AN EVANESCENT PERSPECTIVE ON CELLS

Thesis by

Lawrence A. Wade

In Partial Fulfillment of the Requirements for the

degree of

Doctor of Philosophy in Molecular Biology and

Biochemistry

CALIFORNIA INSTITUTE OF TECHNOLOGY

Pasadena, California

2011

(Defended August 26, 2010)

ACKNOWLEDGEMENTS

Graduate school at Caltech has been a wonderful experience. My thanks to Kai Zinn and the rest of the Biology Division admissions committee for being willing to risk admission of a 47 year-old student into one of the world's finest universities. My thanks also to thesis committee members Pamela Bjorkman and Grant Jensen who took this responsibility very seriously and thereby helped enormously. Towards the end of my studies the Dean of Graduate Studies, Joe Shepherd, worked with real determination to make it possible for me to focus solely on my research and to thereby complete this thesis. It speaks volumes about Caltech that I was not only given an opportunity, but was also provided the tools necessary for success. My supervisors at JPL, Andre Yavrouian and Tim O'Donnell, fought valiantly to help JPL's bureaucracy do the right thing. I am very grateful for all of your efforts.

Much of the richness of life comes from the people you've had an opportunity to work with. I've had the great pleasure and honor to be a friend and colleague of Emil Kartalov throughout my studies. In particular I am very grateful to Rahul Srinivasan for teaching me how to be a hands-on biologist and to Steve Quake for bringing me to Caltech. The Fraser and Lester groups have proven to be collegial, fun, and intellectually adventurous. There are many people whose creativity, warmth and friendship have helped enormously along the way including Chris Richards, Kristy Hilands, Eloisa Imel, officemates Mat Barnet and Cambrian Liu, Mike Roy, Steve Olson, Mary Flowers, Gary Belford, Pat Collier, Jordan Gerton, Rob Sharrow, Jian Li, Guillaume Lessard, Eyal Shafran, Ian Shapiro, Cagdas Son, Fraser Moss, Dan Lo, Le Trinh, Jennifer Yang, David Koos, Carol Readhead, David Kremmers, Christie Canaria, Carole Lu, Luca Caneparo, Sean Megason, Seung-Yong Jung, Maria Esplandiu, Ziyang Ma, Alana Dixon, Arian Forouhar, Mike Tyszka, Rigo Pantoja, Princess Imoukhuede and many, many other wonderful people.

It was my great fortune to have Scott Fraser as my advisor throughout my studies. His unflagging support and keen perception has been crucial.

The last several years of my graduate studies have been spent working with Henry Lester as part of the Lester group. Henry is a scholar and a gentleman. He has continually pushed

me to think deeper and harder. My maturation as a scientist has greatly benefited from his example and teachings.

Of course in the end it all comes down to family. The greatest thanks Arnis and Valda Richters for helping me to realize the importance of gaining a deeper and broader understanding of biology if I wanted to ever work in the field. To my mom, Barbara Siegel, and sister, Janice Otters, your love and enthusiasm has meant everything to me. Finally,

Evi, Thea, and Alec are the best ever.

ABSTRACT

We have optically sectioned living cells to a maximum depth of ~250 nm using a Variable Angle-Total Internal Reflection Fluorescence Microscope (VA-TIRFM). This yields 3D images of cell membranes and nearby organelles similar to that gained by confocal microscopes but with at least an order-of-magnitude greater depth resolution. It also enables cellular membranes to be imaged in near isolation from cell organelles. Key to achieving this resolution was integration of a controllable excitation laser micropositioner into a standard through-the-lens TIRF illuminator and development of a custom culture dish for re-use of expensive high index of refraction cover slips. Images are acquired at several penetration depths by varying the excitation laser illumination angles. At the shallowest penetration depth (~46 nm) just the membrane and a few internal puncta are imaged. As the penetration depth is increased up to 250 nm organelles near the membrane, such as the ER, are imaged as well. The sequence of images from shallow deep is processed to yield a z-stack of images of approximately constant thickness at increasing distance from the coverslip. We employ this method to distinguish membrane-localized fluorophores (α4 GFP β2 nicotinic acetylcholine receptors and pCS2:lyn-mCherry) at the plasma membrane (PM) from those in near-PM endoplasmic reticulum (ERTracker green, α4 GFP β2 nicotinic acetylcholine receptors), on a z-axis distance scale of ~45 to ~250 nm in N2a cells. In doing so we observe occasional smooth ER structures that cannot be resolved as being distinct from the membrane.

In a second project substantial progress has been made towards developing a Tip Enhanced Fluorescence Microscope (TEFM) capable of imaging wet biological samples with ~10 nm resolution. A TEFM combines a TIRFM with an Atomic Force Microscope (AFM) to modulate sample fluorescence through near-field dipole-dipole coupling.

In the third project the capability to consistently produce high quality nanotube AFM probes was developed and a technique for chemically functionalizing the tip of a nanotube AFM probe was invented.

TABLE OF CONTENTS

LIST OF FIGURES

LIST OF TABLES

C h a p t e r 1

INTRODUCTION

Over the course of my studies at the California Institute of Technology I've had the opportunity to work on three lines of research. All of these efforts employed novel imaging techniques to query the organization and composition of surface proteins involved in intercellular signaling. Most of this work was focused on nicotinic acetylcholine receptors (nAChRs).

Neuronal signals are transmitted across a synapse via transmitter-gated ion channels to either skeletal muscle cells or to neuronal cells. Nicotinic acetylcholine receptors are found in many central nervous system and nerve-skeletal muscle postsynaptic membranes. The nAChR has a (pseudo)symmetric pentameric structure comprised of homologous subunits. A wide variety of nAChR stochiometries are possible as the α subunits exist in at least ten different subtypes (α1 through α10) and the β subunits exist in at least four subtypes (β1 through β4).[1] nAChRs can be activated by both acetylcholine and nicotine. Chronic exposure to nicotine has been found to cause upregulation of functional nAChRs with a preferred $(\alpha_4)_2(\beta_2)_3$ stoichiometry.[2, 3, 4, 5, 6, 7]

The capability to image the distribution and composition of nAChRs pre-and post-synaptically in pulse-chase experiments would be very helpful to attempts to untangle the regulatory mechanisms behind nicotine induced upregulation.[8] It would be particularly useful to do so if the functional nAChR composition and distribution (in the membrane) could be resolved or isolated from the composition and distribution of nAChRs sequestered in nearby organelles of living cells.[9] From a larger perspective this is capability would be useful for conducting pulse-chase experiments to illuminate trafficking and regulatory mechanisms of many types of functional surface receptors.

So motivated, I collaborated with the Henry Lester group, to extend Total Internal Reflection Microscopy (TIRFM) to achieve z-axis resolution sufficient to discriminate cellular membranes from nearby organelles via Variable Angle Internal Reflection

Microscopy (VA-TIRFM). We also took initial steps towards using the information acquired while VA-TRIFM imaging to construct three-dimensional images of cell membranes and nearby cellular organelles. We then successfully utilized this technique to image murine neuroblastoma cells (N2a) that had been transfected with fluorescently labeled nAChRs. This technique and our results are described in Chapter 2.

In the second project, we developed a Tip-Enhanced Fluorescence Microscope (TEFM) with the capability to resolve single molecules with <10 nm separation in collaboration with the Quake group.[10,11] Later I attempted to use this technique to image surface proteins in a biological environment (warm and wet) as part of the Scott Fraser group. This effort and its results are described in some detail in Chapter 3.

In the third project, conducted primarily in collaboration with the Pat Collier group, we developed the capability to fabricate nanotube Atomic Force Microscope (AFM) probes.[12] The mechanisms behind nanotube adhesion, and the surprisingly high AFM imaging resolution achieved with nanotube AFM probes, was illuminated through atomistic modeling.[13] Finally we explored utilization of such probes for molecular patterning.[14,15] To enable substrate patterning we invented a novel technique for uniquely functionalizing the end of a nanotube probe. This work is described in Chapter 4.

References

[1] A.R. Tapper, et. al., *Science* **2004**, *306*, 1029-1032.

[2] Buisson B. and Bertrand D., Chronic exposure to nicotine upregulates the human α4β2 nicotinic acetylcholine receptor function. *J Neurosci*, **2001**, *21*, 1819-1829.

[3] Nelson ME, Kuryatov A, Choi CH, Zhou Y, and Lindstrom J, Alternate stoichiometries of α4β2 nicotinic acetylcholine receptors, *Mol Pharmacol* **2003,** *63*, 332-341.

[4] Kuryatov A, Luo J, Cooper J and Lindstrom J, Nicotine acts as a pharmacological chaperone to up-regulate human α4β2 acetylcholine receptors. *Mol Pharmacol*, **2005,** *68*, 1839-1851.

[5] Sallette J, Pons S, Devillers-Thiery A, Soudant M, Prado de Carvalho L, Changeux JP and Corringer PJ, Nicotine upregulates its own receptors through enhanced intracellular maturation, *Neuron*, **2005,** *46*, 595-607.

[6] Vallejo YF, Buisson B, Bertrand D and Green WN, Chronic nicotine exposure upregulates nicotinic receptors by a novel mechanism, *J Neurosci*, **25**, 5563-5572.

[7] Son CD, Moss FJ, Cohen BN and Lester HA, Nicotine normalizes intracellular subunit stoichiometry of nicotinic receptors carrying mutations linked to autosomal dominant nocturnal frontal lobe epilepsy, *Mol Pharmacol* ,**2009**, *75*, 1137-1148.

[8] B.S. Khakh, J.A. Fisher, R. Nashmi, D.N. Bowser, H.A. Lester, *J. Neurosci.* **2005**, *25*, 6911-6920.

[9] Srinvasan, R., Pantoja, R., Moss, F.J., Mackey, E.D.W., Son, C.D., Miwa, J. and Lester, H.A. Nicotine-induced α4β2 nicotinic receptor upregulation: Stoichiometry, β-subunit trafficking motifs, subcellular compartments and endoplasmic reticulum exit sites, submitted for publication **2010**.

[10] J. M. Gerton, L. A. Wade, G. A. Lessard, Z. Ma, and S. R. Quake, Tip-enhanced fluorescence microscopy at 10 nanometer resolution, *Phys. Rev. Lett.*, **2004**, *93*, 180801.

[11] Z. Ma, J.M. Gerton, L.A. Wade and S.R Quake, Fluorescence near-field microscopy of DNA at sub-10 nm resolution, *Phys. Rev. Lett.* **2006,** *97*, 260801.

[12] L. A. Wade, I. R. Shapiro, Z. Ma, S. R. Quake, and C. P. Collier, Correlating AFM Probe Morphology to Image Resolution for Single-Wall Carbon Nanotube Tips, Nano Lett., **2004**, *4*, 725-731.

[13] I. R. Shapiro, S. D. Solares, M. J. Esplandiu, L. A Wade, W. A. Goddard and C. P. Collier, Influence of elastic deformation upon single-wall carbon nanotube AFM probe resolution, J. Phys. Chem. B, **2004,** *108*, 13613-13618.

[14] Method for manufacturing single wall carbon nanotube tips, US 7,211,795 B2, L.A. Wade, P. Collier, S. Quake, I. Shapiro, and Z. Ma issued May 1, 2007.

[15] Selective functionalization of carbon nanotube tips allowing fabrication of new classes of nanoscale sensing and manipulation tools, US 7,514,214, L.A. Wade, I.R. Shapiro, C. P. Collier, M.J. Esplandiu, V.G. Bittner and K.P. Giapis issued April 7, 2009.

Chapter 2

IN-VIVO DISTINCTION BETWEEN PLASMA MEMBRANE AND NEAR-MEMBRANE ORGANELLES USING VARIABLE ANGLE TOTAL INTERNAL REFLECTION FLUORESCENCE MICROSCOPY (VA-TIRFM)

We have optically sectioned living cells to a maximum depth of ~250 nm using a Variable Angle-Total Internal Reflection Fluorescence Microscope (VA-TIRFM). This yields 3D images of cell membranes and nearby organelles similar to that gained by confocal microscopes but with at least an order-of-magnitude greater z resolution. It also enables cellular membranes to be imaged in near isolation from cell organelles. Key to achieving this resolution was integration of a controllable excitation laser micropositioner into a standard through-the-lens TIRF illuminator and development of a custom culture dish for re-use of expensive high index of refraction cover slips. Images are acquired at several penetration depths by varying the excitation laser illumination angles. At the shallowest penetration depth (~46 nm) just the membrane and a few internal puncta are imaged. As the penetration depth is increased up to 250 nm organelles near the membrane, such as the ER, are imaged as well. The sequence of images from shallow deep is processed to yield a z-stack of images of approximately constant thickness at increasing distance from the coverslip. We employ this method to distinguish membrane-localized fluorophores (α4 GFP β2 nicotinic acetylcholine receptors and pCS2:lyn-mCherry) at the plasma membrane (PM) from those in near-PM endoplasmic reticulum (ERTracker green, α4 GFP β2 nicotinic acetylcholine receptors), on a z-axis distance scale of ~45 to ~250 nm in N2a cells. In doing so we observe occasional smooth ER structures that cannot be resolved as being distinct from the membrane.

2.1 Variable Angle Total Internal Reflection Fluorescence Microscopy overview

Total Internal Reflection Fluorescence Microscopy (TIRFM)[1] is a widely used technique for imaging cellular structure near a membrane that is adhered to a thin glass coverslip. This technique takes advantage of a basic principal of optics: the angle of refraction will be greater than the angle of incidence when light reaches an interface where the transport

media sharply changes from a higher to a lower index of refraction. The relationship between these angles is a function of the index of refraction of the two materials as described by Snell's law,

$$n_1 \sin\theta_1 = n_2 \sin\theta_2$$

where θ_1 is the angle of incidence and θ_2 is the angle of refraction for two materials with indexes of refraction n_1 and n_2 as seen in Figure 2.1.

When the angle of refraction is $\geq 90°$ light can no longer cross the material boundary and is reflected from the interface with the lower index of refraction material back into the higher index of refraction material. This can be described as a total internal reflection. The minimum angle at which total internal reflection occurs is called the critical angle. Snell's law can be readily solved for this critical angle:

$$\theta_c = \sin^{-1}(n_2 / n_1)$$

An evanescent field is generated on the lower index of refraction side of this interface. The

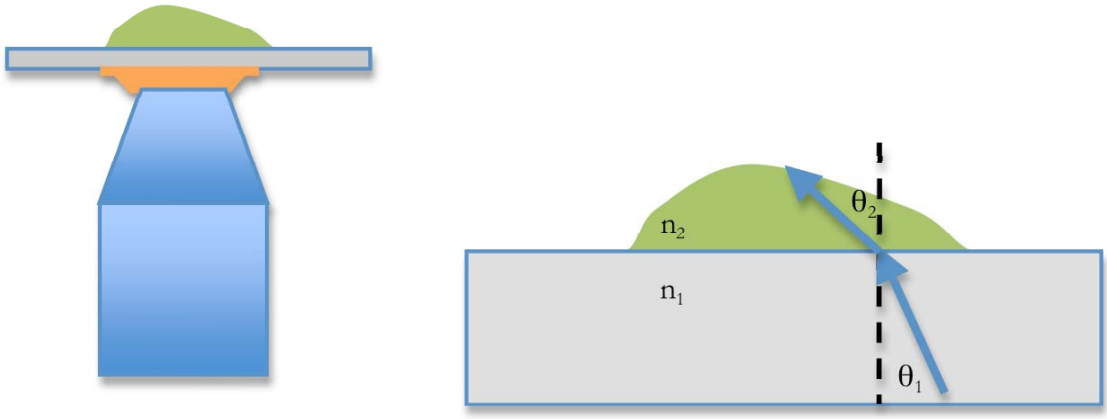

Figure 2.1. An epifluorescence microscope was used in this study. In this type of microscope the objective is under the sample as seen on theleft side of this figure. Immersion oil is used to match the index of refraction of the coverslip. The sample is on top of the coverslip. In objective-based TIRF the excitation laser is focused on the outside edge of the back aperture of the objective. The angle at which the excitation laser light emerges from the objective is determined by the radial positon of the focused excitation beam on the back aperture. θ_1 and θ_2 describe the angle of the excitation laser within the coverslip and in the sample. The index of refraction of the coverslip and the sample are described by n_1 and n_2.

intensity of that evanescent field decays exponentially with distance, z, from the transport media interface as described by

$$I(z) = I(0)e^{-z/d}$$

Where, for surface polarized illumination, the intensity of the evanescent field at the interface

$$I(0) = \frac{4\cos^2\theta}{1-(\frac{n_2}{n_1})^2}$$

The penetration depth of the evanescent field,

$$d = \frac{\lambda}{4\pi n_1}(\sin^2\theta - \sin^2\theta_c)^{-1/2} = \frac{\lambda}{4\pi}(n_1{}^2\sin^2\theta - n_2{}^2)^{-1/2},$$

is defined by the specifics of the situation: the wavelength of the light, the transport media indexes of refraction and the degree to which the angle of incidence exceeds the critical angle. Note that for a given wavelength of light and set of transport media the penetration depth varies considerably. The penetration depth describes the depth at which the evanescent field intensity has decayed to 1/e, or approximately 36.8%, of the field strength at the surface.

The penetration depth is minimized when the angle of incidence is much greater than the critical angle. As the angle of incidence is reduced the penetration depth increases. Therefore a series of images taken of a sample at decreasing angle of incidence will show successively deeper sections of the cell even though all of those images are total internal reflection images. In other words: by controlling the excitation laser angle the thickness of the cell region being imaged can be varied.

This is the basis for the technique called Variable Angle-Total Internal Reflection Fluorescence Microscopy[2] (VA-TIRFM). Since Lanni, Waggoner and Taylor's pioneering work the theory has been expanded, as have the concepts for processing the data. In the

process of advancing VA-TIRFM techniques exploratory studies have been conducted to characterize cell-surface contact topology[2,3,4], image cellular focal adhesion sites[5], determine secretory vesicle motion in 3 dimensions[6,7,8], measure protein and polymer film thickness[9], solute depth dependent concentration profiles[10,11] and determine the length of λ-DNA strands.[12]

These exploratory studies successfully confirmed the theory developed for VA-TIRFM data analysis and refined instrument concepts. They also demonstrated the potential utility of this technique for studying cellular events near the membrane.

However no significant scientific insights have been derived through application of VA-TIRFM, nor has it become widely utilized in studies despite the proliferation of TIRF capable microscopes. Why has the promise yielded so little?

Unfortunately the efficacy of VA-TIRFM was severely limited by the numerical aperture of available objectives. The numerical aperture (NA) can be used to describe the maximum angle of incidence light that can be transmitted through transport media, such as a coverslip, by a microscope objective. Specifically:

$$\theta_{\max} = \sin^{-1}\frac{n_1}{NA}$$

A given microscope objective can be used for objective based TIRF if $\theta_{max} \geq \theta_c$. In other words a microscope objective can only be used for objective based TIRF if $NA > n_2$. Consider a sample with index of refraction n_2 on a coverslip with index of refraction n_1. A microscope objective can be used for TIRF imaging a thin sample in air if microscope NA>1. Objective based TIRF can be accomplished with water if its NA>1.33. Cells can barely be imaged in TIRF with a 1.4 NA objective and more commonly require a 1.45 NA objective since the average cellular index of refraction is 1.385.[13]

All four of the major microscope manufacturers have produced objectives with NA's as high as 1.45 since 2005. Unfortunately many cellular organelles have indexes of refraction that approach 1.45 and some that exceed that value. The index of refraction of lysosomes

and melanin even exceeds the 1.52 index of refraction typical of glass coverslips. Table 2.1 presents a list of cellular components and their indexes of refraction.

Cell Component	Index of refraction
Extracellular fluid	1.35–1.36[14]
Cytoplasm	1.36–1.375[15]
Nucleus	1.38–1.41[16]
Mitochondria	1.40[17]
Lipid	1.48[18]
Lysosomes	1.60[19]
Melanin	1.6–1.7[20]

Table 2.1 The index of refraction of several cellular components.

As was seen earlier, confinement of the evanescent field depends significantly on the difference between the index of refraction of the coverslip and that of the specimen. The importance of these observations is demonstrated in Figure 2.2 where it is demonstrated that in a typical TIRF imaging configuration no cellular components with indexes of refraction greater than 1.42 will be in TIRF. Given the highly inhomogeneous nature of cells all that can be confidently claimed is that a cell is TIRF imaged with a 1.45 NA objective over a wide, ill-defined depth that varies across the image depending on the cell's specific characteristics. The penetration depth ranges from ~130 nm for n=1.385 to ∞ for n>1.42 at the extreme outer edge of the objective for a 1° beam width centered in the TIRF range. From there it rapidly degrades should the beam be adjusted closer to the critical angle. It is also clear from Figure 2.2 that the results of previous investigators using VA-TIRM were significantly limited by the index of refraction of glass and the NA of typical TIRF objectives. Hence we can conclude that VA-TIRFM cannot effectively discriminate between cellular components located within about 200 nm of the surface if a glass coverslip and 1.45 NA objective are used.

Olympus also makes an APO 1.65 NA/100x objective. Two barriers have impeded the widespread use of this objective: the 1.8 index of refraction immersion oil is both toxic and unpleasant and the 1.8 index of refraction coverslips cost $40 each. As a result this objective is very rarely used and is still produced only by Olympus.

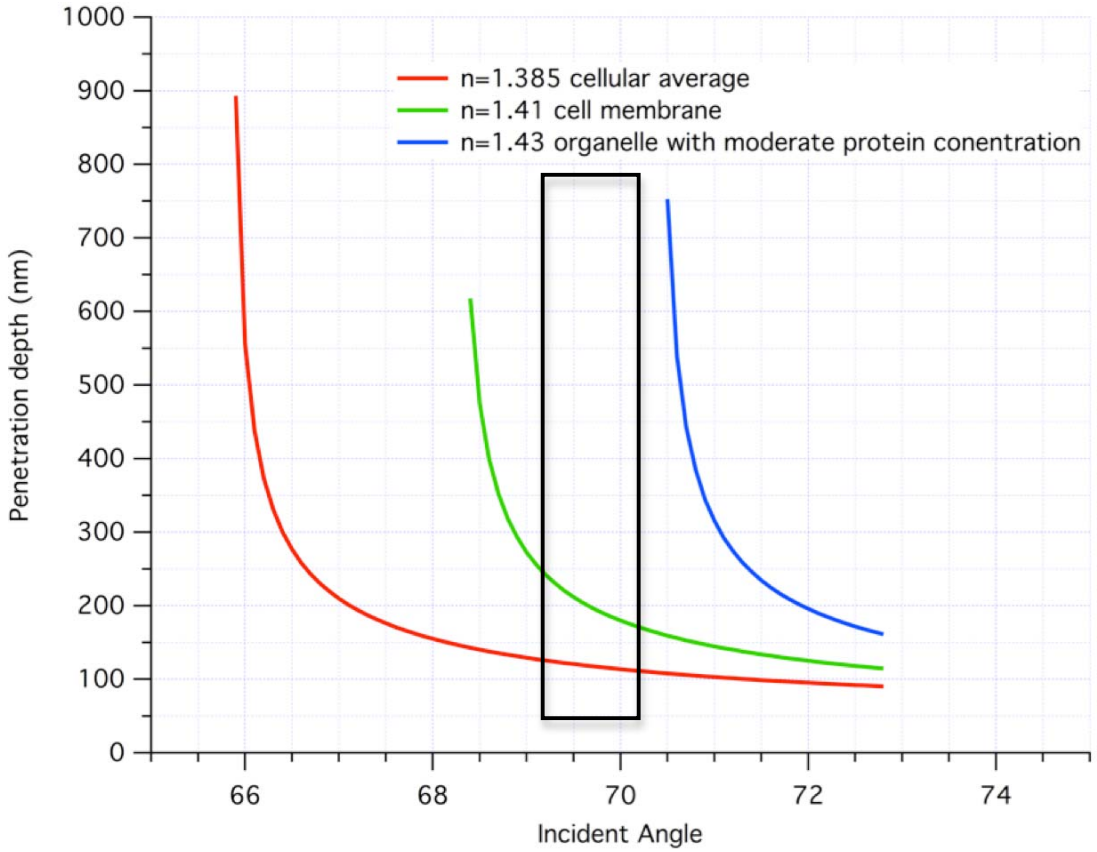

Figure 2.2. A typical TIRF microscope cannot distinguish a cell membrane from its organelles as the cellular indexes of refraction are similar to the 1.45 NA of the microscope objective. As result, the depth TIRF imaged at any given incident angle will vary considerably with cellular structure. The evanescent field penetration depths shown here were calculated for the indexes of refraction of several common cellular organelles. The values presented assume objective-based TIRFM through a 1.45 NA objective with a 488 nm wavelength excitation laser through a glass coverslip. The rectangular box is 1.0° wide and located at the center of the TIRF angular range for this combination.

The penetration depth as a function of angle of incidence and cell component index of refraction are shown in Figure 2.3 for a 1.65 NA objective. These calculations were performed for a 488 nm excitation laser and N-LAF21 coverslip (n=1.7993 at 488 nm)[21]. It is clearly seen that the high index of refraction coverslip results in very tight confinement of the evanescent field. In addition, the variation in the index of refraction of cellular components is small in comparison with the difference between their values and the 1.65 objective's. In combination, the result is that the penetration depth is very shallow and nearly constant across most of the TIRF angular range. Therefore this opens the possibility to vary the incident angle to optically section a cell, and thereby to characterize the fluorescent density as a function of depth.

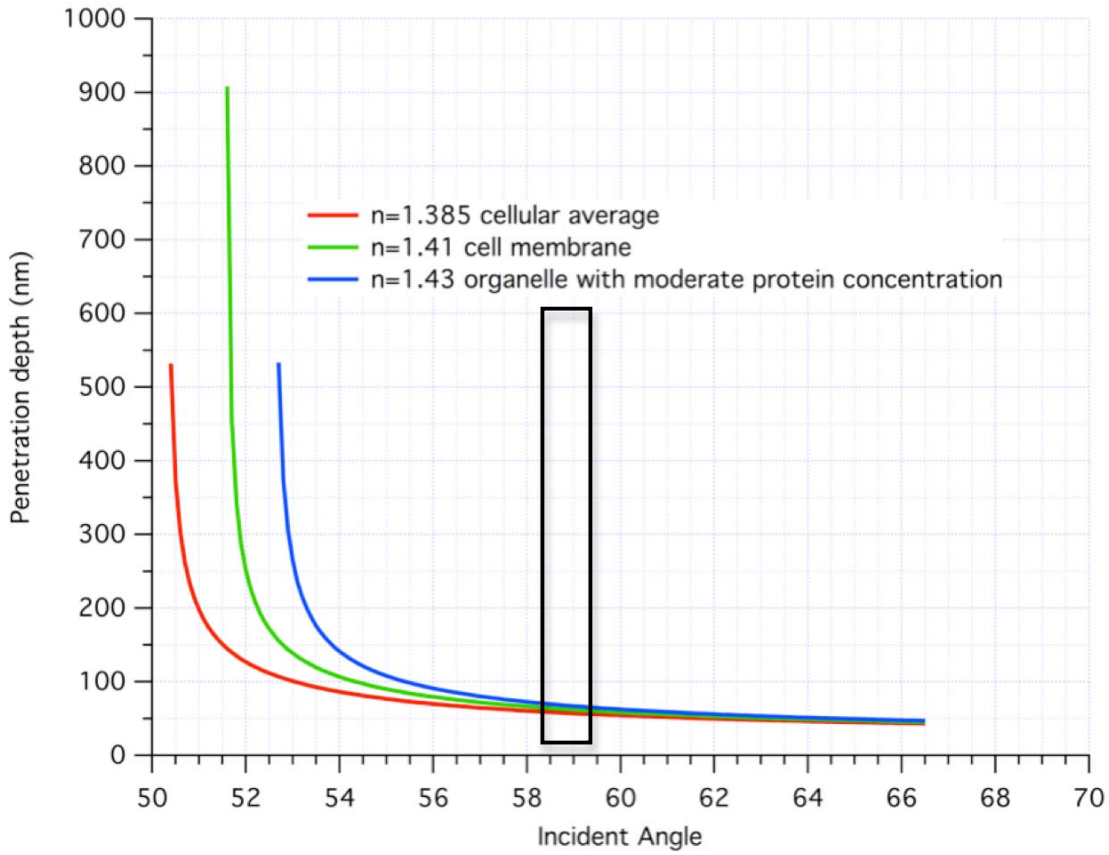

Figure 2.3. A cell can be imaged in pure TIRF (no far field component) with uniform z-thickness, regardless of cellular index of refraction, using a 1.65 objective. Over the boxed range of incident angles, the penetration depth is 60 nm for a 1.385 cellular average index of refraction. There is little difference in penetration depth as a function of cellular component index of refraction. The black rectangular box is 1.0 degree wide and approximates the full width 20% max beam width of our 488 nm excitation laser. The box is centered in the TIRF range for this objective when looking at cells. This figure shows the calculated penetration depth as a function of incident angle and index of refraction for a 1.65 NA objective. These calculations were made for 488 nm laser excitation and assume the use of a N-LAF21 coverslip with an index of refraction of 1.7993 at 488 nm.

In summary: VA-TIRFM is a good idea with a sound, and well-developed, theoretical basis. Initial experiments used 1.45 NA microscope objectives that did not permit sufficient discrimination in z for this approach to provide new insights. However, we demonstrate here that useful VA-TIRFM becomes a real possibility with a 1.65 NA objective and n≅1.8 coverslips.

2.2 VA-TIRFM image processing

One of the most carefully considered VA-TIRFM image processing techniques is the

inverse Laplace transform.[22,23,24] Recall that the intensity of the evanescent field in z is described by

$I(z) = I(0)e^{-z/d}$ where z is the distance to the coverslip surface, d is the penetration depth and the evanescent field intensity at the coverslip surface is

$$I(0) = \frac{4\cos^2\theta}{1-(\frac{n_2}{n_1})^2}$$ for s-polarized excitation.

The product of the distribution of fluorophore concentration in z with the variation in fluorophore collection efficiency with z can be described by $D(z)$.[25] Then the measured fluorescence for a given $D(z)$, assuming that the brightness of a given fluorophore is only a function of the evanescent field intensity and the distance from the fluorophore to the coverslip surface, is

$$F(\theta) = I(0,\theta)\int_0^\infty D(z)e^{-z/d(\theta)}dz.$$

Extending this to describe a two dimensional surface, the z distribution of fluorophores is

$$F_{x,y}(\theta) = I_{x,y}(0,\theta)\int_0^\infty D_{x,y}(z)e^{-z/d(\theta)}dz.$$

Also recall that a Laplace transform of a function $f(t)$ is formally defined as

$$F(s) = \int_0^\infty f(t)e^{-st}dt$$

Then the expression that describes $F_{x,y}(\theta)$ is the Laplace transform of $D_{x,y}(z)$.

As $F_{x,y}(\theta)$ is the Laplace transform of $D_{x,y}(z)$ it is reasonable to attempt to use the inverse Laplace transform of $F_{x,y}(\theta)$ to solve for $D_{x,y}(z)$. This approach assumes that the evanescent field intensity is both constant and uniform over the x-y plane. It also assumes

that the field distribution over x-y is uniform and only varies with θ as described above. Successful application of an inverse Laplace transform on appropriate VA-TIRFM data would enable complete deconvolution of the three-dimensional distribution of fluorophore concentration.

Unfortunately the TIRFM that we used for this experiment evidences a very significant interference pattern across the coverslip that changes sharply with angle. The resulting variation in evanescent field intensity makes the inverse Laplace transform approach to reconstructing the continuous 3D profile of fluorophore concentration challenging.

We note that the variation in field due to the interference pattern is small compared with that caused by large changes in incident angle. Such large changes in incident angle also result in large changes in penetration depth as the critical angle is approached. In other words: the signal-to-noise ratio is significantly improved when images of significantly different penetration depth are differenced instead of using finely incremented images.

The theory above suggested a novel and relatively simple method for 3D image reconstruction using VA-TIRFM: treat the difference between a series of images taken with increasing penetration depth as being representative of the cell structure as function of depth. This approach formed the basis for the work presented in this chapter.

If the difference in the evanescent field strength at the coverslip, I(0), is accounted for sequential images can be directly compared. As an example, with the excitation beam closest to the maximum angle, an approximately 45 nm thick image of the cell is captured. Another image can be taken closer to the critical angle such that the penetration depth is increased to 90 nm. These images can be multiplied by a normalization factor that accounts for the change in evanescent field intensity. By subtracting the first image from the second after normalization, a pair of optically sectioned images is obtained: each of which is ~45 nm thick.

Here we chose to discriminate cellular structure in z by analyzing the difference between images taken at five different angles ranging from the something very close to the critical

angle to something very close to the maximum angle of the 1.65 NA objective was. Surprisingly this simple approach to 3D image reconstruction has not been previously reported

In Figure 2.4 an example of optical sectioning is presented in which a sequence of images is captured at several angles of incidence. The first image primarily shows the 48 nm closest to the coverslip. A second image is taken at a penetration depth of 72 nm. This second image can be considered to contain all of that information found in image 1, plus

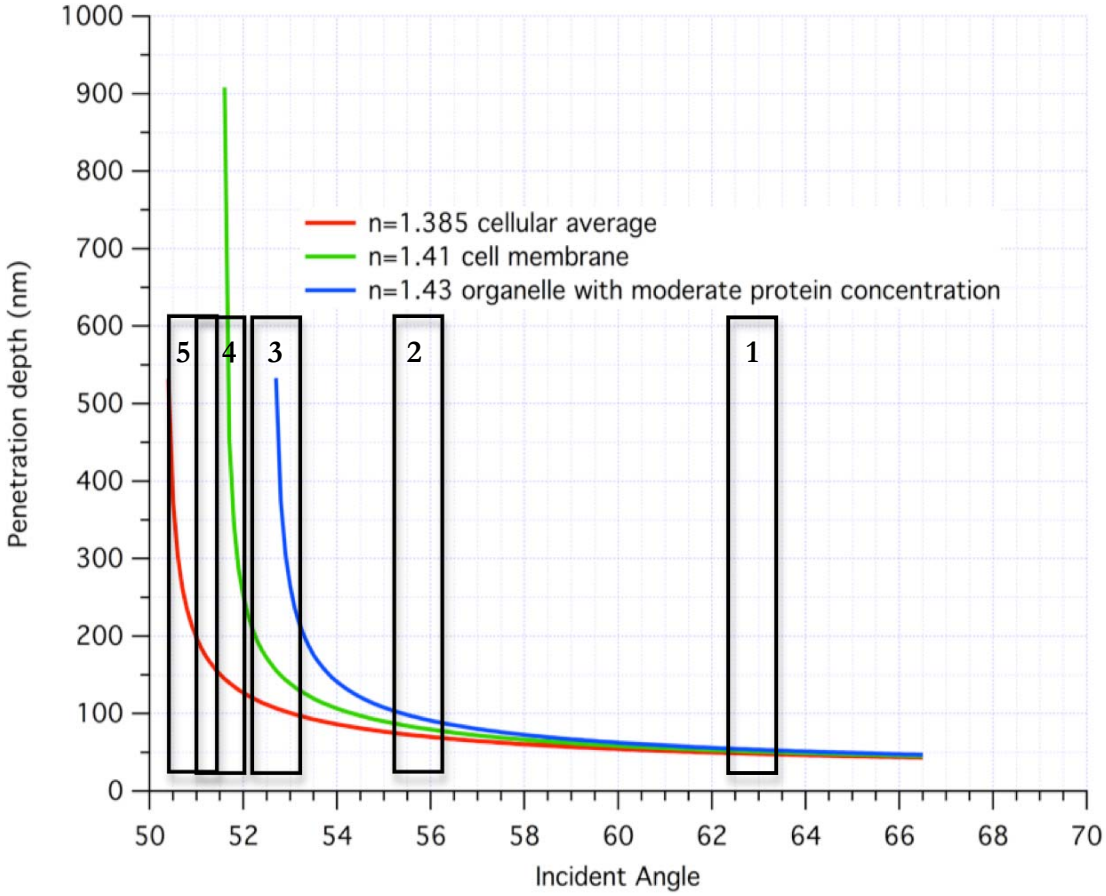

Figure 2.4. A five image VA-TIRFM sequence is shown relative to cellular organelle indexes of refraction. The five black rectangular boxes each represent an image in this sequence. Optical sectioning is achieved by choosing excitation laser incident angles such that the average penetration depth of each successive image is 1.5 times that of the previous one (Table 5.3). The image boxes are 1.0 degree wide and match the full width 20% max beam width of our 488 nm excitation laser. The 5th image (far left box) is centered on a penetration depth of 243 nm for a cell's average index of refraction (1.385). Because of the beam width this image includes incident angles that result in penetration depths ranging between 160 nm up to ~700 nm. That real beam size effectively limits the center penetration depth to ~250 nm for a pure TIRF image (no far-field content). The calculations shown above assume a 1.65 NA objective, 488 nm laser excitation and the use of a N-LAF21 coverslip with an index of refraction of 1.7993 at 488 nm.

that of the next 24 nm. Several of these differenced images can be used to build a 3 dimensional image of the 250 nm closest to the coverslip. In doing so the fluorescent content of the membrane is largely isolated from the fluorescent content of the Endoplasmic Reticulum (ER) and other cellular organelles close to the membrane.

The width of the focused excitation laser beam on the back aperture of the objective was measured and found to be ~42 microns (full width at 20% max height) or about 1° in terms of the incident angle variation near the critical angle. Therefore the width of the boxes shown in Figure 2.4 represent a 1° beam width. The penetration depth is seen to range from ~700 nm to 160 nm across a 1° wide box centered at 50.8° incidence angle for cell with an average index of refraction of 1.385 adhered to a coverslip with an index of refraction of 1.7993. The penetration depth is 240 nm at the center of the box.

We conclude from this that a single image, containing only TIRF and no far-field illumination, has a practical depth limit of about 250 nm using this specified microscope. However we noted that a difference image, produced by subtracting an image taken at a somewhat greater incident angle from one taken proximate to the critical angle, and show detail at depths greater than 250 nm while still being in TIRF.

What image sequence should be selected? Since we have measured the variation in field intensity with angle, and can use those values to normalize, it is not an important factor in selecting the specific angles for the image sequence. The two most important factors are penetration depth and field intensity.

The integrated evanescent field at any incident angle is

$$\int_0^\infty I(z)dz = \int_0^\infty I(0)e^{-z/d}dz = I(0)\int_0^\infty e^{-z/d}dz = I(0)(d)$$

Consider the integrated field intensity ratio between images taken at two angles such that $d_2 = 2d_1$. We have already noted that normalization is done to account for the change in evanescent field intensity $I(0)$ with the change in incident angle. Therefore the

Integrated intensity angle 1/angle 2= $\frac{I(0)d_1}{I(0)d_2} = \frac{d_1}{2d_1} = \frac{1}{2}$

We see that the integrated field intensity is directly proportional to penetration depth once the field intensity at the surface as a function of angle has been normalized! Twice the penetration depth results in twice the normalized integrated evanescent field intensity.

To implement this technique the relationship between beam position, as measured by the closed-loop controller, and the incident angle of the excitation beam in the coverslip was determined. We also determined the actual variation in evanescent field strength as a function of beam position. Using this information we can then choose which incident angles to image knowing the penetration depth at each location. The calibrations were also used to appropriately normalize the measured intensity of the field strength and thereby to enable to direct image differentiation.

In Appendix A we present the details of the critical calibrations that were used to define and normalize the image sequence. These calibrations include the measured relationships between the excitation beam position and excitation beam angle of incidence. Also presented in Appendix A is the measured field intensity as a function of angle (and beam position) at the coverslip surface. This is compared with the field variation with incident angle predicted by theory. We find that the surface evanescent field intensity was approximately 10% less than that predicted by theory over the TIRF range of incident angles. At present we can only speculate as to the origin of this discrepancy. One possibility is that the evanescent field intensity is diminished across the coverslip in the direction of propagation due to scattering caused by the sample and coverslip surface roughness. An alternative explanation is that the difference is due to my measurement and/or data analysis error. A third is that a small fraction of the excitation energy within the evanescent region might contain some vertically polarized energy.

Using these calibrations, difference processing a stack of images taken at different incident angles is straightforward. As an example: having taken an image at each of five incident angles, the background is then subtracted from each. The field intensity variation with angle at the surface can be readily normalized since we have measured this. Then each

image is multiplied by a normalization factor to account for the change in field intensity with angle. Then image 1 is subtracted from image 2. Image 2 is subtracted from image 3. Image 3 is subtracted from image 4. And finally Image 4 is subtracted from image 5. ImageJ v1.44c[26] was used to perform the image processing steps involved in producing the results presented in this thesis.

The resulting stack of images includes the section nearest the coverslip, the section just above this and so on. This information contained in this group of images is analogous to a z-stack of images taken by a confocal microscope albeit with much finer z-axis resolution. This image stack can then be viewed as a three dimensional image using ImageJ or a variety of other programs. All of the 3D visualizations presented in this thesis were created using Imaris 7.0[27] in the Beckman Imaging Center at Caltech.

Since the normalized integrated field intensity is directly proportional to penetration depth, the most obvious imaging sequence strategy is to use even steps in penetration depth. The shallowest section is 48 nm. Therefore in Table 2.2 an imaging sequence is described where the penetration depth of each image is incremented by 48 nm. This approach enables a 5 slice image to be acquired with the deepest slice having a 240 nm penetration depth.

Image number	Penetration depth	Δ depth	Incident angle
1	48 nm	48 nm	63°
2	96 nm	48 nm	53.3°
3	144 nm	48 nm	51.6°
4	192 nm	48 nm	51.1°
5	240 nm	48 nm	50.9°

Table 2.2 Five image sequence with each image being the same thickness.

Another reasonable approach would be to image in even logarithmic steps so that an even multiple of energy is contained in the sequential images after normalization for the chance in z=0 evanescent field strength. An alternate approach is to choose incident angles so that the thickness change is constant through the sequence. Post-normalization sequential image subtraction produces a differential image in the axial direction.

Table 2.3 shows the parameters for a logarithmic sequence in which five successive images contain 1.5 times as much energy (same thing as saying 1.5 times the penetration depth) as the previous image did after normalization.

Image number	Penetration depth	Δ depth	Incident angle
1	48 nm	48 nm	63°
2	72 nm	24 nm	55.7°
3	108 nm	36 nm	52.7°
4	162 nm	54 nm	51.4°
5	243 nm	81 nm	50.9°

Table 2.3 Five image sequence-logarithmic. Each image has 1.5 times the penetration depth of the previous one. This sequence is also shown in Figure 2.4.

For both of the idealized solutions just discussed, noise is an issue. Camera noise, light leakage throughout the path, secondary reflection induced interference of excitation beam, non-uniformity of excitation beam due to alignment errors, laser intensity fluctuation, photobleaching are all concerns. Paucity of signal (photon starvation) is always a concern as well. The differencing technique we propose to use for VA-TIRFM image processing is less sensitive to some of these issues than most direct imaging techniques (e.g. background noise is exactly subtracted out from successive images along with the shallower TIRF information).

Sources of error that change between images are particularly troubling. As noted earlier, the most significant of these appears to be variation of the excitation field intensity due to interference. Such interference between the main excitation beam and reflections within the optical path could be caused by misalignment, non-ideal optical anti-reflection coatings and immersion oil mismatch of index of refraction. The effect of laser interference on differenced images is seen in Figure 2.5.

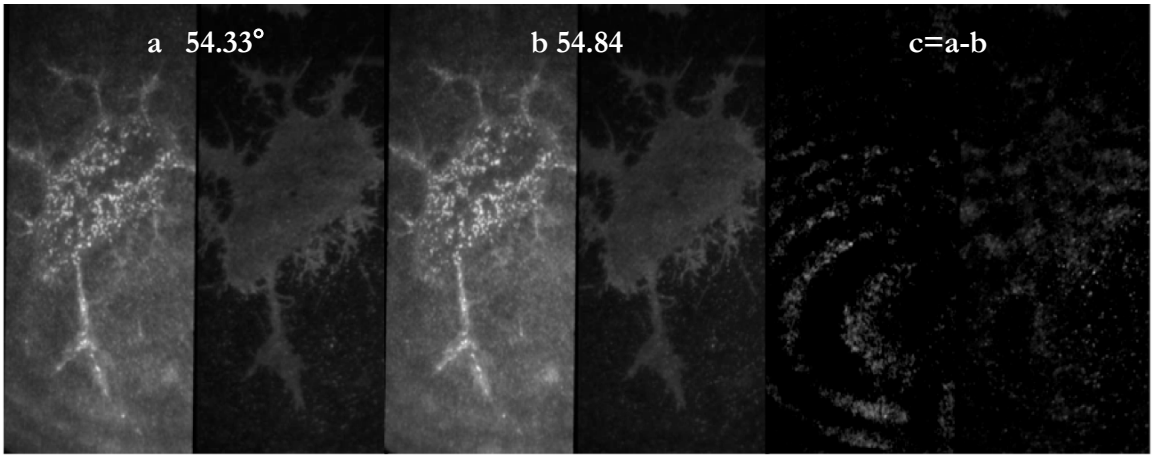

Figure 2.5. Differenced images taken with small changes in incident angle yield little information. The pictures **a** and **b** were captured with at nearly the same incident angle so that there is almost no change in penetration depth. As a result the images are nearly identical and differencing them gives a near-zero result. The three images above are a N2a cell stained with ERTracker green on the left and the membrane localized protein pCS2:lyn-mCherry (20100604 D1 C11b). Image **a** was taken with a 54.33° incident angle. Image **b** was captured at a 54.84° incident angle. Image **c** is the result of subtracting image **b** from image **a**. The impact of changes in the secondary interference pattern is evident.

In finely parsed sequences, the change in image content from one incident angle to another small compared to the change in excitation as the interference pattern is shifted. Subtracting images that differ only slightly exaggerates the variation of excitation due to laser interference. In effect Figure 2.5 demonstrates the magnitude of error seen in many calculations that involve a small difference between two large values.

The ideal solution for eliminating interference fringe variations is to rapidly rotate the excitation beam on the back aperture of the objective. If the image, is taken with a time scale much longer than the rate of rotation, the interference patterns can be nearly completely averaged out.[28] Another solution is to illuminate an annulus on the back aperture rather than at a point. This can be implemented by imaging an optical mask on the back aperture. Neither of these solutions were utilized in this study.

This study instead used the less ideal approach of averaging several (2-5) adjacent images captured at slightly different incident angles. As an example 5 images taken at incident angles 64.3°, 63.5°, 62.9°, 62.3° and 61.6° can be averaged (increments of 10 μm in beam position). The penetration depths of these images vary between 46 and 50 nm. Averaging them significantly suppresses excitation fringe effects without significantly altering the information content.

However there is a limit to how many images can be averaged. Near the maximum angle taking several images causes the loss of very little depth resolution as the change in depth with angle is so small. Referring back to Figure 2.4, we see that the change in penetration depth becomes very large for small angle changes as you approach the critical angle. Therefore averaging must be done over a narrower range of incident angles as the critical angle is approached. In this study five images were averaged near the objective's maximum incident angle. The number of images averaged was reduced to 4, 3 and then 2 as the critical angle was approached. No averaging was done for the images captured closest to the critical angle. Image averaging also has the advantage of further reducing random high frequency noise in the final image. A complete table of the specific images averaged in this study is given in Appendix A.

In future studies angular oversampling could be implemented by finely parsing the incident angle change when sampling (imaging) between the maximum angle of the objective and the critical angle. A running average solution could be implemented for such a dataset to provide far more than the 3 to 5 sections in a 3D image derived for this study. Such a running average could be accomplished by directly averaging adjacent images to yield a long sequence of images with reduced interference effects. Appropriately the images at the ends of this sequence would be minimally processed by this approach.

In this study adjacent images were differenced (subtracted). Doing the same with a finely parsed sequence does not work well as the change in image content from one incident angle to another that is very slightly different, is so small as to exacerbate the impact of error sources such as secondary reflection interference (see Figure 2.5).

Subtracting images using a running difference would provide meaningful information about the distribution of fluorescence concentration in z with a great deal more resolution than in the approach used in this study. As an example images in a sequence with a penetration depth difference of 30 nm could be differenced to result in a sequence of differences with much greater discrimination of fluorescence in z.

2.3 Methods

Total internal reflection fluorescence (TIRF) microscopy. Neuro2a cells cultured in glass-bottom culture dishes were transfected with appropriate plasmids and imaged at 48 h post transfection. TIRF images were obtained using an inverted microscope (Olympus IX71) equipped with an Olympus Apo 100X 1.65 numerical aperture oil objective. eGFP, ER Tracker green and mCherry fluorophores were excited with a 488-nm air-cooled argon laser (P/N IMA101040ALS) and an Optosplit II image splitter (Cairn Research) was used to simultaneously detect fluorescence emission from eGFP and mCherry. Images were aptured with an Andor Technology iXON+ DU-897 back-illuminated EMCCD camera. Data acquisition was accomplished using Andor IQ 1.10.1 software.

The excitation laser incident angle was controlled by an actuated stage with closed-loop controller.[29] Closed-loop control enables reproducible angle of incidence selection with high resolution (specs: 100 nm precision, 3 μm accuracy over the 230 μm TIRF range). The laser alignment and positioning assembly is pictured in Appendix A.

All of the specific incident angle images captured during this study were taken as 64 images sequences. These images were co-added (i.e. are processed to yield an average value z-projection image) to improve signal-to-noise by averaging out rapidly fluctuating noise sources such as shot noise.

Sample exposure rate, percent laser transmission, and gain parameters were initially adjusted for each cell to utilize the full intensity range of the camera while excited by a laser close to the critical angle. Images were acquired beginning at the maximum angle and then sequentially incremented towards the critical angle. The 488 and 561 nm laser lines were linearly s-polarized as revealed using an achromatic 400 to 800 nm 1/2 wave plate (Thorlabs AQWP05M-600).

Cell culture chamber. To reduce the expense of coverslips, I designed a chamber, pictured in Figure 2.6, which is compatible with delicate cell cultures. This chamber itself is fabricated from virgin Teflon. It is sized to match a 35 mm culture dish so that normal culture dish covers can be used. The dish-coverslip junction is sealed via a dry silicon o-ring. As a result the cells are confined in volume that appears, from the health and proliferation of the cells, to have an *in vivo* cytotoxicity comparable to that of commercial culture dishes. This assembly is attached to a stainless steel baseplate via machine screws. The baseplate has a recess sized to hold the 20 mm diameter N-LAF21 coverslips. Screwing the assembly together also provides the force necessary to squeeze the o-ring and thereby to achieve a liquid-tight seal. After some practice, coverslip breakage was reduced

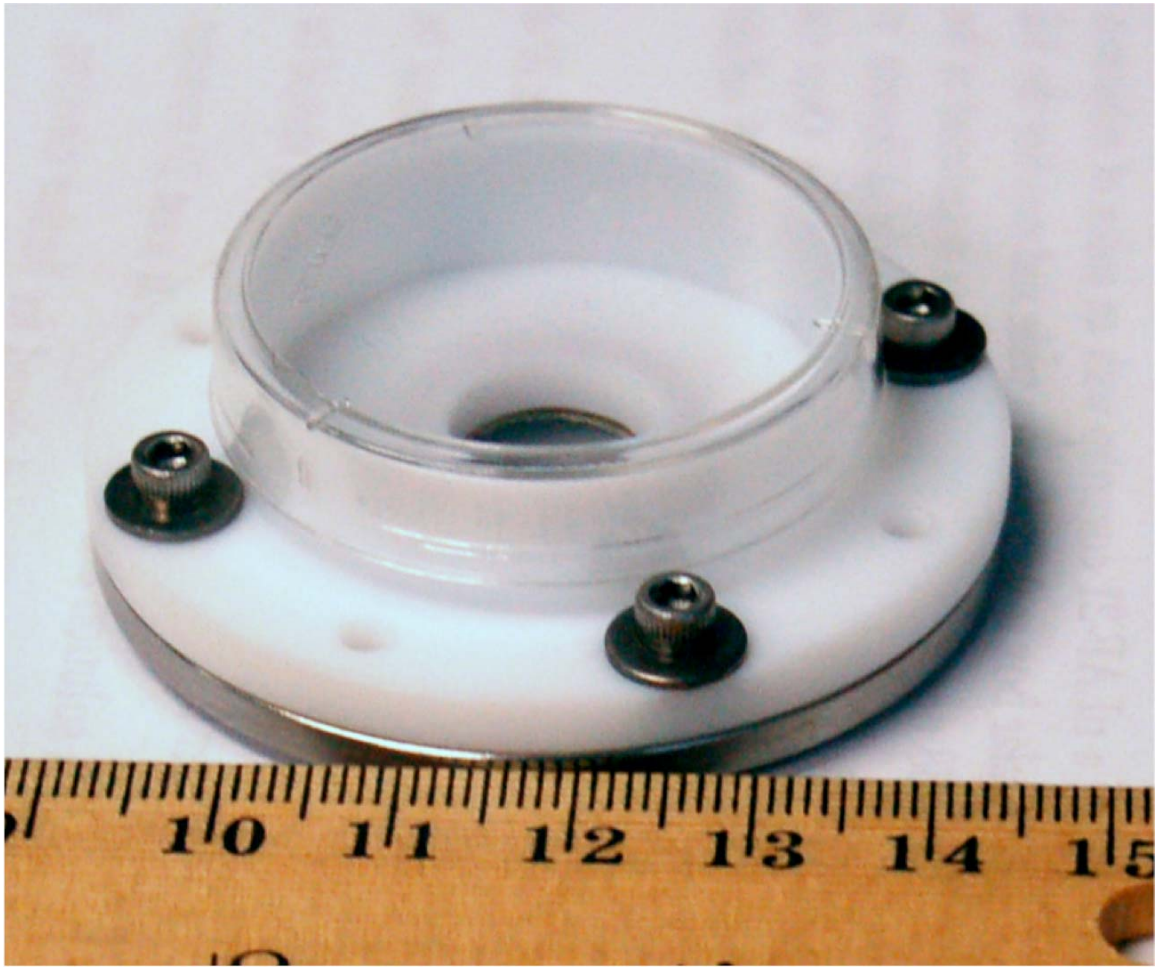

Figure 2.6. A cell culture chamber was fabricated from virgin Teflon that matched the inner and outer diameter, and depth of a commercial 35 mm dish. A silicon o-ring seals the coverslip and chamber so that it is cell media tight. Machine screws are used to assemble this chamber onto a stainless steel baseplate.

to approximately 1 per 20 dishes. The parts, from which the cell culture chamber was assembled, are pictured in Appendix A.

Additionally it should be noted that Delrin was used rather than Teflon in the first version of this chamber. I found that all of the cells died in the dishes fabricated from Delrin. Many variations were explored to try and understand the reason for this without success. Finally new dishes were fabricated from virgin Teflon with the result that the cells thrived. Further literature searches indicate that formaldehyde leaches from Delrin.[30,31]

Stringent cleaning of the culture dish parts is critical. The final assembly must be both sterile and clean of particulate and other contaminates. After use the dishes should be filled with 70% ethyl alcohol or 10% bleach solution and left to sit for at least 20 minutes. Then the dishes should be wiped dry with paper towels and stored for further cleaning. Teflon dishes, baseplates, screws and silicon o-rings are typically cleaned by hand washing in warm, soapy water, followed by 30 minutes sonication in a 2% micro90/DI water solution, followed by extensive rinses in 18 MΩ DI water, followed by 30 minute sonication in acetone in a covered crystallization dish. Then the outside of the crystallization dish containing these parts is very liberally sprayed with 70% ethyl alcohol and it is passed into a sterile tissue culture hood. The parts are individually removed from the acetone dish and blown dry by a high pressure stream of <1μm filtered nitrogen gas. The parts are then stored in a clean, sterile, covered crystallization dish in a sterile tissue culture hood. Assembly is done in the tissue culture hood using sterile tools.

Coverslip cleaning is done separately from the cell culture dish components. The coverslip cleaning protocol is presented in detail in Appendix B. To briefly summarize the procedure: the coverslips are placed in a specially made virgin Teflon carrier, pictured in Figure 2.6, which is in turn is placed in a crystallization dish. The coverslips are sonicated for 20 minutes in a 2% micro90/DI water solution and then rinsed aggressively with DI water. Following this a 2 step RCA cleaning procedure is followed. The first step is to immerse the coverslips in a boiling SC-1 solution (3:2:1 ratio high-purity H2O, 30% NH4OH, 30% H2O2) for 20 min followed by thorough rinsing in 18MΩ DI water. In the

second step the coverslips are immersed in a boiling SC-2 solution (14:3:1 ratio) high-purity water, 30% H2O2, 37% HCl) for 10 minutes followed by stringent rinsing in 18 MΩ water. After rinsing the crystallization dish is refilled with 18 MΩ water, covered, sprayed with 70% ethyl alcohol and stored in a sterile tissue hood. Materials and reagents. Mouse Neuro2a cells (CCL-131) were obtained from American Type Culture Collection (ATCC). Dulbecco's modified Eagle's medium (DMEM) with 4 mM L-glutamine, OptiMEM 1, Leibovitz L-15 imaging medium, ER-Tracker Green and fetal bovine serum (FBS) were purchased from Invitrogen. Expressfect transfection reagent was purchased from Denville Scientific.

Mouse wildtype (wt) α4 and β2 constructs were obtained from Dr. Jerry Stitzel. Mouse α4-eGFP was engineered as previously described.[32] Briefly, eGFP was introduced in frame into the α4 BstEII site with an upstream HA tag after residue 426 in the M3-M4 intracellular loop. eGFP was PCR amplified from the peGFPN1 vector using the forward primer 5'-TTT TGG TCA CCC TAT CCT TAT GAC GTC CCA GAC TAC GCC ATG GTG AGC AAG GGC GAG GAG CTG-3' and the reverse primer 5'-AAAA GGC GTA GTC TGG GAC GTC ATA AGG ATA GG TGA CCT CTT GTA CAG CTC GTC CAT GCC GAG-3'. The PCR product was cut with BstEII and ligated into the *wt* α4 construct to create α4-eGFP. Mutations were introduced into the α4-eGFP and β2-*wt* constructs using the appropriate primers and Quikchange II XL site-directed mutagenesis kit to create the α4L358A-eGFP and the β2-365AAQA368L349M constructs. Plasma membrane reporter, pCS2:lyn-mCherry was obtained from Dr. Scott Fraser. (300 ng per 35-mm dish), to express a red fluorescent protein (pmCherry FP), which is targeted to the plasma membrane. The construct contains two copies of a myristoylation signal sequence subcloned from the Lyn Kinase gene. The signal sequence is immediately upstream of the FP gene and targets the FP to the plasma membrane.

Cell culture and transfections. Mouse Neuro2a cells were cultured using standard tissue culture techniques and maintained in DMEM + 10 % FBS.[33] Plasmid concentrations used for transfection were as follows: 500 ng of each nAChR and GluCl subunit, 75 ng of pCS2:lyn-mCherry. 90,000 cells were plated in the earlier described culture dishes. The following day, plasmid DNA was mixed with cationic lipids by adding appropriate DNA

concentrations to 4 µl of Expressfect transfection reagent in 200 µl DMEM final volume and incubated for 20 min at room temperature to form cationic lipid-DNA complexes. DMEM + DNA-lipid complexes were added to Neuro2a cells in 1 ml of DMEM + 10 % FBS and incubated at 37 ˚C for 4 h, following which, cells were rinsed 2X with DMEM, replaced with 3 ml of DMEM + 10 % FBS and incubated at 37 ˚C for 48 h. For nicotine treatments, a concentration of 0.1 and 1 µM was used for 48 h and 20 min respectively, since these concentrations respectively mimic the nicotine concentrations achieved in smoker's brains in between cigarettes (0.1 µM, 48 h) and during smoking (1µM, 20 min).

2.4 Results

Variable-angle TIRFM is provides the ability to image well-defined layers, or thicknesses, of a cell near a coverslip. By changing the incident angle of the excitation laser we can capture a thinner or thicker optical section. With our current VA-TIRF microscope the thinnest optical section we could image had a ~46 nm penetration depth and the thickest pure TIRF image had a ~250 nm penetration depth.

To test the ability to define layers within the 250 nm closest to the coverslip, we transfected pCS2:lyn-mCherry membrane localized protein into a N2a cell. Just prior to imaging we then stained the cells with ERTracker green. In Figure 2.7**a,** a 46 nm penetration depth image is shown. The mCherry labeled cell membrane is clearly imaged while the darkest part of the ERTracker image is seen in the center of the image where the cell membrane sealed the surface and prevented exposure to the stain. Figure 2.7**a** shows that the cell membrane is imaged in isolation from ER located inside the cell.

To test the ability to isolate deeper cellular organelles we imaged that same cell at two penetrations depths: 240 nm and 80 nm. The 240 and 80 nm images were normalized to account for the change in intensity as a function of incident angle. Then the 80 nm image was subtracted from the 240 nm image to test whether cellular organelles near the membrane could be imaged without interference the plasma membrane. The result is seen in Figure 2.**7b**. The membrane localized mCherry emission is very nearly entirely subtracted out showing that the membrane labeled proteins could be successfully removed.

The ERTracker labeled image in contrast was very bright showing that the ER was well captured up to the ~240 nm penetration depth of that image.

Figures 2.7**a** and **b** together indicated that a cell membrane and ER can be imaged without interference from each other (ie. optically isolated) in living cells.

We then explored whether this would still prove true if a single color was used to image a membrane-bound receptor. To do this we transfected N2a cells with α4 eGFP, β2 wt nicotinic Acetylcholine Receptor (nAChR) subunits and pCS2:lyn-mCherry. In Figure 2.7**c** we see a 46 nm penetration depth image. The mCherry labeled membrane is bright and the α4 eGFP β2 wt nAChR's appear to be uniformly distributed in the membrane with some puncta visible. The 240-80 nm penetration depth image in 7**d** shows that the mCherry labeled membrane is seen at low level while the GFP labeled nAChR α4 subunits are seen in quantity in interior cell organelles.

This experiment was repeated after transfecting a N2a cell with α4 eGFP, β2-365AAQA368L349M nAChR subunits. The mutation in the β2 subunit results in increased transport of nAChRs to the cell membrane. In 7**e** the cell is shown at 46 nm penetration depth. The membrane is clearly seen and evidences labeled nAChRs uniformly across the membrane. There are additionally some small puncta and tubular structures in that image close to the membrane. In 7**f** a 240-80 nm image of the same cell shows extensive ER structure deeper in the cell.

Therefore we conclude that the membrane is significantly isolated from other cellular organelles in the thinnest penetration depth images despite substantial expression of fluorophores located internal to the membrane. We also conclude that the ER and other internal organelles can be imaged with only minor interference from the cell membrane, labeled with the same fluorophores, enabling direct response comparison in future experiments.

Our first goal was to capture a series of VA-TIRFM images that are well discriminated in depth and then to use them to build a 3D image that is representative of the cellular structures within 250 nm of the coverslip. To do this we transfected N2a cells with

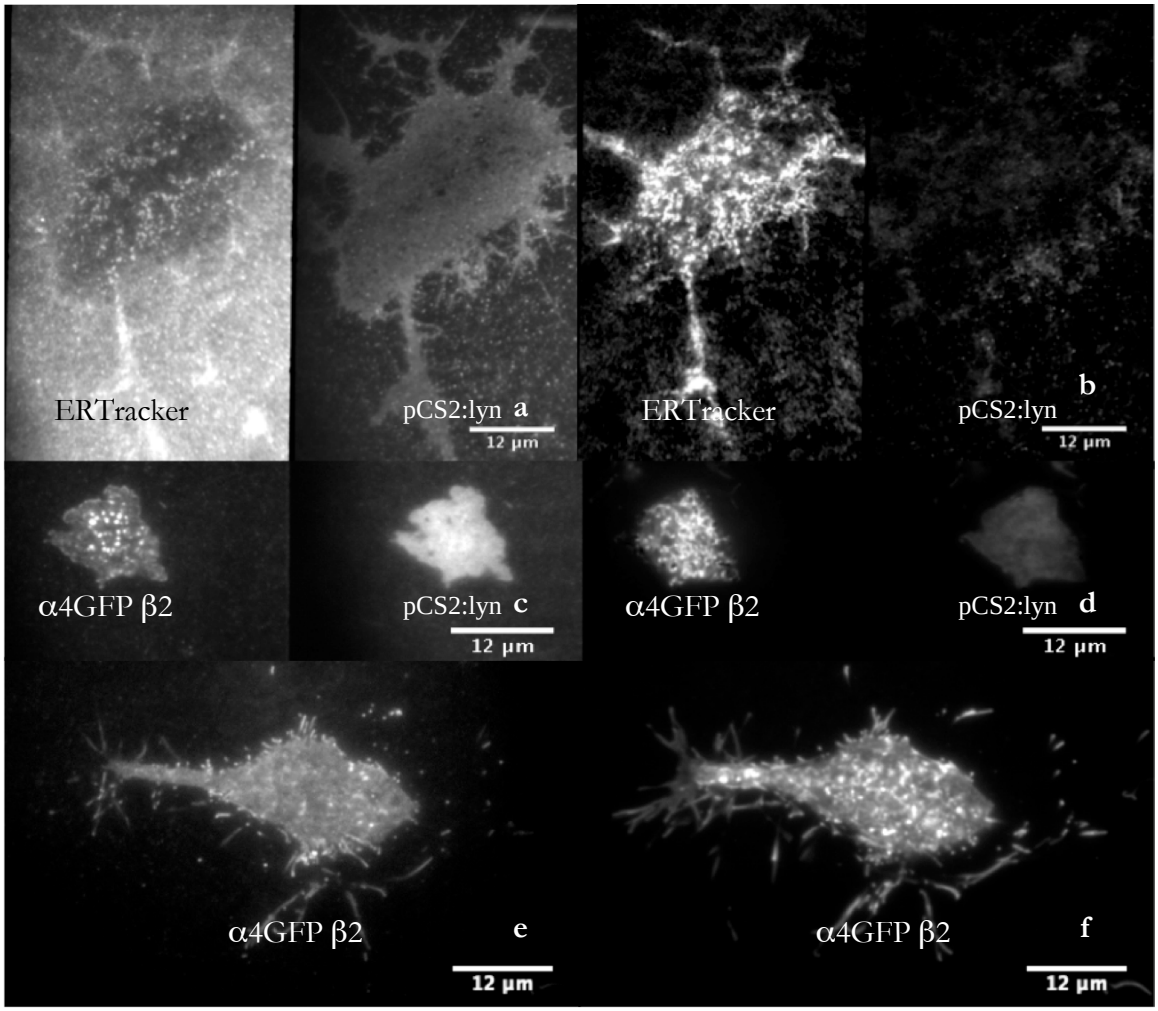

Figure 2.7. A control experiment (**a**) demonstrates that VA-TIRFM is capable of isolating the cell membrane from cell organelles. Additionally it is shown (**b**) that differenced images give information about cell organelles without contamination from membrane signal. Finally it is demonstrated (**c, d, e, f**) that a cell membrane and cell organelles can be imaged in isolation for membrane-expressed proteins labeled with GFP. TIRFM images **a**, **c** and **e** were captured at a penetration depth of 48 nm. TIRFM images **b**, **d**, and **f** are the residual after subtracting an 80 nm penetration depth image from a 240 nm penetration depth image. The 48 nm images are the thinnest which can be captured of a cell using a 1.65 NA objective and a N-LAF21 coverslip. Because these images (**a**, **c**, **e**) are so thin they primarily capture the cell membrane and ER or vesicles that are in contact with, or very close to, the membrane. ~240 nm penetration depth is the deepest that can be captured with this same arrangement and the real beam size of our microscope while remaining in pure TIRF. The residual (**b**, **d**, **e**), after subtracting an 80 nm penetration depth image from a 240 nm penetration depth image, is primarily ER. Images **a** and **b** are control images: the left half of images a and b show ERTracker green stain. Because the cell seals the coverslip from the ERTracker stain the 48 nm image **a** shows a black region where the cell is centered while **b**, the 240-80 nm slice image, shows primarily ER. The right half of images **a**, **b**, **c** and **d** show cells expressing pCS2:lyn-mCherry membrane localized protein. Note that the 48 nm image captured the membrane while very little signal is added in the greater penetration depth images. The cell seen in images **c** and **d** is expressing α4-eGFP β2 wt nAChRs (left) and pCS2:lyn-mCherry (right). The cell in **e** and **f** is expressing α4-eGFP β2-365AAQA368L349M nAChRs (left) and pCS2:lyn-mCherry (right). Camera noise of 110 counts/pixel was subtracted from all of the above images.

α4L358A-eGFP β2 wt nAChR subunits and pCS2:lyn-mCherry. The α4 mutation (L358A)

renders a transport motif inactive. As a result the eGFP labeled subunits accumulate inside the cell. So this experiment, like that seen in 7**a** and **b**, enables us to image the mCherry labeled membrane and eGFP labeled organelles and thereby compare the imaged locations and the fidelity of the 3D model derived from our data.

The imaging results of this experiment are seen in Figure 2.8. On the left is a sequence of VA-TIRFM images taken at 48, 72, 108, 162 and 243 nm penetration depths. These figures capture the total fluorescence within the evanescent field illuminated volume. The mCherry labeled membrane is clearly seen in the 48 nm penetration depth image (top left) and remains approximately the same for the rest of the sequence. In contrast the GFP labeled α4 subunits are more faintly seen in the shallowest image and gain in intensity and structure as the images gain depth. The only processing of these images was camera background subtraction and contrast-brightness adjustment so that they would be visible to the reader.

On the left side of Figure 2.8 are the differenced images defined in Table 5.3 and shown in Figure 2.4. Before differencing, the image intensities of the figures seen on the left are normalized to account for the variation in I(0) as a function of incident angle. The first image in the TIRFM image z-stack is the 46 nm penetration depth image seen in the top right of Figure 2.8. The next down is the difference between the 72 nm image and the 46 nm images. The third down is the difference between the 108 nm and the 72 nm images (2nd and 3rd from the top on the left column). The fourth on the right is the difference between the fourth and the third images (162 nm-108 nm images) on the left. The fifth on the right is the difference between the fifth and the fourth on the left (243 nm-162 nm images). The difference images are the additional fluorescence that is captured each time the incident angle is changed so that a deeper section of the cell is imaged. As such, they approximate the label cellular structure as a function of depth.

The 5 images on the right side of Figure 2.8 were then assembled as a z-stack and converted into a 3D image. The depth was increased by a factor of ~10 (to an apparent 2.5 μm rather than the actual 243 nm) to allow the ER structure to be visible. Because of software limitations the sections are treated as being of equal thickness (500 nm each x 5

layers). Nine views of the resulting 3D image are shown in Figure 2.9. On the top left is an image of the GFP imaged α4 nAChR subunits and next to it is the mCherry labeled membrane. A view of the GFP and mCherry labeled cell 3D model is shown every 22.5° as it is rotated in 8 steps about a vertical axis.

Figures 2.8 and 2.9 together demonstrate that 3D reconstruction captures an appropriately representative thin mCherry labeled membrane, and the much thicker GFP labeled ER and vesicles. Therefore, it appears that VA-TIRFM can be used to create representative 3 D models of cellular structure near the membrane.

We then explored a single label 3D imaging of a membrane embedded protein by transfecting N2a cells with α4-eGFP β2-365AAQA368L349M nAChRs. This β2 mutant increases membrane transport of assembled nAChRs. The cells were also transfected with pCS2:lyn-mCherry membrane localized protein as a control. Similar to what is seen in Figures 2.8 and 2.9 we found that the mCherry labeled membrane image was appropriately represented (not shown).

In Figure 2.10 we see the 3D fluorescence image from the perspective of being in the cell and looking out. The image on the right shows detected fluorescence directly. The image on the left shows a thresholded surface (497 counts per pixel) overlaid on the fluorescence image. The same logarithmic imaging sequence was used to construct this image that was used in Figures 2.8 and 2.9.

In Figure 2.10, the smooth ER and many vesicles are clearly seen. Behind these (closer to the cell surface) the membrane can be seen. In Figures 2.11, 2.12 and 2.13 the 3D model of the cellular structure is further magnified and examined from several angles. As in Figure 2.9, the 5 imaged layers were treated as being equal thickness and magnified by an average factor of ~10. This resulted in an apparent total thickness of 2.5 μm (5 layers, each 500 nm thick in z) as opposed to the actual value of ~243 nm overall.

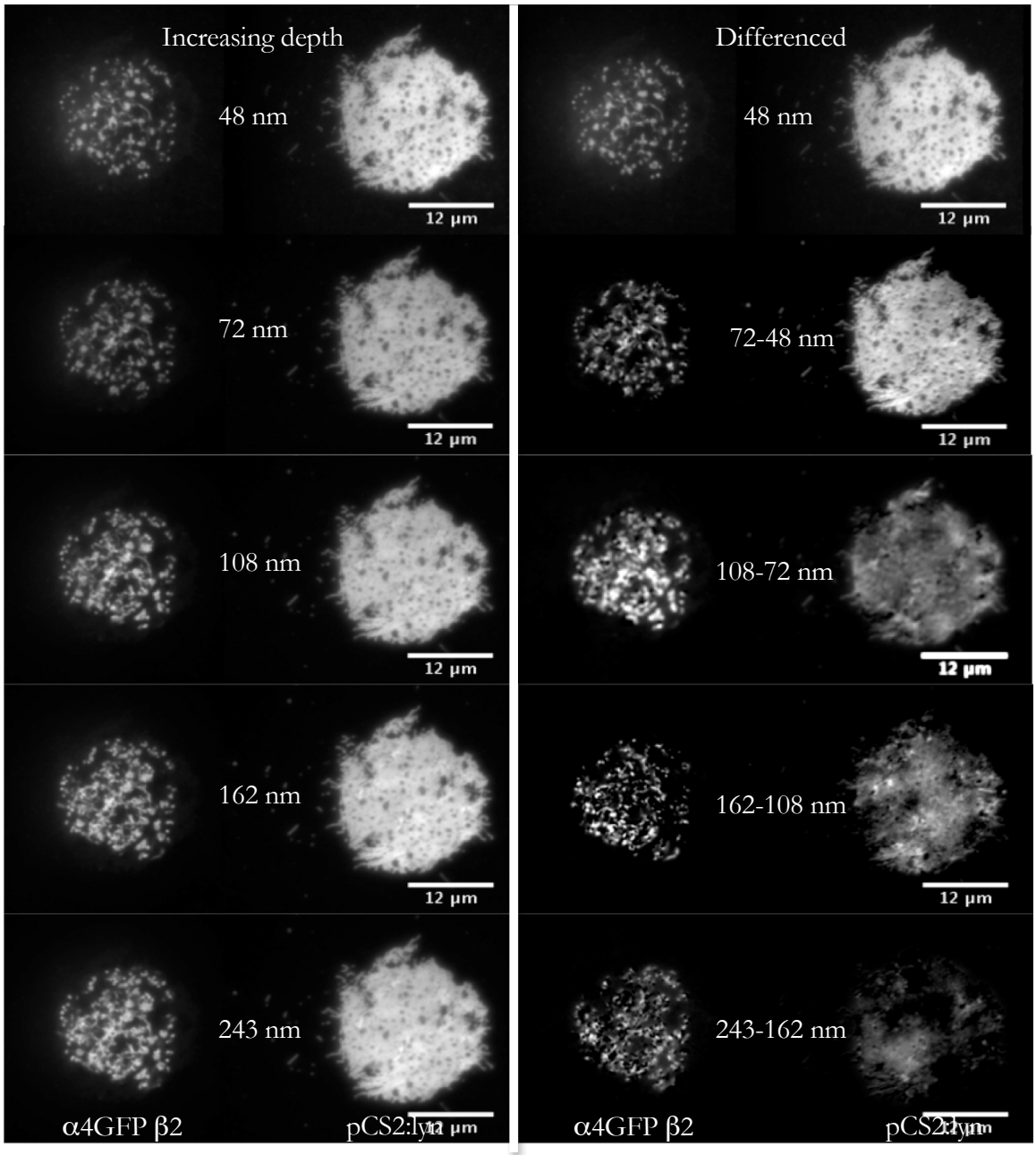

Figure 2.8. A second control experiment demonstrates that a cell membrane and cell organelles can be imaged in isolation. The imaging sequence shown in Figure 2.4 is demonstrated here with a N2a cell. The left column images were captured at penetration depths of 48, 72, 108, 162, and 243 nm (from top to bottom) (Table 5.3). The right column contains the resulting images after differencing (1, 2-1, 3-2, 4-3, 5-4). The differenced images are the additional signal that is captured each time the incident angle is changed to give a thicker image depth The right image in each pair is labeled with pCS2:lyn-mCherry and has the scalebar. The set on the left shows α4L358A-eGFP β2 wt nAChRs. A L358A mutation in the α4 subunit interrupts the transport motif that would normally enable nAChRs to be membrane localized. Therefore this sequence of images provide a side-by-side comparison of the change in signal with increasing penetration depth of an primarily ER localized protein (α4L358A-eGFP on the left) and a membrane localized protein (pCS2:lyn-mCherry on the right).

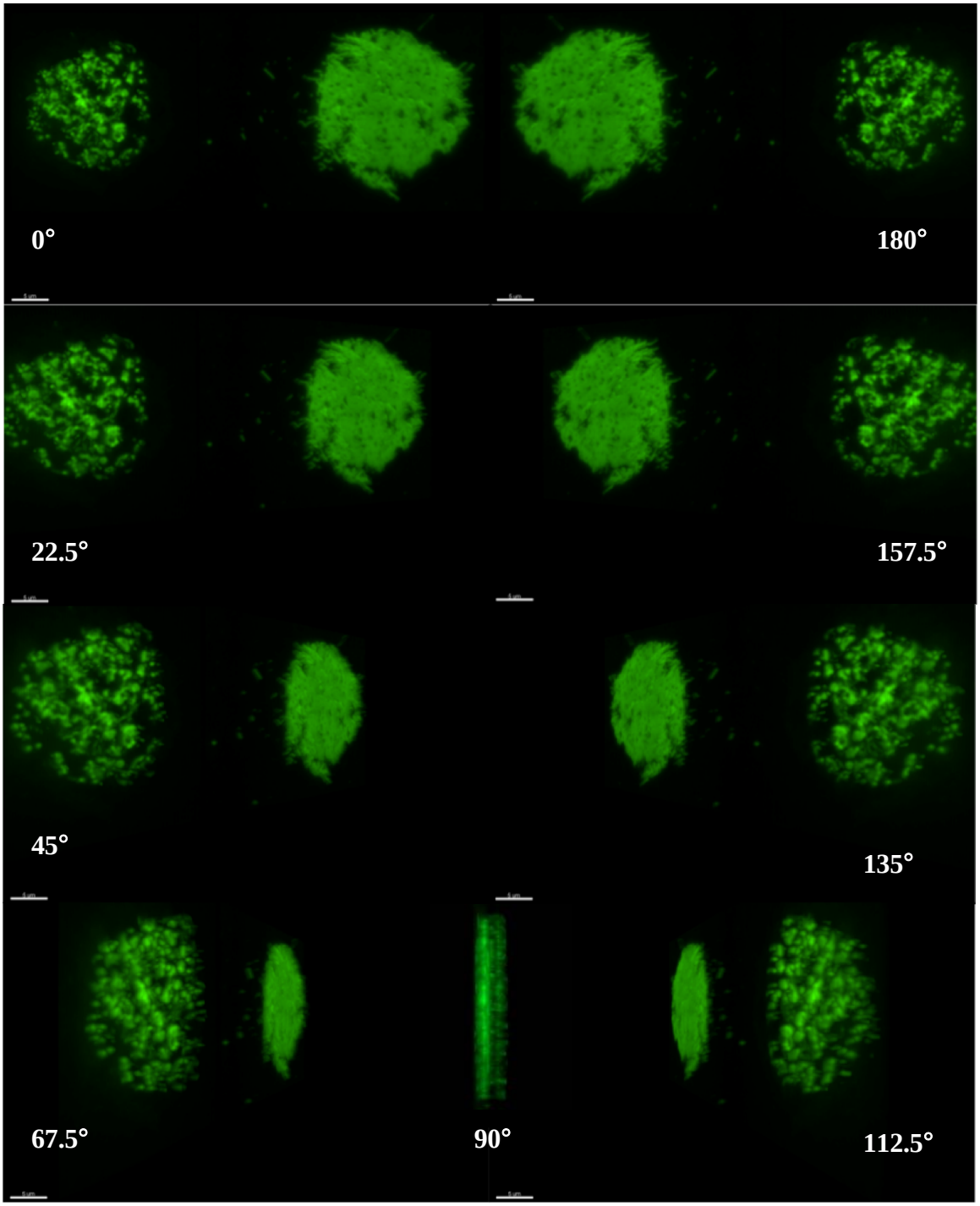

Figure 2.9. A 3D image of a N2a cell is constructed from the differenced images shown in Figure 2.8. Nine views of a three dimensional image are shown being rotated 180° on a central, vertical axis. This 3D image was reconstructed from the five differenced images shown in Figure 2.8 using Imaris software. The scale bar in the bottom left corner of each image is 5 μm long. The total depth of this image was ~240 nm. The z-axis in this figure's images is exaggerated by 10x (expanded to 2.4 microns) for visibility. Magnification in one axis 'stretches' the image such that a normally spherical object becomes cylindrical in appearance (see edge on view in the center bottom). The images were taken face on. The top left perspective is looking out from the center of the cell and the top right from the outside looking in. Each of the successive images is rotated 22.5° from the precious view. Both the GFP labeled nAChRs (outside) and the mCherry labeled membrane (center) are seen.

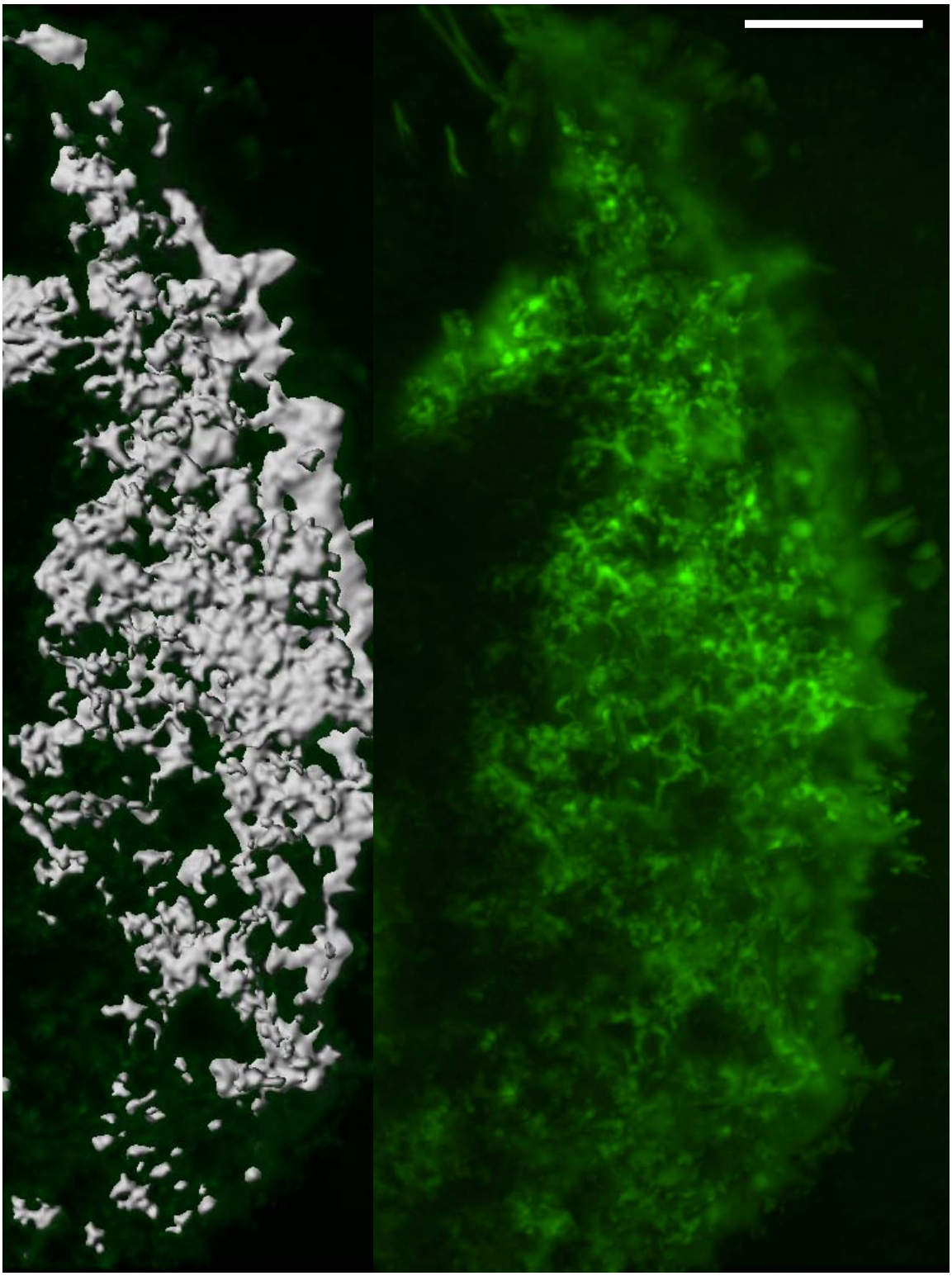

Figure 2.10. A 3D image of cell structures provides information within 250 nm of the membrane with high fidelity. These images show the view from the inside looking out of a 3 D reconstruction that was made from differenced images in using the identical techniques that generated Figure 2.9. On the right, a 240 nm penetration depth TIRFM image is shown of a N2a cell that was transfected with α4-eGFP β2-365AAQA368L349M nAChRs. On the left is a thresholded surface image (497 counts/pixel after background subtraction and normalization) of the same cell. The scale bar at the upper right is 12 μm long.

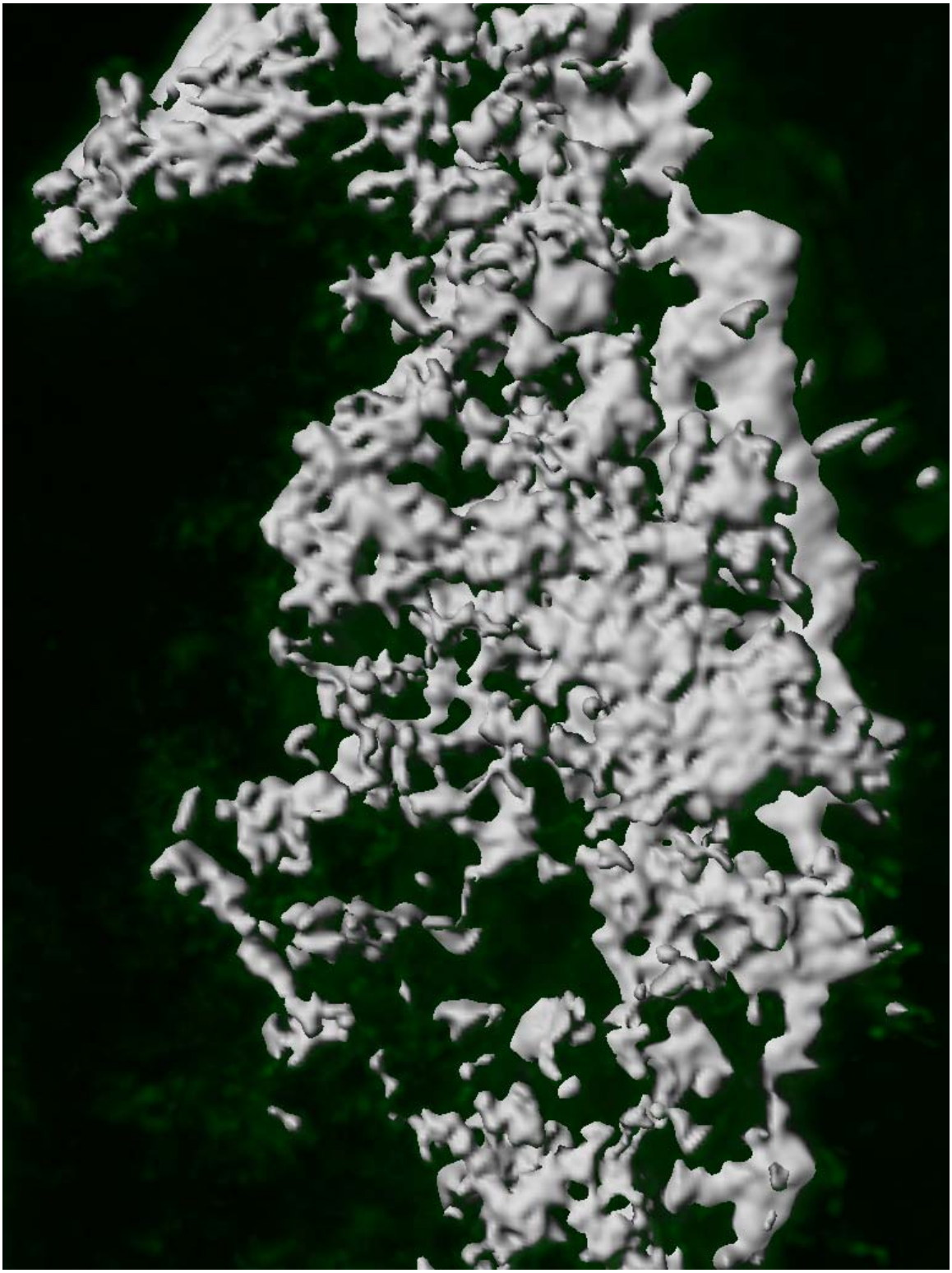

Figure 2.11. A 250 nm thick 3D VA-TIRFM image shows fine structural detail. This view, slightly rotated from that seen in Figure 2.10, implies connections exist between the cell membrane and the smooth ER. In those locations, the separation cannot be resolved by the most shallow TIRM image possible: 46 nm evanescent field penetration depth and 50% illumination at 32 nm. Here the thresholded surface image (identical to Figure 2.10) is overlaid on the green 3 D reconstructed imaged. This view is from the inside looking out. The rotation is on a vertical axis with the left hand side moved (up) out of the page.

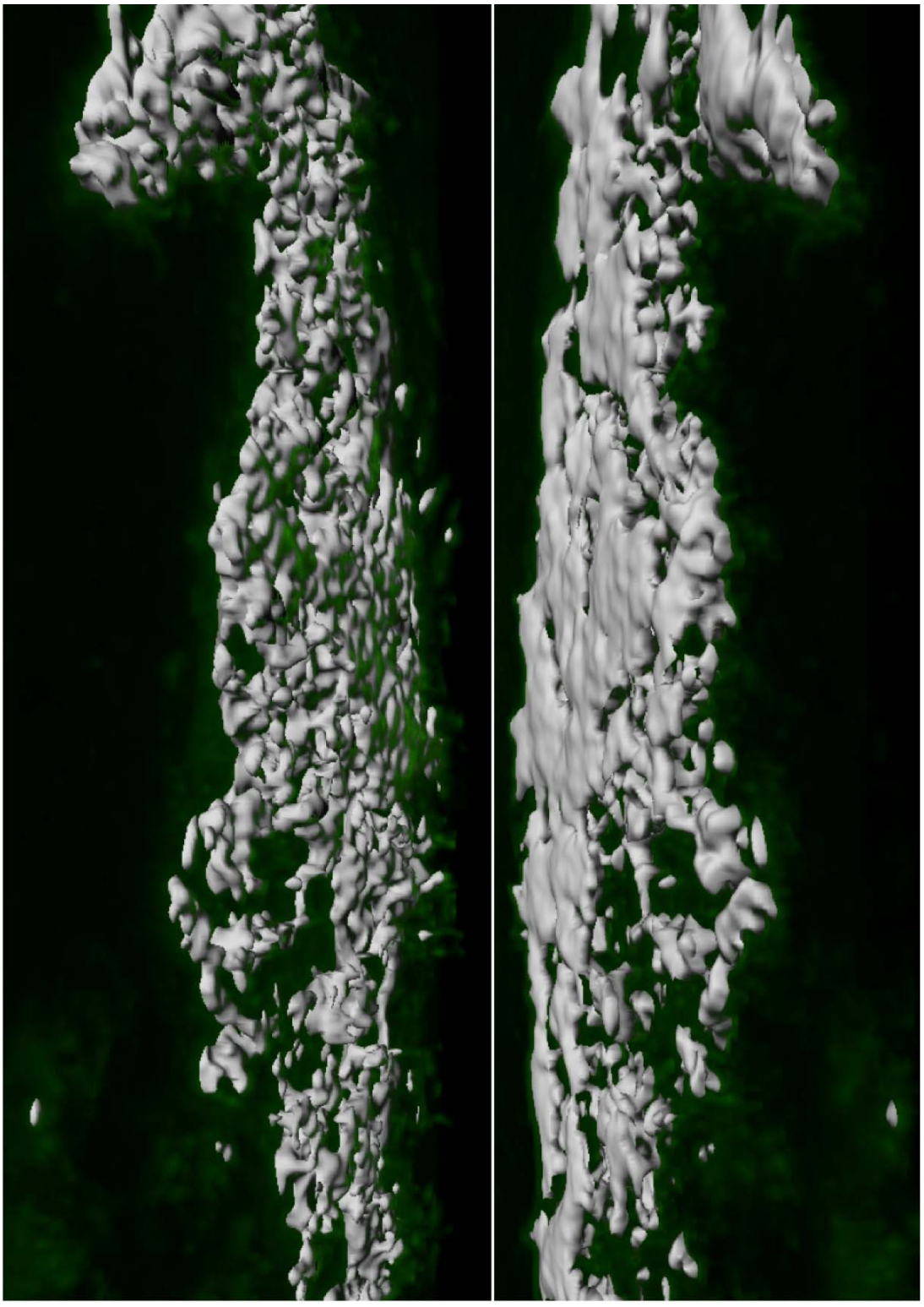

Figure 2.12. Intricate detail is visible indicating that there are many places where parts of the smooth ER are proximate to the membrane such that they cannot be resolved as independent structures. This is the same 3D reconstruction seen in Figures 2.10 and 2.11, of a N2a cell transfected with α4-eGFP β2-365AAQA368L349M nAChRs. The image on the left is further rotated so that the left hand edge seen in Figure 2.10 is nearly perpendicular to the page. The direction of rotation is continued so that the view shows the reconstructed 3D cell image from the membrane side looking in.

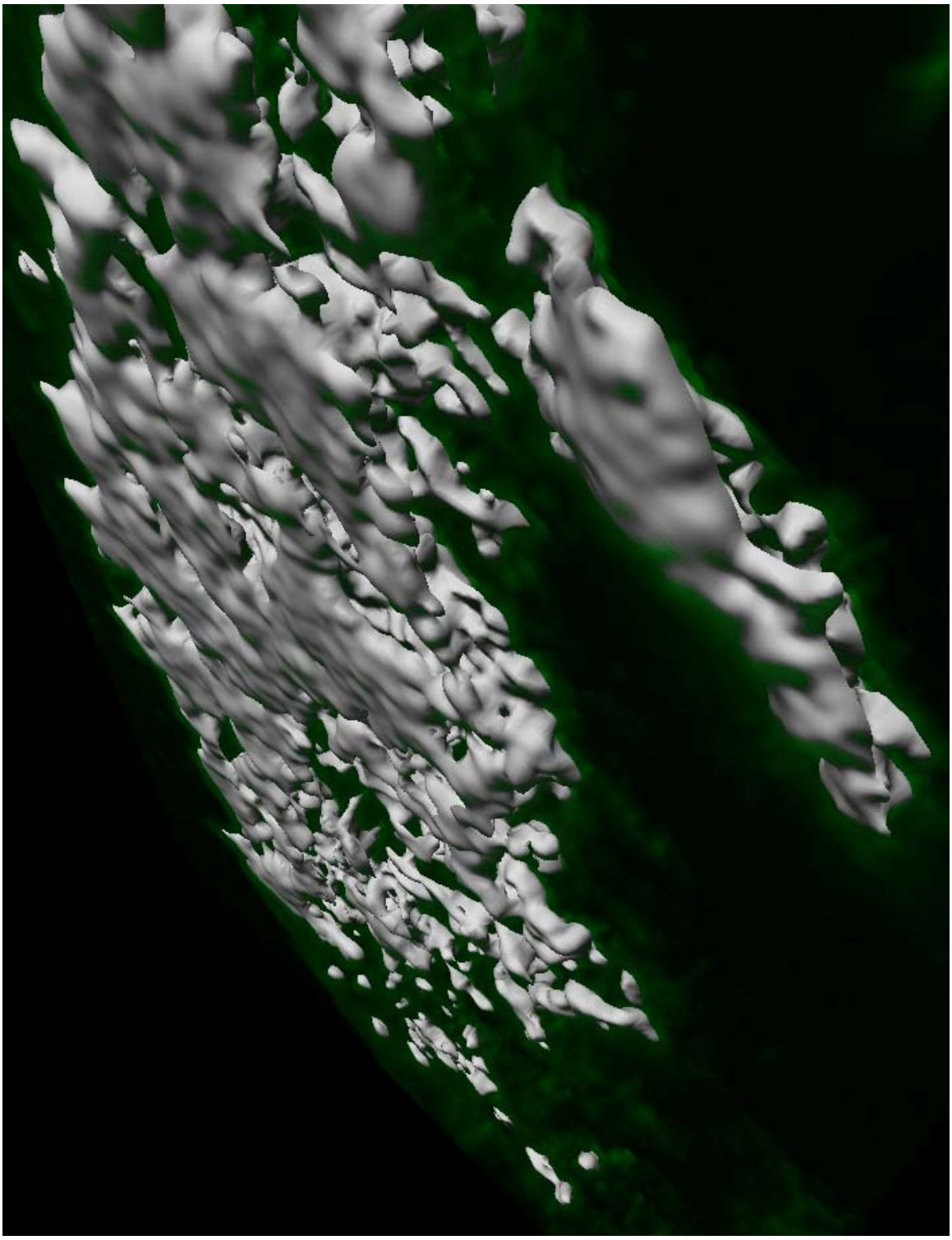

Figure 2.13. Many regions of apparent contact or unresolved proximity between the cell outer membrane and the smooth ER. The rotation of the cell seen in Figures 10, 11, and 12 is continued and the cell is tilted some as well (bottom of the cell rotated into the page). Like Figures 11 and 12 this image too is a combination of thresholded surface and full dynamic range image. This view is from the membrane side of the cell looking in.

A 3D model of a second cell is presented in Figures 2.14 and 2.15. It too is a N2a cell that was transfected with with α4-eGFP β2-365AAQA368L349M nAChRs. As with the other cells, this one was also transfected with pCS2:lyn-mCherry membrane localized protein as a control. Similar to what is seen in Figures 2.8-2.13 we found that the mCherry membrane image was appropriately represented (not shown). The acquisition and processing of this image stack was identical to that used to produce Figures 2.8-2.13. The thresholding surface image was generated at 497 counts per pixel as were those in Figures 2.10-2.13.

The thresholded image too shows a surprisingly complex cellular structure in the 250 nm closest to the coverslip. It also appears that the structure is interconnected. The model indicates sites where the smooth ER either contacts the cell membrane or is sufficiently close that it cannot be resolved as a separate structure.

This raises the question of how unique these features are. In Figure 2.16 three cells are shown. The cells in 2.16**a** and **c** are both transfected with α4-eGFP β2 wt nAChRs. The cell in image 2.16**e** was transfected with α4-eGFP β2-365AAQA368L349M nAChRs and was exposed to 100nM nicotine for 48 hours prior to imaging. Images **a**, **c**, and **e** were taken at 46 nm penetration depth. Images **b**, **d**, and **f** were captured at 200 nm penetration depth. These are full thickness images in that no subtraction was done to localize features. There are bright puncta on the membranes of these three cells.

In image 2.16**b** there are several puncta circled that are located very close to the membrane. In image 2.16**d** it appears that those puncta did not connect to any structure above the membrane. Presumably the puncta imaged in 2.16**b** and 2.16**d** were vesicles. However in the other two cells it appears that puncta did connect to deeper structures. Note that similar features can be seen in Figure 2.7**c** and **e**.

In summary, both α4-eGFP β2 wt and α4-eGFP β2-365AAQA368L349M nAChRs as expressed in N2a cells appear to have junctions where either the smooth ER makes contact with the cell membrane or is so close that it cannot be resolved via TIRFM.

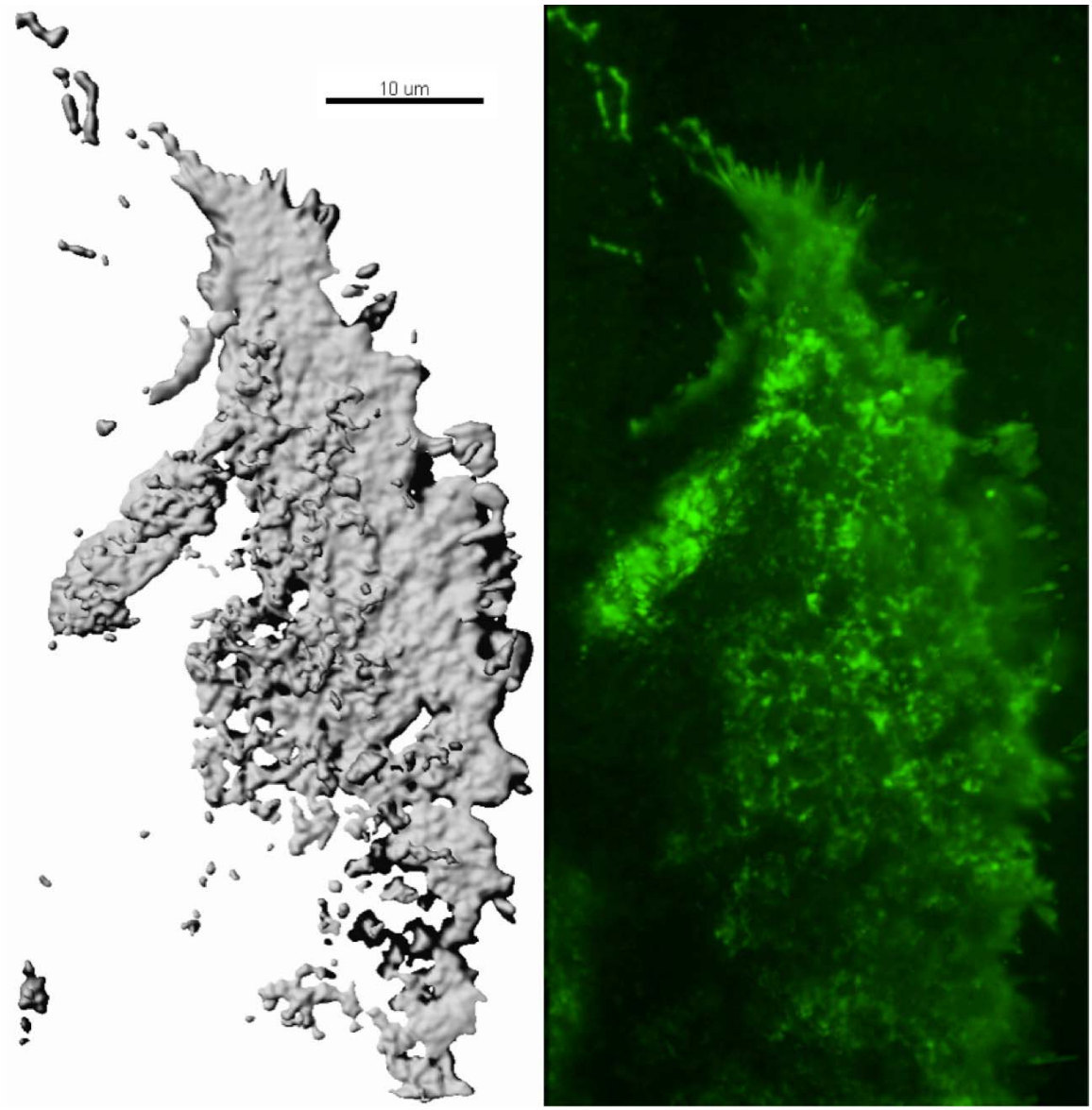

Figure 2.14. A different N2a cell is pictured here with detail shown at a level comparable to that seen in Figures 9-13. On the right, a 240 nm penetration depth TIRFM image is shown of a N2a cell that was transfected with α4-eGFP β2-365AAQA368L349M nAChRs. On the left is a thresholded surface image (497 counts/pixel after background subtraction and normalization) of the same cell. This 3D model was constructed from 5 differenced slices ranging from 46 nm to 240 nm in penetration depth (sequence in Table 5.2).

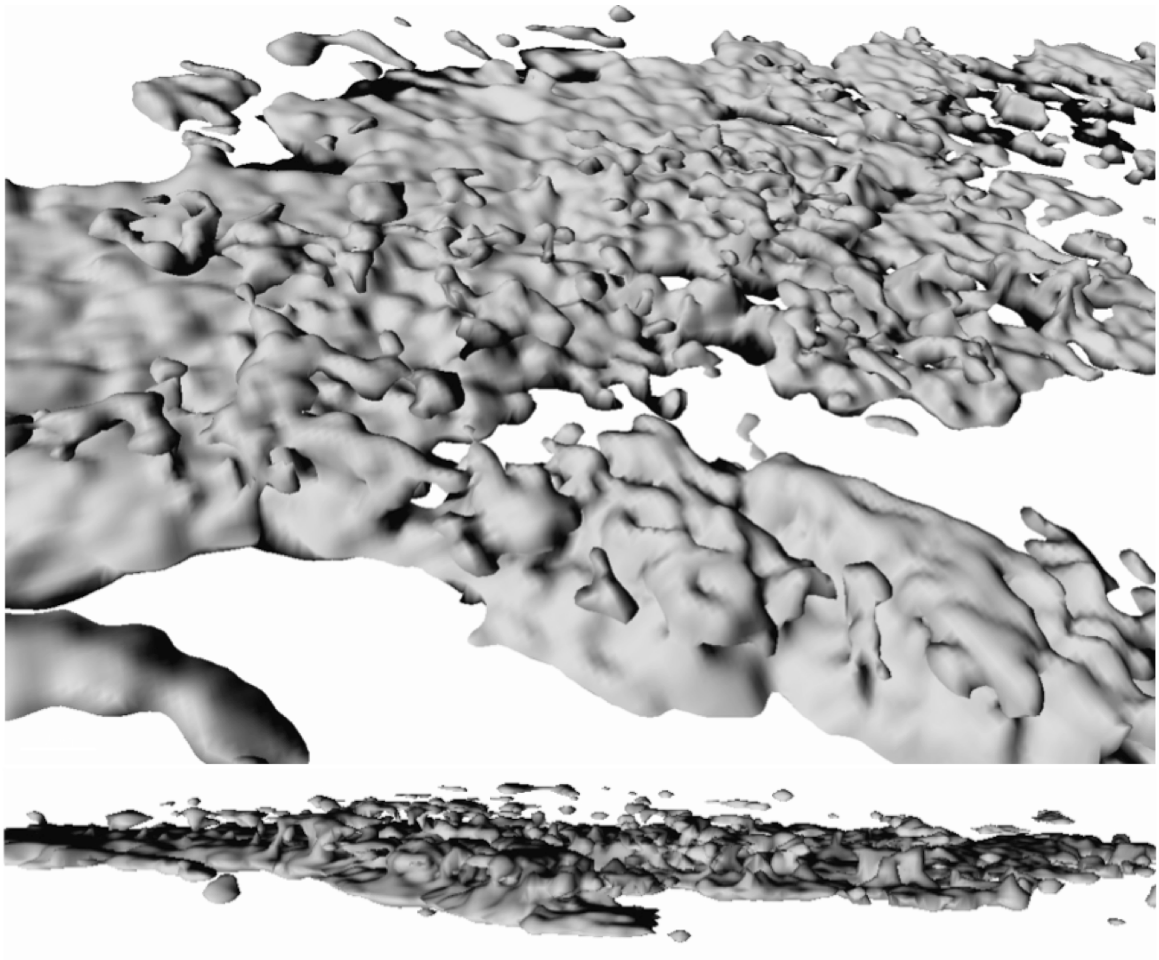

Figure 2.15. Two views are given from the perspective of being on the inside of the cell while looking out. The views above have been rotated ~90 counterclockwise as well as tilted in comparison with the images seen in Figure 2.14. As with the cell in Figures 10-13 there are high intensity regions (>497 counts per pixel after background subtraction) where the isointensity structures shown in threshold surface images seem to indicate either that there is contact between the cell and the smooth ER or alternately that they are so close that they can not be resolved by a 46 nm penetration depth TIRF image.

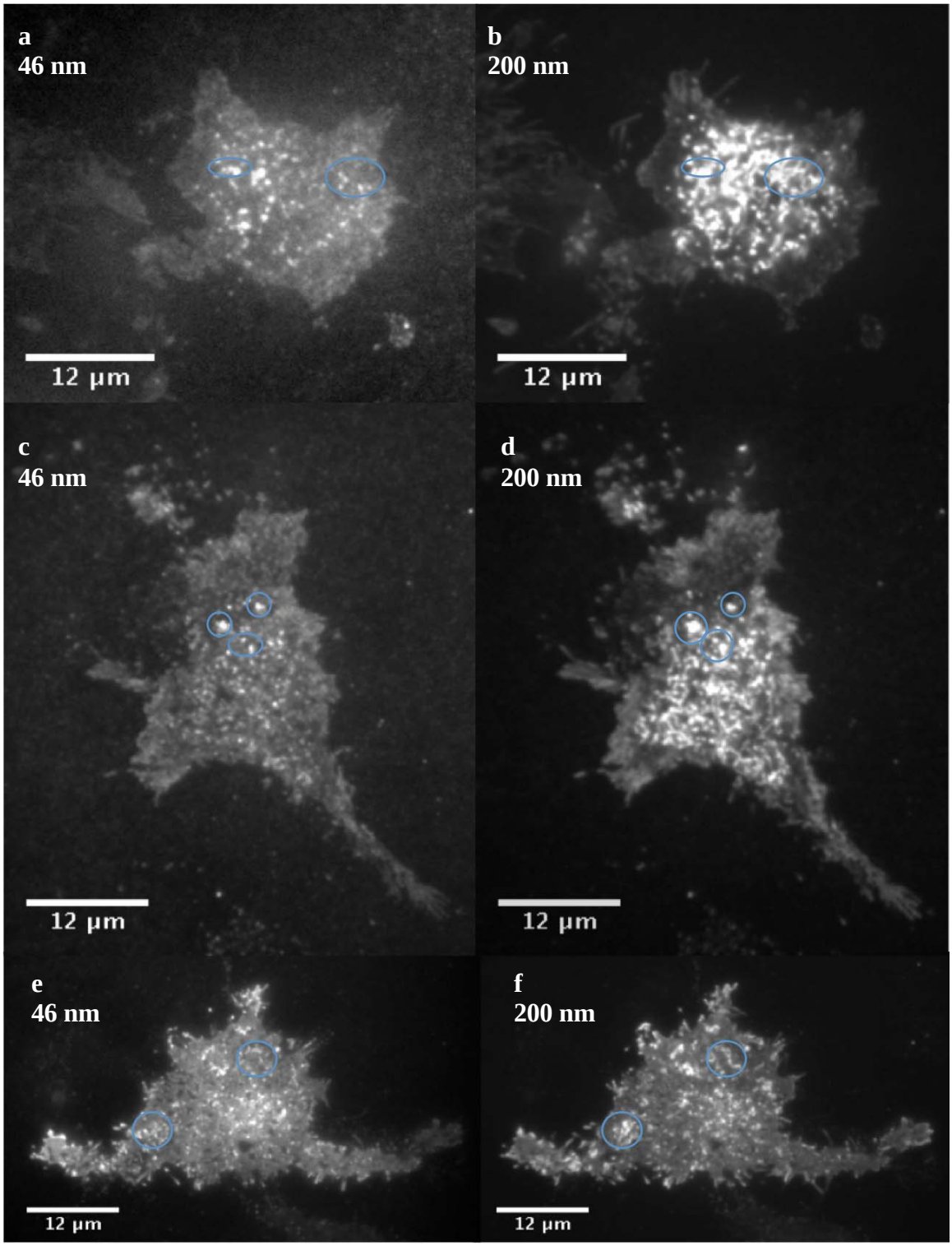

Figure 2.16. Bright nAChR puncta on membrane could be connections between the smooth ER and membrane, localized vesicles (probably the case for circled features in the middle image of this figure) or locations where ER structures are so close to the cell membrane that they cannot be resolved. The left TIRFM images are ~46 nm penetration depth. The right images are approximately 200 nm penetration depth (total power, no differencing). Frequently a bright spot (circled) is seen on the membrane in the thinnest possible TIRF image that appears to be part of a deeper structure. Similar features are seen in nearly all healthy cells with nAChRs that include a membrane transport motif.

2.5 Discussion

It appears that we have detected puncta that may be locations where the smooth ER is in contact with the cell membrane. We know for sure that some detected puncta are so close to the membrane that we cannot detect any separation. How proximate to the membrane are these structures?

The resulting 3D structure is surprisingly detailed. The images indicate that there are direct connections between the membranes and the smooth ER. It appears from this 3D image that these locations are not just self-contained vesicles or invaginations.

In the literature it was reported that smooth ER to cell membrane connections[34,35] have been imaged via electron tomography. Hysashi (ref 34) in particular observed murine neuron cultures with dynamin 1 KO. They observed a great increase in the number of clathrin coated pits in inhibitory synapses and the occurrence of a dynamin 1 independent form of bulk endocytosis. They noted that the observed heterogeneity in the mode of synaptic vesicle recycling in different synapses and function states implied that independent trafficking mechanisms to clathrin mediated endocytosis might exist in normal cells. In addition smooth ER connections with the membranes of other organelles via EM tomography have also been observed.[36]

Therefore it appears plausible that apparent intersections between the smooth ER and outer cell membrane reported here might be real. If so, then VA-TIRFM could be a very useful method for studying the regulatory pathways controlling this potential trafficking mechanism in live cells.

A critical issue with any microscopy technique is: how reliable is this data? Over the index of refraction range of a cell, using a 1.65 objective and N-LAF21 coverslips, a penetration depth of ~46 nm can be achieved. It is critical to remember that the evanescent field decays exponentially. In other words fluorophores near the coverslip surface are more strongly illuminated than those further from the surface. The evanescent field intensity has dropped to ~ 37% at one penetration depth from the surface. Yet even at three times the penetration depth the evanescent field is still ~5% of the intensity at the coverslip surface. Hence an

image taken at a given incident angle, and thereby with a well-defined penetration depth, entangles information from considerably deeper than the penetration depth with that from shallower sections of the cell.

Perhaps the best way to view an individual image is to state that there is a 1-sigma probability that the fluorescence concentration is located within the penetration depth of that image. Therefore the differential technique that was utilized in this VA-TIRFM study optimally yields 3D images in which the fluorophore concentration distribution in z is certain to ~1 sigma.

A 1-sigma certainty is more stringent than the gold standard for defining optical resolution: the Rayleigh criterion.[37] Rayleigh defined a pair of point sources, assuming equal brightness and spectral content, as being resolved when the central diffraction disks are just touching at 50% of maximum. The separation then is equal to the Full Width Half Maximum (FWHM) of one of the beams. 1-sigma certainty is more stringent than the Raleigh criterion as the intensity at that point is only $1/e \approx 37\%$ of maximum rather than at 50%.

The early attempts at VA-TIRFM 3D image reconstruction reported here do not achieve 1-sigma certainty due to non-uniformity of the excitation beam. However they do approach and likely exceed the Rayleigh criterion in terms of vertical resolution. This implies that we have achieved a vertical resolution of <50 nm.

A more rigorous deconvolution of the continuous fluorophore distribution is required to do significantly better than 1-sigma certainty. This could be accomplished via the inverse Laplace transform approach described earlier. An alternate method for disentangling fluorescence that originated at different z distances in an evanescent field would be to use a finite difference technique similar to that used to solve heat transfer and fluid flow problems.

During the course of this study a variety of different imaging strategies were explored. It is clear (see Figure 2.5) that direct differencing very, very finely parsed images is ineffective

as the variation of illumination intensity due to interference patterns is greater than the additional signal detected due to increased penetration depth.

For simple direct differencing with our current microscope we have found that five slices probably represents the most that can be useful. In comparing the efficacy of several approaches we found that five slice z-stacks in general appear to have fewer artifacts than 4, which in turn is better than 3 image z-stacks. Even spaced 5 layer images were constructed and give nearly identical results (not shown) to the 5 slice logarithmic z-stacks. In all cases the 4 slice even space approach gave better results than the 4 slice logarithmic approach. It is not clear to what degree this is due to limitations in the image processing software.

Image fidelity or goodness was here evaluated in a fashion similar to that used when evaluating AFM images: by how sharply defined features are and by an absence of artifacts. Here we define artifacts as repeated structures across an image. As an example, an artifact in a reconstructed image could be identified if the visualized structures have relatively round, twisted shapes throughout most of a cells were connected in one, cell-wide, section with a parallel set of cylindrical or conical features. So the images were examined for features or associations that were repeated as patterns to identify artifacts as would be done when evaluating AFM images.

This kind of artifact is certain to occur when the image is stretched in z (by 10 x in the case of the papers presented herein). It is also likely to occur when the collected image stack has significantly varying thicknesses. Every image processing software package identified, including ImageJ and Imaris 7.0, reconstruct images assuming that every image in the stack is of equal thickness. If on slice is twice as thick as another the final result will be to artificially stretch or compress those regions in a 3D reconstruction. Therefore it is logical to prefer even spaced (in penetration depth) differenced images when doing 3 D image reconstructions.

As shown earlier (e.g. Figure 2.4) even spaced differential images are limited to a z-stack containing only five slices of ~50 nm thickness (each). Clearly it would be beneficial to get

finer z resolution than this. Alternative approaches would include interleaving images so that two stacks of 50 nm thick images could be offset by 25 nm.

While continuous 3D image reconstruction is a challenging problem, there are clear first steps that can be taken by future researchers. Three major impediments remain to be solved for significantly finer z resolution:

1. Image processing software in which the z value of each image in a stack can be individually set and

2. A substantial reduction in excitation laser interference pattern. The first ways to achieve that are to improve the index of refraction match between the coverslip and the immersion oil and to replace the optics that guide the excitation laser with ones that have high quality antireflection coatings. If that is not sufficient, two methods for ensuring elimination of interference patterns are spinning beam and annular mask. With spinning beam the radius must be increased or decreased to change angle of incidence. Precise control of this is possible but will require some though and very good optical alignment. VA-TIRFM with an annular mask is tougher. Perhaps the image of the mask on the objective back plane could be expanded or contracted optically (in analogy to a zoom lens).

3. A smaller excitation laser beam focal spot would significantly reduce the variation in incident angle across the beam. Therefore more finely parsed images could be taken. A factor of two to three reduction in beam size would be sufficient to enable 10 differential slices to be acquired rather than the current limit of 5.

Summary

We have demonstrated that TIRFM using a 1.65 NA objective enables cellular membranes to be imaged in near isolation from the interior of a cell. Further, by using a close-loop controlled positioner, the incident angle of the excitation laser can be repeatably set. This in turn enables images to be captured with known and controlled evanescent field penetration depths. We have shown that the deepest pure TIRF image that can be taken, even with a 1.65 NA objective and high index N-LAF21 coverslips, is about 250 nm thick.

A novel, and relatively simple image processing technique was developed during this study wherein several images are taken with known penetration depths. By normalizing these images, to account for the change in evanescent field intensity as a function of incident angle, they can be directly subtracted to yield difference images in which cellular structures can be optically isolated to distances within 46 nm of the coverslip surface and thereafter at defined distances up to ~250 nm.

We have also demonstrated that these differenced images can be used to construct detailed cellular structure models of up to 250 nm depth. In doing so it appears that cellular organelles can be located vertically to within ~50 nm at present and with higher precision given further development.

Finally we have detected puncta where the smooth ER may intersect with the cell membrane presumably for the purposes of rapid transport of lipids and membrane bound proteins including nAChRs. Such tubular connections between the ER and outer membrane could represent an alternate trafficking mechanism to transport via discrete vesicles. VA-TIRFM appears to be well suited for investigating mechanisms controlling the assembly of functional receptors or lipid rafts in living cells via pulse-chase experiments.

In conclusion, we confidently expect that VA-TIRFM will provide insight into trafficking mechanisms by enabling imaging of cell membranes discrete from images of nearby cellular components.

Acknowledgements

Thanks to Joe Shepherd, Dan Axelrod, Rahul Srinvasan, Chris Richards, and Henry Lester. I could never have hoped to complete this VA-TIRFM study without the skilled work and kind help of Mike Roy and Steve Olson of the Chemistry Department's Instrument shop.

Caltech Dean Grad Studies/Provost, NS11766, Louis and Janet Fletcher, and The Michael J. Fox Foundation are gratefully thanked for funding.

References

[1] Axelrod, D. Cell-substrate contacts illuminated by total internal reflection fluorescence, J Cell Bio, (1981) **89** 141-145.

[2] Lanni, F., Waggoner, A.S. and Taylor, D.L., Structural organization of interphase 3T3 fibroblasts studied by total internal fluorescence microscopy, J Cell Bio, (1985) **100** 1091-1102.

[3] Olveczky, B.P., Periasamy, N. and Verkman, A.S., Mapping fluorophore distributions in three dimensions by quantitative multiple angle-total internal reflection fluorescence microscopy, Biophysical J (1997) **73** 2836-2847.

[4] Stock, K. et al., Variable-angle total internal reflection fluorescence microscopy (VA-TIRFM): realization and application of a compact illumination device, J Micro, (2003) **211** 19-29.

[5] van't Hoff, M, de Sars, V. and Oheim, M., A programmable light engine for quantitative single molecule TIRF and HILO imaging, Opt Express (2008) **16** 18495.

[6] Steyer, J.A. and Almers, W., Tracking single secretory granules in live chromaffin cells by evanescent-field fluorescence microscopy, Biophys J (1999) **76** 2262-2271.

[7] Loerke, D., Preitz, B., Stuhmer, W. and Oheim, M., Super-resolution measurements with evanescent fluorescence excitation using variable beam incidence, J Biomed Opt (2000) **5** 23-30.

[8] Loerke, D., Stuhmer, W. and Oheim, M., Quantifying axial secretory-granual motion with variable-angle evanescent-field excitation, J Neurosci Meth (2002) **119** 65-73.

[9] Reichert, W.M., Suci, P.A., Ives, J.T. and Andrade, J.D., Evanescent detection of adsorbed protein concentration-distance profiles: fit of simple models to variable-angle total internal reflection fluorescence data, Appl Spec (1987) **87** 503-508.

[10] Rangnekar, V.M. and Oldham, P.B., Investigation of the microenvironment polarity of a chromatographic surface using total internal reflection fluorescence, Anal Chem (1990) **62** 114-1147.

[11] Toriumi, M., Saito, S., Kawaguchi, K. and Aiki, K., Variable-angle ultraviolet total-internal-reflection fluorescence spectroscopy using a white excitation light source, Rev. Sci. Instrum (1995) **66** 3520-3526.

[12] van't Hoff, M., Reuter, M., Dryden, D.T.F. and Oheim, M., Screening by imaging: scaling up single-DNA-molecule analysis with a novel parabolic VA-TIRF reflector and noise-reduction techniques, Phys. Chem. Chem. Phys., (2009) **11** 7713-7720.

[13] Lue, N. et al., Live cell refractometry using microfluidic devices, Optics Lett. (2006) **31** 2759-2761.

[14] Maier, J., Walker, S., Fantini, S., Franceschini, S. and Gratton E., Possible correlation between blood glucose concentration and the reduced scattering coefficient of tissues in the near infrared, Opt. Lett. (1994) **19,** 2062–2064.

[15] Brunsting, A. and Mullaney, P., Differential light scattering from spherical mammalian cells, Biophys. J. (1974) **14** 439–453.

[16] Brunsting, A. and Mullaney, P., Differential light scattering from spherical mammalian cells, Biophys. J. (1974) **14** 439–453.

[17] Beuthan, J., Minet, O., Helfman, J. and Muller, G., The spatial variation of the refractive index in biological cells, *Physics in Medicine and Biology*, (1996) **41**, 369-382.

[18] Beuthan, J., Minet, O., Helfman, J. and Muller, G., The spatial variation of the refractive index in biological cells, *Physics in Medicine and Biology*, (1996) **41**, 369-382.

[19] Wilson, J.D., Cottrell, W.J. and Foster, T.H., Index-of-refraction-dependent subcellular light scattering observed with organelle-specific dyes, J Biomed Optics (2007) **12** 014010.

[20] Vitkin, I., Woolsey, J., Wilson, B., and Anderson, R., Optical and thermal characterization of natural (sepia oficinalis) melanin, Photochem. Photobio. **59** 455–462.

[21] Schott glass N-LAF21: http://refractiveindex.info/?group=SCHOTT&material=N-LAF21.

[22] Reichert, W.M., Suci, P.A., Ives, J.T. and Andrade, J.D., Evanescent detection of adsorbed protein concentration-distance profiles: fit of simple models to variable-angle total internal reflection fluorescence data, Appl Spec (1987) **87** 503-508.

[23] Rangnekar, V.M. and Oldham, P.B., Investigation of the microenvironment polarity of a chromatographic surface using total internal reflection fluorescence, Anal Chem (1990) **62** 114-1147.

[24] Olveczky, B.P., Periasamy, N. and Verkman, A.S., Mapping fluorophore distributions in three dimensions by quantitative multiple angle-total internal reflection fluorescence microscopy, Biophysical J (1997) **73** 2836-2847.

[25] Hellen, E.H. and Axelrod, D., Fluorescence emission at dielectric and metal-film interfaces, J.Opt Soc Am B (1987) **4**, 337-350.

[26] ImageJ v1.44c is supported by the National Institute of Health. It can be downloaded at: http://rsbweb.nih.gov/ij/

[27] Bitplane Scientific Software: http://www.bitplane.com/

[28] Mattheyses, A.L., Shaw, K. and Axelrod, D., Effective elimination of laser interference fringing in fluorescence microscopy by spinning azimuthal incidence angle, Microsc. Res. Tech. (2006) **69** 642-647.

[29] Thorlabs pn PT1Z8 motorized translation stage with pn TDC001 T-cube DC motor controller. Thorlabs, 435 Route 206 North, Newton, NJ 07860, USA.

[30] LaIuppa, J.A., McAdams, T.A., Papoutsakis, E.T. and Miller, W.M., Culture materials affect ex vivo expansion of hematopoietic progenitor cells, JBiomedMatlsRes (1997) **36** 347-359.

[31] Ata, S.O. and Yavuzyilmaz, H., In vitro comparison of the cytotoxicity of acetal resin, polymerized resin and auto-polymerized resin as denture base materials, JBiomedMatlsRes PtB (2009) **91B** 905-909.

[32] Nashmi, R., Dickinson, M.E., McKinney, S., Jareb, M., Labarca, C, Fraser, S.E., Lester, H.A., Assembly of $\alpha_4\beta_2$ nicotinic acetylcholine receptors assessed with functional fluorescently labeled subunits: effects of localization, trafficking, and nicotine-induced upregulation in clonal mammalian cells and in cultured midbrain neurons. J Neurosci (2003) **23** 11554-11567.

[33] Son, C.D., Moss, F.J., Cohen, B.N., and Lester, H.A., Nicotine normalizes intracellular subunit stoichiometry of nicotinic receptors carrying mutations linked to autosomal dominant nocturnal frontal lobe epilepsy, Mol Pharmacol (2009) 75 1137-1148.

[34] Spacek, J. and Harris, K.M., Three-Dimensional Organization of Smooth Endoplasmic Reticulum in Hippocampal CA1 Dendrites and Dendritic Spines of the Immature and Mature Rat, J Neurosci (1997) **17** 190-203.

[35] Hayashi, M., et al., Cell- and stimulus-dependent heterogeneity of synaptic vesicle endocytic recycling mechanisms revealed by studies of dynamin 1-null neurons, PNAS (2008) 105 2175-2180.

[36] Yla-Anttila, P., Vihinen, H., Jokitalo, E. and Eskelinen, E.L., 3D tomography reveals connections between the phagophore and endoplasmic reticulum, Autophagy (2009) 1180-1185.

[37] Strutt, J.W., Investigations in optics, with special reference to the spectroscope, Philosophical Magazin, (1879) 8 261-274, 403-411, 477-486 and (1880) 9 40-55.

Chapter 3

TOWARDS IMAGING FLUORESCENLY LABELED PROTEINS WITH TIP-ENHANCED FLUORESCENCE MICROSCOPY (TEFM)

In collaboration with the Quake group of Caltech, we demonstrated sub-10 nm optical resolution with a Tip-Enhanced Fluorescence Microscope (TEFM) imaging quantum dots[1] and single-molecules[2] on a dry surface. TEFM is a hybrid microscope that combines an Atomic Force Microscope (AFM) with a custom Total Internal Reflection Fluorescence Microscope (TIRFM). A 543 nm excitation laser beam is focused through a microscope objective at the top surface of a glass coverslip to stimulate an evanescent field. Emitted fluorescence is collected by the microscope objective and then directed onto an avalanche photodiode (APD) through a system of spectral filters. In Figure 3-1 the major components in a TEFM are shown schematically. The two patents awarded for this microscope are Appendices C and D.

After joining the Scott Fraser group this instrument was substantially enhanced to enable imaging of proteins in a biologically relevant warm, wet environment. In collaboration with the Henry Lester group, a prolonged attempt was made to utilize this Wet-TEFM for imaging nicotinic acetylcholine receptors on living cells. However, the complexities of the tip-sample interaction with living cells, combined with the complexities of tip-evanescent field interactions in extracellular liquid, precluded confident interpretation of the resulting data. As a result I was not able to apply this instrument to study

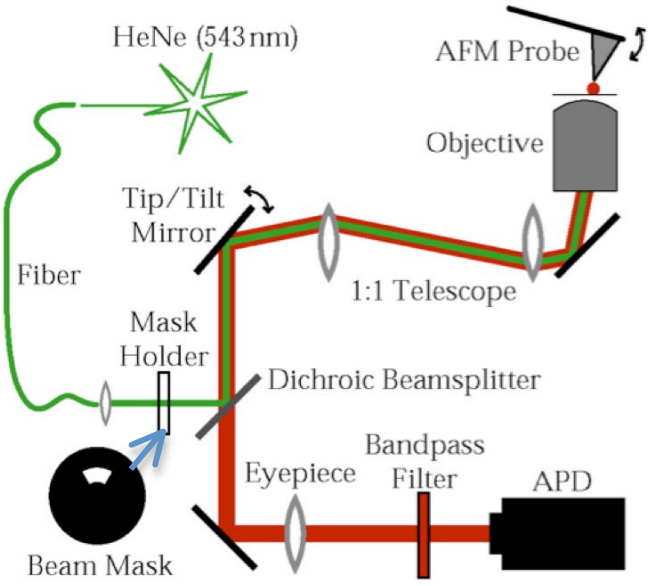

Figure 3.1 The major components in a TEFM are schematically shown above. In essence the TEFM is comprised of an AFM and a TIRF microscope.

neuroreceptor organization and composition as intended.

This chapter is organized into two sections. In the first section 'Dry TEFM Imaging' two papers are presented that describe the TEFM principles, instrument and our results in detail. In the second section 'Wet TEFM Imaging of Live Cells and Membrane-bound Proteins' the innovations developed to enable adaptation of TEFM to imaging live cells are summarized, and some preliminary results are presented. Detailed descriptions of the instrument, data acquisition hardware and software and the image processing software developed for wet TEFM imaging, are presented in Appendix E.

3.1 Dry TEFM Imaging

TEFM is a hybrid microscope that combines an Atomic Force Microscope (AFM) with a custom epi-fluorescence optical microscope as shown in Figure 3.2. The excitation laser beam is focused at the top surface of a glass coverslip and emitted fluorescence is directed onto an avalanche photodiode (APD) through a system of spectral filters. Controlled by independent digital feedback loops, the excitation laser focus spot tracks the lateral motion of the AFM probe with a tip/tilt servo mirror.

The TEFM concept couples an AFM probe to a vertically polarized excitation laser, giving substantial enhancement of the optical field strength in analogy with a lightning rod.[3,4,5] The probe apex electric field intensity is enhanced through a geometric lightning-rod effect: resulting in an increase in the fluorescence of samples being imaged by up to 25x (quantum dots). In the context of near-field microscopy, field enhancement near the tip of a sharp probe has been used to generate optical contrast via elastic light scattering,[6,7] Raman scattering,[8] two-photon fluorescence,[4] single-photon fluorescence[9,10,11], and optical second-harmonic generation.[12] The promise of

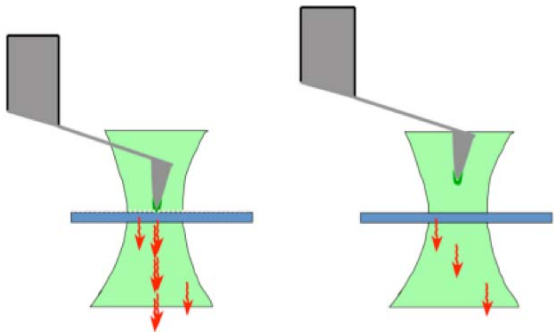

Figure 3.2 Emission is stimulated when the AFM probe tip is proximate to a fluorescent sample. When separated by from the sample by >10 nanometers (left) only the excitation laser stimulated emission can be detected.

these “apertureless” techniques is that spatial resolution is limited only by the sharpness of the tip, overcoming limits imposed by the optical skin-depth in more conventional “aperture” techniques. We reported the first rigorous measurements of the magnitude and spatial extent of the enhanced field near the tip of a silicon atomic force microscope (AFM) probe.[1] The measurements unambiguously confirm an r^6 power-law decay whose spatial dependence is moderated by a tip sharpness parameter. Fluorescence from five nm diameter CdSe-ZnS core-shell quantum-dots decay to half their peak value within 1.7 nm of the tip apex. This fluorescence decay-length is several times smaller than previous measurements for either silicon[9] or metal[4,8,11,13]tips.

In air, the silicon AFM probe oscillates above the sample surface with peak-peak amplitude typically between 10 and 40 nm. The tip-enhanced fluorescence signal is superimposed on a significant far-field fluorescence background induced by the diffraction limited excitation laser focus spot.[5] Oscillating the probe with amplitude three or more times the decay length decouples the tip-enhanced field from the background by inducing a strong modulation of the fluorescence photon count rate.[14] Data is recorded in the form of two primary streams: one that marks the arrival time of each detected photon, and one that timestamps the vertical position of the probe. Because the raw data is inherently digital in nature, multiple analysis algorithms can be applied to the data simultaneously without degradation of the signal. By filtering the data at the tapping frequency we suppress the background and generate single-photon fluorescence images of isolated quantum dots with lateral resolution below 10 nm.

References 1 and 2 are included below (J. M. Gerton, L. A. Wade, G. A. Lessard, Z. Ma, and S. R. Quake, Tip-enhanced Fluorescence Microscopy at 10 nanometer Resolution, *Phys. Rev. Lett.*, 2004, *93*, 180801 and Z. Ma, J.M. Gerton, L.A. Wade and S.R Quake, Fluorescence Near-Field Microscopy of DNA at sub-10 nm Resolution, *Phys. Rev. Lett.* **97**, 260801 (2006)) courtesy of the American Physical Society to whom they are copyrighted.

Tip-Enhanced Fluorescence Microscopy at 10 Nanometer Resolution

Jordan M. Gerton,* Lawrence A. Wade, Guillaume A. Lessard, Z. Ma, and Stephen R. Quake

Department of Applied Physics, California Institute of Technology, MC 128-95, Pasadena, California 91125, USA

(Received 12 December 2003; published 28 October 2004)

We demonstrate unambiguously that the field enhancement near the apex of a laser-illuminated silicon tip decays according to a power law that is moderated by a single parameter characterizing the tip sharpness. Oscillating the probe in intermittent contact with a semiconductor nanocrystal strongly modulates the fluorescence excitation rate, providing robust optical contrast and enabling excellent background rejection. Laterally encoded demodulation yields images with <10 nm spatial resolution, consistent with independent measurements of tip sharpness.

DOI: 10.1103/PhysRevLett.93.180801 PACS numbers: 07.79.Fc, 42.50.Hz, 61.46.+w, 78.67.Bf

The potential of near-field microscopy to optically resolve structure well below the diffraction limit has excited physicists, chemists, and biologists for almost 20 years. Conventional near-field scanning optical microscopy (NSOM) uses the light forced through a small metal aperture to locally excite or detect an optical response. The spatial resolution in NSOM is limited to 30–50 nm by the penetration depth of light into the metal aperture. More recently, apertureless-NSOM (ANSOM) techniques were developed which leverage the strong enhancement of an externally applied optical field at the apex of a sharp tip for local excitation of the sample [1–11]. The promised advantage of ANSOM is that spatial resolution should be limited only by tip sharpness (typically $\sim$10 nm). The resolution in most previous ANSOM experiments, however, was at best marginally better than NSOM and was inferior to expectations based on tip sharpness alone. Further, the external field used to induce enhancement led to a substantial background signal and to assertions that one-photon fluorescence is not appropriate for ANSOM [12,13]. These experiments fell short of their potential because they maintained a tip-sample gap of several nanometers, and thus did not thoroughly exploit the tightly confined enhancement.

Here, we demonstrate an ANSOM technique that fully exploits the available contrast and leads to spatial resolution that is limited only by tip sharpness. The problems associated with a tip-sample gap are overcome by oscillating the probe in intermittent contact with the sample. The detected signal is then composed of a modulated near-field portion that is superimposed on the far-field background. Subsequent demodulation decouples the two components and thus strongly elevates the near-field signal relative to the background. With this technique, we measured <10 nm lateral resolution via one-photon fluorescence imaging of isolated quantum dots, consistent with independent measurements of tip sharpness. The measured resolution is >3 times better than previous reports for quantum dots using one-photon fluorescence [8,9], and is $\sim$2 times better than previous measurements using higher-order optical processes (two-photon fluorescence [6], Raman scattering [4,5]) despite predictions to the contrary [12,13].

To better understand the advantages of this technique and to facilitate development of accurate physical models, it is crucial to rigorously characterize the spatial confinement of the enhancement effect. Previous investigations did not attain the level of precision necessary to differentiate between various theoretical models [4,7,14] and there was no experimental or theoretical consensus regarding either the functionality or the set of parameters governing the spatial confinement [12,15–18]. In this Letter, we show unambiguously that the enhancement decays strictly according to a power-law functionality moderated by a single parameter that characterizes the tip sharpness. The collective results shown here will impact not only nano-optics research, but also the application of ANSOM to a wide range of nanoscale systems at the interface between physics, biology, and chemistry.

Our instrument combines a custom optical layout with a commercial (Digital Instruments Bioscope) atomic force microscope (AFM). The excitation laser beam is focused through a glass coverslip (spot size: 350×1000 nm) using a 1.3 N.A. oil-immersion objective lens. The objective simultaneously collects fluorescence, which is then directed onto an avalanche photodiode through a system of spectral filters (background rejection-ratio $\sim 10^{10} : 1$). A beam-shaping mask is inserted into the excitation beam to generate a purely evanescent field above the glass interface (decay length: 120–250 nm) with a large polarization component along the probe axis [19] as required for field enhancement [15,20]. The focal spot is aligned with the AFM probe by means of a piezoactuated tip-tilt mirror, and the lateral position of the probe is controlled by closed-loop feedback. Uncorrected residual drift (0.05–0.2 nm/s) is the dominant source of uncertainty in the probe position.

The silicon AFM probe oscillates [21] with a typical peak-peak amplitude of 30–40 nm, assuring tip-sample contact at closest approach. In contrast, previous work

used very small oscillations (~1 nm) [7,8] or shear-force feedback [4,6,10,14] to maintain a tip-sample gap of several nanometers. Data are recorded to a computer disk in the form of two independent streams of time stamps: one that marks the arrival time of each detected photon, and one that marks a particular phase in each probe-oscillation cycle. Because the raw data are stored permanently in a lossless digital format, multiple analysis algorithms can be applied without degrading the signal.

Samples are prepared by drying a dilute solution of CdSe-ZnS core-shell quantum dots onto a clean glass coverslip. The dots have a mean diameter of ~5 nm and an emission spectrum centered near $\lambda = 600$ nm. The fluorescence rate is highly dynamic, exhibiting "blinking" and sudden changes in quantum yield (QY), in agreement with previous observations [8,22,23]. When a quantum dot is "on" and in a high QY state, a typical count rate of $\sim 2 \times 10^4$ sec^{-1} is measured with ~300 nW of illumination power.

To determine which parameters influence the tip-enhanced intensity distribution we measure the induced fluorescence rate as a function of tip-sample separation (z). The focal spot and AFM probe are centered on an isolated dot and the photon and probe-oscillation data streams are recorded for several seconds. A histogram of the phase delay (Δ) between the arrival time of each photon and the preceding probe-oscillation time stamp is computed. Each value of Δ is then mapped to the corresponding value of z to produce an approach curve (Fig. 1). Each approach curve is a convolution of the tip-enhanced intensity distribution and the excitation-probability distribution within the target. Thus, the fluorescence decays to half its peak value at larger z for increasing target size: 1.7, 4.3, and 6.3 nm for the quantum dot, nanorod, and sphere, respectively. Because of the convolution, the half-maximum at $z = 1.7$ nm for the quantum dot represents an upper limit for the spatial confinement of the tip-enhanced intensity profile. This value is several times smaller than previous measurements for either silicon [7] or metal [4,6,10,14] tips.

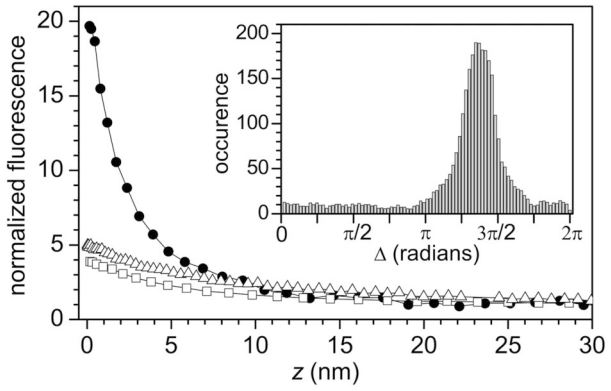

FIG. 1. Enhancement near a sharp silicon probe. Approach curves for a 5 nm diameter quantum dot (solid circles), a 5 × 20 nm CdSe-ZnS nanorod (open squares), and a 20 nm diameter dye-doped latex sphere (open triangles). Additional approach curves extending to $z \sim 150$ nm (not shown) were flat beyond the enhancement region. The vertical scale is normalized to the count rate for a retracted probe. 10% uncertainties in the horizontal and vertical scales originate from calibration of the probe-oscillation amplitude and noise in the normalization factor, respectively. The lines connect the data points. Inset: Histogram of phase delays for the quantum dot.

The fluorescence count rate is enhanced by a factor of 19 for the quantum dot, a factor of 3 for the nanorod, and a factor of 4 for the 20 nm diameter fluorescent sphere. Previous measurements that used silicon tips showed less than a fivefold increase for quantum dots [8,9] and less than a 50% increase for 20 nm spheres [7]. Further, those experiments were complicated by interference effects that yielded a net suppression of the signal relative to the fluorescence background. An additional experiment used a modified aperture-type near-field tip and showed evidence of enhancement that was difficult to quantify [14].

Figure 2 plots each approach curve from Fig. 1 on a log-log scale. Unity is subtracted from the vertical scales of Fig. 1 and the horizontal scales are offset by the fitting parameter a, whose physical relevance is discussed below.

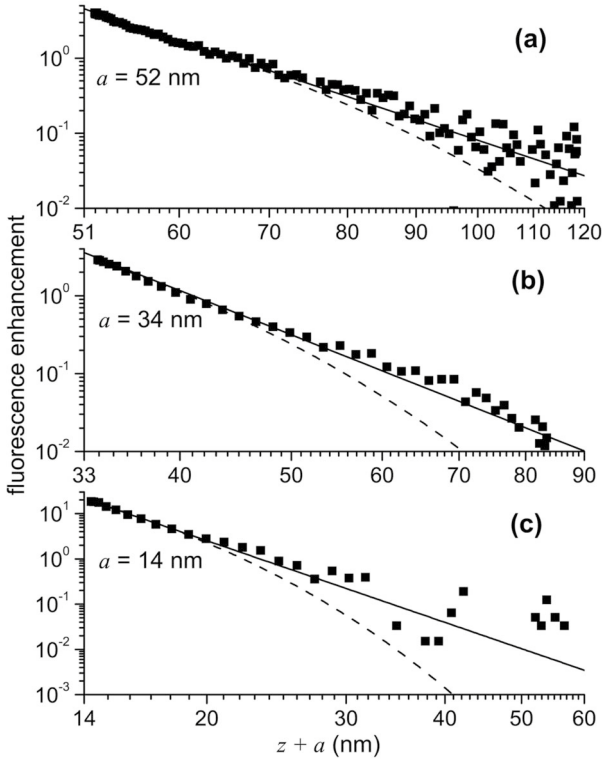

FIG. 2. Least-squares fit to the approach curve for (a) 20 nm diameter dye-doped sphere; (b) nanorod; and (c) spherical quantum dot. Fits to the power law of Eq. (1) (solid curves) and an exponential function (dashed curves) are shown with the data. The horizontal scales are offset by the fitted values of a, and unity is subtracted from the vertical scales.

The linear appearance of the data on the log-log scale indicates a power-law decay, and the fluorescence enhancement (ζ) is fit to the function

$$\zeta = \frac{F(z)}{F_\infty} - 1 = \kappa^2 \left(\frac{a}{z+a} \right)^6, \qquad (1)$$

where $F(z)/F_\infty$ is the detected fluorescence rate normalized to the background rate (F_∞), and κ is the field-enhancement factor. The solid curves show least-squares fits to Eq. (1) (κ, a free parameters) while the dashed curves are exponential decays. The data are clearly consistent with a power law, and deviate systematically from the best exponential fit. Previously, both power law [7,14] and exponential [4] decays were fit to experimental data with equal success. The precision of those experiments was insufficient to differentiate between various models because they did not probe the high-contrast region within several nanometers of tip-sample contact.

The measured $(z+a)^{-6}$ decay corresponds to the "near-field" term in the expression for the field intensity near a point dipole, where z is the distance between the apex of the tip and the sample surface. Thus in the limit of an infinitesimally small target particle, the tip-enhanced field is equivalent to a dipole field whose singularity is located within the probe at a distance a from the apex, where a is the tip radius-of-curvature. For finite-sized target particles, the parameter a is a measure of the degree of convolution between the intensity distribution and the excitation-probability distribution, and as expected the fitted values of a increase for larger targets. For smaller targets, a is converging to a value ($\sim$10 nm) that is characteristic of the silicon probes used here. This is evidence that the field decay is indeed moderated only by the sharpness of the tip.

Because this technique utilizes a large probe-oscillation amplitude, the fluorescence rate is modulated with maximum contrast, from the background level when the tip is 30–40 nm above the sample to the peak enhancement at tip-sample contact (Fig. 1). The tip-enhanced intensity profile has no "far-field" component proportional to r^{-2} (Fig. 2) and the corresponding fluorescence profile arises from the "near-field" intensity distribution only. Thus, the depth of fluorescence modulation that results from oscillation of the probe is decoupled from the far-field background and the near-field signal is easily extracted by subsequent demodulation.

A demodulated fluorescence image of a nanorod is shown in Fig. 3(a). The image was generated by raster scanning the AFM probe at a rate of 4 lines/s and then dividing each line into spatiotemporal pixels. These scan rates are at least 5 times faster than previous work for one-photon fluorescence [7–9] and 10 times faster for both two-photon fluorescence [6] and Raman scattering [4]. Pixel values are computed offline as the component of the photon-time-trace's Fourier power spectrum at the probe-oscillation frequency

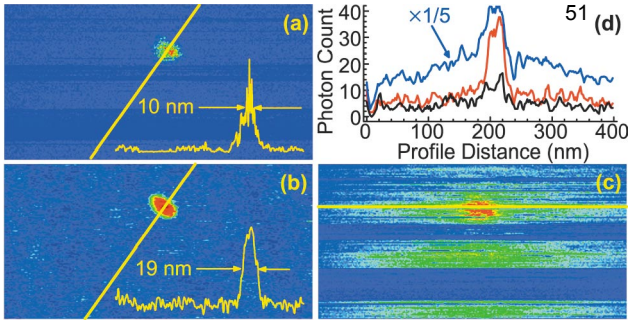

FIG. 3 (color). Tip-enhanced fluorescence image of a nanorod. (a) Fluorescence demodulation signal. (b) AFM probe height (5 nm at peak). (c) Total photon count. Insets in (a) and (b) show signal profiles along the designated axis of length 250 nm. Blue curve in (d) shows the total photon count ($\times$ 0.2) along the horizontal axis in (c), while red and black curves show the photon count within two ranges of tip-sample separation: $0 < z < 0.4$ nm (red) and $2.5 < z < 4.5$ nm (black). Field-of-view is 400 $\times$ 200 nm: 256 lines of 1024 pixels each.

$$P = \left(\sum_i \sin\Delta_i \right)^2 + \left(\sum_i \cos\Delta_i \right)^2, \qquad (2)$$

where Δ_i are the measured phase delays and the summation is over all detected photons for the given pixel. When the probe is in the lateral vicinity of the target, the Δ_i are biased toward the phase value of tip-sample contact where the fluorescence rate is maximally enhanced. Otherwise, the Δ_i are uniformly distributed and P vanishes to within the shot noise. Comparing Figs. 3(a) and 3(b) shows that the spatial resolution of the demodulated image (see below) is comparable to the tip sharpness and surpasses even the AFM resolution. Comparing Figs. 3(a) and 3(c) demonstrates the effectiveness of the analysis [Eq. (2)] in suppressing the fluorescence background.

Figure 3(d) shows three signal profiles along the horizontal axis indicated in Fig. 3(c) corresponding to the summation of photons over the entire probe-oscillation-cycle (blue), and within a tip-sample separation range of $0 < z < 0.4$ nm (red), and $2.5 < z < 4.5$ nm (black). Here, horizontal profiles are chosen to avoid the regions of quantum-dot blinking [dark stripes in Fig. 3(c)]. As indicated on the figure, the data corresponding to the blue profile have been divided by a factor of 5. Nearly 20% of the detected photons are emitted when the tip apex is within 0.4 nm of the sample surface (red curve) even though this corresponds to only $\sim$3% of the oscillation period. The black curve approximates the typical scanning conditions of previous ANSOM experiments which maintained a tip-sample gap roughly in this range [7–9]. Clearly, those conditions yield both inferior contrast and resolution compared to our technique.

The approach curve measurements (Figs. 1 and 2) suggest a straightforward approach for estimating the

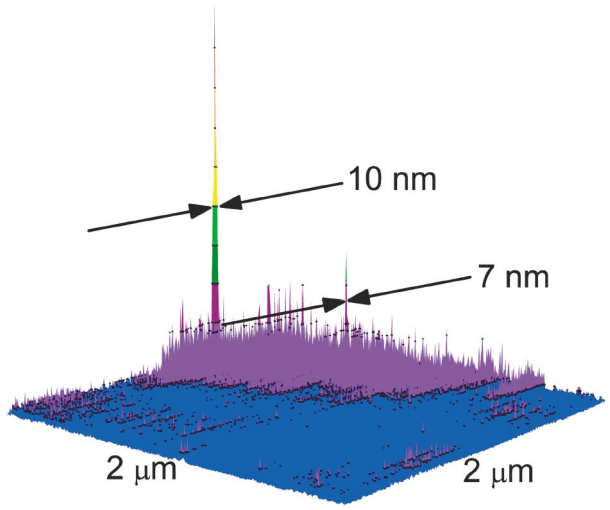

FIG. 4 (color). Tip-enhanced fluorescence image of quantum dots. The degree of contrast is emphasized by false-color relief. The image contains 512 lines of 1000 pixels each. The arrows indicate the measured FWHM for two quantum dots.

spatial resolution. The tip-enhanced field is modeled by a point dipole using a conservative estimate for tip-curvature ($a = 14$ nm) as suggested by the quantum-dot approach curve in Fig. 2(c). A Monte Carlo simulation is then used to generate "mock" data from two hypothetical point sources separated by some distance and the analysis algorithm [Eq. (2)] is applied. The minimum resolvable separation between the point sources is then determined by applying the Sparrow criterion to the demodulated image, i.e., where the central dip between the two sources vanishes [24]. Use of the Sparrow rather than the Rayleigh criterion assures that the estimated resolution is independent of the particular moment calculated in Eq. (2). The simulations suggest a spatial resolution of 11–12 nm for the nanorod images shown in Fig. 3. Figure 4 shows a fluorescence demodulation image of spherical quantum dots in false-color relief. The arrows indicate the measured FWHM for two dots, and the model suggests a spatial resolution of ~8 nm for the smaller one.

In conclusion, we made the first definitive measurement of the tip-enhanced optical field at the apex of a sharp probe and rigorously confirmed a dipolelike model. The technique developed for these measurements overcomes several major obstacles in ANSOM performance and led to the first one-photon fluorescence images with resolution below 10 nm. In contrast to previous work, the tip-enhanced excitation rate is maximized because the probe apex intermittently contacts the sample and thus the enhanced field is probed at atomic-scale distances from the apex. The intermittent tip-sample contact also induces modulation of the excitation rate; demodulating the resultant signal strongly suppresses the problematic far-field background and enables spatial resolution limited only by tip sharpness. The improvements in background suppression and spatial resolution will be even more acute for multiphoton processes (surface-enhanced Raman scattering; coherent anti-Stokes Raman scattering; two-photon fluorescence) compared to one-photon fluorescence, because the induced signal is then more strongly confined at the tip apex. In the future, it may be possible to image samples in a wet environment to measure dynamic processes in molecular-scale structural biology. Finally, it may also be possible to use carbon single-wall nanotubes attached to AFM probes [25,26] to further improve spatial resolution.

We thank Delia Milliron, Ben Boussert, and Paul Alivisatos for the nanocrystals and acknowledge the financial support of Bruce Burrows and Pharmagenomix Inc. J. M. G. was partially supported by the Beckman Institute.

*Permanent address: University of UT, Department of Physics, 115 South 1400 East, Salt Lake City, UT 84112.

[1] F. Zenhausern, Y. Martin, and H. K. Wickramasinghe, Science **269**, 1083 (1995).
[2] H. F. Hamann, A. Gallagher, and D. J. Nesbitt, Appl. Phys. Lett. **73**, 1469 (1998).
[3] R. Hillenbrand and F. Keilmann, Appl. Phys. Lett. **80**, 25 (2002).
[4] A. Hartschuh *et al.*, Phys. Rev. Lett. **90**, 095503 (2003).
[5] T. Ichimura *et al.*, Phys. Rev. Lett. **92**, 220801 (2004).
[6] E. J. Sánchez, L. Novotny, and X. Sunney Xie, Phys. Rev. Lett. **82**, 4014 (1999).
[7] H. F. Hamann *et al.*, J. Chem. Phys. **114**, 8596 (2001).
[8] V. V. Protasenko *et al.*, Opt. Commun. **210**, 11 (2002).
[9] V. V. Protasenko, A. Gallagher, and D. J. Nesbitt, Opt. Commun. **233**, 45 (2004).
[10] A. Kramer *et al.*, Appl. Phys. Lett. **80**, 1652 (2002).
[11] A. Bouhelier *et al.*, Phys. Rev. Lett. **90**, 013903 (2003).
[12] Y. Kawata, C. Xu, and W. Denk, J. Appl. Phys. **85**, 1294 (1999).
[13] L. Novotny, J. Am. Ceram. Soc. **85**, 1057 (2002).
[14] H. G. Frey *et al.*, Appl. Phys. Lett. **81**, 5030 (2002).
[15] L. Novotny, R. X. Bian, and X. S. Xie, Phys. Rev. Lett. **79**, 645 (1997).
[16] J. Azoulay *et al.*, Europhys. Lett. **51**, 374 (2000).
[17] J. L. Bohn, D. J. Nesbitt, and A. Gallagher, J. Opt. Soc. Am. A **18**, 2998 (2001).
[18] Y. C. Martin, H. F. Hamann, and H. K. Wickramasinghe, J. Appl. Phys. **89**, 5774 (2001).
[19] B. Sick *et al.*, J. Microsc. **202**, 365 (2001).
[20] L. Aigouy *et al.*, Opt. Lett. **24**, 187 (1999).
[21] We used NanoDevices Multi75 (50-80 kHz oscillation frequency) and TAP300 (250-350 kHz) cantilevers.
[22] R. G. Neuhauser *et al.*, Phys. Rev. Lett. **85**, 3301 (2000).
[23] M. Kuno *et al.*, J. Chem. Phys. **112**, 3117 (2000).
[24] E. Hecht, *Optics* (Addison-Wesley, Reading, 1990), 2nd ed.
[25] J. H. Hafner *et al.*, J. Phys. Chem. B **105**, 743 (2001).
[26] L. A. Wade *et al.*, Nano Lett. **4**, 725 (2004).

Fluorescence Near-Field Microscopy of DNA at Sub-10 nm Resolution

Ziyang Ma,* Jordan M. Gerton,† Lawrence A. Wade, and Stephen R. Quake*

Applied Physics and Physics, California Institute of Technology, Pasadena, California 91125, USA

(Received 21 October 2005; published 27 December 2006)

We demonstrate apertureless near-field microscopy of single molecules at sub-10 nm resolution. With a novel phase filter, near-field images of single organic fluorophores were obtained with ~sixfold improvement in the signal-to-noise ratio. The improvement allowed pairs of molecules separated by ~15 nm to be reliably and repeatedly resolved, thus demonstrating the first true Rayleigh resolution test for near-field images of single molecules. The potential of this technique for biological applications was demonstrated with an experiment that measured the helical rise of *A*-form DNA.

DOI: 10.1103/PhysRevLett.97.260801 PACS numbers: 07.79.Fc, 42.50.Hz, 87.15.−v, 87.64.Xx

For nano- and molecular science and technology, near-field optical microscopy provides a technique to measure and manipulate structures at subdiffraction limited resolution. The use of a sharp apertureless tip to locally perturb the fields at the sample with apertureless near-field scanning optical microscopy (ANSOM) has allowed spatial resolution at or surpassing 20 nm using elastic scattering [1,2], Raman scattering [3,4], and fluorescence excitation [5,6]. With fluorescence ANSOM, fluorescence of the sample is modified by the proximity of the tip that enhances the excitation field near it, but at the same time induces nonradiative energy transfer (fluorescence quenching) [7]. As a result of the two competitive effects, only single folds of fluorescence enhancement [8–14] or small fractions of fluorescence quenching [15,16] can be measured. Detection of the small high-resolution signal against the classical signal excited by the laser illumination has remained the main concern of fluorescence ANSOM.

Single molecules are widely used as fluorescent tags or reporters in biology [17], sensitive probes in materials and physical chemistry [18], and model single quantum systems for studying light-matter interactions [18]. Near-field optical imaging of single molecules has intrigued scientists since the demonstration by Betzig *et al.* [19]. Unfortunately, it has been a challenge [7,16] to image fluorescent molecules with ANSOM due to the inherent molecular fluorescence fluctuation [inset of Fig. 1(b)] and the limited number of photons available before photochemical destruction (photobleaching) of the molecule. Only two experiments have achieved resolution at 30–40 nm by imaging isolated molecules in vacuum or in a matrix [11] or using a nanofabricated metal tip on top of a fiber aperture [20]. More recently, it was demonstrated that properly designed ''nanoantennas'' can enhance the power of the optical near field by several orders [21,22] or reduce nonradiative energy transfer [23], thus holding promise for imaging single molecules. In this Letter, we demonstrate single-molecule ANSOM imaging at sub-10 nm resolution using a novel phase filter. For the first time, two molecules separated by less than 15 nm can be resolved with ANSOM. We applied this technique to measure the helical rise of *A*-form DNA. The progress we present will accelerate the application of fluorescence ANSOM in the life sciences.

The microscope setup was described previously [6]. Briefly, an atomic force microscope (tapping mode: ~80 kHz) is combined with an inverted confocal optical microscope, with the silicon tip (FESP, Veeco Instruments) aligned with the laser focal spot [Fig. 1(a)]; the fluorescence photons and the beginning of the tip oscillation cycles were recorded as time stamps.

We imaged isolated Cy3 molecules and Cy3 molecule pairs. Each Cy3 molecule is attached to the 5′ end of a

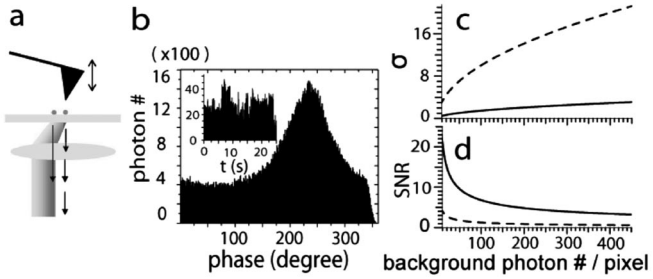

FIG. 1. (a) Illustration of the microscope. The linearly polarized beam, passing through a mask with a wedged window (not shown), is at total internal reflection at the substrate-air interface (focus area ~350 × 1000 nm) to achieve a large field component along the tip axis. (b) Tip-oscillation phase histogram of the photons. The inset is a typical fluorescence time trace of a Cy3 molecule, where the vertical axis is the photon count per 0.01 s. (c) The background noise (standard deviation) obtained from the phase filter (solid curve) and from the unfiltered shot noise, $\sqrt{n}$ (dash curve). The horizontal axis is the same as (d). (d) The SNR calculated as the image pixel signal divided by the background noise from the phase filter (solid curve) and from the unfiltered shot noise (dash curve). The image pixel signal is $0.60fN/3$ (f: fluorescence enhancement; N: photon number per pixel emitted by a typical molecule) for the solid curve according to Eq. (1), and $0.75fN/3$, which is the direct sum of the near-field photons [Fig. 1(b)], for the dash curve. For both curves, we used $f = 5$, $N = 10$.

60-mer single-stranded DNA (ssDNA). Each pair of Cy3 molecules is linked by a 60 bp double-stranded DNA (dsDNA), prepared by annealing two complementary 5′-labeled ssDNA. The dsDNA chain is shorter than the DNA persistence length (~150 bp), so it is rigid. To obtain topographical atomic force microscope (AFM) images of the DNA molecules, we used glass–mica hybrid slides [24]. To prepare the samples, 1 μl of 10 nM DNA solution was spread on the mica surface and evaporated dry, then the surface was rinsed with deionized water and dried with nitrogen gas. The majority of the molecules on the surface produced more than 10^5 photon counts, allowing >20 s imaging time.

The signal of fluorescence ANSOM contains the near-field and far-field components excited by the optical near-field and propagating laser illumination, respectively. With single molecules, fluorescence enhancement is only ~twofold to fivefold [Fig. 1(b)], comparable to the fluctuation of the far-field signal [inset of Fig. 1(b)]. In previous work [6], we demonstrated that signal demodulation separates the far-field and near-field signals successfully. This method, however, requires a large number of photons and works only for intense targets, such as quantum dots (Fig. 4 of Ref. [6]). To find an efficient separation method, we studied the 2×10^5 fluorescence photons from an isolated Cy3 molecule probed by an oscillating tip. Figure 1(b) is the tip-oscillation phase histogram of the photons, from which phase ϕ_0 for the maximum fluorescence enhancement can be determined. It was found from experiments that ϕ_0 remains the same with the same type of tip, and the profile of fluorescence enhancement can be approximated by

$$g[\phi - \phi_0] = \exp\left(-\frac{|\phi - \phi_0|_p^2}{60^2}\right) \qquad (0 \le \phi, \phi_0 < 360)$$

where $|\phi - \phi_0|_p$ is defined as $\min(|\phi - \phi_0|, |360 - |\phi - \phi_0||)$. We calculated the raw near-field signal S_{rn} of a pixel as

$$S_{rn} = \sum_{|\phi-\phi_0|_p \le 60} \exp\left(-\frac{|\phi - \phi_0|_p^2}{60^2}\right) D[\phi], \qquad (1)$$

where $D[\phi]$ is the number of photons at phase ϕ. This formula is a bandpass phase filter that passes photons within 60 deg of ϕ_0 [Fig. 1(b)] with weights determined from g. The width of the bandpass window was optimized to increase the passed photons and to reduce the bleed-through between the near-field and far-field signals. The far-field signal S_f was calculated as

$$S_f = \sum_{|\phi-(\phi_0-180)|_p \le 60} \exp\left(-\frac{|\phi - (\phi_0 - 180)|_p^2}{60^2}\right) D[\phi] \qquad (2)$$

such that molecules outside the near-field volume of the tip contribute equally to S_{rn} and S_f. S_f was then averaged with those of its four neighboring pixels to get $\bar{S}_f$. The[54] pixel signal was calculated as $S_n = S_{\mathrm{rn}} - \bar{S}_f$ for $S_{\mathrm{rn}} > \bar{S}_f$ and $S_n = 0$ for $S_{\mathrm{rn}} < \bar{S}_f$.

The phase filter effectively suppresses the noise of the background, where we refer to the background as an area without near-field images. One can estimate the effect of the filter by approximating g with a top hat function, with which we can calculate the mean and variance of the background as $\tilde{x} = \sum_{i=0}^{\infty}\sum_{j=0}^{\infty} jP(5i, 5n/3) \times P(i + j, n/3)$ and $\tilde{\sigma}^2 = \sum_{i=0}^{\infty} P(5i, 5n/3)\{\sum_{j=0}^{\infty}(j - \tilde{x})^2 P(i + j, n/3) + \sum_{j=0}^{i} \tilde{x}^2 P(j, n/3)\}$, respectively, where i and j are dummy variables, n is the average photon number per pixel in the background, and $P(a, b) = (e^{-b}b^a)/a!$ is the Poisson probability density. The effect of using a Gaussian for g causes only a small change in the standard deviation of the background, giving $\sigma = 0.75\tilde{\sigma}$. Compared with the unfiltered shot noise, the background noise is effectively suppressed with the phase filter [Fig. 1(c)], which provides ~sixfold improvement in the signal-to-noise ratio (SNR) and makes it possible to image multiple fluorescent targets in the focal spot [Fig. 1(d)]. Assuming that a far-field illuminated molecule emits 10 photons per pixel, good SNR (>7) can be obtained with up to ten molecules in the focal spot and fair SNR (>3) with several tens of molecules in the focal spot [Fig. 1(d)]. The SNR obtained in experiments (Figs. 2 and 4), determined as the difference between the peak image signal and the background baseline divided by the variation of a 100 × 100 nm background area, is in good agreement with the calculation [Fig. 1(d)].

We imaged 211 isolated single Cy3 molecules. The images are either symmetric [Fig. 2(a)] or elongated [Fig. 2(b)], due to different molecular dipole orientations

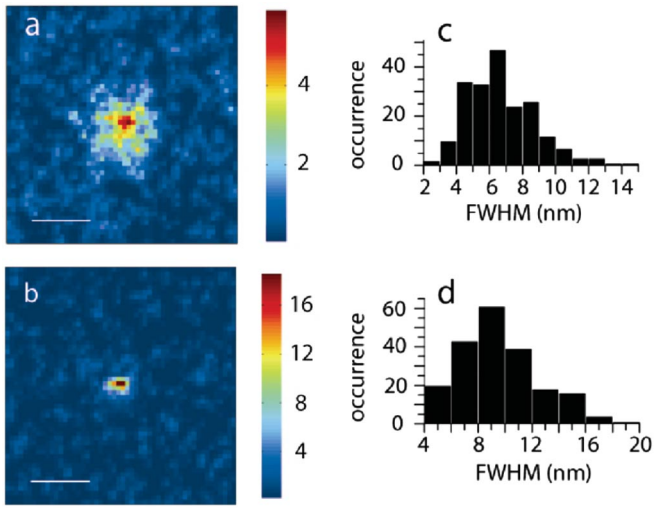

FIG. 2 (color). (a), (b) Near-field images of isolated Cy3 molecules. Each figure was extracted from a 1 × 1 μm, 512 × 512 pixel image. The SNR for (a) and (b) is 16.2 and 25.5, respectively. Scale bars: 25 nm. (c), (d) Histograms of FWHM measured along the minor and major directions, respectively.

(discussed below). Histograms of full width at half maximum (FWHM) measured along the minor and major directions of the 211 images are shown in Figs. 2(c) and 2(d), with the average at 6.8 and 9.6 nm, respectively. It is clear that simply choosing the linewidth of a single image is not an accurate method for determining resolution, for the images are highly variable. Here we define an average resolution of 8.2 nm, which is ~3–4 times better than the previous best ANSOM measurements and close to 1 order better than typical results of apertured near-field microscopy.

To better understand the results, we simulated images of single molecules using the electrostatic dipole model of the tip. This model was adopted in both fluorescence ANSOM and scattering ANSOM [1,25] and was supported by numerical simulations [26]. According to the model, the total field amplitude is

$$\vec{E}(\vec{r}) = E_0\left[\hat{z} + \alpha\left(\frac{3z}{r^4}\hat{r} - \frac{1}{r^3}\hat{z}\right)\right], \quad (3)$$

where E_0 is the external laser field, α is determined experimentally and the coordinate origin is at the tip center. Using $[E(r) \cdot p(\theta, \varphi)]^2$ as the image intensity, simulation results [Fig. 3(a)] show that as $\vec{p}$ tilts away from the tip axis, the image becomes elongated and the image center shifts away from the molecule; when $\vec{p}$ is perpendicular to the tip axis ($|\theta - 90°| \leq 0.8°$), the image has two symmetric "lobes"; when θ is close to 90° ($0.8° \leq |\theta - 90°| \leq 20°$), there is a small region where the signal is below the background. For nonzero φ, the images are simply φ-degree rotation of those for $\varphi = 0$ [Fig. 3(a)], for the field is symmetric about the tip axis. Simulation patterns for θ at or close to 90° were experimentally observed [Figs. 3(b)–3(d)], providing direct support for the electrostatic dipole model.

Measuring true resolution has long been a challenge in near-field microscopy; one of the strongest tests is to make a "Rayleigh" resolution measurement, in which two proximate point sources are resolved. To our knowledge there have been no rigorous near-field measurements such as this made with single molecules, which are excellent approximations of a point source. With the phase filter, we were able to resolve two Cy3 molecules linked by a 60 bp dsDNA oligonucleotide. Figures 4(a)–4(c) are the near-field optical images of such molecule pairs, where Figs. 4(d)–4(f) are the corresponding topographical AFM images. ANSOM has a better resolution than AFM even with the same tip, because the force involved in AFM, which is proportional to the inverse of the tip-sample distance [27], decays much more slowly than the optical near field. There are no previous AFM experiments that resolved DNA molecules as short as 15 nm; instead, round images for short DNA molecules were observed in this [Fig. 4(d)] and previous experiments [28].

We imaged a total of 389 dsDNA oligonucleotides, 29% of which showed resolvable Cy3 pairs. The Cy3 labeling efficiency for each DNA strand is about 80%, so we expect that 67% of the optically detectable DNA oligonucleotides are actually labeled with two Cy3 molecules. Factors such as imperfect annealing, photobleaching, and worn tips can all contribute to the failure to resolve the rest. As a control experiment, the 211 images of single Cy3 molecules were analyzed in the same fashion and double-lobed artifacts were found in only 4% of the images [Fig. 4(h)], which is a

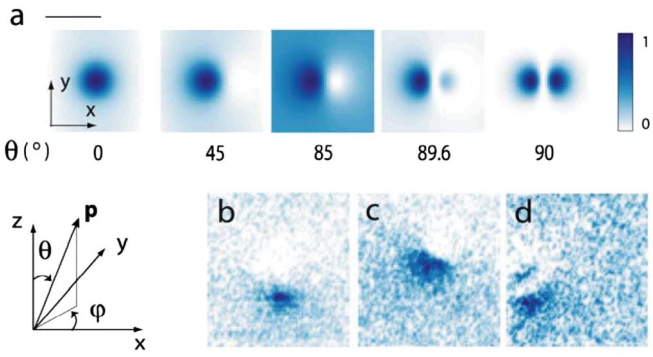

FIG. 3 (color). (a) Simulated images with the tip radius at 10 nm and fluorescence enhancement at 5. Scale bar: 20 nm. (b)–(d) Experimental images (150 × 150 nm) showing the same patterns as the simulated ones. In these images, S_{rn} was used as the pixel signal.

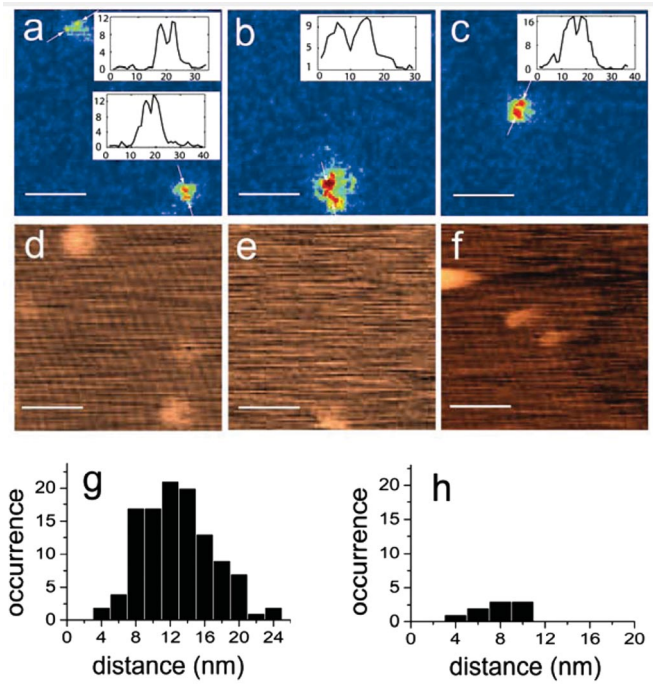

FIG. 4 (color). (a)–(c) Near-field images of Cy3 pairs. The SNR is 12.4 and 15.9 for (a), 16.1 for (b), and 20.4 for (c). The insets show the profiles with line cut through the image centers (indicated by arrows), where the horizontal axis is in pixels (1 pixel = 1.95 nm) and the vertical axis is the pixel signal. (d)–(f) AFM images corresponding to images (a)–(c), respectively. Scale bars: 50 nm. (g) Histogram of distances between the resolved Cy3 molecules. (h) Histogram of distances between the two artifactual lobes of single Cy3 molecules.

vast improvement over a previous method which has artifacts in all images [20].

With the resolved Cy3 molecule pairs, the end-to-end distances of the 60 bp DNA oligonucleotides can be measured [Fig. 4(g)]. The statistical result is 13.0 nm ± 4.1 nm (standard deviation) with standard error of the mean $\sigma_\mu = 0.4$ nm. Random factors that contribute to the distribution of the measurements include limited precision in determining the image centers, shifting of the images, and the flexible carbon linker (~0.6 nm) between the Cy3 molecule and DNA. Systematic errors also exist in the result. Simulation shows that the two images shift toward each other because the tip enhances both molecules when it is in between them; the shift increases with larger tip radius. The linewidth of the majority of the images indicates an upbound of the tip radius at 15 nm, at which a 2.5 nm shift was simulated for two molecules separated by 15 nm. Therefore, the precision of our measurement of the DNA length has a statistical error of 3% and a systematic error up to 20%.

DNA structure depends strongly on humidity and takes the *A*-form and *B*-form structure at low and high humidity, respectively. It is now understood that DNA-binding drugs and proteins can induce local conformational conversion between the two forms [29]. In our experiments, the DNA molecules were imaged at humidity (~30%) well below the 73% threshold for the *A*-form DNA. An unresolved paradox in x-ray diffraction studies of *A*-form DNA is that fibers of long DNA molecules with mixed sequences yield a consistent value of 2.6 Å/bp for the helical rise [30], but crystal structures of small oligonucleotides (~10 bp) reveal an average value of 2.83 Å/bp with a standard deviation of ~0.36 Å/bp across different sequences [31]. The source of the discrepancy is as yet unresolved, although crystal artifacts, molecular weight effects, and incomplete sequence sampling may all play a role. Our measurements described above allow an independent determination of the helical rise, and do not suffer from artifacts due to crystal packing or small molecular weights. The result (2.17 Å/bp) agrees with the x-ray data of fibers within one sigma of our largest estimated experimental error and falls within the two sigma limit of the sequence-dependent variation observed in crystal structure data.

The phase filtering method should be applicable to nanoantennas [21–23] and supersharp carbon nanotube probes [32] with which both the resolution and the precision can be improved. With the advances of AFM technology, such as imaging in water and fast frame imaging speeds, it may ultimately be possible to combine optical resolution approaching that of electron microscopy with the ability to image biomolecules in physiological conditions.

The authors thank G. Lessard for contributions to the development of initial data acquisition and data analysis algorithms. This work was supported by Pharmagenomix Inc. and the NIH Director's Pioneer program.

*Present Address: Dept. of Bioengineering, Stanford University and Howard Hughes Medical Institute, Stanford, CA 94305, USA.

†Present Address: University of Utah, Dept. of Physics, 115 South 1400 East, Salt Lake City, UT 84112.

[1] F. Zenhausern, Y. Martin, and H. K. Wickramasinghe, Science **269**, 1083 (1995).
[2] R. Hillenbrand and F. Keilmann, Appl. Phys. Lett. **80**, 25 (2002).
[3] A. Hartschuh *et al.*, Phys. Rev. Lett. **90**, 095503 (2003).
[4] T. Ichimura *et al.*, Phys. Rev. Lett. **92**, 220801 (2004).
[5] E. J. Sánchez, L. Novotny, and X. S. Xie, Phys. Rev. Lett. **82**, 4014 (1999).
[6] J. M. Gerton *et al.*, Phys. Rev. Lett. **93**, 180801 (2004).
[7] J. Azoulay *et al.*, Europhys. Lett. **51**, 374 (2000).
[8] H. F. Hamann, A. Gallagher, and D. J. Nesbitt, Appl. Phys. Lett. **76**, 1953 (2000); H. F. Hamann *et al.*, J. Chem. Phys. **114**, 8596 (2001).
[9] V. V. Protasenko *et al.*, Opt. Commun. **210**, 11 (2002).
[10] V. V. Protasenko, A. Gallagher, and D. J. Nesbitt, Opt. Commun. **233**, 45 (2004).
[11] V. V. Protasenko and A. C. Gallagher, Nano Lett. **4**, 1329 (2004).
[12] J. Azoulay *et al.*, J. Microsc. **194**, 486 (1999).
[13] N. Hayazawa, I. Inouye, and S. Kawata, J. Microsc. **194**, 472 (1999).
[14] A. Kramer *et al.*, Appl. Phys. Lett. **80**, 1652 (2002).
[15] T. J. Yang, G. A. Lessard, and S. R. Quake, Appl. Phys. Lett. **76**, 378 (2000).
[16] W. Trabesinger *et al.*, J. Microsc. **209**, 249 (2003); W. Trabesinger *et al.*, Appl. Phys. Lett. **81**, 2118 (2002).
[17] S. Weiss, Science **283**, 1676 (1999).
[18] W. E. Moerner and M. Orrit, Science **283**, 1670 (1999).
[19] E. Betzig and R. J. Chichester, Science **262**, 1422 (1993).
[20] H. G. Frey *et al.*, Phys. Rev. Lett. **93**, 200801 (2004).
[21] P. J. Schuck *et al.*, Phys. Rev. Lett. **94**, 017402 (2005).
[22] P. Mühlschlegel *et al.*, Science **308**, 1607 (2005).
[23] J. N. Farahani *et al.*, Phys. Rev. Lett. **95**, 017402 (2005).
[24] A thin layer (~2 μm) of mica was lifted off a mica sheet and placed on a clean glass cover slide; bonding between the two surfaces is immediate, probably due to van der Waals forces. The mica surface was treated with 20 mM $MgCl_2$ and rinsed by deionized water.
[25] B. Knolland and F. Keilmann, Nature (London) **399**, 134 (1999).
[26] A. Bouhelier *et al.*, Phys. Rev. Lett. **90**, 013903 (2003).
[27] F. J. Giessibl, Rev. Mod. Phys. **75**, 949 (2003).
[28] H. G. Hansma, Nucleic Acids Res. **24**, 713 (1996).
[29] X.-J. Lu, Z. Shakked, and W. K. Olson, J. Mol. Biol. **300**, 819 (2000).
[30] S. B. Zimmerman, Annu. Rev. Biochem. **51**, 395 (1982).
[31] X.-J. Lu and W. K. Olson, Nucleic Acids Res. **31**, 5108 (2003).
[32] J. H. Hafner *et al.*, J. Phys. Chem. B **105**, 743 (2001); L. A. Wade *et al.*, Nano Lett. **4**, 725 (2004).

3.2 Wet TEFM Imaging of Live Cells and Membrane-bound Proteins

The basic concepts that enable wet TEFM imaging are very similar to those upon which the dry TEFM microscope was built. Wet TEFM also relies on the modulation of fluorescence when the tip is proximate to a fluorophore. As with the original microscope the wet imaging TEFM also combined a homebuilt TIRF optical microscope with an atomic force microscope.[15] Detailed pictures of the wet TEFM instrument and filter specifics are presented in Appendix E. The data acquisition system specification and design is also included in Appendix E along with the complete image processing code developed for this project.

TEFM imaging of live cells is substantially more difficult than imaging hard, dry samples on atomically smooth surfaces. To a large extent this is true because this technique fundamentally relies on tip stimulated, and modulated, fluorescence. Achieving near-field, tip stimulated fluorescence essentially requires that the AFM probe contact the sample fluorescent labels. It also requires that the AFM probe be oscillated, so that tip-sample contact is periodic, to enable modulation of the sample fluorescence.

In AFM terms, probe oscillation with periodic contact is referred to as 'tapping mode' operation. Unfortunately wet tapping mode imaging of living cells is very, very difficult. Instead of tapping mode, contact mode, in which the tip remains in constant contact with the sample being imaged, is used by the AFM community for imaging biological samples. Also, there were no prior studies, theoretical or experimental, of tip-enhanced fluorescence in a liquid environment.

This discussion is focused on those issues that are specific and unique to wet-sample TEFM imaging. As a result of these challenges, many innovations were developed to enable the capability to image live cells. Some of these challenges, and the solutions that solved them, are described below.

The objects being observed (cells) are large compared with the ~7 micron Field-of-View (FoV) our microscope was capable of.

In the dry TEFM, the sample was kept still as the laser and AFM probe were synchronously rastered over it. The FoV of the microscope described in our PRL publications was limited by the range of the tip-tilt mirror that directed the excitation laser such that it stayed focused on the tip of the AFM probe as it was rastered over the sample. Therefore a new mode of operation, sample scanning, was introduced. To accomplish this an nPoint piezoelectric X-Y sample scanning stage with a 100 micron range[16] was installed. The data acquisition and control software and image processing software were also modified to enable operation in this new mode. With the sample stage in place the laser focal spot was focused onto the AFM probe tip. The laser and AFM probe were then held stationary in X-Y while the sample was rastered. With this change the largest area that could be scanned was increased from ~49 square microns to ~10,000 square microns. This is large enough to fully capture one or more N2a cells.

To image a sequence of cells within a given culture dish the nPoint sample stage was mounted to a second, long-range X-Y translation stage. This long-range X-Y translation stage is driven with two manual 100-pitch thumbscrews. These move the nPoint sample stage approximately 125 microns with one half-turn.

The microscope objective used in our previous work was incompatible with doing TIRF with water above the coverslip.

Total internal reflection fluorescence microscopy, as implemented in our TEFM, relies on an excitation laser the exits the microscope objective at such an extreme angle that it reflects at the glass coverslip-sample interface rather than transmitting. The reflected light, being electromagnetic radiation, induces an evanescent field on the sample side of this interface. It is this evanescent field that we use for exciting fluorescence in the sample.

The maximum angle at which a collimated laser beam can leave an objective is described by the objective's Numerical Aperture (NA). The higher the NA value, the greater the maximum angle is for a given transmitting media.

The infinity corrected microscope objective used for all of our dry sample TEFM imaging was only a 1.3 NA oil immersion objective.[17] Since water has an index of refraction of 1.33 this objective would not be used to do objective-based TIRF of a wet sample. A 1.45 NA oil immersion microscope objective[18] was procured that was compatible with wet sample TIRF.

An unusual feature of this TIRFM was that the excitation laser entered the back aperture as a collimated beam and so was focused at the coverslip surface. As a result, the sample was not illuminated by the laser until the image was actually being acquired. This helped to reduce photobleaching of the sample. In contrast, most objective-based TIRFMs, including the one described in Chapter 2 of this thesis, are designed so that the excitation laser is focused on the objective back aperture and so achieve a uniform illumination over a large area at the cost of additional photobleaching of the sample.

Normal AFM probe holders are capable of tapping mode oscillation are not compatible with imaging in water.

The normal tapping mode AFM tip holder is designed to work on dry samples. Among other issues it has exposed electrical connections to power the tiny piezo chip that drives the high frequency oscillation in z. An alternate method for driving tip oscillation in liquid is called z-demodulation. In that mode the entire piezo column is oscillated. The probe holder acts like a piston that oscillates the entire end of the AFM. Doing so alternately pressurizes and depressurizes the liquid (and cell). The probe tip position oscillates relative to the sample holder because due to interaction with the liquid environment. However I found that this mode of operation significantly distorted live cells. In addition, the Veeco Nanoscope IV AFM control electronics incorporated a low-pass filter in the z-demodulation circuit that was set at 20 kHz. Since silicon AFM

probes that will perform tapping mode in water oscillate at frequencies between 16 and 70 kHz I discovered that the AFM drive circuitry was attenuating it's own drive signal.

To solve this a liquid-compatible probe holder made by Veeco[19] was procured, in which the piezo chip and its electrical connections were encapsulated. This device was intended for tapping mode operation in water. Since the drive signal comes through the tapping mode circuit in the AFM controller rather than the z-demodulation circuit there was no issue with self-attenuation using this holder. The direct drive probe holder is relatively large however and so the AFM stand had to be raised to accommodate it. The size of the tip holder also precluded the use of small cell culture dishes. MatTek manufactures cell culture dishes with a 50 mm diameter, and a large coverslip compatible with this larger AFM probe holder.[20] The glass coverslip was a number 0 thickness, which was compatible with doing TIRF through the new 1.45 NA microscope objective.

TEFM requires that the AFM probe tip oscillate (tap) in such a manner that the probe alternately makes contact with the sample and then oscillates above the sample. Such 'tapping-mode' AFM imaging is done at a frequency near the resonant frequency of the AFM probe cantilever. In air there is very little damping of this oscillation. However, the viscous nature of water substantially damps the AFM probe oscillation and thereby precludes imaging at the very high frequencies (200-400 kHz) typical. In addition, wet cells and membranes are soft resulting in tip-induced physical deformation of the cells.

As described in the 'Dry Imaging' section, the TEFM is fundamentally based on combining an AFM with a TIRFM. The advantage of this technique comes from interactions between the AFM probe tip and the TIRF evanescent field. The large electric field resulting from these interactions at the tip of the probe in turn stimulates fluorescence through a non-radiative dipole-dipole near-field interaction. This $1/r^6$ nature of near-field fluorescence stimulation requires that the tip either touch the

fluorophore significant or approach to within a nanometer if near-field fluorescence enhancement is to be observed.

Normal tapping mode AFM probes are designed to oscillate at high frequency in air. Much of the positional uncertainty in this system is due to chaotic oscillation modes. As a result the primarily random noise in any one image-pixel is reduced by the square root of the number of taps within it. As a result: the higher the tapping frequency the faster an image can be made without degrading image quality. The stiffness of a typical silicon AFM probe cantilever ranges between 40 and 50 N/m. A live cell is much softer than such a probe. So commercially available probes that are designed for tapping mode imaging are inappropriate for imaging live cells in liquid.

Therefore a softer cantilever was required if the soft sample was not to be significantly deformed during contact. Most 'soft' cantilever AFM probes are made of silicon nitride, which is an insulator. We found previously that the best tip enhancement occurred with doped-silicon AFM probes and that silicon nitride cantilevers produced no tip enhancement.

After investigating many options it was discovered that silicon force mode AFM probes were capable of tapping mode imaging in water. In particular I found that Nanosensors ATEC-FM and PPP-FMR AFM probes[21] worked reasonably well on firm wet samples although less well on live cells. These silicon AFM probes typically operate at ~30 kHz in water with a cantilever stiffness of 2.8 N/m. No solution was found that enabled high quality tapping mode imaging of live cells using a semi-conductive probe.

AFM tip alignment with the excitation laser is much more difficult in water as the alignment laser is refracted by the water and its container. In addition, cell covered coverslips are not atomically smooth or essentially free of fluorescent contamination as the dry samples previously imaged were.

Tip alignment with the focal spot of the excitation laser is critical in tip-enhanced imaging. It was found that the AFM probe can be illuminated in water with a 670 nm

laser diode[22] such that it produces a very clearly defined diffraction pattern (see Figure 3.1 a). If water is just pooled over the sample, refraction of the alignment laser normally precluded alignment. However it was found that the side of a cell culture dish is sufficiently flat that this technique works in water as well as in air. This diffraction pattern can be imaged by the optical microscope objective (see Figure 3.1b-d) when this probe is in contact with, or very close to, the glass surface. By comparing the relative positions of the reference laser spot and the probe diffraction pattern as imaged by the microscope objective it is easy to consistently position the AFM probe within ~λ/25 (~30 nm) of a defined point.

In some cases the cells on the surface would scatter the alignment laser light so much as to make it hard to differentiate the tip diffraction pattern. In that situation, the laser was initially aimed higher up the AFM such that the beam is bounced off the dichroic directly down onto the cantilever. The shadow of the cantilever can be used to put the tip very close to the excitation laser backscatter. Final tip-laser alignment could then be carried out in the normal manner.

Most biological experiments based on fluorescence imaging require the detection of at least two fluorophore colors. Such two color imaging often requires excitation at several different laser wavelengths.

To accomplish this a second TEFM was constructed capable of imaging in two colors and using three fiber-coupled excitation lasers (442 nm, 502 nm and 543 nm). This optical and mechanical configuration of this microscope is shown Appendix E. Another significant difference in this microscope is that it utilizes two methods of producing a p-polarized evanescent field. One is based on the mask technique used previously. The second is based on use of a radial polarization filter.[23] The radially polarized beam that emerges from that filter has several more complicated modes. So the beam is then focused on a pinhole chosen and positioned to transmit only radially polarized light. In this microscope excitation beam alignment is done using a tip-tilt mirror through a 1:1 telescope in a manner similar to the earlier instrument. AFM positioning is done using

X and Y translation stages driven by actuators. The same nPoint sample scanning stage is used along with the same gross positioning X-Y translation stage. All of the filters were custom made by Chroma and suitable for single molecule imaging.[24]

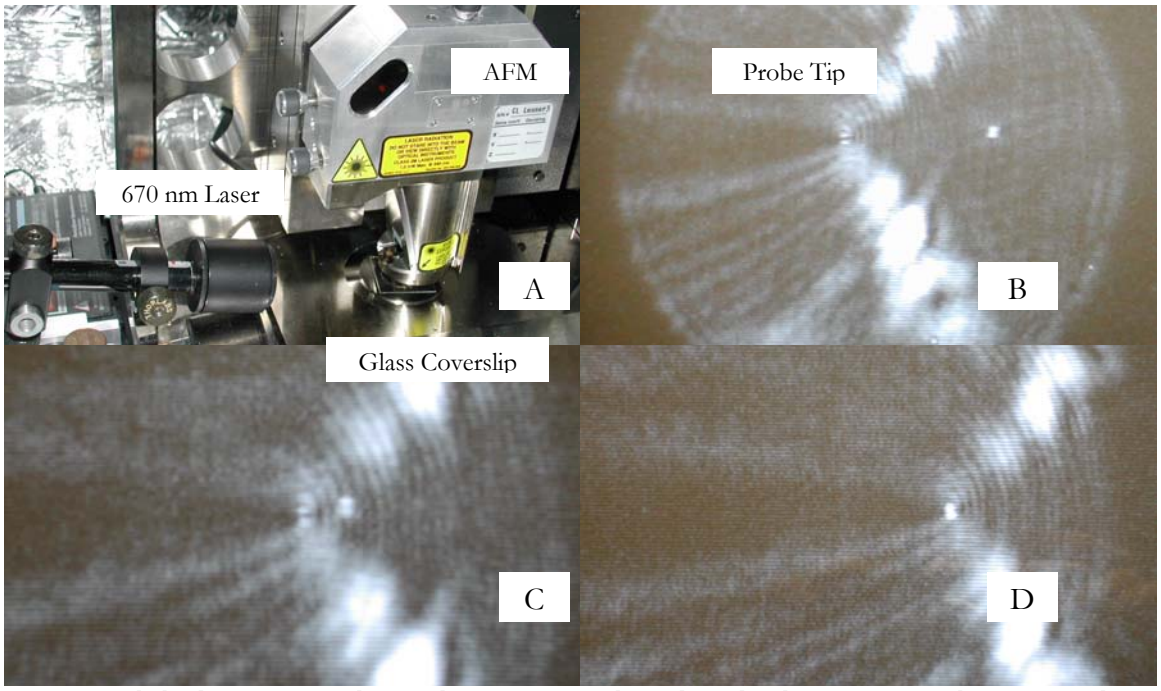

Figure 3.3. A hybrid AFM/Inverted Optical microscope with single molecule sensitivity is shown in panel A. A diffraction pattern is cast by the tip of the AFM probe (panel B) when <50 nm off the coverslip surface under illumination from the laserpointer. The 543 nm reference spot, seen to the left of this pattern, is approximately 9 μm from the probe tip. In panel C, the diffraction pattern is 1.45 μm in X and 450 nm in Y from the reference spot. In panel D the two are aligned.

Even in optimal conditions, AFM imaging of live cells using tapping mode is problematic due to the forces involved. In addition the evanescent field has a typical penetration depth of 100-200 nm in cells. Cells are thicker than 200 nm. As a result imaging the top of the cell will not result in significant tip enhanced fluorescence emission because the evanescent field will have completely decayed by the top of the cell.

While required for efficient stimulated emission, contact with the typical, stiff AFM probe tends to deform the cell surface. As mentioned earlier one way to minimize that distortion is to image with soft AFM probes. Another method for minimizing sample

distortion is to not image a live cell. Instead the cell can be adhered to the surface of a cell. Such adhesion can be achieved by growing the cell on an APTES coated coverslip. Extracellular proteins can be covalently attached to such a surface. Alternately, an APTES coated coverslip can be placed on top of cultured cells. The membrane-bound proteins can be made to covalently bond to the coverslip. After attachment, by cytolysis, the cell can be ruptured and the membrane skeletal membrane gently washed off.

The remaining attached membrane ghost can be imaged directly. The membrane ghost, being attached directly to the coverslip, is in the strongest portion of the evanescent field. The fluorescent labeling is best located on the cytosolic side of the cell membrane for this approach. In that fashion the tip can directly approach the fluorescent label. Protocols used to successfully produce such specimens are presented in Appendix B. The protocols included in Appendix B detail APTES coating the coverslip, cell adhesion, hypotonic cell lysis, cell plating and transfection.

In summary, this approach has the advantages of placing the sample within the maximum intensity of the evanescent field, exposing cytosolically labeled proteins directly to the AFM probe, and minimizing mechanical distortion. Imaging membrane ghosts rather than live cells should be the clear choice of preference in any future studies.

Wet tapping mode imaging can only be done at line scan rates of 3 lines/second or fewer. Typically 1 line per second was used for imaging. A 512 line image therefore typically took 512 seconds to acquire. The large (~1 GB) dataset acquired took 20-40 minutes to transfer and process before an image could be seen. This made it very difficult to scan a culture dish to identify healthy cells. As a result imaging 10 cells took at least 14 hours.

A method for normal real-time fluorescence imaging was developed and incorporated into the TEFM. A photon counter[25] was used that output a DC voltage directly proportional to the photon flux seen by the detector. The optical image was displayed

on the monitor as it was acquired, via the Nanoscope control software (v5.12), by connecting the photon counter output signal to an auxiliary port on the Nanoscope IV AFM controller.

The dry imaging data acquisition system included 27 electronics boxes and several sets of software. This hard-wired system was not adaptable to wet imaging.

A new Data Acquisition and Control (DAC) system was developed using National Instruments cards and LabView software. The flexibility of this system enabled the microscope to be adapted for imaging wet environments. A description of this DAC is provided in Appendix E.

It was desirable to produce combined AFM-optical images that were easily interpreted by eye.

Digital images are typically encoded in RGB. The difficulty with that is that the gray scale is entangled with the color information. An additional difficulty is that the eye is more sensitive to some colors (e.g. green) than to others (e.g. red). As a result, the grayscale must be changed after combining RGB encoded images. While doing so the user has a tendency to rebalance the image: to emphasize specific colors to be more esthetically pleasing. The result does not maintain data integrity.

Alternative method of encoding images is based on Hue, Saturation and Value (HSV). In this system all three components are independent. Hue is color. Saturation is the depth of the color. Value is grayscale. This system can be used to encode the AFM topographic image in value. Each of the emission spectral bands detected can be assigned a different hue. The saturation of that hue is the direct representation of intensity. Since each of these parameters are independent, co-localization is nicely accounted for in the color mathematics by assigning the appropriate intermediate hues. The specific hue can be assigned depending on the relative intensity of the two spectral

bands with the saturation representing the combined intensity. Other researchers can then disentangle the specific band intensities at each pixel without loss of information (2 variables, 2 knowns). Later, this image can be converted back to RGB for presentation. Data integrity is preserved by eliminating any need to rebalance the combined image.

HSV is presented in more detail in Appendix F.

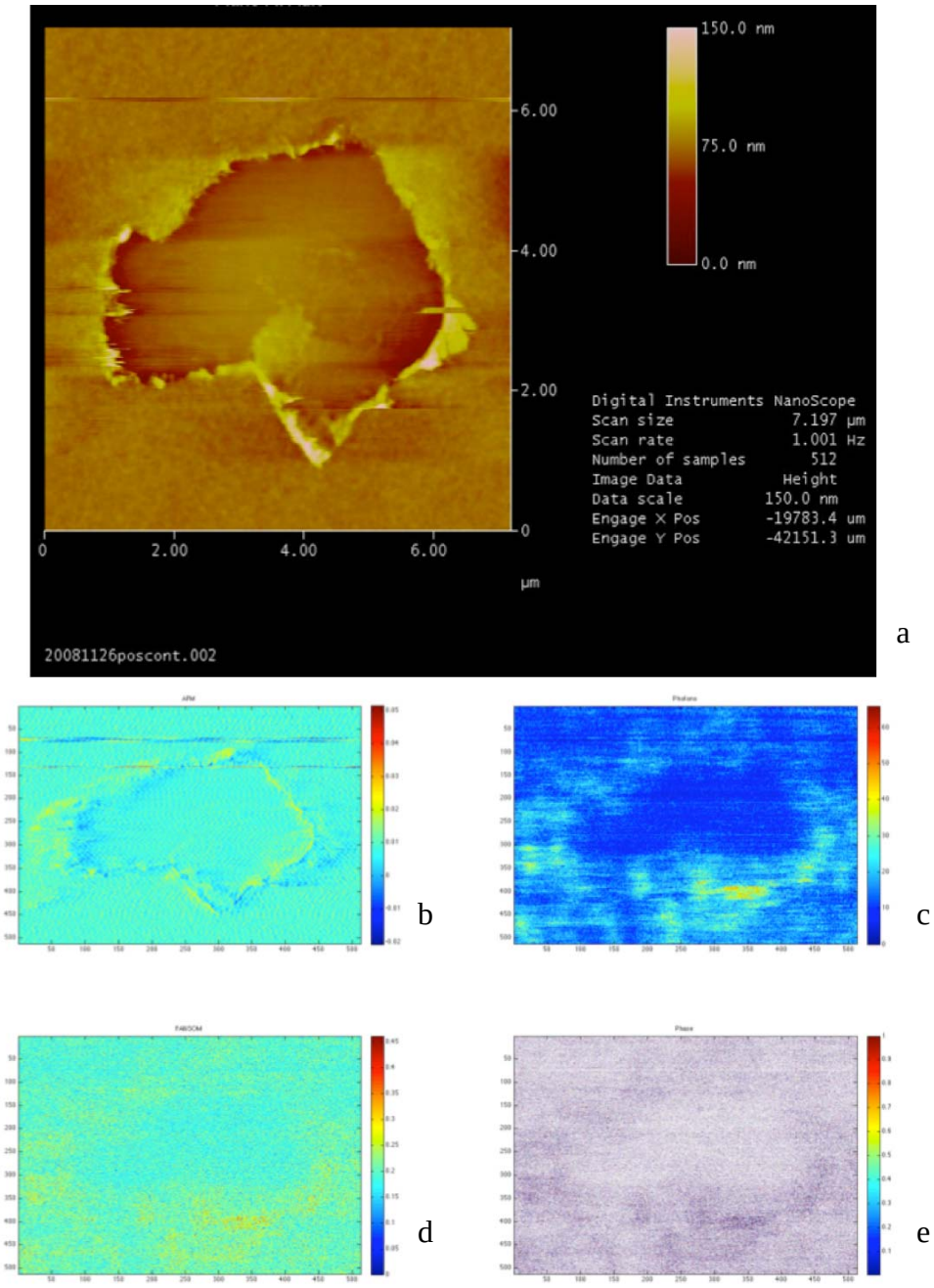

Figure 3.4 An AFM image of a wet membrane ghost from a N2a cell that was attached to a glass coverslip was generated using Veeco Nanoscope software. It was labeled by a mCherry tagged membrane-bound protein. b shows the AFM image computed by the Matlab image processing software we developed. The Matlab scripts for this software are given, in their entirety in Appendix E. c shows the total photon count and is essentially a normal TIRF image. d shows a near-field image computed using the same method described in the 2004 PRL by Gerton et al. e shows a vector summed image indicative of stimulated emission.

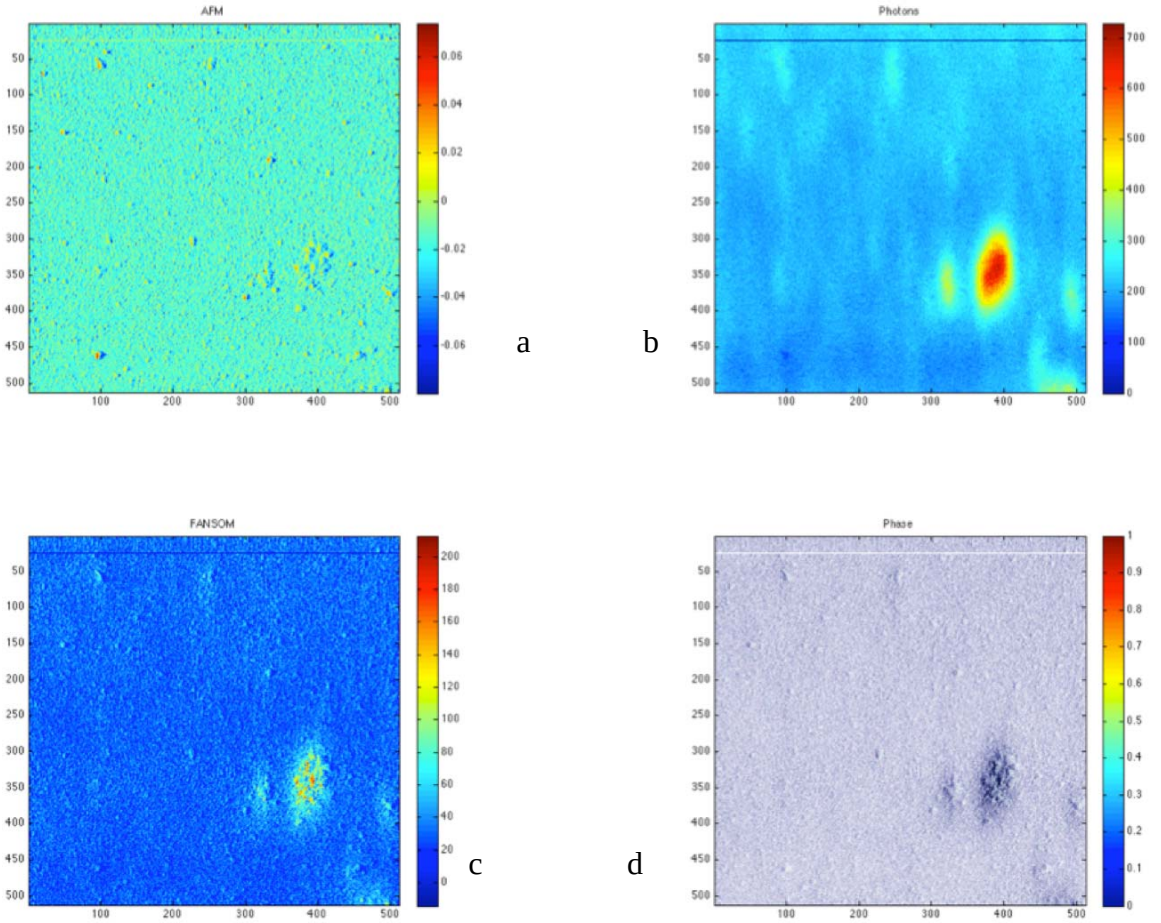

Figure 3.5 An AFM image computed by our Matlab image processing software (Appendix E) for a N2a cell transfected with α4 mCherry β2 wild type. b shows the total photon count and is essentially a normal TIRF image. c shows a fansom computed image using the same method described in the 2004 PRL by Gerton et al. d shows a vector summed image indicative of stimulated emission.

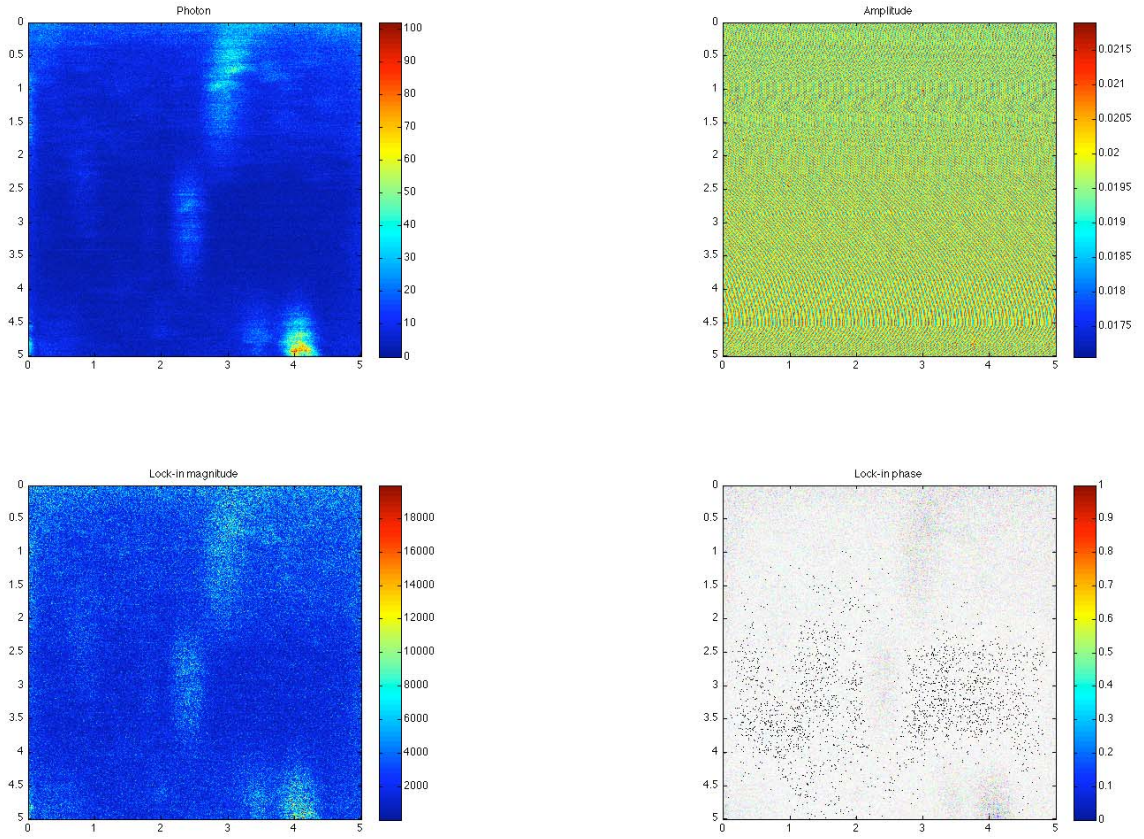

Figure 3.6 Measurement 20091106Wbd1. Top left is the AFM image computed by our Matlab image processing software (Appendix E) for extracellular fluid immersed 20 nm latex beads adhered to a class coverslip. The beads are labeled with red fluorescent dye. Top right is the total photon count image and is essentially a normal TIRF image. Bottom left shows a near-field image computed using the same method described in the 2004 PRL by Gerton et al. Bottom right is a vector summed near-field image indicative of stimulated emission. The FoV is 5 microns.

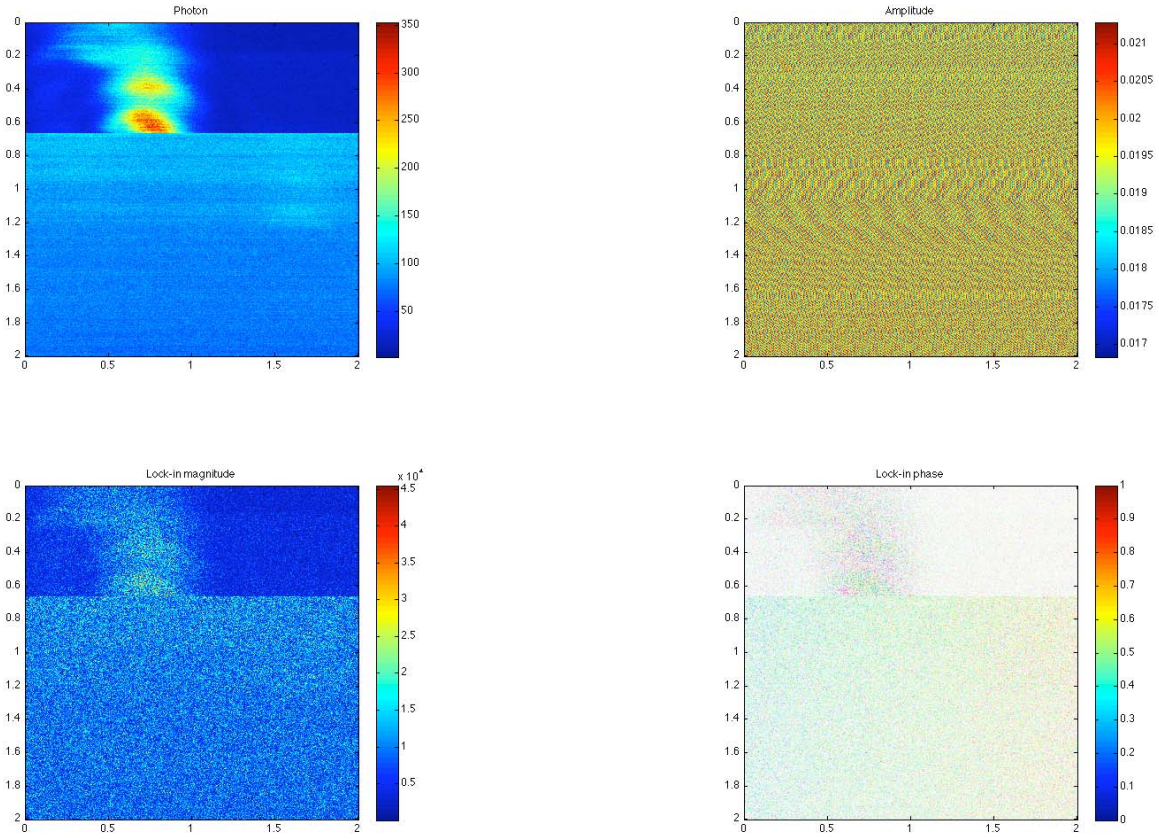

Figure 3.7 Measurement 20091106Wbd3. Top left is the AFM image computed by our Matlab image processing software (Appendix E) for 20 nm latex beads adhered to a class coverslip and immersed in extracellular liquid. The beads are labeled with red fluorescent dye. Top right is the total photon count image and is essentially a normal TIRF image. Bottom left shows a near-field image computed using the same method described in the 2004 PRL by Gerton et al. Bottom right is a vector summed near-field image indicative of stimulated emission. The FoV is 2 microns. Note that the image suddenly changes at 0.7 microns on the y-axis. That is because a bead stuck to the AFM tip partway though the image.

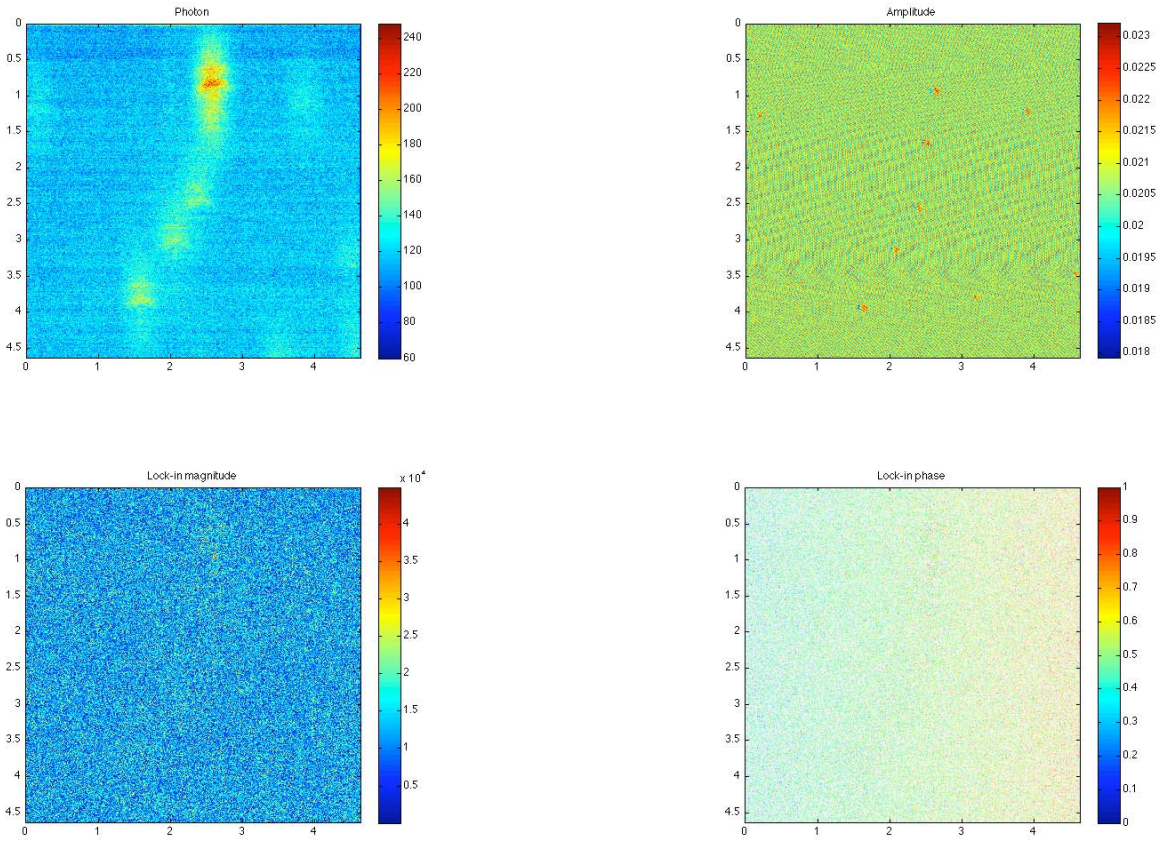

Figure 3.8 Measurement 20091106Wbd5. Top left is an AFM image computed by our Matlab image processing software (Appendix E) for extracellular fluid immersed 20 nm latex beads adhered to a class coverslip. The beads are labeled with Red fluorescent dye. Top right is the total photon count image and is essentially a normal TIRF image. Bottom left shows a near-field image computed using the same method described in the 2004 PRL by Gerton et al. Bottom right is a vector summed near-field image indicative of stimulated emission. The FoV is 4.6 microns.

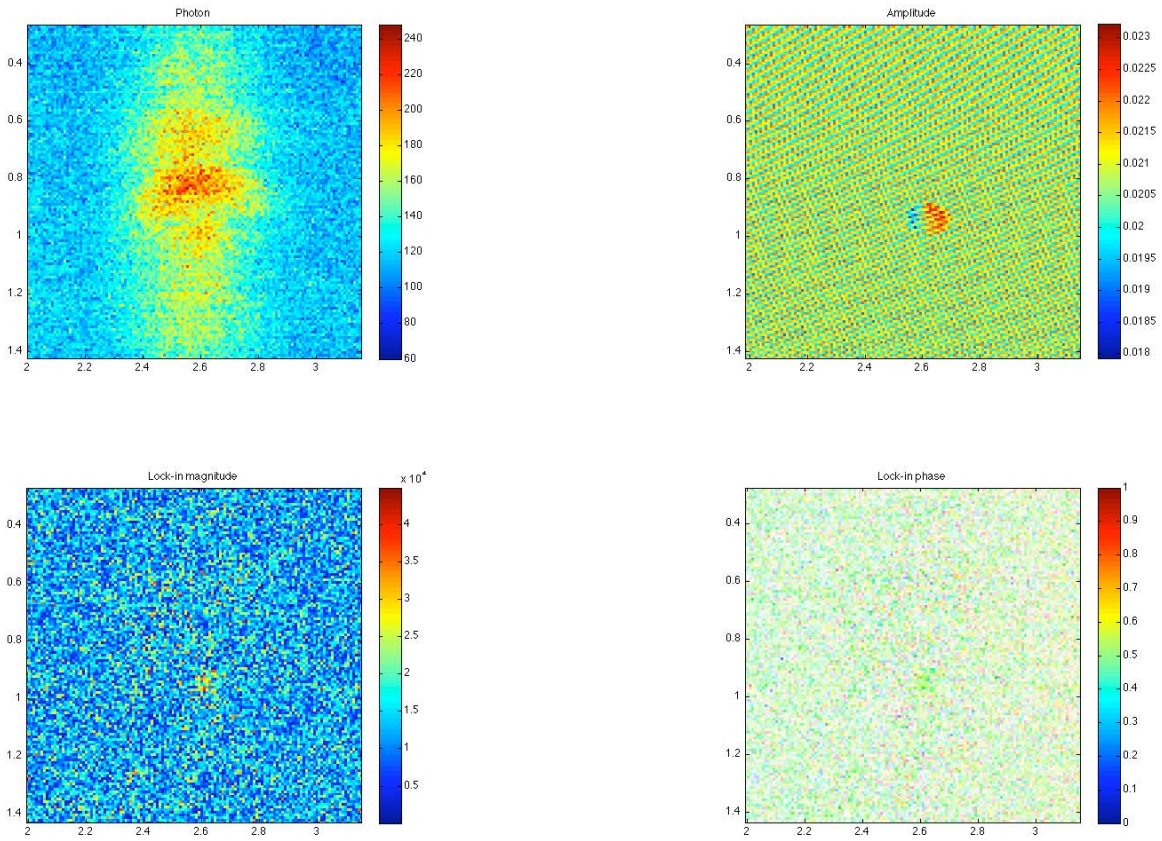

Figure 3.9 Measurement 20091106Wbd5 zoomed in to show a region ~1.2 microns across from Figure 3.6. Top left is a AFM image computed by our Matlab image processing software (Appendix E) for extracellular fluid immersed 20 nm latex beads adhered to a class coverslip. The beads are labeled with red fluorescent dye. Top right is the total photon count image and is essentially a normal TIRF image. Bottom left shows a near-field image computed using the same method described in the 2004 PRL by Gerton et al. Bottom right is a vector summed near-field image indicative of stimulated emission.

3.3 Summary and Conclusions

A TEFM was modified to enable imaging of wet samples. As examples a membrane ghost image is presented in Figure 3.2 and a typical cell image is presented in Figure 3.3. A second version of this microscope was built with greatly increased capability including simultaneous detection of two colors, excitation at three laser wavelengths in either of two modes of vertical polarization.

While many hundreds of cells and cell membrane ghosts were imaged during this effort the results were inconsistent. Figures 3.4-3.7 show images of 20 nm beads in extracellular solution. Clearly there is coupling between the tip and sample. What it means however is uncertain. Resolution of these inconsistencies will require careful study of the tip-laser interactions in water and cell media.

Acknowledgements

After Stephen Quake left Caltech for a faculty position at Stanford, he committed to leave the TEFM at Caltech for the duration of the studies reported herein. This is a remarkable act of generosity for which I am very, very grateful. Thanks also go to Eyal Shafran (Un. Utah) and Daniel Lo (Caltech) for assistance with the detection software, David Kremmers for suggesting HSV for combining images, Jian Li (JPL) and Mike Gordon (UCSB) for assistance with the data acquisition software and Rob Sharrow for a great deal of help with both. Building the two color TEFM would have been impossible without the sage advice and craftsmanship of Mike Roy and Steve Olson of the Chemistry Department's Instrument shop. Finally, thanks to Paul Millman and Chroma Technology for quickly making custom filters of incredibly high quality. Funding from the JPL Research and Technology Development and BioNano programs, NASA-PRSGC IDEAS-ER grant, NIH, NSF, NS-11756, DA-17279, and the Philip Morris External Research Program is gratefully acknowledged.

Reference

[1] Gerton, J. M., Wade, L. A., Lessard, G. A.. Ma, Z. and Quake, S. R., Tip-enhanced fluorescence microscopy at 10 nanometer resolution, *Phys. Rev. Lett.*, (2004) **93** 180801.

[2] Ma, Z., Gerton, J.M., Wade, L.A. and Quake, S.R., Fluorescence near-field microscopy of dna at sub-10 nm resolution, *Phys. Rev. Lett.* (2006) **97** 260801.

[3] Novotny, L., Bian, R. X. and Xie, X. S., Phys. Rev. Lett.(1997) **79** 645.

[4] Sanchez, E. J., Novotny, L. and Xie, X. S. Phys. Rev. Lett. (1999) **82** 4014.

[5] Novotny, L., J. Am. Cer. Soc. (2002) **85** 1057.

[6] Hamann, H. F., Gallagher, A. and Nesbitt, D. J., Appl. Phys. Lett. (1998) **73** 1469.

[7] Hillenbrand, R. and Keilmann, F. Appl. Phys. Lett. (2002) **80** 25.

[8] Hartschuh, A., Sanchez, E. J., Xie, X. S., and Novotny, L., Phys. Rev. Lett. (2003) **90** 0995503.

[9] Hamann, H. F., Kuno, M., Gallagher, A. and Nesbitt, D. J., J. Chem. Phys. (2001) **114** 8596.

[10] Protasenko,V.V., Kuno, M., Gallagher, A. and Nesbitt, D. J. Opt. Comm. (2002) **210** 11.

[11] Kramer, A., Trabesinger, W., Hecht, B. and Wild, U. P., Appl. Phys. Lett. (2002) **80** 1652.

[12] Bouhelier, A., Beversluis, M., Hartschuh, A. and Novotny, L. Phys. Rev. Lett. (2003) **90** 013903.

[13] Sick, B., Hecht, B., Wild, U. P. and Novotny, L., J. Micr. (2001) **202** 365.

[14] Yang, T. J., Lessard, G. A. and Quake, S. R., Appl. Phys. Lett. (2000) **76** 378.

[15] Closed-Look Bioscope with Nanoscope IV controller, Veeco Metrology, 112 Robin Hill Road, Santa Barbara, CA 93117, USA.

[16] nPoint closed-loop AFM scanner, pn iCXY100LA-BO with nPoint C300 DSP Controller. nPoint, 3030 Laura Ln Suite 100, Middleton, WI 53562 USA.

[17] Olympus UPlanFl 100x/1.30 Oil. Olympus America Inc., 3500 Corporate Parkway, Center Valley, PA, USA

[18] Zeiss α Plan-Fluar 100x/1.45 Oil, pn 000000-1084-514. Carl Zeiss MicroImaging, Inc., One Zeiss Drive, Thornwood, NY 10594, USA.

[19] Veeco Direct Drive Fluid Cantilever Holder, pn 013-410-000. Veeco Metrology, 112 Robin Hill Road, Santa Barbara, CA 93117, USA.

[20] MatTek pn P50G-0-30F. MatTek Corporation, 200 Homer Avenue, Ashland, MA 01721, USA.

[21] Nanosensors, Rue Jaquet-Droz 1, Case Postale 216, CH-2002 Neuchatel, Switzerland.

[22] Thorlabs pn CPS186. Thorlabs, Newton, New Jersey, USA.

[23] ARCopix Radial Polarization Converter with USB ARCoptix LC driver. ARCotix S.A., Rue de la Maladiere 71, 2000, Neuchatel, NE, Switzerland.

[24] Chroma Technology Corp. • 10 Imtec Lane • Bellows Falls, VT 05101 USA.

[25] SRS400 Gated Photon Counter. Stanford Research Systems, Inc., 1290-D Reamwood Ave., Sunnyvale, CA 94089, USA.

Chapter 4

NANOTUBES, IMAGING AND PROTEINS

An atomic force microscope can image the height (z) of a surface with extraordinary resolution. For a smooth surface it is relatively easy to achieve 0.25 Å in height resolution. However when the topography becomes more convoluted the detected height at any given point can be strongly influenced by the shape of the AFM probe. This becomes particularly apparent when determining the width of an object. The surface resolution (x-y) of an atomic force microscope is limited by the width of its tip (typically 5-10 nm radius).

The advantages of nanotube AFM probes are that they are very small in diameter and that the sides are vertical. As a result nanotube probes offer the potential for AFM imaging surface topography with minimal distortion due to the shape and size of the probe. Therefore we developed, in collaboration with the Pat Collier group, the capability to fabricate nanotube Atomic Force Microscope (AFM) probes.[1] In this paper we present how to grow nanotube substrates and fabricate nanotube AFM probes. As part of this effort we characterized the diameter of the nanotubes on the substrate. We also examine the resolution that nanotube AFM probes could achieve.

To our surprise we found that images taken with nanotube probes frequently demonstrated resolution better than could be expected given the apparent diameter of the nanotubes that were grown on the substrates that we used to supply nanotubes for attachment.

Therefore we (in an effort primarily conducted by Santiago Solaris of the Goddard group) used atomistic modeling to study the balance of forces that enabled nanotube attachment.[2] As a result of this effort we gained real insight into the basis for the surprisingly high imaging resolution we achieved with nanotube AFM probes.

Both of the papers referenced above are included in this chapter, along with their supporting material, courtesy of the American Chemical Society to whom they are copyrighted.

A US patent issued for the methods we invented for nanotube tip attachment to an AFM probe is included in Appendix G.[3] Appendix H is a patent[4] that describes a method of functionalizing nanotube tips. Specifically, it describes methods for coating the nanotube tipped probe to preclude non-specific binding or other chemical interactions with the probe and then chemically functionalizing the end of the nanotube tipped probe with a carboxyl group or amine group so that further chemical modification can be made. This unique chemical functionalization of the nanotube tip can be used to attach a single protein or a specific group of proteins. Such a modified tip can then be used for sensing unique chemical motilities or triggering specific reactions with extraordinary spatial resolution. Functionalized nanotube tips can be used to pattern a substrate for future sensing or chemical logic use.

NANO LETTERS

2004
Vol. 4, No. 4
725−731

Correlating AFM Probe Morphology to Image Resolution for Single-Wall Carbon Nanotube Tips

Lawrence A. Wade,[†,‡] Ian R. Shapiro,[§] Ziyang Ma,[‡] Stephen R. Quake,[‡] and C. Patrick Collier*[,§]

Jet Propulsion Laboratory and Departments of Applied Physics and Chemistry, California Institute of Technology, Pasadena, California 91125

Received January 2, 2004; Revised Manuscript Received January 31, 2004

ABSTRACT

Scanning and transmission electron microscopy were used to image hundreds of single-wall carbon nanotube probes and to correlate probe morphology with AFM image resolution. Several methods for fabricating such probes were evaluated, resulting in a procedure that produces image-quality single-wall nanotube probes at a rate compatible with their routine use. Surprisingly, about one-third of the tips image with resolution better than the nanotube probe diameter and, in exceptional cases, with resolution better than 1 nm. This represents the highest lateral resolution reported to date for a SWNT probe.

Single-wall carbon nanotubes (SWNTs) have shown great potential as high-resolution AFM imaging probes.[1−3] The level of resolution possible for both single molecule imaging and force transduction in AFM is ultimately limited by the structure of the tip. Commercially available silicon probe tips have radii of curvature of 5−15 nm. The finest commercially available Si tips are very delicate, leading to substantial variation in tip shape and size even between successive images. SWNTs, on the other hand, have diameters between 1.5 and 6 nm, providing resolution comparable to molecular scale dimensions. Carbon nanotubes are chemically and mechanically robust, with axial Young's moduli of about 1.25 TPa,[4,5] resulting in a tip structure that is stable over prolonged imaging periods.[6] Finally, SWNTs can be chemically functionalized uniquely at their very ends, permitting a broad array of applications in nanotechnology and biotechnology.[7] Nevertheless, it is difficult to reproducibly assemble large quantities of high-quality single-wall nanotube AFM tips. To fully realize the promise of these probes for high-resolution AFM, a better physical understanding is needed of how the geometry of the mounted SWNT on its AFM tip support affects image quality.

Successfully fabricating a probe suitable for AFM imaging in air involves several steps: attaching the nanotube to a silicon AFM tip, shortening it sufficiently to enable high resolution imaging, characterizing its quality, and storing it for later use. Building upon previously reported techniques, we have conducted a comparative survey of fabrication methods to produce a protocol that routinely results in high quality probes. The quality of the AFM images taken with the resultant probes, along with the frequency and ease of success, was used to distinguish between the several approaches studied. In addition, SEM and TEM images of hundreds of nanotube AFM probes were used to evaluate the efficacy of different probe attachment and shortening techniques and to improve the accuracy of our interpretation of AFM imaging and force calibration results. For the first time, the AFM resolution achieved when imaging with nanotube probes was directly correlated to TEM images taken of these same probes. This allowed us to carry out a rigorous examination of nanotube morphology and its influence on image resolution and quality, by directly correlating nanotube geometry, as determined with TEM imaging, with their performance as AFM probes. As a result, we gained significant new insights that are important for research groups performing AFM imaging with SWNT tips.

In this paper, we summarize the results of these studies and describe a procedure that enables consistently successful nanotube probe fabrication. The lateral resolution of these probes when used to image 3 nm diameter SWNTs was typically less than 4 nm, and in one case, 5 Å.[8] This is an improvement by a factor of 4 over the best resolution reported to date using a SWNT probe, which is 2.0 nm.[9] The systematic correlation of TEM images of SWNT probes with the effective lateral resolution obtained when using these probes for topographical imaging indicates that approxi-

* Corresponding author. E-mail: collier@caltech.edu.
† Jet Propulsion Laboratory.
‡ Department of Applied Physics.
§ Department of Chemistry.

10.1021/nl049976q CCC: $27.50
Published on Web 02/17/2004

mately one-third of the probes demonstrated resolution smaller than the diameter of the nanotube probe itself when imaging nanotubes on a smooth substrate. For example, we have measured 1.2 nm lateral resolution from a SWNT scanning probe that was 5.5 nm in diameter.

These TEM−AFM correlations provide experimental evidence consistent with previous mechanical modeling carried out by Snow, et al.[10] Additionally, whereas previous investigations have shown nanotube buckling to be an elastic process,[2,3,9,11] we have found that under some circumstances, a SWNT probe can buckle inelastically, resulting in probe damage and corresponding image artifacts.

Finally, we have found that nanotubes picked up by AFM tips can have larger diameters (by about a factor of 2) than the diameters of nanotubes imaged on the surface of the growth substrate, as determined from height measurements with a conventional AFM tip. A better understanding of this discrepancy is needed for optimizing the yield and reproducibility of nanotube probe fabrication. The AFM image resolution statistics we report here underscore the variability between probes fabricated by different methods.

Digital Instruments BioScope and Multimode atomic force microscopes were used with Nanoscope IV controllers for this work. Transmission electron microscopy was performed with a Phillips EM430, and scanning electron microscopy was performed with a Hitachi 4100.

We compared several methods for attaching nanotubes to silicon AFM tips: manual assembly, direct growth, and pickup. Smalley's group reported the first example of the use of carbon nanotubes as AFM tips in 1996.[11] Manual assembly of AFM probes was found to be relatively simple, although the nanotubes had to be large enough to be seen and manipulated under an optical microscope, and thus did not yield high-resolution probes. While direct growth[12−14] offers the potential for parallel fabrication of SWNT AFM probes, we found that the yield was quite low. We also determined that the rate-limiting step in probe fabrication was the nanotube shortening step rather than attachment. Therefore, we focused our efforts on the pick-up technique for nanotube attachment, as shown in Figure 1.

The pick-up technique, developed by Lieber et al.,[15] is an efficient and consistent method for mounting SWNTs in the proper orientation. When SWNTs are grown on a flat substrate, a small percentage of the tubes are oriented vertically, and can be picked up when the AFM tip scans across the surface in tapping mode. The nanotube binds to the side of the pyramidal AFM tip via attractive van der Waals forces, and usually remains attached firmly enough that it can be repeatedly pressed into and scanned across the substrate surface. We found that it was important to reduce the field of view (e.g., from 10 μm to 10 nm) or retract the tip as soon as a nanotube was successfully picked up in order to minimize the probability of picking up additional nanotubes (see Supporting Information). Multiple attached tubes or bundles can lead to AFM image artifacts.

It is also important to note that the ambient humidity appears to affect the efficiency of the pickup method. We found it nearly impossible to pick up nanotubes from a

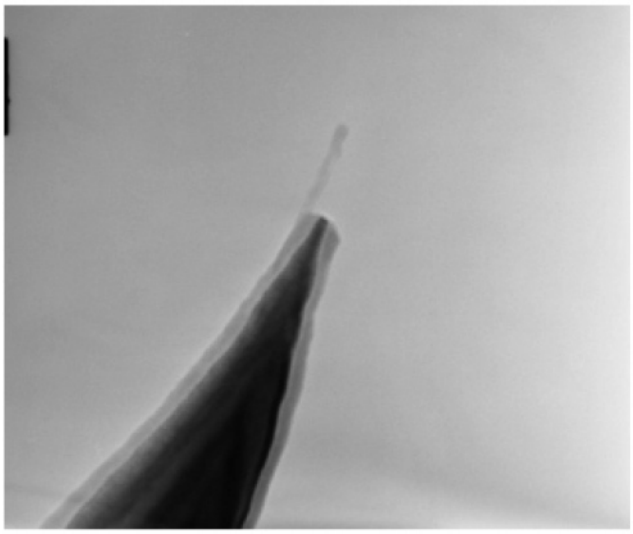

Figure 1. TEM image of a single-wall carbon nanotube picked up from a silicon substrate.

substrate under high humidity conditions. Enclosing the AFM in a glovebag under a flow of dry nitrogen for about 30 min rejuvenated the process. We speculate that an increase in the relative humidity makes it more difficult to pick up nanotubes for two main reasons. First, at higher humidity values, it is harder to overcome capillary forces due to the build up of a surface layer of water on the growth substrate. More force is necessary to pry a prone nanotube off the surface due to increased adhesion. Second, increasing water build up on the tip decreases the attractive interactions of the nanotube to the silicon surface of the AFM tip during pick up. It is known that the van der Waals interactions at the nanotube−AFM tip interface are not strong enough to keep the tube attached to the tip in liquid water.[9] Nanoscopic condensation of water between the AFM tip and the growth substrate at high relative humidity may have an analogous effect on the success rate for picking up a nanotube.

SWNTs were grown via chemical vapor deposition (CVD) on 4 mm to 8 mm square, 500 μm thick p-doped Si wafers. Four different methods were used to coat the substrates with iron catalyst for growing nanotubes suitable for pickup: spin coating a solution of $Fe(NO_3)_3 \cdot 9H_2O$ in isopropyl alcohol,[9] thermal evaporation of iron onto the substrate, electron beam evaporation of iron onto the substrate,[15] and incubation with ferritin. We achieved the most uniform deposition of small (1−2 nm) catalytic sites with high spatial density by using ferritin-derived iron nanoparticles, prepared as described by Dai and co-workers.[16]

CVD growth was performed in a 22 mm inner diameter Lindberg/Blue M quartz tube furnace with a single heating zone 312 mm long, as shown in Figure 2. Five wafers are positioned 12.5 mm apart in a specially designed quartz holder, oriented vertically and with the catalyst-coated side facing away from the direction of the incoming gas. A significant advantage of this holder is that it enables up to three small substrates to be mounted side-by-side in each slot for parallel comparison of growth results under nearly identical temperature and gas flow conditions.

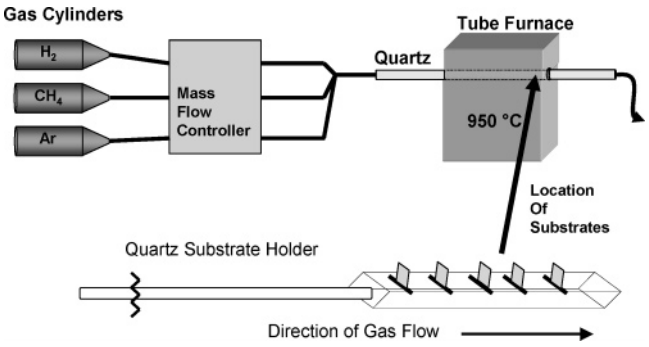

Figure 2. Diagram of CVD apparatus for production of nanotube substrates.

We found that growth was faster (5 μm long nanotubes within one minute) and the distribution of tube lengths increased when the catalyst-coated surface was facing away from the incoming gas flow. We speculate that this is due to increased turbulence of the gas flow at the catalyst coated side after passing over the edges of the substrate. Induced turbulence should minimize the role of diffusion-limited growth relative to nucleation rate in the growth kinetics, but at the expense of uniform growth. These growth procedures generate SWNTs on the substrate with diameters ranging from 1.6 to 3.0 nm, and lengths between 100 nm and 5 μm, as imaged with AFM and SEM.

The distribution of tube diameters varied with the size of the catalytic sites. For example, we found that spin coating many drops of dilute solution of the iron nitrate catalyst to give a high density of small catalytic sites gave a slightly broader tube diameter distribution than did ferritin. In contrast, depositing a few drops of higher density iron solutions yielded broad size distributions and larger average tube diameters. Based on AFM analyses of these substrates, it appears that the larger tube diameters resulted from larger catalytic sites on the substrate. No MWNTs have been observed on these substrates.

The long-term stability of pickup substrates appears to vary depending on how they were prepared. Ferritin and ferric nitrate substrates appear to be substantially less effective for pickup attachment after 4 to 6 months. We hypothesize that this is due to the relatively weak mechanical attachment of the catalytic site to the substrate. Over time, vertically oriented tubes that are attached to loosely bound catalytic sites apparently physisorb onto the substrate. Enclosing the AFM in a glovebag with a flow of dry nitrogen for about 30 min substantially enhanced pickup with these older substrates. In contrast, substrates that had the catalytic sites deposited by molecular beam epitaxy (MBE) have demonstrated reliable pickup of nanotubes with an AFM tip over several years without special care.[15]

The diameters of the picked up tubes measured with TEM were typically between 4 and 6 nm. In comparison, the diameters of nanotubes lying horizontally on the substrate, determined by AFM height measurements, were only 2−3 nm. We have ruled out TEM and AFM calibration errors as the cause of this discrepancy. We have also ruled out compression of the imaged nanotubes by the AFM tip, which would result in a decreased apparent diameter. Deformation of the horizontal nanotubes due to van der Waals forces has also been modeled using realistic molecular dynamics simulations based on quantum mechanical calculations, and found insufficient to explain this discrepancy.[17] It appears that this disparity is real and not just an artifact due to tube distortion or measurement error.

This indicates a strong preference for larger diameter tubes to be picked up by silicon AFM probes. There are two plausible explanations for this disparity. One possibility is that larger diameter nanotubes have a higher probability of remaining vertically oriented on the growth substrate over time than smaller diameter tubes. Only the population of smaller diameter nanotubes adsorbed to the growth substrate can be imaged by AFM. Hence, AFM images will be biased toward this part of the distribution of nanotube diameters.

Alternatively, this disparity may be explained by the binding energy of the nanotube to the AFM cantilever tip relative to the binding energy of the nanotube to the substrate. Once a SWNT has been picked up by a scanning AFM tip, there are two kinds of motions that impose stress on the system. The AFM cantilever has a net motion parallel to the substrate. During pick-up, typical horizontal velocities are on the order of 30 000 nm/s. This motion imposes three kinds of stress on the system: shear, bending, and tension. In addition, the cantilever has a rapid vertical oscillation, typically 70−250 kHz, with an amplitude of 40−50 nm, that imposes additional bending and tension stresses.

The mechanical stresses imposed by the cantilever motion on a nanotube attached on one end to the AFM tip, and on the other end to the surface of the growth substrate, will result in one of two outcomes: the nanotube either slips off the cantilever tip and remains attached to the substrate, or the nanotube separates from the substrate interface and is "picked up". The discriminator between these two outcomes is the binding energy at the attachment site of the nanotube to the silicon tip relative to that of its attachment to the substrate. These binding energies will depend on many factors that are virtually impossible to characterize fully, such as the relative lengths of the nanotube adsorbed onto the tip versus the substrate, as well as details of the chemical, physical, and mechanical interactions between the nanotube and these surfaces during scanning in tapping mode. It is known, however, that binding energy scales with the tube diameter, which can be determined directly from both AFM and TEM images.

The strength of nanotube attachment can be approximated as being linearly proportional to the nanotube diameter using the thin-walled cylinder approximation. At the attachment site with the AFM cantilever tip, the nanotube can be considered fixed until the binding energy is exceeded at this interface by the imposed stresses. This binding force increases linearly with diameter, but at a rate 1.6 times faster for tubes greater than 2.7 nm diameter than it does for smaller diameter nanotubes.[18] The increased binding energy for nanotubes greater than 2.7 nm could result in larger diameter nanotubes being preferentially picked up. The relative adhesion strength of the catalytic particle to the tube versus

the substrate could also have a significant influence on the diameters of the tubes that are picked up.

As seen in Figure 1, more than 100 nm of a nanotube typically protrudes from the end of the AFM tip after pick-up. High-resolution imaging is not possible with such a long nanotube tip due to thermal fluctuations and bending. Pick-up SWNT tips were shortened by a combination of push shortening, an approach developed by Hafner and Lieber,[13] and electrical pulse etching.[2,12] An HP 8114A pulse generator was used in combination with a Digital Instruments signal access module for all of our pulse shortening experiments.

Push shortening is done by incrementally decreasing the tip−sample separation distance during successive force calibrations to push the nanotube up along the side of an AFM tip. This process requires a picked-up tube of very specific length. Tubes longer than 100 nm tend to buckle inelastically during this process, after which they cannot be shortened by further pushing. Push shortening is superior to pulse etching when further shortening nanotubes less than 100 nm long in very small increments.

We obtain similar results for electrical pulse etching with native oxide coated p-doped silicon, 300 nm thick thermally grown oxide-coated p-doped silicon, and gold-plated silicon substrates. This finding indicates that the entire probe fabrication procedure can be carried out on a single unpatterned, doped-silicon substrate. Thermally grown oxide substrates typically required higher voltages to successfully pulse-shorten than did either native oxide or gold-coated silicon substrates.

Using electrical pulse shortening and push shortening in combination on the same tip relaxes the constraints for obtaining high-quality probes from the nanotube growth substrate and increases yield. Long tubes can be coarsely shortened with electrical pulses until their lengths are less than 100 nm. Push shortening can then be used for finer control in adjusting the probe length.

We frequently found that electrostatic forces would strip nanotubes off the AFM tips when they had been stored in a nonconductive container. An aluminum box with a narrow strip of double-sided tape or a conductive Gel-Pak container both seemed to solve this problem. Prior to use of conductive boxes for nanotube tip storage, we were unsuccessful in TEM imaging the attached nanotube probes.

To characterize the effective resolution of our SWNT probes, we imaged nanotubes resting flat on the silicon growth substrate, using a scanning field of view of 100−350 nm. We define resolution as the full width of the imaged tube measured at the noise floor, minus the measured tube height. While nanotubes are convenient samples for determining resolution, they are not infinitely rigid. Dekker's group has shown that the apparent height of a nanotube measured by tapping mode imaging can decrease substantially at high oscillation amplitudes, even with conventional silicon tips.[19] We have observed similar effects with nanotube probes.[20] For this study, the oscillation amplitude was maintained close enough to its freely oscillating value in air to limit this effect to be within 10% of the true nanotube height.

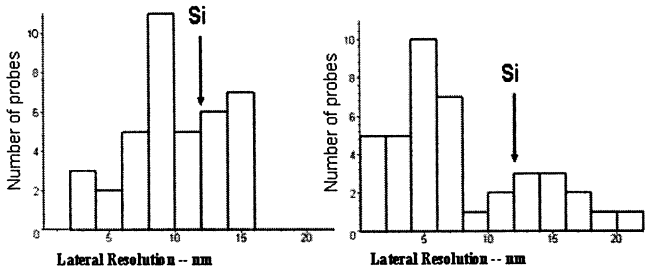

Figure 3. The left histogram summarizes the resolution for 39 probes fabricated on a substrate coated with ferric nitrate catalyst. The right histogram shows the resolution distribution of 40 probes made from nanotubes picked up from a substrate coated with ferritin. Included is the typical resolution obtainable with a conventional silicon AFM tip.

Figure 3 shows histograms of the lateral resolutions obtained with SWNT probes fabricated using a growth substrate coated with ferric nitrate catalyst versus those fabricated using ferritin as the catalyst. The variation in nanotube probe performance was greater than we expected based on previous reports. Leiber et al. had examined the image quality of different nanotube types (MWNTs and SWNTs).[21] In contrast, we compared 39 SWNTs made from the same iron nitrate-coated substrate and 40 from a ferritin substrate. The wide range in resolution found, between the two different kinds of substrate (ferritin vs iron nitrate), as well as from the same substrate, was surprising and underscores the importance of specific nanotube characteristics in determining the maximum achievable resolution.

There is a clear shift in the distribution toward higher resolution probes when ferritin was used as the catalyst, consistent with a narrower catalyst size distribution. It is not clear how much technique improvements rather than the switch to ferritin from ferric nitrate coated substrates played in the comparative distribution. Most of the latter tips were fabricated using ferritin substrates. By that time, we were more careful to reduce the field of view immediately after pick-up to minimize bundle formation. This could explain why there are fewer 10−15 nm resolution tips. However, it is clear that significantly more probes with resolution better than 5 nm were fabricated using ferritin substrates.

Nearly 100 probes were imaged by TEM to characterize the efficacy of different fabrication techniques. Of these, fourteen SWNT probes imaged by TEM had previously been used for tapping-mode topographic imaging. Table 1 presents a summary of probe characteristics determined by TEM−AFM correlations for the fourteen SWNT probes. Entries in bold correspond to probes that demonstrated lateral resolution less than the actual nanotube probe diameter.

Image quality is a function of many factors including: tube diameter and length, contact angle, number of nanotubes extending past the silicon tip, thermal noise, and contamination. These factors can lead to substantial variability in resolution. By correlating probe structure and orientation seen in the TEM images with topographic imaging performance, we can provide experimental evidence consistent with previous mechanical modeling carried out by Snow et al.,[10] who have shown that lateral tip−sample forces can bend

Table 1. TEM−AFM Correlation Table for Single-Wall Carbon Nanotube Scanning Probes

tip type	tube diameter	tube length	aspect ratio	deviation from perpendicular	lateral resolution (full width-height)	lateral resolution/ probe diameter
SWNT	**4.2 nm**	**10 nm**	**2.4**	**10°**	**2.8 nm**	**0.67**
Bundle	**9.3 nm**	**77 nm**	**8.3**	**20°**	**4.0 nm**	**0.43**
SWNT	4.0 nm	112 nm	28	30°	10.4 nm	2.60
SWNT[a]	4.0 nm	19 nm	4.8	40°	4.6 nm	1.15
SWNT	**5.5 nm**	**40 nm**	**7.3**	**20°**	**1.2 nm**	**0.22**
Bundle	**8.0 nm**	**35 nm**	**4.4**	**15°**	**5.6 nm**	**0.70**
SWNT	3.7 nm	30 nm	8.1	30°	5.8 nm	1.56
SWNT[a,b]	4.2 nm	33 nm	7.9	20°	6.0 nm	1.43
SWNT	5.4 nm	38 nm	7.0	10°	5.9 nm	1.09
SWNT	3.5 nm	15 nm	4.3	20°	4.4 nm	1.26
Bundle	5.5 nm	51 nm	9.3	0°	21 nm	4.0
SWNT	**5.3 nm**	**55 nm**	**10.4**	**0°**	**3.9 nm**	**0.74**
SWNT	**6.5 nm**	**42 nm**	**6.5**	**0°**	**4.3 nm**	**0.66**
SWNT	5.4 nm	26 nm	4.8	10°	8.0 nm	1.48

[a] Probe showed a "shadowing" artifact. [b] Nanotube appeared buckled 16 nm from the end of the tube.

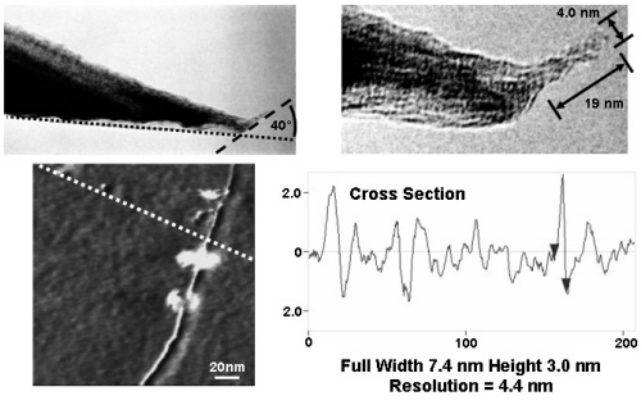

Figure 4. Correlation of image showing artifact due to large contact angle with substrate. Additionally, this nanotube appears to be buckled near the silicon tip. The dotted black line in the upper left image is perpendicular to the substrate.

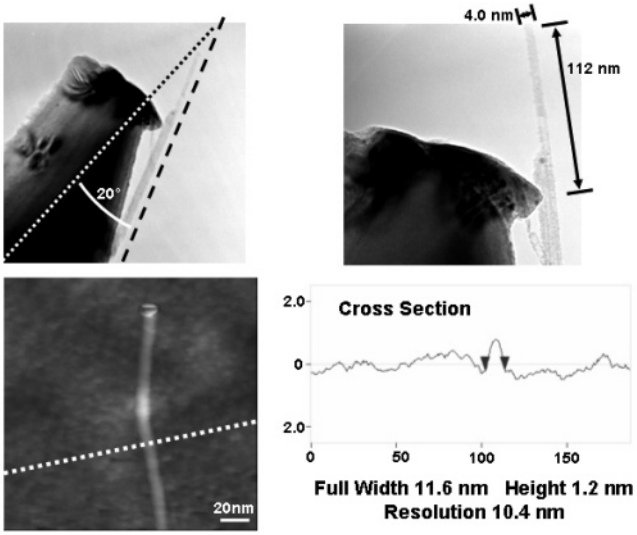

Figure 5. Image artifacts due to bending are significant for long nanotubes. Note that there are a number of picked up nanotubes at the base of this tip. The damage to the silicon tip probably occurred during repeated force calibrations.

single-wall nanotubes or cause snap-to-contact behavior when the tubes exceed either a critical length or a critical angle relative to the substrate surface normal. These effects introduce a significant degree of broadening and the appearance of image artifacts.

If the nanotube is presented to the sample surface at an angle deviating from the surface normal by more than ∼30°, poor resolution and obvious image artifacts result due to tip−sample forces having a significant component perpendicular to the nanotube axis. For example, Figure 4 shows a 19 nm long, 4 nm diameter nanotube projecting from the probe tip at an angle of 40°. This probe produced an image that contained a positive height "shadowing" artifact approximately 10 nm in width parallel to each sample nanotube. This artifact resulted from the nonideal orientation of the probe. Additionally, the TEM image showed that the nanotube is buckled near the silicon tip. Previous reports have described reversible *elastic* buckling of the nanotube, which did not have a serious impact on image quality.[5,9,21] Our TEM correlations indicate, however, that buckling can, under some circumstances, be inelastic, resulting in irreversible structural changes. This structural defect results in an effectively lower stiffness for the probe, which we believe is responsible for the decreased resolution and imaging artifacts we observe (shadowing features). Similar artifacts were seen with SWNT ropes (multiple SWNTs bundled together) for the same reason; the layered structure of a bundle of nanotubes attached to the AFM tip results in stiffness variation along the probe length.

SWNTs must also have aspect ratios less than ∼10 to be adequate for imaging purposes. Figure 5 shows a 4 nm diameter nanotube protruding 112 nm from the end of the AFM tip, but at an angle deviating from the surface normal by less than 20°. The resulting lateral resolution was still 2.5 times the probe tube diameter. This broadening of the image is due in small part to thermal vibrations. However, mechanical modeling studies have indicated that for a nanotube of this geometry, the root-mean-squared thermal vibrations of the end of the tube should be less than 2 Å.[22] Nanotube bending due to lateral tip−sample forces is most likely the principal contribution to the degraded resolution.

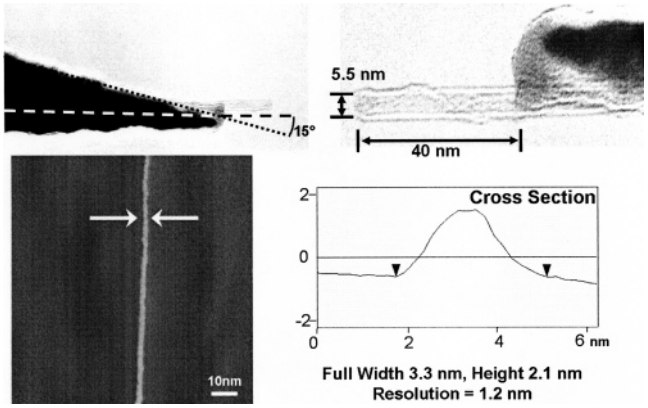

Figure 6. TEM−AFM correlation of a SWNT probe that demonstrated an effective lateral resolution that was 22% of the probe diameter.

Images taken with high quality nanotube probes show no sign of artifacts. These probes all had the nanotubes oriented on the tip at angles close to the substrate surface normal (within 10−20°) and had protrusion lengths ≤40 nm. By directly measuring the nanotube width from each TEM image and comparing that to the obtained AFM resolution, we have determined the average ratio of AFM resolution to tube diameter for SWNT probes in this class to be 1.17. This is a reasonable value, given that thermal vibrations and bending of the nanotube will always slightly increase its effective imaging diameter.

In about 1/3 of the high quality nanotube probes made from the ferritin substrate, as shown in Figure 6, it was found that the effective lateral resolution was significantly *better* than the nanotube probe diameter measured directly with TEM. Figure 6 shows a nanotube probe 5.5 nm in diameter that demonstrated a lateral resolution of 1.2 nm, just 22% of the diameter of the nanotube. It is likely that this enhanced resolution occurs when the nanotube contacts the substrate being imaged with either an asperity or at a specific angle such that only an edge of the nanotube is in contact with the substrate. Imaging a small object with an asperity or an open edge of the tube could lead to the high resolutions observed. Molecular dynamics simulations of surface−nanotube and nanotube−nanotube interactions indicate that other phenomena may also be important, including elastic deformation of the sample nanotube relative to the probe nanotube.[17]

In conclusion, we have combined elements from several previously reported techniques for producing nanotube tips suitable for AFM imaging dry samples that significantly reduce the time of manufacture while improving reproducibility and performance. Feedback from SEM and TEM images of the nanotube probes was used to directly evaluate the effectiveness of the different techniques employed for each of the steps in the fabrication procedure. The optimal process involves the following six steps. (1) Grow nanotubes from ferritin-derived iron nanoparticles on conductive silicon substrates coated only with its native oxide. (2) Pick up a SWNT by imaging the substrate with a 10 μm field of view in tapping mode. (3) Quickly reduce the field of view to approximately 10 nm so that additional tubes are not picked up. (4) Shorten the tube to an appropriate length for imaging without changing substrates using a combination of electrical pulse and push shortening techniques. (5) Image a 100−500 nm region of the substrate to characterize the probe quality. (6) Store shortened nanotube probe in a conductive box.

By growing nanotubes directly on a conductive p-doped silicon substrate with only a native oxide layer, it is possible to pick up, shorten, and test the probe resolution without having to switch samples. This proved to be a significant timesaving optimization. We have found that the resulting nanotube growths (diameter and length) are very similar for all of the investigated catalyst deposition techniques if the spatial density and diameters of catalytic sites are similar. Rates of production have typically reached one probe per hour for several consecutive hours. On exceptional days, the rate can be as high as several per hour. This success has been duplicated with incoming group members.

Overall, we have found AFM image quality to be consistently and significantly better with nanotube tips than with the best silicon AFM tips. Correlations of TEM images of SWNT probes with the effective lateral resolution obtained when using these probes for topographical imaging with AFM indicate that approximately one-third of the probes demonstrate resolution better than the diameter of the nanotube probe itself when imaging nanotubes on a smooth substrate. The methodology described here has resulted in a sufficiently high level of productivity to enable development of single-molecule probes and sensors using functionalized nanotube tips, and has proven capable of fabricating AFM probes with the highest resolution reported to date.

Acknowledgment. The authors thank Jason Hafner, Jim Hone, and Jordan Gerton for fruitful discussions and suggestions. We also thank Carol Garland for many patient hours of TEM imaging and NanoDevices, Santa Barbara, CA for providing direct growth nanotube tips for characterization. Wade, Ma, and Quake were supported by a grant from Pharmagenomix; Shapiro and Collier were supported by Caltech startup funds. Wade, Shapiro, and Collier were also supported by the Caltech President's Fund and NASA contract NAS7-1407.

Supporting Information Available: Experimental procedures for SWNT growth and AFM probe fabrication. This material is available free of charge via the Internet at http://pubs.acs.org.

References

(1) Hafner, J. H.; Cheung, C.-L.; Wooley, A. T.; Lieber, C. M. *Prog. Biophys. Mol. Biol.* **2001**, *77*, 73.
(2) Wong, S. S.; Harper, J. D.; Lansbury; P. T., Jr.; Lieber, C. M. *J. Am. Chem. Soc.* **1998**, *120*, 603.
(3) Wong, S. S.; Woolley, A. T.; Odom, T. W.; Huang, J. L.; Kim, P.; Vezenov, D. V.; Lieber, C. M. *Appl. Phys. Lett.* **1998**, *73*, 3465.
(4) Krishnan, A.; Dujardin, E.; Ebbesen, T. W.; Yianilos, P. N.; Treacy, M. M. J. *Phys. Rev. B* **1988**, *58*, 14013.
(5) Wong, E. W.; Sheehan, P. E.; Lieber, C. M. *Science* **1997**, *277*, 1971.
(6) Larsen, T.; Moloni, K.; Flack, F.; Eriksson, M. A.; Lagally, M. G.; Black, C. T. *Appl. Phys. Lett.* **2002**, *80*, 1996.
(7) Wong, S. S.; Joselevich, E.; Wooley, A. T.; Cheung C.-L.; Lieber, C. M. *Nature* **1998**, *394*, 52.

(8) Wade, L. A.; Shapiro, I. R.; Ziyang, M.; Quake, S. R.; Collier, C. P. *Nanotech 2003* **2003**, *3*, 317.
(9) Hafner, J. H.; Cheung, C.-L.; Oosterkamp, T. H.; Lieber, C. M. *J. Phys. Chem. B* **2001**, *105*, 743.
(10) Snow, E. S.; Campbell, P. M.; Novak, J. P. *Appl. Phys. Lett.* **2002**, *80*, 2002.
(11) Dai, H.; Hafner, J. H.; Rinzler, A. G.; Colbert, D. T.; Smalley, R. E. *Nature* **1996**, *384*, 147.
(12) Cooper, E. B.; Manalis, S. R.; Fang, H.; Dai, H.; Minne, S. C.; Hunt, T.; Quate, C. F. *Appl. Phys. Lett.* **1999**, *75*, 3566.
(13) Hafner, J. H.; Cheung, C. L.; Lieber, C. M. *J. Am. Chem. Soc.* **1999**, *121*, 9750.
(14) Hafner, J. H.; Cheung, C.-L.; Lieber, C. M. *Nature* **1999**, *398*, 761.
(15) Hafner, J.; Rice University, private communication, March, 2002.
(16) Li, Y.; Kim, J. W.; Zhang, Y.; Rolandi, M.; Wang, D.; Dai, H. *J. Phys. Chem. B* **2001**, *105*, 11424.
(17) Shapiro, I. R.; Solares, S.; Esplandiu, M. J.; Wade, L. A.; Quake, S. R.; Goddard, W. A.; Collier, C. P., manuscript in preparation.
(18) Hertel, T.; Walkup, R. E.; Avouris, Ph. *Phys. Rev. B* **1998**, *58*, 13870.
(19) Postma, H. W. C.; Sellmeijer, A.; Dekker, C. *Adv. Mater.* **2000**, *12*, 1299.
(20) Esplandiu, M. J.; Shapiro, I. R.; Solares, S.; Matsuda, Y.; Goddard, W. A.; Collier, C. P., manuscript in preparation.
(21) Cheung, C. L.; Hafner J. H.; Lieber, C.; M. *Proc. Natl. Acad. Sci. U.S.A.* **2000**, *97*, 3809.
(22) Yakobson, B. I.; Avouris, Ph. *Topics Appl. Phys.* **2001**, *80*, 287.

NL049976Q

Supplemental information for NanoLetters, 2004, Vol. 4, 725-731.

Correlating AFM Probe Morphology to Image Resolution for Single Wall Carbon Nanotube Tips

*Lawrence A. Wade,[1,2] Ian R. Shapiro,[3] Ziyang Ma,[2] Stephen R. Quake,[2] C. Patrick Collier[3]**

[1]Jet Propulsion Laboratory, [2]Department of Applied Physics, [3]Department of Chemistry

California Institute of Technology, Pasadena, CA 91125

collier@caltech.edu

Supporting Information:

Nanotube AFM Tip Attachment

Methods we compared for attaching nanotubes to silicon AFM tips include manual assembly, direct growth and pickup.

Smalley's group reported the first example of the use of carbon nanotubes as AFM tips in 1996.[1] They manually attached multi-wall carbon nanotubes (MWNT) and ropes of individual SWNTs to the apex of silicon pyramidal tips using tape adhesive and a micromanipulator in an optical microscope. The main drawback to this method is that MWNT tips large enough to be seen optically did not improve the resolution much beyond standard silicon tips when imaging isolated amyloid fibrils.[2]

We found it fairly efficient to manually attach MWNTs to silicon AFM cantilevers with a 1000x optical microscope. In particular, the rate of assembly was quite high when a 15 V potential was applied between the silicon probe and the nanotubes. This resulted in nearly perfect and rapid alignment of the nanotube to the silicon tip. However, there was not a clear path to doing so with the thin SWNTs required for very high-resolution imaging.

Lieber[3,4] and Quate's[5] groups later showed that individual single wall carbon nanotubes could be directly grown by chemical vapor deposition (CVD) on the silicon tips themselves by first pre-coating the tip with a metal catalyst. In the CVD synthesis of carbon nanotubes, metal catalyst nanoparticles are heated in the presence of a hydrocarbon gas or carbon monoxide; the gas molecules dissociate on the catalyst surface and carbon is adsorbed into the particle. As the carbon precipitates, a carbon nanotube is grown with a diameter similar to that of the catalyst particle.

Two techniques for direct growth have been reported. One involves creating nanopores at the apex of the silicon tip by etching with hydrofluoric acid. Catalyst particles are then deposited inside the nanopores. Carbon nanotubes grown via CVD from such a tip have an appropriate geometry for AFM imaging. While this approach enables fabrication of SWNT tips, the preparation of the porous layer in the silicon is time consuming and placement of the nanotube at the optimal location near the tip apex is

often not achieved. In addition nanotubes typically grew at perhaps 1% of catalytic sites for the growth procedures we have explored. To ensure a moderate probability of having a nanotube grown on a given tip, a large number (20 or more) of etched holes with catalytic particles could be fabricated. However, any given tip might have no tubes, one tube or several tubes.

Direct surface growth of SWNTs by CVD on catalyst-coated silicon tips has also been demonstrated, without the use of pores. We have analyzed approximately 300 tips prepared this way with scanning electron microscopy (SEM) and dozens of tips with transmission electron microscopy (TEM). As seen in Figure 1, we most commonly found densely coated tips with ropes and bundles of SWNTs extending from all sides of the silicon pyramid. These ropes often form complex loop structures not suitable for AFM work. About 1/3 of the tips examined had no tubes near the tip although they may have been covered by nanotubes elsewhere. Only a few percent of the probes had single nanotubes at the tip. Even fewer were oriented vertically.

The mechanical stability of the nanotubes directly grown on the silicon tips was found to be quite poor. As a control, we briefly imaged a smooth surface in tapping mode with tips having nanotubes at the end, as determined by SEM, before any attempts at electrical pulse shortening of the tubes. Afterwards, these probes were re-imaged by SEM. The nanotubes were lost from 7 of 9 tips used in this control experiment. It was also frequently observed during electrical pulse shortening that the tubes would fall off. The final yield of useful nanotube tips was therefore on the order of 1% of the number of originally fabricated probes using the direct growth method. While these results represent early attempts at developing nanotube AFM tips, and there was clearly significant progress possible with continued process development, we decided to focus on the technically simpler problem of developing suitable substrates for nanotube pickup.

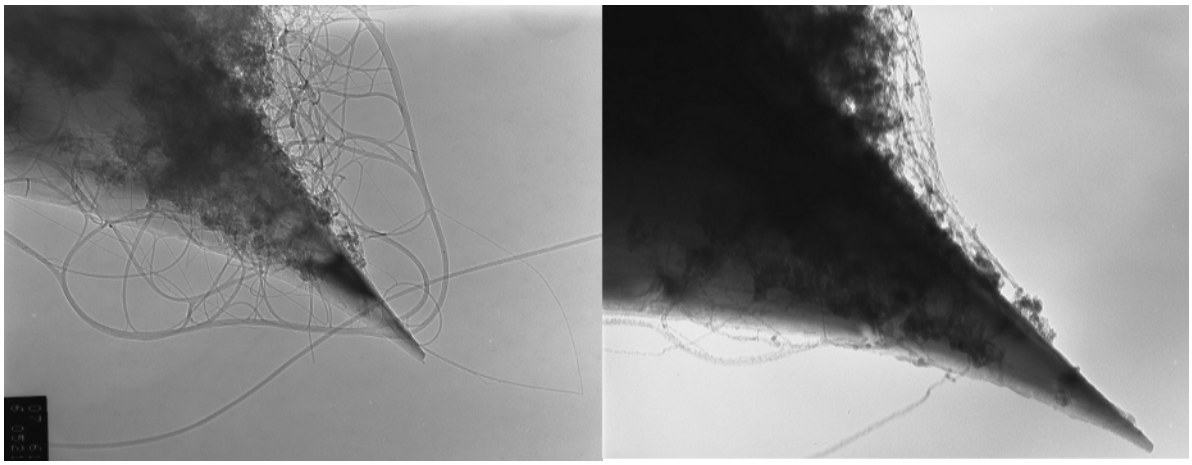

Figure 1. TEM images of nanotubes grown on AFM tip include ropes, multi-walled and single-walled tubes. Note that most of the growths consist of ropes.

Pick-up Substrate Preparation and Nanotube Growth

The pick-up technique is an efficient and consistent method for mounting SWNTs in the proper orientation. When SWNTs are grown on a flat substrate, a small percentage of the tubes are oriented vertically, and can be picked up when the AFM tip scans across the surface in tapping mode. Typically, 1 to 4 tubes can be picked up from a 10 μm square region. Given this tube density, a 6 mm substrate could in theory be used nearly a million times. Nanotube substrates suitable for pickup were produced using four methods of catalyst deposition and compared in side-by-side CVD growths. We achieved similar results with each of these techniques. The suitability of a substrate for nanotube pickup appears to depend primarily on the density and size distribution of the catalytic sites and not on how they were

deposited.

Pick-up of a nanotube is readily observed by monitoring the height signal of the AFM image while looking for a significant step change in the average position. The nanotube binds to the side of the pyramidal AFM tip via attractive van der Waals forces, and usually remains attached firmly enough that it can be repeatedly pressed into and scanned across the substrate surface. A picked up tube can be removed by holding the tip a few hundred nanometers above the substrate and applying a 50V, 100 μs pulse. The removal mechanism is not clear but probably involves either electrostatic attraction or ablation.

Nanotube pick up can reoccur several times, resulting in a 'bundle' of nanotubes attached to the tip. In figure 2, two bundles are shown that most likely were picked up sequentially, although it is possible that they grew this way on the substrate.

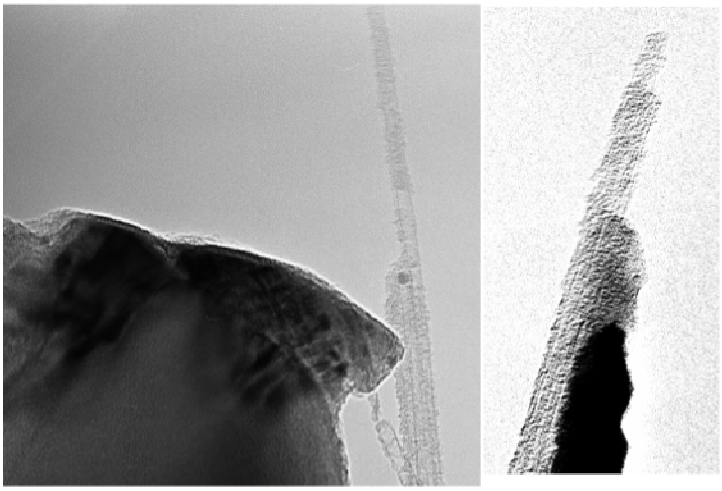

Figure 2. Several tubes have been picked up and stacked in 'bundles' on silicon AFM probes.

Silicon substrates were cleaved under cleanroom conditions, and cleaned by sonicating for 15 minutes at 25 ºC first in toluene, then in acetone, and finally in electronics-grade isopropyl alcohol. To coat the substrates with catalytic iron nanoparticles, 1-30 drops of 1-30 μg/mL $Fe(NO_3)_3 \bullet 9H_2O$ solution in electronics-grade isopropyl alcohol were applied while spinning substrates at 3000 r.p.m., waiting approximately 10 seconds between drops to permit the solvent to evaporate. We found that the catalytic sites would be considerably larger and often less homogeneously distributed over the surface at higher concentrations (e.g. 100-300 μg/mL $Fe(NO_3)_3 \bullet 9H_2O$). The nanotube growths on such substrates were correspondingly larger in diameter and sparser. Again, the critical factor is achieving a high density of very small catalytic sites.

Alternately, some silicon substrates were coated under high vacuum with ~1/40 monolayer of iron applied by thermal or electron beam evaporation. In general, the deposited catalyst sites were large and not optimal for SWNT growth. However, with continued development an optimal pickup substrate could most likely be fabricated via molecular beam epitaxy of the iron catalyst at patterned growth sites. Such a substrate can achieve a nearly uniform catalyst site size and therefore will grow a more uniform distribution of nanotubes; a high density of 1-3 nm diameter tubes with lengths less than 1 μm would be ideal. In addition, such a substrate is substantially more stable over time and can be used for nanotube pickup successfully for several years.

Other silicon substrates were incubated overnight at 4 ºC in a 44 μM solution of ferritin containing ~200 Fe atoms/protein, prepared as described by Dai and coworkers.[6] In this process, a calcination step is required after coating the substrate to remove all organic material originating from the ferritin protein, leaving behind only nanoparticles of iron oxide. This is done by heating the coated substrate in a furnace to 800 ºC in air and holding at that temperature for 10 minutes. This process gave the smallest catalyst size distribution and therefore yielded the most consistent nanotube growths. The catalytic site size distribution and the resultant growths were very consistent with those reported by Dai. The results from

a typical ferritin growth are depicted in Figure 3.

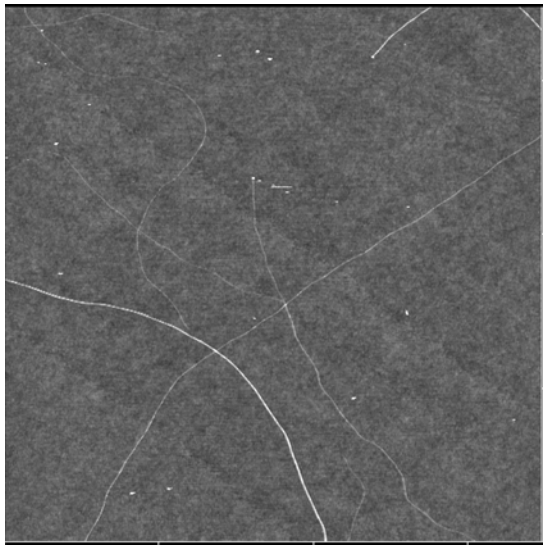

Figure 3. AFM height image of nanotubes grown from ferritin coated oxidized silicon substrate. Field of view is 3 x 3 μm. The height range is 10 nm.

CVD growth was performed in a 22 mm inner diameter Lindberg/Blue M quartz tube furnace with a single heating zone 312 mm long. Five wafers are positioned 12.5 mm apart in a specially designed quartz holder, oriented vertically and with the catalyst coated side facing away from the direction of the incoming gas. A significant advantage of this holder is that it enables up to three small substrates to be mounted side-by-side in each slot for parallel comparison of growth results under nearly identical temperature and gas flow conditions. Optimal nanotube growth is obtained when the holder is positioned at the leeward end of the quartz tube, with the last wafer approximately 2 mm from the end of the heating zone.

The quartz tube is then flushed for 15 minutes with argon gas (Matheson, 99.9995% purity, 440 sccm). The furnace is heated at 950˚ C for approximately 20 minutes, and then held at 950˚C for 15 minutes, both under a flowing atmosphere of Argon (440 sccm) and H_2 (Matheson, research grade, 125 sccm). The furnace is held at this temperature for 5 additional minutes while being flushed with Ar (440 sccm). Growth of nanotubes is then carried out for 0.5 to 2 minutes at 950˚C with CH_4 (Air Liquide, Ultra High Purity, 1080 sccm) and H_2 (125 sccm). Following this growth step, the furnace is again flushed with Argon (440 sccm) and held at 950˚C before rapidly cooling to less than 250˚C, after which the substrates are removed from the furnace.

Substantial variations in growth density occurred between substrates mounted at different positions in the furnace or between identically placed substrates on different runs, which we attribute to temperature variations in the furnace. It was found that the substrate temperature could differ by as much as 20 ˚C with a 1 cm change in position in the furnace or upon changes in the gas composition and mass-flow. A three-stage furnace would likely help improve reproducibility.

Shortening AFM Nanotube Tips

Push and electrical pulse techniques for shortening nanotube AFM tips were examined individually and in combination. This was done on several different surfaces. The most efficient method was to combine pickup, pulse and push shortening all on a single substrate. Force calibration measurements were employed to establish the length of the nanotube tips using the method described by Cooper, *et al*.[5] This approach was found to be suitable for both push and electrical pulse shortening techniques. Once a nanotube has been picked up and shortened, the probe can be used for high-resolution imaging, biomolecular manipulations or force spectroscopy.

A general method for shortening utilizes electrical pulses.[2,7] The procedure to shorten the SWNT in air consists of applying +5 to +30 volt pulses of 20 to 100 μs duration between the AFM tip and a grounded, conductive substrate. Presumably the electrical pulse shortens the nanotube by ablation due to the very high electric field generated at the nanotube end. These pulses are supplied from a Hewlett-Packard 8114A pulse generator and routed to the tip through a Digital Instruments Signal Access Module, or “break-out” box, which is connected to the MultiMode AFM. The pulses are applied while tapping the surface at approximately 70 kHz or 300 kHz, which are the resonance frequencies of the

cantilevers we used (FESP and TESP cantilevers, Digital Instruments). While both work, we tend to prefer the softer FESP probes.

For a given SWNT tip, larger voltage pulses shorten the tube in larger increments, as do pulses of longer duration. But the voltage necessary to carry out shortening varies drastically between individual tubes. This is believed due both to the environmental conditions (especially humidity), and to the widely varying conductivities associated with nanotubes of slightly different molecular structure, for example, between semiconducting and metallic nanotubes. Nanotubes can be shortened precisely with steps as small as 2 nm per pulse. The main drawback to this technique is that the nanotube length removed can vary significantly from one pulse to another and one day to another. Hence to successfully employ this technique one must be careful and attentive. A secondary drawback is that electrical pulsing can dislodge the nanotube electrostatically from the AFM tip. Nevertheless, this second effect can also be exploited to controllably deposit nanotubes precisely on substrates for device fabrication.[8]

Push shortening of short, <100nm long tubes is accomplished by taking successive tip-substrate distance-sweep measurements, and incrementing the sweep start point by ~5 nm at a time.[9] By doing this, the tube can be pushed up along the tip. We find electrical pulse shortening to be more effective than push shortening in terms of being able to shorten a nanotube significantly (e.g. by several hundred nm in 20 nm steps).

For substrates with tubes of significantly varying length that are typically too long the combined approach, pulse shortening followed by push shortening has significant advantages. We have avoided the need for multiple substrates or a patterned substrate that includes pickup and separate shortening regions by reducing the field-of-view to ~10 nm during shortening.

Once the nanotube probe has been shortened to a useful length, the field of view can be increased to 100-500 nm so that a nanotube laying flat on the substrate can be imaged. An AFM image of a horizontal nanotube is a very good way to determine the quality of the final probe. Keeping the field of view small minimizes the chance that another nanotube is picked up.

Imaging with Nanotube Probe Tips

Table 1 in the manuscript lists the properties of 14 nanotube probes that were determined by TEM-AFM correlations described in the text. We have found that topographic image resolution when using SWNT probes was more sensitive to imaging conditions, particularly oscillation amplitude, than conventional silicon probes. This may be due to the small interaction area and compressibility of SWNTs. In addition, in about a third of the cases, the observed AFM resolution was significantly better than would be predicted from the nanotube probe diameter. We have also found that, at a given oscillation amplitude, a small change in drive frequency or in amplitude setpoint can improve image resolution when compared with the optimal settings used for imaging with a bare silicon probe. In particular, the amplitude set point for a nanotube probe can often be as high as 95% of the free oscillation amplitude in air and still permit high resolution imaging. A high amplitude setpoint corresponds to small tip-sample forces, which is desirable for imaging delicate biological macromolecules.

When imaging with SWNT tips in tapping mode AFM, care must be taken to recognize imaging artifacts. Imaging artifacts can be introduced through bending and thermal vibration.[10] In addition, buckled nanotubes frequently demonstrate degraded resolution or artifacts. We have also seen multiple tubes at the tip of some probes, either bundled together to form a “broom”, or attached to different faces of the silicon AFM tip oriented at an angle relative to one another. The data in table 1 of the main paper show that high resolution imaging without artifacts was only accomplished with probes consisting of single tubes that had not been previously buckled.

The TEM images also show the presence of a low density contaminant coating on the probes. Evidence suggests that this material is deposited by silicone oil outgassing from the "gel-pack" in which most of the probes were stored.[11] This is supported by the significant amount of movement of this contaminant over the nanotube observed during TEM imaging. We have found via TEM imaging that gel-free clamshell tip wafer enclosures deposit about an order-of-magnitude less contamination on silicon AFM probes than gel-pack enclosures. This will be important for those wishing to perform dip pen nanolithography or nanotube probe functionalization. However, the contaminant had a limited effect for AFM imaging in air.

References

[1] Dai, H.; Hafner, J.H.; Rinzler, A.G.; Colbert, D.T.; Smalley, R.E. *Nature* **1996,** *384*, 147-150.
[2] Wong, S.S.; Harper, J.D.; Lansbury, P.T.; Lieber, C.M.:*J. Am. Chem. Soc.* **1998,** *120*, 603-604.
[3] Hafner, J.H.; Cheung, C.-L.; Lieber, C.M. *Nature* **1999,** *398*, 761-762.
[4] Hafner, J.H.; Cheung, C.L.; Lieber, C.M. *J. Am. Chem. Soc.* **1999**, 121, 9750-9751.
[5] Cooper, E.B.; Manalis, S.R.; Fang, H.; Dai, H.; Minne, S.C.; Hunt, T.; Quate, C.F. *Appl. Phys. Lett*. **1999,** *75*, 3566-3568.
[6] Li, Y.; Kim, W.; Zhang, Y.; Rolandi, M.; Wang, D.; Dai, H. *J. Phys. Chem. B* **2001,** *105*, 11424-11431.
[7] Wong, S.S.; Joselevich, E.; Wooley, A.T.; Cheung C.-L.; Lieber, C.M.:*Nature* **1998,** *394*, 52-55.
[8] Cheung, C.-L.; Hafner, J.H.; Odom, T.W.; Kim, K.; Lieber, C.M.:*Appl. Phys. Lett.* **2000**, *76*, 3136-3138.
[9] Hafner, J.; Rice University, private communication, March 2002.
[10] Snow, E.S.; Campbell, P.M.; Novak, J.P. *Appl. Phys. Lett.* **2002**, *80*, 2002-2004.
[11] Lo, Y.S.; Huefner, N.D.; Chan, W.S.; Dryden, P.; Hagenhoff, B.; Beebe, T.P. *Langmuir* **1999**, 15, 6522-6526.

Influence of Elastic Deformation on Single-Wall Carbon Nanotube Atomic Force Microscopy Probe Resolution

Ian R. Shapiro,[†] Santiago D. Solares,[‡,§] Maria J. Esplandiu,[†,⊥] Lawrence A. Wade,[||] William A. Goddard,[*,†,§] and C. Patrick Collier[*,†]

Jet Propulsion Laboratory and Departments of Chemistry, Chemical Engineering, and Applied Physics, California Institute of Technology, Pasadena, California 91125

Received: May 14, 2004

We have previously reported that 4−6 nm diameter single-wall carbon nanotube (SWNT) probes used for tapping-mode atomic force microscopy (AFM) can exhibit lateral resolution that is significantly better than the probe diameter when prone nanotubes are imaged on a flat SiO_2 surface. To further investigate this phenomenon, accurate models for use in atomistic molecular dynamics simulations were constructed on the basis of transmission electron microscopy (TEM) and AFM data. Probe−sample interaction potentials were generated by utilization of force fields derived from ab initio quantum mechanics calculations and material bulk and surface properties, and the resulting force curves were integrated numerically with the AFM cantilever equation of motion. The simulations demonstrate that, under the AFM imaging conditions employed, elastic deformations of both the probe and sample nanotubes result in a decrease of the apparent width of the sample. This behavior provides an explanation for the unexpected resolution improvement and illustrates some of the subtleties involved when imaging is performed with SWNT probes in place of conventional silicon probes. However, the generality of this phenomenon for other AFM imaging applications employing SWNT probes remains to be explored.

Introduction

To date, numerous papers have described the preparation of both multiwall and single-wall carbon nanotube (SWNT) atomic force microscopy (AFM) probes.[1−5] SWNT probes offer topographic imaging resolution superior to that of conventional silicon AFM tips, due to their unique chemical and mechanical properties, high aspect ratios, and molecular-scale dimensions.[6−10] In a recent publication we have described an efficient SWNT probe fabrication methodology and correlated the structures [acquired by transmission electron microscopy (TEM)] of 14 probes with the quality of AFM images they produced when imaging a prone SWNT sample.[11] By comparing the observed AFM resolution with the diameter of the probe nanotube measured from the TEM image, we found that the lateral resolution is on average 1.2 times the nanotube probe diameter. This value approaches the expected ideal ratio of unity in the absence of thermal vibrations and bending effects of the probe.[12]

Surprisingly, we have found that for some cases the apparent lateral resolution of the probe nanotube was actually *better* than expected on the basis of its diameter. In one case (shown in Figure 6 of ref 11), which forms the basis for the computational work presented here, we found that the lateral resolution from a 5.5 nm diameter SWNT probe was 1.2 nm, just 22% of the probe diameter. Here and in previous investigations, we define the lateral resolution of a SWNT probe as the difference between the measured height of a sample, which can be determined to high precision with AFM, and the measured diameter (full width at the noise floor), as outlined in Figure 1. In an ideal case, the limiting resolution equals the diameter of the probe. This simplified model, in which the probe and sample are considered to be incompressible objects, has commonly been used to describe AFM resolution.[2,4,5] However, simple geometrical arguments alone cannot explain the subdiameter resolution we observed. The potential for SWNT AFM probes to be used as common research tools requires a more thorough understanding of how the physical, chemical, and mechanical properties of SWNT probes affect image resolution.

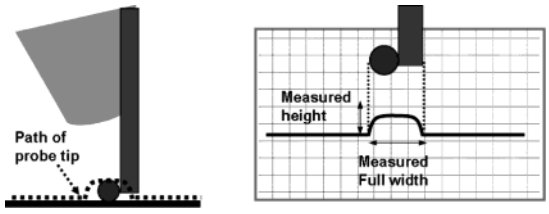

Figure 1. Schematic illustration of the relationship between probe diameter and lateral resolution. The left panel shows a model for a SWNT probe imaging a prone nanotube on a flat surface. The right panel shows the resulting cross-sectional profile, from which the width and height of the imaged nanotube are measured. In this simple geometric model, the full width is equal to the sum of the diameters of the probe and sample nanotubes.

To this end, we present here a quantitative atomistic molecular dynamics investigation of SWNT AFM probe behavior in the context of tapping-mode topographic imaging. The dimensions of the probes and samples are on the order of 1−50 nm, placing them within the range of atomistic simulations. To elucidate the actual tip−sample interactions that give rise to the observed phenomena, we have used TEM−AFM correlation data[11] to construct realistic molecular models of an open-ended SWNT probe interacting with a prone SWNT sample on a flat hydroxyl-

* Corresponding authors: e-mail collier@caltech.edu (C.P.C.), wag@wag.caltech.edu (W.A.G.).
† Department of Chemistry.
‡ Department of Chemical Engineering.
§ Materials and Process Simulation Center.
|| Department of Applied Physics and Jet Propulsion Laboratory.
⊥ Current address: Departament de Quimica, Universitat Autonoma de Barcelona, Barcelona, Spain.

10.1021/jp047937x CCC: $27.50
Published on Web 08/17/2004

TABLE 1: Tapping-Mode AFM Parameters Used for Numerical Simulations

cantilever spring constant	$k = 4.8$ N/m
cantilever quality factor	$Q = 150$
cantilever resonant frequency	$\omega/2\pi = 47.48$ kHz
free air oscillation amplitude	$A_0 = 39$ nm
amplitude set-point	$A_{sp} = 15.4$ nm
excitation force	$F_0 = 1.25$ nN

terminated silicon surface. These models were used to generate accurate potential curves at different positions of the probe relative to the sample. Integration of the resulting forces into the equation of motion for an oscillating cantilever yielded simulated topographic cross-section profiles that corroborate the experimental results. These simulations indicate that, under the AFM conditions employed, both probe bending and localized deformations of the probe and sample SWNTs strongly influence the topographic profile measured with AFM. The reversible elastic nature of these deformations is demonstrated both experimentally and in simulations.

Methods

Fabrication, characterization, and imaging with SWNT AFM probes has been described previously.[11] The effective lateral resolution of each probe was obtained by imaging, under ambient conditions in air, a carbon nanotube lying prone on a flat native-oxide silicon surface. To acquire accurate sample height and width measurements by use of amplitude-modulated AFM, it was necessary to first carefully calibrate the response of the system over a wide range of operational parameters, most importantly, the oscillation amplitude of the SWNT probe. For example, to understand the effects that vertical compression of a sample nanotube by the AFM probe had on the lateral resolution, repeated measurements of the sample nanotube height as a function of probe oscillation amplitude were performed for both conventional silicon and SWNT AFM tips. In all cases, the driving amplitudes employed were kept below the limit corresponding to a 10% reduction in the apparent height of the sample nanotube due to compression. In addition, we measured force calibration curves, which consist of scans of the damped oscillation amplitude as a function of the average tip−sample separation for a given cantilever driving force. The force calibration curves revealed the presence of coexisting attractive and repulsive tip−sample interaction regimes.[13,14] Bistable switching of the cantilever oscillation between the two regimes manifests itself as sudden changes in the observed sample height and width.[15] In general, we avoided these amplitude instabilities and the concomitant experimental artifacts by operating the AFM cantilever with a driving force sufficient to give a free-air oscillation amplitude greater than 20 nm. Consequently, all AFM data presented here can be considered in the repulsive regime or "intermittent contact" mode.

The simulation of the AFM tip motion was carried out by integration of the equation of motion for a damped harmonic oscillator at each AFM scan point on the sample, with the experimental parameter values contained in Table 1:

$$m\frac{d^2z(Z_c, t)}{dt^2} = -kz(Z_c, t) + m\frac{\omega_0}{Q}\frac{dz(Z_c, t)}{dt} + F_{ts}(z_{ts}) + F_0 \cos(\omega t) \quad (1)$$

where $z(Z_c, t)$ is the instantaneous tip position with respect to its average position (Z_c), k is the harmonic force constant for the displacement of the tip with respect to its equilibrium rest position, m is the effective mass, $\omega_0 = \sqrt{k/m}$, the free resonant frequency, Q is the quality factor, z_{ts} is the instantaneous tip position *with respect to the sample*, $F_{ts}(z_{ts})$ the calculated tip−sample interaction force, and $F_0 \cos(\omega t)$ is the oscillating driving force applied to the cantilever.

The use of this equation to describe the tip motion approximates the SWNT tip−cantilever ensemble as a point-mass harmonic oscillator. Nevertheless, this model has been used extensively for numerical treatment of tapping-mode AFM with conventional probes. Although the actual dynamics of the oscillating cantilever in the presence of the probe−sample interactions are nonlinear, the validity of the harmonic approximation for modeling conventional tapping-mode AFM imaging in air has been demonstrated with both theory and experiment for the range of parameters used here.[13,16−19]

Prior to integrating eq 1 we obtained the required tip−sample interaction forces using atomistic models, as explained in detail below. All molecular dynamics (MD) simulations were carried out with Cerius2 molecular simulations software (Accelrys, San Diego, CA). The MD force-field parameters were optimized by fitting the material bulk and surface properties such as elasticity moduli, vibrational frequencies, and surface geometry both to experimental data and to rigorous quantum mechanics calculations on clusters representative of the silicon and graphene systems under study. Equation 1 was integrated by use of the Verlet algorithm to fourth-order accuracy for the tip position and second-order accuracy for the tip velocity.[20]

Realistic atomistic models were constructed for the SWNT probe used for tapping-mode AFM imaging. Every effort was made to match the model structures and simulation conditions as closely as possible to corresponding experimental values, including the nanotube probe diameter, length, angle relative to the substrate normal, and the fine structure at the probe end. All silicon surfaces were (100) and were terminated with hydroxyl groups. The probe was a (40,40)[21] armchair SWNT (5.4 nm diameter, 45 nm length, with 5 nm of fixed atoms at one end of the probe to simulate its attachment site at the AFM tip) constructed from approximately 25 000 carbon atoms. The sample was a (16,16) armchair SWNT (2.2 nm diameter, 10 nm length) constructed from approximately 2600 carbon atoms. The sample SWNT was kept fixed at both ends during the calculations to simulate a very long nanotube, which is unlikely to displace laterally during AFM tapping. Similar models were generated for a conventional silicon tip interacting with the sample nanotube. Several of these models are shown in Figure 2.

The tip−sample interaction potentials were constructed by vertically approaching the sample with the probe nanotube at 0.05 nm intervals, at each point optimizing the system geometry by minimization of the potential energy (additional calculations performed at 300 K showed that the potentials did not significantly change with inclusion of thermal vibrations at room temperature; see Supporting Information). The gradient of this energy−position function with respect to the vertical tip position is the tip−sample interaction force.

To reduce the computational cost of the molecular simulations, each model of a nanotube on the surface included only a small section of the silicon surface, sufficient to obtain an accurate description of the SWNT probe interactions with the sample. This does not give an accurate description of the interaction of the tip with the silicon surface for the cases in which the SWNT tip deforms and slips against one side of the sample nanotube and makes contact with the underlying

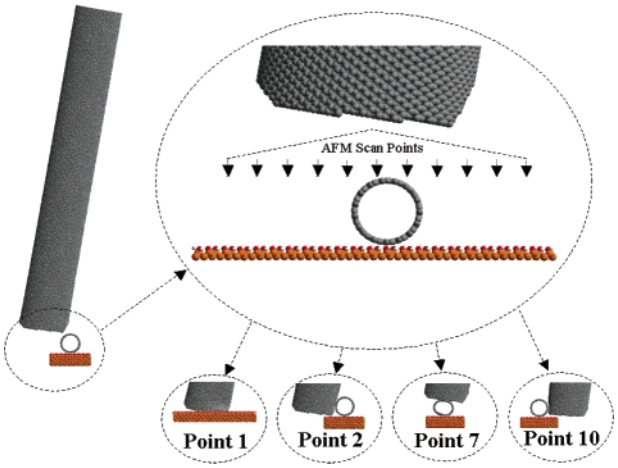

Figure 2. Illustration of the models used to construct the tip−sample interaction profile. The models were constructed on the basis of experimental TEM and AFM data. The final tip position during the AFM scan is shown for four of these points. The corresponding force curves are shown in Figure 3.

substrate. To correct this, another model was constructed *without* a sample nanotube on the substrate to obtain the interaction forces between the tip and the bare silicon surface. The deformation of the tip was considered in all cases when the relative position of the surface and the end of the tip was calculated for each scan point.

This procedure provides a discrete set of points, and so regression analysis with simple functional forms (e.g., polynomials or functions of the form $1/r^n$) was performed in order to obtain continuous force−position curves, which can be programmed easily into the AFM dynamics integration code. The forces for a given vertical position of the tip may have different values, depending on whether the tip has slipped relative to the sample SWNT. This was accounted for during the construction of the force−position curves and incorporated into the integration of the cantilever equation of motion.

Results and Discussion

A series of 11 curves showing probe−sample force versus height were generated at evenly spaced points along the line perpendicular to the axis of the sample nanotube. The separation between adjacent points was 1 nm. Figure 2 shows the location of the 11 scan points relative to the sample nanotube, and four of the corresponding tip−sample force curves are shown in Figure 3 (all 11 energy-position curves, from which these force curves were obtained by differentiation, are provided in the Supporting Information). The abscissa on all graphs in Figure 3 corresponds to the distance between the lowest atom on the SWNT tip and the highest atom of the Si(100)−OH surface. Negative values on this axis correspond to elastic deformations in nanotube and surface geometry, including local deformation of the probe, as well as slight deformation of the Si−OH surface.

Each of the 11 probe−sample force curves generated along the scan line was then inserted into eq 1 and integrated for the average tip positions relative to the substrate (Z_c) ranging from 50 to 0 nm, by use of actual imaging parameter values.[11] For each scan point and tip position, eq 1 was integrated numerically for 0.02 s with a 0.1 ns integration step (to fourth-order accuracy with respect to the time step size) to determine the oscillation amplitude of the cantilever as a function of its vertical position [the initial tip position was set equal to its equilibrium position, i.e., $z(Z_c, 0) = 0$, and the initial velocity was set to zero in all cases]. This numerical procedure is analogous to acquiring a "force calibration curve" for each scan point in Figure 2.

The result of these calculations was a curve showing the cantilever equilibrium oscillation amplitude as a function of the average vertical position of the tip for each point along the scan direction. Two of these curves are shown as insets in Figure 5. The simulated cross-section trace in Figure 5 was then constructed by plotting the locus of tip position values which maintained the oscillation amplitude at the set-point value of 15.4 nm. Note that the average tip−sample separation for each scan point is given relative to the value obtained when imaging the bare silicon oxide substrate.

The construction of tip−sample interaction force curves through molecular simulations of large finite systems underestimates the long-range attractive forces present in the system. This is because the calculation of nonbonded interaction energies between pairs of atoms is generally limited to a cutoff radius on the order of 1 nm or less to reduce the cost of the computation (the number of nonbonded interactions, which scales with the square of the number of atoms in the simulation, can account for over 90% of the computation costs of a typical system). Underestimating the long-range attractive forces, and hence the region of positive force gradient, can alter the predicted regions of amplitude bistability.[13] However, at the free oscillation amplitude employed here, $A_0 = 39$ nm, the average force will be determined almost exclusively by the repulsive part of the tip−sample interaction potential,[16] and thus the underestimation of the attractive contribution will have negligible influence on the simulated topographic profile.

Under ambient conditions, a thin film of water is adsorbed on hydrophilic surfaces such as SiO_2. The formation of a meniscus or liquid bridge between the surface and the probe will result in an additional attractive capillary force that depends on probe−sample distance.[22] We did not include the effects of adsorbed water in our model. We do not expect that inclusion of these effects will significantly change the nanoscopic interactions between the probe and sample nanotubes predicted by the simulations. Future work will address this issue.

Simple models of AFM resolution assume that the probe is a rigid, incompressible cylinder with a flat or hemispherical end. In practice this is not the case. High-magnification TEM images show that the ends of the probe nanotubes are generally open due to ablation from an electrical etching procedure used to shorten the nanotube probes to useful lengths.[2,4] Purely geometric arguments suggest that an open-ended tube with protruding asperities could, for extremely low-relief samples, provide resolution comparable to the asperity diameter rather than the full diameter of the probe, in direct analogy to results published for silicon probes.[23] However, probe asperities are unlikely to be important when imaging a sample nanotube that has a diameter (height above the surface) comparable to that of the probe.

The Young's modulus of SWNTs is approximately 1.25 TPa along the tube axis.[24] Because of this very high stiffness, only a small amount of longitudinal compression of the tube occurs during AFM imaging. However, Snow et al.[12] have shown that SWNT probes are susceptible to bending due to their high aspect ratio if not oriented vertically relative to a surface. Image artifacts from bending can be minimized by shortening the nanotube probe so that it protrudes less than 100 nm beyond the supporting silicon tip.

While SWNTs have exceptional longitudinal stiffness, radially they are far more compliant,[25] a characteristic that permits localized deformation of the nanotube walls. The likelihood of deformation is further increased due to the structural discontinu-

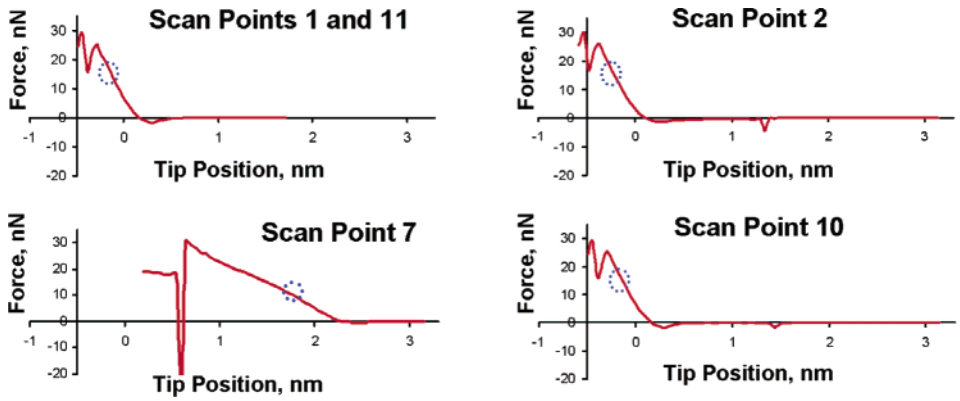

Figure 3. Tip−sample force curves calculated for four of the 11 scan points shown in Figure 2. The abscissa on all graphs corresponds to the distance between the lowest atom on the SWNT tip and the highest atom of the Si(100)−OH surface. The small blue circle in each plot indicates the lowest position that the probe tip reached during the subsequent AFM imaging simulation.

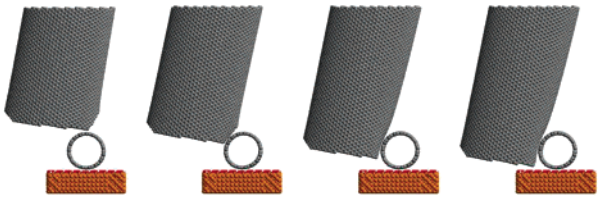

Figure 4. Illustration of the slipping phenomenon of the SWNT probe past the SWNT sample for scan point 3. Both bending along the length of the probe and local deformation contribute to slipping. The picture shows that the simulated probe is more susceptible to deformation, although the sample nanotube does deform slightly. This is due to the larger diameter of the probe (5.4 vs 2.2 nm) and the fact that its end is opened, which decreases its radial rigidity.

ity at the opened end of the nanotube probe. The susceptibility of nanotubes to radial deformation is predicated upon two competing effects: the energy cost associated with strain of the nanotube as it is deformed from its equilibrium cylindrical geometry, and the stabilization that a compressed nanotube gains due to increased interlayer van der Waals attractions. These two competing effects scale in opposite directions with increased nanotube diameter, such that larger SWNTs are easier to deform radially than smaller diameter tubes.[26] We have previously observed that SWNTs attached to silicon AFM tips via the "pick-up" method tend to be 4−6 nm, which is larger than the tubes observed lying prone upon the pick-up substrate (1−3 nm).[11] We postulated that the increase in net binding energy with larger diameter nanotubes stems from the interplay between van der Waals forces and the geometric stiffness of a nanotube. The resulting radial "softness" of these larger nanotubes not only increases the energy with which they bind to a silicon probe during pick-up but also has significant implications when they are subsequently used for AFM imaging.

Our molecular dynamics simulations show lateral slipping of the probe nanotube relative to the sample nanotube, due both to bending along the length of the probe and to localized radial deformation of the probe and sample at the point of contact (illustrated in Figure 4 and Supporting Information). This behavior is a function of the structures and relative orientations of the probe and sample nanotubes, the applied tip−sample force, and the position (in the $x-y$ plane) of the probe nanotube relative to the sample nanotube. The smaller the $x-y$ distance between the center of the probe tube and the axis of the sample tube, the larger the force required to deform the nanotubes and cause them to slip past one another. That is, when the probe presses on the edge of the sample nanotube, a smaller amount of force is required to cause it to slip laterally than when it presses on the crown of the sample nanotube. The simulations show this deformation behavior to be completely reversible and elastic (images illustrating reversibility are provided in the Supporting Information). Experimentally, the elasticity is demonstrated by the fact that we have not observed the topographic cross sections to change significantly during imaging at a given amplitude set-point, and the TEM images taken of each probe after AFM imaging show no alterations of the nanotube structure, such as kinks or buckles.

This lateral slipping and deformation of the probe nanotube explains the observation of sub-probe-diameter effective resolution. In amplitude−feedback tapping-mode AFM, modulation of the cantilever oscillation amplitude depends on the average strength of the tip−sample forces.[27] The AFM controller adjusts the extension of the z-piezoelectric element in order to hold the amplitude of the cantilever oscillation at the fixed value designated by the amplitude set-point (an independent variable set by the user). The resulting z-piezo voltage corrections are converted to units of length and output as the topographic height data. If the probe and sample deform negligibly under the associated tapping forces, the sample height can be measured accurately to within the precision of the piezoelectric element, typically <1 Å. However, if either material is significantly deformable, the resultant z-piezo data represents a more complex convolution of probe and sample structure.

The simulations conducted here indicate that when the probe SWNT is tapping on an edge of the sample SWNT, the subsequent repulsive forces deform *both* nanotubes sufficiently to allow them to slip past one another without significantly influencing the cantilever oscillation amplitude. In fact, when the very edges of the probe and sample tubes come into contact, the net tip−sample force is actually attractive rather than repulsive, due to the large area of favorable contact between the graphitic surfaces. This is illustrated in the force curves for scan points 2 and 10 by the fact that the net force is negative between the two local minima, corresponding to the region in which the probe and the sample are slipping past one another. Once lateral slipping takes place, the resulting tip−sample interaction is dominated by the repulsive forces between the probe SWNT and the Si/SiO_2 surface. Thus, for that particular $x-y$ position, the AFM controller does not "see" the sample nanotube. Only when the probe SWNT is positioned closer to the crown of the prone sample SWNT are the interaction forces between the probe and sample nanotubes high enough to cause sufficient damping of the cantilever oscillation amplitude. At scan point 7, which corresponds to the probe tapping on the crown of the sample nanotube, no slipping can take place under

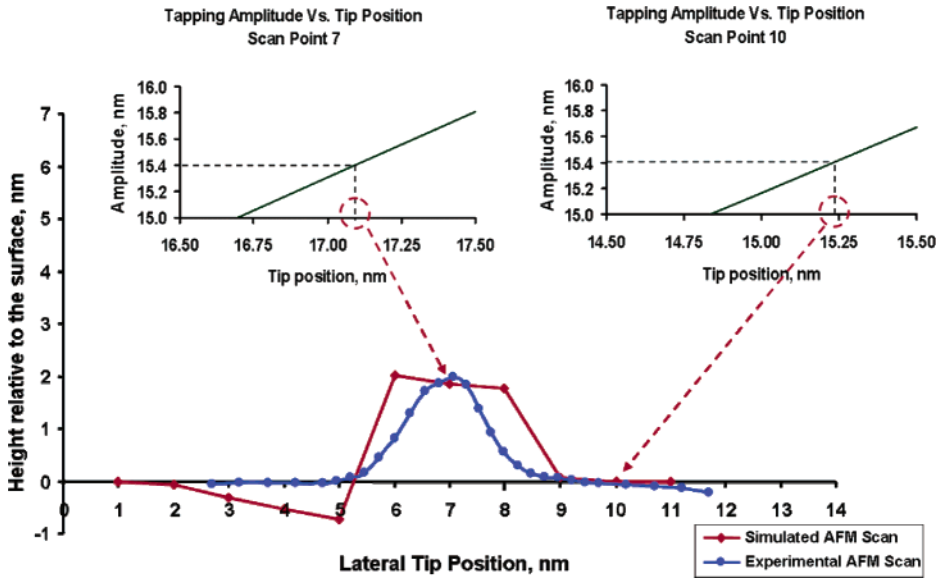

Figure 5. Schematic depiction of the construction of an AFM scan from molecular and AFM dynamics simulations. The two inset amplitude−distance curves illustrate how the measured height is obtained for each scan point at an amplitude set-point of 15.4 nm. The resulting AFM cross-sectional height is given relative to the average tip separation from the bare SiO_2 surface. The horizontal axis corresponds to the scan points shown in Figure 2. For comparison, the cross section from experimental data has been overlaid on the same scale with its center point arbitrarily positioned to match up with the center of the simulated cross section.

the imaging conditions given in Table 1, because the maximum tip−sample repulsive force does not exceed the necessary threshold, ∼30 nN. Here, the cantilever amplitude is damped by the sample nanotube and the AFM records the interaction. The net result is that the topographic data indicates an apparent nanotube width that is smaller than the sum of the probe and sample SWNT diameters.

A quantitative representation of this phenomenon is illustrated in Figure 5. The lower half of the figure shows the effective cross section of a sample nanotube, calculated from the MD and AFM dynamics simulations, obtained when a SWNT probe is used under the repulsive tapping conditions given in Table 1. This scan shows two important features that are also observed experimentally. First, the apparent probe resolution for this simulation is 2.0 nm, 37% of the probe diameter. Additionally, the simulated cross section is asymmetric, which is a direct consequence of the specific SWNT probe geometry, particularly the tilt angle, that favors probe−sample slipping more on one side of the sample than on the other.

In contrast, MD simulations have shown that a conventional silicon probe does not slip under the same imaging conditions. This is because the rigidity of the silicon probe requires higher forces to induce deformation, while the larger radius of curvature of the probe tip actually generates smaller lateral forces compared to a SWNT probe. The different behavior is also due to the chemical properties of crystalline silicon, which strongly influence the surface−surface interactions with the SWNT sample, as well as the attractive van der Waals forces between the larger silicon tip and the silicon surface. These two parameters in particular, probe compressibility and adhesion forces, are transformed in a highly nonlinear way by the response of the oscillating tip.[28] Thus, SWNT probes perform in a fundamentally different manner than silicon probes, not merely when imaging prone carbon nanotubes but for a variety of samples.

We have also simulated a smaller diameter SWNT probe since previous reports have described nanotube probes in the 1−3 nm diameter range.[1,2,4,7] Smaller diameter nanotube probes should be far less susceptible to localized radial deformation, due to their increased resistance against compression (as seen with the sample nanotube, Figure 4). However, the bending mode along the length of a thinner probe is actually softer, since the flexural rigidity scales as r^4.[29] The probe was a (16,16) armchair SWNT (2.2 nm diameter, 20 nm length) that had approximately the same aspect ratio as the larger 5.4 nm probe used in this study. As before, the probe nanotube was oriented at 15° relative to the surface normal and the sample nanotube was 2.2 nm in diameter and 10 nm in length. Images from the simulation are incorporated in the Supporting Information and show that slipping also occurs for the thinner probe when tapping on the edge of the sample nanotube. For this probe, the slipping is almost entirely due to bending and not to local deformation. The corresponding tip−sample force curve indicates that the force opposing the slipping motion of the probe was negligible.

Dekker and co-workers[30] have reported previously that as a function of driving amplitude in tapping-mode imaging, a conventional silicon AFM probe can vertically compress a 1.4 nm single-wall nanotube lying on a flat surface, resulting in a decreased apparent *height*. This experimental observation is consistent with previously reported experimental measurements and molecular dynamics simulations, which described radial deformation of 1−3 nm single-wall carbon nanotubes by both van der Waals forces and external static loads.[31−33] Here we show that in tapping-mode AFM, the associated forces deform the probe nanotube in addition to the sample, strongly influencing the subsequently measured effective *lateral* resolution.

Our molecular dynamics simulations confirm that some vertical compression of a prone sample nanotube occurs under standard tapping-mode AFM conditions, for both conventional silicon AFM probes and SWNT probes. However the simulations predict that this effect is, at most, 10% of the sample tube diameter for 1−3 nm SWNTs and occurs primarily when the probe nanotube is tapping on the crown of the sample nanotube (see, for example, point 7 in Figure 2). This corresponds well with our experimental calibration of sample tube compression under the tapping-mode operating parameters employed. The enhanced lateral resolution, on the other hand, is due to the

highly localized deformation and bending of the probe nanotube along the edges of the sample nanotube, and is therefore not affected significantly by vertical compression.

Conclusion

By correlating experimental data with atomistic molecular dynamics simulations, we have characterized how the unique properties of SWNT AFM probes can strongly influence topographic imaging fidelity. Probe bending and mutual local deformation of both the probe and sample nanotubes under typical tapping-mode AFM forces can result in a reduction of the measured width of the sample tube, and consequently an ostensive improvement of the lateral resolution, to the extent that the resolution can appear to be better than expected from the measured diameter of the nanotube probe. We are interested in determining whether a similar improvement of apparent resolution is observed when imaging less compliant samples of different material composition, such as metallic or semiconducting nanoparticles.

Given the interest in nanoscale physical and biological phenomena, SWNT probes are likely to evolve into a more common research tool. A complete understanding of probe behavior in the context of atomic force microscopy is therefore critical. It is important to note that the lateral resolution reported here is an apparent value, arising from the simplified definition set forth in the Introduction, and was studied for the specific case of 4−6 nm diameter open-ended SWNT probes imaging 2−3 nm diameter SWNTs adsorbed on a flat surface. In practice, the resolving power of an AFM probe is dependent upon the experimental context. It is of particular importance to determine whether the observed deformation phenomenon results in a net gain or loss of structural information when SWNT probes are used to image soft nanoscale samples, such as biological macromolecules. The improvement in the apparent resolution due to deformation of the probe and sample nanotubes in this study was a consequence of the relatively high driving forces applied to the AFM cantilever. Tapping-mode AFM imaging performed in this repulsive regime with conventional probes has been shown to damage biomolecules.[14] In addition, resolution less than the probe diameter could complicate interpretation of AFM images quantitatively.

The combination of probe structure determination, characterization of imaging resolution, and simulated dynamic behavior described here has highlighted practical differences between carbon nanotube probes and conventional silicon probes. This work also underscores the usefulness of atomistic simulations in describing the dynamic nanoscale interactions involved in scanning probe microscopy.

Acknowledgment. We thank Professor Stephen Quake, Dr. Jordan Gerton, and Ms. Yuki Matsuda for essential discussions. I.R.S., M.J.E., and C.P.C. were supported by Caltech startup funds and by Arrowhead Research. S.D.S. and W.A.G. were supported by NSF-NIRT Grant CTS-0103002, and by the Microelectronics Advanced Research Corporation (MARCO) and its Focus Center on Function Engineered NanoArchitectonics (FENA). L.A.W. was supported by the Caltech President's Fund and NASA Contract NAS7-1407.

Supporting Information Available: Simulated energy−distance and force−distance curves, force-field parameters, effects of thermal vibrations, illustrations of bending and local deformation modes of a 5.4 nm diameter SWNT probe, of lateral slipping of a 2.2 nm diameter SWNT probe, and the elastic nature of nanotube deformation. This material is available free of charge via the Internet at http://pubs.acs.org.

References and Notes

(1) Cheung, C.-L.; Hafner, J. H.; Odom, T. W.; Kyoungha, K.; Lieber, C. M. *Appl. Phys. Lett.* **2000**, *76*, 3136.
(2) Wong, S. S.; Wooley, A. T.; Joselevich, E.; Cheung, C. L.; Lieber, C. M. *J. Am. Chem. Soc.* **1998**, *120*, 8557.
(3) Campbell, P. M.; Snow, E. S.; Novak, J. P. *Appl. Phys. Lett*. **2002**, *81*, 4586.
(4) Hafner, J. H.; Cheung, C. L.; Oosterkamp, T. H.; Lieber, C. M. *J. Phys. Chem. B* **2001**, *105*, 743.
(5) Choi, N.; Uchihashi, T.; Nishijima, H.; Ishida, T.; Mizutani, W.; Akita, S.; Nakayama, Y.; Ishikawa, M.; Tokumoto, H. *Jpn. J. Appl. Phys.* **2000**, *39*, 3707.
(6) Dai, H.; Hafner, J. H.; Rinzler, A. G.; Colbert, D. T.; Smalley, R. E. *Nature* **1996**, *384*, 147.
(7) Wong, S. S.; Woolley, A. T.; Odom, T. W.; Huang, J.-L.; Kim, P.; Vezenov, D. V.; Lieber, C. M. *Appl. Phys. Lett.* **1998**, *73*, 3465.
(8) Hafner, J. H.; Cheung, C. L.;. Wooley, A. T.; Lieber, C. M. *Prog. Biophys. Mol. Biol*. **2001**, *77*, 73.
(9) Stevens, R. M. D.; Frederick, N. A.; Smith, B. L.; Morse, D. E.; Stucky, G. D.; Hansma, P. K. *Nanotechnology* **2000**, *11*, 1.
(10) Nguyen, C. V.; Stevens, R. M. D.; Barber, J.; Han, J.; Meyyapan, M. *Appl. Phys. Lett.* **2002**, *81*, 901.
(11) Wade, L. A.; Shapiro, I. R.; Ma, Z.; Quake, S. R.; Collier, C. P. *Nano Lett*. **2004**, *4*, 725.
(12) Snow, E. S.; Campbell, P. M.; Novak, J. P. *Appl. Phys. Lett.* **2002**, *80*, 2002.
(13) García, R.; San Paulo, A. *Phys. Rev. B.* **1999**, *60*, 4961.
(14) San Paulo, A.; García, R. *Biophys. J*. **2000**, *78*, 1599.
(15) García, R.; San Paulo, A. *Phys. Rev. B.* **2000**, *61*, R13381.
(16) San Paulo, A.; García, R. *Phys. Rev. B.* **2002**, *66* R041406.
(17) San Paulo, A.; García, R. *Phys. Rev. B.* **2001**, *64*, 193411.
(18) Rodriguez, T. R.; García, R. *Appl. Phys. Lett.* **2002**, *80*, 1646.
(19) Cleveland, J. P.; Anczykowski, B.; Schmid, A. E.; Elings, V. B. *Appl. Phys. Lett.* **1998**, *72*, 2613.
(20) For an explanation of (*n*, *m*) designation, see Jeroen, W. G.; Wildoer, L. C.; Venema, A. G.; Rinzler, R.; Smally, E.; Dekker, C. *Nature* **1998**, *391*, 59.
(21) Frenkel, D.; Smit, B. *Understanding Molecular Simulation*; Academic Press: San Diego, CA, 2002; pp 69−71.
(22) García, R.; Calleja, M.; Rohrer, H. *J. Appl. Phys.* **1999**, *86*, 1898.
(23) Engel, A.; Müller, D. *Nat. Struct. Biol.* **2000**, *7*, 715.
(24) Krishnan, A.; Dujardin, E.; Ebbesen T. W.; Yianilos, P. N.; Treacy, M. M. J. *Phys. Rev. B* **1998**, *58*, 14013.
(25) Shen, W.; Jiang, B.; Han, B. S.; Xie, S.-S. *Phys. Rev. Lett.* **2000**, *84*, 3634.
(26) Gao, G.; Çağin, T.; Goddard, W. A. *Nanotechnology* **1998**, *9*, 184.
(27) García, R.; Perez, R. *Surf. Sci. Rep*. **2002**, *47*, 197.
(28) Lee, S. I.; Howell, S. W.; Raman, A.; Reifenberger, R. *Phys. Rev. B.* **2002**, *66*, 115409.
(29) Wilson, N. R.; Macpherson, J. V. *Nano Lett.* **2003**, *3*, 1365.
(30) Postma, H. W. C.; Sellmeijer, A.; Dekker, C. *Adv. Mater*. **2000**, *12*, 1299.
(31) Hertel, T.; Walkup, R. E.; Avouris, P. *Phys. Rev. B* **1998**, *58*, 13870.
(32) Li, C.; Chow, T.-W. *Phys. Rev. B* **2004**, *69*, 073401.
(33) Ruoff, R. S.; Tersoff, J.; Lorents, D. C.; Subramoney, S.; Chan, B. *Nature* **1993**, *364*, 514.

Supplemental information for J.Phys.Chem.B 2004, Vol. 108, 13613-13618.

Influence of Elastic Deformation on Single-Wall Carbon Nanotube AFM Probe Resolution

Ian R. Shapiro, Santiago D. Solares, Maria J. Esplandiu, Lawrence A. Wade, William A. Goddard, and C. Patrick Collier**

Supporting Information

Tables of force field parameters:

TABLE 1: Force Field Energy Expression

Total Energy	$E = E_{\text{bond stretch}} + E_{\text{angle bend}} + E_{\text{torsion}} + E_{\text{stretch-bend-stretch}} + E_{\text{stretch-stretch}} + E_{\text{van der Waals}}$ *
Bond Stretch Energy Type Harmonic	$E = \frac{1}{2} K_b (R - R_o)^2$
Bond Stretch Energy Type Morse	$E = D_o (e^{-\alpha(R-R_o)} - 1)^2$ where $\alpha = \sqrt{\frac{K_b}{2D_o}}$

Angle Bend Energy Theta Harmonic	$E = \frac{1}{2} K_\theta (\theta - \theta_o)^2$
Angle Bend Energy Cosine Harmonic	$E = \frac{1}{2Sin^2\theta_o} K_\theta (Cos\theta - Cos\theta_o)^2$
Torsion Energy Dihedral	$E = \frac{1}{2} K_t [1 - d_t Cos(n_t \phi)]$
Stretch-Bend-Stretch Energy R-Cosine	$E = (Cos\theta - Cos\theta_o)[C_{ij}(Rij - Rij_o) + C_{jk}(Rjk - Rjk_o)]$
Stretch-Stretch Energy R-R	$E = K_{ss}(Rij - Rij_o)(Rjk - Rjk_o)$
Van der Waals Energy Morse	$E = D_o(\chi^2 - 2\chi)$ where $\chi = e^{\frac{-\gamma}{2}(\frac{R}{R_o} - 1)}$
Van der Waals Energy Lennard-Jones 6-12	$E = D_o((\frac{R_o}{R})^{12} - 2(\frac{R_o}{R})^6)$

* The present study did not consider charged samples or probes; hence the energy expression does not include electrostatic energy terms.

TABLE 2: Force Field Atom Types

H_	Non-acid hydrogen
H___A	Acid hydrogen
C_3	SP^3 carbon
C_2G	SP^2 graphite carbon
O_3	SP^3 oxygen
Si0	Bulk silicon
SiS	Surface silicon
SiOH	Surface silicon connected to OH group
SiH	Surface silicon connected to H_

TABLE 3: Harmonic Bond Stretch Parameters

Atom 1	Atom 2	K_b	R_o
SiOH	O_3	700.0000	1.5870
O_3	H___A	500.0000	1.0000
C_3	H_	662.6080	1.1094
C_3	C_3	699.5920	1.5140
C_2G	H_	700.0000	1.0200
C_2G	C_3	739.8881	1.4860
H_	H_	700.0000	0.7500

TABLE 4: Morse Bond Stretch Parameters

Atom 1	Atom 2	K_b	R_o	D_o
SiOH	H_	382.3870	1.4830	92.6000
SiH	H_	382.3870	1.4830	92.6000
Si0	Si0	193.0936	2.3810	73.7000
SiOH	Si0	193.0936	2.3810	73.7000
SiH	Si0	240.0660	2.3810	73.7000
SiOH	SiOH	193.0936	2.3810	73.7000
SiH	SiH	193.0936	2.3810	73.7000
C_2G	C_2G	720.0000	1.4114	133.0000
SiS	Si0	193.0936	2.3810	73.7000
SiS	SiS	193.0936	2.3810	73.7000

TABLE 5: Angle Bend Parameters

Atom 1	Atom 2	Atom 3	Type	K_θ	θ_o
C_2G	C_2G	C_2G	Cosine harmonic	196.1300	120.0000
C_2G	C_2G	C_3	Cosine harmonic	196.1300	120.0000
C_3	C_2G	C_3	Cosine harmonic	188.4421	120.0000
C_2G	C_3	C_2G	Cosine harmonic	220.2246	109.4710
C_3	C_3	C_3	Cosine harmonic	214.2065	109.4710
C_3	C_2G	H_	Cosine harmonic	98.7841	120.0000
Si0	SiH	H_	Cosine harmonic	42.2500	115.1400
Si0	Si0	Si0	Cosine harmonic	31.2682	105.0467
C_3	C_3	H_	Cosine harmonic	117.2321	109.4710
C_2G	C_3	H_	Cosine harmonic	121.6821	109.4710
C_2G	C_3	C_3	Cosine harmonic	220.2246	109.4710
C_2G	C_2G	H_	Cosine harmonic	103.1658	120.0000
Any	O_3	Any	Theta harmonic	100.0000	104.5100
H_	SiOH	H_	Cosine harmonic	58.2560	110.9530
Si0	SiOH	O_3	Cosine harmonic	102.7429	109.4710
SiOH	SiOH	Si0	Cosine harmonic	31.2682	105.0467
SiOH	Si0	Si0	Cosine harmonic	31.2682	105.0467
SiOH	Si0	SiOH	Cosine harmonic	31.2682	105.0467
SiH	SiH	Si0	Cosine harmonic	31.2682	105.0467
Si0	SiH	Si0	Cosine harmonic	31.2682	105.0467
SiH	Si0	SiH	Cosine harmonic	31.2682	105.0467
SiS	Si0	Si0	Cosine harmonic	31.2682	105.0467
SiS	Si0	SiS	Cosine harmonic	31.2682	105.0467
Si0	SiOH	Si0	Cosine harmonic	31.2682	105.0467
SiOH	SiOH	O_3	Cosine harmonic	102.7429	109.4710
SiH	SiH	H_	Cosine harmonic	42.2500	115.1400

Si0	SiS	Si0	Cosine harmonic	31.2682	105.0467	100
SiS	SiS	Si0	Cosine harmonic	31.2682	105.0467	
O_3	SiOH	H_	Cosine harmonic	57.6239	109.4710	

TABLE 6: Torsion Parameters

Atom 1	**Atom 2**	**Atom 3**	**Atom 4**	**K_t**	**n_t**	**d_t**
C_2G	C_2G	C_2G	C_2G	85.1200	2.0000	1.0000
Any	C_2G	C_2G	Any	100.0000	2.0000	1.0000
Any	C_2G	C_3	Any	2.0000	3.0000	-1.0000
Any	C_3	C_3	Any	2.0000	3.0000	-1.0000
Any	SiOH	O_3	Any	2.0000	3.0000	-1.0000

TABLE 7: Stretch-Bend-Stretch Parameters

Atom 1	**Atom 2**	**Atom 3**	**Rij**	**Rjk**	**θ_o**	**C_{ij}**	**C_{jk}**
Si0	Si0	Si0	2.3810	2.3810	109.4712	-14.8184	-14.8184

TABLE 8: Stretch-Stretch Parameters

Atom 1	**Atom 2**	**Atom 3**	**K_{ss}**	**Rij_o**	**Rjk_o**
Si0	Si0	Si0	3.6001	2.3810	2.3810

TABLE 9: van der Waals Parameters

Atom 1	**Atom 2**	**Type**	**D_o**	**R_o**	**γ**
H_	H_	Morse	0.018145	3.56979	10.70940

H___A	H___A	LJ 6-12	0.000099	3.19499	N/A	101
C_3	C_3	LJ 6-12	0.146699	3.98300	N/A	
C_2G	C_2G	Morse	0.098999	3.993999	10.96300	
O_3	O_3	LJ 6-12	0.095700	3.404599	N/A	
Si0	Si0	LJ 6-12	0.310000	4.269999	N/A	
SiS	SiS	LJ 6-12	0.310000	4.269999	N/A	
SiOH	SiOH	LJ 6-12	0.310000	4.269999	N/A	
SiH	SiH	LJ 6-12	0.310000	4.269999	N/A	
C_2G	H_	Morse	0.034710	3.744610	12.25614	
SiOH	C_2G	LJ 6-12	0.175186	4.132000	N/A	
Si0	C_2G	LJ 6-12	0.175186	4.132000	N/A	
SiH	C_2G	LJ 6-12	0.175186	4.132000	N/A	
SiS	C_2G	LJ 6-12	0.175186	4.132000	N/A	
O_3	C_2G	LJ 6-12	0.097336	3.699299	N/A	

The original parameters used to create these force fields were developed in the Materials and Process Simulation Center (California Institute of Technology).[1,2,3] Additional parameters were added to study mixed systems (containing silicon, graphitic systems, oxygen and hydrogen) by applying arithmetic and/or geometric combination rules to existing parameters, by quantum mechanics calculations conducted by Weiqiao Deng, Richard Muller and William A. Goddard III or by using generic terms from the Dreiding force field.[4]

Energy-position and force-position curves from MD simulations:

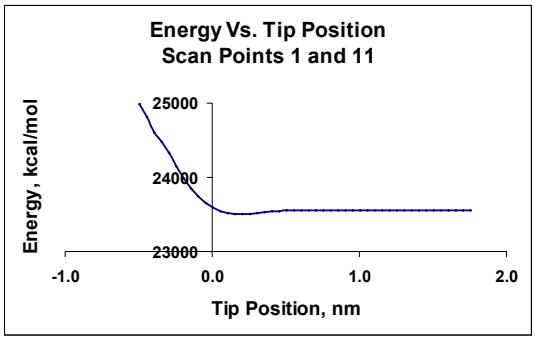

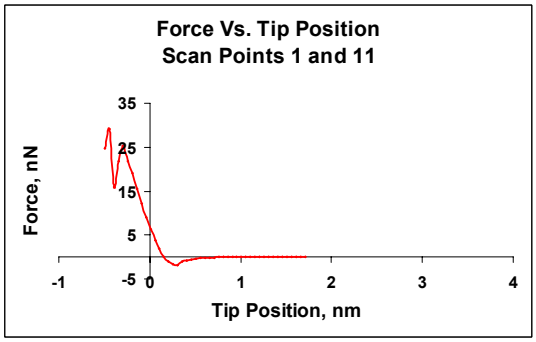

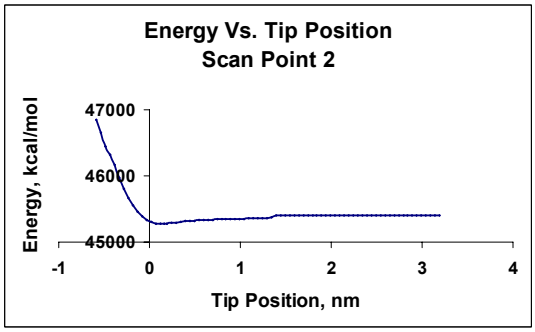

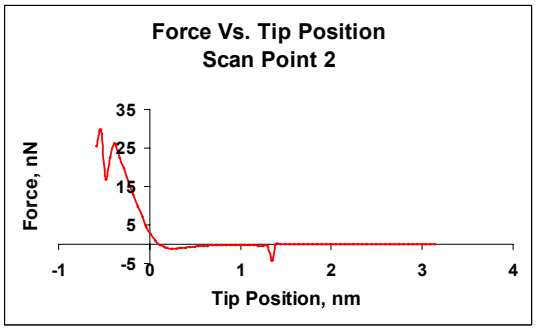

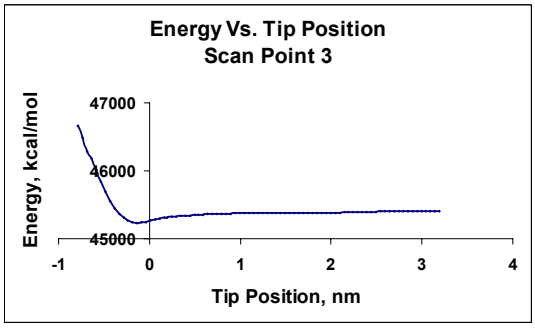

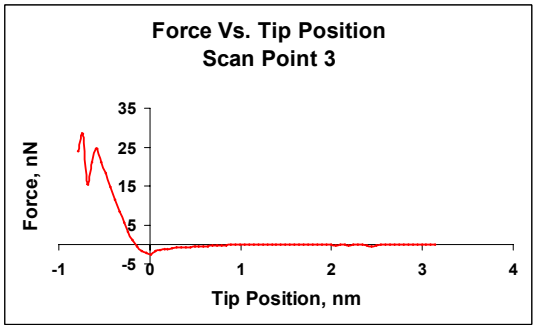

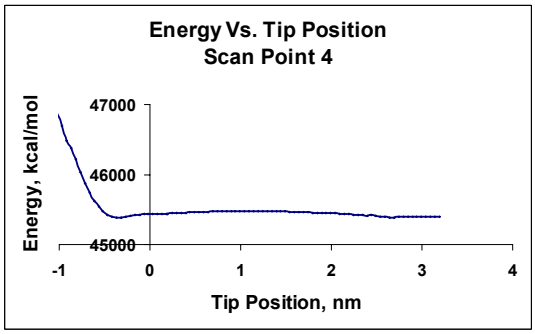

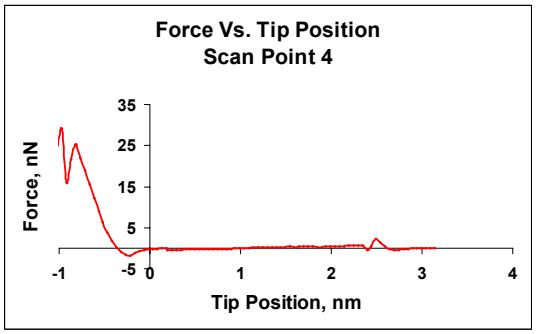

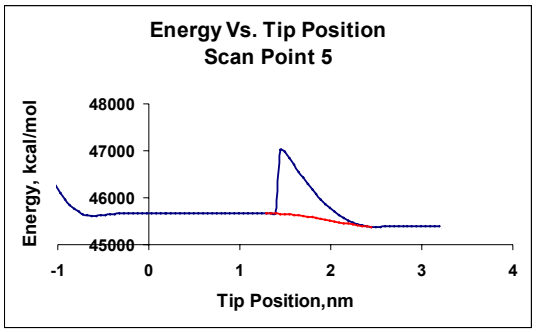
Energy Vs. Tip Position
Scan Point 5
Energy, kcal/mol
48000
47000
46000
45000
-1
0
1
2
3
4
Tip Position,nm

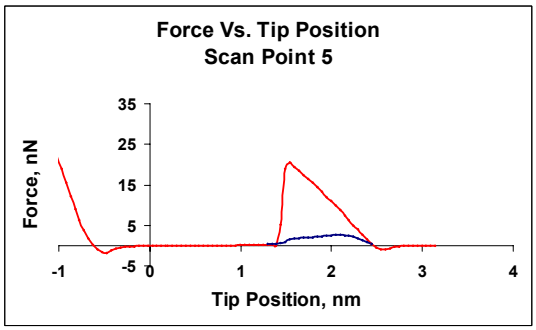
Force Vs. Tip Position
Scan Point 5
Force, nN
35
25
15
5
-5
-1
0
1
2
3
4
Tip Position, nm

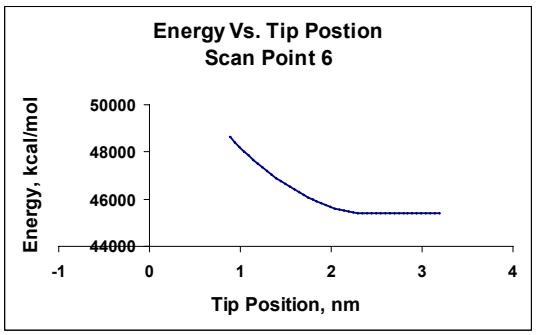
Energy Vs. Tip Postion
Scan Point 6
Energy, kcal/mol
50000
48000
46000
44000
-1
0
1
2
3
4
Tip Position, nm

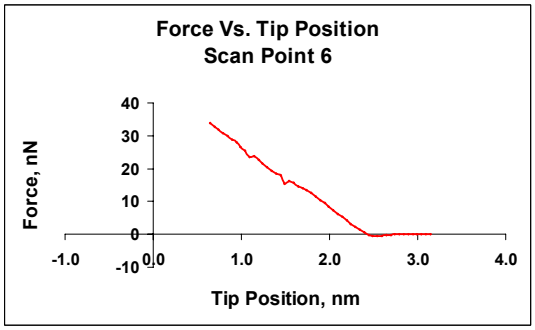
Force Vs. Tip Position
Scan Point 6
Force, nN
40
30
20
10
0
-10
-1.0
0.0
1.0
2.0
3.0
4.0
Tip Position, nm

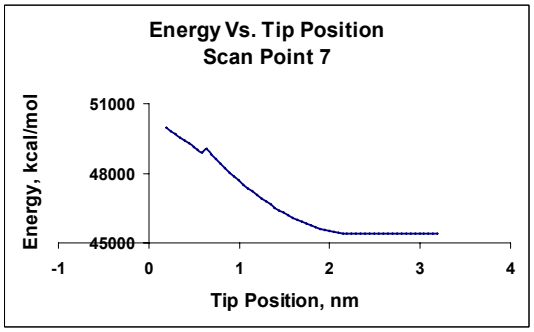
Energy Vs. Tip Position
Scan Point 7
Energy, kcal/mol
51000
48000
45000
-1
0
1
2
3
4
Tip Position, nm

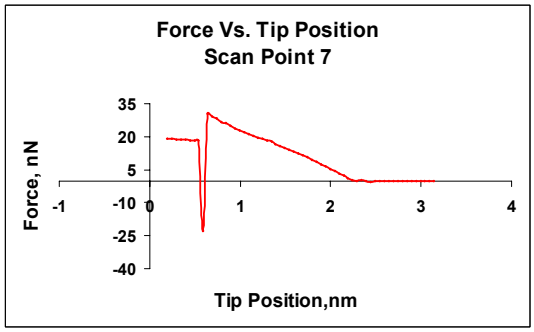
Force Vs. Tip Position
Scan Point 7
Force, nN
35
20
5
-10
-25
-40
-1
0
1
2
3
4
Tip Position,nm

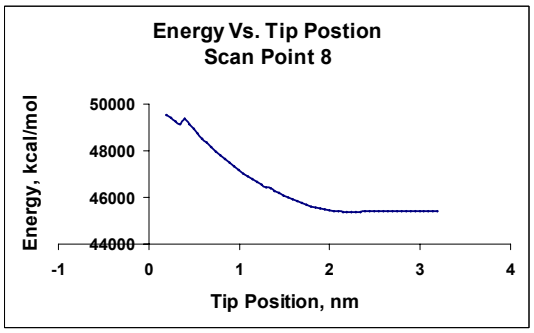
Energy Vs. Tip Postion
Scan Point 8
Energy, kcal/mol
50000
48000
46000
44000
-1
0
1
2
3
4
Tip Position, nm

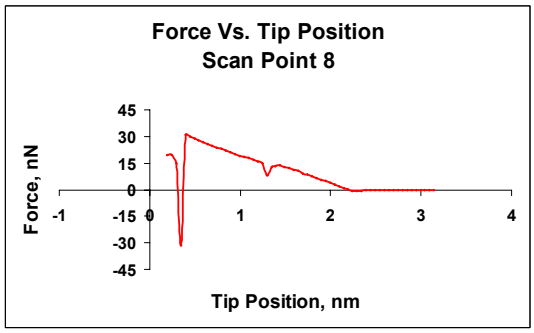
Force Vs. Tip Position
Scan Point 8
Force, nN
45
30
15
0
-15
-30
-45
-1
0
1
2
3
4
Tip Position, nm

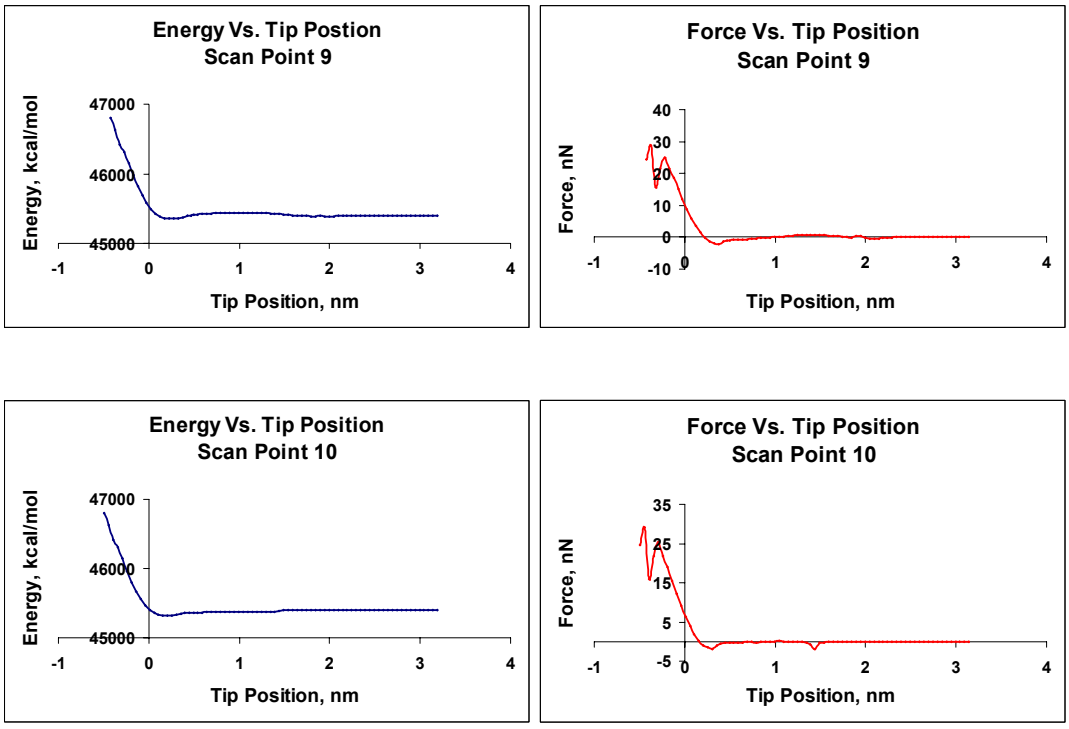

Figure S-1: Energy-distance and force-distance profiles generated for various probe positions, corresponding to the scan points in figure 2 of the manuscript.

Effect of thermal vibrations:

The tip-sample potentials and the corresponding force curves were constructed at zero kelvin to minimize the cost of the simulations. However, thermal vibration calculations at 300 K show that the potentials would not be significantly different at room temperature. The additional thermal energy would have the effect of lowering the energy barriers that the system needs to overcome in order for the probe to slip off the sample. This is only relevant for scan points 6, 7 and 8, for which the probe did not slip at the tip-sample forces present during tapping mode imaging. Only at much higher forces (~30 nN) did the probe slip off the sample nanotube at these points. The force and energy curves presented here show that the energy requirement to cause these points to slip is the same as that required to longitudinally compress the probe by one full nm, which is much greater than the available thermal energy. Our calculations show that the maximum horizontal displacement of any atom on the tip of the probe at 300 K is below 0.095 nm (less than 1.8% of the probe width), which would not significantly

change the relative position of probe and sample. The amplitude of the vertical vibrations is less than 0.055 nm.

Characterization of SWNT deformation modes:

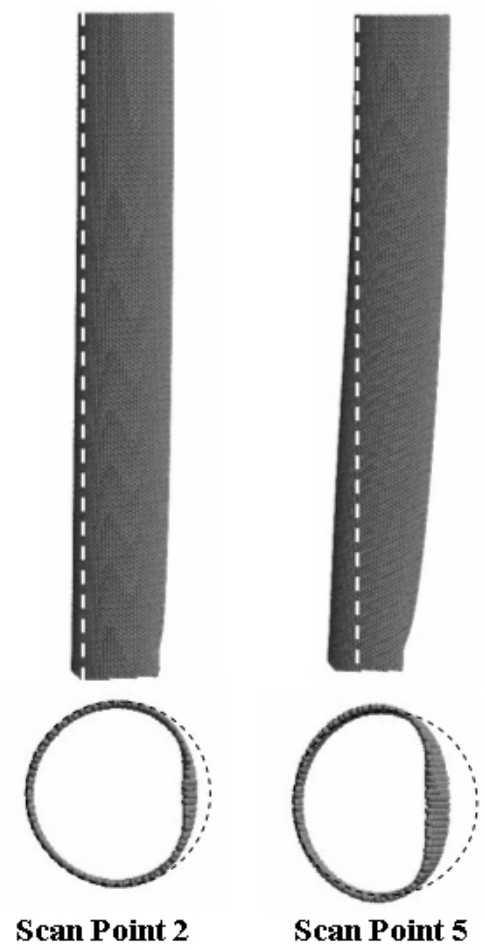

Figure S-2: Degree of probe bending shown for two extreme cases: scan point 2, the point on the scan where the 5.4 nm diameter probe nanotube first comes into contact with the sample nanotube, and scan point 5, the last point for which slipping occurred during the imaging simulation. The probe images have been rotated from their original tilted position to illustrate the amount of bending that the probe undergoes. The local deformation of the tip is also shown in the bottom pictures. The images show that both bending and local deformation contributes significantly to the reduction in the probe's effective resolution for this SWNT diameter.

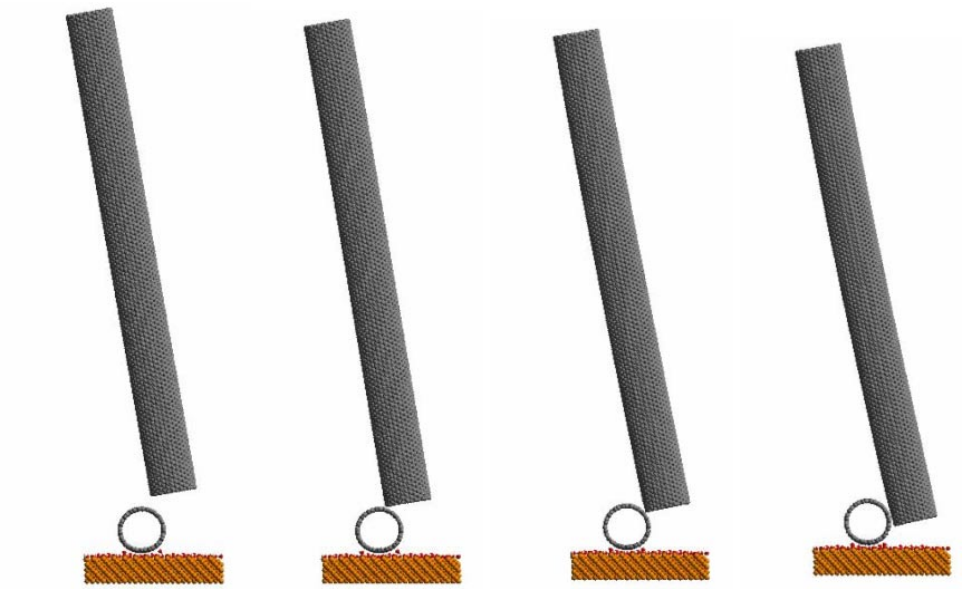

Figure S-3: The images from the simulation with the 2.2 nm diameter probe show that slipping also occurs for smaller probes, although it is primarily due to bending and not to local deformation, due to the higher radial stiffness for the thinner SWNT probes. In order to slip, the probe needed to displace laterally a distance of approximately 0.5 nm (22% of the sample diameter).

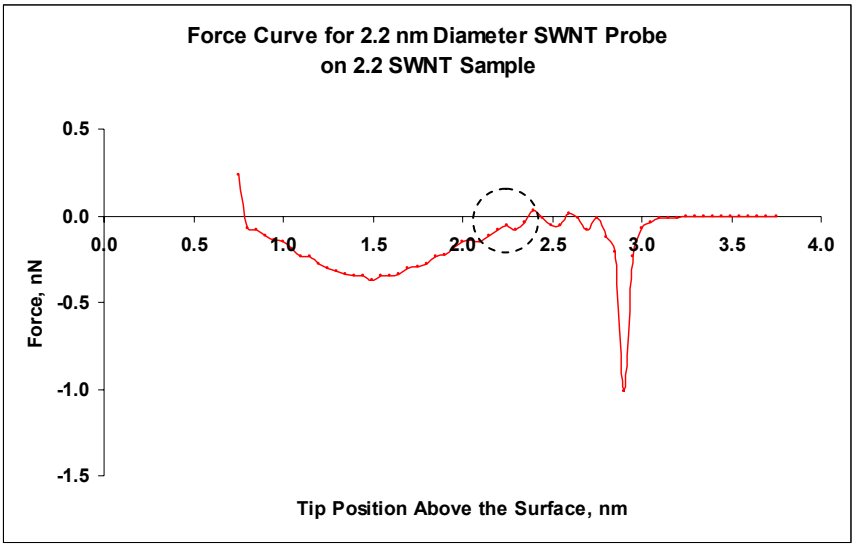

Figure S-4: Force curve for the 2.2 nm SNWT probe. The dashed circle shows the region where slipping occurs. As the graph shows, there is no significant force opposing the slipping motion of the probe. The negative peak in the force is due to snap-to-contact as the probe first approaches the sample.

Illustration of reversibility in SWNT probe-sample interaction:

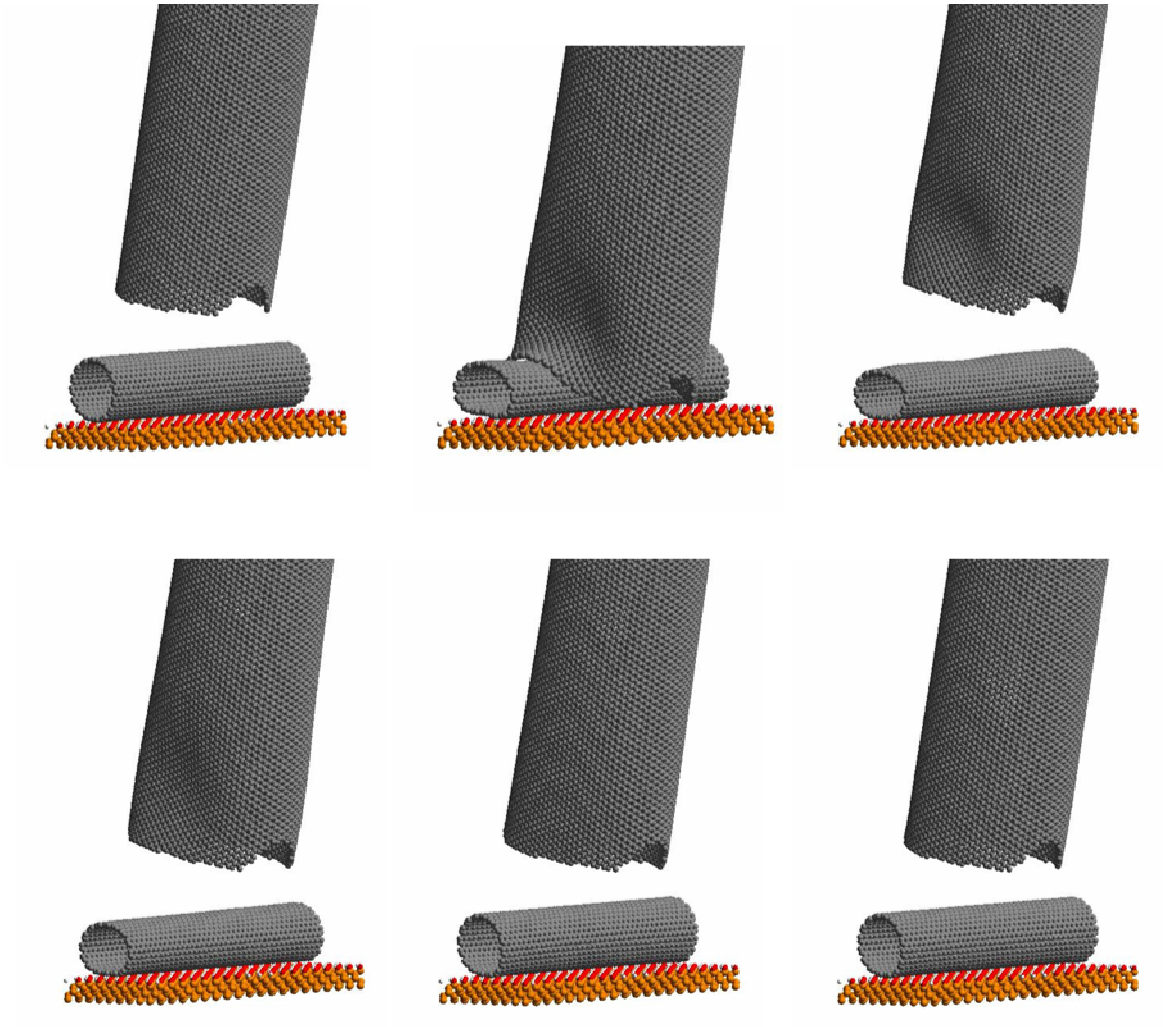

Figure S-5: Sequential images illustrating the reversible elastic nature of the deformation phenomenon. The top image on the left corresponds to the SWNT tip and sample before contact for scan point 6. The second image corresponds to the tip compressing the SWNT with a force of 33 nN (approximately twice the maximum tip-sample force observed during imaging). Images 3-6 correspond to intermediate geometry relaxation steps of the probe and sample after the probe has retracted. Note that the time required for geometry relaxation is on the order of 20 *ps,* one order of magnitude smaller than the integration time step used for AFM dynamics simulations (0.1 *ns*). This guarantees that the probe and sample are able to relax before the tip impacts the sample a second time.

References:

1. Musgrave, C.B., **1995.** PhD Dissertation Thesis: *"Molecular Mechanics and ab Initio Simulations of Silicon (111) Surface Reconstructions, Semiconductors and Semiconductor Superlattices, H Abstraction Tool for Nanotechnology, Polysilanes, and Growth of CVD Diamond"* California Institute of Technology.

2. Guo, Y.J. **1992.** PhD Dissertation Thesis: *"Molecular Simulations of Buckyball Fullerenes. Quantum Chemistry Studies on High Tc Superconductors"* California Institute of Technology.

3. Guo, Y.J.; Karasawan N.; Goddard W.A. III. *Nature,* **1991,** *351*, 6326.

4. Mayo, S.; Olafson, B.; Goddard, W. A. III. *J. Phys. Chem*. **1990**, 94, 8897.

Acknowledgements

My particular thanks to Pat Collier, Ian Shapiro, Maria Jose Esplandiu, and Santiago Solaris for being wonderful collaborators. Thanks also to Carol Garland for all of the TEM imaging used in this study. I gratefully acknowledge the help and advice of Jason Hafner who shared the pioneering nanotube fabrication techniques he developed without reservation. Funding for these efforts, provided by the Caltech President's Fund, JPL Research and Technology Development Program, Arrowhead Research and Pharmagenomix, is gratefully acknowledged.

References

[1] L. A. Wade, I. R. Shapiro, Z. Ma, S. R. Quake, and C. P. Collier, Correlating AFM Probe Morphology to Image Resolution for Single-Wall Carbon Nanotube Tips, Nano Lett., **2004**, 4, 725-731.

[2] I. R. Shapiro, S. D. Solares, M. J. Esplandiu, L. A Wade, W. A. Goddard and C. P. Collier, Influence of Elastic Deformation upon Single-Wall Carbon Nanotube AFM Probe Resolution, J. Phys. Chem. B, **2004,** *108*, 13613-13618.

[3] Method for Manufacturing Single Wall Carbon Nanotube Tips, US 7,211,795 B2, L.A. Wade, P. Collier, S. Quake, I. Shapiro, and Z. Ma issued May 1, 2007.

[4] Selective functionalization of carbon nanotube tips allowing fabrication of new classes of nanoscale sensing and manipulation tools, US 7,514,214, L.A. Wade, I.R. Shapiro, C. P. Collier, M.J. Esplandiu, V.G. Bittner and K.P. Giapis issued April 7, 2009.

Appendix A

VA-TIRFM supporting information

The following are included in this appendix:

A.1 Relationships between excitation laser beam position and angle of incidence in the coverslip

A.2 Evanescent field intensity as a function of angle of incidence

A.3 Imaging sequence table including which images are averaged

A.4 Andor iXonem+ 897 camera background

A.5 Photographs of Teflon cell culture chamber

A.6 Photographs of TIRF microscope and excitation positioning assembly

A.1 Relationships between excitation laser beam position and angle of incidence in the coverslip

Prism based TIRF angle measurement (July 1-6, 2010)
These values were used for all of the data analysis presented in this thesis.

Excitation laser distance from start of TIRF (microns)	Excitation laser distance from actuator 'Home' (mm)	Incidence angle at N-LAF21 coverslip-air interface
30	9.54	62.20011804
40	9.55	61.56618627
50	9.56	60.97517815
60	9.57	60.36034276
70	9.58	59.75822335
80	9.59	59.15776225
90	9.6	58.57997814
100	9.61	58.09803605
110	9.62	57.47241837
120	9.63	56.94762434
130	9.64	56.49142547
140	9.65	55.87686581
150	9.66	55.38603725
160	9.67	54.84467262
170	9.68	54.37578342
180	9.69	53.84137628
190	9.7	53.36306498
200	9.71	52.85593721
210	9.72	52.38820027
220	9.73	51.89360491
230	9.74	51.3740835
240	9.75	50.89504964
250	9.76	50.42415964
260	9.77	49.87027422
270	9.78	49.43323141
280	9.79	48.96066402
290	9.8	48.51270569
300	9.81	48.06056125
310	9.82	47.57803314
320	9.83	47.121313
330	9.84	46.65059582
340	9.85	46.23064973

Table A.1 Angle as a function of beam position. This measurement was made in the TIRF region using a SF-2 equilateral prism (n=1.648) to project the beam onto lab wall. Then the beam angle in air was calculated, then the beam angle in the prism and then that in the coverslip using a coverslip index of refraction-1.7993 and a 488 nm laser.

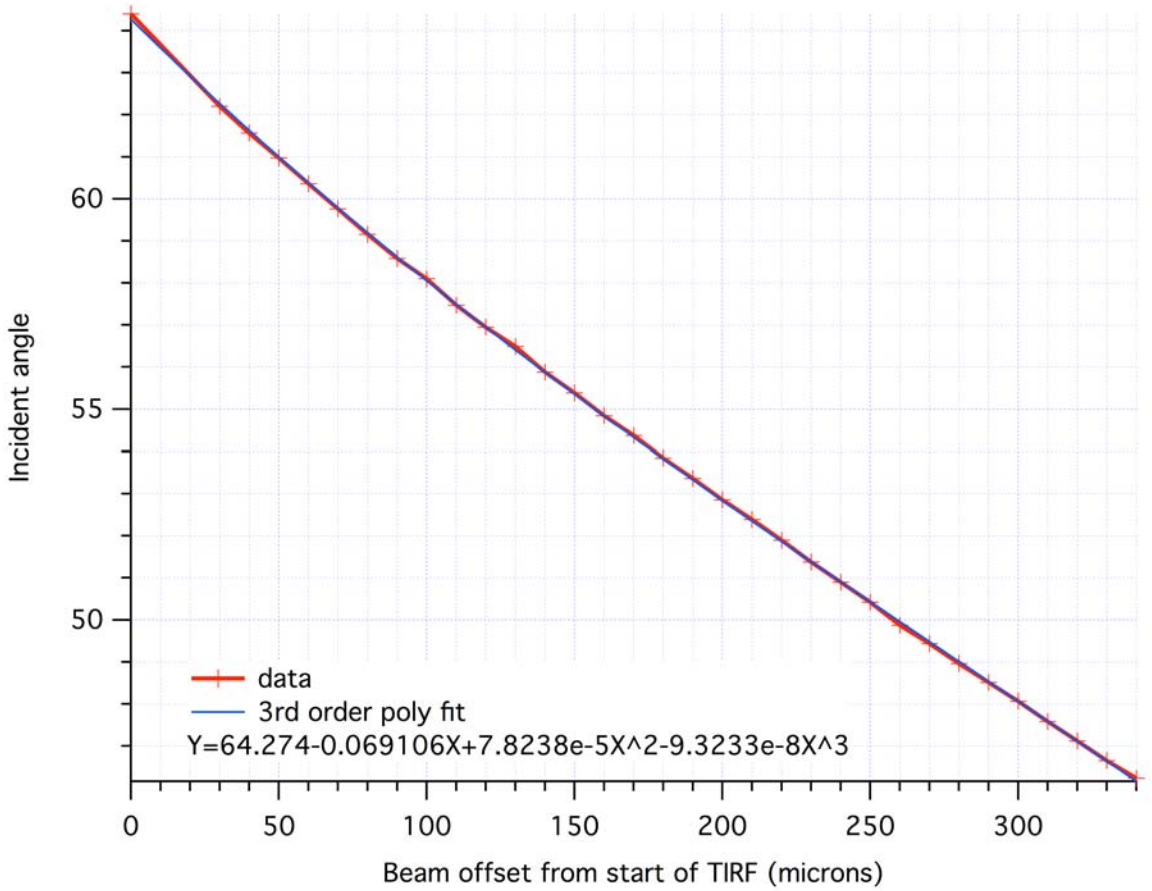

Figure A.1 Angle of incidence as a function of beam offset. This is from the prism-based measurement of beam angle as a function of position. The curve fit relation was used to relate the position data in my lab notebook to the angle of incidence. That angle of incidence was in turn used to establish penetration depth. Therefore this figure was used to select which images to use for image processing in every case for the data presented in Chapter 2 of this thesis. This relation was used rather than absolute beam position because at times there was some drift in the measured position. In that case I would use the offset from onset of TIRF (defined by the maximum angle allowed by the back aperture) to determine what the angle and thereby the penetration depth were.

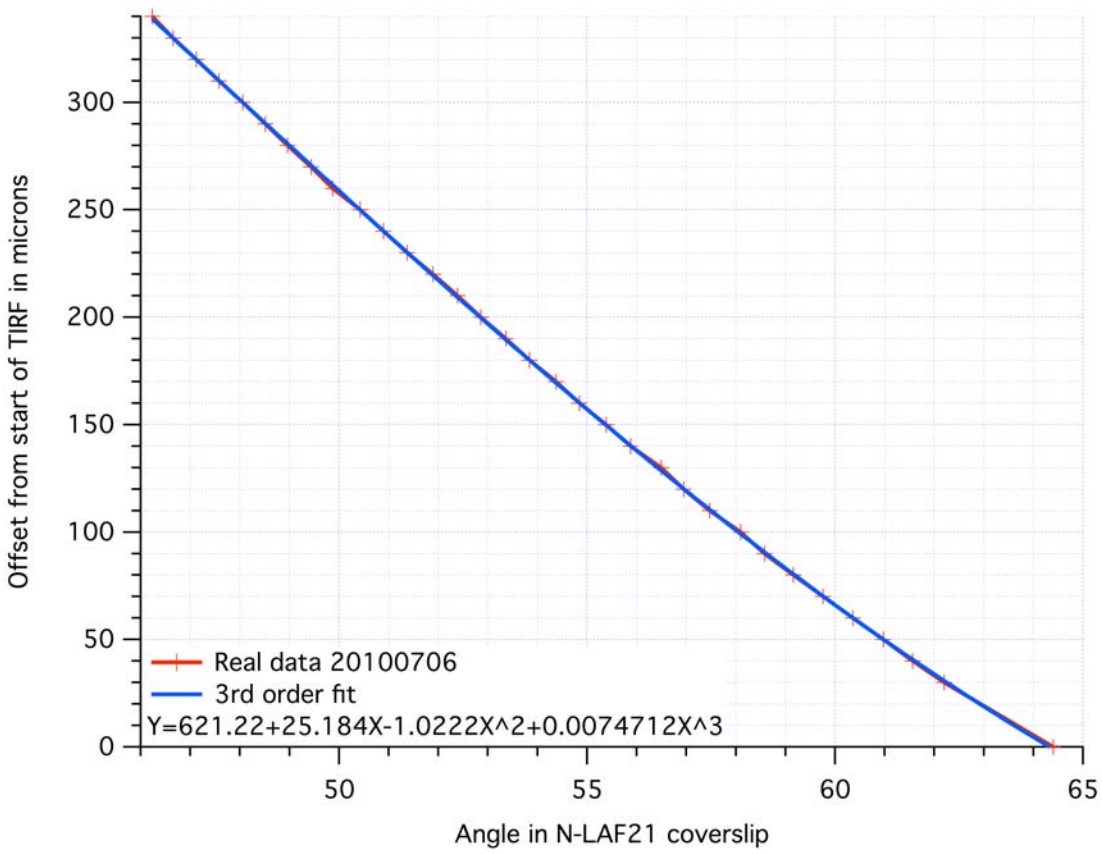

Figure A.2 Prism based TIRF measurement fit and data: Offset laser position as a function of angle. This is the inverse plot from that in Figure A.1.

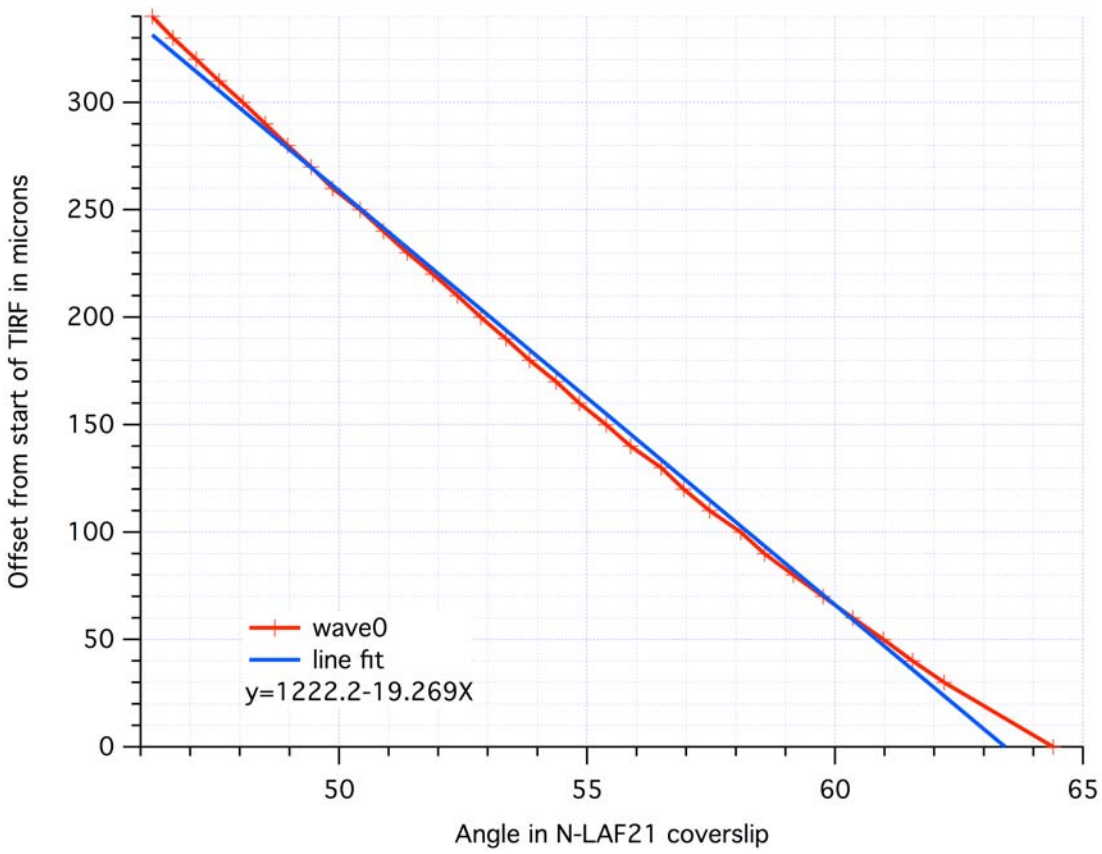

Figure A.3 Prism TIRF data compared to a linear fit: it is really close.

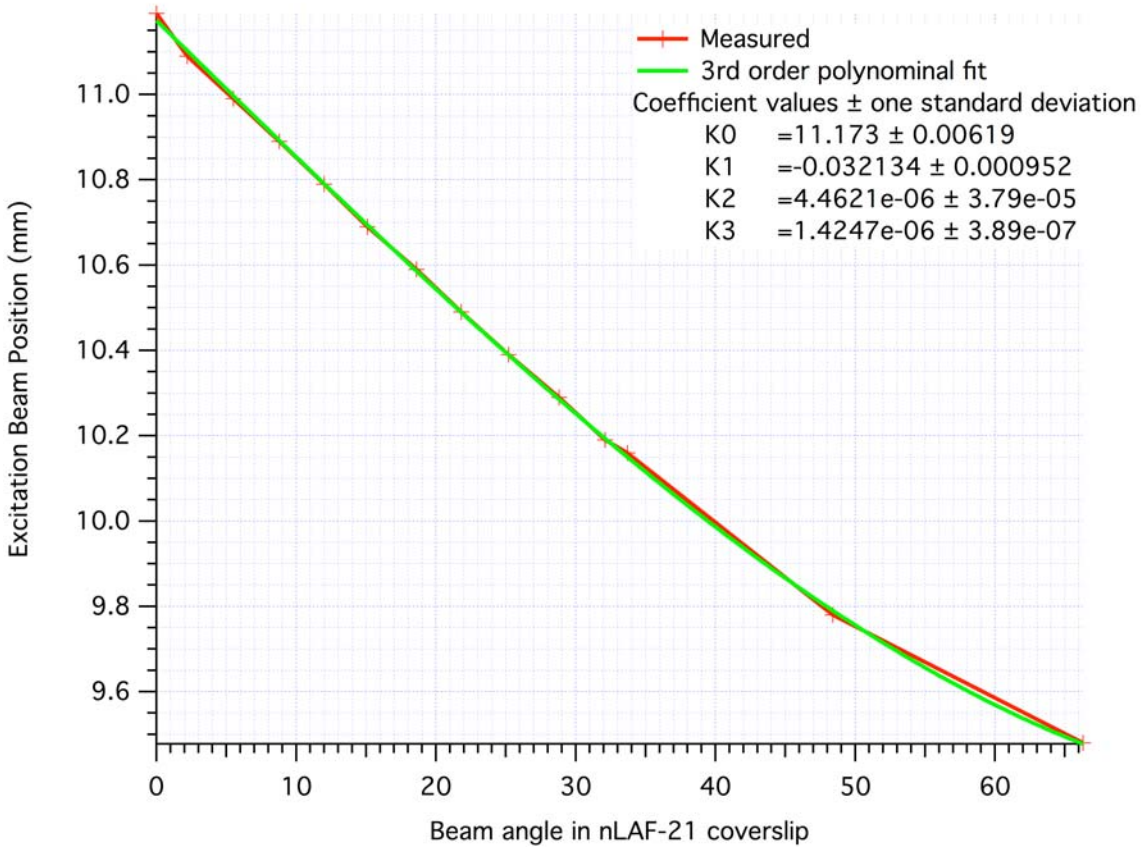

Figure A.4 Full scale fit from the laser in Epi (pointed vertically) to sealing down to the critical angle (data points from 0° to ~34°). It also includes a waterbased TIRF onset datapoint and another at the extreme edge of the back aperture point. The units on the excitation beam position are distance in (mm) from the actuator 'homed' position.

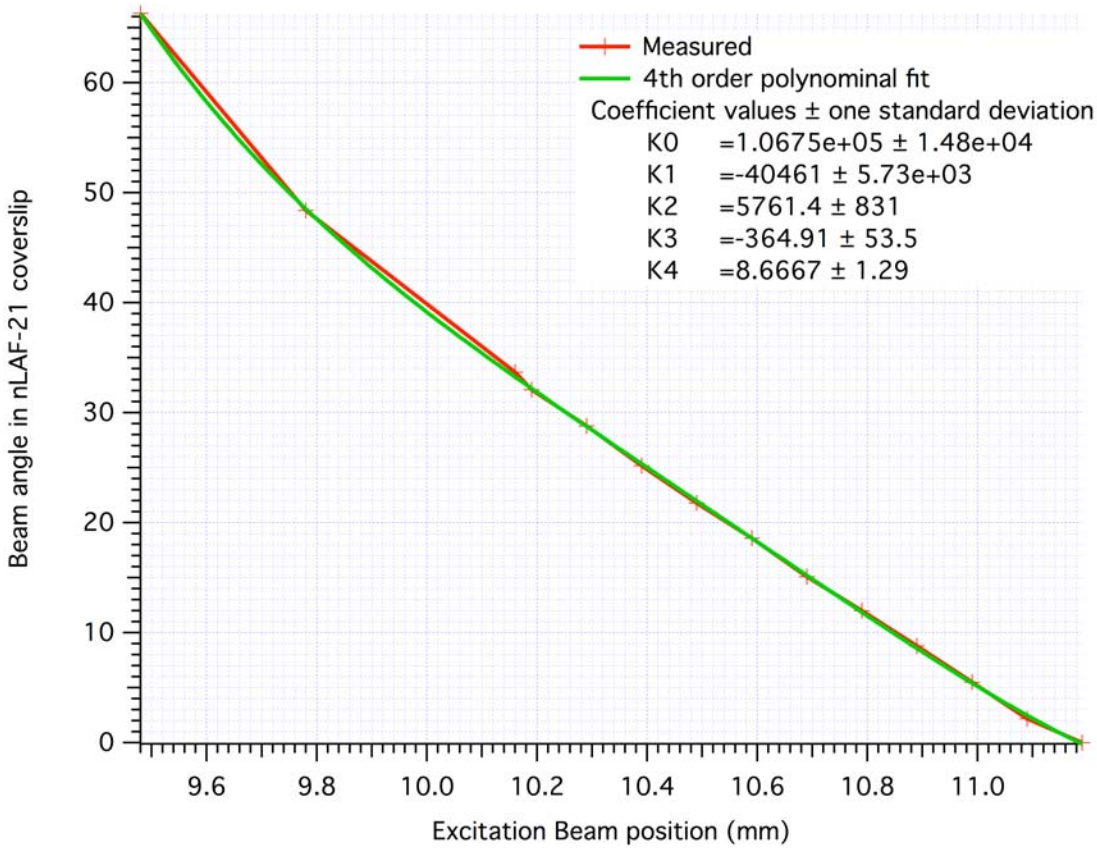

Figure A.5 Beam angle as a function of excitation beam position. Full scale fit from the laser in Epi pointed vertically to sealing down to the critical angle (data points from 0° to ~34°). It also includes a water-based TIRF onset datapoint and the extreme edge of the back aperture point. The units on the excitation beam position are distance in (mm) from the actuator 'homed' position. This is the inverse of Figure A.4.

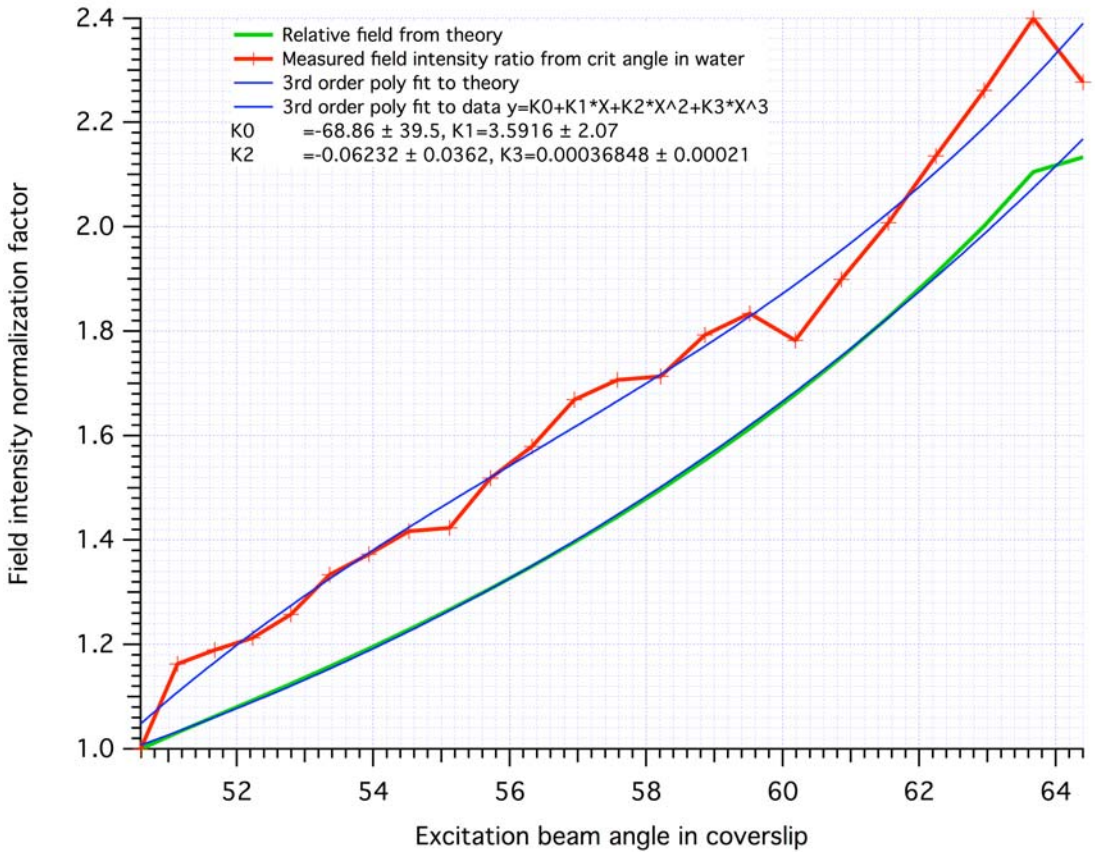

Figure A.6 The measured field intensity averaged was about 10% (on average) lower than that predicted by theory over the TIRF range of incident angle. At present we can only speculate as to the origin of this discrepancy. One possibility is that the evanescent field intensity is diminished across the coverslip in the direction of propagation due to scattering caused by the sample and coverslip surface roughness. An alternative explanation is that the difference is due to my measurement and/or data analysis error. A third is that a small fraction of the excitation energy within the evanescent region might contain some vertically polarized energy

As a result the normalization factor was increased by 10% from theory to account for this difference.

A.2 Evanescent field intensity as a function of angle of incidence

Microns offset	position (mm)	angle	Penetration Depth (nm)	Calc Intensity	Normalization	ADJ+ 10%
0	9.51	64.274	46.11099207	1.849497093	2.153675043	2.369
10	9.52	63.590	47.13495262	1.941917327	2.051176781	2.256
20	9.53	62.922	48.22529751	2.033929283	1.958384574	2.154
30	9.54	62.268	49.38857035	2.125454198	1.874053902	2.061
40	9.55	61.628	50.63245181	2.21642634	1.797134269	1.976
50	9.56	61.002	51.96600732	2.306792179	1.726733673	1.899
60	9.57	60.389	53.40000522	2.39650959	1.662090462	1.828
70	9.58	59.787	54.94733027	2.485547091	1.602550902	1.762
80	9.59	59.198	56.6235278	2.573883125	1.547551127	1.702
90	9.6	58.620	58.44753042	2.661505365	1.496602556	1.646
100	9.61	58.052	60.44264372	2.748410064	1.449279998	1.594
110	9.62	57.494	62.63790777	2.834601432	1.405211924	1.545
120	9.63	56.946	65.07001602	2.920091055	1.364072441	1.500
130	9.64	56.407	67.78608288	3.004897335	1.32557465	1.458
140	9.65	55.876	70.84774223	3.089044974	1.289465115	1.418
150	9.66	55.353	74.33740586	3.172564475	1.255519238	1.381
160	9.67	54.838	78.36817005	3.255491682	1.22353737	1.345
170	9.68	54.329	83.1001824	3.337867337	1.193341535	1.312
180	9.69	53.826	88.76912127	3.419736672	1.164772646	1.281
190	9.7	53.328	95.73903929	3.501149013	1.137688147	1.251
200	9.71	52.836	104.6087792	3.582157416	1.111959992	1.223
210	9.72	52.348	116.4508049	3.662818315	1.087472921	1.196
220	9.73	51.864	133.4349282	3.743191193	1.064122971	1.170
225	9.735	51.623	145.2559639	3.783288968	1.052844698	1.158
230	9.74	51.384	160.8804372	3.823338265	1.041816197	1.145
235	9.745	51.144	182.9217212	3.86334724	1.031027108	1.134
240	9.75	50.906	217.4781111	3.903324181	1.020467568	1.122
245	9.755	50.668	283.9205354	3.943277501	1.010128182	1.111
250	9.76	50.430	521.9432409	3.983215732	1	1

Table A.2 Evanescent field intensity at the coverslip surface as a function of angle of incidence. The +10% values in the far right column were used for all images processed in Chapter 2 of this thesis.

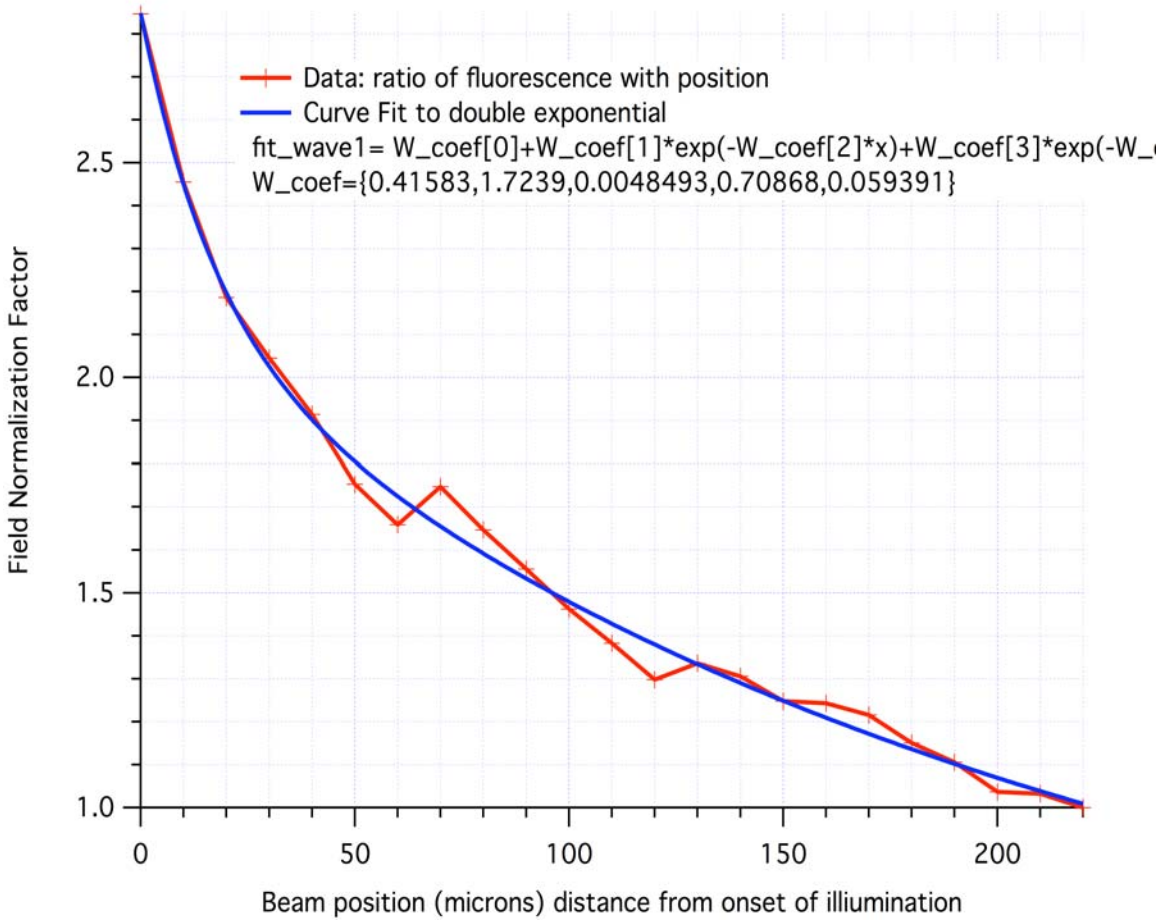

Figure A.7 The measured field normalization factor as a function of offset beam position from the onset of illumination (at the outside edge of objective). The actual onset was considered to be once the full beam was past the edge of the objective. That onset was found to be 20 microns past the point where light would first start to leak past the edge. The evanescent field intensity was determined by measuring the fluorescence intensity from 20 nm beads stuck on a N-LAF21 coverslip with more beads in solution above the coverslip. To make this measurement, the average of a very small region of interest was defined in ImageJ. Four sets of measurements were made across the 220 micron TIRF range. A new region of interest was selected for each of those runs. The average intensity within that ROI was measured in 10 micron increments. The intensity for the four runs at each position was then averaged. That yielded the data plotted here. When beads became continuously visible in any part of the image, the limit of TIRF was considered to have been reached. From this point it was ~20 microns further in beam position before the full field would be far-field illuminated...presumably due to beam width again.

A.3 Imaging sequence table including which images are averaged

Assume that images were taken every 10 microns from the onset of TIRF (as defined above), then those images can be numbered. Image 1 was the very first image taken at the onset of TIRF. Image 26 was then taken after shifting the beam position 250 microns towards being centered.

These assume five slice image stacks as defined in Tables 2.2 and 2.3.

z-stack from most extreme TIRF towards critical angle	5 image logarithmic defined in Table 2.3	5 image even-spaced defined in Table 2.2
Stack Image 1	Average images 1-5	Average images 1-5
Stack Image 2	Average images 13-17	Average images 19-21
Stack Image 3	Average images 21-22	Average images 23-24
Stack Image 4	Image 24	Image 25
Stack Image 5	Average images 25-26	Image 26 if very clean else just use 4 stack

Table A.3 Images selected and averaged for z-stack to be used for 3D image generation.

A.4 Andor iXonem+ 897 camera background

A 200 image sequence was acquired with the camera stable at -85°C. During these images the 488 laser was on but the shutter was off. Also the room light was off but computer monitors were on. A z-stack was then assembled and averaged. The histogram of that image showed values at 109, 110 and 111 counts per pixel with 110 having more pixels than the other two combined.

The camera background value of 110 counts per pixel was therefore used for all calculations within this thesis.

A.5 Photographs of Teflon cell culture chamber

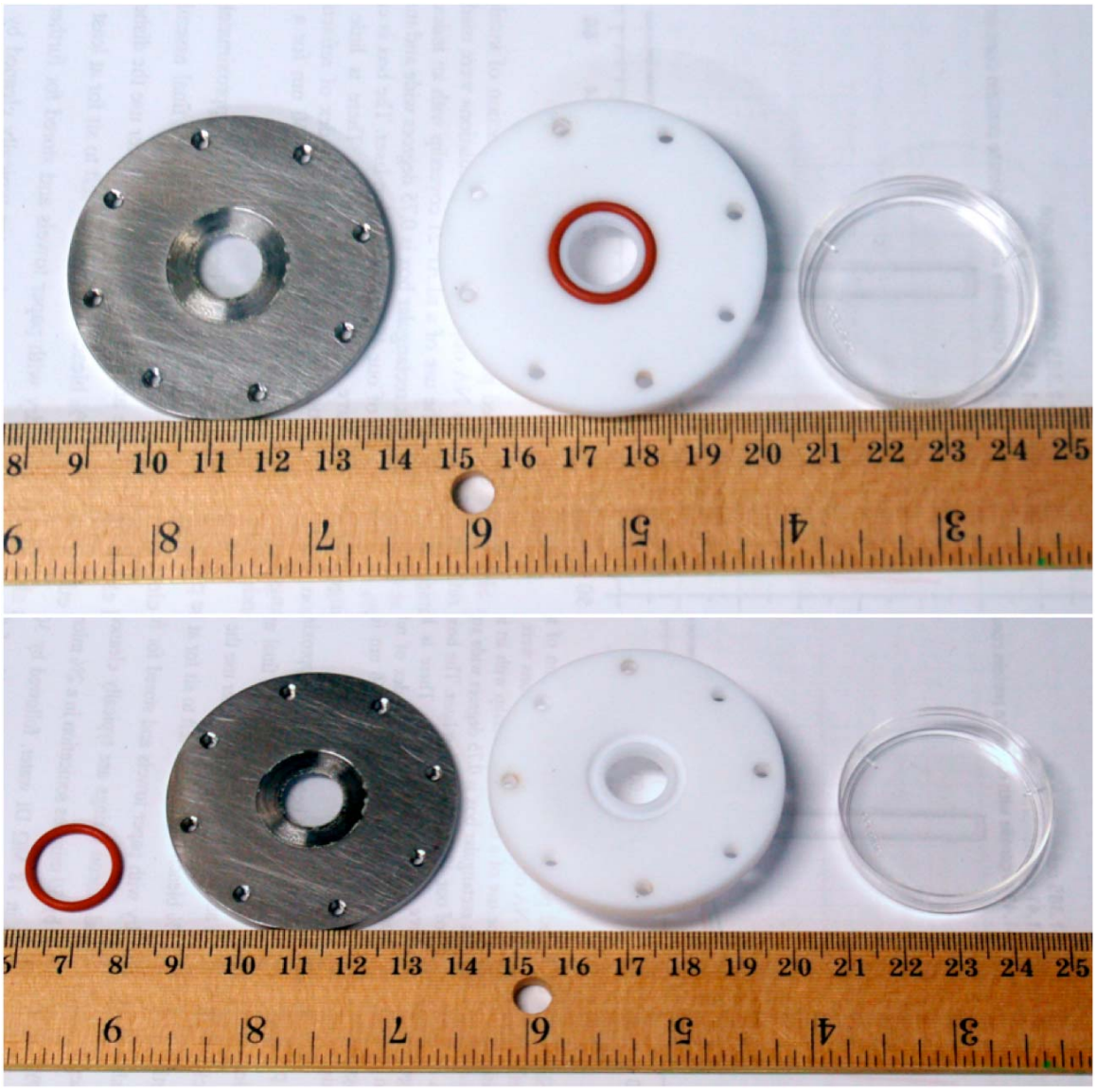

Figure A.8 Cell culture chamber parts. The baseplate was made of stainless steel. The chamber was made from virgin Teflon and sealed with a silicon o-ring. The chamber was covered with a commercial 35 mm culture dish top (to ensure proper circulation of air in the incubation chamber).

Figure A.9 An assembled cell culture dish is shown on the left with a commercial 35 mm cover.

Figure A.10 A fully assembled culture dish is shown above from the top and also from the bottom.

A.6 Photographs of TIRF microscope and excitation positioning assembly

Figure A.11 The complete Olympus IX71 microscope used for the VA-TIRFM study reported in this thesis is shown here. Note the laser positioning assembly on the right.

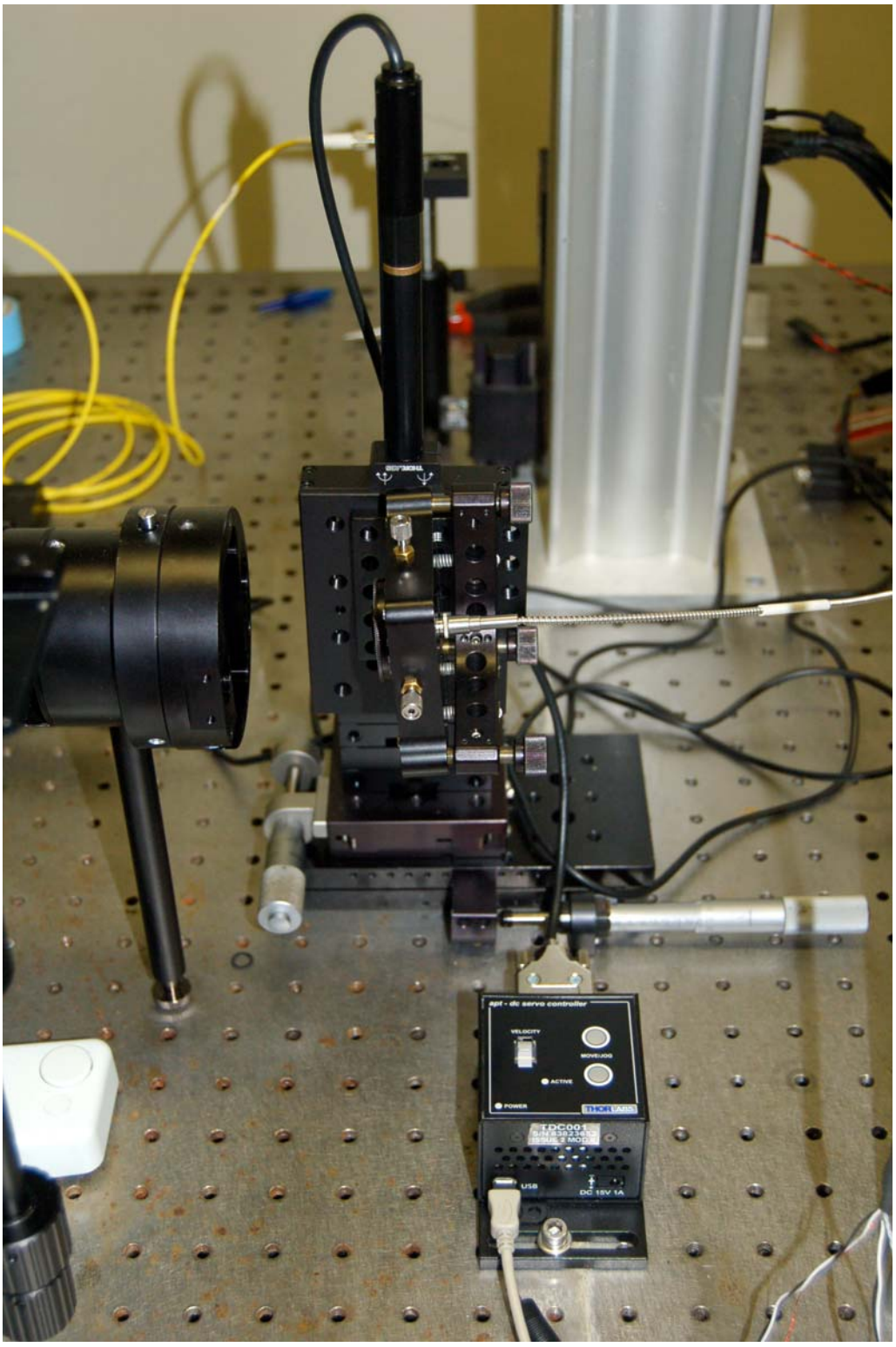

Figure A.12 Laser alignment and positioning assembly with control electronics.

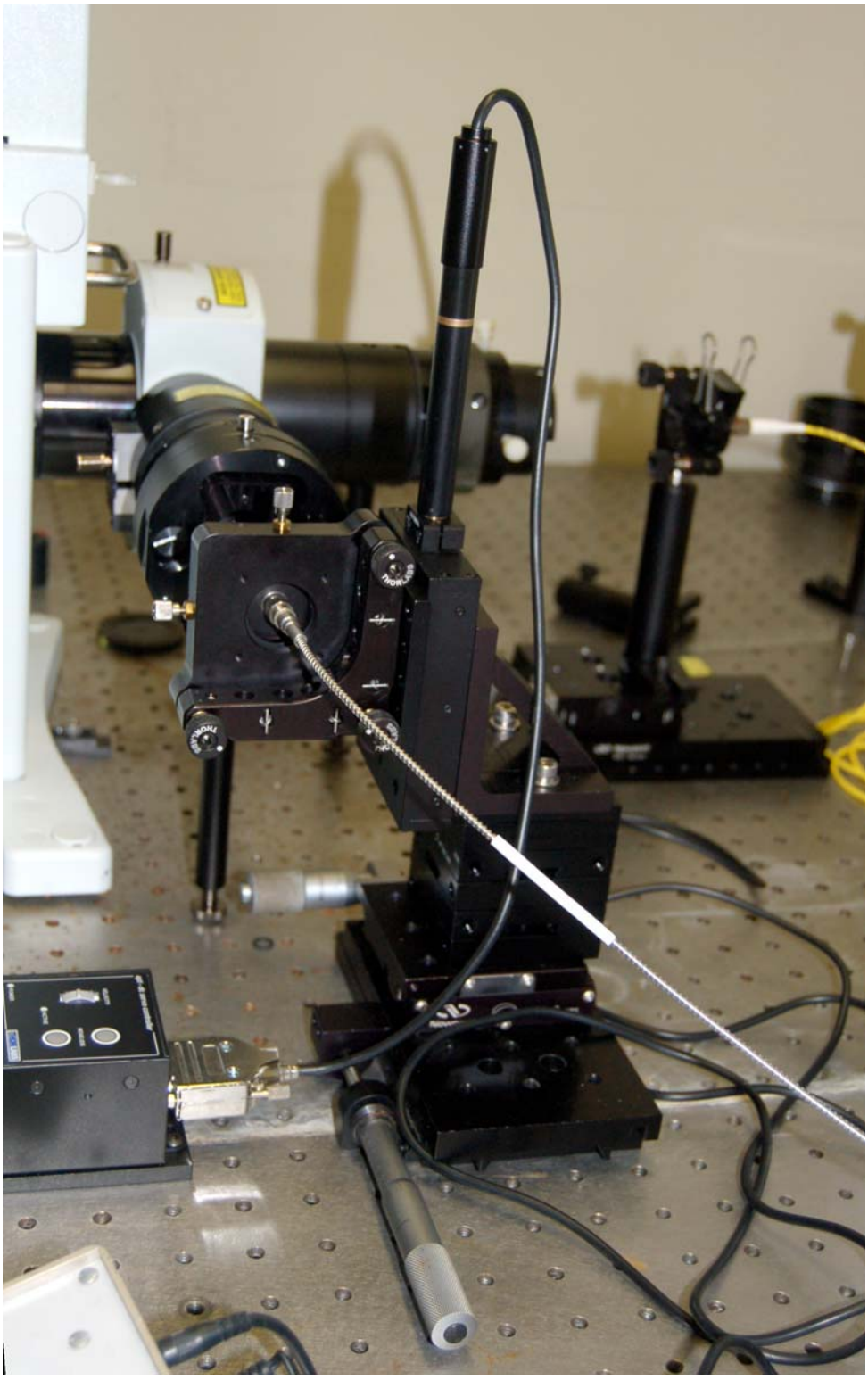

A.13 View of laser positioning assembly facing the microscope.

Appendix B

Cell, Cleaning and Surface Chemistry Protocols

Protocols presented:

- N2a cell plating
- N2a cell transfection
- N2a cell media
- N2a cell media-clear
- Intracellular Fluid
- Extracellular Liquid
- Coverslip cleaning
- Cell Lysis
- Membrane patch preparation
- N2a cell top membrane adhesion
- Linking carboxylated beads to APTES coated coverslip
- APTES coating glass coverslips

N2a cell plating protocol

L. Wade
April 13, 2009
This protocol is for splitting flasks of N2a cells and for plating cells into new culture dishes.

Basics:
Sterilize everything with 70% ethanol. Then put into hood
Spray hands too....every time you touch something outside the sterile box.
Wear short sleeves or roll up long sleeves.
Stay sterile
Toss anything that touches anything else

Fluids used:
TrypLE express (Gibco 12605)
This is basically trypsin. It is used to separate the cells from the flask in which they've been growing.

N2a Cell Media Protocol for 500 ml solution:

a. DMEM, high Glucose, 4mMl-glutamine (Gibco 11965-092)	222.5 ml
b. Fetal Bovine Serum, Qualified (Gibco 26140-079)	50 ml
c. Optimem1	222.5 ml
d.Pen/Strep (100x) (Mediatech 30-009-CI/Gibco 15140-122)	5 ml

-note this is a mix of the antibiotics Penicillin and Streptomycin

Add together, stir, and then 0.22 μm filter into sterile 500 ml container.
I checked pH: 7.42 without titration.

Flask Splitting protocol:
Prepare three 50 ml centrifuge tubes.
Add 5 ml of TrypLE (avoids contamination of main bottle) to one of the tubes.
Transfer 50 ml of N2a growth media into the second tube.
Spray and pass the third tube into the sterile hood to hold cells later in protocol.
Separate cells from flask.
Evacuate all serum from flask.
Use 5 ml pipette to add a couple ml of N2a cell media.
Roll this around flask and then evacuate this media.
Add 2-3 ml of trypsin, roll it around flask and then set flask in incubator for 2 to 4 minutes.
Add 10 ml of N2a growth media to flask.
Suck back into 10 ml pipette, then back out then back in.
Repeat this a total of 3 to 4 times.
Suck up the ~12 to 13 ml of cells-in-media solution and put into the previously sterilized empty 50 ml bottle.
Suck about 1 ml of this media (for 10:1 split...or ~2.5 ml for 5:1 split) and put into a new sterile flask.

Add 13 ml of N2a cell media to this new flask.
Label flask with the passage number, the date of plating, your name, the cell type.
Place new flask in incubator.
Discard old flask and TrypLE containing 50 ml bottle.

Notes: p30 is the end of a cell line's useful life. More than p25 is pretty old, and p28 and more is aged severely. My experience is that old cell lines are less vital and express (the desired) proteins at much lower levels than new cell lines do.

Plate cells into new culture dishes:
Pass new culture dishes into the sterile hood after spraying liberally with ethanol.
Calibrate the cell density in the 50 ml tube left over from splitting the cells from old flask:

Turn 50 ml tube up and down a couple times to mix the cells in the media.
Pipette out ~100µl of this solution.
Wick into hemacytometer with coverslip.
I use one made by Hausser Scientific, model 3500, 'Levy Hemacytometer, improved Neubauer.' Each group of 16 squares has a volume of 0.1 µl.
Count the number of cells in each of the four 16 grid locations.
Count cells on the top and lefthand lines but not those on the bottom or righthand lines.
Divide the total by four.
The density in the 50 ml flask is therefore this number times 10,000 per ml.
For example: a total count of 236 mean that there were an average of 59 cells per 16 grid location and that the flask has a density of 590,000 cells per ml of media/cell solution.

We want to plate about 90,000 cells into each new culture dish. So in the case described above we want to put 90,000 cells/ 590,000 cells/ml = 0.15 ml of solution pipetted into each culture dish (this is for large dishes (50-60 mm dia)). For my teflon 35 mm dishes I plated 25,000 cells.
For my 35 mm teflon dishes with 20 mm coverslips try 10,000 cells.
Also add 4 ml of N2a cell growth media into each culture dish.
Gently swish cells in a figure 8 until well mixed.
No opaque clump in center should be visible.
Put into incubator.
Dispose of everything and spray everything in sterile hood with ethanol including the suction tube.

Longevity
Cells in culture dish ready for transfection in ~1 day.
Cells in flask will live for 3-4 days and then need to be split again.

Cell transfection protocol

L. Wade
April 13, 2009
This protocol is for transfecting DNA plasmids into N2a cells.

Basics:

1. Sterilize everything with 70% ethanol. Then put into hood.
    a. Spray hands too....every time you touch something outside the sterile box.
    b. Wear short sleeves or roll up long sleeves.
2. Stay sterile.
    a. Toss anything that touches anything else.

Fluids used:

DMEM (Gibco 11965)
ExpressFect Transfection Reagent (Denville Scientific)
DNA Plasmids to be transfected
N2a cell growth Media (only needed for final step)

Transfection solution preparation:

1) Pass one ~1ml centrifuge tube into the sterile hood for each dish being prepared, plus One extra.
2) Transfer 100μl DMEM into one centrifuge tube for each dish to be prepared.
3) Add plasmid to each centrifuge tube for each dish in the appropriate amount:
    a. 75 ng of mCherry labeled lyn kinase (membrane localized protein) is 0.46 μl (160 ng/μl).
    b. 500 ng of α4 with GFP or β2 with or w/o GFP. Density is 100 ng/μl so for these transfer 5μl into each tube.
4) Prepare 'master mix':
    a. Into extra tube transfer 100 μl of DMEM plus 8μl of Expressfect for each 50 mm dish being prepared (4 μl for a 35 mm dish).
    b. Gently tap bottom of this master mix several times to mix.
5) Pipette 104 μl of 'master mix' into each centrifuge tube (one per dish).
6) Vortex and then let sit for 15-20 minutes.

Transfect culture dishes:

1) Pipette ~3ml media from culture dishes to be transfected.
    a. Leaves about 1.5 mm deep media in each dish.
    b. Put removed media into a 50 ml tube for future disposal.
2) Pipette all liquid from one centrifuge tube (about 205 to 210 μl each) and transfer into a culture dish.
3) Gently swirl each of the dishes to mix fluids.
4) Place all transfection culture dishes into incubator and wait 4 hours.
5) Wipe everything down with ethanol mixture (70%)
6) <u>After four hours</u> evacuate transfection mixture out of each dish and immediately add ~4 ml of N2a cell media.
7) Swirl some and suction up again.
8) Once again immediately add 4 ml of N2a cell media and then place sealed dish in incubator.

9) Dish will be ready to image in 48 hours (optimally).
    a. Can be imaged as early as 24 hours with low levels of protein expression.
    b. 36 to 60 hours is the optimal range.

N2a Cell Media Protocol

500 ml solution

DMEM, high Glucose, 4mMl-glutamine (Gibco 11965-092)	222.5 ml
Fetal Bovine Serum, Qualified (Gibco 26140-079)	50 ml
Optimem1	222.5 ml
Pen/Strep (100x) Mediatech 30-009-CI/Gibco 15140-122)	5 ml

(note this is a mix of the antibiotics Penicillin and Streptomycin)

Add together, stir, and then 0.22 μm filter into sterile 500 ml container.

I checked pH today: 7.42 without titration.

N2a Cell Media-clear

445 ml of DMEM without phenol red
5 ml of penicillin streptomysin (we have aliquots)
50 ml of FBS

Intracellular fluid

Rev 2 with recommended changes by Fraser Moss on 9 January 2009:

mM	Compound	Fw	100 ml (1X)	150ml (1X)
130	KCl	74.55	969.2 mg	1.454 g
6	MgCl2.6H2O	203.3	122.0 mg	183 mg
5	EGTA	380.4	190.2 mg	275.3 mg
10	HEPES	238.3	238.3 mg	357.5 mg

Titrate the pH of this solution to ~7.4 using **KOH** NOT NaOH.
Also check the osmolarity of this solution. Typically mammalian cells in culture will be in media of 296mOsm/kg. Try and get your solutions in this ballpark (+/- 10% max). Add glucose to increase and water to decrease. Check that the concentrations above have not been changed if water is added.

The solution below includes ATP, which is not necessary for today's work (membrane patches) as my cell is not functioning:

mM	Compound	Fw	100 ml (1X)
110	K-gluconate	234.25	2.577 g
20	KCl	74.55	149.1 mg

1	MgCl2.6H2O	203.3	20.3 mg
5	EGTA	380.4	190.2 mg
5	MgATP	507.2	253.6 mg
10	HEPES	238.3	238.3 mg

Titrate the pH of this solution to ~7.4 using **KOH**.

For whole cell patch clamping use:

From Nashmi-JNeuro-2007

Whole-cell recordings were performed with glass electrodes (2–5 MΩ) filled with an internal solution [88 mM KH2PO4, 4.5 mM MgCl2, 0.9 mM EGTA, 9 mM HEPES, 0.4 mM CaCl2, 14 mM creatine phosphate (Tris salt), 4 mM Mg-ATP, and 0.3 mM GTP (Tris salt), pH 7.4 with KOH.] (Nashmi et al., 2003; Fonck et al., 2005). Also used in Drenan, MolPharm-2008.

Extracellular Liquid-ECL (or Solution-ECS or Fluid-ECF)

After Clemens, Sodickson DL and Bean BP (1998) J. Neurosci. **18,** 8153-8162**.**

	GMW	mM	X1 1l(g)	10X 1l(g)
NaCl	58.44	150	8.766	87.66
KCl	74.55	4	0.298	2.98
Hepes	238.3	10	2.383	23.83
$MgCl_2$	203.3	2	0.407	4.07
$CaCl_2$	110.99	2	0.222	2.22
Glucose	180.16	10	1.802	18.02

Adjust to pH 7.4 with NaOH

Coverslip cleaning summary

This is for starting with dirty coverslips and going all the way.

To clean new coverslips, that do not need a specific surface charge, you can simply sonicate in spectroscopic grade acetone and then blow dry.

My standard Glass Cleaning Proceedure
June 8, 2010
This is a variation of the RCA method

In the "RCA" method, coverslips and slides were:
1. sonicated in a surfactant solution (2% Micro-90) for 20 min,
2. washed for 3min in a stream of deionized water,
3. rinsed thoroughly with 18.3 MΩ-cm and 0.22μm filtered water,
4. then immersed in boiling RCA solution (3:2:1 high-purity H_2O, 30% NH_4OH, 30% H_2O_2) for 20 min.
a. Temperature was 78C and the fluid was boiling.
b. e.g. for 420 ml of RCA solution (SC-1) combine 210 ml of water with 140 ml of NH_4OH with 70 ml of H_2O_2.
5. Coverslips were rinsed and stored in high purity water to avoid particulate contamination. High-purity water was 18.3 MΩ-cm and 0.22μm filtered.
6. Rinses: rinsed 6 times, vigorously in 18.3 MΩ-cm and 0.22μm filtered water, filled to brim and vigorously agitated.
7. Immerse in boiling acid solution (SC-2): combine (14:3:1 ratio) 350 ml of water with 75 ml of H_2O_2 with 25 ml of HCl (37%) for 450 ml solution for 10 minutes.
a. Remember to add acid to water.
8. Rinses: rinsed 6 times, vigorously in 18.3 MΩ-cm and 0.22μm filtered water, filled to brim and vigorously agitated.
9. Store in the same crystallization dishes filled with a 7th round of 18.3 MΩ-cm and 0.22μm filtered water.
10. Immediately before use, coverslips were blown dry with filtered nitrogen (MMCFA02 filter: 0.01 μm filtered, oil removed to 1 part per trillion of line input; Airmaze, Stow, OH, USA).

Alternate methods:
The one step RCA method is probably less aggressive to the glass but it can leave organic stuff behind. All of the methods described below leave the coverslip highly hydrophobic. It may therefore be necessary to coat with poly-DL-lysine afterward for cells to happily bind to the glass surface.

1. RCA cleaning is the industry standard for removing contaminants from wafers. Werner Kern developed the basic procedure in 1965 while working for RCA (Radio Corporation of America) - hence the name.

In the "RCA" method, coverslips and slides were:
1. sonicated in a surfactant solution (2% Micro-90) for 20 min,
2. washed for 3min in a stream of deionized water,
3. rinsed thoroughly with 18.3 MΩ-cm and 0.22µm filtered water,
4. then immersed in boiling RCA solution (6:4:1 high-purity H2O, 30% NH4OH, 30% H2O2) for 1 h.
a. Temperature was 78C and the fluid was boiling.
b. e.g. for 440 ml of RCA solution combine 240 ml of water with 160 ml of NH4OH with 40 ml of H2O2.
5. Coverslips were rinsed and stored in high purity water to avoid particulate contamination. High-purity water was 18.3 MΩ-cm and 0.22µm filtered.
6. Rinses: rinsed 6 times, vigorously in 18.3 MΩ-cm and 0.22µm filtered water, filled to brim and vigorously agitated.
7. Store in the same crystallization dishes filled with a 7th round of 18.3 MΩ-cm and 0.22µm filtered water.
8. Immediately before use, coverslips were blown dry with filtered nitrogen (MMCFA02 filter: 0.01 µm filtered, oil removed to 1 part per trillion of line input; Airmaze, Stow, OH, USA).

An updated version of RCA (from: http://fabweb.ece.uiuc.edu/recipe/rca.aspx) recommends:
1. starting with Acetone,
2. DI water rinse
3. Put in an acid rinse: 50:1 H20, HF (hydrofluoric acid) for 30 seconds.
4. DI water rinse
5. Then use RCA solution. Their solution uses the same components but in different ratios: 10 (H2O), 2 (H202), 1 (NH4OH). They also use a temp of 75 C. They leave their wafers (coverslips for me) there for ~20 minutes (~10 minute warmup and 10 minutes at 75 C). While this is going on, prepare the next solution.
6. Rinse with DI water
7. Then use a second solution in the ratio (17 (H20), 3 (H202), 1 (H2SO4-sulfuric acid)). Remember the AAA rule: Always add acid to water! Sulfuric acid reacts violently with water: add it very slowly, and only if the temperature of the water is below 30°C. Put wafers in this solution and then heat to 75 C. Then remove wafer (so time to 75C is ~10 min?).
8. Then do another 50:1 DI:SF etch for 15 seconds (strips hydrous oxides)
9. Rinse in DI water
10 Place wafers back into the 17:3:1 H2O:H2O2:H2SO4 solution (now heated to 75C). Leave it there for 10 minutes.
11. Rinse in DI water
12. Blow dry with Nitrogen gas.

Third variation: The RCA clean first uses an H_2O-NH_4OH-H_2O_2 solution (standard clean 1; SC1) to remove organic contaminants and particles. After rinsing with dilute HF, a second standard solution (SC2) uses a H_2O-HCl-H_2O_2 mixture to remove metal contaminants. A final rinse prepares the wafer for further processing.

Fourth variation is copied from Wikipedia: http://en.wikipedia.org/wiki/RCA_clean

The RCA clean is a standard set of wafer cleaning steps which needs to be performed before high temp processing steps (oxidation, diffusion, CVD) of silicon wafers in semiconductor manufacturing. RCA cleaning includes RCA-1 and RCA-2 cleaning procedures. RCA-1 involves removal of organic contaminants, while RCA-2 involves removal of metallic contaminants.
Werner Kern developed the basic procedure in 1965 while working for RCA, the Radio Corporation of America [1] It involves the following :

1. Removal of the organic contaminants (Organic Clean)
2. Removal of thin oxide layer (Oxide Strip)
3. Removal of ionic contamination (Ionic Clean)

The wafers are prepared by soaking them in DI water. The first step (called SC-1, where SC stands for Standard Clean) is performed with a 1:1:5 solution of NH_4OH (ammonium hydroxide) + H_2O_2 (hydrogen peroxide) + H_2O (water) at 75 or 80 °C[1] typically for 10 minutes. This treatment results in the formation of a thin silicon dioxide layer (about 10 Angstrom) on the silicon surface, along with a certain degree of metallic contamination (notably Iron) that shall be removed in subsequent steps. This is followed by transferring the wafers into a DI water bath.

The second step is a short immersion in a 1:50 solution of HF + H_2O at 25 °C, in order to remove the thin oxide layer and some fraction of ionic contaminants.

The third and last step (called SC-2) is performed with a 1:1:6 solution of HCl + H_2O_2 + H_2O at 75 or 80 °C. This treatment effectively removes the remaining traces of metallic (ionic) contaminants[1].

The RCA cleaning procedures leaves hydroxyl groups on the glass surface, which is deprotonated at the pH used here, and thus impart negative charge to the surface (making it hydrophilic). While this charge can provide some electrostatic shielding against non-specific adsorption of tagged nucleotides, the surface charge density is very low.

Notes:
H2O2 is hydrogen peroxide
NH40H is ammonia hydroxide

A more aggressive method:

1) Fill a clean teflon rack with coverslips (VWR, No.1, 1" square) and place in a clean crystallization dish.
2) Cover the glass coverslips with Micro-90 cleaning solution. Sonicate for 30 min and rinse in DI water.
3) Fill the crystallization dish with 30 % (w/w) NaOH. Sonicate the totally immersed coverslips at room temperature for 1 h.
4) The coverslips must be rinsed in DI water again, until they reach pH = 6.5 (pH of our laboratory water).
5) Steps 3) and 4) are repeated with 1 N HCl.
6) Refill and store coverslips in 18 MΩ water

Cell Lysis

AfCS Solution Protocol
Reagent name: Hypotonic cell lysis buffer stock, pH 7.4, 2X
Reagent name abbreviation: 2X HSE, pH 7.4
Protocol ID: PS00000678
Version: 01
Volume: 250 ml

Components: Reagent	Source	Catalog or Protocol No.	F.W. or Stock Conc.	Quantity	Final Concentration
HEPES	Invitrogen	15630080	1 M	10 ml	40 mM
Sodium chloride (NaCl)	None	PS00000677	4 M	2.5 ml	40 mM
EDTA, pH 8.0	None	PS00000026	0.5 M	5 ml	10 mM
Hydrochloric acid (HCl)	None	PS00000034	1 N	titrate	NA
Sodium hydroxide (NaOH)	None	PS00000038	1 N	titrate	NA

Preparation:
1. Pipette HEPES, NaCl, and EDTA in order into a 250-ml beaker.
2. Add purified water to a volume of approximately 220 ml.
3. Adjust pH to 7.4 with 1 N HCl or 1 N NaOH.
4. Adjust volume to 250 ml with purified water in a graduated cylinder.
5. Sterilize by autoclaving or filtration and divide into 50-ml aliquots.

Storage:
Temperature: 4 °C
Aliquot size: 50 ml
Author: Leah Santat
Date: 09/01/04
Approved: Iain Fraser

Membrane patch preparation:

Adhere the cell onto an APTES coated glass coverslip. Plate cells on coverslip and let grow.
Prepare coverslips using the Pierce protocol.

Wash with ice cold PBS once to remove loose cells

Pour into edge of dish and let sit for 1 min., then pour out

Lyse the cell:
Low concentration ionic buffer solution: 18 MΩ water with 5 mM NaH2PO4 and 1 mM EDTA (pH 7.1). **Do this in the refrigerator**. Let sit for 12.5 minutes.

Cell lysis (splitting of cells) is when a cell gets so fat from all the hypertonitation that it just explodes. Cytolysis is the lysis of cells in a hypotonic environment. Cytolysis is caused by excessive osmosis, or movement of water, towards the inside of a cell (hyperhydration). The cell membrane cannot withstand the osmotic pressure of the water inside, and so it explodes. Osmosis occurs from a region of high water potential to a region of low water potential passing through a semipermeable membrane, so these bursting cells are located in hypotonic environments. (from wikipedia). EDTA chelates Ca ions involved in intercellular and intra-cellular adhesion and results in better breakdown of cells.

Wash the cells to remove everything but the adhered membranes. **Do this with ice cold solution.**
Wash in ice cold PBS.
Again **pour into edge of dish, let sit for 1 min. then pour out**
Replace with PBS and then look under microscope to make sure the patches look good.

Try imaging membrane patches with the membrane skeletal structure intact in PBS.

Dissolve the membrane skeletal structure
Remove the filamentous actin/spectrin mesh by incubation with a 0.5 mM Na phosphate buffer (0.5 mM NaH2PO4, 0.05 mM EDTA, pH 7.4) at 37 °C for 30 min.
Place cells in incubator in hallway.

Gently wash again with PBS.

Image wet in PBS.

Mixing Protocols:
Lysing solution: 5 mM NaH2PO4 and 1 mM EDTA (pH 7.1)
Make about ½ liter.

Start with 500 ml of 18 MΩ water in a flask

½ liter x 0.005 M x 137.99 g/Mol=0.345 g of NaH_2PO_4 H_2O
Add 0.345 g of NaH_2PO_4 H_2O

We have 0.5 M EDTA. And want 1mM (500 times more dilute).
Add 1 ml EDTA for 500 ml.

Mix using a stirring bar and measure pH. Add NaOH until at pH=7.1.

Then vacuum feed and filter into 500 ml container.

Membrane skeletal structure removal: 0.5 mM NaH2PO4, 0.05 mM EDTA, pH 7.4

Make about ½ liter.

Start with 500 ml of 18 MΩ water in a flask

½ liter x 0.0005 M x 137.99 g/Mol=0.0345 g of NaH_2PO_4 H_2O
Add 0.0345 g of NaH_2PO_4 H_2O

We have 0.5 M EDTA. And want 0.05mM (10000 times more dilute).
Add 50 μl EDTA for 500 ml.

Mix using a stirring bar and measure pH. Add NaOH until at pH=7.4.

Then vacuum feed and filter into 500 ml container.

N2a cell top membrane adhesion to coverslip

February 6, 2009

Use an APTES coated coverslip
Prepare using Pierce instructions and product #80370:

Protocol for Amino-Silylation of a Glass Surface

1. Thoroughly wash and dry the glass, silica or quartz surface to be coated.

Note: Perform steps 2 and 3 in a fume hood.

2. Prepare a 2% solution of 3-Aminopropyltriethoxysilane in acetone. For example, mix 1 part Amino-silane Reagent with 49 parts dry (i.e., water-free) acetone. Prepare a volume sufficient to immerse or cover the surface material.
3. Immerse surface in the diluted reagent for 30 seconds.
4. Rinse surface with acetone.
5. Allow surface to air-dry.

Note: The dried silylated surface may be stored for later use.

Plate and transfect N2a cells as normal in Matek dish with 30 mm hole/coverslip
Wash out N2a cell media and replace with ECL
Place APTES coated 25mm round coverslip on top of cells
First try laying gently on top...if no adhesion try giving a very gentle push on each corner to ensure cell contact
Incubate cells for 30 min at 37 C to give time for adhesion to occur
Lift up coverslip (tearing cells) and place in dish
Wash both coverslips (with cell bottom and top membranes respectively) with intracellular fluid
Image the coverslip with the adhered membranes isolated from the cell top will need to be imaged 'open' (not in a dish) under a meniscus of intracellular fluid.

Linking carboxylated beads to APTES coated coverslip

EDAC is a water-soluble carbodiimide
EDC (also EDAC or EDCI, acronyms for 1-ethyl-3-(3-dimethylaminopropyl) carbodiimide)
http://en.wikipedia.org/wiki/1-Ethyl-3-%283-dimethylaminopropyl%29carbodiimide

http://en.wikipedia.org/wiki/Carbodiimide

MES is http://en.wikipedia.org/wiki/MES_(buffer)

2-(N-morpholino)ethanesulfonic acid is MES buffer

The MES I bought makes 0.1M at 4.7 pH. Dilute with DI water to 50 mM. Then titrate with NaOH to pH 6.0 (maybe 6.5 TBD).

To link carboxylated beads to amine groups (APTES coated glass)

Some variant: 50 mM MES at pH 6, add microspheres. Then add 4 mg fresh EDAC to a 1 ml MES/Bead mixture. Let incubate on amine (APTES) coated slide for 15 minutes at room temperature. If want to avoid non-specific binding at this point passivate with dilute BSA.

The MES causes the carboxyl groups to be exposed and active. Otherwise they tend to be shielded due to charge. However the beads should not be in an environment < 5 pH. pH 6.0 is probably optimal and stay in the range of 5.5 < pH< 6.5.

APTES coating glass coverslips

Silanization procedure:

1) First the described cleaning procedure must be applied to the coverslips.
2) The surfaces are placed in a polymethylpentene (PMP) jar with 0.6 mM APTES solution in 100 % ethanol (for APTES see Sigma Aldrich catalog).
3) The coverslips are stored in this solution for 48 h.
4) After drying the coverslips should be used for imaging during the next few hours.

Appendix C

US patent 6,953,927
Method and system for scanning apertureless fluorescence microscope

This patent was issued for the tip enhanced fluorescence microscopy technique. The 58 claims awarded here were for the methods detailed in Chapter 3 (esp. section 3.1 Dry imaging). This patent was issued on October 11, 2005 to Steven Quake, Guillaume Lessard, Lawrence Wade and Jordan Gerton. These four inventors made equal contributions to this invention.

US006953927B2

(12) **United States Patent**
Quake et al.

(10) **Patent No.: US 6,953,927 B2**
(45) **Date of Patent: Oct. 11, 2005**

(54) **METHOD AND SYSTEM FOR SCANNING APERTURELESS FLUORESCENCE MICROSCOPE**

(75) Inventors: **Stephen R. Quake**, San Marino, CA (US); **Guillaume Lessard**, Pasadena, CA (US); **Lawrence A. Wade**, La Canada, CA (US); **Jordan M. Gerton**, Upland, CA (US)

(73) Assignee: **California Institute of Technology**, Pasadena, CA (US)

(*) Notice: Subject to any disclaimer, the term of this patent is extended or adjusted under 35 U.S.C. 154(b) by 0 days.

(21) Appl. No.: **10/616,896**

(22) Filed: **Jul. 9, 2003**

(65) **Prior Publication Data**

US 2004/0089816 A1 May 13, 2004

Related U.S. Application Data

(60) Provisional application No. 60/402,351, filed on Aug. 9, 2002.

(51) **Int. Cl.**[7] **H01J 3/14**; H01J 40/14; H01J 5/16

(52) **U.S. Cl.** **250/234**; 250/458.1

(58) **Field of Search** 250/234, 458.1; 356/72–73, 301, 318; 977/DIG. 1

(56) **References Cited**

U.S. PATENT DOCUMENTS

5,479,024	A	* 12/1995	Hillner et al.	250/458.1
6,002,471	A	12/1999	Quake	
6,046,448	A	* 4/2000	Sato et al.	250/234
6,643,012	B2	11/2003	Shen et al.	
6,681,133	B2	1/2004	Chaiken et al.	
2002/0109082	A1	8/2002	Nakayama et al.	

OTHER PUBLICATIONS

H. Gersen et al., "Near–field effects in single molecule emission", Journal of Microscopy, vol. 202, Pt 2, May 2001, pp. 374–378.

H. Gersen et al., "Influencing the Angular Emission of a Single Molecule", Physical Review Letters, vol. 85, No. 25, Dec. 18, 2000, pp. 5312–5315.

J.M. Gerton et al., "Fluorescence Apertureless Near–field Optical Microscope for Biological Imaging", The 7th International Conference on Near–field Optics and Related Techniques, Aug. 11–15, 2002, p. 71.

T.J. Yang et al., "An Apertureless Near–field Microscope for Fluorescence Imaging", Applied Physics Letters vol. 76, No. 3, Jan. 17, 2000, pp. 378–380.

Guillaume A. Lessard et al., "A Scanning Apertureless Fluorescence Microscope", Department of Applied Physics, California Institute of Technology, Pasadena, California, pp. 1–8.

* cited by examiner

Primary Examiner—David Porta
Assistant Examiner—Patrick J. Lee
(74) *Attorney, Agent, or Firm*—Townsend and Townsend and Crew LLP

(57) **ABSTRACT**

Methods and systems for operating an apertureless microscope for observing one or more features to a molecular sensitivity on objects are described. More particularly, the method includes moving a tip of a probe coupled to a cantilever in a vicinity of a feature of a sample, which emits one or more photons at a detected rate relative to a background rate of the sample based upon the presence of the tip of the probe in the vicinity of the feature. The method modifies the detected rate of the feature of the sample, whereupon the modifying of the detected rate causes the feature of the sample to enhance relative to background rate of the feature.

55 Claims, 38 Drawing Sheets

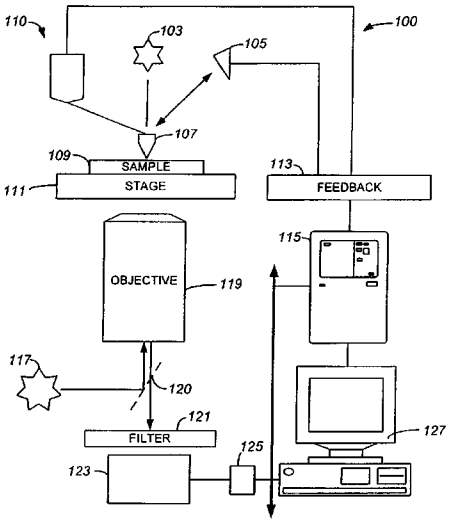

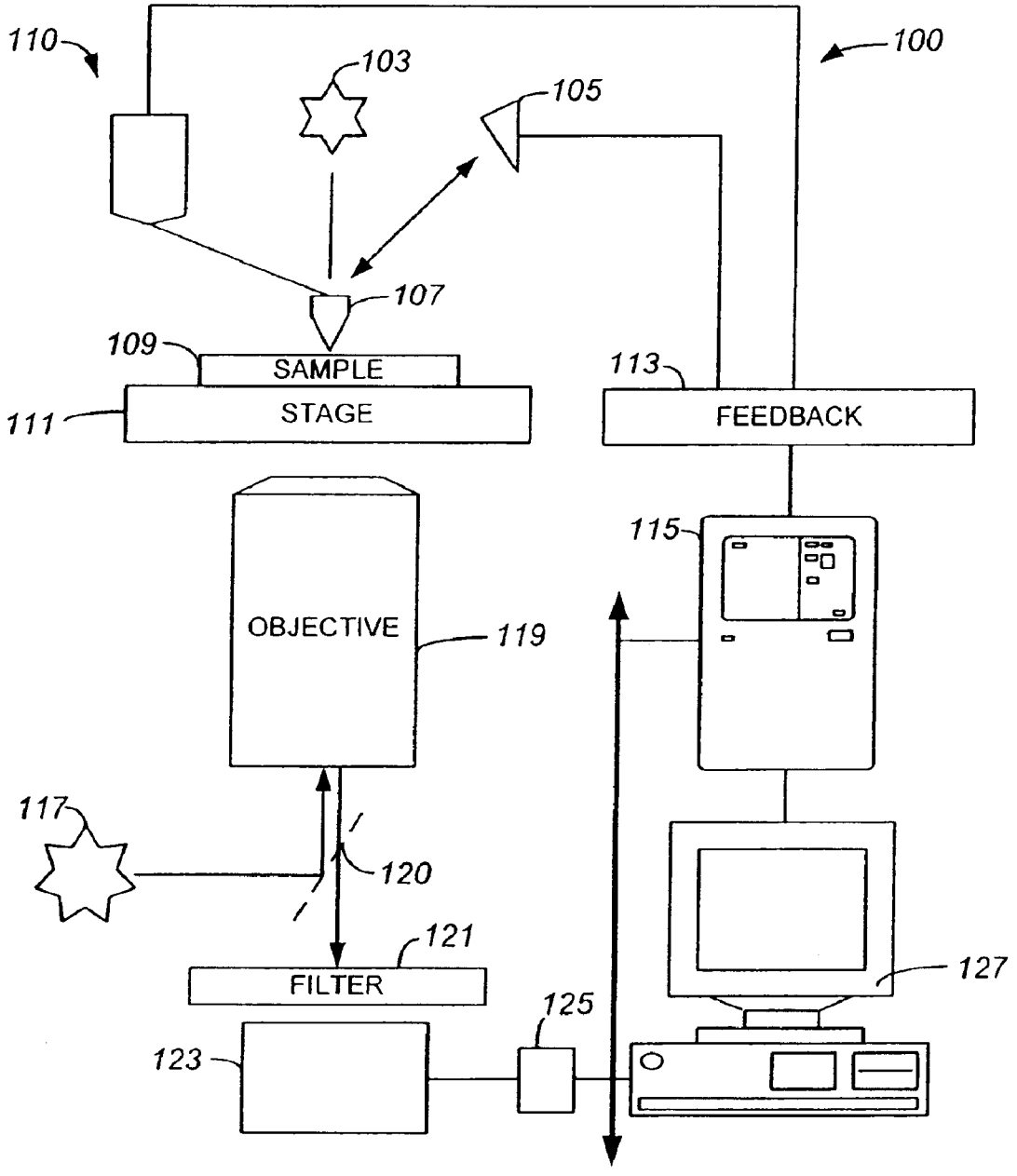
110
100
103
105
107
109
SAMPLE
111
STAGE
113
FEEDBACK
115
OBJECTIVE
119
117
120
121
FILTER
123
125
127

FIG. 1

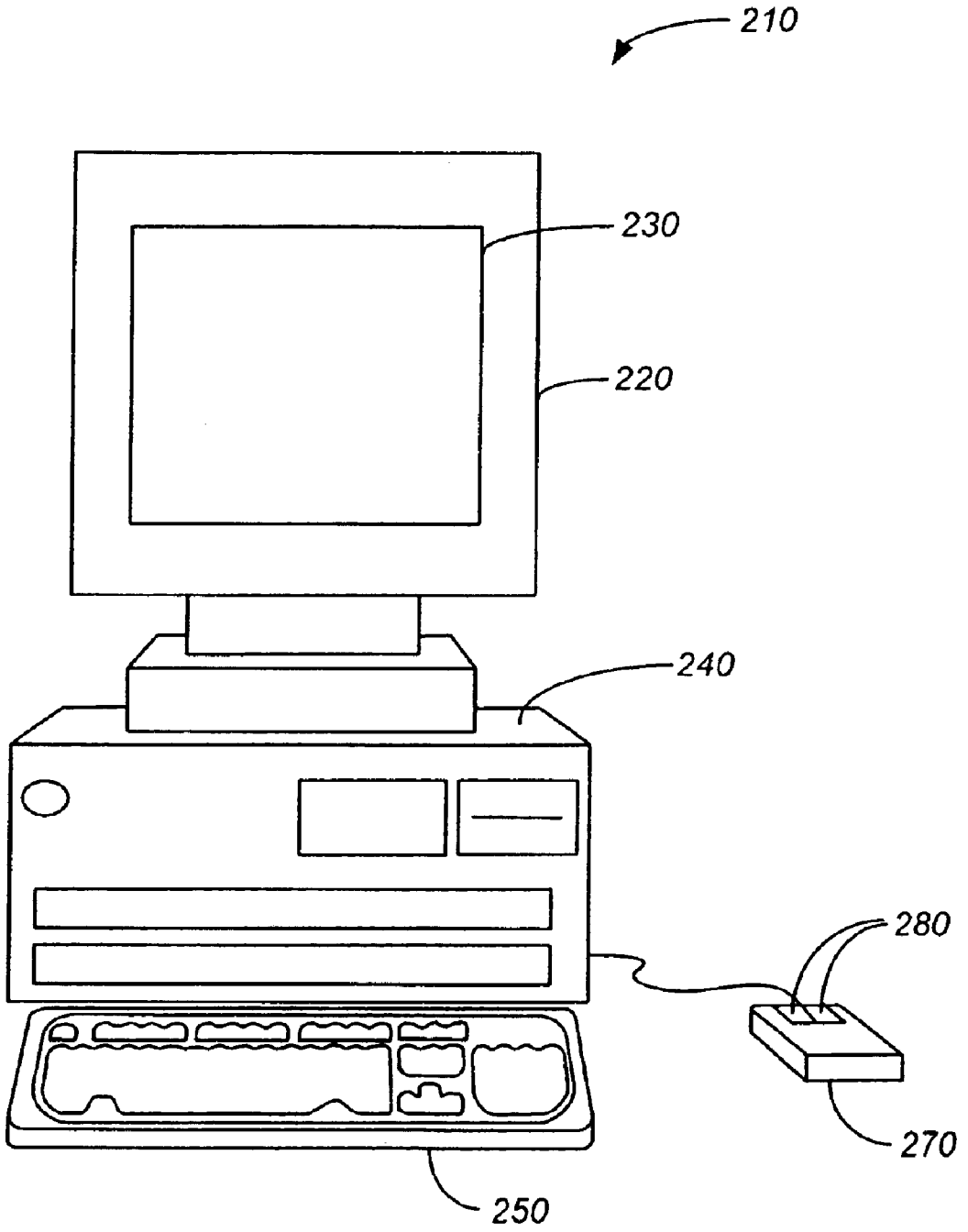

FIG. 2

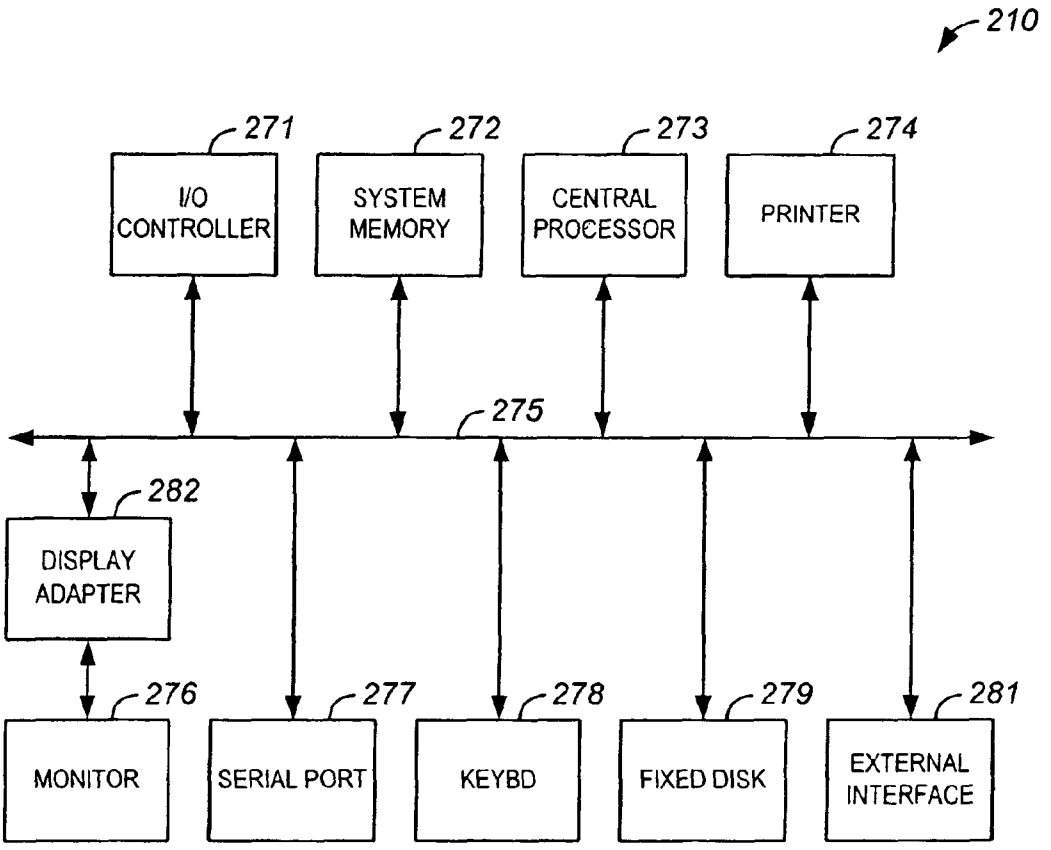
210
271
I/O CONTROLLER
272
SYSTEM MEMORY
273
CENTRAL PROCESSOR
274
PRINTER
275
282
DISPLAY ADAPTER
276
MONITOR
277
SERIAL PORT
278
KEYBD
279
FIXED DISK
281
EXTERNAL INTERFACE

FIG. 2A

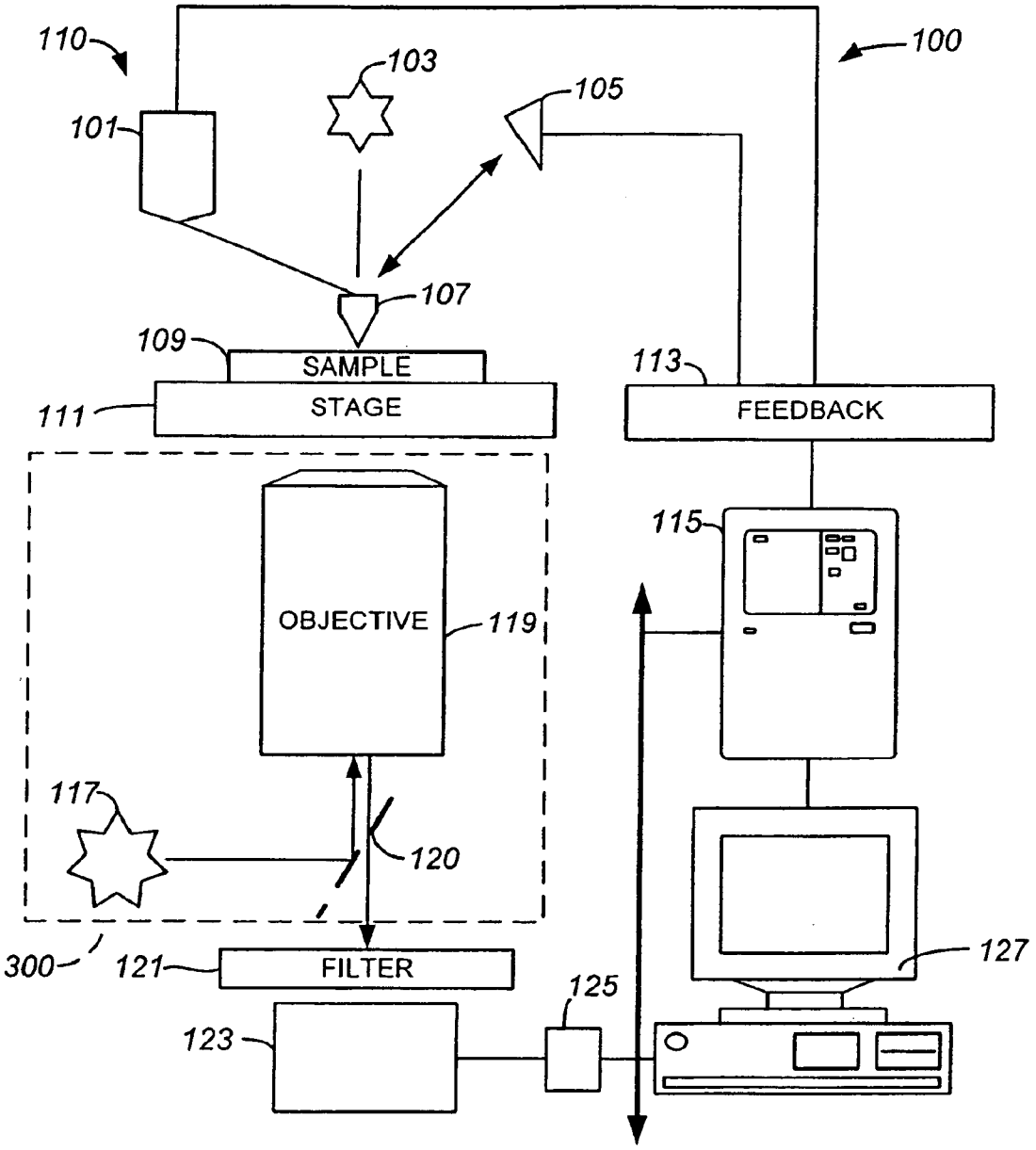
110
100
103
105
101
107
109
SAMPLE
113
111
STAGE
FEEDBACK
115
OBJECTIVE
119
117
120
300
121
FILTER
125
127
123

FIG. 3

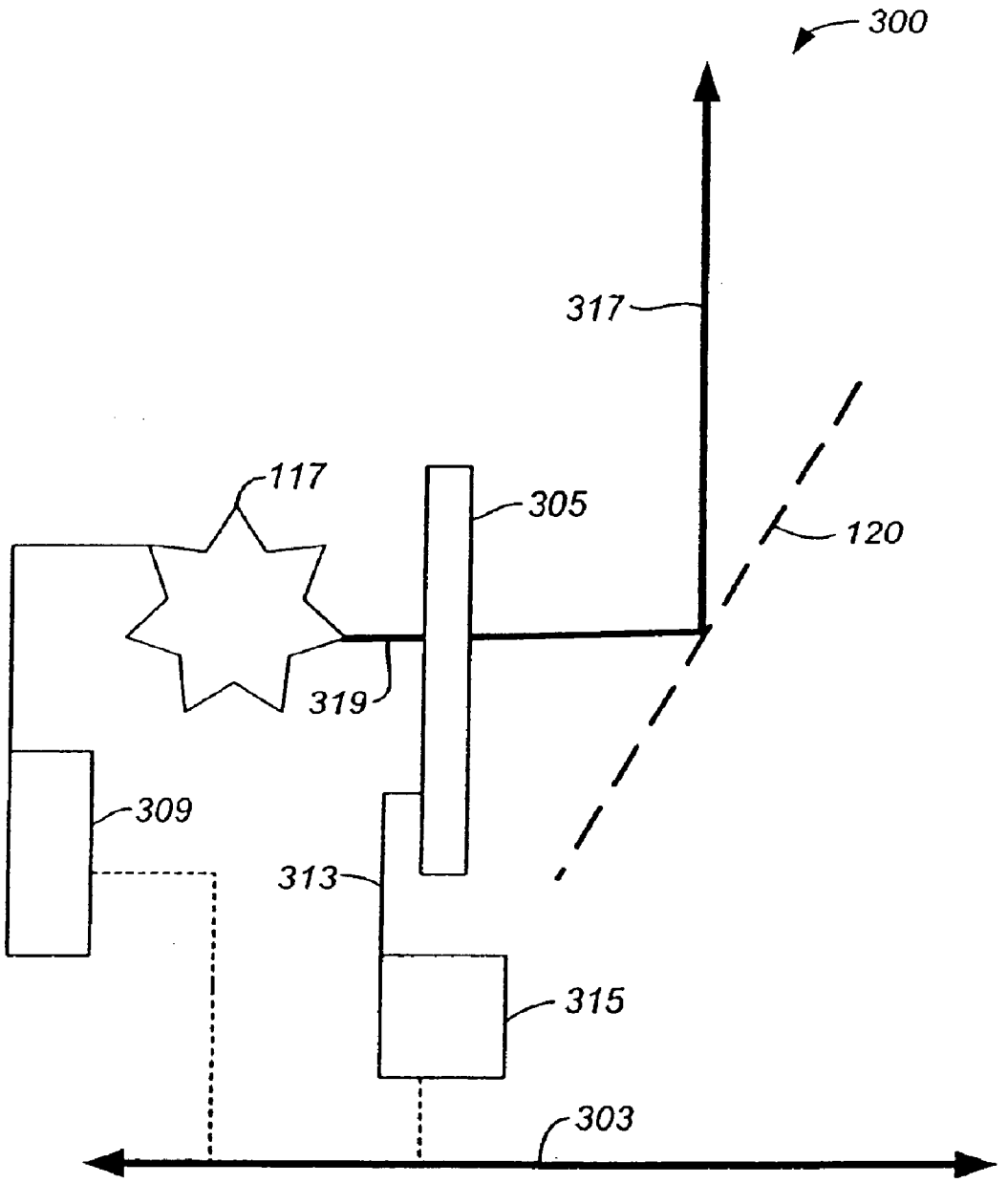

FIG. 3A

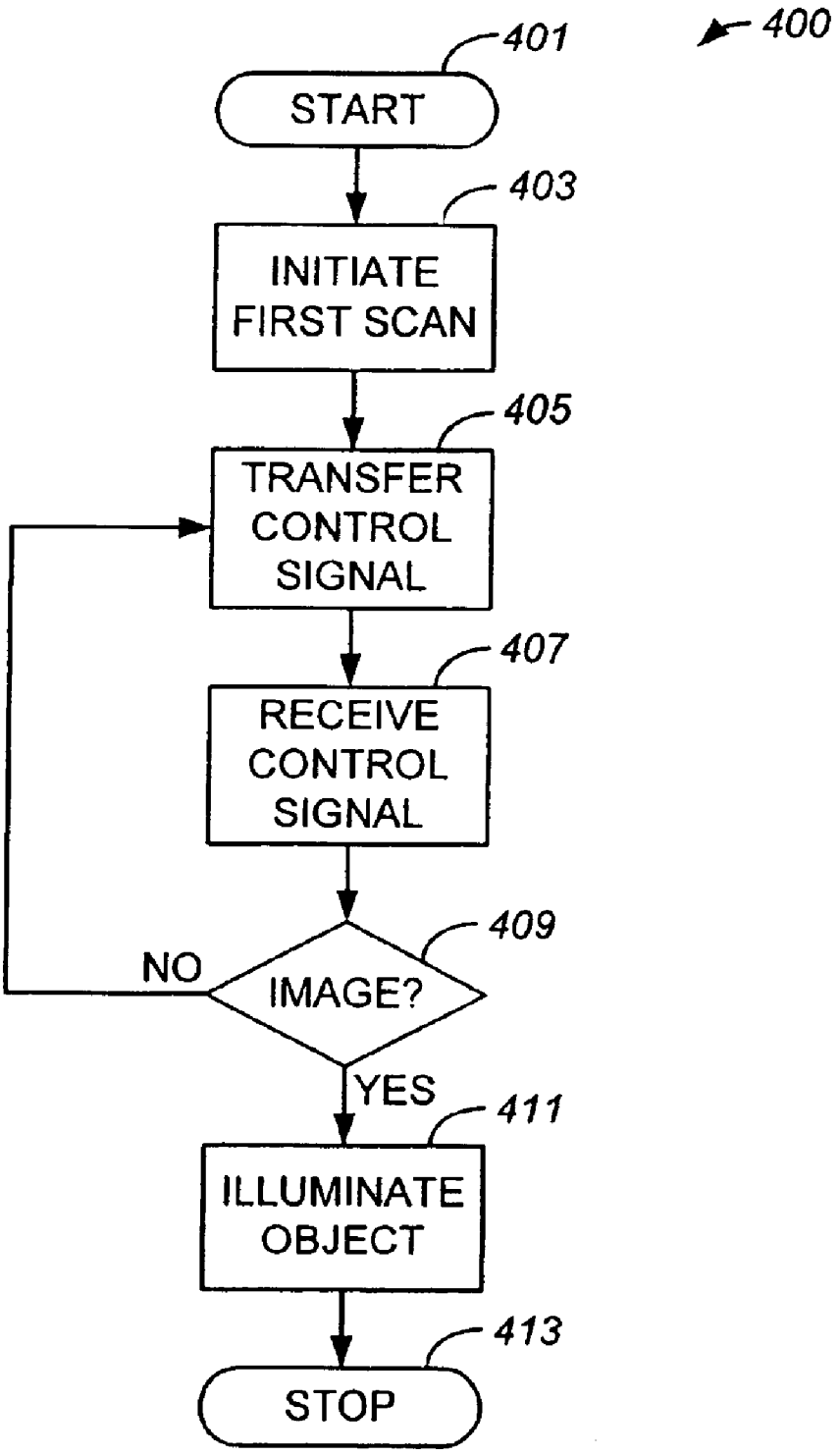
400
401
START
403
INITIATE FIRST SCAN
405
TRANSFER CONTROL SIGNAL
407
RECEIVE CONTROL SIGNAL
409
IMAGE?
NO
YES
411
ILLUMINATE OBJECT
413
STOP

FIG. 4

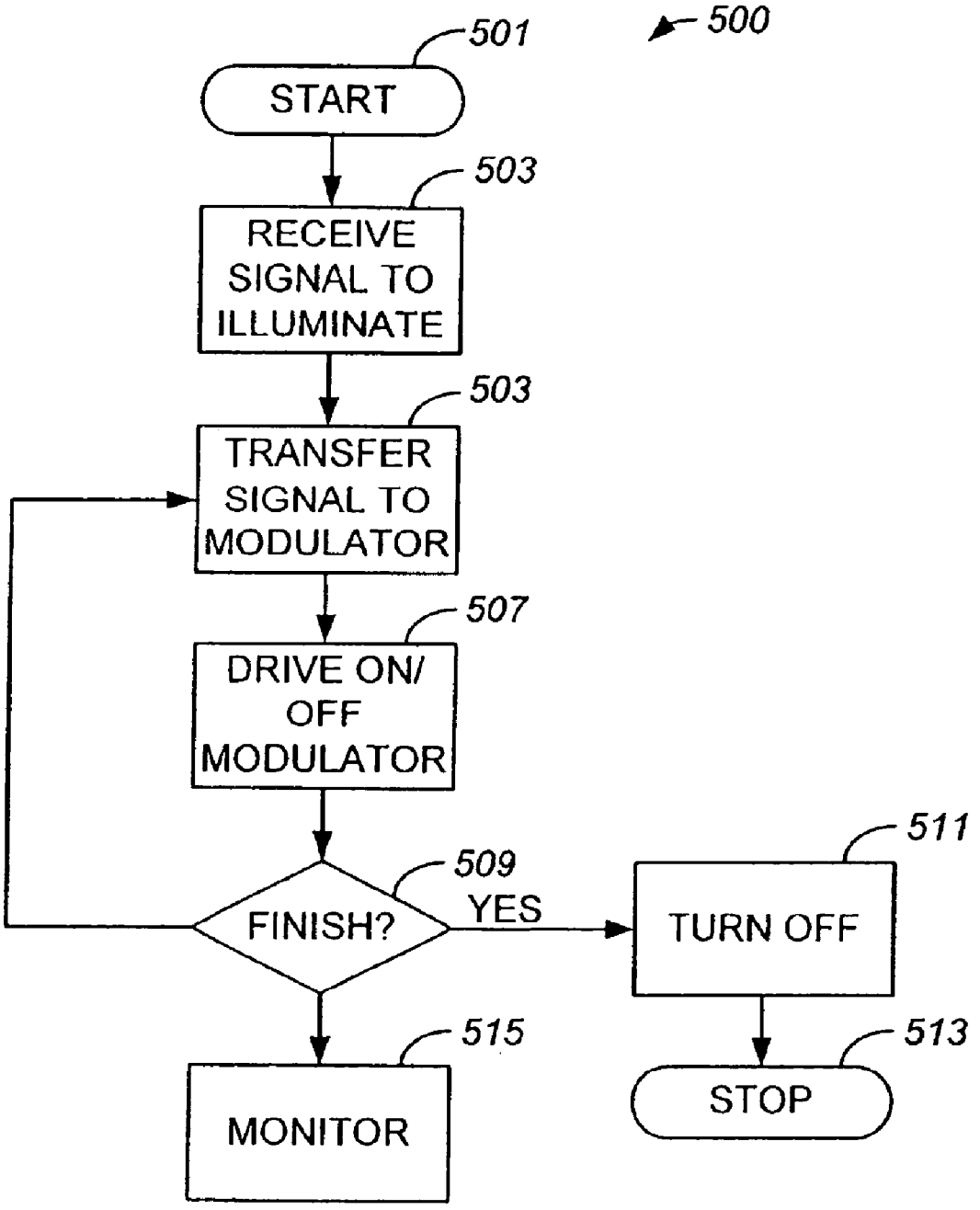
500
501
START
503
RECEIVE SIGNAL TO ILLUMINATE
503
TRANSFER SIGNAL TO MODULATOR
507
DRIVE ON/ OFF MODULATOR
509
FINISH?
YES
511
TURN OFF
513
STOP
515
MONITOR

FIG. 5

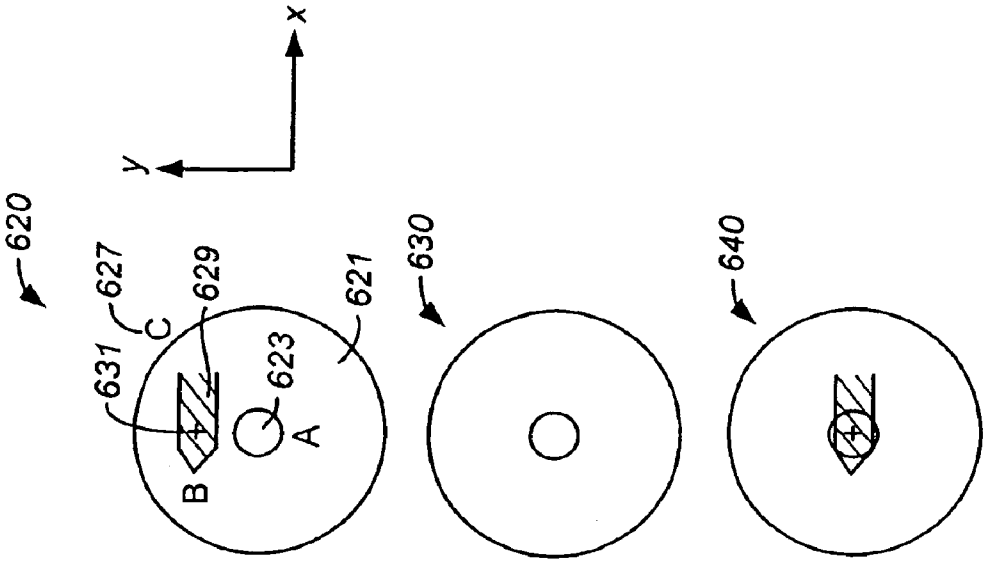
x
y
620
627
C
629
631
623
A
B
621
630
640

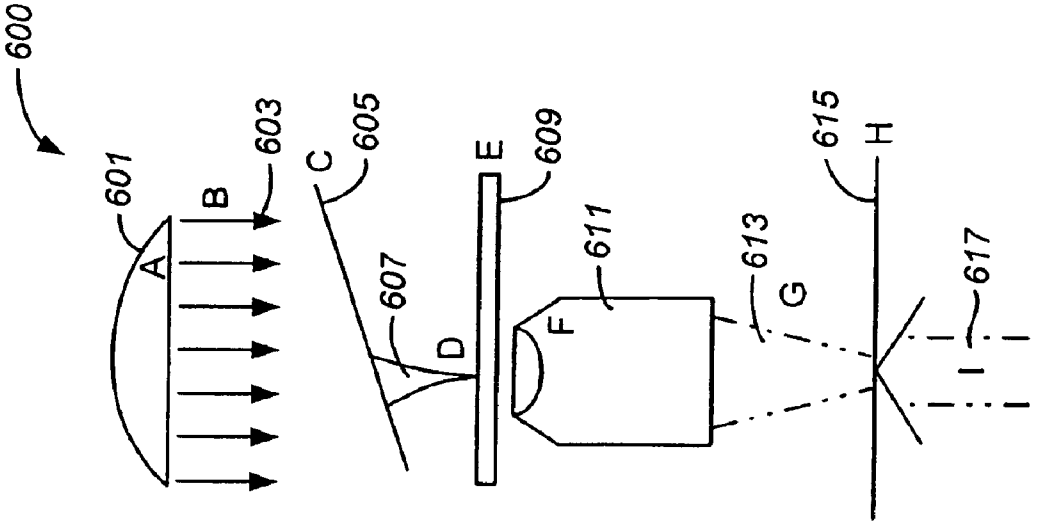
600
601
A
B
603
C
605
607
D
E
609
611
F
613
G
615
H
617
I
I

FIG. 6

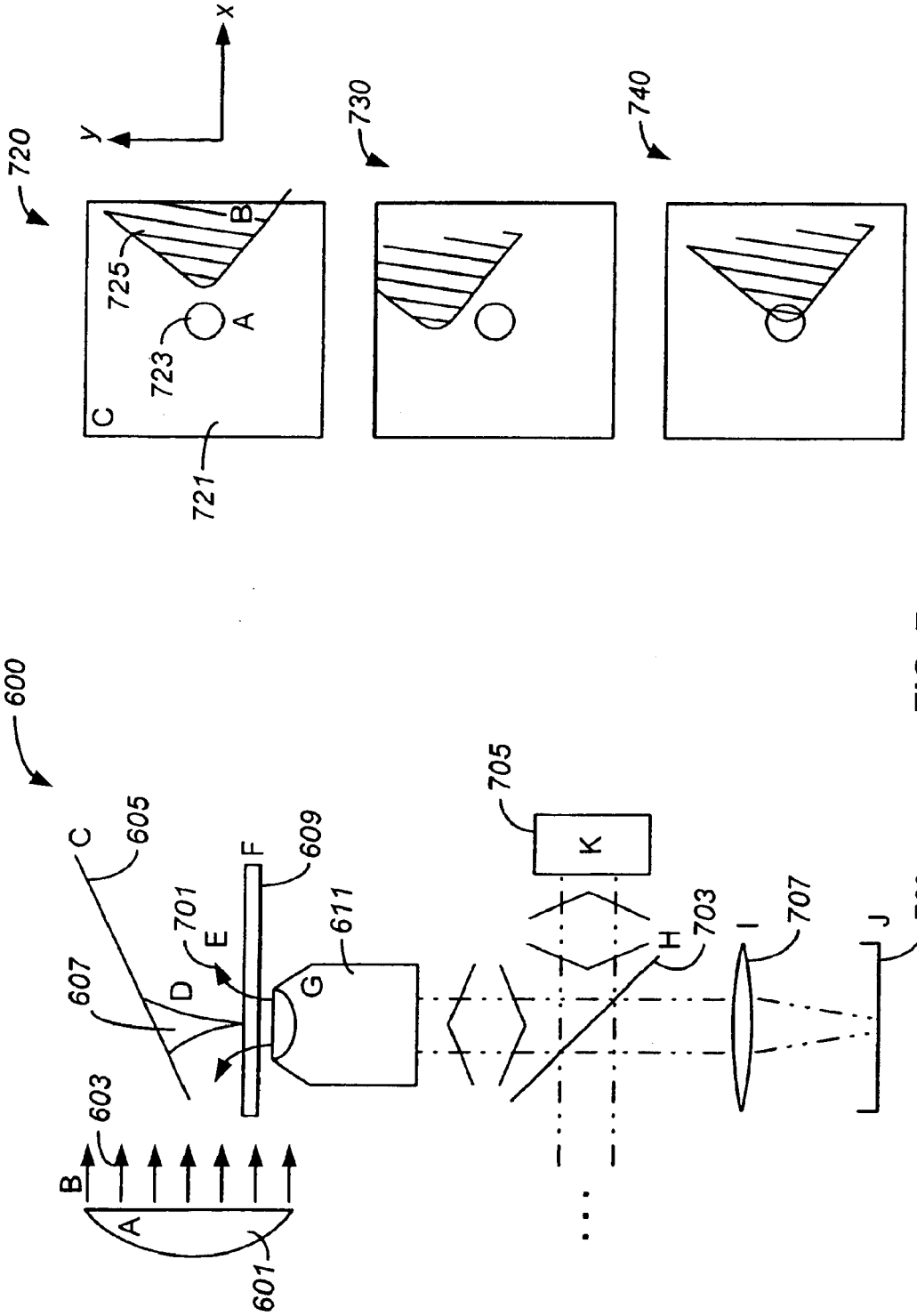
720
730
740
x
y
A
B
C
723
725
721
600
601
603
605
607
609
611
701
703
705
707
709
D
E
F
G
H
I
J
K

FIG. 7

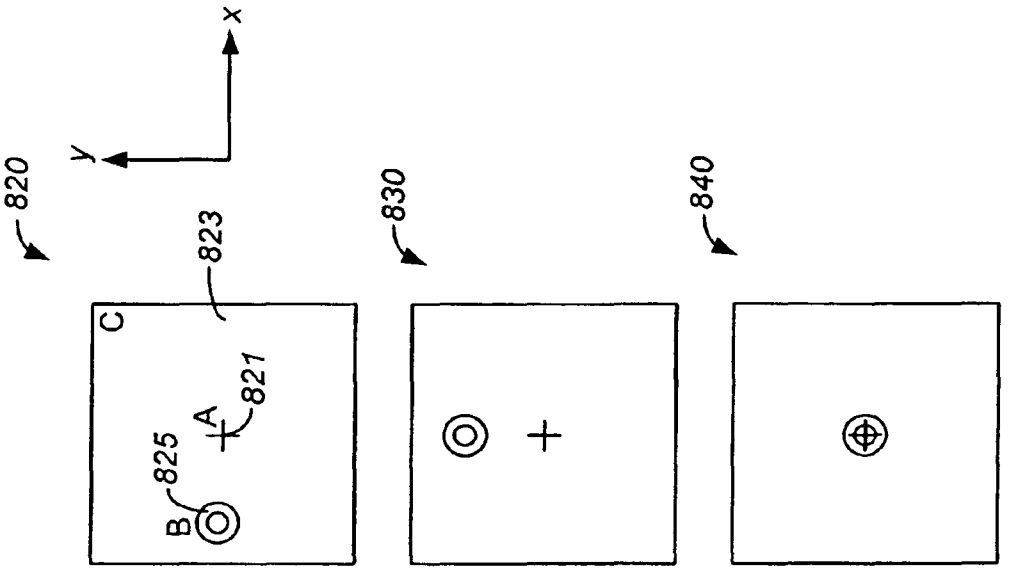
x
y
820
823
830
840
C
A
821
825
B

FIG. 8

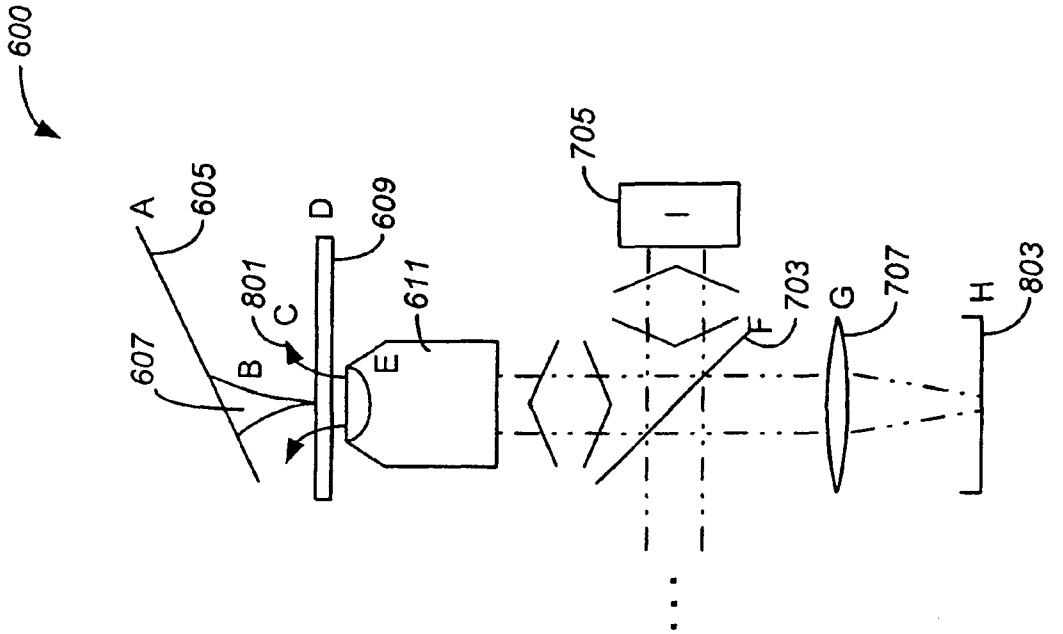
600
A
605
607
B
801
C
D
609
611
E
705
703
F
G
707
H
803

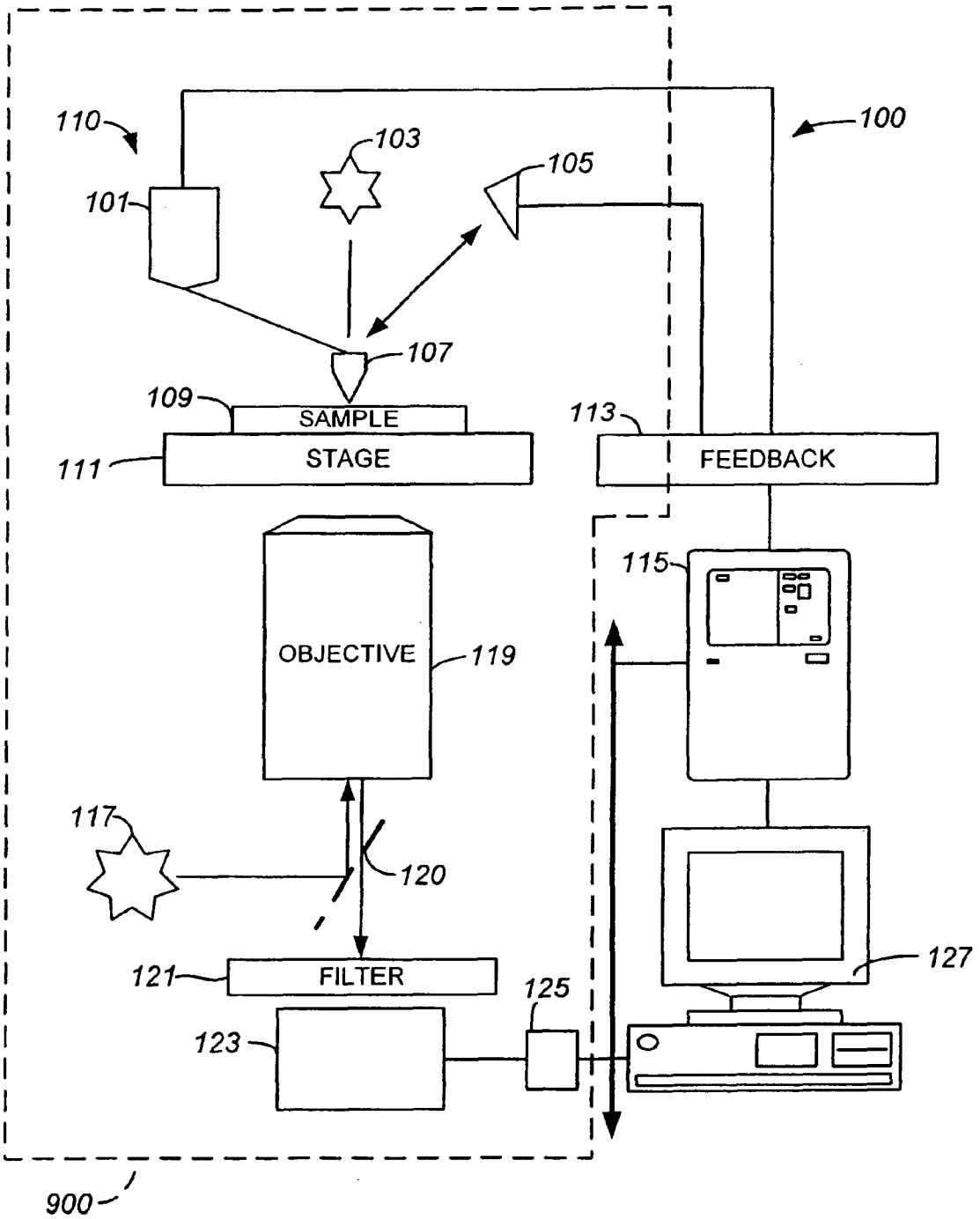
110
100
103
105
101
107
109
SAMPLE
113
111
STAGE
FEEDBACK
115
OBJECTIVE
119
117
120
121
FILTER
125
127
123
900

FIG. 9

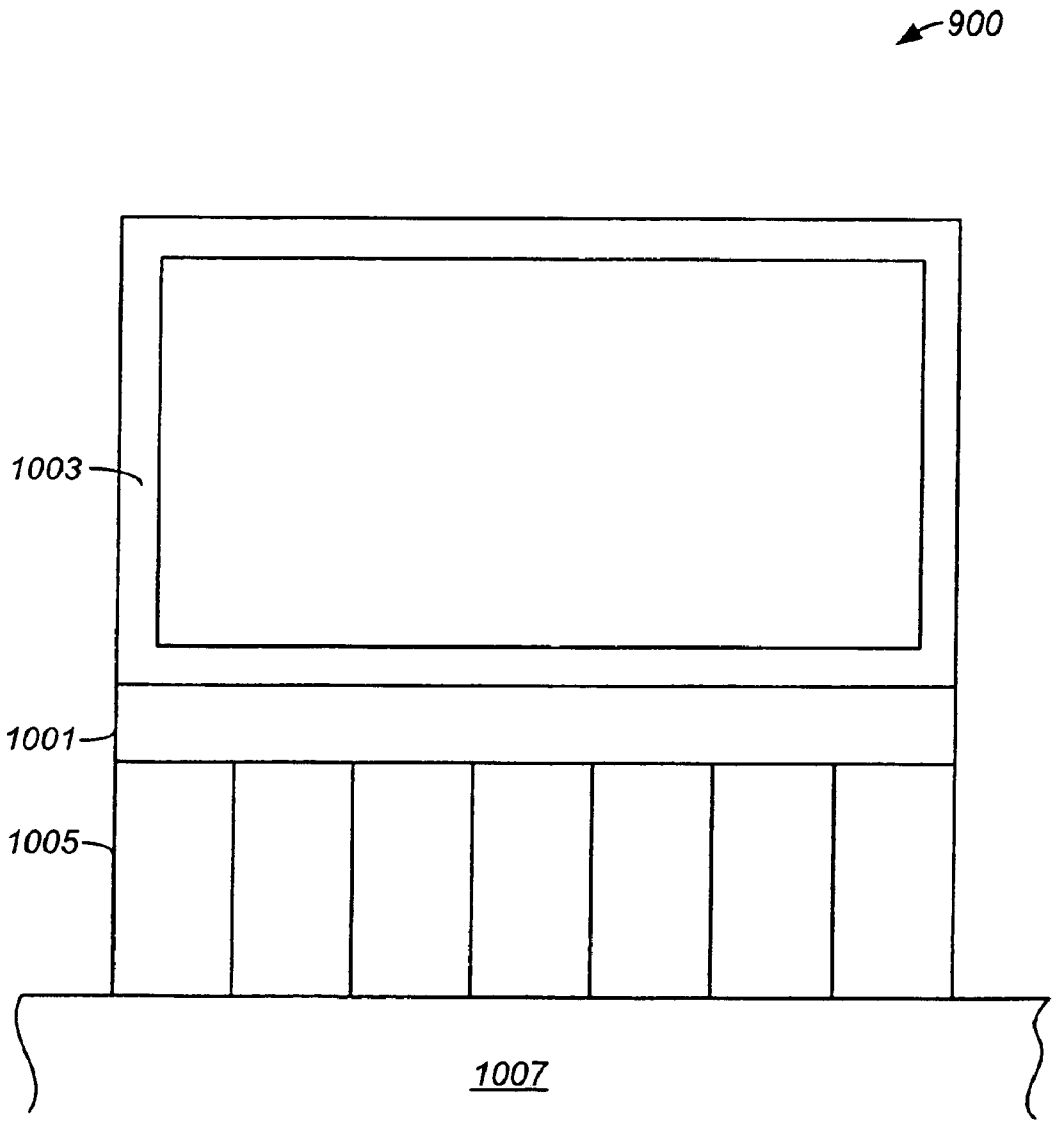

FIG. 10

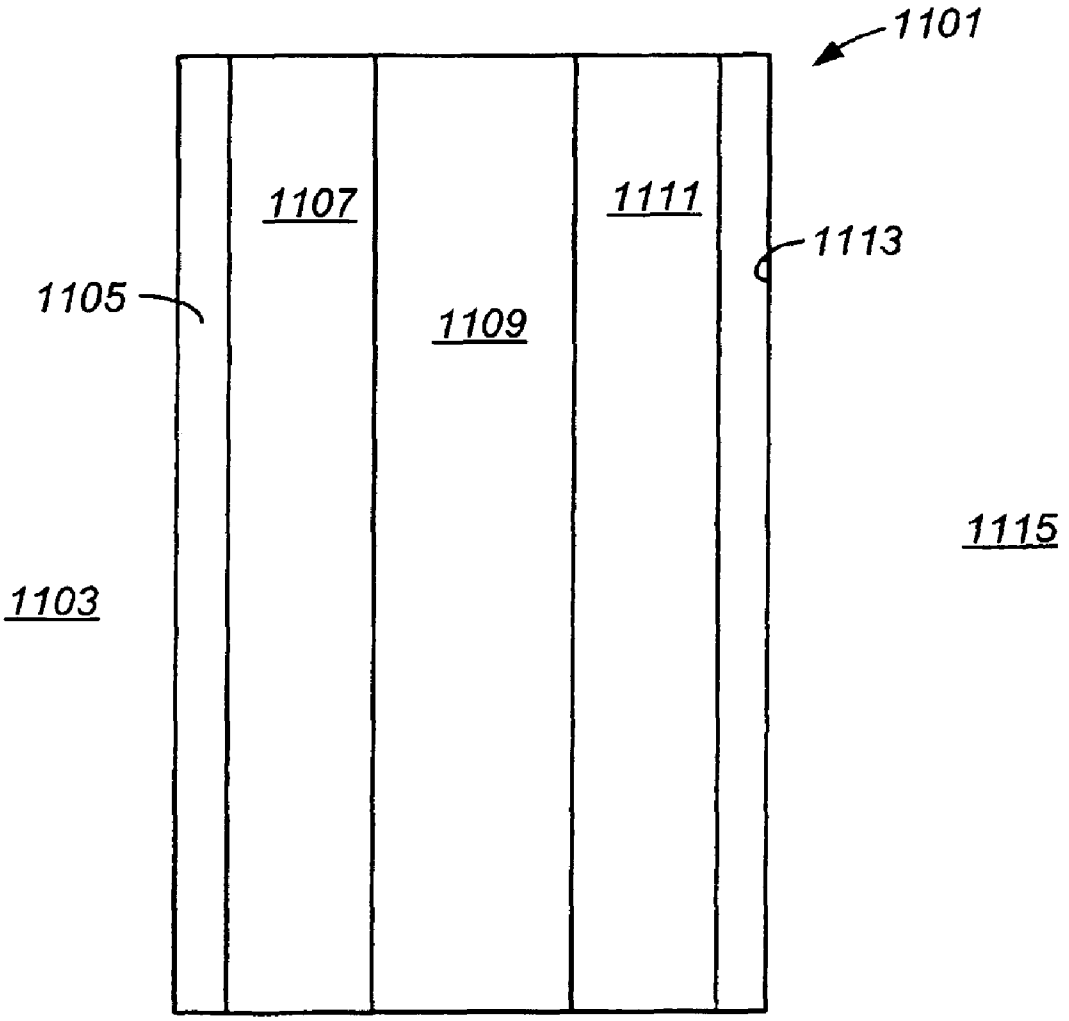

FIG. 11

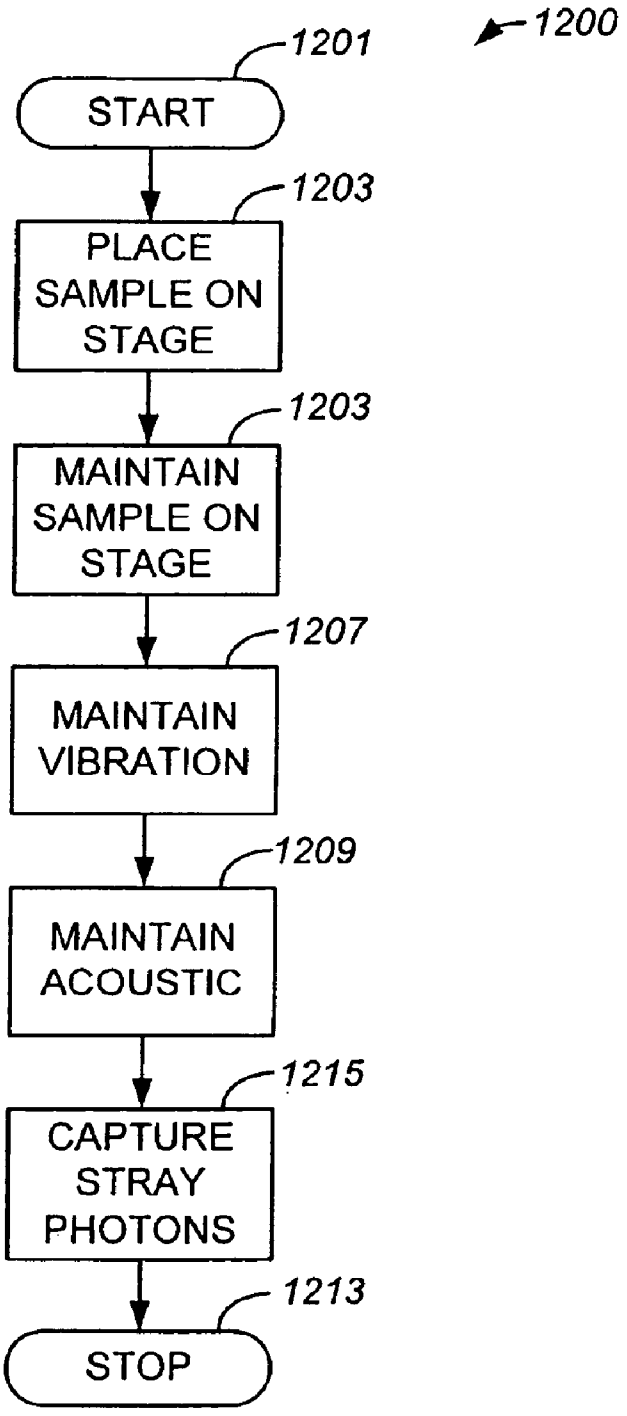
1200
1201
START
1203
PLACE SAMPLE ON STAGE
1203
MAINTAIN SAMPLE ON STAGE
1207
MAINTAIN VIBRATION
1209
MAINTAIN ACOUSTIC
1215
CAPTURE STRAY PHOTONS
1213
STOP

FIG. 12

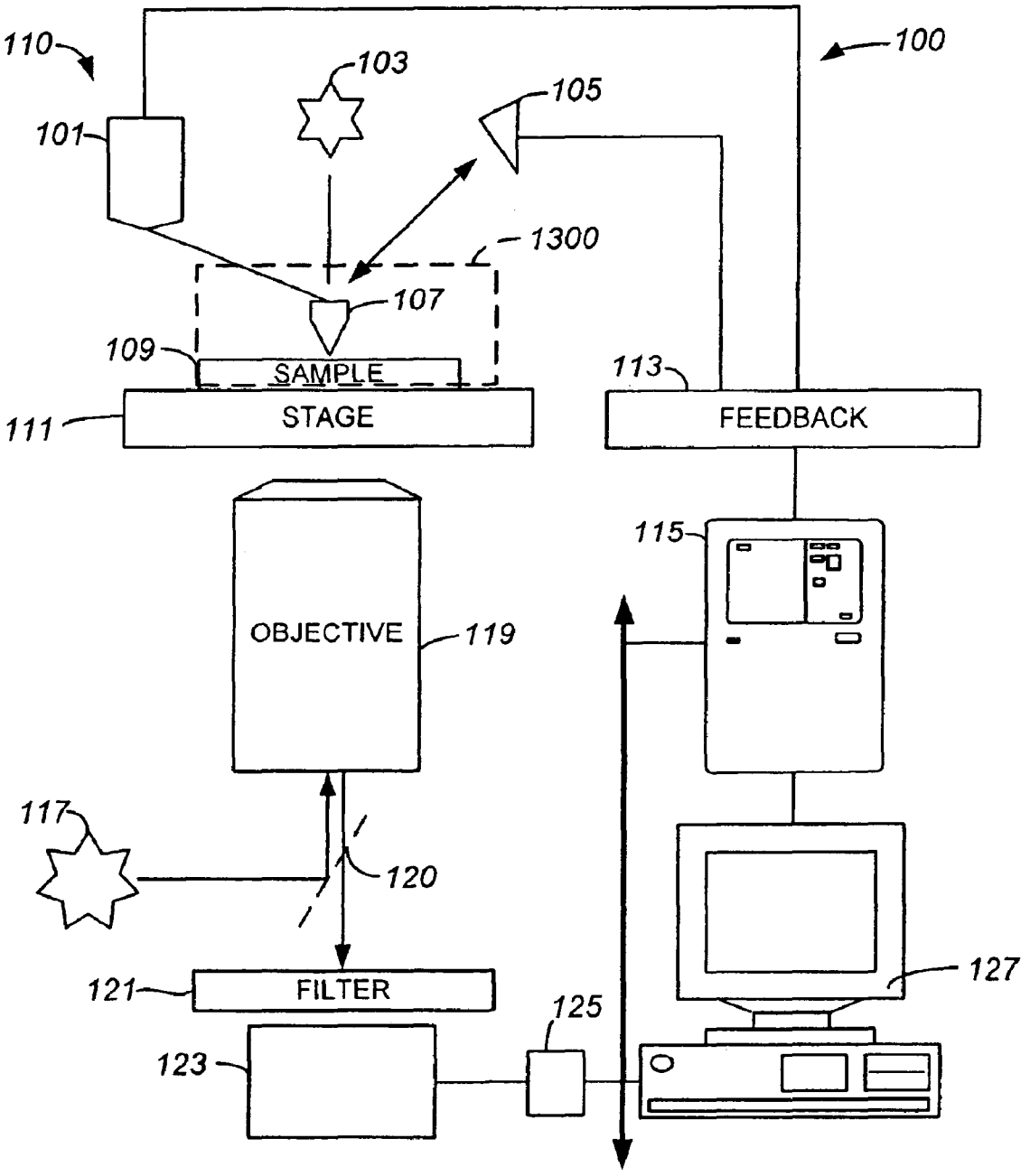
110
100
103
105
101
1300
107
109
SAMPLE
113
111
STAGE
FEEDBACK
115
OBJECTIVE
119
117
120
121
FILTER
125
127
123

FIG. 13

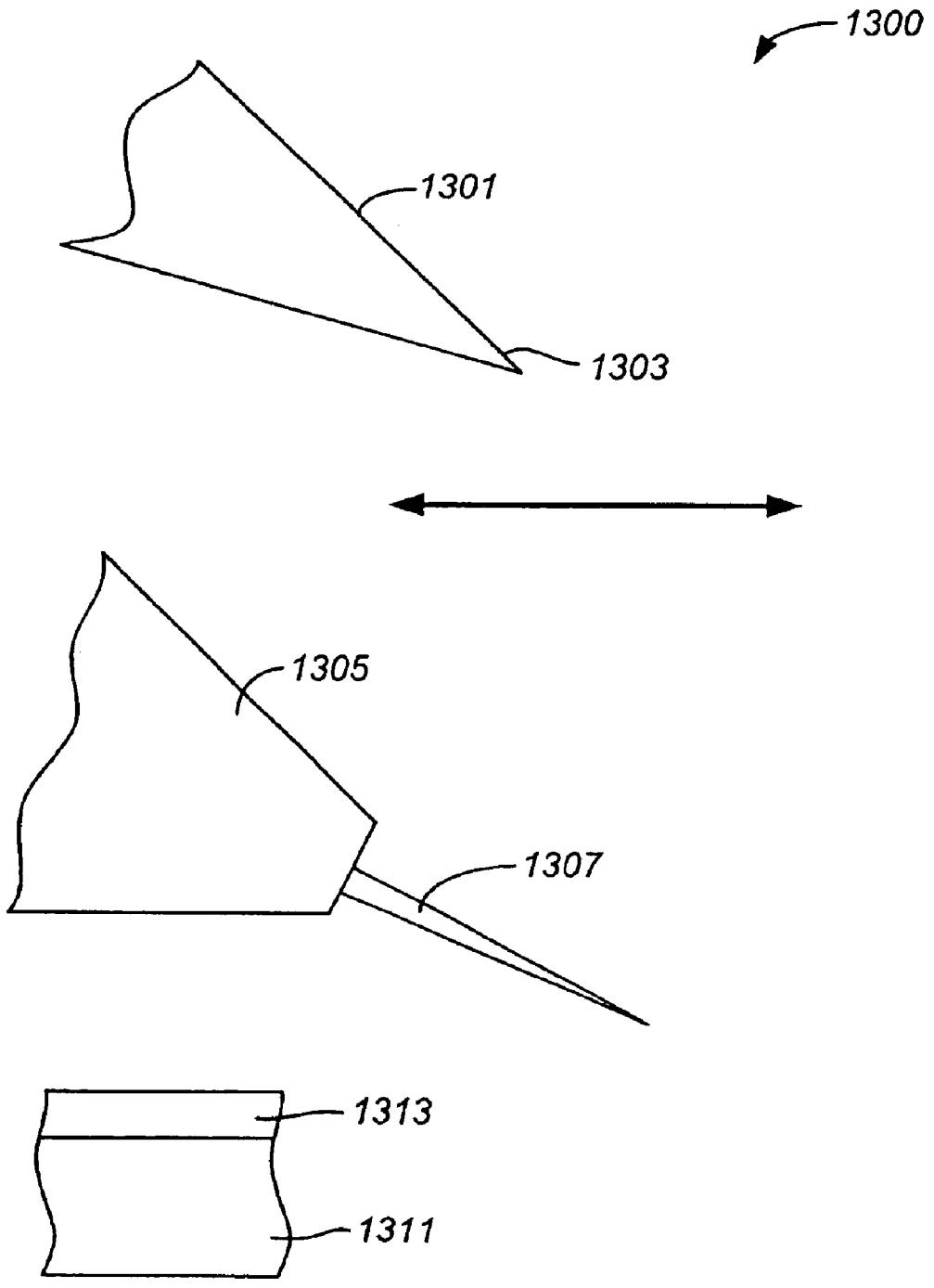

FIG. 14

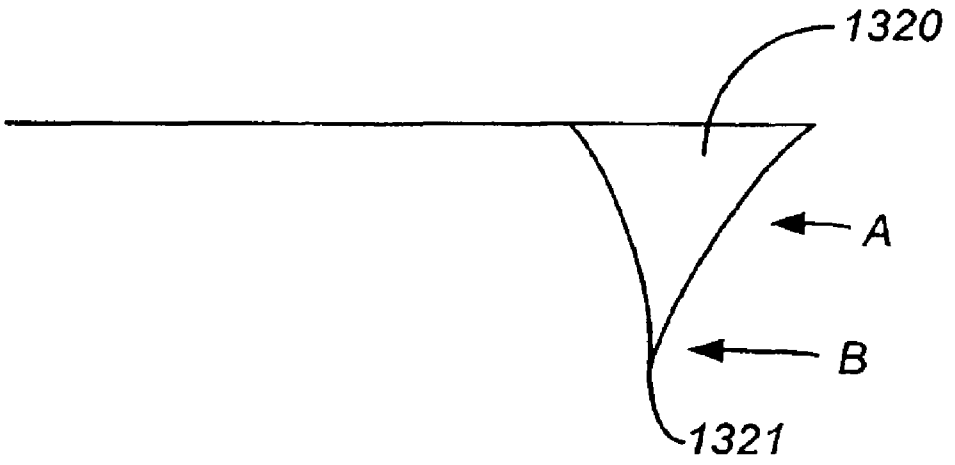

FIG. 14A

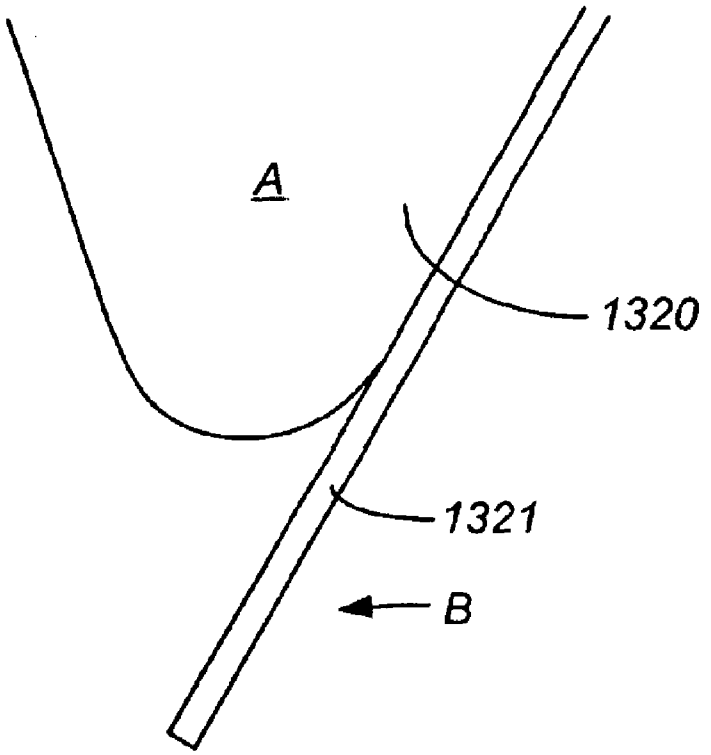

FIG. 14B

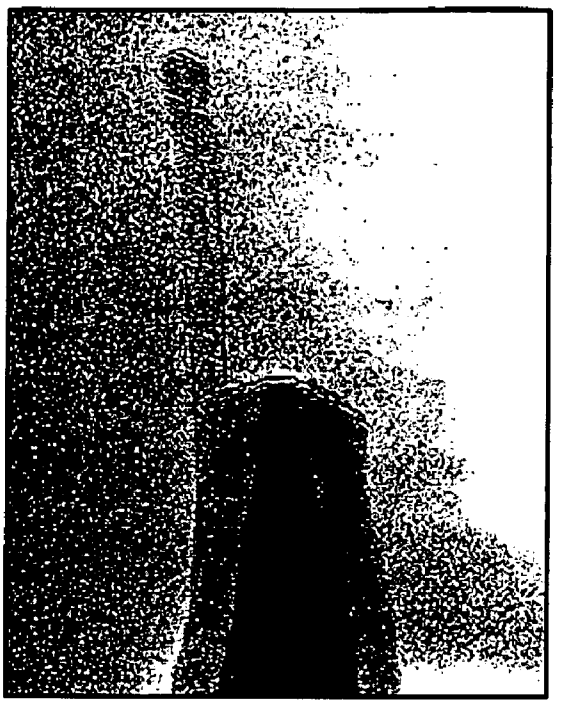

FIG. 14C

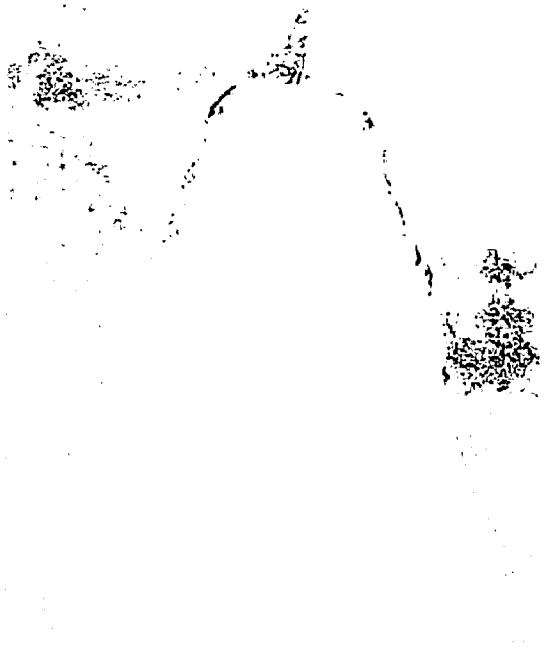

FIG. 14D

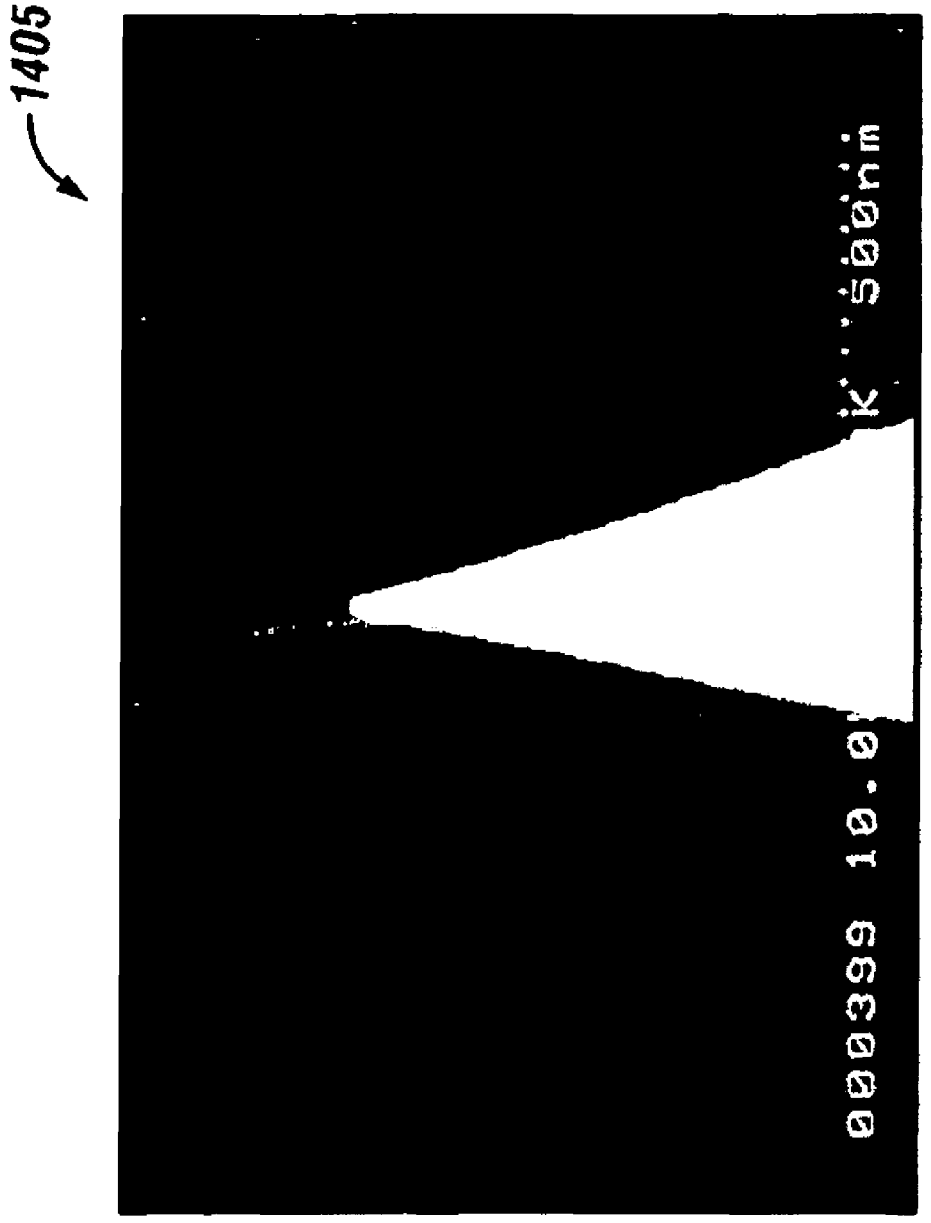

FIG. 14E

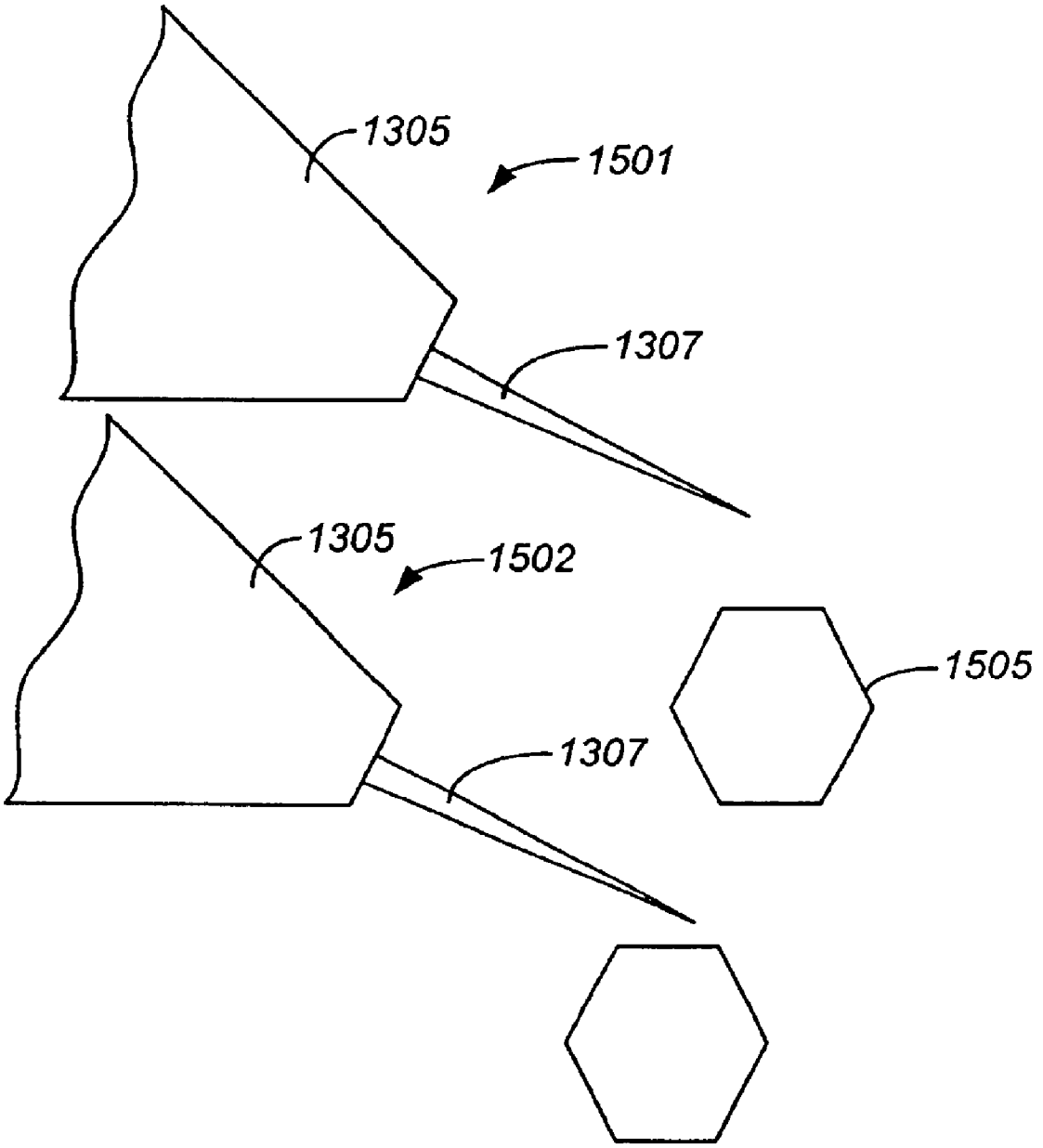

FIG. 15

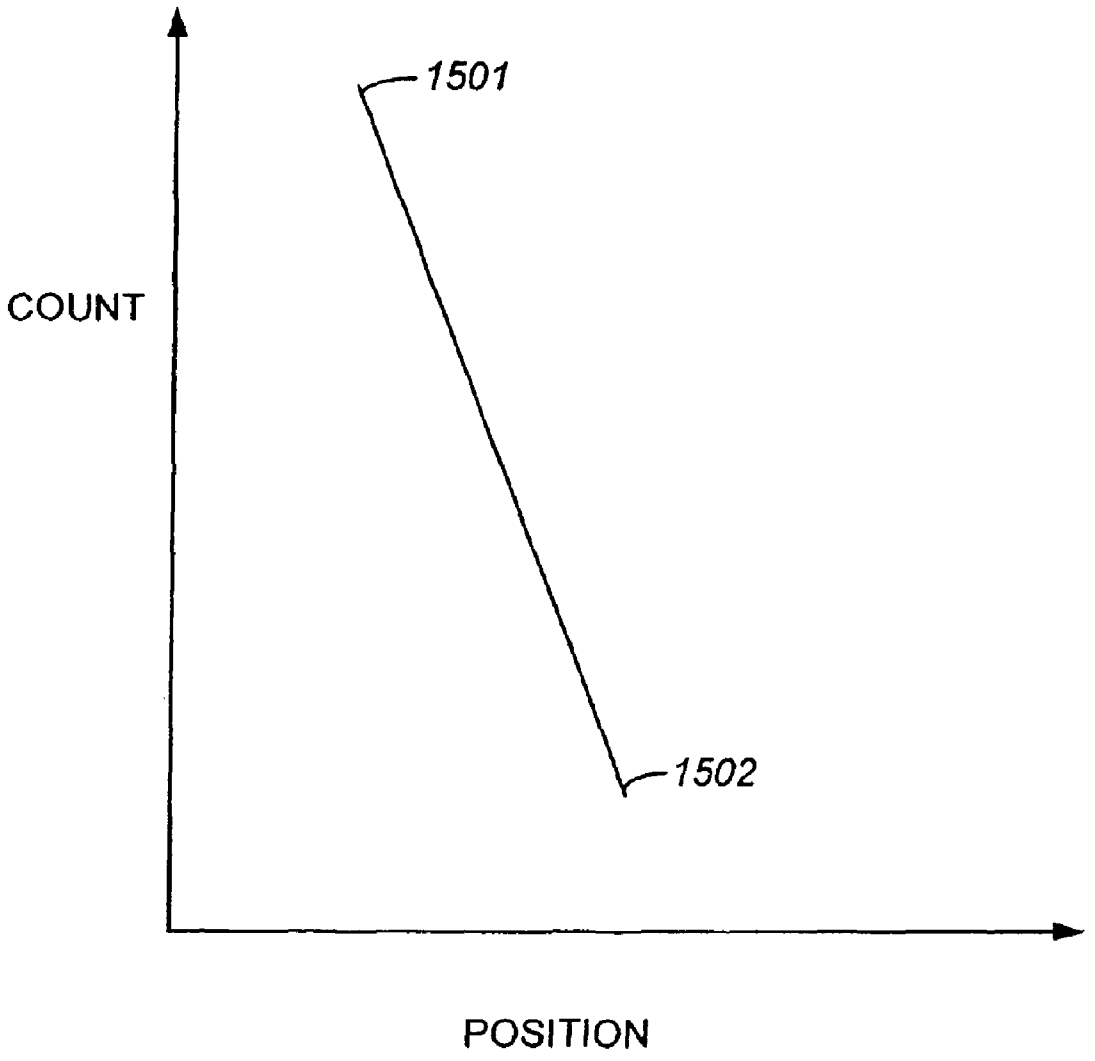

FIG. 16

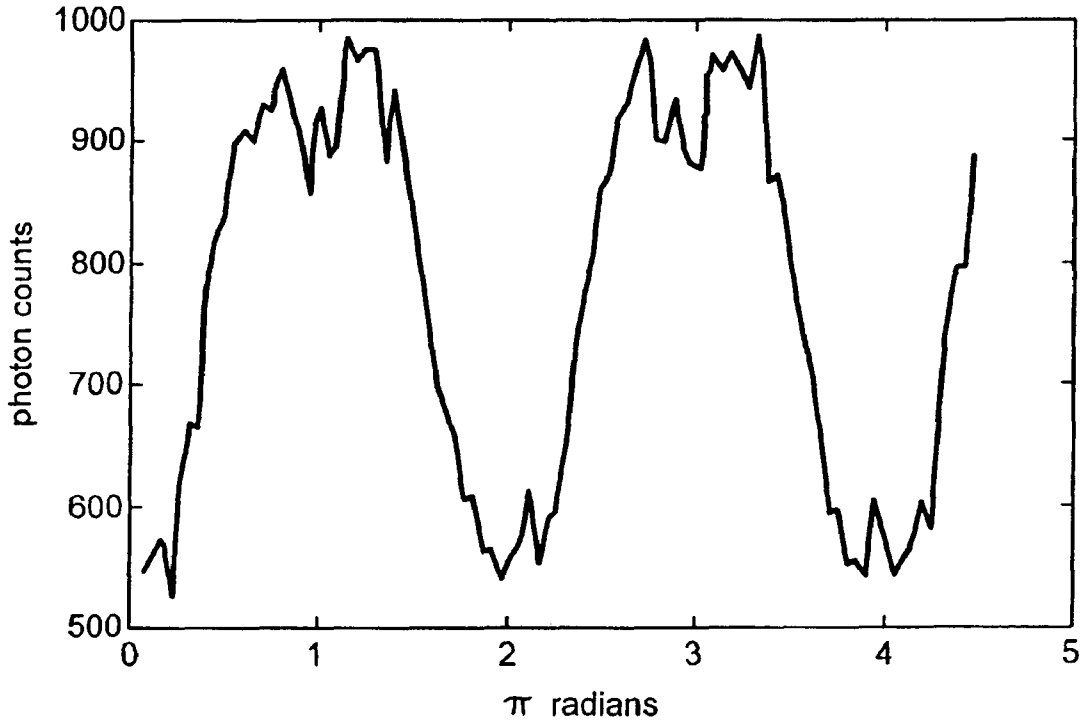

FIG. 17

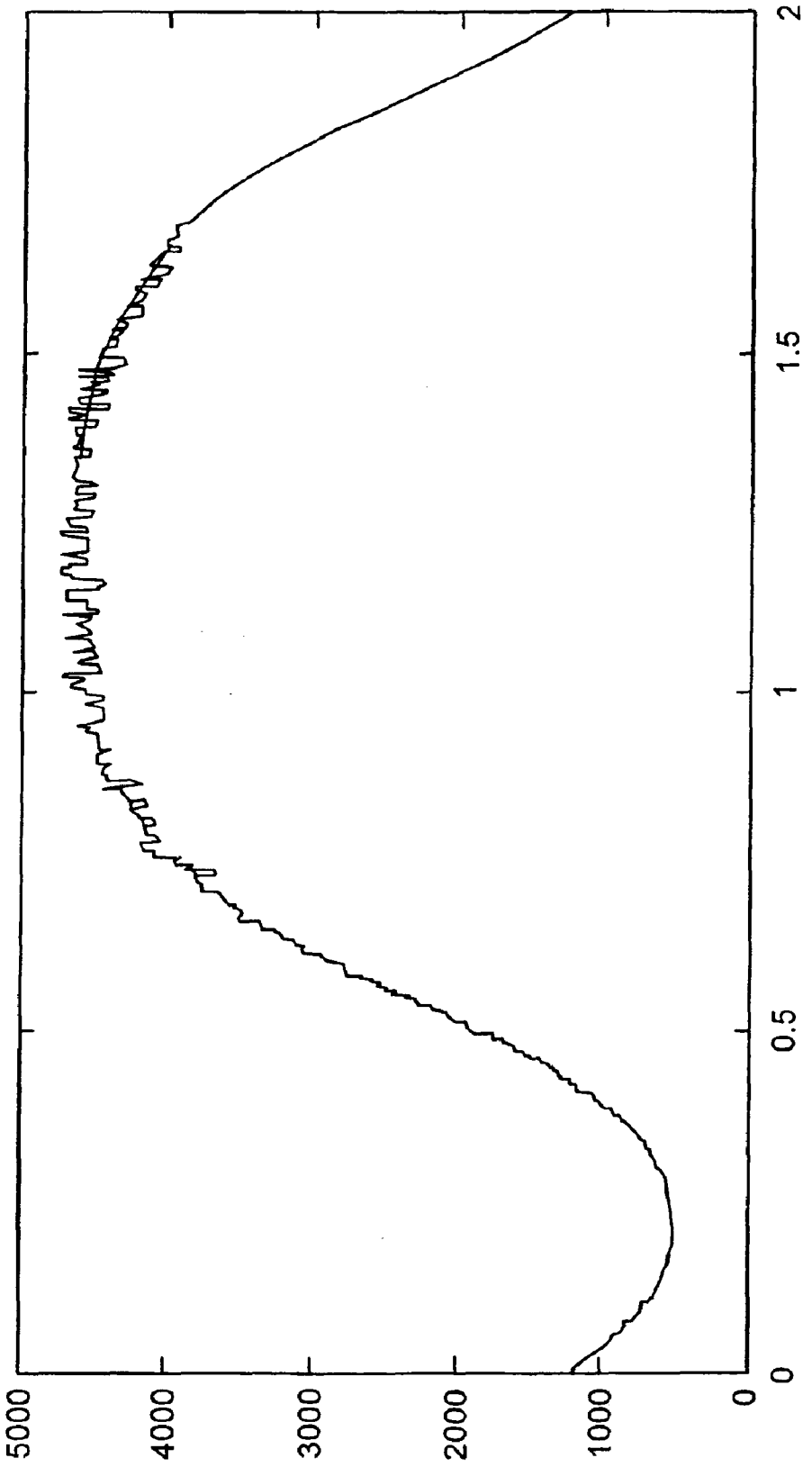

FIG. 18

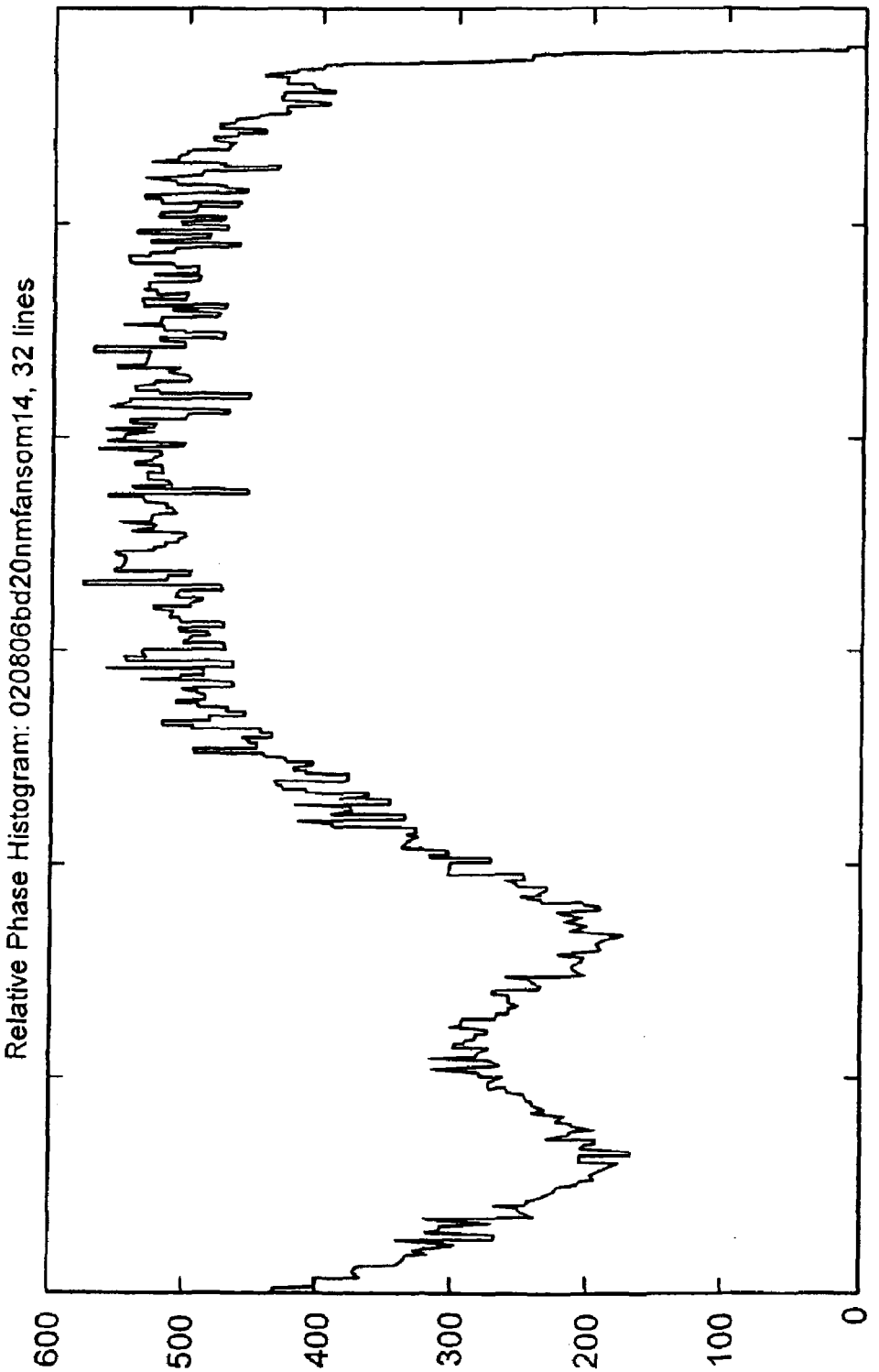
Relative Phase Histogram: 020806bd20nmfansom14, 32 lines
600
500
400
300
200
100
0

FIG. 19

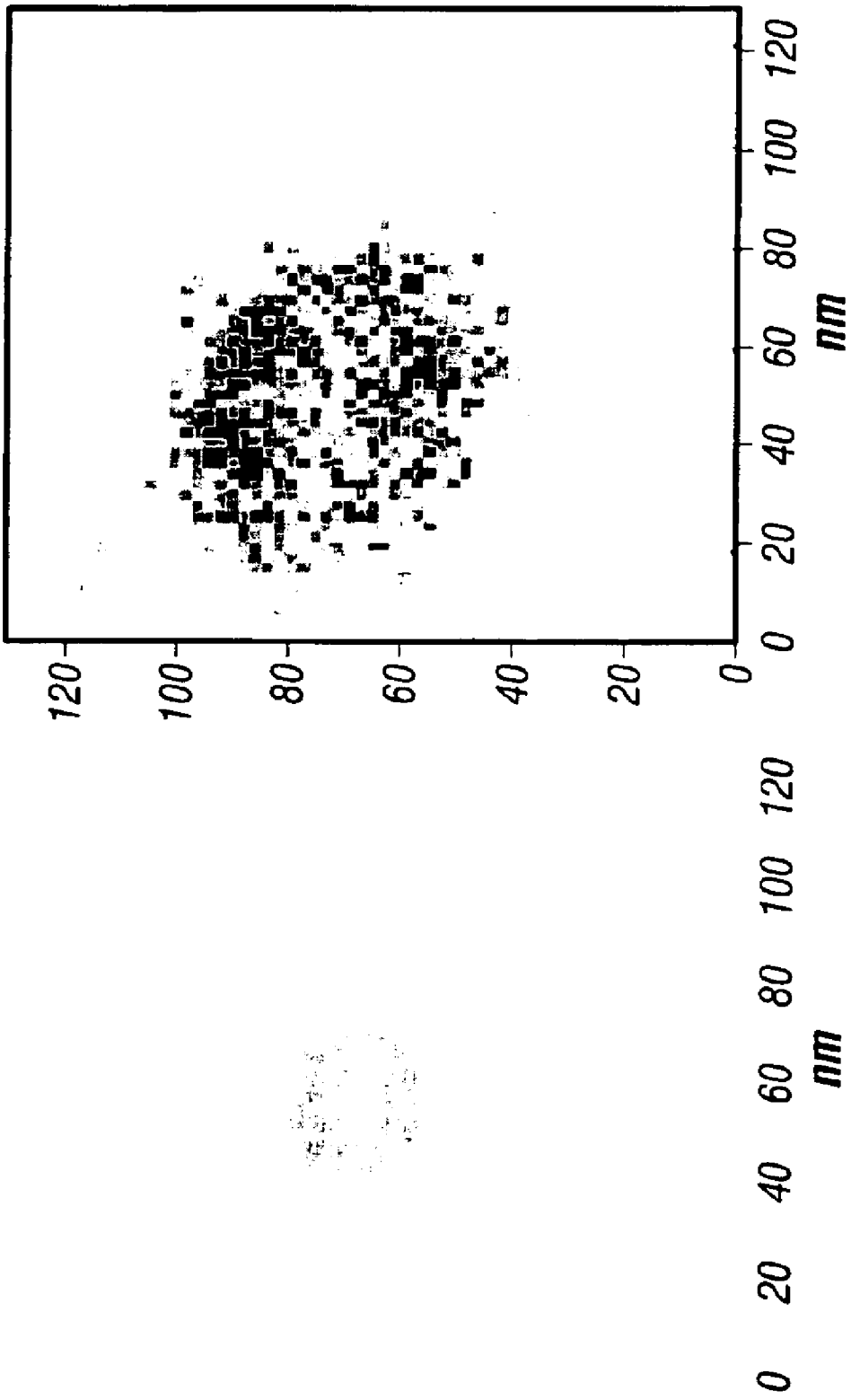

FIG. 20

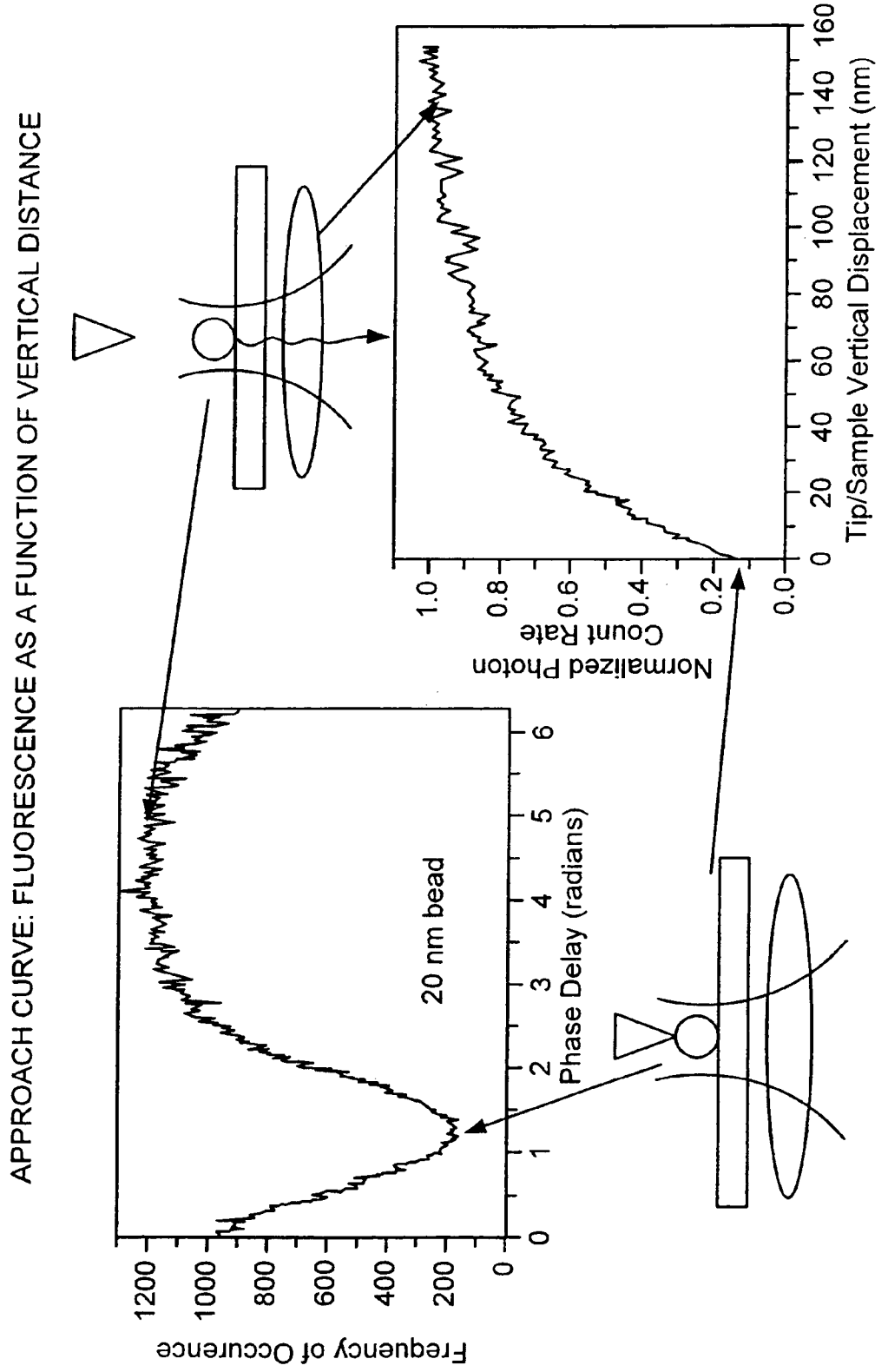
APPROACH CURVE: FLUORESCENCE AS A FUNCTION OF VERTICAL DISTANCE
Frequency of Occurence
0
200
400
600
800
1000
1200
20 nm bead
Phase Delay (radians)
0
1
2
3
4
5
6
Normalized Photon Count Rate
0.0
0.2
0.4
0.6
0.8
1.0
Tip/Sample Vertical Displacement (nm)
0
20
40
60
80
100
120
140
160

FIG. 20A

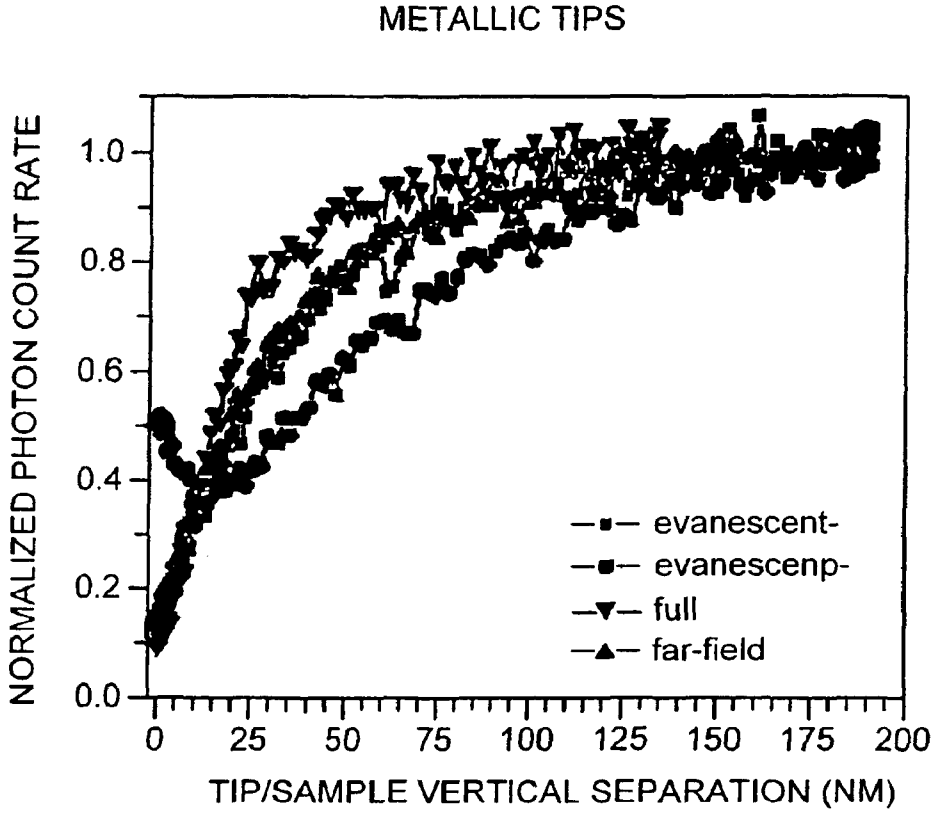

- PLATINUM-IRIDIUM COATED TIPS (COMMERCIAL)
- 85-90% SUPPRESSION OF FLUORESCENCE
- PARTIAL RECOVERY OF FLUORESCENCE FOR *P*-POLARIZATION

FIG. 20B

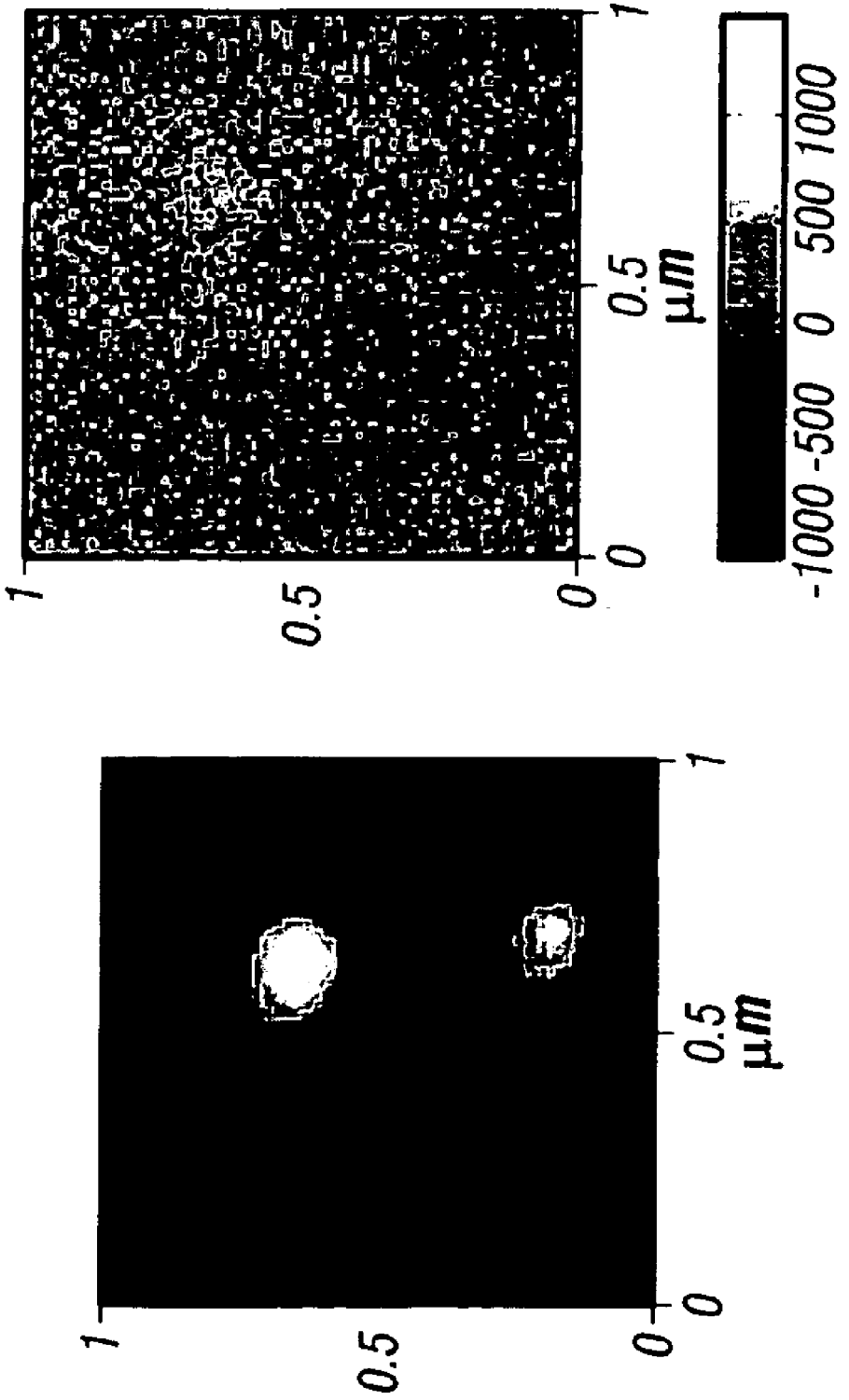

FIG. 21

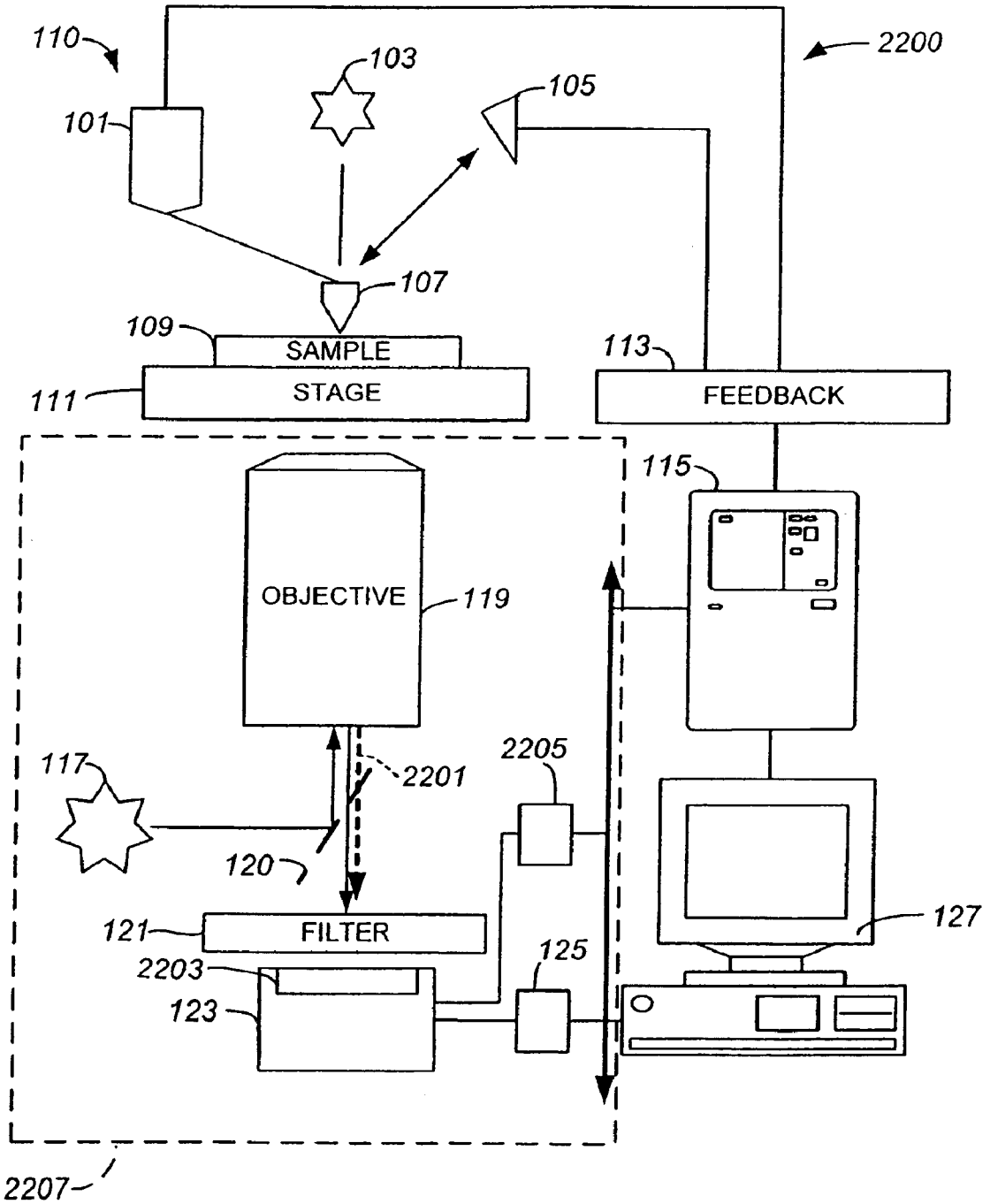
110
103
105
2200
101
107
109
SAMPLE
113
111
STAGE
FEEDBACK
115
OBJECTIVE
119
117
2201
2205
120
121
FILTER
127
125
2203
123
2207

FIG. 22

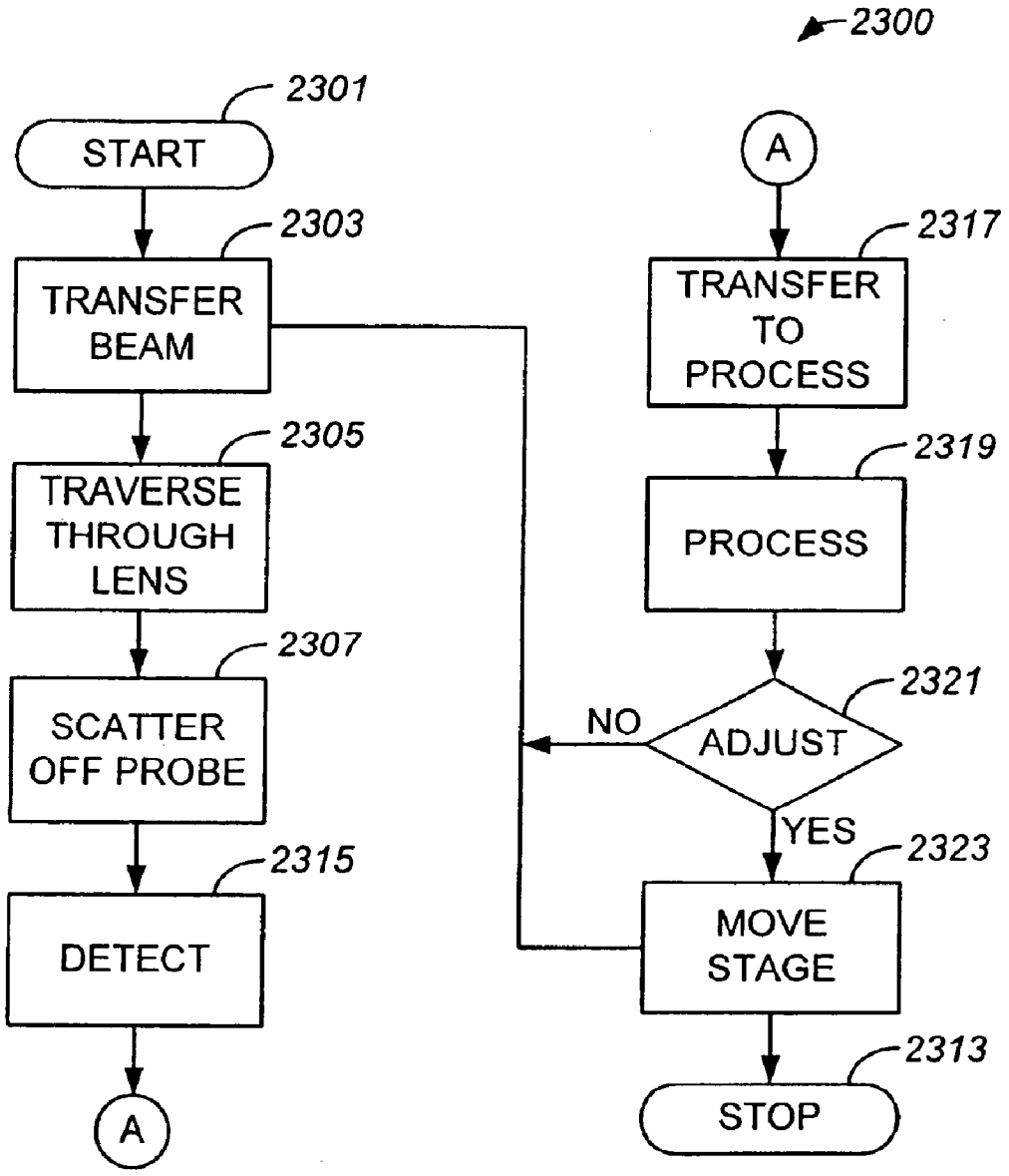
2300
2301
START
2303
TRANSFER BEAM
2305
TRAVERSE THROUGH LENS
2307
SCATTER OFF PROBE
2315
DETECT
A
A
2317
TRANSFER TO PROCESS
2319
PROCESS
2321
ADJUST
NO
YES
2323
MOVE STAGE
2313
STOP

FIG. 23

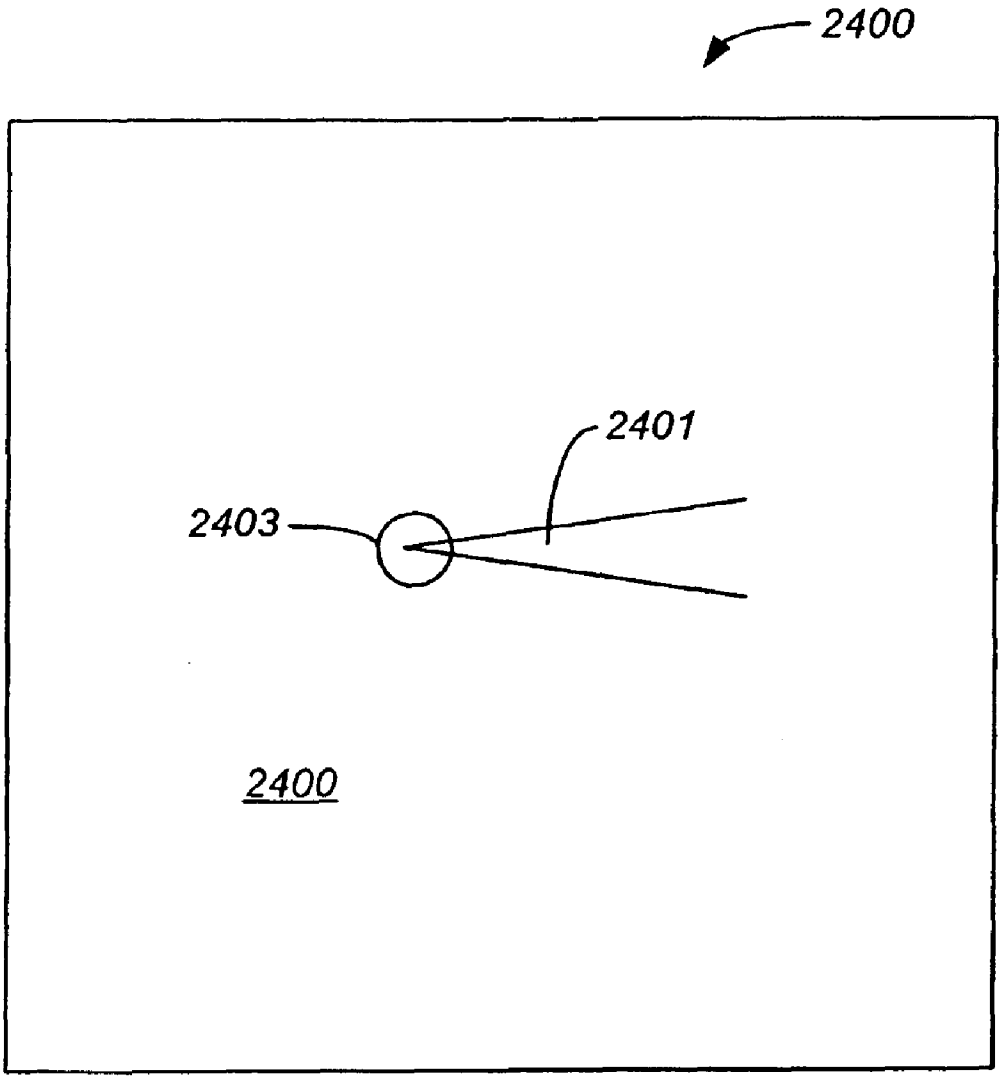

FIG. 24

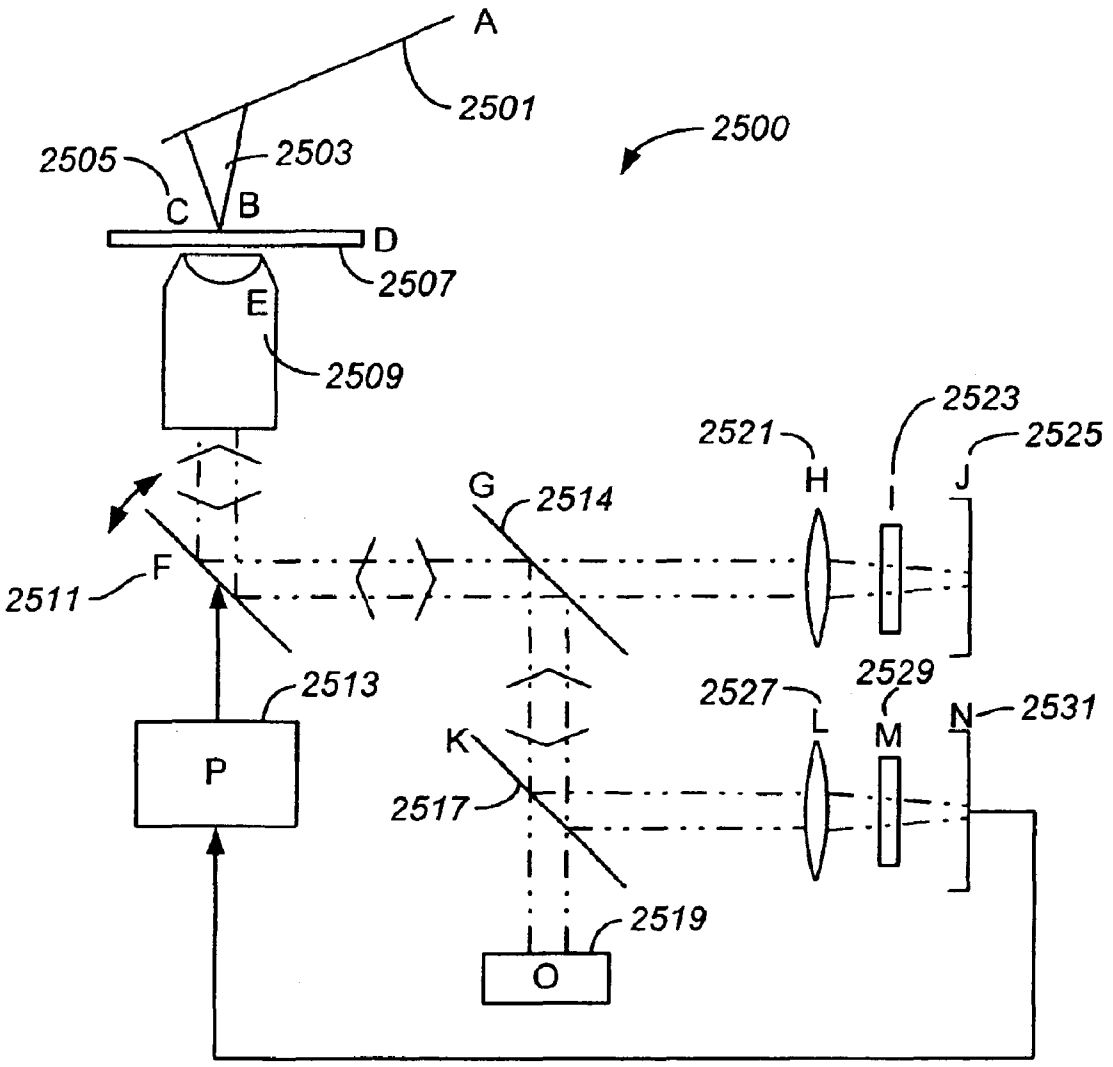
A
2501
2500
2505
2503
C
B
D
2507
E
2509
2523
2521
2525
H
J
G
2514
F
2511
2513
2529
2527
L
M
N
2531
K
P
2517
2519
O

FIG. 25

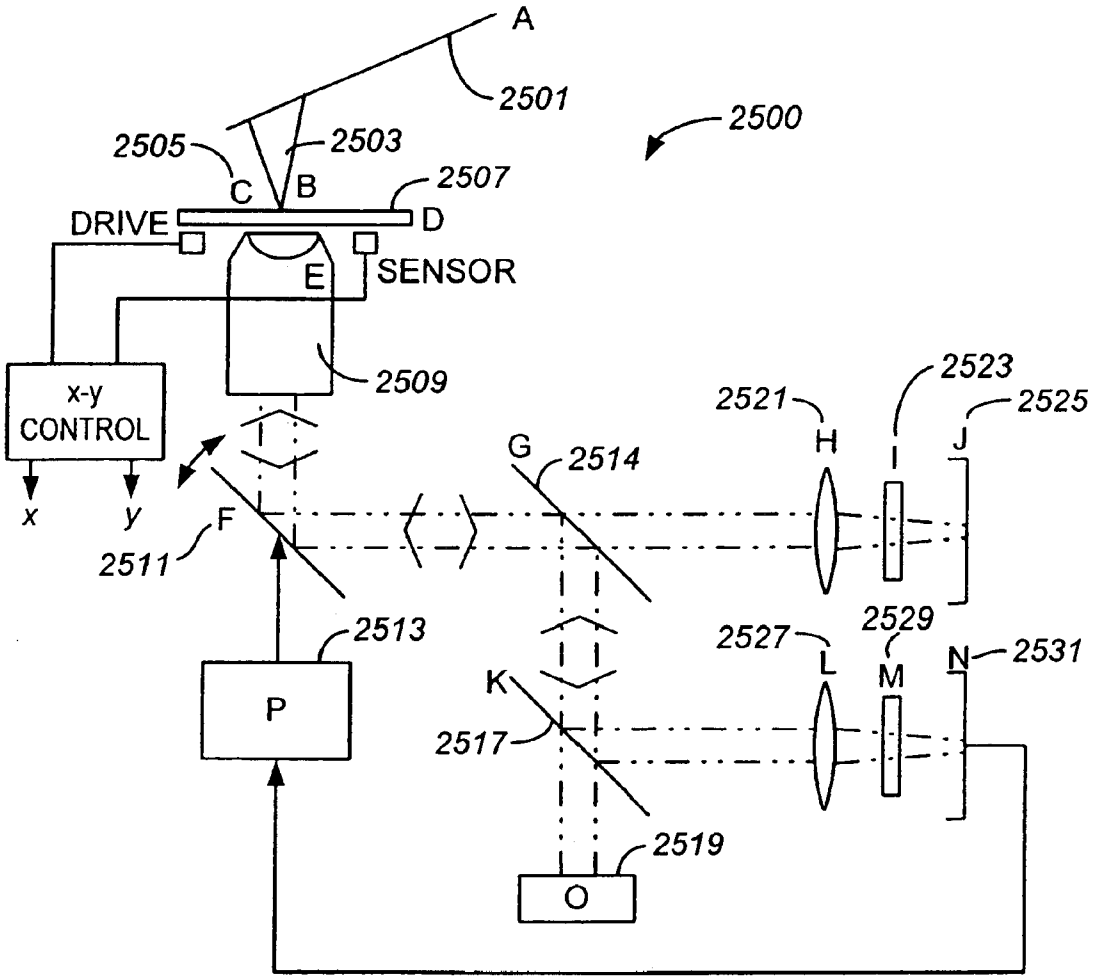
A
2501
2500
2505
2503
C
B
2507
DRIVE
D
E
SENSOR
2509
x-y
CONTROL
x
y
F
2511
2513
P
G
2514
2521
H
2523
I
2525
J
2527
L
2529
M
N
2531
K
2517
2519
O

FIG. 25A

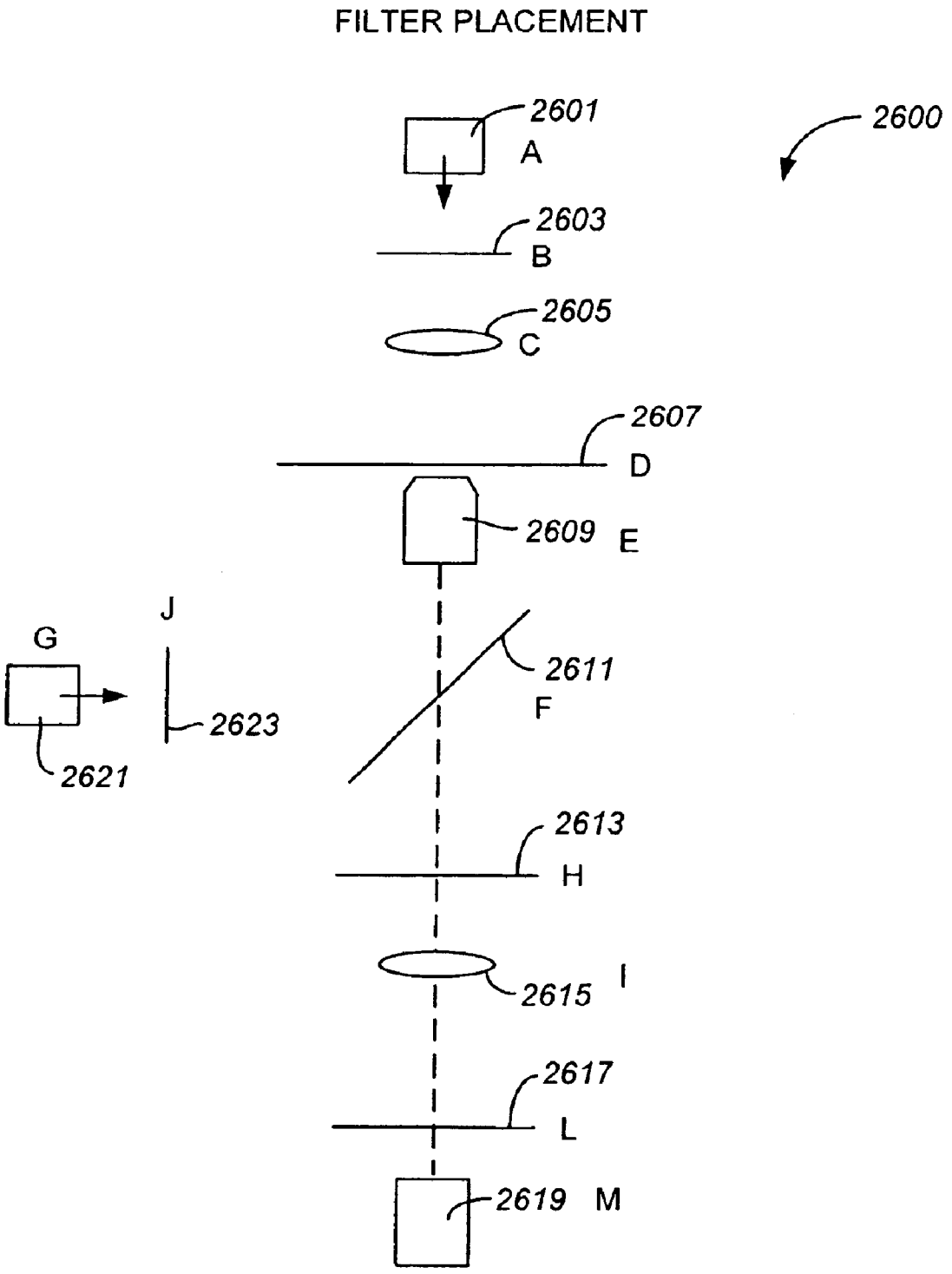
FILTER PLACEMENT
2600
2601
A
2603
B
2605
C
2607
D
2609
E
J
G
2611
F
2623
2621
2613
H
2615
I
2617
L
2619
M

FIG. 26

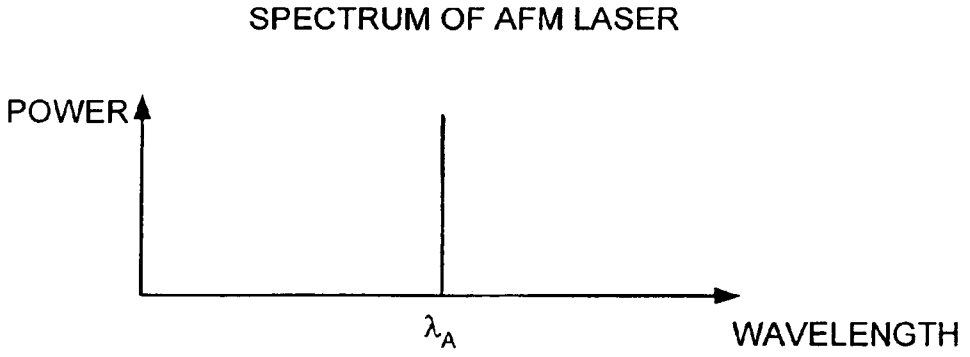

FIG. 27

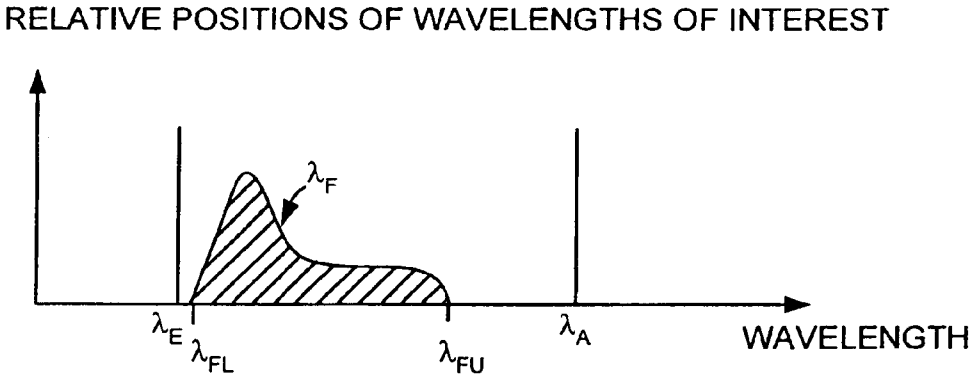

FIG. 28

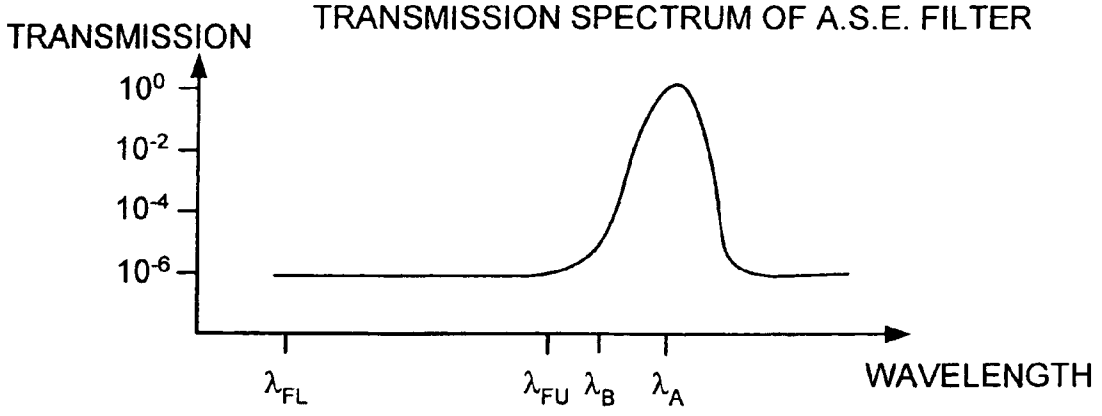

FIG. 29

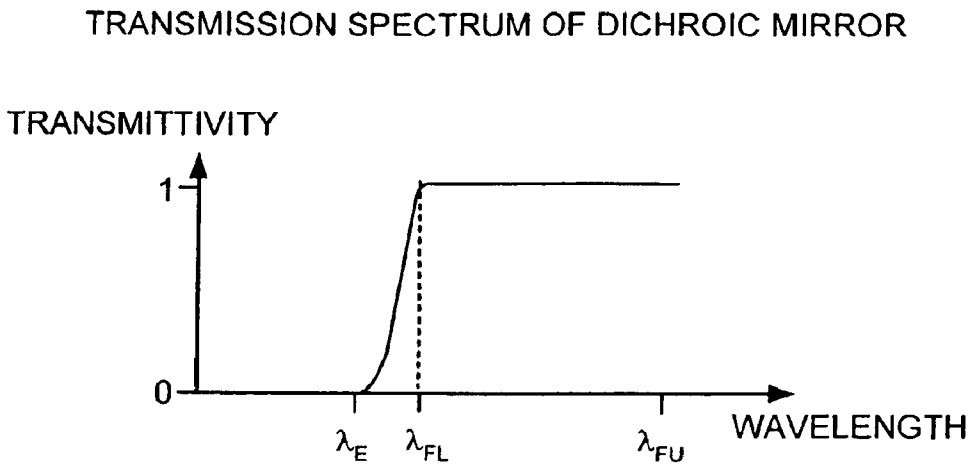
TRANSMISSION SPECTRUM OF DICHROIC MIRROR
TRANSMITTIVITY
1
0
λ_E
λ_{FL}
λ_{FU}
WAVELENGTH

FIG. 30

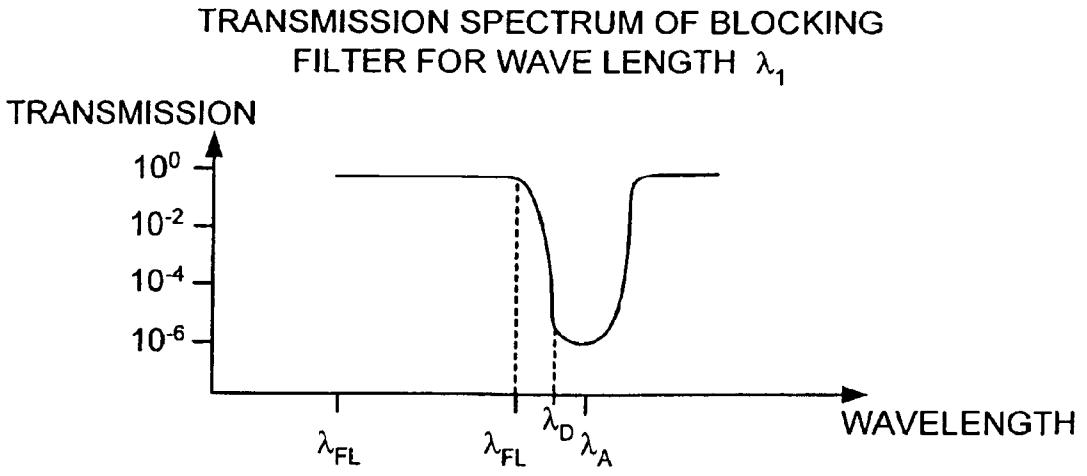
TRANSMISSION SPECTRUM OF BLOCKING FILTER FOR WAVE LENGTH λ_1
TRANSMISSION
10^0
10^{-2}
10^{-4}
10^{-6}
λ_{FL}
λ_{FL}
λ_D
λ_A
WAVELENGTH

FIG. 31

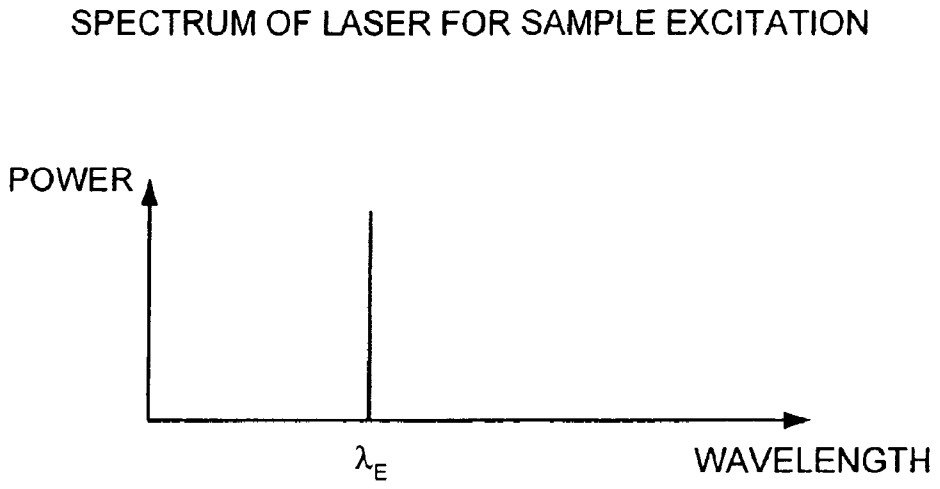
SPECTRUM OF LASER FOR SAMPLE EXCITATION
POWER
λ_E
WAVELENGTH

FIG. 32

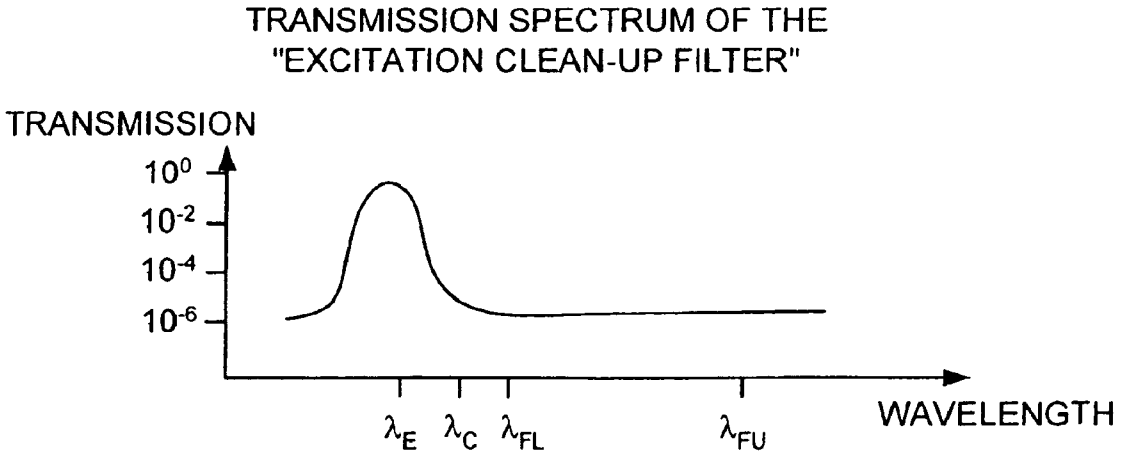
TRANSMISSION SPECTRUM OF THE
"EXCITATION CLEAN-UP FILTER"
TRANSMISSION
10^0
10^{-2}
10^{-4}
10^{-6}
λ_E
λ_C
λ_{FL}
λ_{FU}
WAVELENGTH

FIG. 33

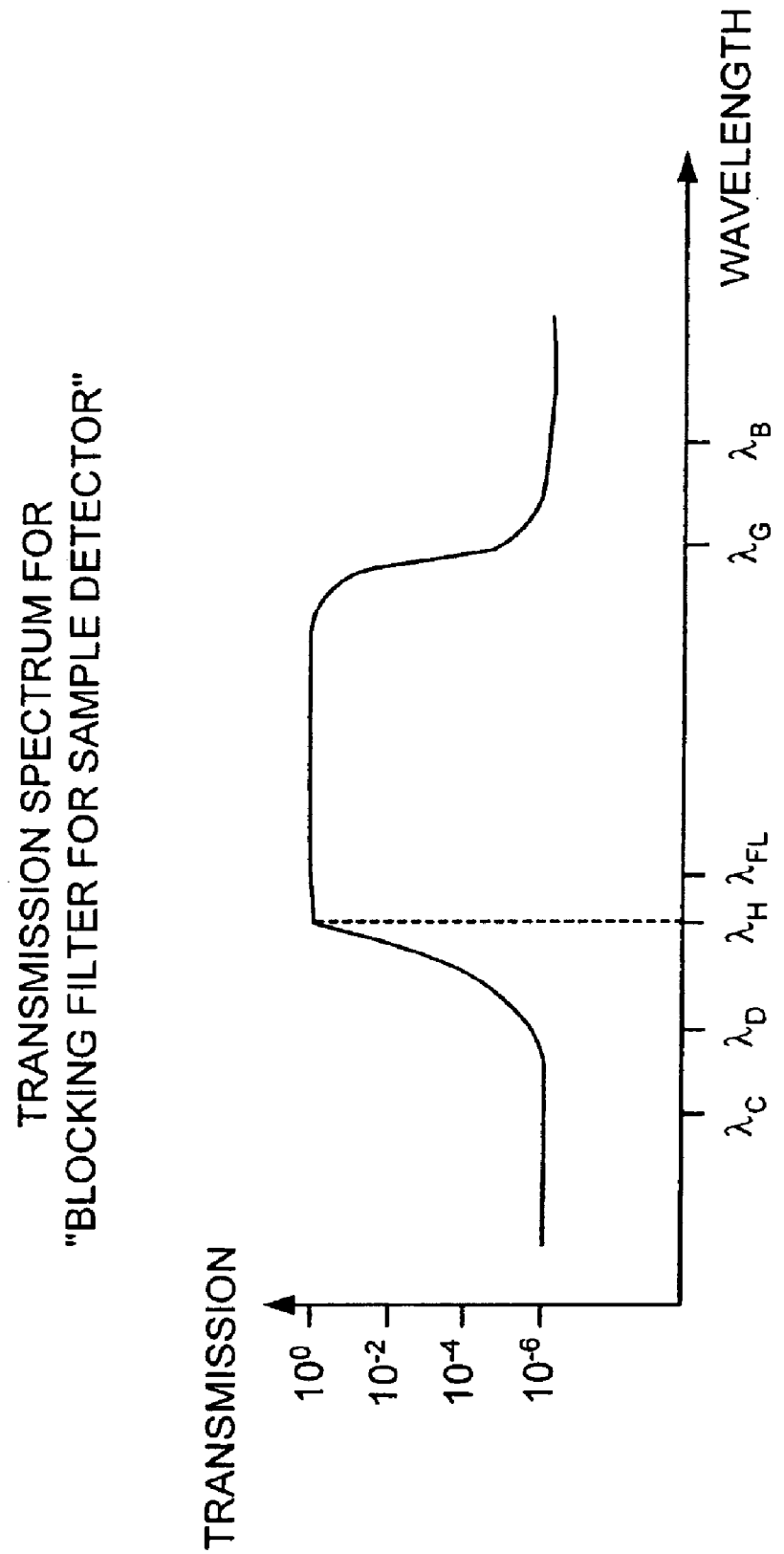
TRANSMISSION SPECTRUM FOR
"BLOCKING FILTER FOR SAMPLE DETECTOR"
TRANSMISSION
10^{0}
10^{-2}
10^{-4}
10^{-6}
λ_C λ_D λ_H λ_{FL} λ_G λ_B
WAVELENGTH

FIG. 34

METHOD AND SYSTEM FOR SCANNING APERTURELESS FLUORESCENCE MICROSCOPE

CROSS-REFERENCES TO RELATED APPLICATIONS

This application claims priority to U.S. Provisional No. 60/402,351 filed Aug. 9, 2002, which is incorporated by reference herein.

STATEMENT AS TO RIGHTS TO INVENTIONS MADE UNDER FEDERALLY SPONSORED RESEARCH OR DEVELOPMENT

The U.S. government has rights in the disclosed invention pursuant to National Science Foundation Grant No. DMR-0080065 to the California Institute of Technology.

REFERENCE TO A "SEQUENCE LISTING," A TABLE, OR A COMPUTER

PROGRAM LISTING APPENDIX SUBMITTED ON A COMPACT DISK

Not Applicable

BACKGROUND OF THE INVENTION

The present invention relates generally to high resolution microscopy techniques. More particularly, the invention provides methods and systems for improved high resolution scanning using apertureless near field scanning optical microscopes ("ANSOM") that image one or more fluorescent samples with single photon excitation, which we call fluorescence ANSOM ("FANSOM"). But it would be recognized that the invention has a much broader range of applicability. For example, the invention can be applied with other types of images such as Raman scattering, and other multiphoton processes. Additionally, the samples can range from a variety of different fields such as electronics, semiconductor, organic chemistry, life sciences, biotechnology, micro and nanomachining and micro and nanodevices, molecular and biological circuits, and others.

Over the years, significant development of different types of microscopy has occurred. As merely an example, visible light optical microscopy using far field optics including lenses and light evolved from a simple compound microscope that is capable of resolving sizes of about 200 nanometers and greater. Examples of samples that are capable of being viewed using far field optics include biological cells and tissues, and others, which are often, bulk in nature. The resolving ability of such far field optical microscopy is generally limited by the diffraction of light. The diffraction limit for optical resolution has been stretched somewhat for far field imaging of very specific samples to perhaps 150 nanometers using confocal microscopes and other, related, approaches. Accordingly, atomic force microscopes ("AFM") and scanning optical microscopes including near field scanning optical microscopes were developed. The AFM and near field scanning optical microscopy ("ANSOM") have been developed to overcome certain limitations of far field optics. The AFM and near field scanning microscopes have also found many applications in biology, chemistry, physics, and materials science.

Near field scanning optical microscopy allows one to take optical images with resolutions below the diffraction limit of light. More particularly, light propagating through a waveguide is forced through a subwavelength aperture, which is then scanned in close proximity to a sample. Such subwavelength aperture techniques create other limitations. Here, physical limitations relate to a skin depth of the metal used to coat the waveguide and various scanning artifacts, which yield resolutions of 30 to 50 nanometers, most typically 50 to 100 nanometers. Apertureless near field scanning microscopes have been proposed and demonstrated to overcome these limitations, among others. Conventional ANSOM often involves using an oscillating sharp probe, which is scanned over the sample. The probe perturbs an incident laser beam, by introducing phase shifts in an electric field or by a periodic occlusion of the sample. Detection techniques are generally used to discriminate light scattered by near field interactions from a far field contribution. Limitations also exist with such ANSOM techniques. Such limitations include contaminated images based upon certain artifacts of the sample topography, and may include others.

A pioneering approach for achieving high resolution spectroscopic information using a scanning microscope is described in U.S. Pat. No. 6,002,471, assigned to California Institute of Technology, Pasadena, Calif., and in the name of Stephen R. Quake ("Quake"). Quake generally provides a system and method for obtaining high resolution spectroscopic information. The system generally includes a support and first optical elements for directing an optical beam at a sample, which is on the support. An optical element for collecting light emitted from the sample to reduce a background noise is also included. Other elements include a spectral dissociating apparatus, a probe, and a probe detection apparatus coupled to the probe. As merely an example, the probe enhances the light level emitted from the sample in the vicinity of the probe. Because this occurs only when the probe is in the immediate vicinity of the sample, detection of this modulation results in very high spatial resolution and chemical detection sensitivity. Fluorescence ANSOM, called FANSOM, has also been demonstrated. Conventional FANSOM often uses a principle of a two photon excitation and electric field enhancement near a tip of the probe. See, T. J. Yang, Guillaume A. Lessard, and Stephen R. Quake, An apertureless near field microscope for fluorescence imaging, Applied Physics Letters, Volume 76, Number 3, Jan. 17, 2000 ("Yang, et al."). Yang, et al. reports certain results achieved using the FANSOM designed to image fluorescent samples with single photon excitation. FANSOM has demonstrated resolutions in the 10–20 nm range. Although FANSOM appears to be promising, certain practical limitations may still exist.

From the above, it is seen that improved high resolution scanning techniques are desired.

BRIEF SUMMARY OF THE INVENTION

According to the present invention, techniques for high resolution scanning are provided. More particularly, the invention provides methods and systems for improved high resolution scanning using apertureless near field scanning microscopes that image one or more fluorescent samples with single photon excitation, which we call fluorescence ANSOM. But it would be recognized that the invention has a much broader range of applicability. For example, the invention can be applied with other types of images such as Raman scattering, multi-photon imaging techniques, and others. Additionally, the samples can be from a variety of different fields such as electronics, semiconductor, organic chemistry, life sciences, biotechnology and others.

In a specific embodiment, the invention provides a method for measuring characteristics of nanoscopic objects

(e.g., 0.1 nanometers to>1,000 nanometers) using detection of photons emitted from the objects, e.g., Proteins or DNA tagged with fluorescent molecules. The method includes moving a tip of a probe coupled to a cantilever toward a feature of a sample to influence and/or modulate a rate of fluorescence from the feature of the sample. The method measures and/or compares the first intensity level of electromagnetic energy from a feature of a sample during a first predetermined portion of movement of the cantilever and records a change in the first intensity level to a second intensity level during a second predetermined portion of movement of the cantilever using a detector or the like.

In an alternative specific embodiment, the invention provides a system for measuring characteristics of nanoscopic objects using detection of photons emitted from the objects. The system has one or more computer memories, which include computer codes. A first code is directed to cause movement of a tip of a probe coupled to a cantilever member toward a feature of a sample to influence a detected rate of fluorescence from the feature of the sample. A second code is directed to apply illumination using a first intensity level of electromagnetic energy to the feature of the sample during a first predetermined portion of movement of the cantilever member to capture a signal from the feature at a detector from the sample. The one or more memories also include a third code directed to output a control signal to switch the first intensity level to a second intensity level during a second predetermined portion of movement of the cantilever member. Depending upon the embodiment, other computer codes can also be used to implement the functionality described herein as well as outside of this specification.

In a specific embodiment, the invention provides a capability to extend the lifetime of fluorescent molecules. Preferably, the method extends the life of such molecules by turning an excitation laser on only during specific periods of the data gathering cycle, which can improve and possibly maximizes a lifetime of the fluorescent molecule by delaying photobleaching or other similar features. Photobleaching is a photo-catalyzed chemical reaction that severely reduces or completely eliminates fluorescence emission. In addition this allows the signal to be maximized during imaging. Image scans often include series of fast probe movements, or line scans, along one axis and backcoupled with a slow continuous movement or discrete set of movements along the orthogonal axis of the sample surface plane-rastering pattern. Such rastering pattern continues until the desired portion of the sample plane is mapped which forms one image frame. The probe is typically made to oscillate rapidly (typically but not limited to 50–400 kilohertz oscillation frequency) up and down so that it lightly "taps" on the sample surface, following the sample topography while being rastered over the surface. When an image frame begins or ends, the probe controller sends a voltage signal that is monitored by the data acquisition computer. Similarly, the probe controller sends a voltage signal when each line scan begins in one direction and another signal at the beginning of the return movement. The image is typically constructed of either all-forward direction line scans or all return line scans in certain embodiments. If forward direction line scans are desired, then the controlling software detects the voltage pulse signaling the onset of forward scanning and in turn sends a voltage signal to an acousto-optic modulator that switches so that the excitation laser transmits into the FANSOM optical system. When the return line begins, a second voltage pulse is generated by the probe controller. As this line is not being used to create the image, the controlling computer stops sending the voltage pulse to the AOM. The AOM then switches so that the excitation laser light is no longer transmitted into the FANSOM optical system and the sample is not illuminated. This process repeats for each line with the sample being illuminated only during forward direction line scans. When the image frame is complete, the laser is commanded to switch off (in this case by stopping the voltage pulse to the AOM) until the initiation of the next image frame.

There can be other modifications, alternatives, and variations. As described above, the triggering of the laser switching can be actuated at the beginning of each line scan. Alternately it could begin based on topographical information from the probe (that is that the probe is over the sample of interest) or on a user defined area or coordinate set. The switching itself can be accomplished in a variety of ways other than the acousto-optical method described above. These other ways include using an electro-optic modulator or a shutter or chopper which is triggered or timed to correspond to the aforementioned inputs (beginning of line, coordinate, topographical information). The use of either an acousto-optic or electro-optic switching method allows for extremely fast (<10 nanosecond) switching times which enables other types of laser-triggering schemes. For instance, the laser may be triggered by the oscillating motion of the probe so that the laser would be on only for a portion of the probe oscillation cycle. This triggering scheme can be used to enhance the optical contrast as well as maximizing and/or improving the fluorescent molecule lifetimes. Other techniques may also use scanners, mirrors (e.g., MEMS), any combination of these and the like.

In an alternative specific embodiment, the invention provides a method for operating an apertureless microscope for viewing microscopic features of objects to molecular sensitivity. The method includes aligning the excitation laser beam to a tip coupled to a cantilever through a probe or a portion of the cantilever within a first assembly. There are several methods for accomplishing such alignment to nanometric accuracy. Gross alignment within a few microns can be achieved by viewing the back reflection of the excitation laser beam and the cantilever laser illumination of the cantilever and either moving the cantilever assembly until the two beams are properly aligned. Alternately or in combination a tip-tilt mirror can be used to move the focus of the excitation laser so that it is properly aligned with the cantilever tip. Additionally, the shadow cast by the cantilever when illuminated by the excitation laser can be visualized or imaged and used to align the tip with the excitation laser. Fine alignment to approximately 1 micron and possibly less can be achieved by illuminating the cantilever with monochromatic light or broadband light such that the optics can image the cantilever tip shadow relative to the excitation laser. Piezoelectric actuators can be used to either move the tip until properly aligned with the excitation laser or to steer the excitation laser until it is properly aligned with the tip. Fine and ultrafine alignment to as little as a few nanometers can be achieved by imaging the backscatter of the excitation laser either when scanning the laser over the cantilever tip or alternately when scanning the tip over a fixed focus excitation laser. The backscatter image gives a high resolution image via the microscope objective which allows the relative positions of the tip and the laser to be established.

Final alignment can then be achieved by either moving the cantilever assembly, moving the cantilever tip or the excitation laser focus point until the excitation laser and the cantilever tip are properly aligned. All of the previously mentioned alignment steps can be carried out separately or in combination. Also they can be carried out in combination

with a properly marked sample substrate which incorporates appropriate position reference points and or structures. Alignment can be maintained while imaging in several ways. It can be achieved by imaging the excitation laser back-reflection. The imaged diffraction pattern can then be used to monitor changes in relative position which can be used to correct any misalignments which develop if the laser tracks the cantilever tip while imaging a sample. Alternately, this imaged pattern information can be used to provide primary commands to move the excitation laser to track a moving cantilever tip. Finally, it can be used to correct other accumulated misalignments including but not limited to thermal drift and piezo and/or other mechanical strain relaxation, hysteresis, and piezo creep. These techniques can be used to achieve and maintain alignment whether the cantilever tip scans a stationary sample and excitation laser, both the cantilever tip and excitation laser scan a stationary sample, the excitation laser scans a stationary cantilever tip and sample, or a stationary cantilever tip and excitation laser scan a moving sample.

In yet an alternative embodiment, the invention provides an apertureless microscope system for viewing one or more features of samples to a resolution of molecular sensitivity. The system has a member for supporting the apertureless microscope system. A support structure is coupled to the member to support the member. A plurality of shock absorbing devices is coupling the support structure and the member. The plurality of shock absorbing devices is capable of substantially eliminating a possibility of mechanical noise from the floor structure. The system also has an enclosure structure coupled to the member and covering the apertureless microscope system. The enclosure houses the apertureless microscope within an opening confined within the enclosure structure. A sound absorbing member is coupled to the enclosure structure to substantially eliminate a possibility of acoustic noise from entering into the opening within the enclosure structure. An inner liner is also coupled within the opening of the enclosure structure to absorb one or more stray photons within the enclosure structure. The inner liner is generally capable of substantially preventing the stray photons from being released back into the enclosure structure.

Still further, the invention provides a method for operating a scanning system in a substantially noise free environment for viewing one or more features of samples to a resolution of molecular sensitivity. The method includes inserting a sample having a molecular feature on a stage of an apertureless microscope system, which has at least a scanning apparatus including a probe coupled to an optical imaging apparatus. The optical imaging apparatus is adapted to capture information having a feature size of less than five nanometers from a portion of the sample. The method also maintains at least the stage and the sample in an opening confined by an enclosure structure, which is coupled to a member for supporting a portion of the apertureless microscope system. The method maintains at least the stage and the sample free from mechanical vibration noise using a plurality of shock absorbing devices coupling the member. The plurality of shock absorbing devices is capable of substantially eliminating a possibility of mechanical vibration noise from an external source. The method further maintains at least the stage and the sample free from acoustic noise using a sound-absorbing member coupled to the enclosure structure to substantially eliminate a possibility of the acoustic noise from interacting with the captured information. A step of capturing one or more stray photons within the opening of the enclosure structure using an inner liner coupled within the enclosure structure to absorb the one or more stray photons within the enclosure structure is included. The inner liner is capable of substantially preventing the one or more stray photons from being released back into the opening of the enclosure structure.

In a specific embodiment, the invention provides a method for operating an apertureless microscope for observing one or more features to a molecular sensitivity on objects. The method includes moving a nanotube based tip of a probe coupled to a cantilever in the near vicinity of a feature of a sample or the sample relative to the nanotube based tip. In common with the previously described embodiments, the nanotube based tip will enhance contrast by interacting with the sample and the excitation light. The same mechanisms described earlier, that reduce the amount of fluoresced and/or detected fluoresced light and increased the amount of fluoresced light, will also occur with this tip in the proximity of the sample and/or illuminated by the excitation light. In addition other effects may serve to enhance contrast. In addition the resolution is increased due to the small diameter (typically 1–3 nm) of a single-walled nanotube. Preferably, the nanotube structure is single walled, although it may be multiwalled or has several single-walled tubes in a rope and/or bundle structure. Preferably, the term rope is a structure made of more than one strand of nanotube material, which may be twisted together or in any other aggregated geometric configurations according to certain embodiments. Additionally, enhanced contrast and resolution may occur through a quenching influence of the one or more photons. As merely an example, enhancement through quenching is shown in the first two (Y axis is photons/sec). The second figure shows, in one case, quenching and enhanced emission simultaneously (see also FIG. **19**). This offers an opportunity for further improvement in resolution.

In an alternative specific embodiment, the invention provides an apertureless microscope system for observing one or more features to a molecular sensitivity on objects. The system comprises a nanotube based tip on a probe coupled to a cantilever operable to move in a vicinity of a feature of a sample. Metallization of the nanotube tip increases the contrast enhancement by increasing the amount of interaction between the tip and the sample and/or the tip and the excitation laser depending on the specifics of the excitation beam and sample. This metallization also increases the nanotube attachment strength to the tip.

In an alternative specific embodiment, the invention provides an apertureless microscope system for observing one or more features to a molecular sensitivity on objects. The system comprises a metallized DNA molecule which is attached to the cantilever tip. The small diameter and high conductivity of this invention enables contrast enhancement and high-resolution FANSOM imaging in a method similar to the nanotube tips.

In a specific embodiment, the invention provides a method for dynamically viewing an increased field of view based upon a smaller fixed field of view to capture an image of features of samples to molecular sensitivity. The method includes illuminating through a fixed lens using a beam a feature of a sample. The beam is directed toward at least one tip of a probe, which is in a vicinity of the feature of the sample. The method scatters a portion of the beam off a portion of the tip of the probe. The method also detects the scattered portion of the beam. The method then processes the scattered portion of the beam to determine a pattern to identify a relationship between the tip and the beam for spatial alignment between the tip and the beam. A step of

adjusting a position of the beam used for illumination based upon at least the pattern to maintain a desired relationship between the tip and the beam is also included.

In an alternative specific embodiment, the invention provides a system for dynamically viewing an increased field of view based upon a smaller field of view to capture an image of features of samples to molecular sensitivity. The system has an electromagnetic energy source (in a specific embodiment this can be a laser), which is capable of emitting a beam. A fixed lens is coupled to the electromagnetic energy source. The fixed lens focuses the beam toward at least one tip of a probe, which is in a vicinity of a feature of a sample to scatter a portion of the beam off a portion of the tip of the probe. A detector is coupled to the fixed lens. The detector detects the scattered portion of the beam. A processor is coupled to the detector. The processor is adapted to process the scattered portion of the beam to determine a pattern to identify a relationship between the tip and the beam for a spatial alignment between the tip and the beam. An adjustment device is coupled to the processor. The adjustment device is adapted to adjust a position of the beam based upon at least the pattern to maintain a desired relationship between the tip and the beam.

In an alternative specific embodiment, the invention provides a scanning microscope for viewing one or more features of molecular scale and below. The system has a support stage for holding an object to be observed. A tip is coupled to a probe, which is configured within a vicinity of a feature of the object. An illumination source is directed to apply electromagnetic radiation from the illumination source to the tip of the probe. This illumination is used to determine the position of the cantilever tip over the sample. The system has a filter coupled to the object to substantially eliminate amplified spontaneous emission (ASE) from a power spectrum of the electromagnetic radiation. Preferably, such filter has a narrow transmission width to block ASE at wavelengths both shorter and longer than a central laser wavelength according to a specific embodiment. Alternately, such filter can be a long pass filter to block ASE with wavelengths shorter than the central laser wavelength. In an alternative embodiment, such filter can be a short pass to block ASE with wavelengths longer than the laser wavelengths longer than the central laser wavelength. The system also has an object illumination source coupled to the support to illuminate at least the feature of the object. Additional filters allow the blocking of the central cantilever illumination and also of the excitation illumination. Finally a filter is used to remove ambient illumination outside the sample fluoresced wavelength(s). These filters serve to block the several sources of photons not emitted by the sample but are highly transmissive in the wavelengths emitted by the sample. In combination, the present filters allow signals at wavelengths longer than the central laser wavelength or shorter than the central laser wavelength to be observed according to a specific embodiment. A detector is coupled to the object to capture signals from at least the feature of the object. The signals are derived from a detection band from the object illumination source.

Many benefits are achieved by way of the present invention over conventional techniques. For example, the present technique provides an easy to use process that relies upon conventional technology. The invention can also provide improved resolution within a predetermined range of spatial feature sizes. Preferably, the invention can be applied to capture images from biological molecules and the like. Depending upon the embodiment, one or more of these benefits may be achieved. These and other benefits will be described in more throughout the present specification and more particularly below.

Various additional objects, features and advantages of the present invention can be more fully appreciated with reference to the detailed description and accompanying drawings that follow.

BRIEF DESCRIPTION OF THE DRAWINGS

FIG. **1** is a simplified diagram of a scanning system **100** according to an embodiment of the present invention;

FIG. **2** is a simplified diagram of a computer system that is used to oversee the system of FIG. **1** according to an embodiment of the present invention;

FIG. **2A** is a more detailed diagram of hardware elements in the computer system of FIG. **2** according to an embodiment of the present invention;

FIG. **3** is a simplified diagram of an improved illumination system for a scanning system according to an embodiment of the present invention;

FIG. **3A** is a more detailed diagram of the improved illumination system according to an embodiment of the present invention;

FIGS. **4** through **5** are simplified diagrams of scanning methods according to embodiments of the present invention;

FIGS. **6** through **8** are simplified diagrams illustrating optical alignment methods for nanoscopic scanning according to embodiments of the present invention;

FIGS. **9** through **12** are simplified diagrams of packaging systems and methods for scanning systems according to embodiments of the present invention;

FIGS. **13** through **16** are simplified diagrams of various tip devices according to embodiments of the present invention;

FIGS. **14A** and **14B** are nanotube based probes according to embodiments of the present invention;

FIGS. **14C** through **14E** are nanotube based probes according to alternative embodiments of the present invention;

FIGS. **17** through **21** are experimental results using selected tip designs according to embodiments of the present invention;

FIG. **22** is a simplified diagram of an alignment subsystem for an optical system according to an embodiment of the present invention;

FIGS. **23** through **25** are simplified diagrams of tip detection alignment methods and systems for the scanning system according to embodiments of the present invention;

FIG. **25A** is a simplified diagram of a FANSOM system using a closed loop feedback loop according to an embodiment of the present invention; and

FIGS. **26** through **34** are simplified diagrams of methods and systems for selectively illuminating one or more samples according to embodiments of the present invention.

DETAILED DESCRIPTION OF THE INVENTION

According to the present invention, techniques for high resolution scanning are provided. More particularly, the invention provides methods and systems for improved high resolution scanning using apertureless near field scanning microscopes that image one or more fluorescent samples with single photon excitation, which we call fluorescence ANSOM microscope. But it would be recognized that the

invention has a much broader range of applicability. For example, the invention can be applied with other types of images such as Raman scattering, multiphoton imaging techniques, and others. Additionally, the samples can be from a variety of different fields such as electronics, semiconductor, organic chemistry, life sciences, biotechnology, and others.

FIG. **1** is a simplified diagram of a scanning system **100** according to an embodiment of the present invention. This diagram is merely an example, which should not unduly limit the scope of the claims herein. One of ordinary skill in the art would recognize many other modifications, alternatives, and variations. As shown, the present microscope system **100** includes a mobile stage **111**, which has x-y-z movement capability. The stage can be moved with a tolerance of less than 40 microns for sample positioning and when used for alignment can be moved with a tolerance of<1 nm. A sample **109** is placed on the stage. Depending upon the application, the sample can include a biological sample, a quantum dots, fluorescently tagged molecules, and Fluorescently tagged nano- or micro-structures, arrays or components. Preferably, the sample can also be in liquids, air, inert gas environments, or in vacuum and at specific temperatures (cryogenic, room temperature, warm to extremely high temperatures), depending upon the application.

The system also includes a tapping mode atomic force microscope ("AFM") **110**. In a specific embodiment, the AFM **110** has various elements such as probe **107**, a cantilever to support the probe, which is coupled to a piezo-electric stack. Such piezo-stack provides for dithering and z-motion of the cantilever. The AFM also includes a driving signal, which is coupled to control electronics **113** for signal detection and correction. Preferably, probe **107** has a pyramidal shape and the tip of the pyramid is coated with silver particles. Alternatively, other particles or coatings can also be used. For example, such coatings include, among others, semiconductor (e.g., silicon, silicon nitride, diamond, etc.), conductors (e.g., platinum, gold, silver alloys, aluminum, platinum-irridium, cobalt and an other metals as well as materials doped to be conductive), as well as combination of these, an the like. The AFM also includes a laser source **103**, which is directed to the cantilever or probe. The laser source is used as a position detector, which provides photons that scatter off of the cantilever and/or probe. Such scattered photons are detected by way of photodetector **105**, which is coupled to control electronics **113**. The AFM is coupled to an inverted optical microscope, as shown.

Preferably, the inverted optical microscope **119** is underlying the AFM, as shown. A laser beam **117** (which in a specific embodiment is from a green HeNe **103** source) is focused on the AFM tip. The laser beam is directed from the source **117** and is adjusted by way of dichroic mirror **120** through the objective **119**, which focuses the beam onto the AFM tip. As the sample is scanned in the x-y plane (which is also in the plane of the paper), fluorescent photons emit from the sample. Such photons pass through the objective through a bandpass filter **121** and are detected by an avalanche photodiode **123**. A gated photon counter **125**, which is coupled to the photodiode, processes the detected photons. The gated photon counter is triggered by a measured height of an AFM cantilever. A signal acquisition and processing apparatus **115** (which includes a microprocessor device and has been used as a "controller" and/or "main controller" herein without unduly limiting the scope of the term processing apparatus), which may be coupled to the counter through a common bus, oversees and performs operation and processing of information. The system also has a display **127**, which can be a computer, coupled to the signal acquisition and processing apparatus. The signal acquisition and processing apparatus is also coupled to the control electronics of the AFM as shown.

In a specific embodiment, the AFM operates using a sinusoidal diving signal coupled to the AFM probe via the piezo-electric stack. The AFM probe is scanned over the surface of the sample, receiving the perturbations caused by the surface of the sample and transmitting the perturbed signal to the position detector. The position detector transmits a position signal to electronic systems for correcting and digitizing the signal. The correction occurs by comparing the position signal to an external height reference signal. The corrected AFM signal and the optical signal are coupled to the digitizing system for the processing of the AFM image of the surface topography and the optical image. Of course, there can be other modifications, alternatives, and variations. Further details of the present system can be found in the Quake patent, which has been previously described. Other details of the present system and methods are provided throughout the specification and more particularly below.

FIG. **2** is a simplified diagram of a computer system **210** that is used to oversee the system of FIG. **1** according to an embodiment of the present invention. This diagram is merely an example, which should not unduly limit the scope of the claims herein. One of ordinary skill in the art would recognize many other modifications, alternatives, and variations. As shown, the computer system **210** includes display device **220**, display screen **230**, cabinet **240**, keyboard **250**, scanner and mouse **270**. Mouse **270** and keyboard **250** are representative "user input devices." Mouse **270** includes buttons **280** for selection of buttons on a graphical user interface device. Other examples of user input devices are a touch screen, light pen, track ball, data glove, microphone, and so forth.

The system is merely representative of but one type of system for embodying the present invention. It will be readily apparent to one of ordinary skill in the art that many system types and configurations are suitable for use in conjunction with the present invention. In a preferred embodiment, computer system **210** includes a Pentium™ class based computer, running Windows™ NT operating system by Microsoft Corporation. However, the system is easily adapted to other operating systems and architectures by those of ordinary skill in the art without departing from the scope of the present invention. As noted, mouse **270** can have one or more buttons such as buttons **280**. Cabinet **240** houses familiar computer components such as disk drives, a processor, storage device, etc. Storage devices include, but are not limited to, disk drives, magnetic tape, solid-state memory, bubble memory, etc. Cabinet **240** can include additional hardware such as input/output (I/O) interface cards for connecting computer system **210** to external devices external storage, other computers or additional peripherals, which are further described below.

FIG. **2A** is a more detailed diagram of hardware elements in the computer system of FIG. **2** according to an embodiment of the present invention. This diagram is merely an example, which should not unduly limit the scope of the claims herein. One of ordinary skill in the art would recognize many other modifications, alternatives, and variations. As shown, basic subsystems are included in computer system **210**. In specific embodiments, the subsystems are interconnected via a system bus **275**. Additional subsystems such as a printer **274**, keyboard **278**, fixed disk **279**, monitor **276**, which is coupled to display adapter **282**, and others are shown. Peripherals and input/output (I/O) devices, which

couple to I/O controller **271**, can be connected to the computer system by any number of means known in the art, such as serial port **277**. For example, serial port **277** can be used to connect the computer system to a modem **281**, which in turn connects to a wide area network such as the Internet, a mouse input device, or a scanner. The interconnection via system bus allows central processor **273** to communicate with each subsystem and to control the execution of instructions from system memory **272** or the fixed disk **279**, as well as the exchange of information between subsystems. Other arrangements of subsystems and interconnections are readily achievable by those of ordinary skill in the art. System memory, and the fixed disk are examples of tangible media for storage of computer programs, other types of tangible media include floppy disks, removable hard disks, optical storage media such as CD-ROMS and bar codes, and semiconductor memories such as flash memory, read-only-memories (ROM), and battery backed memory.

Although the above has been illustrated in terms of specific hardware features, it would be recognized that many variations, alternatives, and modifications can exist. For example, any of the hardware features can be further combined, or even separated. The features can also be implemented, in part, through software or a combination of hardware and software. The hardware and software can be further integrated or less integrated depending upon the application. Further details of the functionality of the present invention can be outlined below according to the Figures.

FIG. **3** is a simplified diagram of an improved illumination system **300** for a scanning system according to an embodiment of the present invention. This diagram is merely an example, which should not unduly limit the scope of the claims herein. One of ordinary skill in the art would recognize many other modifications, alternatives, and variations. Like reference numerals are used in FIG. **3** as certain other figures herein, but ware not intended to be limiting. As shown, the present microscope system **100** includes mobile stage **111**, which has x-y-z movement capability. The system also includes atomic force microscope ("AFM") **110**, which is preferably a tapping mode atomic force microscope, but may also be others. In a specific embodiment, the AFM **110** has various elements such as probe **107**, a cantilever to support the probe, which is coupled to a piezo-electric stack **104**. Such piezo-stack provides for dithering and z-motion of the cantilever. The AFM also includes a driving signal, which is coupled to control electronics **113** for signal detection and correction. The AFM also includes a laser source **103**, which is directed to the cantilever or probe. The laser source is used as a position detector, which provides photons that scatter off of the cantilever and/or probe. Such scattered photons are detected by way of photodetector **105**, which is coupled to control electronics **113**. The AFM is coupled to an inverted optical microscope, as shown.

The inverted optical microscope **119** is underlying the AFM, as shown. The laser beam **117** from the green HeNe **103** source is focused on the AFM tip. The laser beam is directed from the source **117** and is adjusted by way of dichroic mirror **120** through the objective **119**, which focuses the beam onto the AFM tip. The system also has the bandpass filter **121** and avalanche photodiode **123**. The gated photon counter **125** processes the detected photons. The gated photon counter is triggered by a measured height of the AFM cantilever. Signal acquisition and processing apparatus **115**, which may be coupled to the counter through a common bus, oversees and performs operation and processing of information. Other features are also included.

Preferably, the system includes illumination system **300** that selectively adjusts an illumination level. Here, a shutter and/or a modulator material can selectively adjust the beam **117** from a first state to a second state. The first state can correspond to an on-state and the second state can correspond to an off-state. The on-state allows the beam to traverse through the modulator material. The off-state blocks the beam. As merely an example, a blocking material or filter can be used between the beam **117** and mirror **120**. Such blocking material can include, among others, a modulator material. The modulator material can be coupled to the processing apparatus through the bus. Preferably, the modulator material is an acousto-optic ("AO") modulator, which will be described in more detail below. Of course, there can be other modifications, alternatives, and variations. For example, the modulator material can be replaced with a mechanical shutter, an electro-optic modulator, any combination of these, and the like.

FIG. **3A** is a more detailed diagram of the improved illumination system according to an embodiment of the present invention. This diagram is merely an example, which should not unduly limit the scope of the claims herein. One of ordinary skill in the art would recognize many other modifications, alternatives, and variations. As shown, the system includes common elements from other figures herein without unduly limiting the scope of the invention. The illumination system **300** includes laser beam **117** coupled to the objective through dichroic mirror **120**. An AO modulator **305** is coupled between the beam and mirror in a specific embodiment. The modulator is made of suitable material to diffract the beam upon command such that it is no longer coupled into the fiber optic cable, thereby blocking transmission to the sample. An example of such a material is lead molybate. The material also has to have a certain speed characteristic. That is, the modulator material should be able to change states within 0.1 milliseconds seconds and less. Preferably, the modulator material changes where the light is bent in a different direction which no longer corresponds to the fiber, i.e., the modulator is in fact blocked. An example of such a material is from ISOMET Corporation: According to a specific embodiment, when aligned at the Bragg angle which correctly corresponds to the laser wavelength and RF frequency being applied, the modulator material diffracts a portion of the beam passing through it (zeroth order) into an adjacent location (first order). The first order beam is normally used for most applications. The intensity of the first order light is controlled by the amplitude of the RF signal. Either digital (on-off) or analog (video) modulation of the first order spot can be produced, depending on the type of driver selected. Of course, the type of material used depends upon the application.

The modulator is coupled to input/output device **315** through line **313**. The input/output device may also include driving circuits, depending upon the application. Alternatively, the modulator has integrated driving circuits. Laser beam **117** is coupled to input/output device **309** and is also coupled to bus **303**, which connects to the processing apparatus. Similarly, input/output device **315** couples to bus **303**, which connects to the processing apparatus. A simple switching method can be provided using the present system.

In a specific embodiment, the modulator includes at least two states corresponding to an on-state and an off-state. In an on-state, the modulator allows beam **319** to traverse through the modulator material and reflect off of mirror **120** to enter **317** into the objective. As merely an example, the modulator material is in a transparent state, which allows the beam to traverse therethrough. Alternatively, the modulator material can be in the off-state, where the terms "off" and "on" are merely be used for descriptive purposes without

limiting the scope of the claims herein. In the off-state, the modulator/optical assembly material blocks beam **319** and does not allow beam **317** to traverse therethrough (not shown). In a specific embodiment, the processing apparatus oversees the operation of the modulator material in reference to the operation of the present methods described herein as well as outside of this specification. Of course, there can be other modifications, alternatives, and variations. For example, the modulator material can be replaced with a mechanical shutter, an electro-optic modulator, any combination of these, and the like. The modulator is preferred in most embodiments (rather than adjusting the laser beam that should often be stabilized before use in the present method and system). Other details of the present system and methods are provided throughout the specification and more particularly below.

An illumination method used for operating the scanning apparatus according to an embodiment of the present invention is provided as follows.

1. Begin process for scanning using FANSOM a feature of an object;

2. Initiate line scan process for a line along a first direction (which is different from a second direction to be described below);

3. Transfer control signal from probe controller to main controller at beginning the scan along the first direction;

4. Determine if an image is to be constructed using the main controller;

5. If the image is to be constructed, send signal from main controller to modulator to allow beam to traverse through the modulator;

6. Illuminate the feature of the object while capturing information for the image of the feature;

7. Complete scanning of the object in the first direction while constructing the image of the feature;

8. Transfer control signal from probe to controller with beginning a scan along a second direction, which is different from the first direction;

9. Determine if an image is to be constructed;

10. If the image is to be constructed along the first direction, send signal from controller to modulator to allow beam to traverse through the modulator;

11. Alternatively, send signal (or no signal) form the controller to the modulator to prevent beam from traversing through the modulator;

12. Illuminate the feature of the object or maintain the object without illumination depending upon steps 10 and 11;

13. Complete scanning in the second direction; and

14. Perform other steps as desired.

As shown, the present method provides ways to turn on and turn off illumination of a beam used for a feature of an object. In a specific embodiment, the process repeats for each line with the feature of the object being illuminated only during left to right scans as an image is built up. Once the image is complete, the laser is commanded to switch off (in this case by stopping the signal to the modulator) until initiation of the next image scan. Further details of this method are described according to the Figures below.

FIGS. **4** through **5** are simplified diagrams of scanning methods **400**, **500** according to embodiments of the present invention These diagrams are merely examples, which should not unduly limit the scope of the claims herein. One of ordinary skill in the art would recognize many other modifications, alternatives, and variations. As shown, the method begins at start, step **401**. Here, the image scan includes a series of scans from right to left and back again, although these directions could be changed in the specific embodiment. When a line scan begins (step **403**) a probe controller, which is coupled to the probe, sends (step **405**) a voltage signal that is monitored (step **407**) by a controlling computer and/or main controller. The voltage signal is often a pulse, which is sent from the probe controller at a beginning of each scan line from left to right and again on a return right to left line. If an image is to be constructed (step **409**) of scans from left to right, the method detects the voltage pulse signaling the onset of scanning using computer software. The method sends a voltage signal to initiate illumination, step **411**. Alternatively, if the image is not being constructed for the scan, the method returns via a branch back to step **405**. The method also stops at step **413**. Depending upon the embodiment, there can be many modifications, variations, and alternatives.

Referring to FIG. **5**, the method includes using a modulator to turn-on and turn-off illumination of a feature of an object. As shown, the method begins at start, step **501**. Here, the image scan includes a series of scans from right to left and back again, although these directions could be changed in the specific embodiment. When a line scan begins a probe controller, which is coupled to the probe, sends a voltage signal that is monitored by a controlling computer and/or main controller. The voltage signal is often a pulse, which is sent from the probe controller at a beginning of each scan line from left to right and again on a return right to left line. If an image is to be constructed of scans from left to right, the method detects (step **503**) the voltage pulse signaling the onset of scanning using computer software. The method sends a voltage signal to initiate illumination. Alternatively, if the image is not being constructed for the scan, the method does not illuminate the feature of the object.

Preferably, the method includes transferring a control signal from the controller to a controller of an acousto-optic modulator. The control signal is used to drive (step **507**) the modulator such that it switches the beam into the FANSOM optical system. The method continues to determine if the scan is finished, step **509**. Depending upon the embodiment, the method can also monitor (step **515**) the scan and whether illumination is desired during the scan. Alternatively, the method completes the scan and returns to step **503** for another scan, which may or may not drive the modulator to allow the beam into the FANSOM system. Preferably, when the return line scan begins, a second voltage pulse is generated by the probe controller. As the return line is not being used to create the image according to the preferred embodiment, the controller sends a voltage pulse (or no voltage pulse) to the modulator such that light no longer transmits into the FANSOM optical system and the feature of the object is not illuminated.

Depending upon the embodiment, the method repeats for each line with the feature of the object being illuminated only during left to right scans as the image is built up. Once the image is complete, the laser is commanded to switch off (also step **507**) (in this case by stopping the voltage pulse to the modulator) until initiation of the next image scan. A triggering of each line scan can be actuated at the beginning of each line. Alternately it could begin based on topographical information from the probe (that is that the probe is over the sample of interest). Alternately the switching could be based on a user defined area or coordinate set. The switching itself can be accomplished in a variety of ways. These include using a shutter or chopper which is triggered or timed to correspond to the aforementioned inputs (beginning of line, coordinate, topographical information).

Depending upon the embodiment, there can be many benefits over conventional techniques. In a specific embodiment, the invention provides a capability to extend the lifetime of fluorescent molecules by turning the excitation laser on only during data gathering. Turning the laser off when the fluorescent molecules are not being imaged often ensures maximizes the life of the fluorescent molecule by preventing photobleaching. In addition this allows the signal to be maximized during imaging. Depending upon the embodiment, one or more of these benefits may be achieved. These and other benefits will be described in more throughout the present specification and more particularly below.

Although the above has been illustrated in terms of specific software and/or hardware features, it would be recognized that many variations, alternatives, and modifications can exist. For example, any of the hardware features can be further combined, or even separated. The features can also be implemented, in part, through software or a combination of hardware and software. The hardware and software can be further integrated or less integrated depending upon the application. Of course, one of ordinary skill in the art would recognize many other modifications, variations, and alternatives.

In an alternative specific embodiment, the invention provides a method for operating an apertureless microscope for viewing microscopic features of objects to molecular sensitivity. Conventional techniques have proved to be difficult in aligning laser sources with optical systems. Such difficulties have been overcome by way of the present method and system resulting therefrom. The method is provided as follows:

1. Couple a first assembly including a probe coupling a cantilever to an optical sub-system to facilitate spatial movement between the first assembly and the optical sub-system through a spatial translation axis;

2. Adjust the tip or the portion of the cantilever toward a test surface to focus the tip to a predetermined region of the test surface on the optical sub-system using the spatial translation axis;

3. Adjust a relationship between the alignment beam and the first assembly to an excitation laser such that the tip or the portion of the cantilever in the first assembly is within a vicinity of 1 micron of the excitation laser; and

4. Fine tune the excitation laser to align the tip or the portion of the cantilever using movement of the first assembly on the spatial translation axis.

The above sequence of steps provides a way to adjust a first assembly having a probe and cantilever to an optical sub-system, where the probe becomes aligned with the optical sub-system. Examples of such a probe and optical sub-system have been previously described herein, but can also be outside of the present specification. As can be seen, there is a general course alignment and fine alignment steps, and may also be others depending upon the application. Further details of the present method can be found throughout the specification and more particularly to the figures below.

FIGS. **6** through **8** are simplified diagrams illustrating optical alignment methods for nanoscopic scanning according to embodiments of the present invention. As shown, the invention provides a method for operating an apertureless microscope for viewing microscopic features of objects to molecular sensitivity. The method includes aligning the excitation laser beam to a tip coupled to a cantilever through a probe or a portion of the cantilever within a first assembly. There are several methods for accomplishing such alignment to nanometric accuracy. Gross alignment within a few microns can be achieved by viewing the back reflection of the excitation laser beam and the cantilever laser illumination of the cantilever and either moving the cantilever assembly until the two beams are properly aligned. Alternately or in combination a tip-tilt mirror can be used to move the focus of the excitation laser so that it is properly aligned with the cantilever tip. Additionally, the shadow cast by the cantilever when illuminated by the excitation laser can be visualized or imaged and used to align the tip with the excitation laser.

Referring to FIG. **6**, illustrated is a simplified system diagram **600** including a lamp **601**, which outputs white light **603**. A cantilever **609** is coupled to prove tip **607**. The probe tip is faced toward cover slip **609**, which also may be a plane of a sample. A microscope objective **611** is coupled to the probe. The system also has shadow formation region **613**, which is projected to screen **615**, which may be temporary and/or removable. The system also has excitation laser source **617** which projects onto the backside of the screen. The excitation laser source which projects through the objective. Other features of the present system have been previously described above, but can also be found throughout this specification.

The method performs a gross alignment step, which aligns the laser, which is on a lower subsystem to the probe tip, which is on an AFM subsystem or assembly. As shown, reference numeral **620** illustrates a projection on the screen, which is transparent in nature. Laser spot is illustrated by reference numeral **623**. The projection also includes a shadow of cantilever **629** and perimeter of field of view **627**. The probe tip, which is coupled to a larger assembly, is adjusted relative to the laser spot. A mis-aligned cantilever along the positive y-axis is shown by reference numeral **620**. A mis-aligned cantilever along the x-axis is shown by reference numeral **630**. An aligned cantilever and laser spot are provided in the illustration of reference numeral **640**. Such aligned cantilever aligns the probe to the laser, which is coupled to the lower optical system.

In a specific embodiment, the method performs another alignment step, which aligns the laser to the probe in a finer manner. Such fine alignment to approximately 1 micron can be achieved by illuminating the cantilever either with monochromatic light or broadband light such that the optics can image the cantilever tip shadow relative to the excitation laser. Piezoelectric actuators can be used to either move the tip until properly aligned with the excitation laser or to steer the excitation laser until it is properly aligned with the tip. Alignment is achieved by way of an optical subsystem, which can be viewed using a display coupled to an image capturing camera or the like.

FIG. **7** is a simplified system diagram **600** including image capturing device which is coupled to a display device. Like reference numerals are used in this diagram as the prior diagram merely for illustration. The system includes lamp **601**, which outputs white light **603**. The cantilever **609** is coupled to prove tip **607**. The probe tip is faced toward cover slip **609**, which also may be a plane of a sample. The microscope objective **611** is coupled to the probe. The system also has photons from the excitation laser diverging from the objective **611**. The system has dichroic mirror **703**, which directs radiation from laser **705** through the objective. An image captured from the probe via white light traverse through eyepiece lens **707** from objective and through mirror. Such white light is captured via image capturing device **709**, which is a CCD camera or the like. Other features of the present system have been previously described above, but can also be found throughout this specification.

A relationship between the probe tip and laser beam is illustrated by reference numerals **720**, **730**, and **740**. As shown, a display **721** is coupled to the camera, which captures the white light images. The display illustrates laser spot **723** and probe tip **725**. Reference numeral **720** illustrates a mis-aligned probe tip along an x-axis direction from the beam. Reference numeral **730** illustrates a y-direction mis-alignment. An aligned probe tip and laser beam are illustrated by way of reference numeral **740**. Such alignment provides the finer alignment according to an embodiment of the present invention. By way of example only, the relationship between the probe and the laser is adjusted by way of an automated x-y-z state, which has automated and/or semi-automatic control features according to a specific embodiment.

The method also performs a fine alignment between the probe and the laser beam according to preferred embodiments. Referring to FIG. **8**, illustrated is a system including a raster image using an avalanche photo diode or the like. Like reference numerals are used in this diagram as the prior diagram merely for illustration. The system includes cantilever **609** coupled to prove tip **607**. The probe tip is faced toward cover slip **609**, which also may be a plane of a sample. The microscope objective **611** is coupled to the probe. The system also has photons from the excitation laser diverging from the objective **611**. The system has dichroic mirror **703**, which directs radiation from laser **705** through the objective which is backscattered from the probe tip. Back scattered light from the probe traverse through eyepiece lens **707** from objective and through mirror. Such backscattered light is captured via avalanche photo diode **803**. Other features of the present system have been previously described above, but can also be found throughout this specification.

A relationship between the probe tip and laser beam is illustrated by reference numerals **820**, **830**, and **840**. As shown, a display **823** is coupled to the avalanche photodiode, which captures the backscattered images. The display illustrates laser spot **825** backscatter and a center **821** of a raster field of view, which is the alignment point. Reference numeral **820** illustrates a mis-aligned probe tip along an x-axis direction from the beam. Reference numeral **830** illustrates a y-direction mis-alignment. An aligned probe tip and laser beam via raster field of view are illustrated by way of reference numeral **840**. Such alignment provides the finer alignment according to an embodiment of the present invention. By way of example only, the relationship between the probe and the laser is adjusted by way of an automated x-y-z state, which has automated and/or semi-automated control features according to a specific embodiment.

As noted, the method includes fine and ultrafine alignment to as little as a few nanometers. Such alignment can be achieved by imaging the backscatter of the excitation laser either when scanning the laser over the cantilever tip or alternately when scanning the tip over a fixed focus excitation laser. The backscatter image gives a high resolution image via the microscope objective which allows the relative positions of the tip and the laser to be established. Final alignment can then be achieved by either moving the cantilever assembly, moving the cantilever tip or the excitation laser focus point until the excitation laser and the cantilever tip are properly aligned. All of the previously mentioned alignment steps can be carried out separately or in combination. Also they can be carried out in combination with a properly marked sample substrate which incorporates appropriate position reference points and or structures. Alignment can be maintained while imaging in several ways. It can be achieved by imaging the excitation laser back reflection. The imaged diffraction pattern can then be used to monitor changes in relative position which can be used to correct any misalignments which develop if the laser tracks the cantilever tip while imaging a sample. Alternately, information associated with the pattern can be used to provide primary commands to move the excitation laser to track a moving cantilever tip. Finally it can be used to correct other accumulated misalignments including but not limited to thermal drift and strain relaxation, hysteresis, and piezo creep. These techniques can be used to achieve and maintain alignment whether the cantilever tip scans a stationary sample and excitation laser, both the cantilever tip and excitation laser scan a stationary sample, the excitation laser scans a stationary cantilever tip and sample, or a stationary cantilever tip and excitation laser scan a moving sample.

Although the above has been illustrated in terms of specific hardware and/or software features, it would be recognized that many variations, alternatives, and modifications can exist. For example, any of the hardware features can be further combined, or even separated. The features can also be implemented, in part, through software or a combination of hardware and software. The hardware and software can be further integrated or less integrated depending upon the application. One of ordinary skill in the art would recognize many alternatives, variations, and modifications.

FIGS. **9** through **12** are simplified diagrams of packaging systems **900** and methods **1200** for scanning systems according to embodiments of the present invention. These diagrams are merely examples, which should not unduly limit the scope of the claims herein. One of ordinary skill in the art would recognize many other variations, modifications, and alternatives. As shown, the system includes a package **900** to protect an environment of sensitive scanning and measurement equipment. Preferably, the scanning system is an apertureless microscope system for viewing one or more features of samples to a resolution of molecular sensitivity. The system maintains a controlled environment for elements including sample **109** coupled to stage **111**. The elements also include AFM probe **107**, which is coupled to drive **101**, through cantilever member. Source **103** and detector **105** are also enclosed in the environment. Other elements include objective **119** coupled to mirror **120** and laser source **117**. Filter **121** is coupled to sensor **123** and is coupled to detector **125**. Each of these elements are also included in the controlled environment. Of course, some of these elements may be removed while others added without departing from the scope of the claims herein. Preferably, at least the AFM probe **107**, sample **109**, stage **111** and objective **119** are included in the controlled environment.

The controlled environment allows for accurate measurement of one or more features on a sample. Depending upon the embodiment, the controlled environment has a predetermined temperature, lighting, pressure, gas mixture, any combination of these, and the like. The environment can also be free from contaminants, e.g., organic, inorganic. Preferably, the environment is free from coupled mechanical vibration, i.e., equivalent to less than 1% of an output signal of measurement, although others may work as well. Other embodiments may require an oxygen rich environment. Still others may include a non-reactive environment, which is rich with nitrogen bearing particles and/or non-reactive noble gases, any combination of these, and the like. In many cases, the sample may be maintained and imaged in a biologically relevant fluid environment. Of course, the environment depends highly upon the particular application.

Referring to FIG. **10**, the controlled environment is provided using system **900**. The system has a member **1007** for supporting the apertureless microscope system. A support structure **1001** is coupled to the member to support the member. A plurality of shock absorbing devices **1005** is coupling the support structure and the member. The plurality of shock absorbing devices is capable of substantially eliminating a possibility of mechanical noise from the floor structure. Preferably, the shock absorbing device is a sorbothane manufactured by Sorbothane corp., but can also be others. The shock absorbing device has a suitable length and capable of supporting 2 or more pounds. At least all vibration sensitive elements, and vibration producing elements (e.g. those with fans are included. Preferably, the shock absorbing devices substantially eliminate high frequency (e.g., >10 Hz) noise from entering the controlled environment through the floor structure.

The system also has an enclosure structure **1003** coupled to the member and covering the apertureless microscope system. The enclosure houses the apertureless microscope within an opening confined within the enclosure structure. The enclosure can be made of a suitable material that is rigid and can maintain the environment. Preferably, the enclosure is made of a plastic, a metal, or wood, as well as any combination of these. As merely an example, the enclosure is made of wood, but can also be made of other materials. A cross-sectional-view of the enclosure has been provided by FIG. **11**, which is not intended to be limiting.

As shown, the cross-sectional view includes an outer region exposed to an outer environment **1103** and an inner region exposed to the controlled environment **1115**. The outer environment is often a laboratory or other location where human beings often work. The controlled environment is a region occupied by the scanning system, as previously noted. The enclosure includes rigid structure **1109**. As noted, the rigid structure can be made of a suitable material for supporting the enclosure and overlying materials. The enclosure may also include a frame to support the rigid structure or semi-rigid structure. Such frame can also include walls according to specific embodiments. A sound absorbing member **1111** is coupled to the enclosure structure to substantially eliminate a possibility of acoustic noise from entering into the opening from an external source within the enclosure structure. Preferably, the sound absorbing member is a foam composite, but can also be other sound deadening materials. An inner liner **1107** is also coupled within the opening of the enclosure structure to absorb one or more stray photons within the enclosure structure. The inner liner is generally capable of substantially preventing the stray photons from being released back into the enclosure structure. As an example, the inner liner is a composite manufactured by EAR Composites Inc. A reflective member (e.g., aluminum or other metal, or aluminized mylar or dense plastic) **1105**, **1113** can be formed overlying outer surfaces of the enclosure structure. The outer reflective member is configured to substantially eliminate a desired acoustic noise from entering into the opening within the enclosure structure by reflecting a desired acoustic noise on the reflective surface. Depending upon the embodiment, there can be other layers, which are interposed between any pair of layers described. Some of these layers may be sound absorbing or serve to support the reflective layers. Other embodiments may remove one or more of the layers. Additionally, each layer can be a single material, a composite, or multi-layered, depending upon the embodiment.

Although the above has been illustrated in terms of specific hardware features, it would be recognized that many variations, alternatives, and modifications can exist. For example, any of the hardware features can be further combined, or even separated. Further details of the functionality of the present invention can be outlined below.

According to the present invention, a method for operating a scanning system in a substantially noise free environment is provided as follows.

1. Insert a sample having a molecular feature on a stage of an apertureless microscope system, which has at least a scanning apparatus including a probe coupled to an optical imaging apparatus;

2. Capture information having a feature size of less than five nanometers from a portion of the sample;

3. Maintain at least the stage and the sample in an opening confined by an enclosure structure, which is coupled to a member for supporting a portion of the apertureless microscope system;

4. Maintain at least the stage and the sample free from mechanical vibration noise using a plurality of shock absorbing devices coupling the member, where the plurality of shock absorbing devices is capable of substantially eliminating a possibility of mechanical vibration noise from an external source;

5. Maintain at least the stage and the sample free from acoustic noise using a sound absorbing member coupled to the enclosure structure to substantially eliminate a possibility of the acoustic noise from interacting with the captured information; and

6. Capture one or more stray photons within the opening of the enclosure structure using an inner liner coupled within the enclosure structure to absorb the one or more stray photons within the enclosure structure.

The above sequence of steps is used to perform a method for operating a scanning system in a substantially noise free environment for viewing one or more features of a sample(s) to a resolution of molecular sensitivity. The method allows users of the scanning system to work around it without substantial interference of measurements derived from the system. Further details of the present method are provided throughout the present specification and more particularly below.

Referring to FIG. **12**, the method **1200** begins with start, step **1201**. The method includes inserting (step **1203**) a sample having a molecular feature on a stage of an apertureless microscope system, which has at least a scanning apparatus including a probe coupled to an optical imaging apparatus. An example of such an apparatus has been described above, but can also be outside of this specification according to certain embodiments. Alternatively, the apparatus can be sample scanning with fixed optics and probe, probe scanning with fixed sample and optics, optically scanned with fixed sample and probe, and probe and optically scanned with fixed sample. The optical imaging apparatus is adapted to capture information having a feature size of less than five nanometers from a portion of the sample in preferred embodiments.

Once the sample has been placed on the stage, the method maintains a controlled environment. In a specific embodiment, the method maintains (step **1203**) at least the stage and the sample in an opening confined by an enclosure structure. Preferably, the enclosure structure is coupled to a member for supporting a portion of the apertureless microscope system. The method maintains at least the stage and the sample free from mechanical vibration noise (step **1207**) using a plurality of shock absorbing devices coupling the

member. The plurality of shock absorbing devices is capable of substantially eliminating a possibility of mechanical vibration noise from an external source. Other techniques could also be used, as well.

The method further maintains at least the stage and the sample free from acoustic noise (step **1209**) using a sound absorbing member. Preferably, the sound absorbing member is coupled to the enclosure structure to substantially eliminate a possibility of the acoustic noise from interacting with the captured information. An example of such a sound absorbing member has been provided. The method then has a step of capturing (step **1215**) one or more stray photons within the opening of the enclosure structure using an inner liner. Such inner liner is coupled within the enclosure structure to absorb the one or more stray photons within the enclosure structure. The inner liner is capable of substantially preventing the one or more stray photons from being released back into the opening of the enclosure structure. Depending upon the embodiment, there may be other steps that are included and/or possibly removed.

Although the above has been illustrated in terms of specific hardware and/or software features, it would be recognized that many variations, alternatives, and modifications can exist. For example, any of the hardware features can be further combined, or even separated. The features can also be implemented, in part, through software or a combination of hardware and software. The hardware and software can be further integrated or less integrated depending upon the application. One of ordinary skill in the art would recognize many alternatives, variations, and modifications.

FIGS. **13** through **16** are simplified diagrams of various tip devices according to embodiments of the present invention. These diagrams are merely examples, which should not unduly limit the scope of the claims herein. One of ordinary skill in the art would recognize many other variations, modifications, and alternatives. As shown, the system includes common elements as the prior figures without unduly limiting the scope of the claims herein. The present tip devices are provided within the region surround by the dotted line and indicated by reference numeral **1300**. As shown, the tip **107** is coupled to a cantilever, which is coupled to a drive device. Preferably, the tip is a nanotube based structure, but can also be like structures, depending upon the embodiment. Referring to FIG. **14**, the nanotube structures **1300** include at least a pyramid shaped structure **1301**, which includes tip **1301**. Additionally, such structures include a multi-diameter structure **1305**, which includes tip **1307**. The nanotube structure can be single walled, multiwalled, or any combination of these. Preferably, the nanotube structure is single walled and made of pure or doped carbon. Alternately the nanotube could be made of doped carbon. As merely an example, such single walled structure is a PIT tip from a company called Nanosensors of Germany, but can also be others (for example AC240TM tips from Olympus of Japan). In certain embodiments, the nanotube structure **1311** is coated with an overlying layer **1313**. Here, the nanotube structure can be a semiconductor or conductor. The overlying layer or layers (if multilayered) is a conductor, e.g., metal. The metal's used include platinum, gold, silver alloys, aluminum, platinum-iridium, cobalt and many others. Preferably, the metal is high purity gold or platinum. The nanotube structure can also include a length of less than 250 nanometers in certain embodiments, but will generally have a range of length, e.g., 5–100 nanometers, 10–30 nanometers, depending upon the application.

The metal is deposited using a deposition process. Such deposition process includes evaporation, chemical vapor deposition, sputtering, or molecular beam epitaxy. Preferably, the deposition process is molecular beam epitaxy, which forms a high quality layer of single crystal metal. The thickness of such metal is preferably less than 3 nm, although other thicknesses can be used. The combination of nanotube structure and overlying layer is less than 5 nm diameter near a tip region in preferred embodiments. This compares with commercially available metalized AFM probe diameters of 30 nm from Olympus of Japan. The coated nanotube structures should enhance coupling with an excitation laser light according to certain embodiments. Alternative embodiments are provided by the simplified diagrams of FIGS. **14**A and **14**B, which are nanotube based probes. Such probes include AFM probe **1320** coupled to nanotube probe **1321**. Depending upon the application, there can be many other variations, modifications, and alternatives.

According to an alternative embodiment, metal coating is used for one or more sides of a DNA molecule. Such coated DNA molecule is attached to the probe such that it provides higher resolution images while still modulating the optical signal from the sample being imaged. A DNA molecule coated with gold on one side can have a typical diameter of less than 8 nm.

Other alternative embodiments are illustrated by the photographs **1401**, **1403**, **1405** of FIGS. **14**C, D, and E. Referring to FIGS. **14**C and D, TEM images of shortened nanotube ropes attached by pickup are shown. As shown, nanotube rope dimensions on the right side axis and are approximately 8 nm in width by 62 nm in length. The nanotube tip on the left is approximately 12 nm long and 5 nm in diameter. Referring to FIG. **14**E, scanning electron micrographs of an individual, unshortened carbon nanotube mounted on silicon AFM probe is illustrated. The nanotube was picked up from a flat substrate supporting SWNTs grown by metal catalyzed chemical vapor deposition. Of course, there would be many other alternatives, variations, and modifications.

In a specific embodiment, a method for using the coated nanotube probe can be illustrated by way of FIG. **15**. As shown, the nanotube probe includes a first state **1501** and a second state **1502**. A sample **1505** is also included. The first state has the probe above the sample while the second state is on or in a vicinity of the surface of the sample as shown. As merely an example, an output detected by the present system is shown in the simplified plot of FIG. **16**. The plot includes vertical axis, which is photon count, along probe position. Further details of such plot are provided throughout the specification and more particularly below.

Although certain figures have been described in terms of a specific nanotube structure, one of ordinary skill in the art would recognize many variations, alternatives, and modifications. For example, the nanotube material can be made of homogeneous material, a composite, or even a coated structure. The coating may be a metal, as noted. The metal can include a conductive metal such as platinum, gold, silver, cobalt, and various alloys of such metals such as platinum iridium alloy and the like. Of course, there can a variety of variations without departing from the scope of the claims herein.

Experimental Results:

To prove the principle and operation of the present invention, we performed experiments. The present invention used the FANSOM system, which has been previously described. Such FANSOM used a Digital Instruments BioScope AFM, which had a controller. The controller was a NanoScope IIIa, also manufactured by Digital Instruments

of Santa Barbara, Calif. A second closed-loop BioScope AFM has also been used with a NanoScope IV controller. The microscope objective is a 1.3 NA 100× oil immersion objective, which was manufactured by Olympus of Japan. The system used a PIT tip coated with platinum and iridium manufactured by NanoSensors of Germany. Such tip had a 75 kHz. The samples prepared 20 nanometer (nm) latex beads from a company called Interfacial Dynamics of Portland, Oreg. Such beads were coated with a fluorescent dye, e.g., Nile Red 2 dye. The experiments were performed in room temperature at atmospheric pressure. Although these parameters have been used, there can be many other variations, modifications, and alternatives.

Using the experiment, we demonstrated the probe. Referring to FIG. **17**, as the probe came within a vicinity of a surface of the sample, photon counts decreased. As merely an example, the high photon count corresponded to a 120 nanometer distance between the surface of the sample and the probe. The lower photon counts corresponded to contact between the probe and the sample. As shown, a rate of fluorescence is shown modulated as the cantilever tip oscillates above the sample.

Another example of our experiment is provided by the simplified diagram of FIG. **18**. As shown, a number of photons (y-axis) emitted by a 20 nm fluorescent bead as a function of phase (shown in π radians on the x-axis). At a phase of 0.3 π radians, the tip is closest to the bead and the fluorescence is reduced or even minimized. When the tip is far from the bead the fluorescence is increased or even maximized. The tip is in a stationary X-Y position over the center of the 20 nm bead for a long time, e.g., ten seconds and more. The tip oscillates in the z (vertical) axis and the bead is continuously illuminated. In this combination of illumination (including phase and evanescent components) only a reduced detection rate is illustrated.

Another illustration is provided by the simplified diagram of FIG. **19**, which plots photon count in the vertical axis against radians, i.e., phase, which are along the horizontal axis. A strong polarized evanescent component that has increased fluorescence is seen only when the tip is very close to the bead. At longer range the fluorescence is maximized as the tip to sample distance increases in a manner similar to that seen in FIG. **18**.

We also imaged the bead using AFM only and FANSOM. Referring to FIG. **20**, the 20 nm fluorescent bead has been imaged by AFM (left) and FANSOM (right). The full width-half max (FWHM) diameter is measured on both images as 40 nm. The resolution of the FANSOM is therefore demonstrated to be at least 20 nm for this large sample. Accordingly, FANSOM resolution appears to be limited by the imaging capability of the probe and matches the best available via AFM. In other experiments, we prepared approach curves using a closed loop AFP (See, for example, FIGS. **20**A and **20**B), which provided improved positioning to a resolution of 10 nanometers and better. The closed loop AFM reduced or even minimized the relative drift of the probe over the sample. Partially by minimizing the relative drift error source, it can be expected that 10 nm resolution can be achieved using the present tips. In the present experiments, we used a NanoScope IV controller rather than the IIIa, which had been previously used. As noted above, we used the Digital Instruments BioScope with NanoScope IIIa controller to take the AFM image. Most of the presented FANSOM data was taken with the same optics coupled to a Closed-loop BioScope with NanoScope IV controller. The FANSOM resolution should improve with better probes (e.g. nanotubes) and smaller targets (e.g. quantum dots, biological molecules, etc.).

We also discovered that FANSOM can be used to distinguish different types of materials. For example, images of the bead and a dust particle have been captured. Such images are provided by the diagrams in FIG. **21**. As shown, a 100 nm fluorescent bead and a dust particle are illustrated. On the left hand side using an AFM, the dust particle and bead are nearly indistinguishable (since they each appear as bright spots along a black background.) On the right hand side, they are imaged by FANSOM which clearly distinguishes the fluorescent spherical bead from the dust particle. Depending upon the embodiment, there can be many other variations, modifications, and alternatives.

Although the above has been illustrated in terms of specific hardware features, it would be recognized that many variations, alternatives, and modifications can exist. For example, any of the hardware features can be further combined, or even separated. The features can also be implemented, in part, through software or a combination of hardware and software. The hardware and software can be further integrated or less integrated depending upon the application. One of ordinary skill in the art would recognize many alternatives, variations, and modifications.

FIG. **22** is a simplified diagram of an alignment subsystem **2200** for an optical system according to an embodiment of the present invention. This diagram is merely an example, which should not unduly limit the scope of the claims herein. One of ordinary skill in the art would recognize many other variations, modifications, and alternatives. As shown, a system **2200** for dynamically viewing an increased field of view based upon a smaller field of view to capture an image of features of samples to molecular sensitivity is included. Like reference numerals are used in this figure as the prior figures without limiting the scope of the claims herein. The system has an electromagnetic energy source (in a specific embodiment this can be a laser) **117**, which is capable of emitting a beam. A fixed lens **119** is coupled to the electromagnetic energy source. The fixed lens focuses the beam toward at least one tip of a probe **107**, which is in a vicinity of a feature of a sample to scatter a portion of the beam off a portion of the tip of the probe. A detector **2203** is coupled to the fixed lens. The detector detects the scattered portion of the beam. As shown, the scattered portion of the beam traverses through objective, through mirror **120**, through filter (optional), to the detector. A processor **115** is coupled to the detector via input/output device **2205**. The processor is adapted to process the scattered portion **2201** of the beam to determine a pattern to identify a relationship between the tip and the beam for a spatial alignment between the tip and the beam. As merely an example, conventional image processing techniques can be used. An adjustment device **111** is coupled to the processor. The adjustment device is adapted to adjust a position of the beam based upon at least the pattern to maintain a desired relationship between the tip and the beam. As merely an example, the adjustment device can be an x-y-z state or the like. Further details of the present system can be described with way of the following methods described below.

A method according to an embodiment of the present invention for dynamically viewing an increased field of view based upon a smaller fixed field of view to capture an image of features of samples to molecular sensitivity is provided as follows.

1. Output a beam from a laser coupled to an optical system, which is coupled to an AFM system;

2. Illuminate through a fixed lens coupled to the optical system using the beam of the laser a feature of a sample on a stage coupled to the AFM system;

3. Direct the beam toward at least one tip of a probe coupled to the AFM, which is in a vicinity of the feature of the sample;

4. Scatter a portion of the beam off a portion of the tip of the probe;

5. Traverse scattered portion through the fixed lens;

6. Detect the scattered portion of the beam using a detector;

7. Transfer signal indication from scattered portion being detected to a processor;

8. Process the signal indication of the scattered portion of the beam to determine a pattern to identify a relationship between the tip and the beam for spatial alignment between the tip and the beam;

9. If necessary, adjust a position of the beam used for illumination based upon at least the pattern to maintain a desired relationship between the tip and the beam; and

10. Maintain the alignment between the tip and the beam using one or more of the steps above.

These steps provide a way to align the probe tip of the AFM to the optical subsystem, which is coupled to the AFM. Such steps are provided as the AFM is operational or in-situ in some embodiments. These steps are used by way of a combination of computer hardware and/or software depending upon the embodiment. Further details of these steps are provided throughout this specification and more particularly below.

FIGS. **23** through **24** are simplified diagrams of tip detection alignment methods **2300** for the scanning system according to embodiments of the present invention. These diagrams are merely examples, which should not unduly limit the scope of the claims herein. One of ordinary skill in the art would recognize many other variations, modifications, and alternatives. The scanning system can be one or more of the ones that were previously described, as well as others. As shown, the method begins at start, step **2300**. Here, the method for dynamically (e.g., moving) viewing an increased field of view based upon a smaller fixed field of view to capture an image of features of samples to molecular sensitivity. The method emits a beam from a laser for transfer, step **2303**.

The method also includes illuminating (step **2305**) through a fixed lens using the beam a feature of a sample. The beam is directed toward at least one tip of a probe, which is in a vicinity of the feature of the sample. Next, the method scatters (step **2307**) a portion of the beam off a portion of the tip of the probe. The scattered beam traverses back through the lens. Optionally, the beam also scatters through a filter. The method detects (step **2315**) the scattered portion of the beam using a detector. The detector can include a CCD camera, an avalanche photodiode, or the like.

The method then transfers (step **2317**) signals associated with the detector to a processor. The method then processes (step **2319**) the scattered portion of the beam to determine a pattern to identify a relationship between the tip and the beam for spatial alignment between the tip and the beam. The processing can be done on a conventional signal processor and/or computer or the like. The processor determines of the tip is aligned to the beam, step **2321**. If so, the method continues to transfer the beam, which may have been continuously transferred, as the probe and sample move relative to each other in the scanning method. If not, the method adjusts (step **2323**) a position of the beam used for illumination based upon at least the pattern to maintain a desired relationship between the tip and the beam. Such adjustment may occur using an automated x-y-z stage or the like. The method continues via the branch to step **2303**. The method also stops at step **2313**.

Referring to FIG. **24**, the present method maintains alignment between the probe tip and laser beam. As noted above, such alignment is generally for precision measurement of the features of the sample. The probe tip **2401** should be aligned with the beam **2403**, which can be viewed on display **2400**. Such display can be coupled to the processor, which processes the signals of the image. Of course, there can be other modifications, alternatives and variations.

Preferably, the present method is provided on a secondary illumination system **2500**, which is coupled to the FANSOM. Referring to FIG. **25**, the system **2500** includes various elements, which can be found in the other systems described herein. Additionally, the system includes an independent or secondary illumination sub-system, which transmits and receives scattered light from the probe using a different wavelength of light than the main detector, which is used for the imaging. As shown, the system includes cantilever **2501**, which is coupled to tip **2503**. A sample **2505** such as a bead, fluorophore, DNA, quantum dot, or others is included. The sample is provided on cover slip **2507**. An objective **2509** is coupled to the probe. A tip/tilt mirror **2511** directs light between dichroic mirror **2514** and objective. The dichroic mirror reflects an excitation laser and transmits the backscattered signal. As shown, the excitation laser **2519** transmits light through beam splitter **1517** to the mirror, which transmits the light to the probe. Such probe scatters light and directs it back through the secondary optical subsystem. The scattered light goes from the probe, through the objective, through a secondary eyepiece **2527**, which is coupled to secondary bandpass filter **2529**, which is coupled to a secondary detector **2531**, which receives scattered light from the probe. The system also has primary eye piece **2521** coupled to primary filter **2523**, which is coupled to primary detector **2525**. Control electronics **2517** is coupled to the secondary detector **2531**. The solid arrows and lines represent control signals and the other lines represent light paths. Of course, there can be many variations, alternatives, and modifications.

Although the above has been illustrated in terms of specific hardware and/or software features, it would be recognized that many variations, alternatives, and modifications can exist. For example, any of the hardware features can be further combined, or even separated. The features can also be implemented, in part, through software or a combination of hardware and software. The hardware and software can be further integrated or less integrated depending upon the application. One of ordinary skill in the art would recognize many alternatives, variations, and modifications.

FIG. **25A** is a simplified diagram of a FANSOM system using a closed loop feedback loop according to an embodiment of the present invention. This diagram is merely an example, which should not unduly limit the scope of the claims herein. One of ordinary skill in the art would recognize many other limitations, variations, and modifications. Preferably, the system includes use of a closed-loop AMF position information directly in combination with the tip-tilt mirror position information to maintain alignment while scanning large fields of view or while taking a series of high resolution small FOV images of many samples spread over a larger area (e.g. a 100 micron square region).

According to a specific embodiment to maintain the initial alignment while imaging a series of samples. Alignment established as above (e.g. paragraphs numbered 90–93), both are commanded to new location, maintaining the earlier established alignment, then imaging commences as above. The location of each of these series of samples could be determined before either by patterning, by taking a large

FOV image (for example using a CCD array) and determining the coordinates of each sample within the image, or by taking an AFM image of the sample and determining the coordinates of each sample. The series of sample coordinates then are used to direct both the closed-loop AFM and the tip-tilt mirror such that the sample is illuminated while maintaining alignment with the probe tip. A high resolution, high sensitivity image can then be taken of each sample in sequence.

Alternately, after achieving alignment in a method such as that outlined in 90–93, the closed loop AFM can be used to image a large FOV. The position information from the closed loop head can then be used to direct the tip-tilt mirror in such a manner as to maintain alignment as the area to be imaged is rastered over. In an alternate configuration the tip-tilt mirror is commanded to image a large FOV and the position information is used to direct the closed-loop AFM such that alignment is maintained between the probe tip and the excitation laser. Of course, there can be many variations, alternatives, and modifications depending upon the embodiment.

FIGS. **26** through **34** are simplified diagrams of methods and systems for selectively illuminating one or more samples according to embodiments of the present invention. These diagrams are merely examples, which should not unduly limit the scope of the claims herein. One of ordinary skill in the art would recognize many other variations, modifications, and alternatives. As shown, the system includes, among other elements, an AFM source (e.g., laser diode) **2601**. The source is characterized by a certain wavelength of such as λ_A. A clean up filter **2603** is disposed between the source and a focusing lens **2605**. The system includes a plane **2607** for a sample. The plane can be provided on a stage, e.g., x-y stage. The system includes a microscope objective **2609** underlying the sample stage for detecting one or more features from the sample. Other elements include a dichroic mirror **2611** coupled to a laser **2621** λ_E for sample excitation. A clean up filter **2623** is disposed between the laser and dichroic mirror. The system also includes detector elements such as blocking filter for wavelength λ_A between lens for sample imaging and dichroic mirror. A blocking filter is disposed between the lens and a sample detector **2617**. Depending upon the embodiment, there can also be other elements. Details with regard to the operation of the system can be illustrated by FIGS. **27** through **34**, which are simplified illustrations.

FIG. **27** is a simplified plot of power against wavelength for a spectrum of the AFM laser according to an embodiment of the present invention. The wavelength of the peak emission of the AFM laser is λ_A. FIG. **28** is a simplified plot of power against wavelength for relative positions of wavelengths of predetermined interest. Here, wavelength parameters are defined by λ_E that corresponds to the wavelength of the peak emission from excitation laser, λ_F that corresponds to a range of wavelengths emitted by a sample, λ_{FL} that corresponds to a lower bound of a sample fluorescence, and λ_{FU} that corresponds to an upper bound of a sample fluorescence. FIG. **29** is a simplified plot of transmission plotted against wavelength for a transmission spectrum of the ASE filter according to an embodiment of the present invention. Here, λ_B is the wavelength at which transmission is down to about 10^{-5} and λ_B is higher than λ_{FU}. FIG. **30** is a simplified plot of transmittivity plotted against wavelength for a transmission spectrum of a dichroic mirror according to an embodiment of the present invention. Here, certain characteristics are reflected at (rather than absorption) and transmission from FIG. **31** is a simplified plot of transmission plotted against wavelength for a blocking filter for a wavelength λ_A, which corresponds to a wavelength at which transmission falls to about 10^{-5} and λ_B is higher than λ_{FU}. FIG. **33** is a simplified plot of transmission plotted against wavelength of an excitation clean-up filter according to an embodiment of the present invention. Here, λ_C corresponds to a wavelength at which transmission falls to 10^{-5} and λ_C is lower than λ_{FL}. FIG. **34** is a simplified plot of transmission as a function of wavelength. Here, λ_J corresponds to a wavelength at which transmission is about 10^{-5} and λ_J is higher than λ_C. Here, λ_H corresponds to a wavelength at which transmission is about 60% and λ_H is lower than λ_{FL}. Here, λ_G corresponds to a wavelength at which transmission is about 10^{-5} and λ_G is lower than λ_B and also lower than λ_D. Of course, there can be other modifications, alternatives, and variations depending upon the embodiment.

It is also understood that the examples and embodiments described herein are for illustrative purposes only and that various modifications or changes in light thereof will be suggested to persons skilled in the art and are to be included within the spirit and purview of this application and scope of the appended claims.

What is claimed is:

1. A method for measuring characteristics of nanoscopic objects using detection of photons emitted from the objects, the method comprising:

moving a tip of a probe coupled to a cantilever toward a feature of a sample to influence a rate of emission from the feature of the sample;

illuminating using a first intensity level of electromagnetic energy the feature of the sample during a first predetermined portion of movement of the cantilever to capture a signal at a detector from the sample; and

changing the first intensity level to a second intensity level during a second predetermined portion of movement of the cantilever.

2. The method of claim **1** wherein the second intensity level is lower than the first intensity level.

3. The method of claim **1** wherein the second intensity level is near zero.

4. The method of claim **1** wherein the movement of the cantilever is a portion of an oscillating action of the cantilever.

5. The method of claim **1** whereupon changing the first intensity level to the second intensity level, the second intensity level being lower than the first intensity level changes a capability of emitting photons from the feature of the sample.

6. The method of claim **5** wherein the capability of emitting photons is increased.

7. The method of claim **1** wherein the changing is provided using a switch that blocks an illumination of the first intensity level.

8. The method of claim **1** wherein the changing is provided by an electro-optic modulator material that blocks an illumination of the first intensity level to cause the second intensity level.

9. The method of claim **1** wherein the changing is provided by an acousto-optic modulator material, the acousto-optic modulator material being adapted to block an illumination at the first intensity level to cause the second intensity level.

10. The method of claim **1** wherein the sample is a fluorophore.

11. The method of claim **1** wherein the sample is selected from a collection of fluorophores, a fluorescent particle, or a bead.

12. The method of claim 1 wherein the sample comprises a biological molecule coupled to a fluorophore, the sample having a pre-determined life.

13. The method of claim 1 wherein the sample is a quantum dot or other solid state entity with tunable fluorescent property.

14. The method of claim 1 wherein the sample is a biological molecule coupled to a quantum dot or other solid state entity.

15. The method of claim 1 wherein the sample is a collection of quantum dots or other solid-state entities.

16. The method of claim 1 wherein the sample is a biological molecule coupled to a plurality of quantum dots or other solid-state entities.

17. A system for measuring characteristics of nanoscopic objects using detection of photons emitted from the objects, the system comprising one or more computer memories, the one or more computer memories including:

a first code directed to cause movement of a tip of a probe coupled to a cantilever member toward a feature of a sample to influence a rate of emission from the feature of the sample;

a second code directed to apply illumination using a first intensity level of electromagnetic energy to the feature of the sample during a first predetermined portion of movement of the cantilever member to capture a signal from the feature at a detector from the sample; and

a third code directed to output a control signal to switch the first intensity level to a second intensity level during a second predetermined portion of movement of the cantilever member.

18. The system of claim 17 further comprising a fourth code directed to provide a control signal to initiate a relative motion between a region of illumination and a portion of the sample.

19. The system of claim 18 further comprising a fifth code directed to provide a control signal to initiate a relative motion between a region of the cantilever member and a portion of the sample.

20. The system of claim 17 wherein the second intensity level is lower than the first intensity level.

21. The system of claim 17 wherein the second intensity level is zero.

22. The system of claim 17 wherein the movement of the cantilever is a portion of an oscillating action of the cantilever.

23. The system of claim 17 whereupon changing the first intensity level to the second intensity level, the second intensity level being lower than the first intensity level changes a capability of emitting photons from the feature of the sample.

24. The system of claim 15 wherein the capability of emitting photons is increased.

25. The system of claim 17 wherein the third code directed to switch is coupled to a switch means that blocks an illumination at the first intensity level.

26. The system of claim 17 wherein the third code directed is coupled to an electro-optic modulator material that blocks an illumination of the first intensity level to cause the second intensity level.

27. The system of claim 17 wherein the third code directed is coupled to an acousto-optic modulator material that blocks an illumination of the first intensity level to cause the second intensity level.

28. The system of claim 17 wherein the sample comprises a biological molecule coupled to a fluorophore, the sample having a pre-determined life.

29. The system of claim 17 wherein the sample is a quantum dot or other solid-state entity with tunable fluorescent property.

30. The system of claim 17 wherein the first code, second code, and third code are provided on a fixed memory.

31. A method for measuring a characteristic of objects using detection of photons associated with objects, the method comprising:

maintaining a sample on a stage, the sample including a feature to be imaged;

providing a tip of a probe to be movable toward the feature of sample to influence an emission of electromagnetic energy associated with the feature of the sample;

illuminating a feature of a sample using electromagnetic energy comprising a first intensity level;

capturing a first signal associated with the feature during a first portion of movement of the tip during a portion of time associated with illuminating the feature of the sample with the electromagnetic energy comprising the first intensity level;

moving the tip of the probe toward a vicinity of the feature of the sample during a second portion of movement of the tip;

providing electromagnetic energy comprising a second intensity level as the tip of the probe moves toward the vicinity of the feature of the sample during the second portion of movement of the tip to cause enhancement of the tip of the probe;

determining a spatial coordinate of the stage on which the sample has maintained;

determining a distance of the tip of the probe relative to the feature of the sample;

capturing a second signal associated with the feature; and

forming an image associated with at least the second signal associated with the feature of the sample.

32. The method of claim 31 wherein the second intensity level is associated with an enhancement or quenching influence of the feature of the sample.

33. The method of claim 31 wherein the first portion and the second portion are provided within an oscillation cycle of the tip of the probe.

34. The method of claim 33 wherein the tip of the probe is maintained in gas and wherein the oscillation cycle is characterized by a frequency ranging from about 50 kilohertz to 250 kilohertz.

35. The method of claim 31 wherein the second intensity level is lower than the first intensity level.

36. The method of claim 31 wherein the vicinity of the feature is in contact with the feature.

37. The method of claim 31 wherein the capturing the first signal and the capturing the second signal are among a plurality of capturing steps.

38. The method of claim 31 further comprising scanning the tip of the probe along a spatial surface region of the sample.

39. The method of claim 31 wherein the first signal is associated with a plurality of photons emitted from the feature of the sample.

40. The method of claim 31 wherein the second signal is associated with a plurality of photons emitted from the feature of the sample, the second signal being greater than the first signal.

41. The method of claim 31 wherein the moving the tip of the probe comprises a portion of an tapping mode of operation.

42. The method of claim 31 wherein the sample and tip are maintained in a liquid.

43. The method of claim 31 wherein the sample and tip are maintained in an inert gas.

44. A method for measuring a characteristic of objects using detection of photons associated with objects, the method comprising:

providing a liquid environment or gas environment;

providing a tip of a probe to be movable toward a feature of a sample in the liquid or gas environment to influence an emission of electromagnetic energy associated with the feature of the sample, the feature and the sample being maintained on a stage;

illuminating the tip of the probe using electromagnetic energy comprising a first intensity level as the tip of the probe moves toward the feature of the sample;

capturing a first signal associated with the feature during a first portion of movement of the tip during a portion of time associated with illuminating the tip of the probe with the electromagnetic energy comprising the first intensity level;

moving the tip of the probe toward a vicinity of the feature of the sample during a second portion of movement of the tip;

providing electromagnetic energy comprising a second intensity level associated with the feature of the sample as the tip of the probe moves toward the vicinity of the feature of the sample during the second portion of movement of the tip to cause enhancement of the tip of the probe to the second intensity level;

determining a spatial coordinate of the stage on which the sample has maintained;

determining a distance of the tip of the probe relative to the feature of the sample; and

capturing a second signal associated with the feature to create an image of the feature of the sample.

45. The method of claim 44 wherein the second intensity level is associated with an enhancement or quenching influence of the feature of the sample.

46. The method of claim 44 wherein the first portion and the second portion are provided within an oscillation cycle of the tip of the probe.

47. The method of claim 46 wherein the oscillation cycle is characterized by a predetermined frequency.

48. The method of claim 44 wherein the second intensity level is lower than the first intensity level.

49. The method of claim 44 wherein the vicinity of the feature is when the tip is in contact with the feature.

50. The method of claim 44 wherein the capturing the first signal and the capturing the second signal are among a plurality of capturing steps.

51. The method of claim 44 further comprising scanning the tip of the probe along a spatial surface region of the sample.

52. The method of claim 44 wherein the first signal is associated with a plurality of photons emitted from the feature of the sample.

53. The method of claim 44 wherein the second signal is associated with a plurality of photons emitted from the feature of the sample, the second signal being greater than the first signal.

54. The method of claim 44 wherein the moving the tip of the probe comprises a portion of an tapping mode of operation.

55. A method for measuring characteristics of nanoscopic objects using detection of photons emitted from the objects, the method comprising:

moving a tip of a probe toward a feature of a sample to influence a rate of emission from the feature of the sample;

capturing a signal associated with illumination of a first intensity level of electromagnetic energy associated with the feature of the sample during a first portion of movement of the probe at a detector;

changing the first intensity level to a second intensity level during a second portion of movement of the probe; and

forming an image based upon at least the second intensity level;

whereupon the second intensity is caused by an enhancement o the tip of the probe as the tip of the probe moves within a vicinity of the feature of the sample.

* * * * *

Appendix D

US patent 7,247,842
Method and system for scanning apertureless fluorescence microscope

This patent adds 12 claims to the 58 claims awarded in US patent 6,953,927. The 12 claims awarded in this patent primarily serve to describe wet imaging: especially the wet imaging of biological samples with TEFM. The work I did on this is described in section 3.2 of Chapter 3. This patent was issued on July 24, 2007 to Steven Quake, Guillaume Lessard, Lawrence Wade and Jordan Gerton. These four inventors made equal contributions to this invention.

US007247842B1

(12) **United States Patent**
Quake et al.

(10) **Patent No.: US 7,247,842 B1**
(45) **Date of Patent: *Jul. 24, 2007**

(54) **METHOD AND SYSTEM FOR SCANNING APERTURELESS FLUORESCENCE MIRCROSCOPE**

(75) Inventors: **Stephen R. Quake**, San Marino, CA (US); **Guillaume Lessard**, Rochester, NY (US); **Lawrence A. Wade**, La Canada, CA (US); **Jordan M. Gerton**, Upland, CA (US)

(73) Assignee: **California Institute of Technology**, Pasadena, CA (US)

(*) Notice: Subject to any disclaimer, the term of this patent is extended or adjusted under 35 U.S.C. 154(b) by 0 days.

This patent is subject to a terminal disclaimer.

(21) Appl. No.: **11/180,976**

(22) Filed: **Jul. 12, 2005**

(51) **Int. Cl.**
H01J 3/14 (2006.01)
H01J 40/14 (2006.01)
H01J 5/16 (2006.01)

(52) **U.S. Cl.** **250/234**; 250/458.1

(58) **Field of Classification Search** 250/234, 250/458.1; 356/72–73, 301, 318
See application file for complete search history.

(56) **References Cited**

U.S. PATENT DOCUMENTS

5,479,024 A 12/1995 Hillner et al.
6,002,471 A 12/1999 Quake
6,046,448 A 4/2000 Sato et al.
6,643,012 B2 11/2003 Shen et al.
6,681,133 B2 1/2004 Chaiken
6,850,323 B2 2/2005 Anderson
6,953,927 B2 * 10/2005 Quake et al. 250/234
2002/0109082 A1 8/2002 Nakayama et al.

OTHER PUBLICATIONS

Gersen et al., "Near-field effects in single molecule emission", *Journal of Microscopy*, vol. 202, Pt 2, May 2001, pp. 374-378.
Gersen et al., "Influencing the Angular Emission of a Single Molecule", *Physical Review Letters*, vol. 85, No. 25, Dec. 18, 2000, pp. 5312-5315.
Gerton et al., Tip-Enhanced Fluorescence Microcopy at 10 Nanometer Resolution, Department of Applied Physics, CALTECH, MC 128-95, Pasadena, CA, 2004.
Gerton et al., "Fluorescence Apertureless Near-field Optical Microscope for Biological Imaging", The 7th International Conference on Near-field Optics and Related Techniques, Aug. 11-15, 2002, p. 71.

(Continued)

Primary Examiner—Georgia Epps
Assistant Examiner—Patrick J. Lee
(74) *Attorney, Agent, or Firm*—Townsend and Townsend and Crew LLP

(57) **ABSTRACT**

Methods and systems for operating an apertureless microscope for observing one or more features to a molecular sensitivity on objects are described. More particularly, the method includes moving a tip of a probe coupled to a cantilever in a vicinity of a feature of a sample, which emits one or more photons at a detected rate relative to a background rate of the sample based upon the presence of the tip of the probe in the vicinity of the feature. The method modifies the detected rate of the feature of the sample, whereupon the modifying of the detected rate causes the feature of the sample to enhance relative to background rate of the feature.

12 Claims, 38 Drawing Sheets

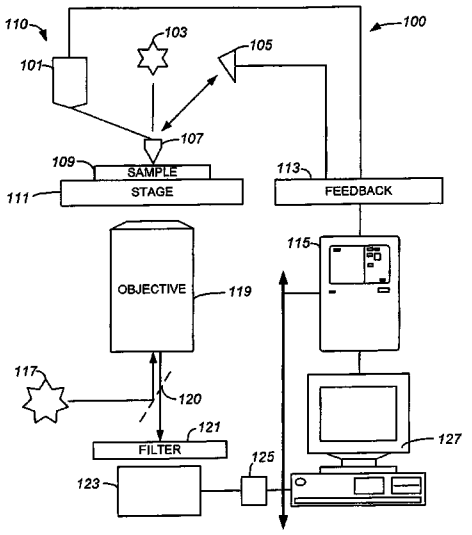

OTHER PUBLICATIONS

Kawata et al., Feasibiltiy of Molecular-Resolution Fluorescence near-field Microscopy using Multi-Photon Absorption and Field Enhancement near a sharp tip, Journal of Applied Physics, vol. 85, No. 3, 1999.

Lessard et al., "A Scanning Apertureless Fluorescence Microscope", Department of Applied Physics, California Institute of Technology, Pasadena, California, pp. 1-8.

Sanchez et al, Near-Field Fluorescence Microscopy Based on Two-Photon Excitation with Metal Tips, Physical Review Letters, vol. 82, No. 20, 1999.

Yang et al., "An Apertureless Near-field Microscope for Fluorescence Imaging", *Applied Physics Letters*, vol. 76, No. 3, Jan. 17, 2000, pp. 378-380.

Bachelot et al., "Apertureless Near-field Optical Microscopy: A Study of the Local Tip Field Enhancement Using Photosensitive Azobenzene-Containing Films," *Journal of Applied Physics* (Aug. 1, 2003), vol. 94, No. 3, pp. 2060-2072.

Brody et al., "Self-Assembled Microlensing Rotational Probe," *Applied Physics Letters* (Jan. 4, 1999) vol. 74, No. 1, pp. 144-146.

Lessard et al., "Ultra High Resolution Optical Microscopy (SIAM)," The Quake Group, downloaded from Internet <<http://thebigone.caltech.edu/quake/research/siam.html>> on Apr. 9, 2002, 2 pages.

Furukawa et al., "Local Field Enhancement with an Apertureless Near Field Microscope Probe," *Optical Communications* (1998) vol. 148, pp. 221-224.

Hamann et al., "Enhance Sensitivity Near Field Scanning Optical Microscopy at High Spatial Resolution," *Applied Physics Letters* (Sep. 14, 1998) vol. 73, No. 11, pp. 1489-1471.

Hamann et al., "Near Field Fluorescence Imaging by Localized Field Enhancement Near a Sharp Probe Tip," *Applied Physics Letters* (Apr. 3, 2000) vol. 76, No. 14, pp. 1953-1955.

Zenhausern et al., "Apertureless Near-Field Optical Microscope," *Applied Physics Letters* (Sep. 26, 1994), vol. 65, No. 13, pp. 1623-1625.

Zenhausern et al., "Scanning Interferometric Apertureless Microscopy: Optical Imaging at 10 Angstrom Resolution," *Science* (Aug. 25, 1995), vol. 269. No. 5227, pp. 1083-1085.

* cited by examiner

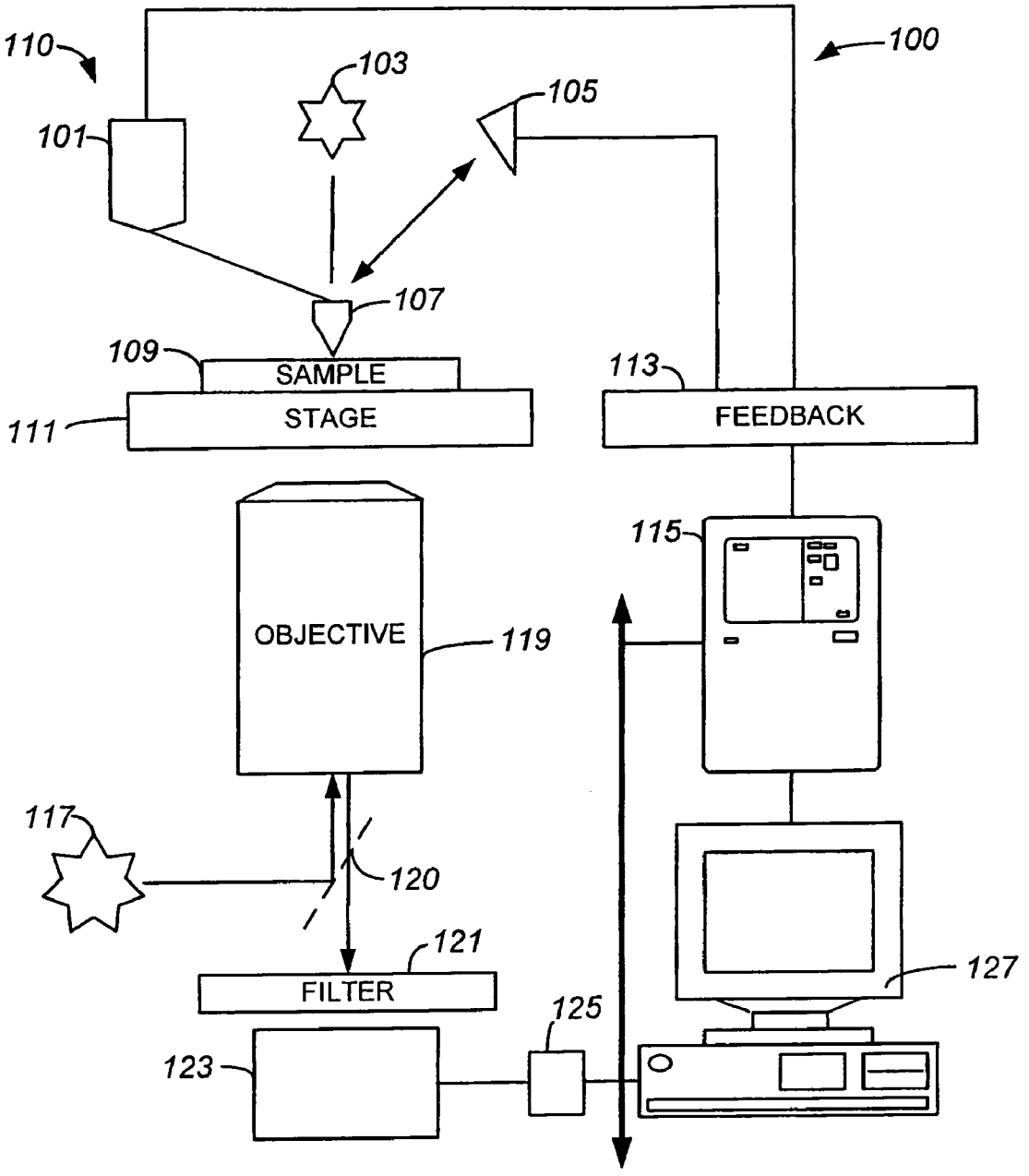
110
100
103
105
101
107
109
SAMPLE
113
111
STAGE
FEEDBACK
115
OBJECTIVE
119
117
120
121
FILTER
127
125
123

FIG. 1

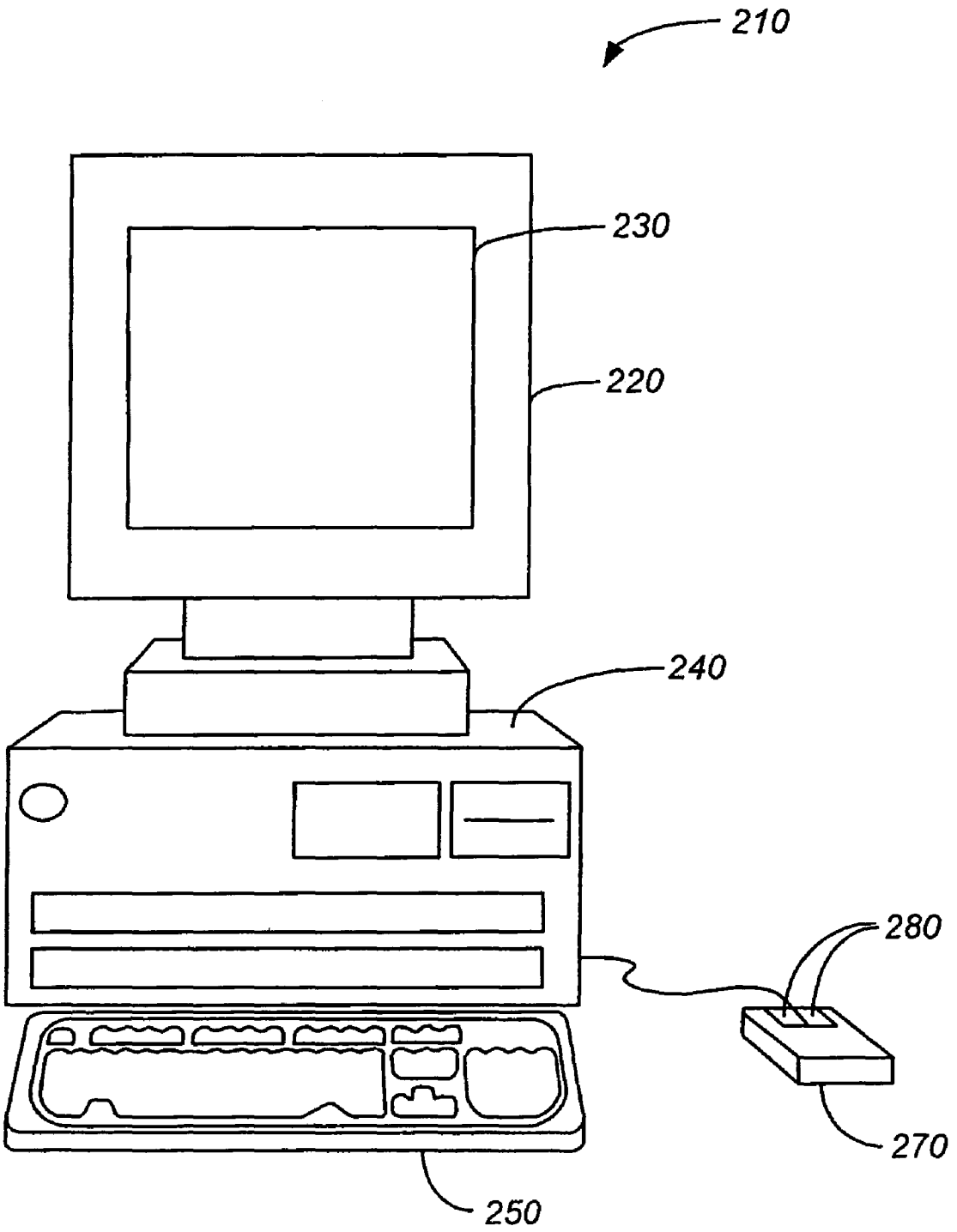

FIG. 2

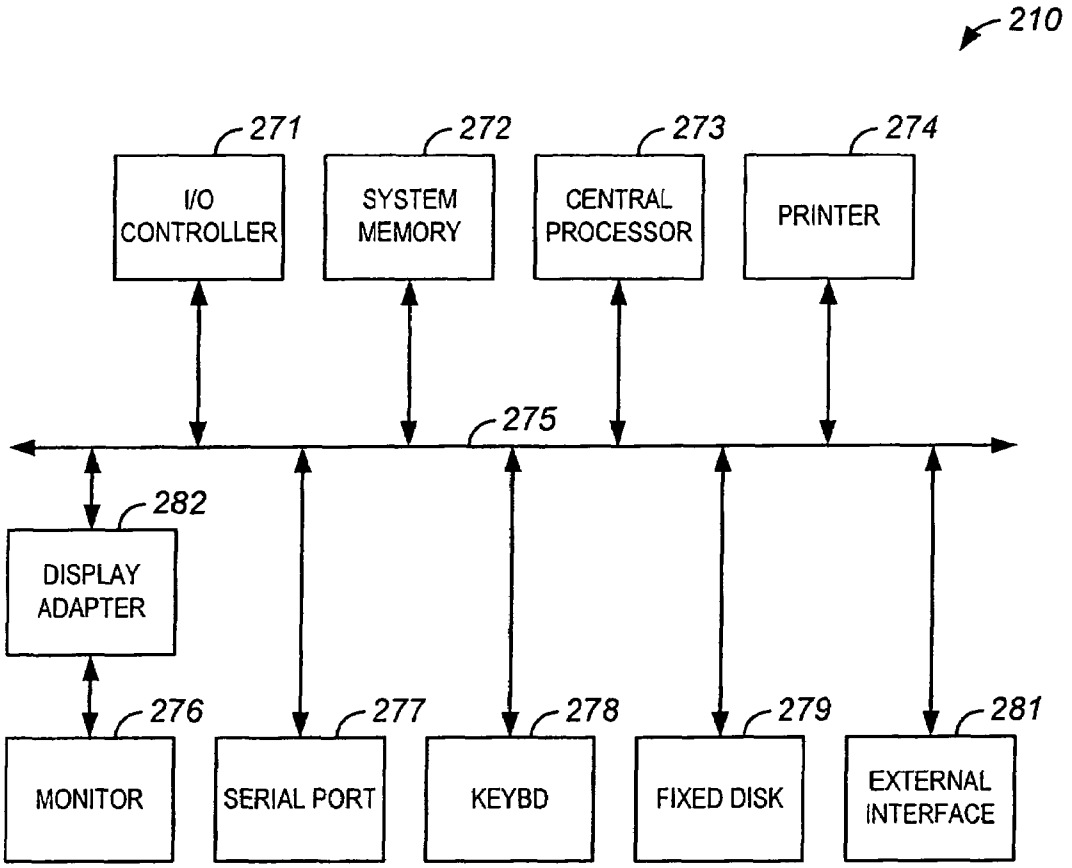
210
271
I/O CONTROLLER
272
SYSTEM MEMORY
273
CENTRAL PROCESSOR
274
PRINTER
275
282
DISPLAY ADAPTER
276
MONITOR
277
SERIAL PORT
278
KEYBD
279
FIXED DISK
281
EXTERNAL INTERFACE

FIG. 2A

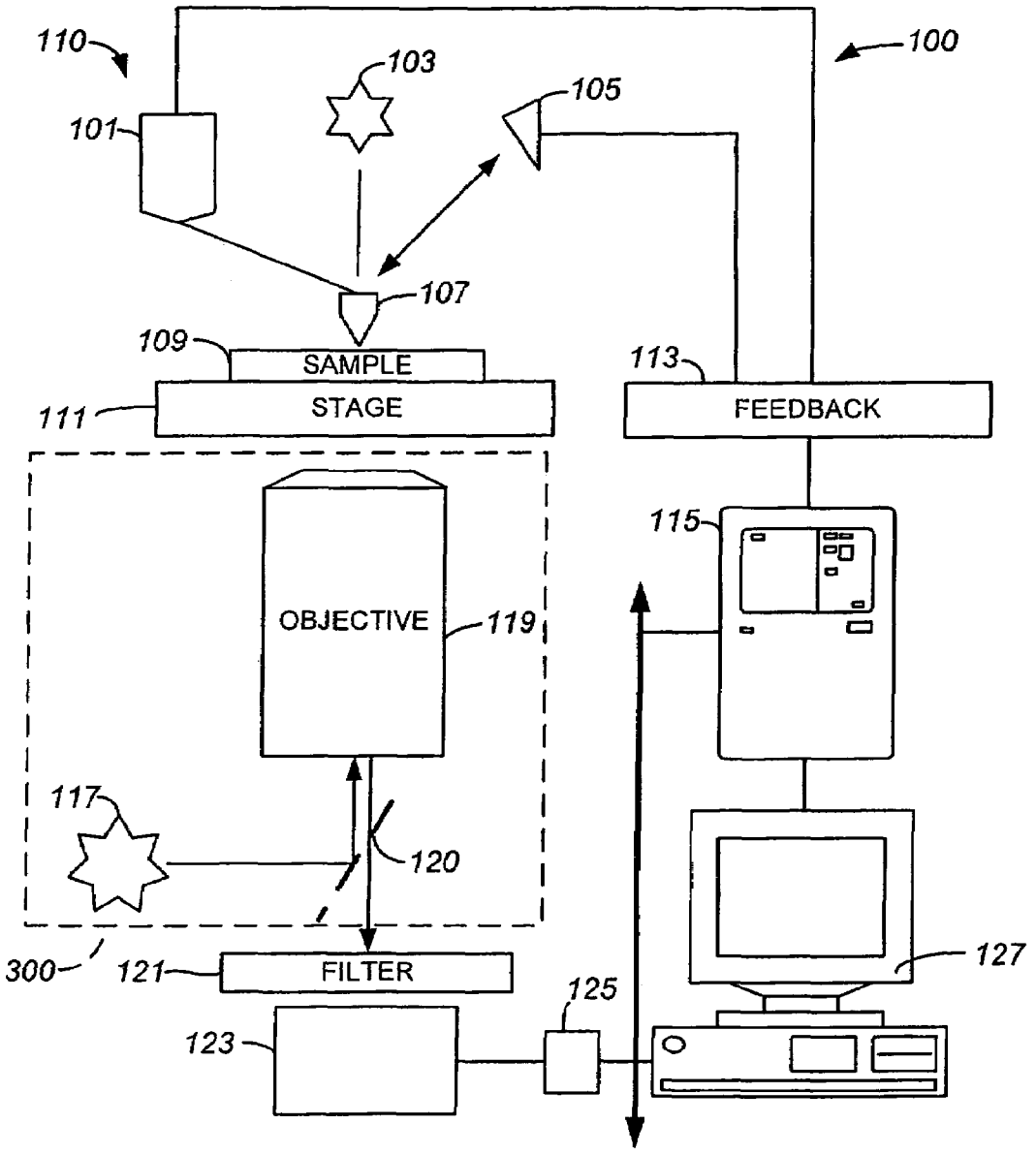
110
100
103
105
101
107
109
SAMPLE
113
111
STAGE
FEEDBACK
115
OBJECTIVE
119
117
120
300
121
FILTER
125
127
123

FIG. 3

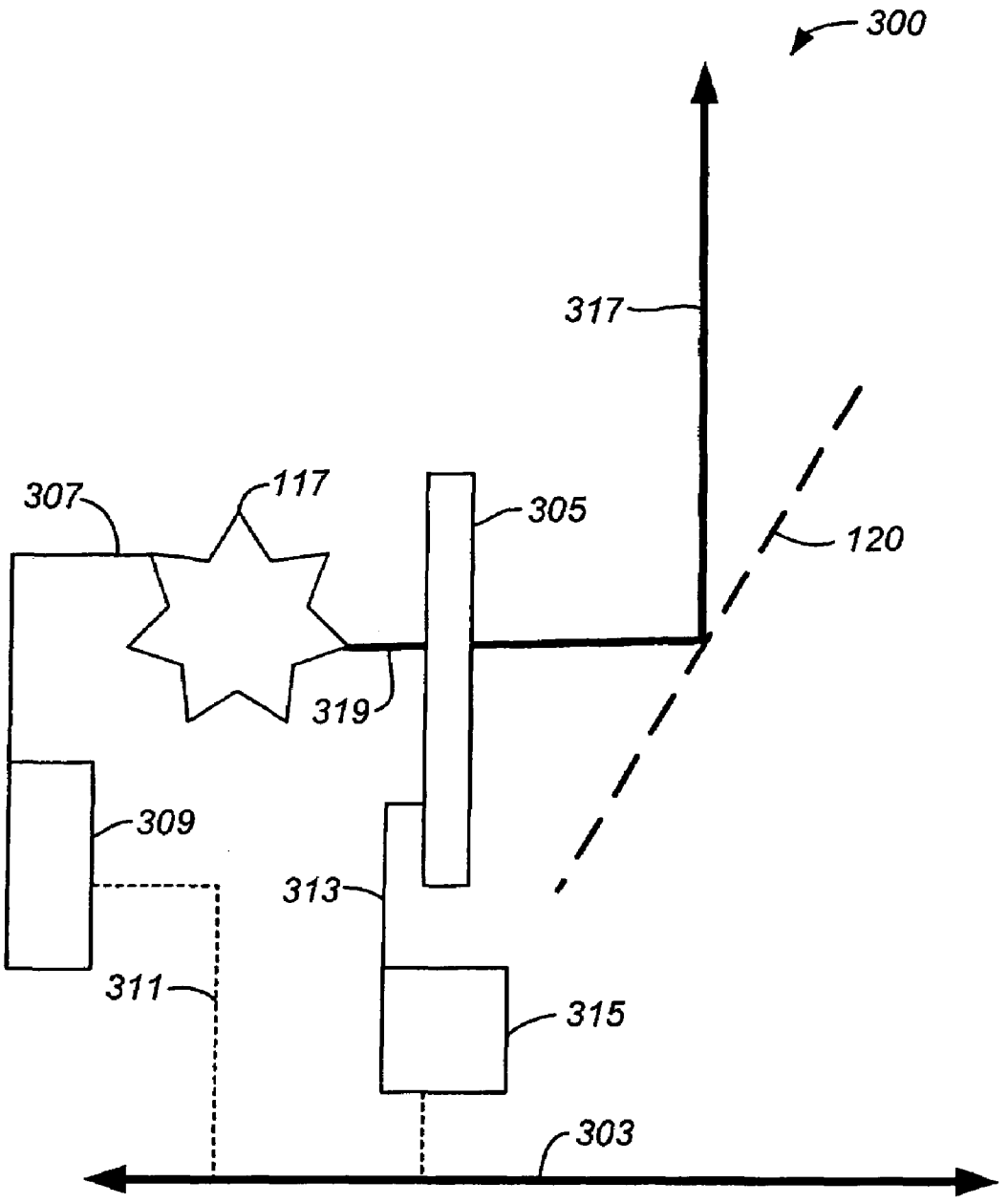

FIG. 3A

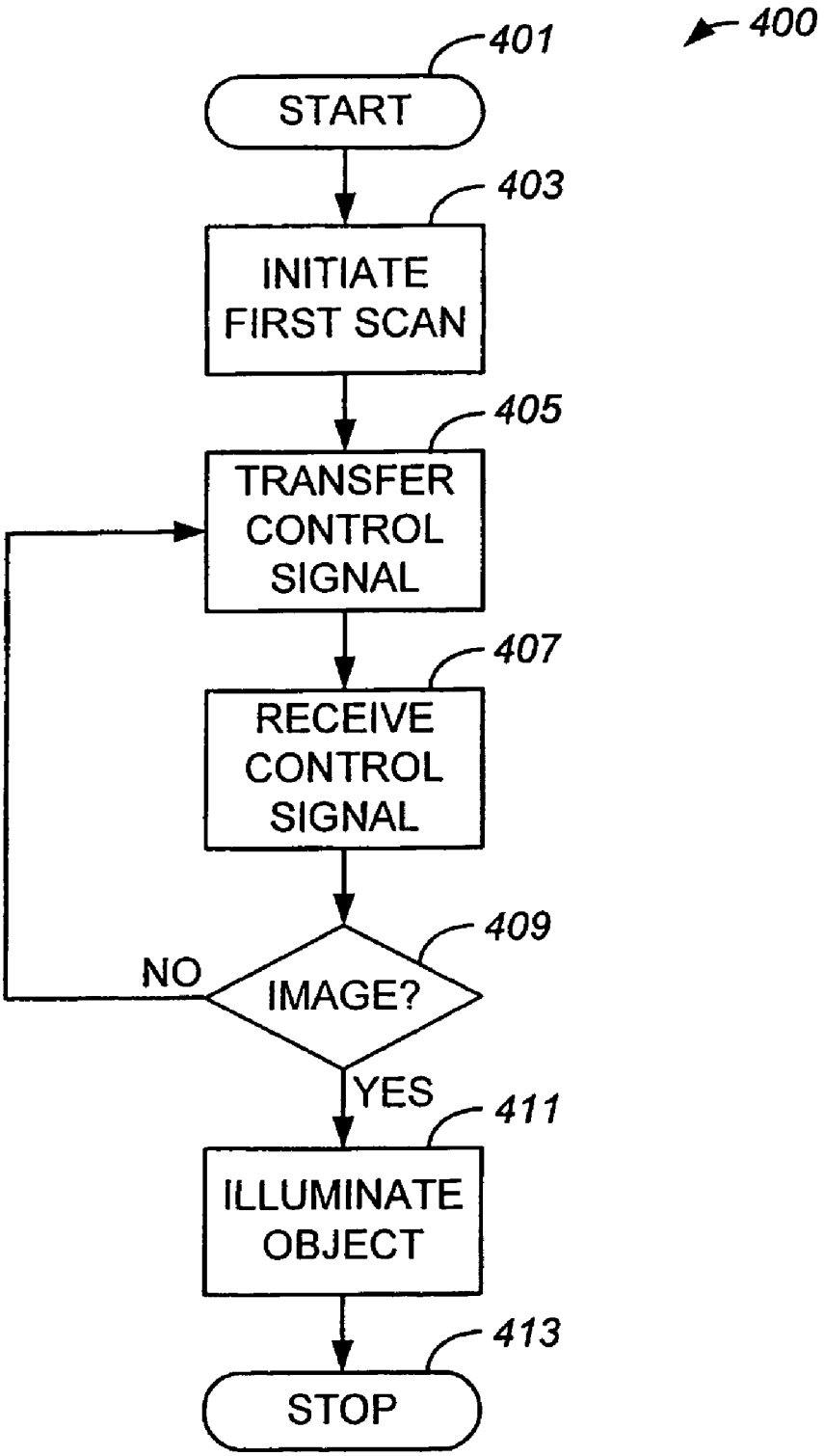
400
401
START
403
INITIATE FIRST SCAN
405
TRANSFER CONTROL SIGNAL
407
RECEIVE CONTROL SIGNAL
409
IMAGE?
NO
YES
411
ILLUMINATE OBJECT
413
STOP

FIG. 4

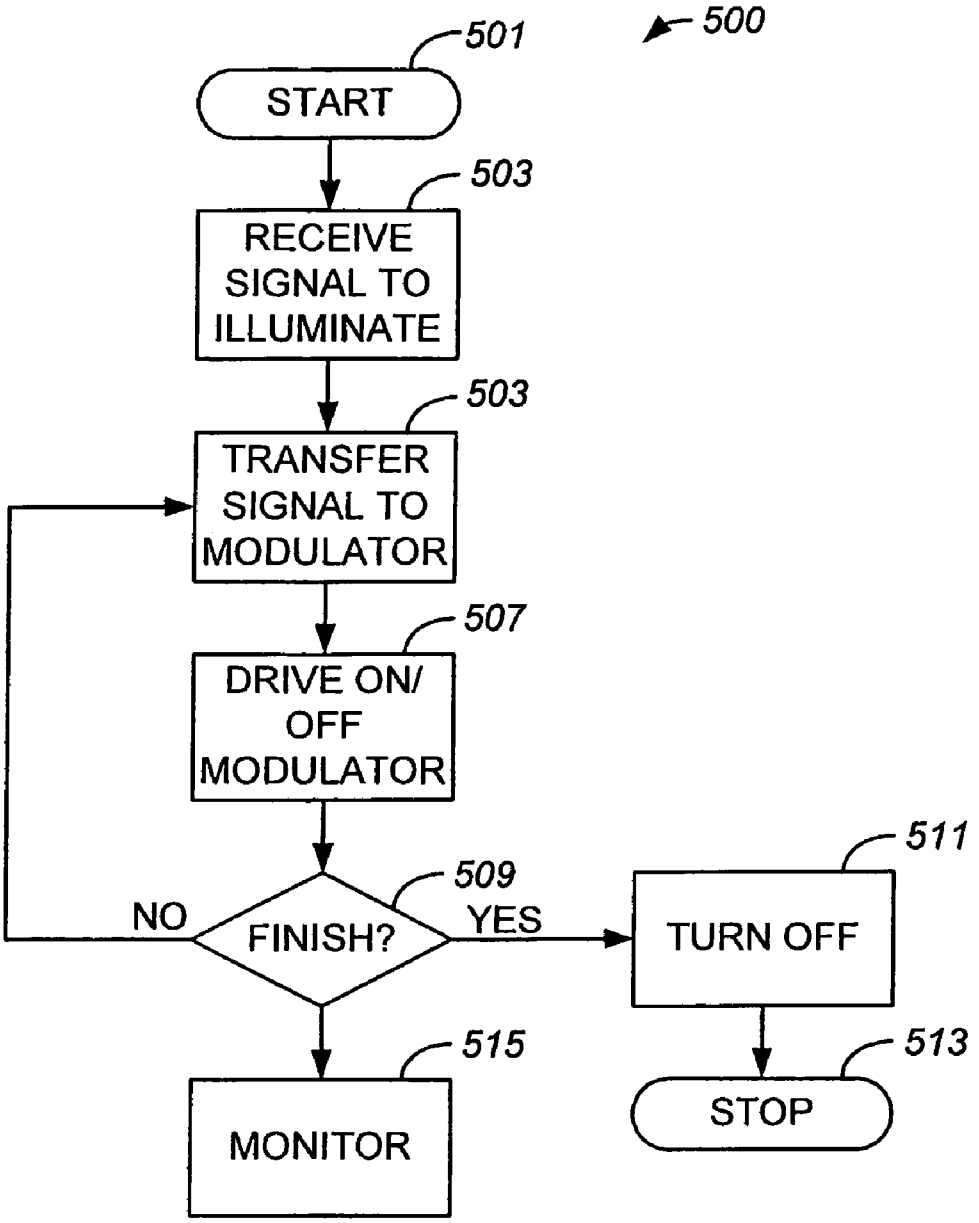
500
501
START
503
RECEIVE SIGNAL TO ILLUMINATE
503
TRANSFER SIGNAL TO MODULATOR
507
DRIVE ON/ OFF MODULATOR
509
FINISH?
NO
YES
511
TURN OFF
513
STOP
515
MONITOR

FIG. 5

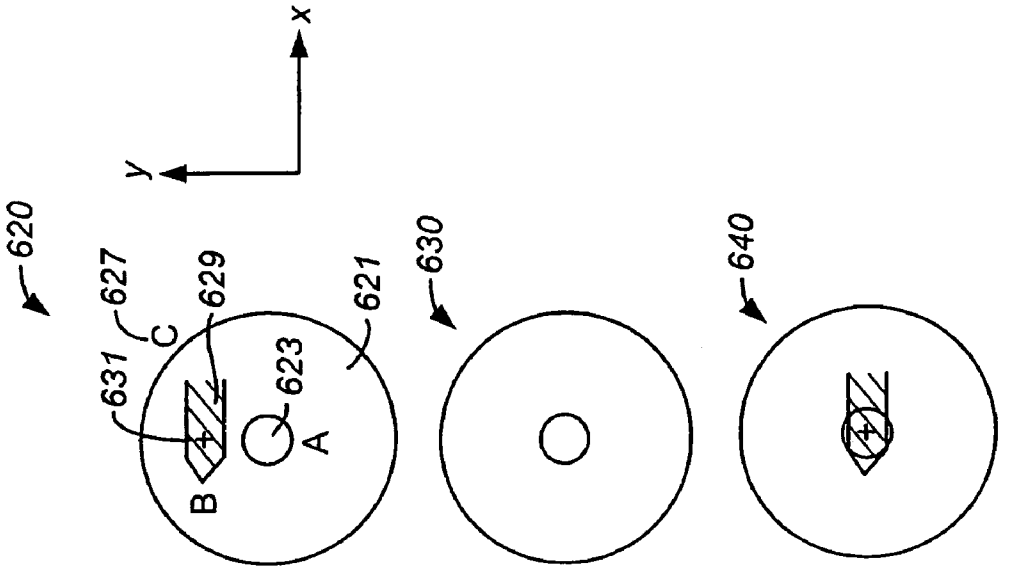
x
y
620
627
C
629
631
623
A
B
621
630
640

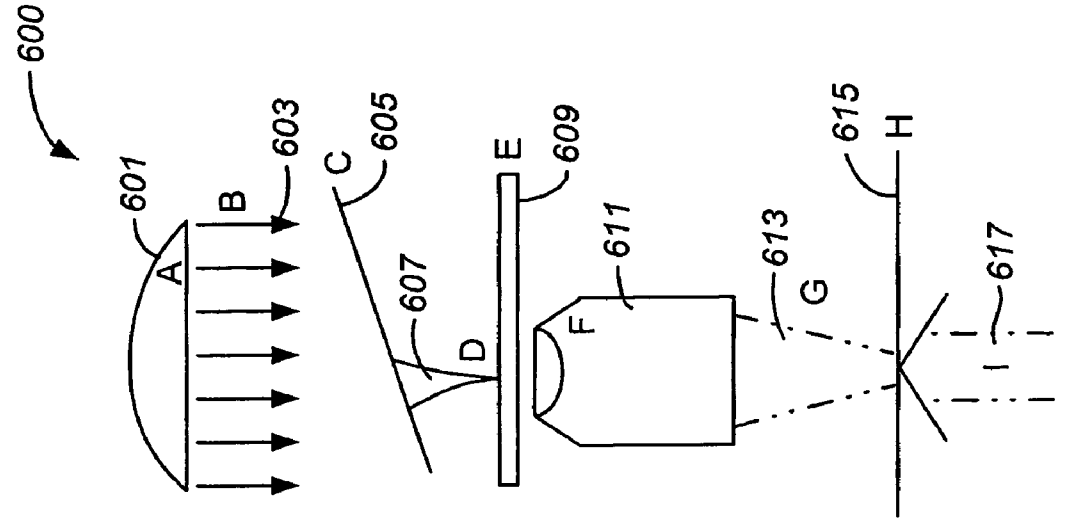
600
601
A
B
603
C
605
607
D
E
609
611
F
613
G
615
H
617
I
I

FIG. 6

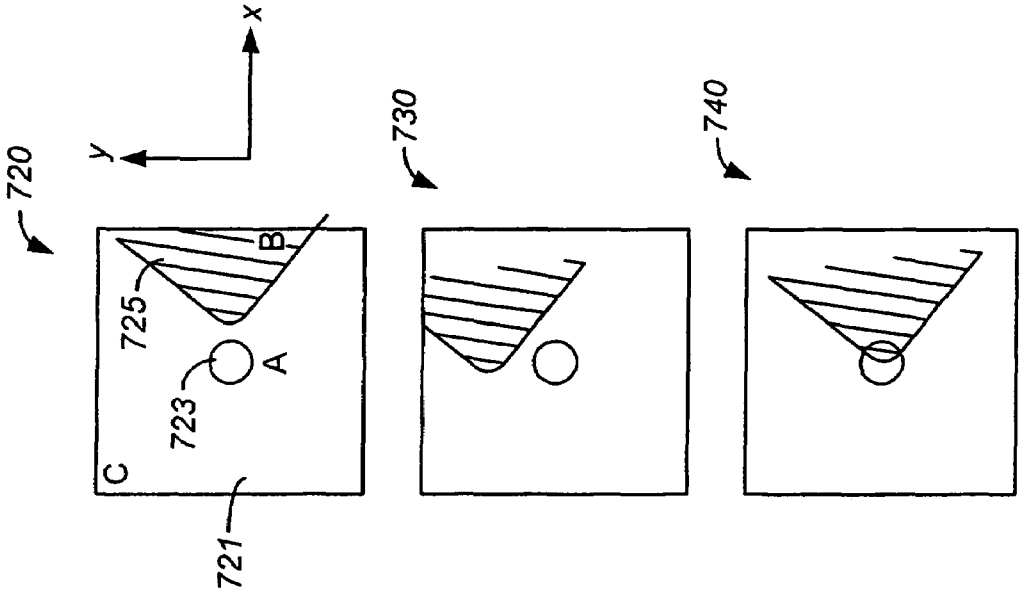
x
y
720
730
740
B
725
A
723
C
721

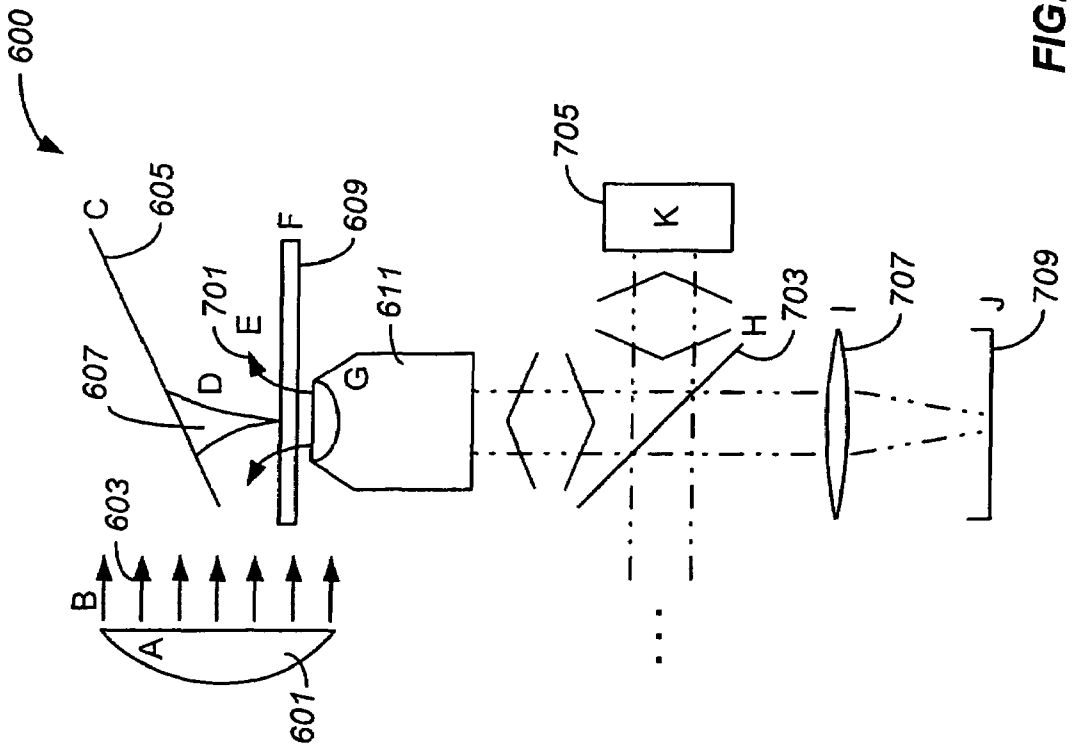
600
C
605
F
609
705
K
701
E
611
607
D
G
H
703
I
707
J
709
603
B
A
601

FIG. 7

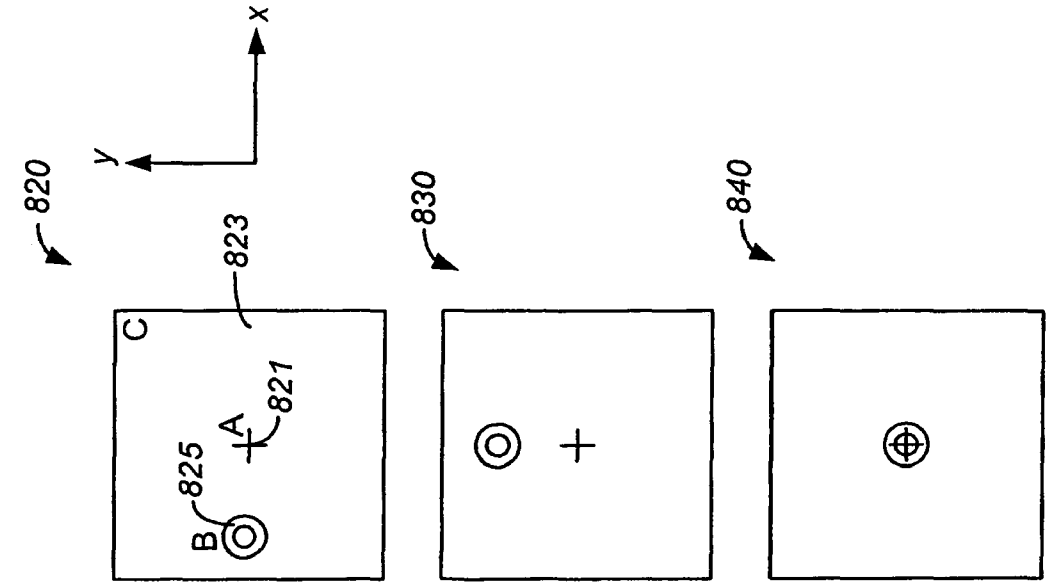
x
y
820
823
C
A
821
825
B
830
840

FIG. 8

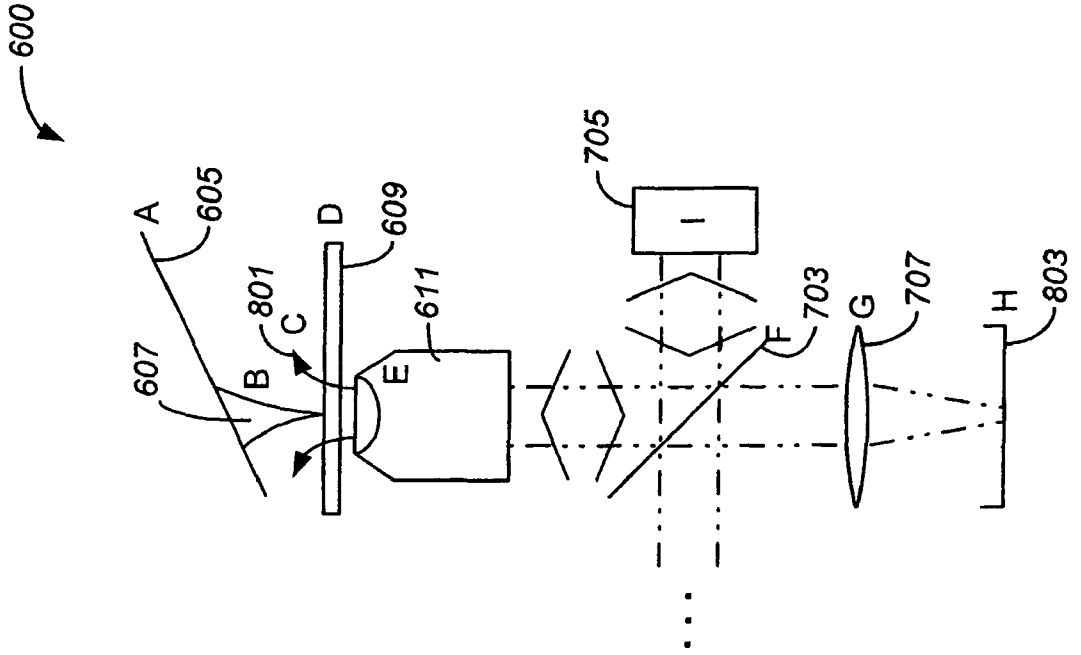
600
A
605
607
B
801
C
D
609
611
E
705
703
F
G
707
H
803

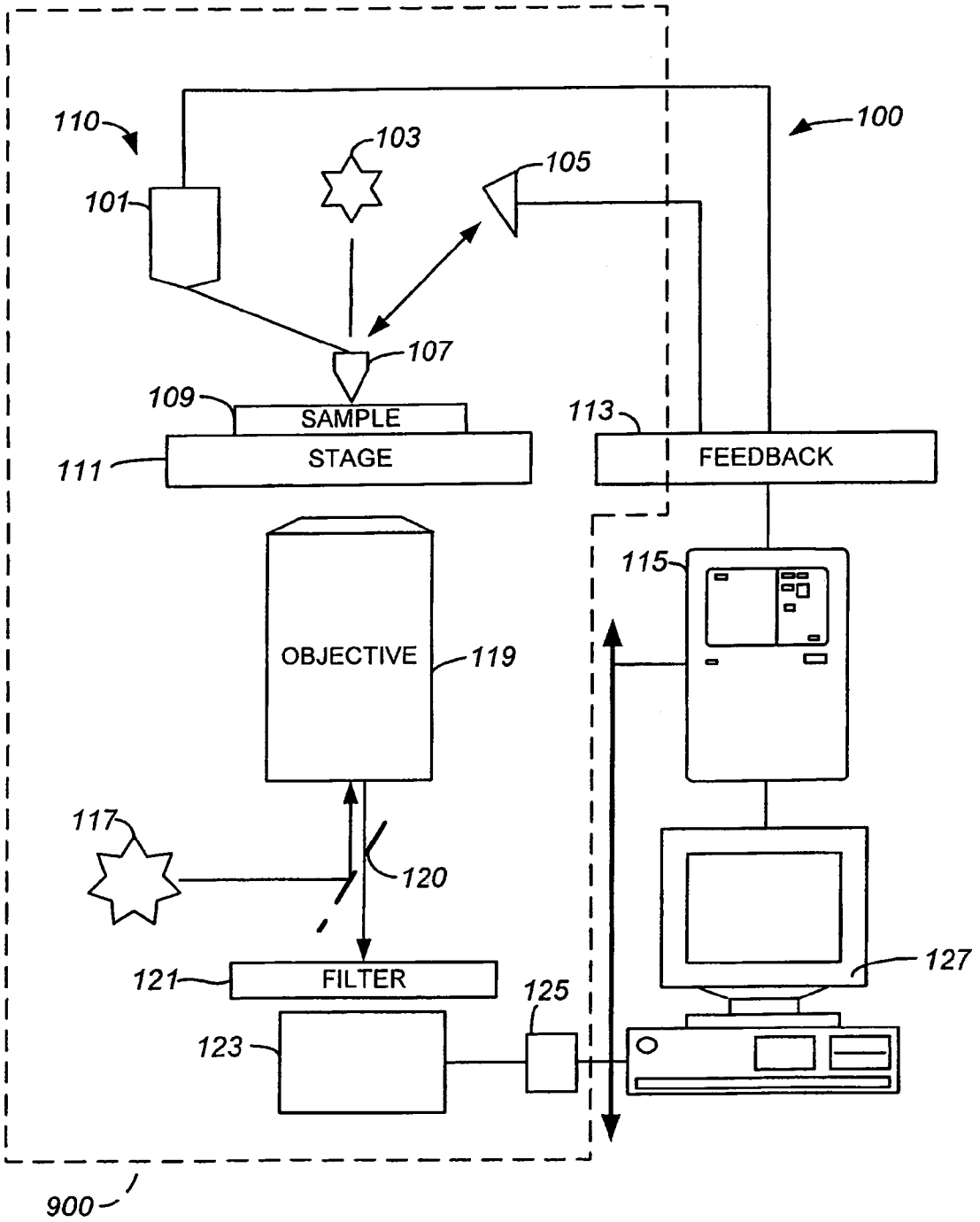
110
100
103
105
101
107
109
SAMPLE
113
111
STAGE
FEEDBACK
115
OBJECTIVE
119
117
120
121
FILTER
125
127
123
900

FIG. 9

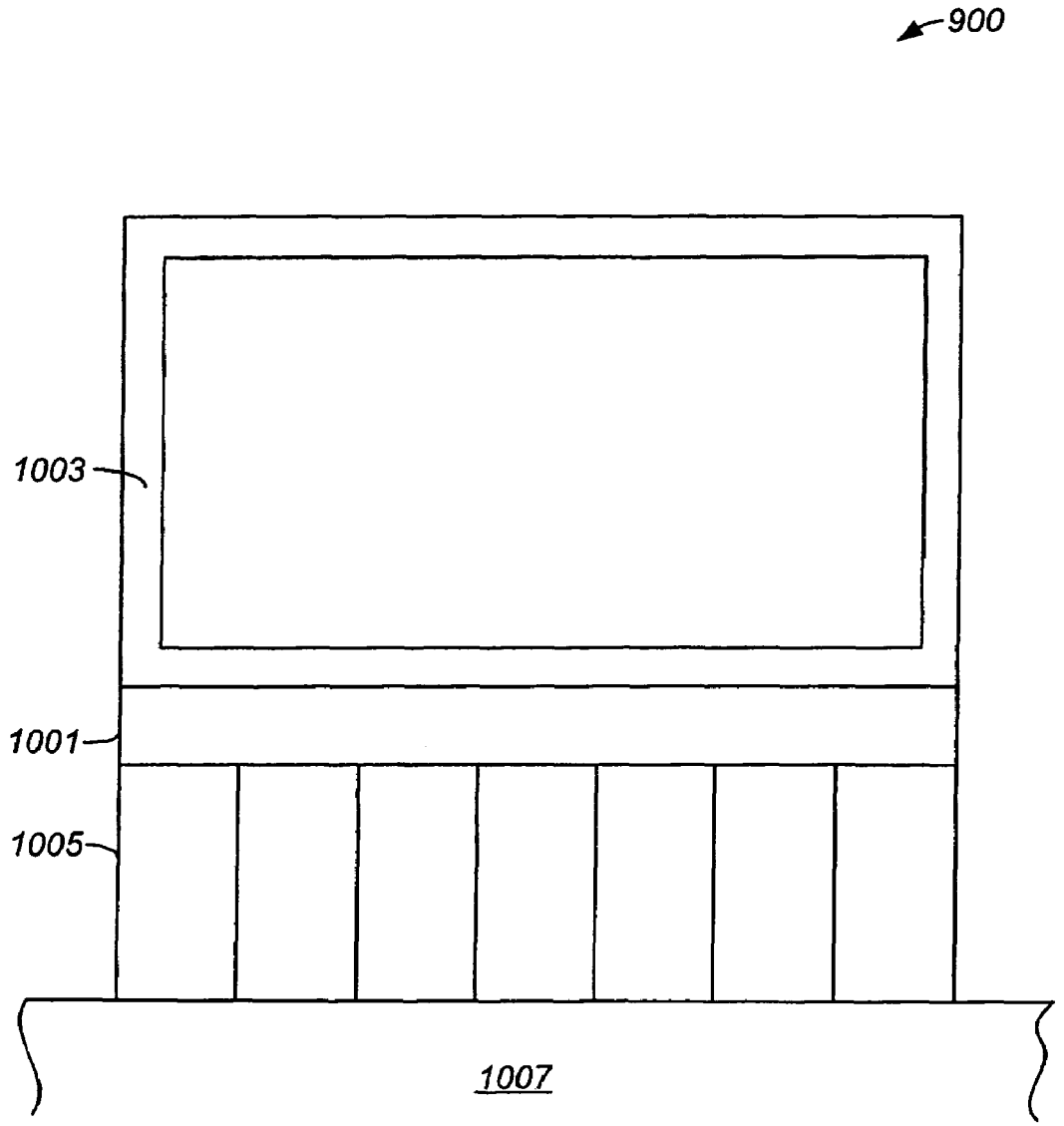

FIG. 10

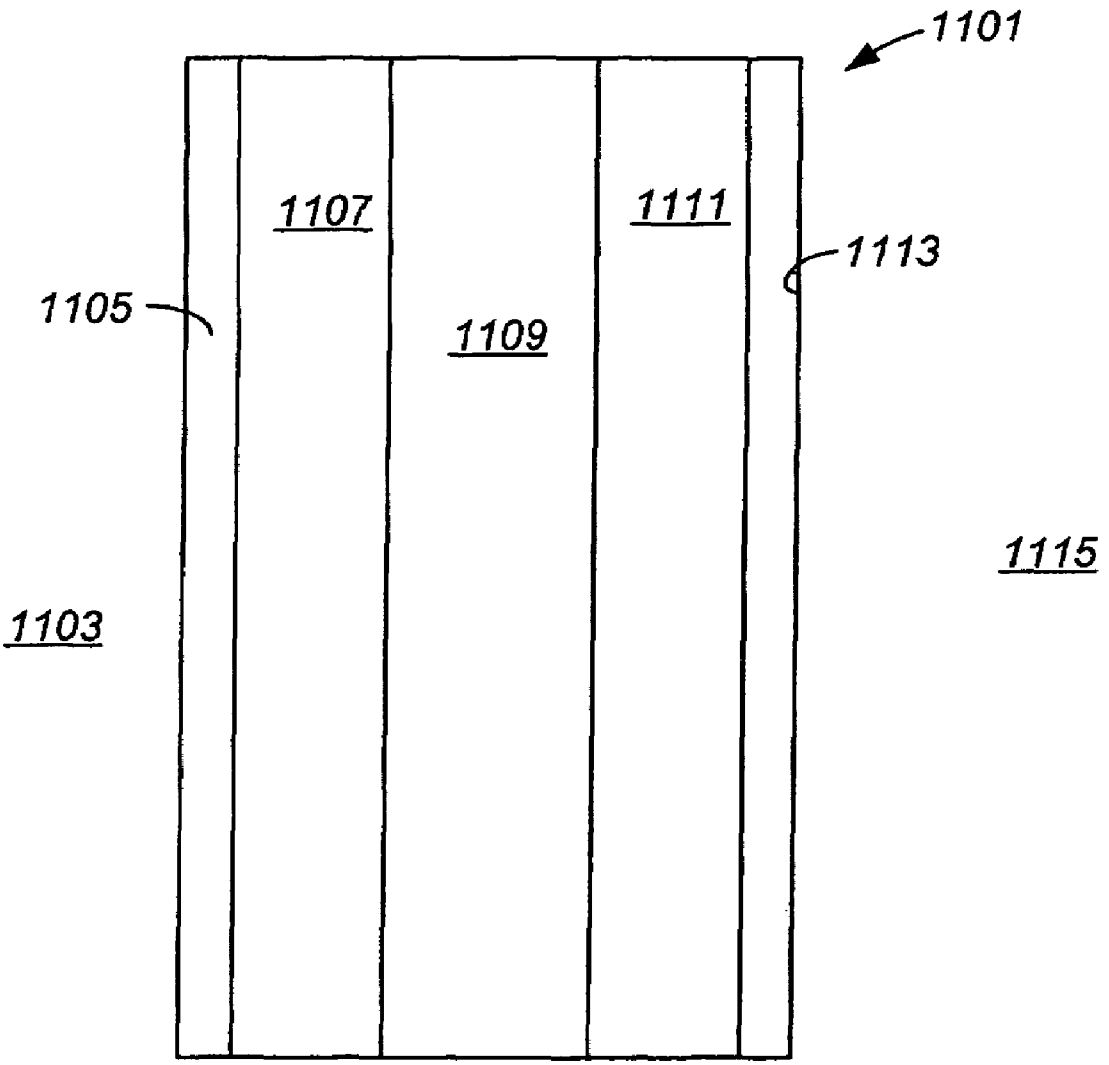

FIG. 11

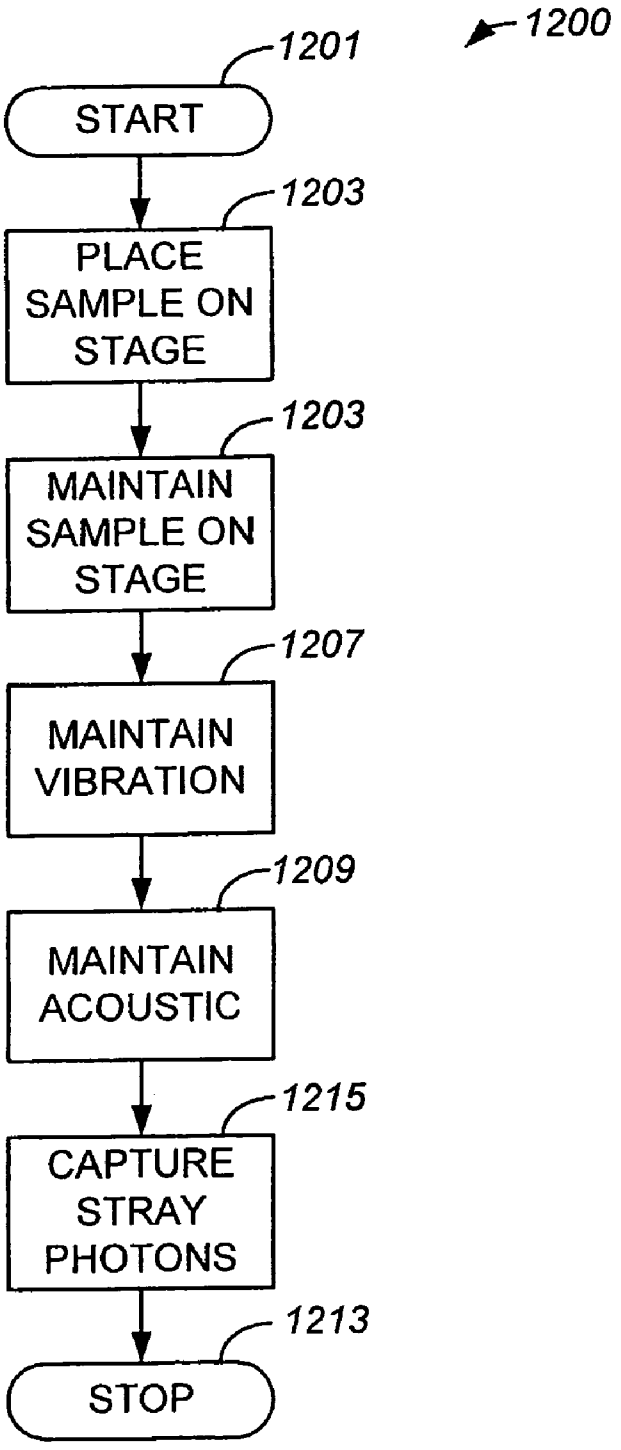
1200
1201
START
1203
PLACE SAMPLE ON STAGE
1203
MAINTAIN SAMPLE ON STAGE
1207
MAINTAIN VIBRATION
1209
MAINTAIN ACOUSTIC
1215
CAPTURE STRAY PHOTONS
1213
STOP

FIG. 12

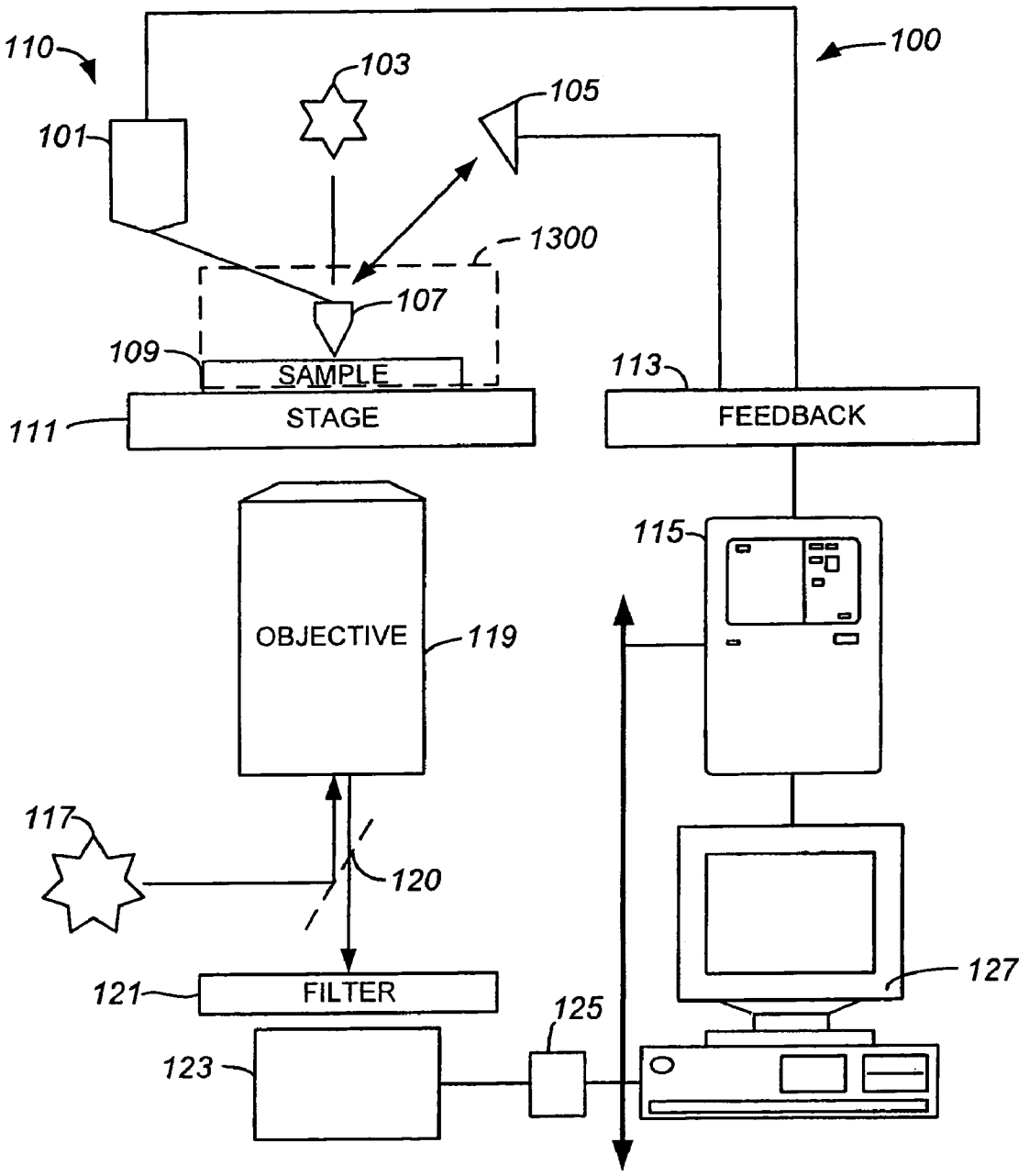
110
100
103
105
101
1300
107
109
SAMPLE
113
111
STAGE
FEEDBACK
115
OBJECTIVE
119
117
120
121
FILTER
125
127
123

FIG. 13

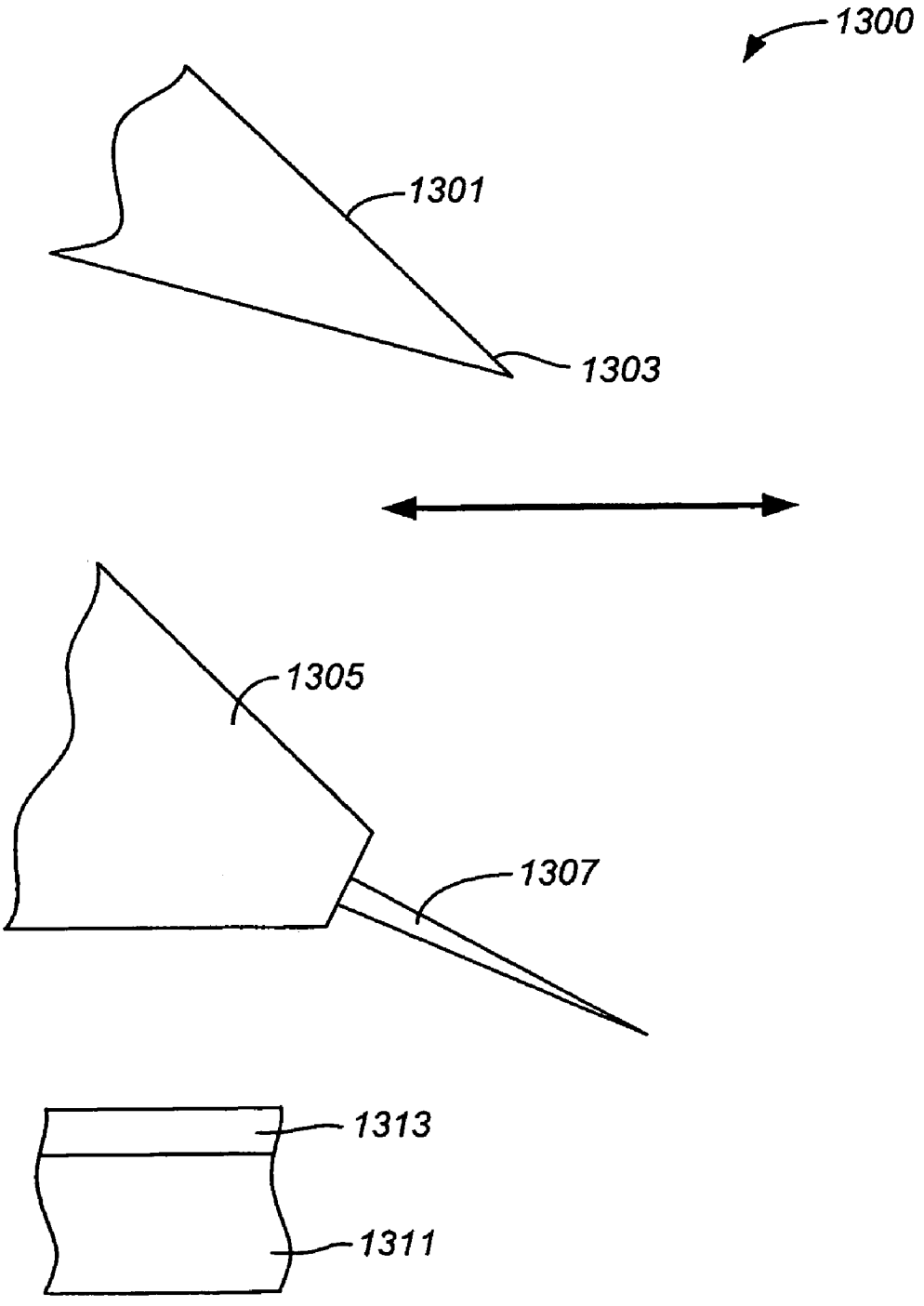

FIG. 14

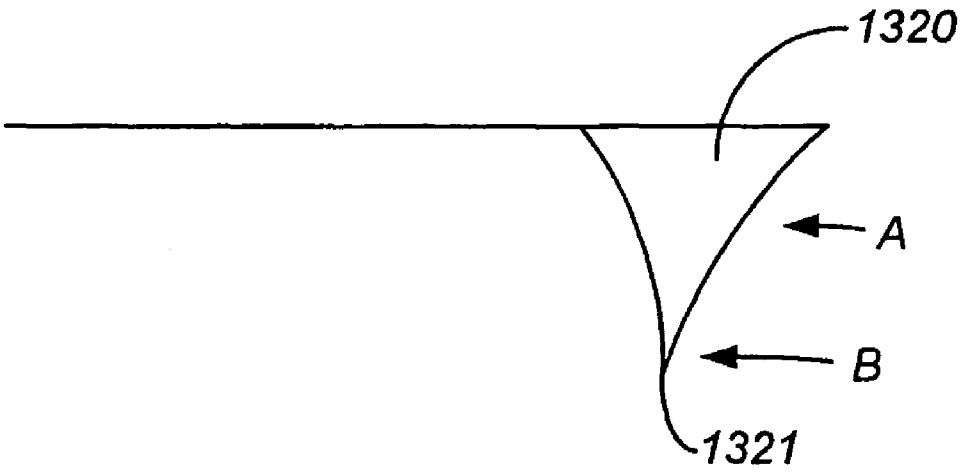

FIG. 14A

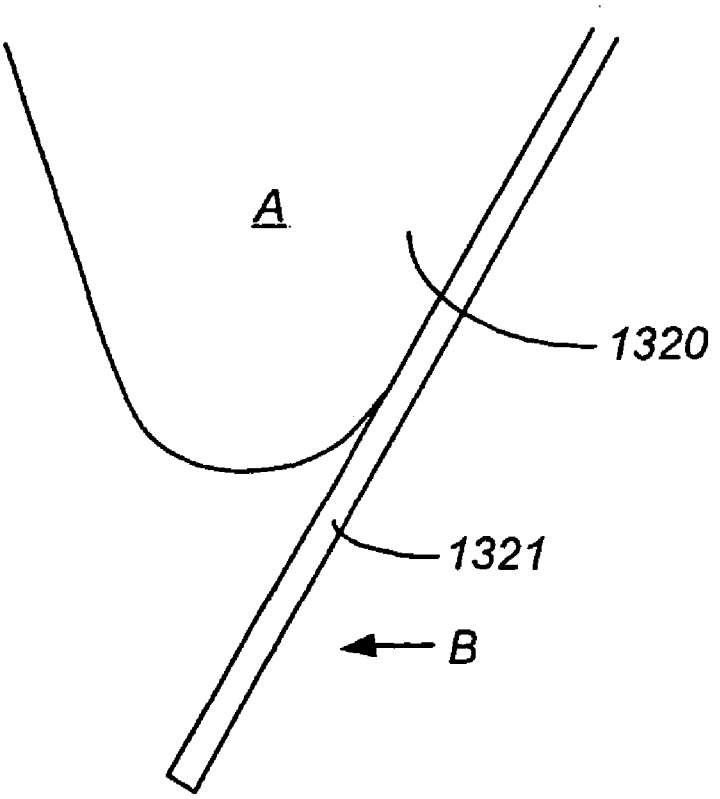

FIG. 14B

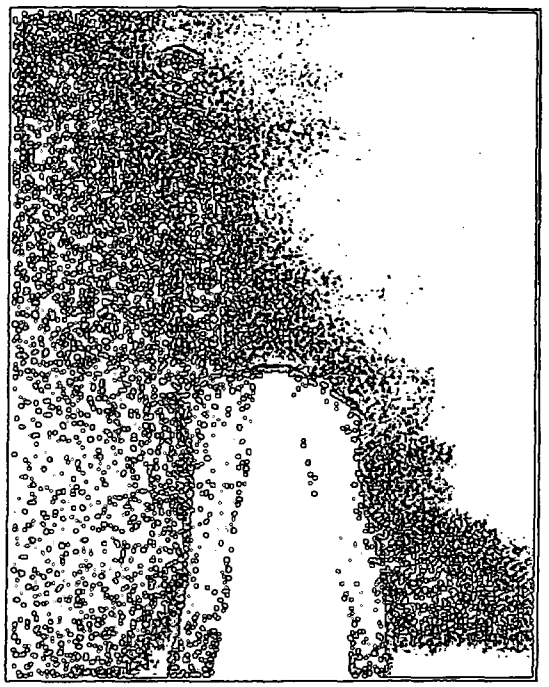

FIG. 14C

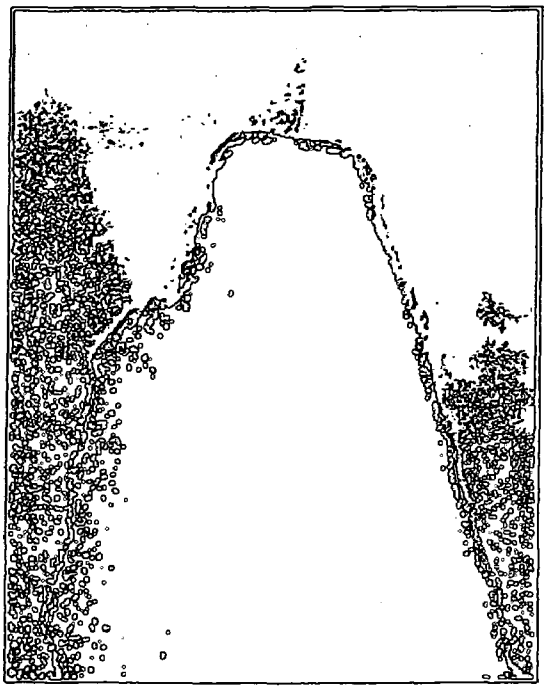

FIG. 14D

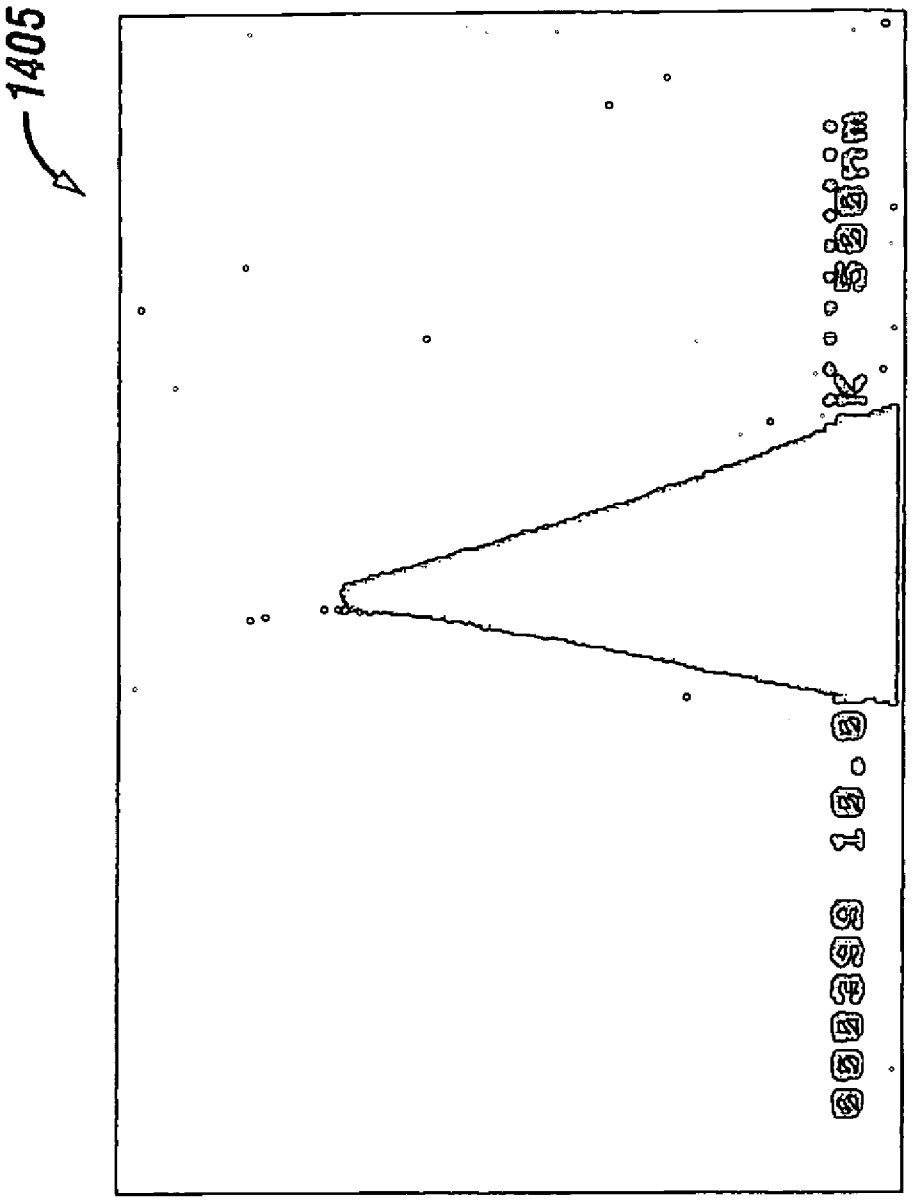

FIG. 14E

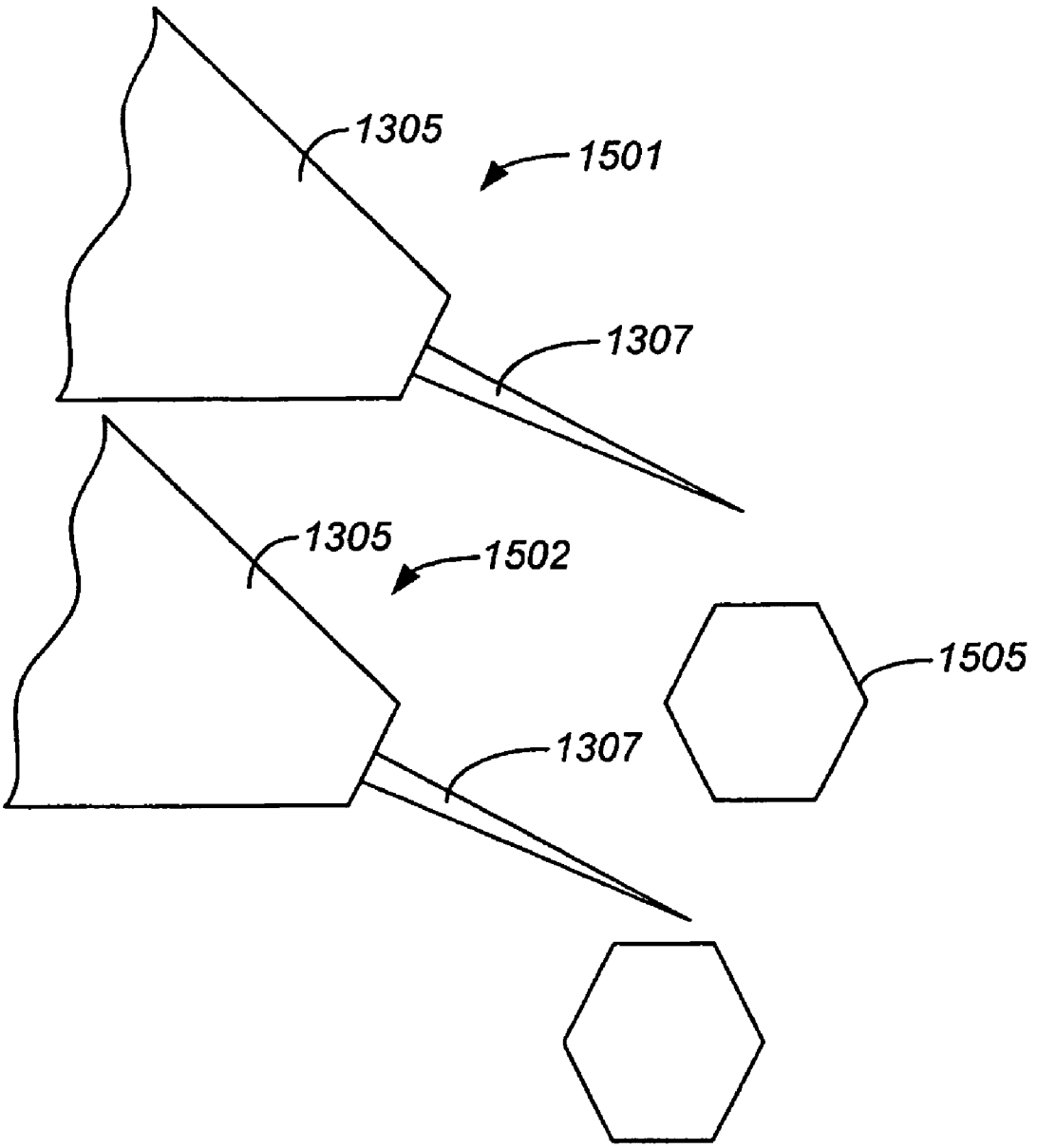

FIG. 15

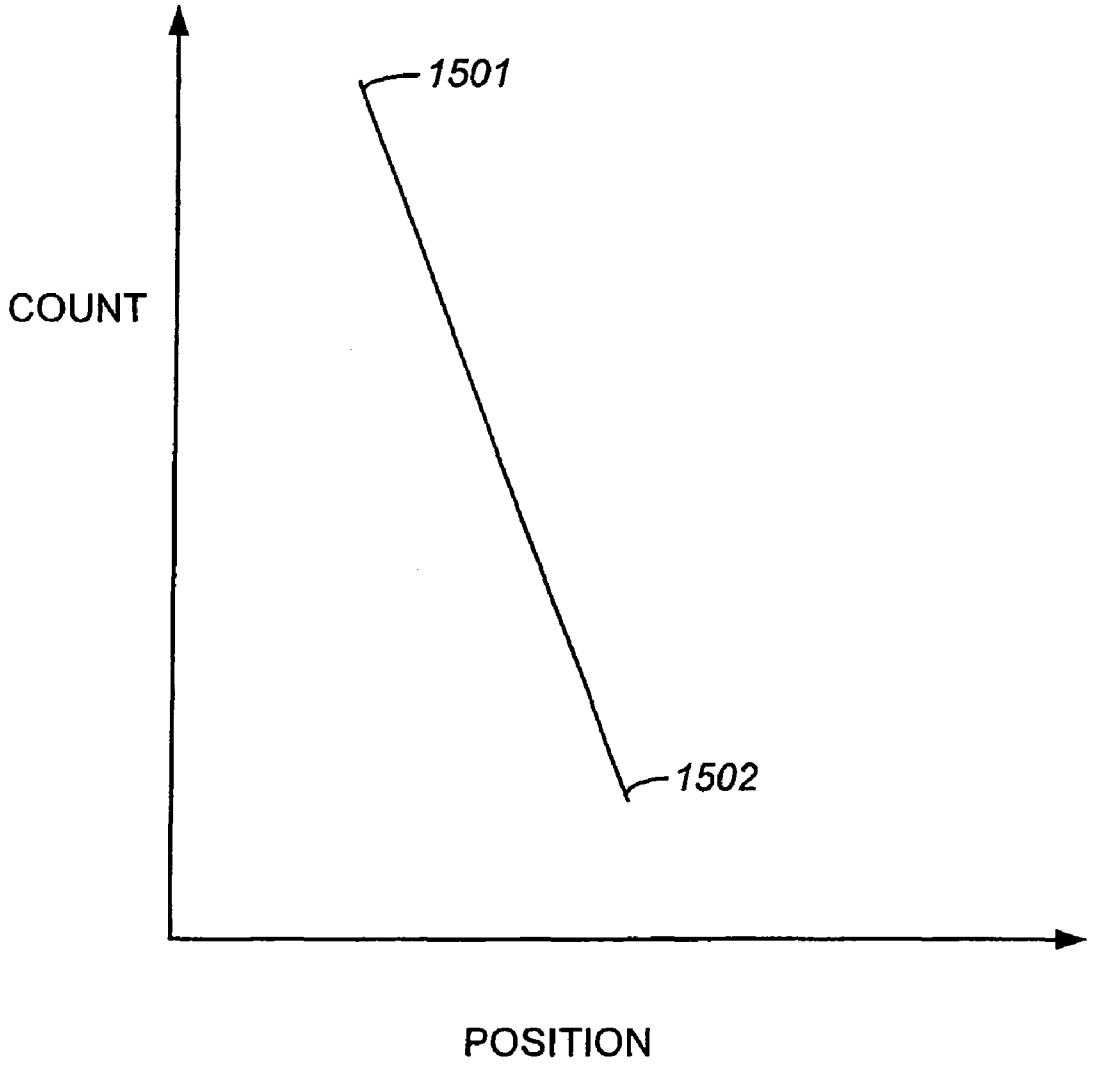

FIG. 16

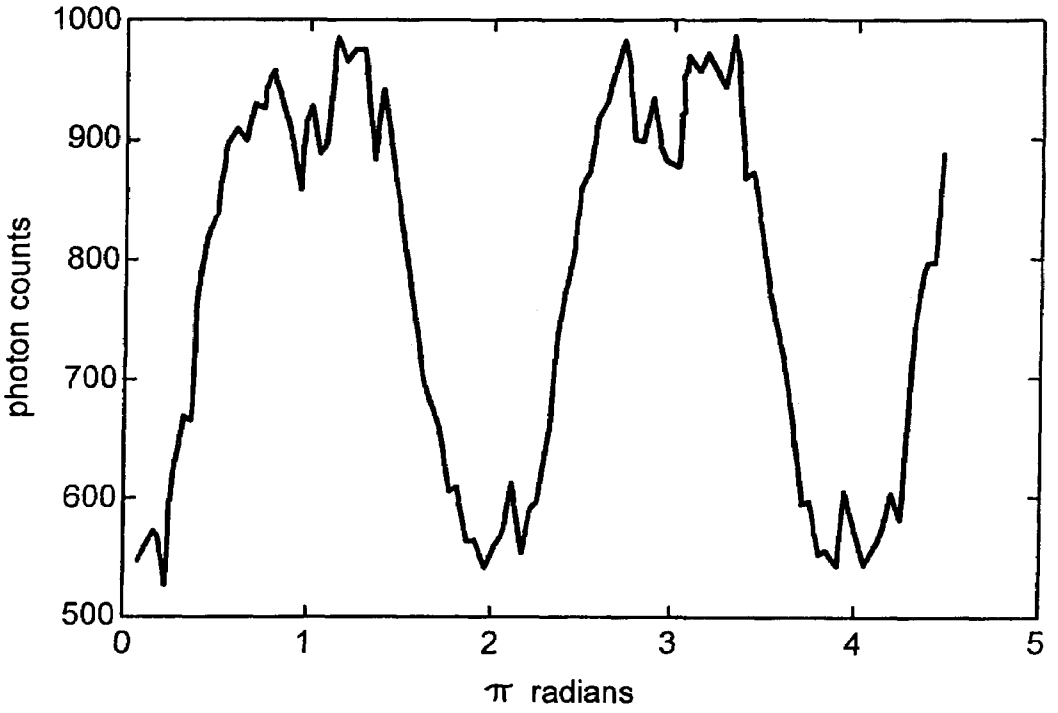

FIG. 17

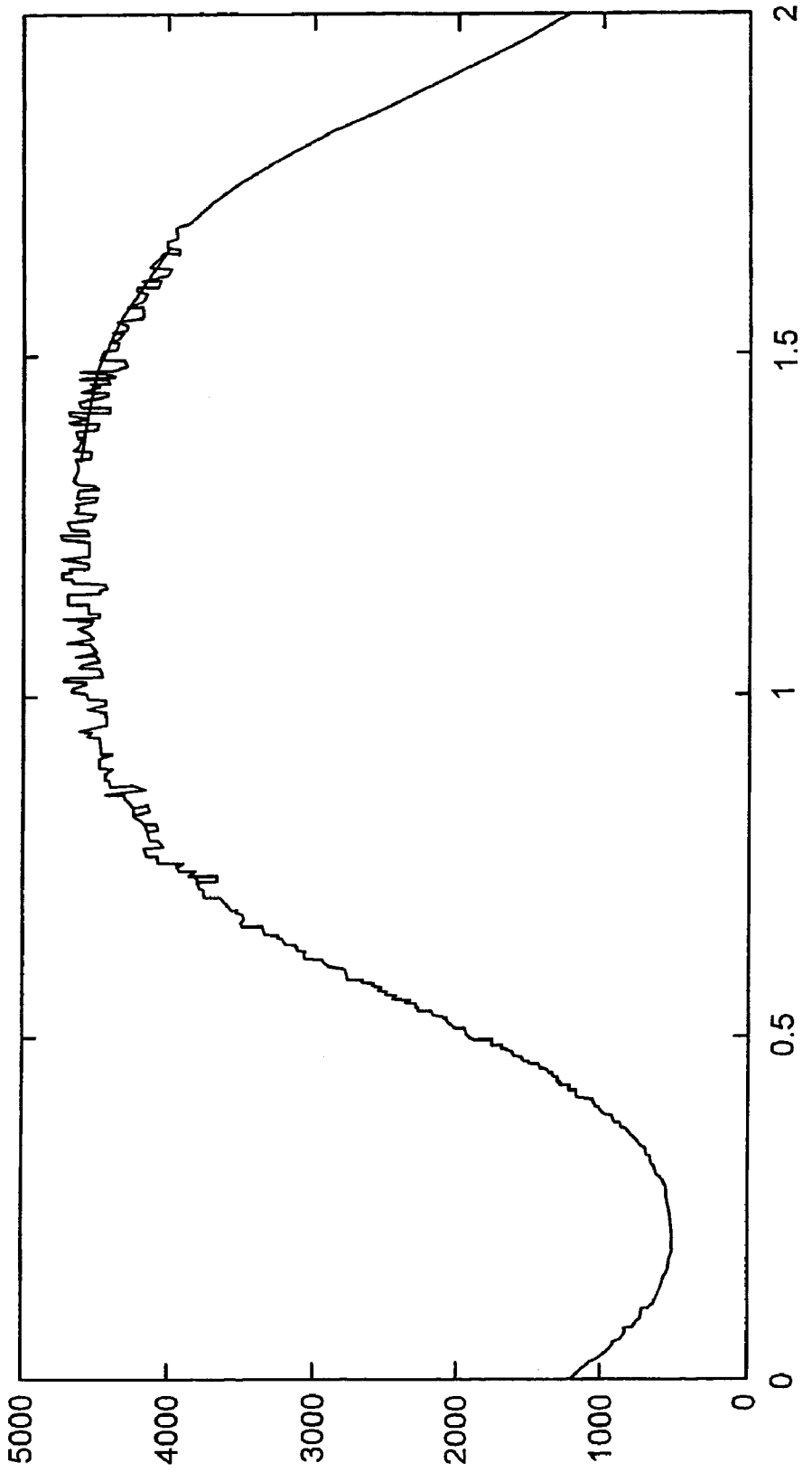

FIG. 18

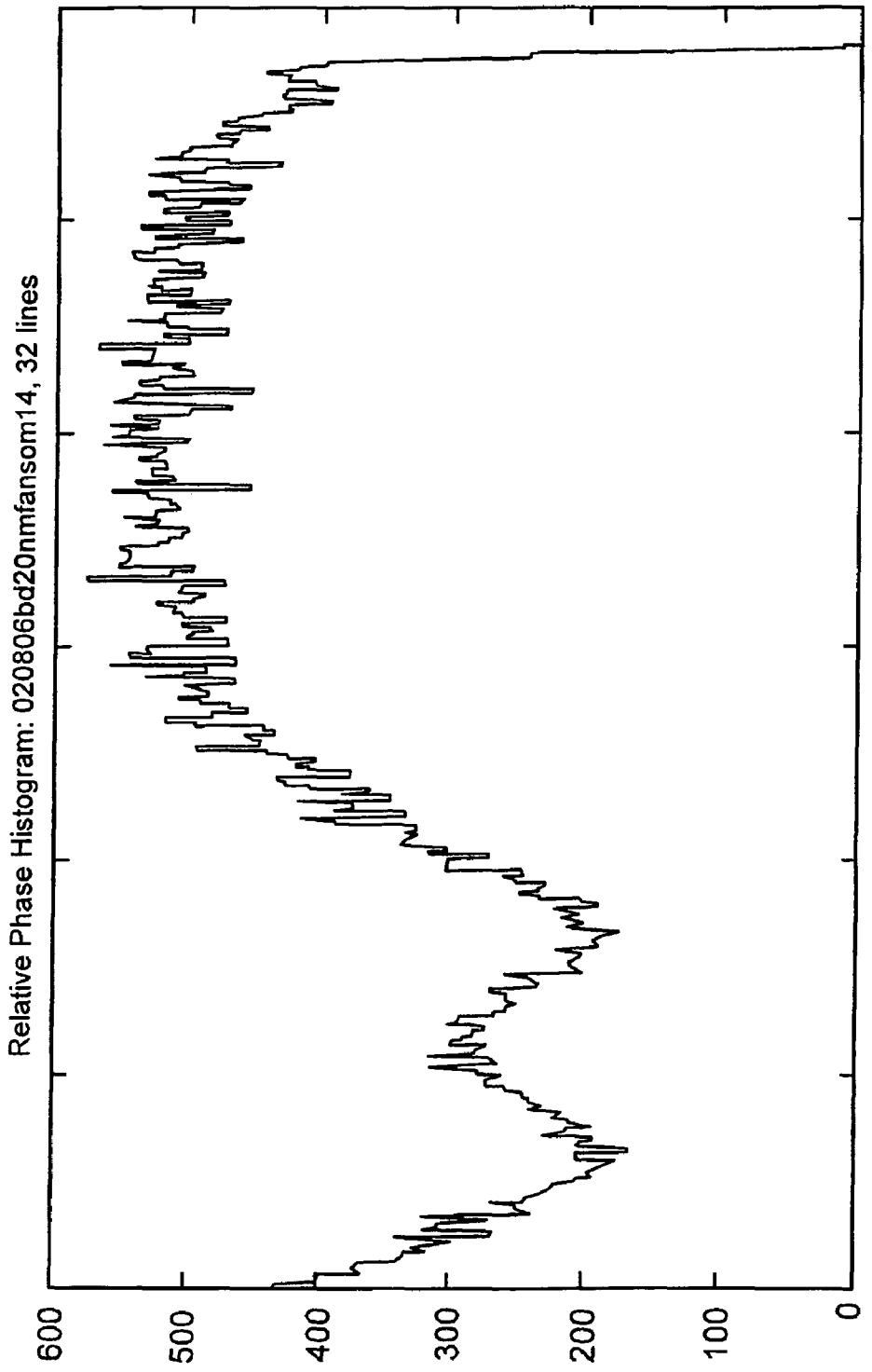
Relative Phase Histogram: 020806bd20nmfansom14, 32 lines
600
500
400
300
200
100
0

FIG. 19

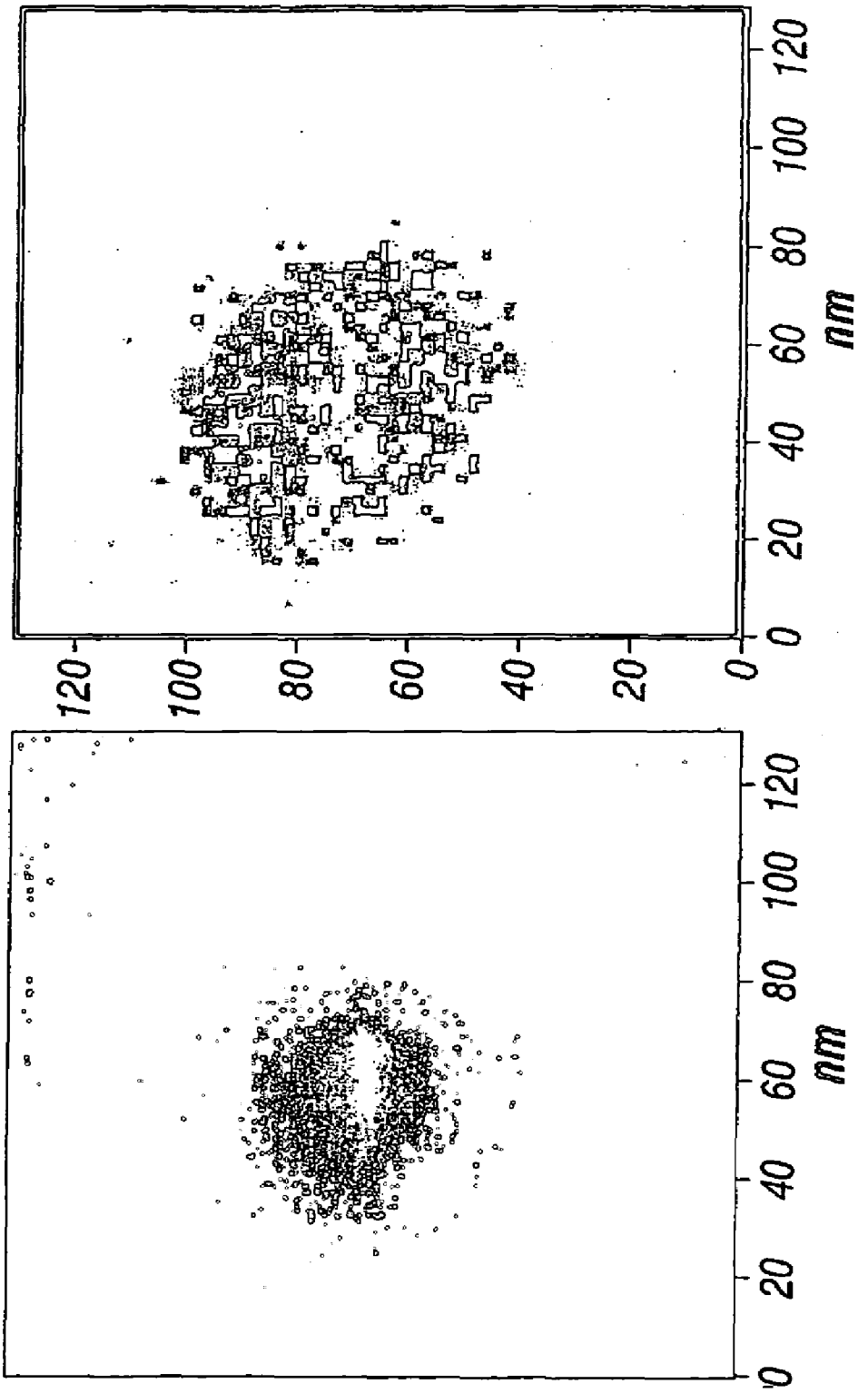

FIG. 20

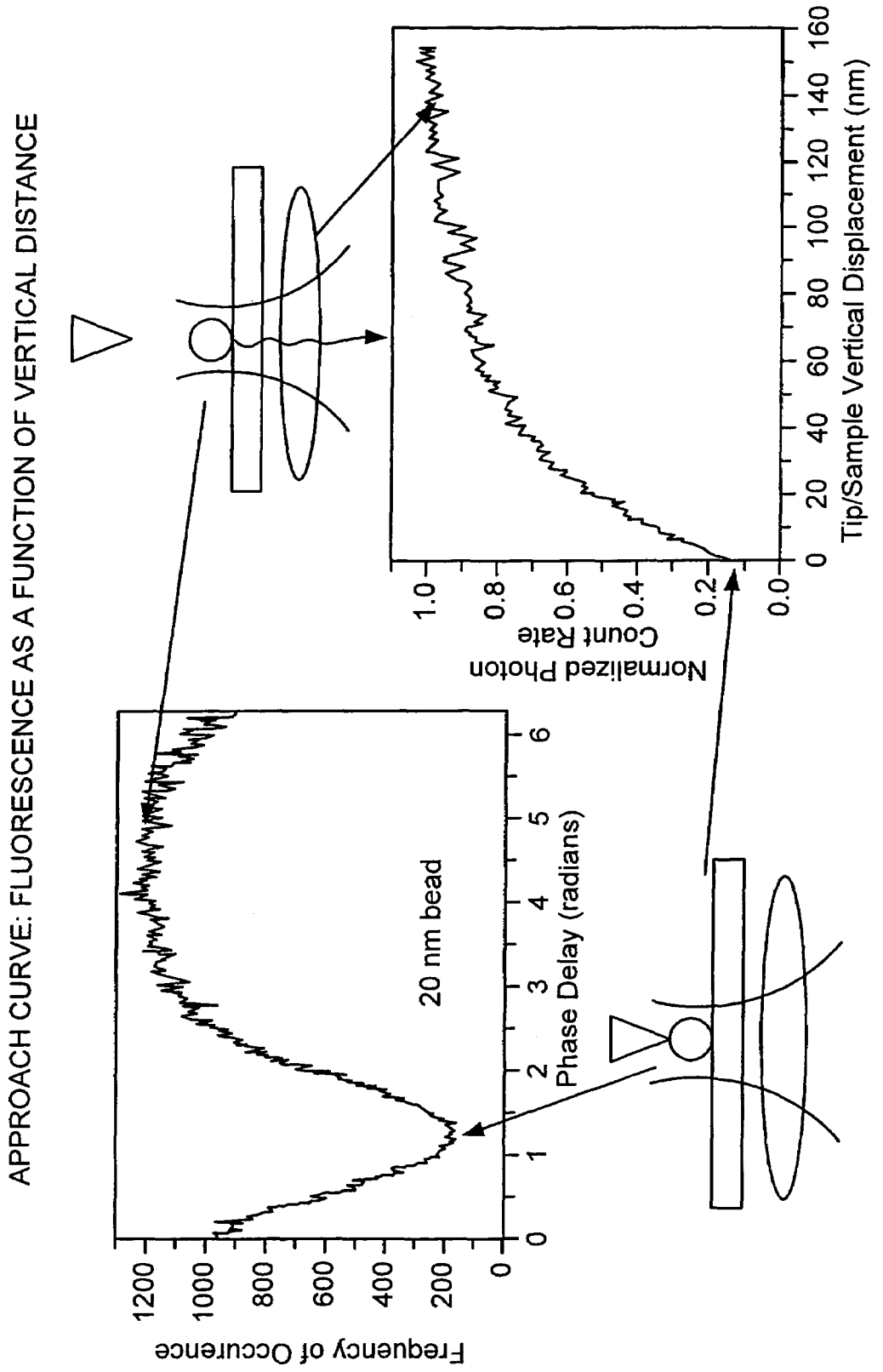
APPROACH CURVE: FLUORESCENCE AS A FUNCTION OF VERTICAL DISTANCE
Frequency of Occurrence
1200
1000
800
600
400
200
0
20 nm bead
0
1
2
3
4
5
6
Phase Delay (radians)
Normalized Photon Count Rate
1.0
0.8
0.6
0.4
0.2
0.0
0
20
40
60
80
100
120
140
160
Tip/Sample Vertical Displacement (nm)

FIG. 20A

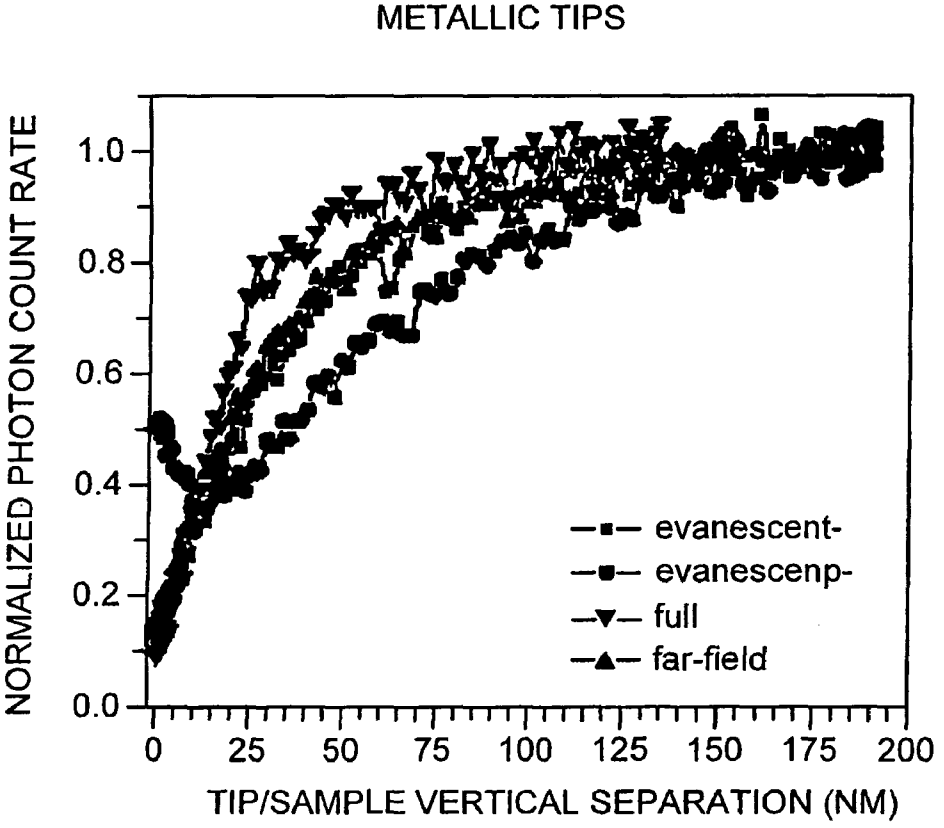

- PLATINUM-IRIDIUM COATED TIPS (COMMERCIAL)
- 85-90% SUPPRESSION OF FLUORESCENCE
- PARTIAL RECOVERY OF FLUORESCENCE FOR *P*-POLARIZATION

FIG. 20B

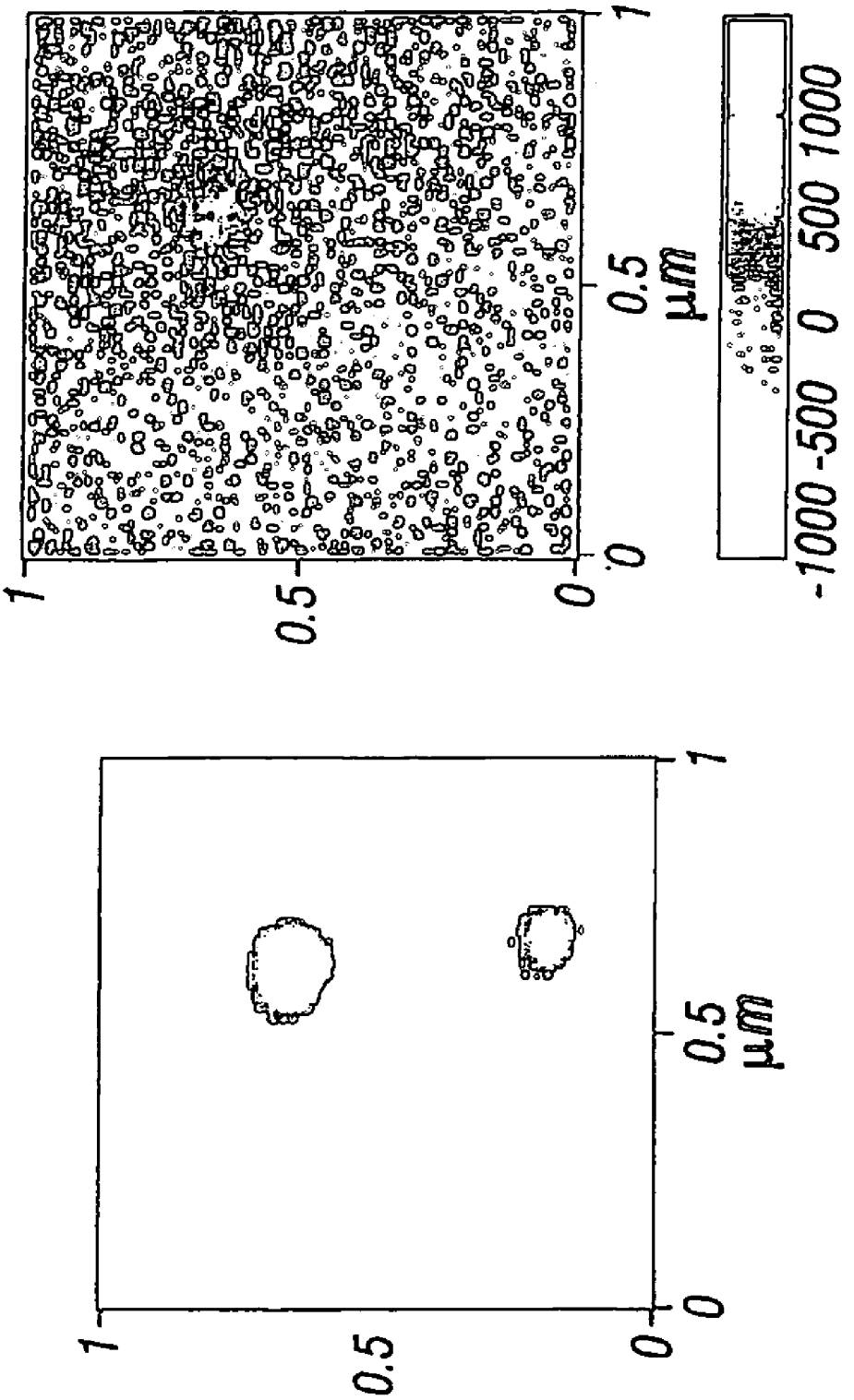

FIG. 21

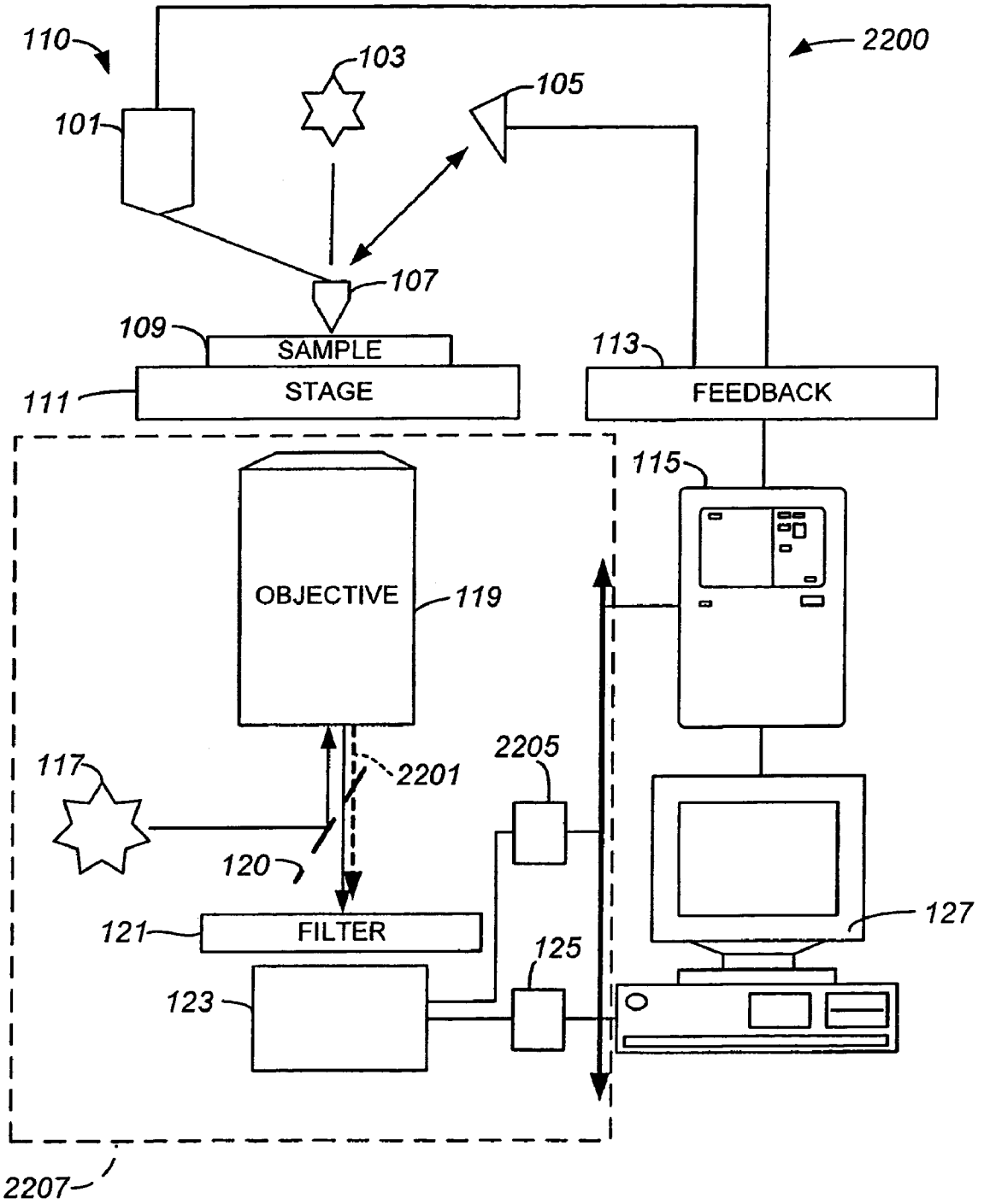
110
103
105
2200
101
107
109
SAMPLE
113
111
STAGE
FEEDBACK
115
OBJECTIVE
119
117
2201
2205
120
121
FILTER
125
127
123
2207

FIG. 22

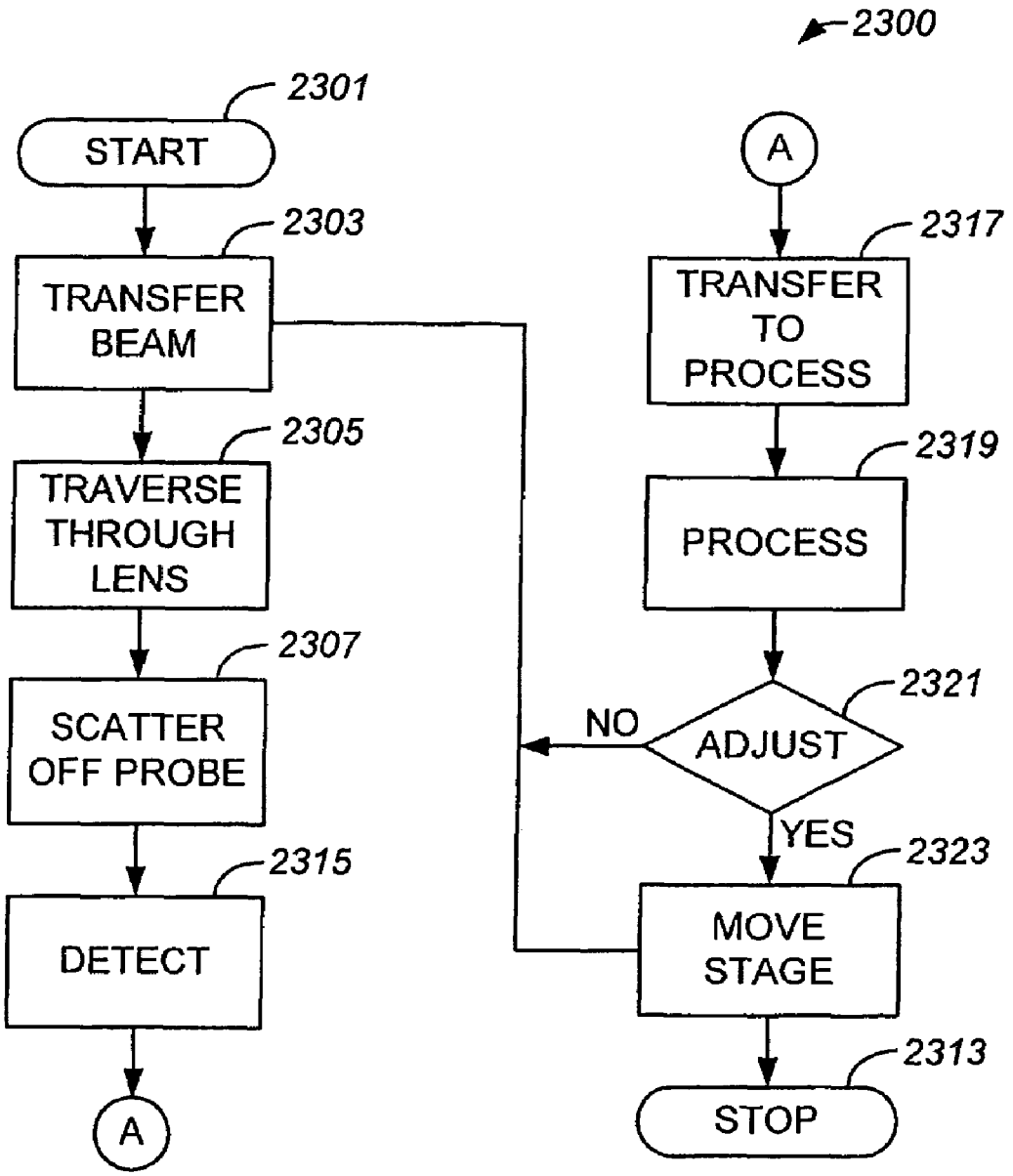
2300
2301
START
2303
TRANSFER BEAM
2305
TRAVERSE THROUGH LENS
2307
SCATTER OFF PROBE
2315
DETECT
A
A
2317
TRANSFER TO PROCESS
2319
PROCESS
2321
ADJUST
NO
YES
2323
MOVE STAGE
2313
STOP

FIG. 23

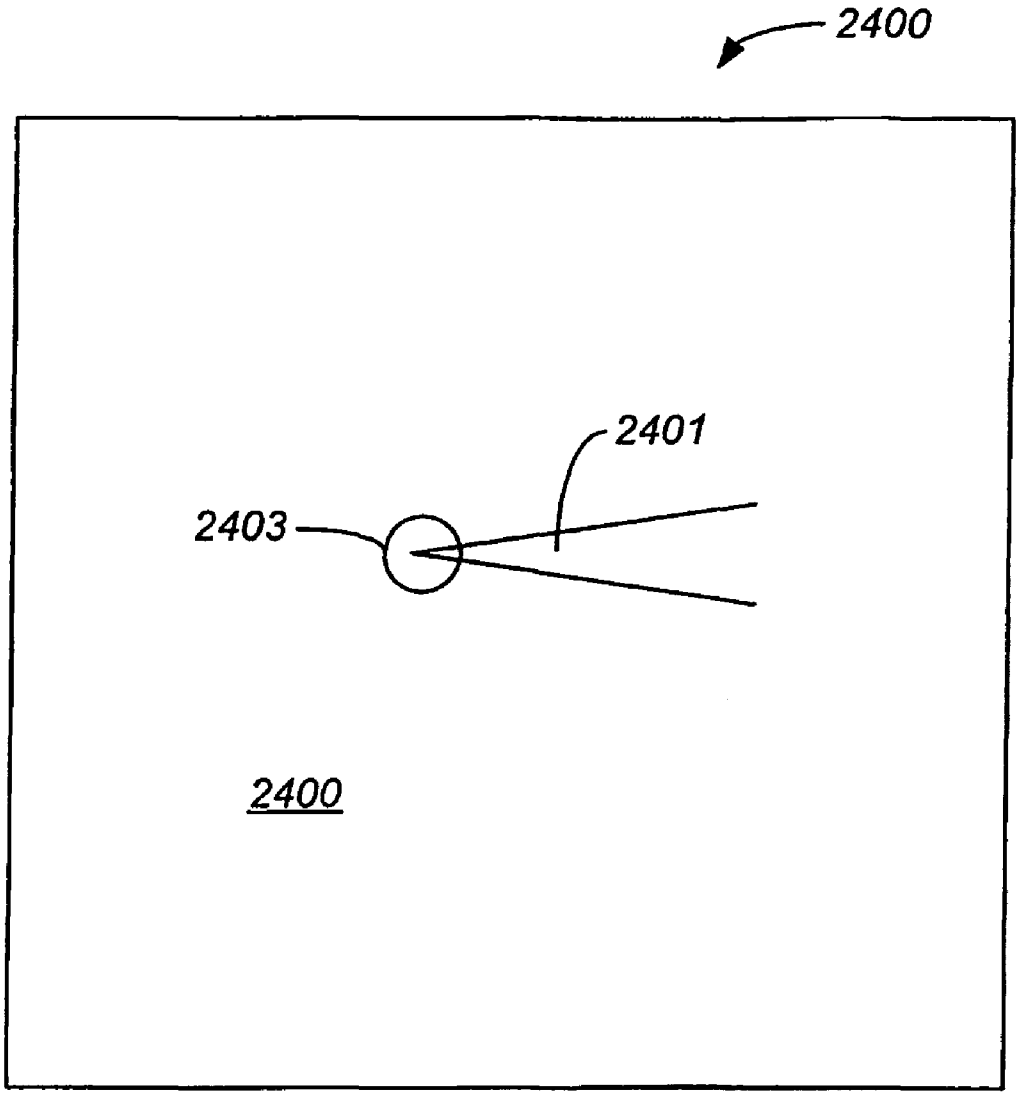

FIG. 24

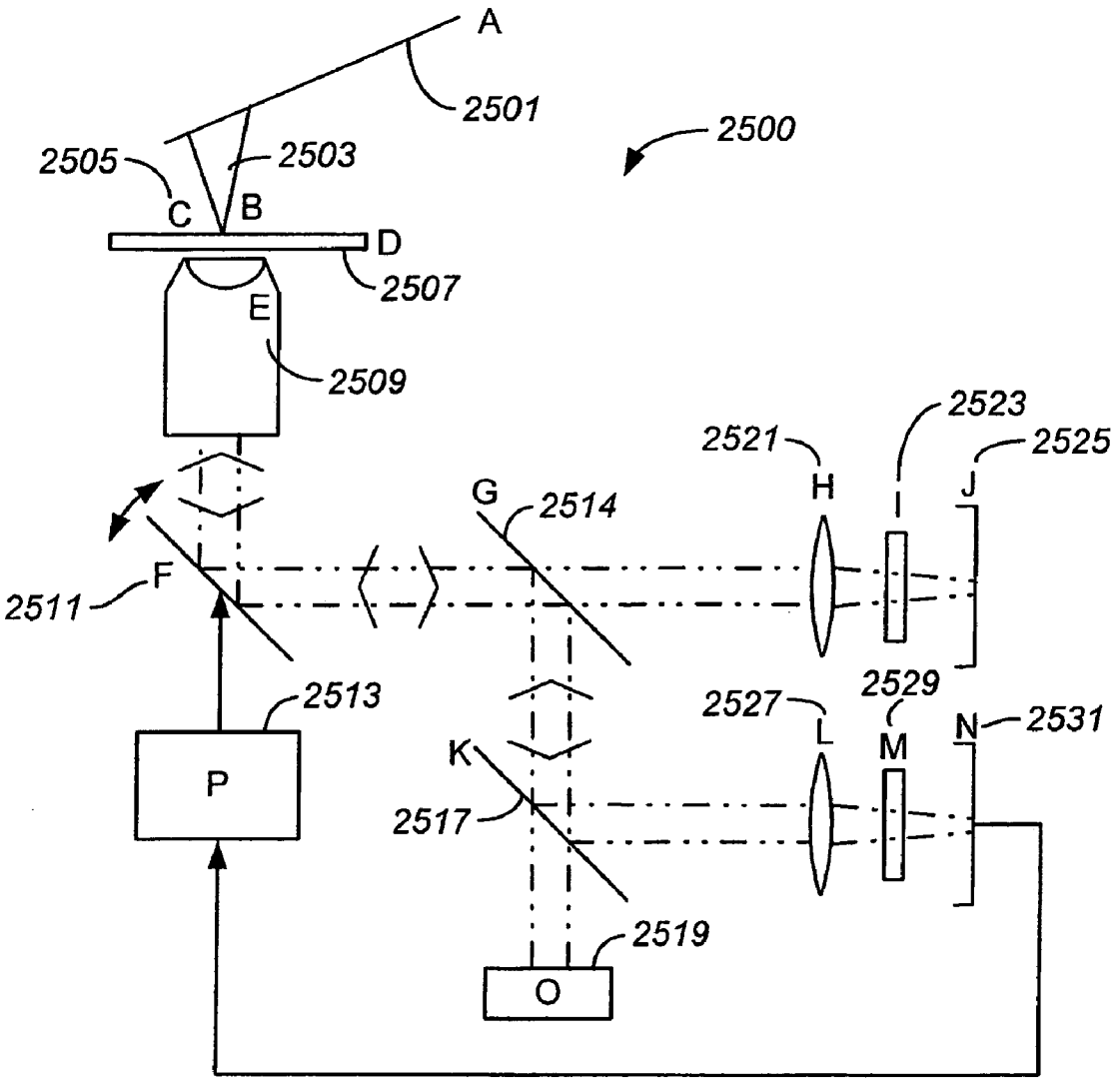
A
2501
2500
2505
2503
C
B
D
2507
E
2509
2523
2521
2525
H
J
G
2514
2511
F
2513
2529
2527
L
M
N
2531
K
P
2517
2519
O

FIG. 25

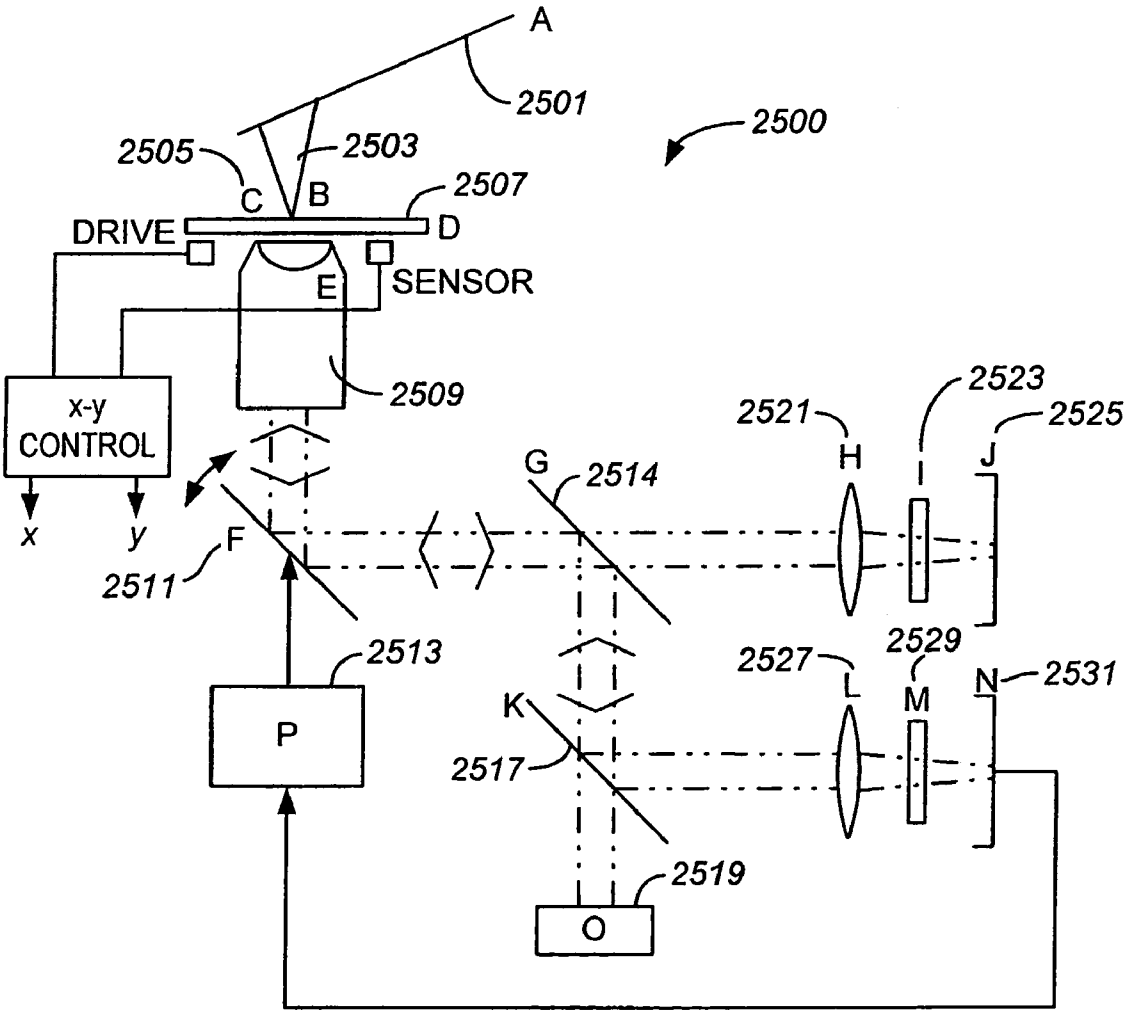
A
2501
2500
2505
2503
C
B
2507
DRIVE
D
E
SENSOR
2509
x-y
CONTROL
x
y
2521
2523
2525
H
I
J
G
2514
F
2511
2513
P
2527
2529
L
M
N
2531
K
2517
2519
O

FIG. 25A

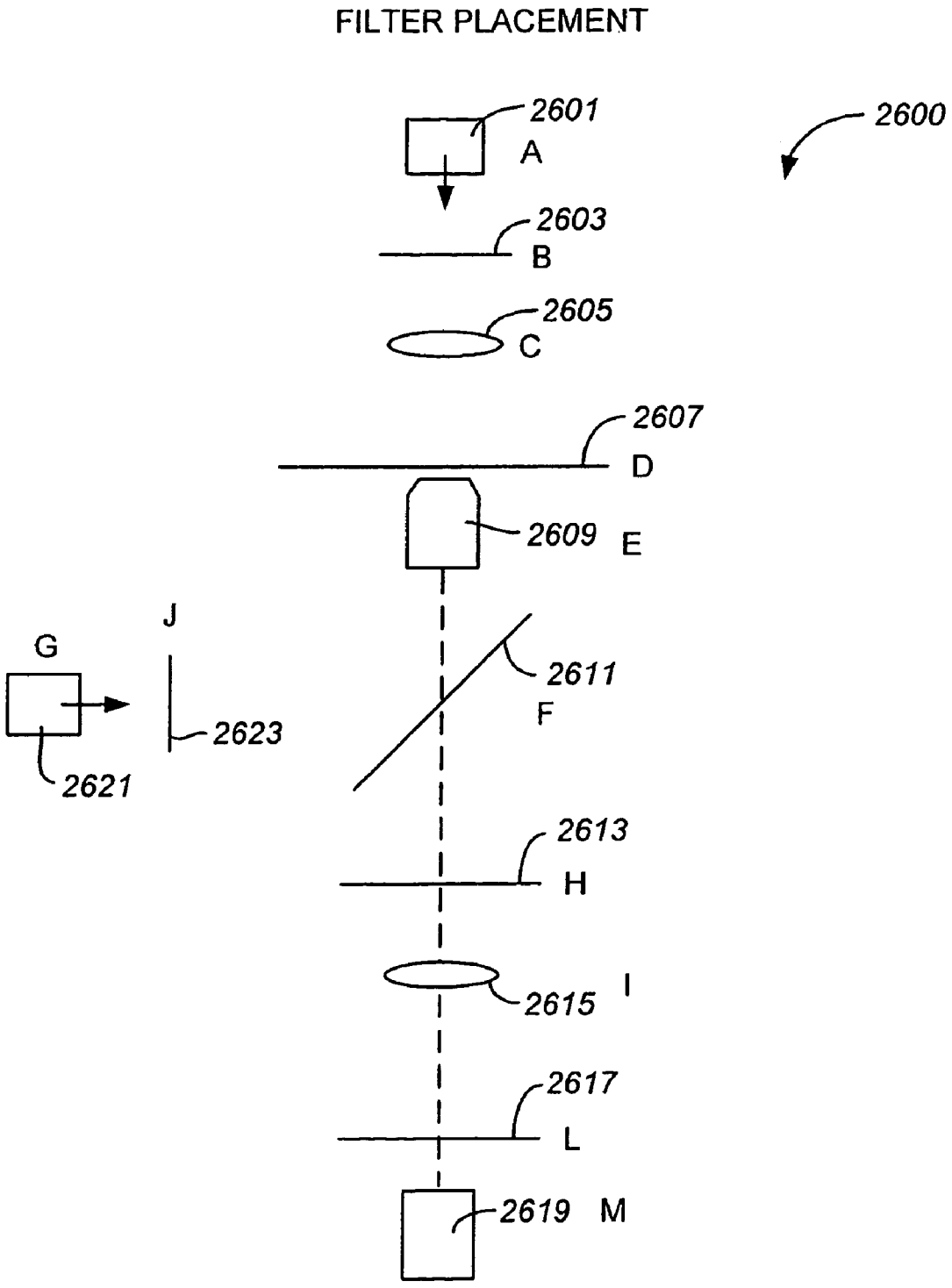
FILTER PLACEMENT
2600
2601
A
2603
B
2605
C
2607
D
2609
E
J
G
2611
F
2623
2621
2613
H
2615
I
2617
L
2619
M

FIG. 26

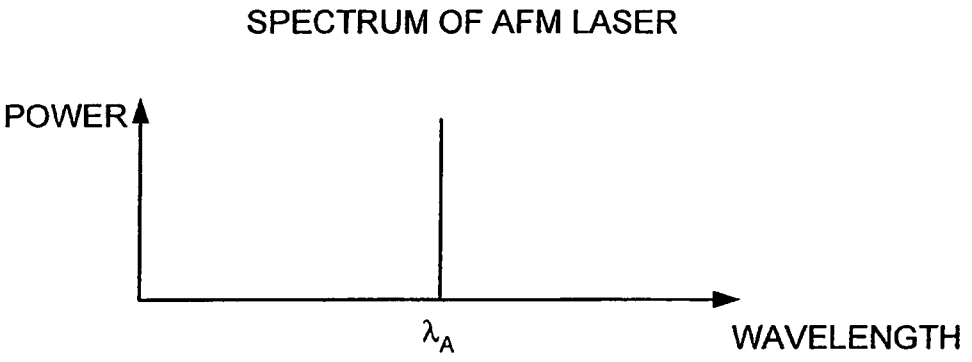

FIG. 27

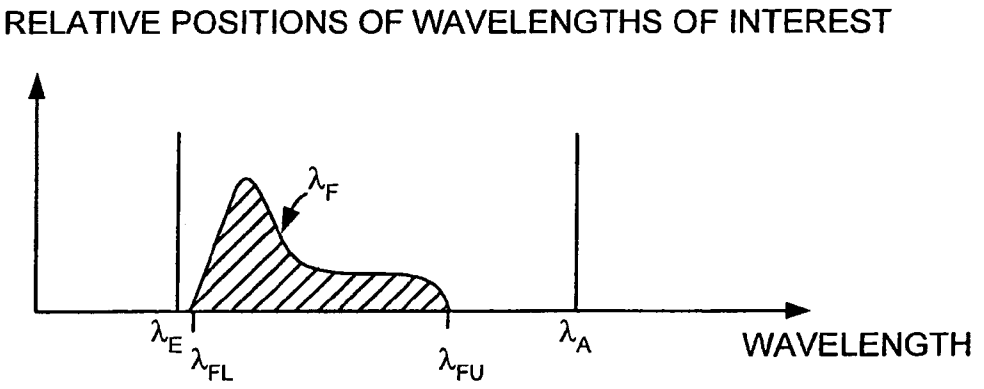

FIG. 28

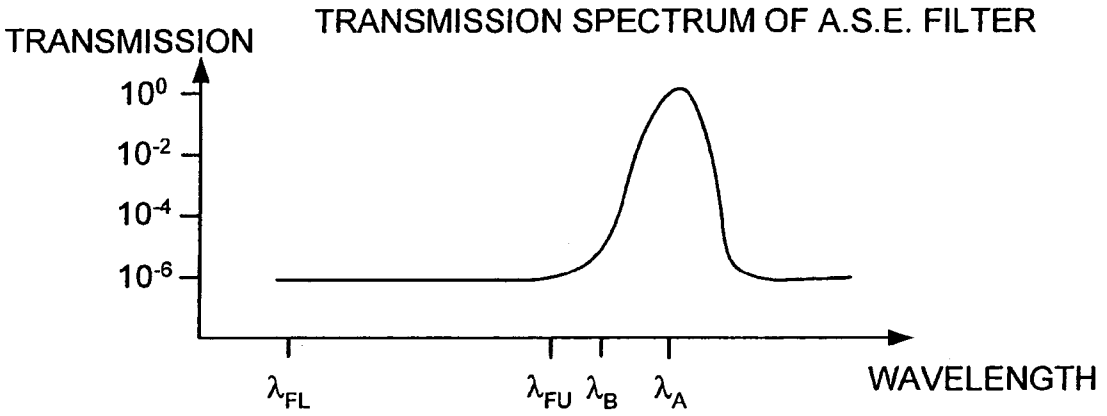

FIG. 29

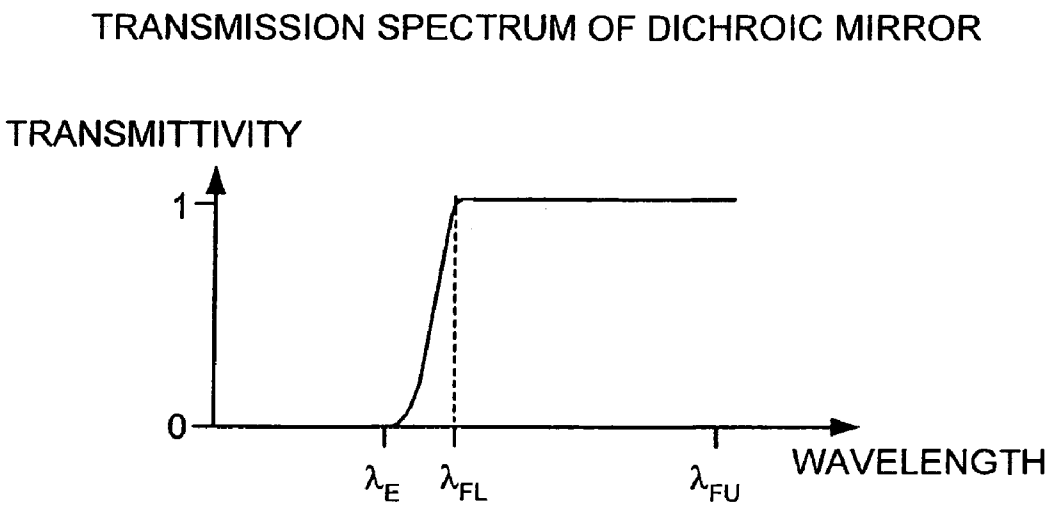
TRANSMISSION SPECTRUM OF DICHROIC MIRROR
TRANSMITTIVITY
1
0
λ_E
λ_{FL}
λ_{FU}
WAVELENGTH

FIG. 30

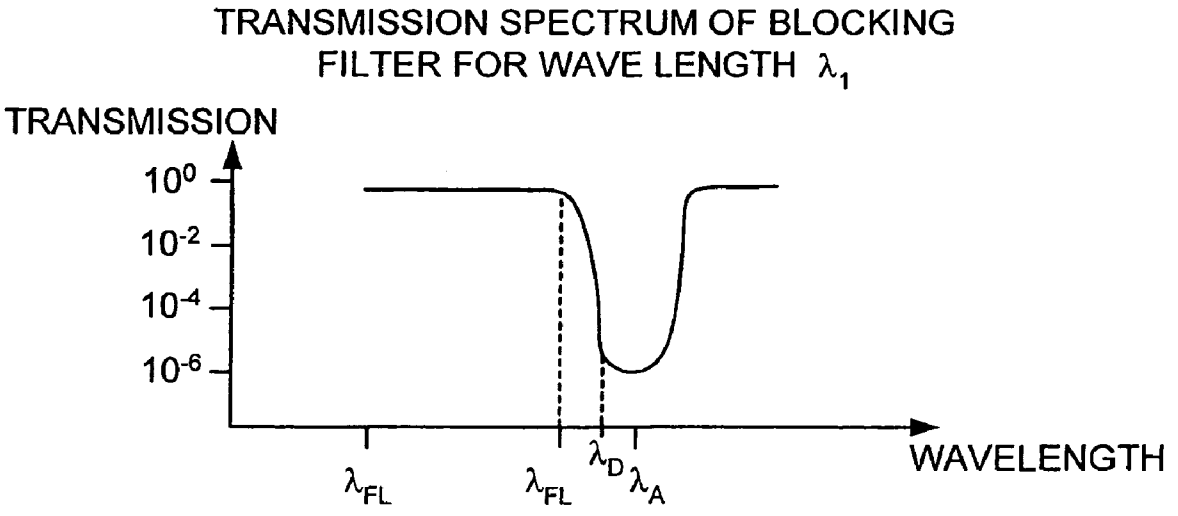
TRANSMISSION SPECTRUM OF BLOCKING FILTER FOR WAVE LENGTH λ_1
TRANSMISSION
10^0
10^{-2}
10^{-4}
10^{-6}
λ_{FL}
λ_{FL}
λ_D
λ_A
WAVELENGTH

FIG. 31

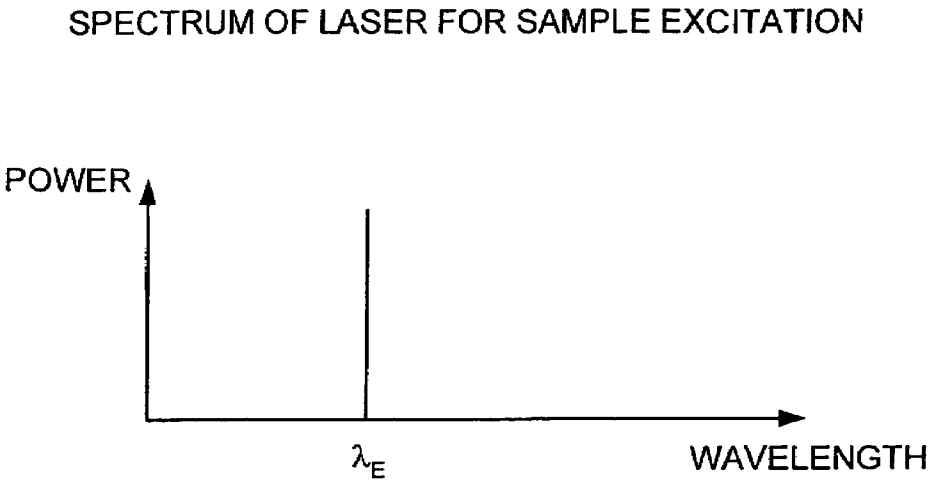
SPECTRUM OF LASER FOR SAMPLE EXCITATION
POWER
λ_E
WAVELENGTH

FIG. 32

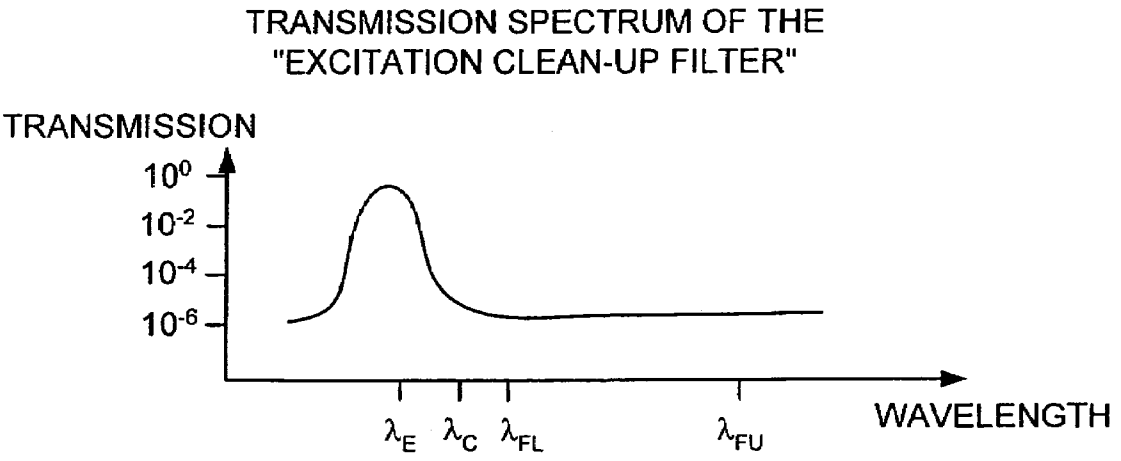
TRANSMISSION SPECTRUM OF THE
"EXCITATION CLEAN-UP FILTER"
TRANSMISSION
10^0
10^{-2}
10^{-4}
10^{-6}
λ_E
λ_C
λ_{FL}
λ_{FU}
WAVELENGTH

FIG. 33

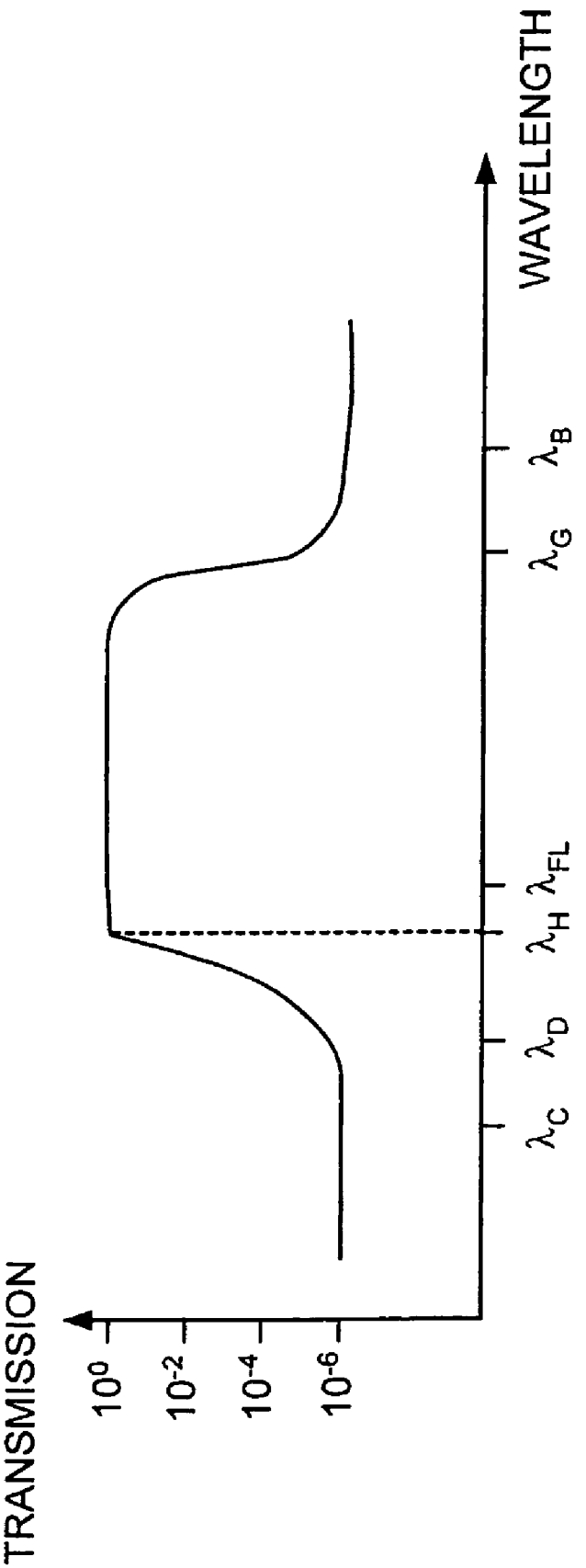
TRANSMISSION SPECTRUM FOR
"BLOCKING FILTER FOR SAMPLE DETECTOR"
TRANSMISSION
10^{0}
10^{-2}
10^{-4}
10^{-6}
λ_C λ_D λ_H λ_{FL} λ_G λ_B
WAVELENGTH

FIG. 34

METHOD AND SYSTEM FOR SCANNING APERTURELESS FLUORESCENCE MIRCROSCOPE

STATEMENT AS TO RIGHTS TO INVENTIONS MADE UNDER FEDERALLY SPONSORED RESEARCH OR DEVELOPMENT

The U.S. government has rights in the disclosed invention pursuant to National Science Foundation Grant No. DMR-0080065 to the California Institute of Technology.

CROSS-REFERENCES TO RELATED APPLICATIONS

This application claims priority to U.S. patent application Ser. No. 10/616,896, filed on Jul. 9, 2003, which claims priority to U.S. Provisional Application No. 60/402,351, filed Aug. 9, 2002, which are incorporated by reference herein.

REFERENCE TO A "SEQUENCE LISTING," A TABLE, OR A COMPUTER PROGRAM LISTING APPENDIX SUBMITTED ON A COMPACT DISK

NOT APPLICABLE

BACKGROUND OF THE INVENTION

The present invention relates generally to high resolution microscopy techniques. More particularly, the invention provides methods and systems for improved high resolution scanning using apertureless near field scanning optical microscopes ("ANSOM") that image one or more fluorescent samples with single photon excitation, which we call fluorescence ANSOM ("FANSOM"). But it would be recognized that the invention has a much broader range of applicability. For example, the invention can be applied with other types of images such as Raman scattering, and other multiphoton processes. Additionally, the samples can range from a variety of different fields such as electronics, semiconductor, organic chemistry, life sciences, biotechnology, micro and nanomachining and micro and nanodevices, molecular and biological circuits, and others.

Over the years, significant development of different types of microscopy has occurred. As merely an example, visible light optical microscopy using far field optics including lenses and light evolved from a simple compound microscope that is capable of resolving sizes of about 200 nanometers and greater. Examples of samples that are capable of being viewed using far field optics include biological cells and tissues, and are capable of being viewed using far field optics include biological cells and tissues, and others, which are often, bulk in nature. The resolving ability of such far field optical microscopy is generally limited by the diffraction of light. The diffraction limit for optical resolution has been stretched somewhat for far field imaging of very specific samples to perhaps 150 nanometers using confocal microscopes and other, related, approaches. Accordingly, atomic force microscopes ("AFM") and scanning optical microscopes including near field scanning optical microscopes were developed. The AFM and near field scanning optical microscopy ("ANSOM") have been developed to overcome certain limitations of far field optics. The AFM and near field scanning microscopes have also found many applications in biology, chemistry, physics, and materials science.

Near field scanning optical microscopy allows one to take optical images with resolutions below the diffraction limit of light. More particularly, light propagating through a waveguide is forced through a subwavelength aperture, which is then scanned in close proximity to a sample. Such subwavelength aperture techniques create other limitations. Here, physical limitations relate to a skin depth of the metal used to coat the waveguide and various scanning artifacts, which yield resolutions of 30 to 50 nanometers, most typically 50 to 100 nanometers. Apertureless near field scanning microscopes have been proposed and demonstrated to overcome these limitations, among others. Conventional ANSOM often involves using an oscillating sharp probe, which is scanned over the sample. The probe perturbs an incident laser beam, by introducing phase shifts in an electric field or by a periodic occlusion of the sample. Detection techniques are generally used to discriminate light scattered by near field interactions from a far field contribution. Limitations also exist with such ANSOM techniques. Such limitations include contaminated images based upon certain artifacts of the sample topography, and may include others.

A pioneering approach for achieving high resolution spectroscopic information using a scanning microscope is described in U.S. Pat. No. 6,002,471, assigned to California Institute of Technology, Pasadena, Calif., and in the name of Stephen R. Quake ("Quake"). Quake generally provides a system and method for obtaining high resolution spectroscopic information. The system generally includes a support and first optical elements for directing an optical beam at a sample, which is on the support. An optical element for collecting light emitted from the sample to reduce a background noise is also included. Other elements include a spectral dissociating apparatus, a probe, and a probe detection apparatus coupled to the probe. As merely an example, the probe enhances the light level emitted from the sample in the vicinity of the probe. Because this occurs only when the probe is in the immediate vicinity of the sample, detection of this modulation results in very high spatial resolution and chemical detection sensitivity. Fluorescence ANSOM, called FANSOM, has also been demonstrated. Conventional FANSOM often uses a principle of a two photon excitation and electric field enhancement near a tip of the probe. See, T. J. Yang, Guillaume A. Lessard, and Stephen R. Quake, An apertureless near field microscope for fluorescence imaging, Applied Physics Letters, Volume 76, Number 3, Jan. 17, 2000 ("Yang, et al."). Yang, et al. reports certain results achieved using the FANSOM designed to image fluorescent samples with single photon excitation. FANSOM has demonstrated resolutions in the 10-20 nm range. Although FANSOM appears to be promising, certain practical limitations may still exist.

From the above, it is seen that improved high resolution scanning techniques are desired.

BRIEF SUMMARY OF THE INVENTION

According to the present invention, techniques for high resolution scanning are provided. More particularly, the invention provides methods and systems for improved high resolution scanning using apertureless near field scanning microscopes that image one or more fluorescent samples with single photon excitation, which we call fluorescence ANSOM. But it would be recognized that the invention has a much broader range of applicability. For example, the invention can be applied with other types of images such as Raman scattering, multi-photon imaging techniques, and

others. Additionally, the samples can be from a variety of different fields such as electronics, semiconductor, organic chemistry, life sciences, biotechnology and others.

In a specific embodiment, the invention provides a method for measuring characteristics of nanoscopic objects (e.g., 0.1 nanometers to >1,000 nanometers) using detection of photons emitted from the objects, e.g., Proteins or DNA tagged with fluorescent molecules. The method includes moving a tip of a probe coupled to a cantilever toward a feature of a sample to influence and/or modulate a rate of fluorescence from the feature of the sample. The method measures and/or compares the first intensity level of electromagnetic energy from a feature of a sample during a first predetermined portion of movement of the cantilever and records a change in the first intensity level to a second intensity level during a second predetermined portion of movement of the cantilever using a detector or the like.

In an alternative specific embodiment, the invention provides a system for measuring characteristics of nanoscopic objects using detection of photons emitted from the objects. The system has one or more computer memories, which include computer codes. A first code is directed to cause movement of a tip of a probe coupled to a cantilever member toward a feature of a sample to influence a detected rate of fluorescence from the feature of the sample. A second code is directed to apply illumination using a first intensity level of electromagnetic energy to the feature of the sample during a first predetermined portion of movement of the cantilever member to capture a signal from the feature at a detector from the sample. The one or more memories also include a third code directed to output a control signal to switch the first intensity level to a second intensity level during a second predetermined portion of movement of the cantilever member. Depending upon the embodiment, other computer codes can also be used to implement the functionality described herein as well as outside of this specification.

In a specific embodiment, the invention provides a capability to extend the lifetime of fluorescent molecules. Preferably, the method extends the life of such molecules by turning an excitation laser on only during specific periods of the data gathering cycle, which can improve and possibly maximizes a lifetime of the fluorescent molecule by delaying photobleaching or other similar features. Photobleaching is a photo-catalyzed chemical reaction that severely reduces or completely eliminates fluorescence emission. In addition this allows the signal to be maximized during imaging. Image scans often include series of fast probe movements, or line scans, along one axis and backcoupled with a slow continuous movement or discrete set of movements along the orthogonal axis of the sample surface plane-rastering pattern. Such rastering pattern continues until the desired portion of the sample plane is mapped which forms one image frame. The probe is typically made to oscillate rapidly (typically but not limited to 50-400 kilohertz oscillation frequency) up and down so that it lightly "taps" on the sample surface, following the sample topography while being rastered over the surface. When an image frame begins or ends, the probe controller sends a voltage signal that is monitored by the data acquisition computer. Similarly, the probe controller sends a voltage signal when each line scan begins in one direction and another signal at the beginning of the return movement. The image is typically constructed of either all-forward direction line scans or all return line scans in certain embodiments. If forward direction line scans are desired, then the controlling software detects the voltage pulse signaling the onset of forward scanning and in turn sends a voltage signal to an acousto-optic modulator that switches so that the excitation laser transmits into the FANSOM optical system. When the return line begins, a second voltage pulse is generated by the probe controller. As this line is not being used to create the image, the controlling computer stops sending the voltage pulse to the AOM. The AOM then switches so that the excitation laser light is no longer transmitted into the FANSOM optical system and the sample is not illuminated. This process repeats for each line with the sample being illuminated only during forward direction line scans. When the image frame is complete, the laser is commanded to switch off (in this case by stopping the voltage pulse to the AOM) until the initiation of the next image frame.

There can be other modifications, alternatives, and variations. As described above, the triggering of the laser switching can be actuated at the beginning of each line scan. Alternately it could begin based on topographical information from the probe (that is that the probe is over the sample of interest) or on a user defined area or coordinate set. The switching itself can be accomplished in a variety of ways other than the acousto-optical method described above. These other ways include using an electro-optic modulator or a shutter or chopper which is triggered or timed to correspond to the aforementioned inputs (beginning of line, coordinate, topographical information). The use of either an acousto-optic or electro-optic switching method allows for extremely fast (<10 nanosecond) switching times which enables other types of laser-triggering schemes. For instance, the laser may be triggered by the oscillating motion of the probe so that the laser would be on only for a portion of the probe oscillation cycle. This triggering scheme can be used to enhance the optical contrast as well as maximizing and/or improving the fluorescent molecule lifetimes. Other techniques may also use scanners, mirrors (e.g., MEMS), any combination of these and the like.oi

In an alternative specific embodiment, the invention provides a method for operating an apertureless microscope for viewing microscopic features of objects to molecular sensitivity. The method includes aligning the excitation laser beam to a tip coupled to a cantilever through a probe or a portion of the cantilever within a first assembly. There are several methods for accomplishing such alignment to nanometric accuracy. Gross alignment within a few microns can be achieved by viewing the back reflection of the excitation laser beam and the cantilever laser illumination of the cantilever and either moving the cantilever assembly until the two beams are properly aligned. Alternately or in combination a tip-tilt mirror can be used to move the focus of the excitation laser so that it is properly aligned with the cantilever tip. Additionally, the shadow cast by the cantilever when illuminated by the excitation laser can be visualized or imaged and used to align the tip with the excitation laser. Fine alignment to approximately 1 micron and possibly less can be achieved by illuminating the cantilever with monochromatic light or broadband light such that the optics can image the cantilever tip shadow relative to the excitation laser. Piezoelectric actuators can be used to either move the tip until properly aligned with the excitation laser or to steer the excitation laser until it is properly aligned with the tip. Fine and ultrafine alignment to as little as a few nanometers can be achieved by imaging the backscatter of the excitation laser either when scanning the laser over the cantilever tip or alternately when scanning the tip over a fixed focus excitation laser. The backscatter image gives a high resolution image via the microscope objective which allows the relative positions of the tip and the laser to be established.

Final alignment can then be achieved by either moving the cantilever assembly, moving the cantilever tip or the excitation laser focus point until the excitation laser and the cantilever tip are properly aligned. All of the previously mentioned alignment steps can be carried out separately or in combination. Also they can be carried out in combination with a properly marked sample substrate which incorporates appropriate position reference points and or structures. Alignment can be maintained while imaging in several ways. It can be achieved by imaging the excitation laser back-reflection. The imaged diffraction pattern can then be used to monitor changes in relative position which can be used to correct any misalignments which develop if the laser tracks the cantilever tip while imaging a sample. Alternately, this imaged pattern information can be used to provide primary commands to move the excitation laser to track a moving cantilever tip. Finally, it can be used to correct other accumulated misalignments including but not limited to thermal drift and piezo and/or other mechanical strain relaxation, hysteresis, and piezo creep. These techniques can be used to achieve and maintain alignment whether the cantilever tip scans a stationary sample and excitation laser, both the cantilever tip and excitation laser scan a stationary sample, the excitation laser scans a stationary cantilever tip and sample, or a stationary cantilever tip and excitation laser scan a moving sample.

In yet an alternative embodiment, the invention provides an apertureless microscope system for viewing one or more features of samples to a resolution of molecular sensitivity. The system has a member for supporting the apertureless microscope system. A support structure is coupled to the member to support the member. A plurality of shock absorbing devices is coupling the support structure and the member. The plurality of shock absorbing devices is capable of substantially eliminating a possibility of mechanical noise from the floor structure. The system also has an enclosure structure coupled to the member and covering the apertureless microscope system. The enclosure houses the apertureless microscope within an opening confined within the enclosure structure. A sound absorbing member is coupled to the enclosure structure to substantially eliminate a possibility of acoustic noise from entering into the opening within the enclosure structure. An inner liner is also coupled within the opening of the enclosure structure to absorb one or more stray photons within the enclosure structure. The inner liner is generally capable of substantially preventing the stray photons from being released back into the enclosure structure.

Still further, the invention provides a method for operating a scanning system in a substantially noise free environment for viewing one or more features of samples to a resolution of molecular sensitivity. The method includes inserting a sample having a molecular feature on a stage of an apertureless microscope system, which has at least a scanning apparatus including a probe coupled to an optical imaging apparatus. The optical imaging apparatus is adapted to capture information having a feature size of less than five nanometers from a portion of the sample. The method also maintains at least the stage and the sample in an opening confined by an enclosure structure, which is coupled to a member for supporting a portion of the apertureless microscope system. The method maintains at least the stage and the sample free from mechanical vibration noise using a plurality of shock absorbing devices coupling the member. The plurality of shock absorbing devices is capable of substantially eliminating a possibility of mechanical vibration noise from an external source. The method further maintains at least the stage and the sample free from acoustic noise using a sound-absorbing member coupled to the enclosure structure to substantially eliminate a possibility of the acoustic noise from interacting with the captured information. A step of capturing one or more stray photons within the opening of the enclosure structure using an inner liner coupled within the enclosure structure to absorb the one or more stray photons within the enclosure structure is included. The inner liner is capable of substantially preventing the one or more stray photons from being released back into the opening of the enclosure structure.

In a specific embodiment, the invention provides a method for operating an apertureless microscope for observing one or more features to a molecular sensitivity on objects. The method includes moving a nanotube based tip of a probe coupled to a cantilever in the near vicinity of a feature of a sample or the sample relative to the nanotube based tip. In common with the previously described embodiments, the nanotube based tip will enhance contrast by interacting with the sample and the excitation light. The same mechanisms described earlier, that reduce the amount of fluoresced and/or detected fluoresced light and increased the amount of fluoresced light, will also occur with this tip in the proximity of the sample and/or illuminated by the excitation light. In addition other effects may serve to enhance contrast. In addition the resolution is increased due to the small diameter (typically 1-3 nm) of a single-walled nanotube. Preferably, the nanotube structure is single walled, although it may be multiwalled or has several single-walled tubes in a rope and/or bundle structure. Preferably, the term rope is a structure made of more than one strand of nanotube material, which may be twisted together or in any other aggregated geometric configurations according to certain embodiments. Additionally, enhanced contrast and resolution may occur through a quenching influence of the one or more photons. As merely an example, enhancement through quenching is shown in the first two (Y axis is photons/sec). The second figure shows, in one case, quenching and enhanced emission simultaneously (see also FIG. **19**). This offers an opportunity for further improvement in resolution.

In an alternative specific embodiment, the invention provides an apertureless microscope system for observing one or more features to a molecular sensitivity on objects. The system comprises a nanotube based tip on a probe coupled to a cantilever operable to move in a vicinity of a feature of a sample. Metallization of the nanotube tip increases the contrast enhancement by increasing the amount of interaction between the tip and the sample and/or the tip and the excitation laser depending on the specifics of the excitation beam and sample. This metallization also increases the nanotube attachment strength to the tip.

In an alternative specific embodiment, the invention provides an apertureless microscope system for observing one or more features to a molecular sensitivity on objects. The system comprises a metallized DNA molecule which is attached to the cantilever tip. The small diameter and high conductivity of this invention enables contrast enhancement and high-resolution FANSOM imaging in a method similar to the nanotube tips.

In a specific embodiment, the invention provides a method for dynamically viewing an increased field of view based upon a smaller fixed field of view to capture an image of features of samples to molecular sensitivity. The method includes illuminating through a fixed lens using a beam a feature of a sample. The beam is directed toward at least one tip of a probe, which is in a vicinity of the feature of the

sample. The method scatters a portion of the beam off a portion of the tip of the probe. The method also detects the scattered portion of the beam. The method then processes the scattered portion of the beam to determine a pattern to identify a relationship between the tip and the beam for spatial alignment between the tip and the beam. A step of adjusting a position of the beam used for illumination based upon at least the pattern to maintain a desired relationship between the tip and the beam is also included.

In an alternative specific embodiment, the invention provides a system for dynamically viewing an increased field of view based upon a smaller field of view to capture an image of features of samples to molecular sensitivity. The system has an electromagnetic energy source (in a specific embodiment this can be a laser), which is capable of emitting a beam. A fixed lens is coupled to the electromagnetic energy source. The fixed lens focuses the beam toward at least one tip of a probe, which is in a vicinity of a feature of a sample to scatter a portion of the beam off a portion of the tip of the probe. A detector is coupled to the fixed lens. The detector detects the scattered portion of the beam. A processor is coupled to the detector. The processor is adapted to process the scattered portion of the beam to determine a pattern to identify a relationship between the tip and the beam for a spatial alignment between the tip and the beam. An adjustment device is coupled to the processor. The adjustment device is adapted to adjust a position of the beam based upon at least the pattern to maintain a desired relationship between the tip and the beam.

In an alternative specific embodiment, the invention provides a scanning microscope for viewing one or more features of molecular scale and below. The system has a support stage for holding an object to be observed. A tip is coupled to a probe, which is configured within a vicinity of a feature of the object. An illumination source is directed to apply electromagnetic radiation from the illumination source to the tip of the probe. This illumination is used to determine the position of the cantilever tip over the sample. The system has a filter coupled to the object to substantially eliminate amplified spontaneous emission (ASE) from a power spectrum of the electromagnetic radiation. Preferably, such filter has a narrow transmission width to block ASE at wavelengths both shorter and longer than a central laser wavelength according to a specific embodiment. Alternately, such filter can be a long pass filter to block ASE with wavelengths shorter than the central laser wavelength. In an alternative embodiment, such filter can be a short pass to block ASE with wavelengths longer than the laser wavelengths longer than the central laser wavelength. The system also has an object illumination source coupled to the support to illuminate at least the feature of the object. Additional filters allow the blocking of the central cantilever illumination and also of the excitation illumination. Finally a filter is used to remove ambient illumination outside the sample fluoresced wavelength(s). These filters serve to block the several sources of photons not emitted by the sample but are highly transmissive in the wavelengths emitted by the sample. In combination, the present filters allow signals at wavelengths longer than the central laser wavelength or shorter than the central laser wavelength to be observed according to a specific embodiment. A detector is coupled to the object to capture signals from at least the feature of the object. The signals are derived from a detection band from the object illumination source.

Many benefits are achieved by way of the present invention over conventional techniques. For example, the present technique provides an easy to use process that relies upon conventional technology. The invention can also provide improved resolution within a predetermined range of spatial feature sizes. Preferably, the invention can be applied to capture images from biological molecules and the like. Depending upon the embodiment, one or more of these benefits may be achieved. These and other benefits will be described in more throughout the present specification and more particularly below.

Various additional objects, features and advantages of the present invention can be more fully appreciated with reference to the detailed description and accompanying drawings that follow.

BRIEF DESCRIPTION OF THE DRAWINGS

FIG. **1** is a simplified diagram of a scanning system **100** according to an embodiment of the present invention;

FIG. **2** is a simplified diagram of a computer system that is used to oversee the system of FIG. **1** according to an embodiment of the present invention;

FIG. **2**A is a more detailed diagram of hardware elements in the computer system of FIG. **2** according to an embodiment of the present invention;

FIG. **3** is a simplified diagram of an improved illumination system for a scanning system according to an embodiment of the present invention;

FIG. **3**A is a more detailed diagram of the improved illumination system according to an embodiment of the present invention;

FIGS. **4** through **5** are simplified diagrams of scanning methods according to embodiments of the present invention;

FIGS. **6** through **8** are simplified diagrams illustrating optical alignment methods for nanoscopic scanning according to embodiments of the present invention;

FIGS. **9** through **12** are simplified diagrams of packaging systems and methods for scanning systems according to embodiments of the present invention;

FIGS. **13** through **16** are simplified diagrams of various tip devices according to embodiments of the present invention;

FIGS. **14**A and **14**B are nanotube based probes according to embodiments of the present invention;

FIGS. **14**C through **14**E are nanotube based probes according to alternative embodiments of the present invention;

FIGS. **17** through **21** are experimental results using selected tip designs according to embodiments of the present invention;

FIG. **22** is a simplified diagram of an alignment subsystem for an optical system according to an embodiment of the present invention;

FIGS. **23** through **25** are simplified diagrams of tip detection alignment methods and systems for the scanning system according to embodiments of the present invention;

FIG. **25**A is a simplified diagram of a FANSOM system using a closed loop feedback loop according to an embodiment of the present invention; and

FIGS. **26** through **34** are simplified diagrams of methods and systems for selectively illuminating one or more samples according to embodiments of the present invention.

DETAILED DESCRIPTION OF THE INVENTION

According to the present invention, techniques for high resolution scanning are provided. More particularly, the invention provides methods and systems for improved high

resolution scanning using apertureless near field scanning microscopes that image one or more fluorescent samples with single photon excitation, which we call fluorescence ANSOM microscope. But it would be recognized that the invention has a much broader range of applicability. For example, the invention can be applied with other types of images such as Raman scattering, multiphoton imaging techniques, and others. Additionally, the samples can be from a variety of different fields such as electronics, semiconductor, organic chemistry, life sciences, biotechnology, and others.

FIG. **1** is a simplified diagram of a scanning system **100** according to an embodiment of the present invention. This diagram is merely an example, which should not unduly limit the scope of the claims herein. One of ordinary skill in the art would recognize many other modifications, alternatives, and variations. As shown, the present microscope system **100** includes a mobile stage **111**, which has x-y-z movement capability. The stage can be moved with a tolerance of less than 40 microns for sample positioning and when used for alignment can be moved with a tolerance of <1 nm. A sample **109** is placed on the stage. Depending upon the application, the sample can include a biological sample, a quantum dots, fluorescently tagged molecules, and Fluorescently tagged nano- or micro-structures, arrays or components. Preferably, the sample can also be in liquids, air, inert gas environments, or in vacuum and at specific temperatures (cryogenic, room temperature, warm to extremely high temperatures), depending upon the application.

The system also includes a tapping mode atomic force microscope ("AFM") **110**. In a specific embodiment, the AFM **110** has various elements such as probe **107**, a cantilever to support the probe, which is coupled to a piezoelectric stack **104**. Such piezo-stack provides for dithering and z-motion of the cantilever. The AFM also includes a driving signal, which is coupled to control electronics **113** for signal detection and correction. Preferably, probe **107** has a pyramidal shape and the tip of the pyramid is coated with silver particles. Alternatively, other particles or coatings can also be used. For example, such coatings include, among others, semiconductor (e.g., silicon, silicon nitride, diamond, etc.), conductors (e.g., platinum, gold, silver alloys, aluminum, platinum-iridium, cobalt and any other metals as well as materials doped to be conductive), as well as combination of these, and the like. The AFM also includes a laser source **103**, which is directed to the cantilever or probe. The laser source is used as a position detector, which provides photons that scatter off of the cantilever and/or probe. Such scattered photons are detected by way of photodetector **105**, which is coupled to control electronics **113**. The AFM is coupled to an inverted optical microscope, as shown.

Preferably, the inverted optical microscope **119** is underlying the AFM, as shown. A laser beam **117** (which in a specific embodiment is from a green HeNe **103** source) is focused on the AFM tip. The laser beam is directed from the source **117** and is adjusted by way of dichroic mirror **120** through the objective **119**, which focuses the beam onto the AFM tip. As the sample is scanned in the x-y plane (which is also in the plane of the paper), fluorescent photons emit from the sample. Such photons pass through the objective through a bandpass filter **121** and are detected by an avalanche photodiode **123**. A gated photon counter **125**, which is coupled to the photodiode, processes the detected photons. The gated photon counter is triggered by a measured height of an AFM cantilever. A signal acquisition and processing apparatus **115** (which includes a microprocessor device and has been used as a "controller" and/or "main controller" herein without unduly limiting the scope of the term processing apparatus), which may be coupled to the counter through a common bus, oversees and performs operation and processing of information. The system also has a display **127**, which can be a computer, coupled to the signal acquisition and processing apparatus. The signal acquisition and processing apparatus is also coupled to the control electronics of the AFM as shown.

In a specific embodiment, the AFM operates using a sinusoidal diving signal coupled to the AFM probe via the piezo-electric stack. The AFM probe is scanned over the surface of the sample, receiving the perturbations caused by the surface of the sample and transmitting the perturbed signal to the position detector. The position detector transmits a position signal to electronic systems for correcting and digitizing the signal. The correction occurs by comparing the position signal to an external height reference signal. The corrected AFM signal and the optical signal are coupled to the digitizing system for the processing of the AFM image of the surface topography and the optical image. Of course, there can be other modifications, alternatives, and variations. Further details of the present system can be found in the Quake patent, which has been previously described. Other details of the present system and methods are provided throughout the specification and more particularly below.

FIG. **2** is a simplified diagram of a computer system **210** that is used to oversee the system of FIG. **1** according to an embodiment of the present invention. This diagram is merely an example, which should not unduly limit the scope of the claims herein. One of ordinary skill in the art would recognize many other modifications, alternatives, and variations. As shown, the computer system **210** includes display device **220**, display screen **230**, cabinet **240**, keyboard **250**, scanner and mouse **270**. Mouse **270** and keyboard **250** are representative "user input devices." Mouse **270** includes buttons **280** for selection of buttons on a graphical user interface device. Other examples of user input devices are a touch screen, light pen, track ball, data glove, microphone, and so forth.

The system is merely representative of but one type of system for embodying the present invention. It will be readily apparent to one of ordinary skill in the art that many system types and configurations are suitable for use in conjunction with the present invention. In a preferred embodiment, computer system **210** includes a Pentium™ class based computer, running Windows™ NT operating system by Microsoft Corporation. However, the system is easily adapted to other operating systems and architectures by those of ordinary skill in the art without departing from the scope of the present invention. As noted, mouse **270** can have one or more buttons such as buttons **280**. Cabinet **240** houses familiar computer components such as disk drives, a processor, storage device, etc. Storage devices include, but are not limited to, disk drives, magnetic tape, solid-state memory, bubble memory, etc. Cabinet **240** can include additional hardware such as input/output (I/O) interface cards for connecting computer system **210** to external devices external storage, other computers or additional peripherals, which are further described below.

FIG. **2A** is a more detailed diagram of hardware elements in the computer system of FIG. **2** according to an embodiment of the present invention. This diagram is merely an example, which should not unduly limit the scope of the claims herein. One of ordinary skill in the art would recognize many other modifications, alternatives, and variations. As shown, basic subsystems are included in computer sys-

tem **210**. In specific embodiments, the subsystems are interconnected via a system bus **275**. Additional subsystems such as a printer **274**, keyboard **278**, fixed disk **279**, monitor **276**, which is coupled to display adapter **282**, and others are shown. Peripherals and input/output (I/O) devices, which couple to I/O controller **271**, can be connected to the computer system by any number of means known in the art, such as serial port **277**. For example, serial port **277** can be used to connect the computer system to a modem **281**, which in turn connects to a wide area network such as the Internet, a mouse input device, or a scanner. The interconnection via system bus allows central processor **273** to communicate with each subsystem and to control the execution of instructions from system memory **272** or the fixed disk **279**, as well as the exchange of information between subsystems. Other arrangements of subsystems and interconnections are readily achievable by those of ordinary skill in the art. System memory, and the fixed disk are examples of tangible media for storage of computer programs, other types of tangible media include floppy disks, removable hard disks, optical storage media such as CD-ROMS and bar codes, and semiconductor memories such as flash memory, read-only-memories (ROM), and battery backed memory.

Although the above has been illustrated in terms of specific hardware features, it would be recognized that many variations, alternatives, and modifications can exist. For example, any of the hardware features can be further combined, or even separated. The features can also be implemented, in part, through software or a combination of hardware and software. The hardware and software can be further integrated or less integrated depending upon the application. Further details of the functionality of the present invention can be outlined below according to the Figures.

FIG. **3** is a simplified diagram of an improved illumination system **300** for a scanning system according to an embodiment of the present invention. This diagram is merely an example, which should not unduly limit the scope of the claims herein. One of ordinary skill in the art would recognize many other modifications, alternatives, and variations. Like reference numerals are used in FIG. **3** as certain other figures herein, but ware not intended to be limiting. As shown, the present microscope system **100** includes mobile stage **111**, which has x-y-z movement capability. The system also includes atomic force microscope ("AFM") **110**. which is preferably a tapping mode atomic force microscope, but may also be others. In a specific embodiment, the AFM **110** has various elements such as probe **107**, a cantilever to support the probe, which is coupled to a piezo-electric stack **104**. Such piezo-stack provides for dithering and z-motion of the cantilever. The AFM also includes a driving signal, which is coupled to control electronics **113** for signal detection and correction. The AFM also includes a laser source **103**, which is directed to the cantilever or probe. The laser source is used as a position detector, which provides photons that scatter off of the cantilever and/or probe. Such scattered photons are detected by way of photodetector **105**, which is coupled to control electronics **113**. The AFM is coupled to an inverted optical microscope, as shown.

The inverted optical microscope **119** is underlying the AFM, as shown. The laser beam **117** from the green HeNe **103** source is focused on the AFM tip. The laser beam is directed from the source **117** and is adjusted by way of dichroic mirror **120** through the objective **119**, which focuses the beam onto the AFM tip. The system also has the bandpass filter **121** and avalanche photodiode **123**. The gated photon counter **125** processes the detected photons. The gated photon counter is triggered by a measured height of the AFM cantilever. Signal acquisition and processing apparatus **115**, which may be coupled to the counter through a common bus, oversees and performs operation and processing of information. Other features are also included.

Preferably, the system includes illumination system **300** that selectively adjusts an illumination level. Here, a shutter and/or a modulator material can selectively adjust the beam **117** from a first state to a second state. The first state can correspond to an on-state and the second state can correspond to an off-state. The on-state allows the beam to traverse through the modulator material. The off-state blocks the beam. As merely an example, a blocking material or filter can be used between the beam **117** and mirror **120**. Such blocking material can include, among others, a modulator material. The modulator material can be coupled to the processing apparatus through the bus. Preferably, the modulator material is an acousto-optic ("AO") modulator, which will be described in more detail below. Of course, there can be other modifications, alternatives, and variations. For example, the modulator material can be replaced with a mechanical shutter, an electro-optic modulator, any combination of these, and the like.

FIG. **3A** is a more detailed diagram of the improved illumination system according to an embodiment of the present invention. This diagram is merely an example, which should not unduly limit the scope of the claims herein. One of ordinary skill in the art would recognize many other modifications, alternatives, and variations. As shown, the system includes common elements from other figures herein without unduly limiting the scope of the invention. The illumination system **300** includes laser beam **117** coupled to the objective through dichroic mirror **120**. An AO modulator **305** is coupled between the beam and mirror in a specific embodiment. The modulator is made of suitable material to diffract the beam upon command such that it is no longer coupled into the fiber optic cable, thereby blocking transmission to the sample. An example of such a material is lead molybate. The material also has to have a certain speed characteristic. That is, the modulator material should be able to change states within 0.1 milliseconds seconds and less. Preferably, the modulator material changes where the light is bent in a different direction which no longer corresponds to the fiber, i.e., the modulator is in fact blocked. An example of such a material is from ISOMET Corporation: According to a specific embodiment, when aligned at the Bragg angle which correctly corresponds to the laser wavelength and RF frequency being applied, the modulator material diffracts a portion of the beam passing through it (zeroth order) into an adjacent location (first order). The first order beam is normally used for most applications. The intensity of the first order light is controlled by the amplitude of the RF signal. Either digital (on-off) or analog (video) modulation of the first order spot can be produced, depending on the type of driver selected. Of course, the type of material used depends upon the application.

The modulator is coupled to input/output device **315** through line **313**. The input/output device may also include driving circuits, depending upon the application. Alternatively, the modulator has integrated driving circuits. Laser beam **117** is coupled to input/output device **309** and is also coupled to bus **303**, which connects to the processing apparatus. Similarly, input/output device **315** couples to bus **303**, which connects to the processing apparatus. A simple switching method can be provided using the present system.

In a specific embodiment, the modulator includes at least two states corresponding to an on-state and an off-state. In an on-state, the modulator allows beam **319** to traverse

through the modulator material and reflect off of mirror **120** to enter **317** into the objective. As merely an example, the modulator material is in a transparent state, which allows the beam to traverse therethrough. Alternatively, the modulator material can be in the off-state, where the terms "off" and "on" are merely be used for descriptive purposes without limiting the scope of the claims herein. In the off-state, the modulator/optical assembly material blocks beam **319** and does not allow beam **317** to traverse therethrough (not shown). In a specific embodiment, the processing apparatus oversees the operation of the modulator material in reference to the operation of the present methods described herein as well as outside of this specification. Of course, there can be other modifications, alternatives, and variations. For example, the modulator material can be replaced with a mechanical shutter, an electro-optic modulator, any combination of these, and the like. The modulator is preferred in most embodiments (rather than adjusting the laser beam that should often be stabilized before use in the present method and system). Other details of the present system and methods are provided throughout the specification and more particularly below.

An illumination method used for operating the scanning apparatus according to an embodiment of the present invention is provided as follows.

1. Begin process for scanning using FANSOM a feature of an object;

2. Initiate line scan process for a line along a first direction (which is different from a second direction to be described below);

3. Transfer control signal from probe controller to main controller at beginning the scan along the first direction;

4. Determine if an image is to be constructed using the main controller;

5. If the image is to be constructed, send signal from main controller to modulator to allow beam to traverse through the modulator;

6. Illuminate the feature of the object while capturing information for the image of the feature;

7. Complete scanning of the object in the first direction while constructing the image of the feature;

8. Transfer control signal from probe to controller with beginning a scan along a second direction, which is different from the first direction;

9. Determine if an image is to be constructed;

10. If the image is to be constructed along the first direction, send signal from controller to modulator to allow beam to traverse through the modulator;

11. Alternatively, send signal (or no signal) form the controller to the modulator to prevent beam from traversing through the modulator;

12. Illuminate the feature of the object or maintain the object without illumination depending upon steps 10 and 11;

13. Complete scanning in the second direction; and

14. Perform other steps as desired.

As shown, the present method provides ways to turn on and turn off illumination of a beam used for a feature of an object. In a specific embodiment, the process repeats for each line with the feature of the object being illuminated only during left to right scans as an image is built up. Once the image is complete, the laser is commanded to switch off (in this case by stopping the signal to the modulator) until initiation of the next image scan. Further details of this method are described according to the Figures below.

FIGS. **4** through **5** are simplified diagrams of scanning methods **400**, **500** according to embodiments of the present invention These diagrams are merely examples, which should not unduly limit the scope of the claims herein. One of ordinary skill in the art would recognize many other modifications, alternatives, and variations. As shown, the method begins at start, step **401**. Here, the image scan includes a series of scans from right to left and back again, although these directions could be changed in the specific embodiment. When a line scan begins (step **403**) a probe controller, which is coupled to the probe, sends (step **405**) a voltage signal that is monitored (step **407**) by a controlling computer and/or main controller. The voltage signal is often a pulse, which is sent from the probe controller at a beginning of each scan line from left to right and again on a return right to left line. If an image is to be constructed (step **409**) of scans from left to right, the method detects the voltage pulse signaling the onset of scanning using computer software. The method sends a voltage signal to initiate illumination, step **411**. Alternatively, if the image is not being constructed for the scan, the method returns via a branch back to step **405**. The method also stops at step **413**. Depending upon the embodiment, there can be many modifications, variations, and alternatives.

Referring to FIG. **5**, the method includes using a modulator to turn-on and turn-off illumination of a feature of an object. As shown, the method begins at start, step **501**. Here, the image scan includes a series of scans from right to left and back again, although these directions could be changed in the specific embodiment. When a line scan begins a probe controller, which is coupled to the probe, sends a voltage signal that is monitored by a controlling computer and/or main controller. The voltage signal is often a pulse, which is sent from the probe controller at a beginning of each scan line from left to right and again on a return right to left line. If an image is to be constructed of scans from left to right, the method detects (step **503**) the voltage pulse signaling the onset of scanning using computer software. The method sends a voltage signal to initiate illumination. Alternatively, if the image is not being constructed for the scan, the method does not illuminate the feature of the object.

Preferably, the method includes transferring a control signal from the controller to a controller of an acousto-optic modulator. The control signal is used to drive (step **507**) the modulator such that it switches the beam into the FANSOM optical system. The method continues to determine if the scan is finished, step **509**. Depending upon the embodiment, the method can also monitor (step **515**) the scan and whether illumination is desired during the scan. Alternatively, the method completes the scan and returns to step **503** for another scan, which may or may not drive the modulator to allow the beam into the FANSOM system. Preferably, when the return line scan begins, a second voltage pulse is generated by the probe controller. As the return line is not being used to create the image according to the preferred embodiment, the controller sends a voltage pulse (or no voltage pulse) to the modulator such that light no longer transmits into the FANSOM optical system and the feature of the object is not illuminated.

Depending upon the embodiment, the method repeats for each line with the feature of the object being illuminated only during left to right scans as the image is built up. Once the image is complete, the laser is commanded to switch off (also step **507**) (in this case by stopping the voltage pulse to the modulator) until initiation of the next image scan. A triggering of each line scan can be actuated at the beginning of each line. Alternately it could begin based on topographical information from the probe (that is that the probe is over the sample of interest). Alternately the switching could be based on a user defined area or coordinate set. The switching

itself can be accomplished in a variety of ways. These include using a shutter or chopper which is triggered or timed to correspond to the aforementioned inputs (beginning of line, coordinate, topographical information).

Depending upon the embodiment, there can be many benefits over conventional techniques. In a specific embodiment, the invention provides a capability to extend the lifetime of fluorescent molecules by turning the excitation laser on only during data gathering. Turning the laser off when the fluorescent molecules are not being imaged often ensures maximizes the life of the fluorescent molecule by preventing photobleaching. In addition this allows the signal to be maximized during imaging. Depending upon the embodiment, one or more of these benefits may be achieved. These and other benefits will be described in more throughout the present specification and more particularly below.

Although the above has been illustrated in terms of specific software and/or hardware features, it would be recognized that many variations, alternatives, and modifications can exist. For example, any of the hardware features can be further combined, or even separated. The features can also be implemented, in part, through software or a combination of hardware and software. The hardware and software can be further integrated or less integrated depending upon the application. Of course, one of ordinary skill in the art would recognize many other modifications, variations, and alternatives.

In an alternative specific embodiment, the invention provides a method for operating an apertureless microscope for viewing microscopic features of objects to molecular sensitivity. Conventional techniques have proved to be difficult in aligning laser sources with optical systems. Such difficulties have been overcome by way of the present method and system resulting therefrom. The method is provided as follows:

1. Couple a first assembly including a probe coupling a cantilever to an optical sub-system to facilitate spatial movement between the first assembly and the optical sub-system through a spatial translation axis;

2. Adjust the tip or the portion of the cantilever toward a test surface to focus the tip to a predetermined region of the test surface on the optical sub-system using the spatial translation axis;

3. Adjust a relationship between the alignment beam and the first assembly to an excitation laser such that the tip or the portion of the cantilever in the first assembly is within a vicinity of 1 micron of the excitation laser; and

4. Fine tune the excitation laser to align the tip or the portion of the cantilever using movement of the first assembly on the spatial translation axis.

The above sequence of steps provides a way to adjust a first assembly having a probe and cantilever to an optical sub-system, where the probe becomes aligned with the optical sub-system. Examples of such a probe and optical sub-system have been previously described herein, but can also be outside of the present specification. As can be seen, there is a general course alignment and fine alignment steps, and may also be others depending upon the application. Further details of the present method can be found throughout the specification and more particularly to the figures below.

FIGS. **6** through **8** are simplified diagrams illustrating optical alignment methods for nanoscopic scanning according to embodiments of the present invention. As shown, the invention provides a method for operating an apertureless microscope for viewing microscopic features of objects to molecular sensitivity. The method includes aligning the excitation laser beam to a tip coupled to a cantilever through a probe or a portion of the cantilever within a first assembly. There are several methods for accomplishing such alignment to nanometric accuracy. Gross alignment within a few microns can be achieved by viewing the back reflection of the excitation laser beam and the cantilever laser illumination of the cantilever and either moving the cantilever assembly until the two beams are properly aligned. Alternately or in combination a tip-tilt mirror can be used to move the focus of the excitation laser so that it is properly aligned with the cantilever tip. Additionally, the shadow cast by the cantilever when illuminated by the excitation laser can be visualized or imaged and used to align the tip with the excitation laser.

Referring to FIG. **6**, illustrated is a simplified system diagram **600** including a lamp **601**, which outputs white light **603**. A cantilever **609** is coupled to prove tip **607**. The probe tip is faced toward cover slip **609**, which also may be a plane of a sample. A microscope objective **611** is coupled to the probe. The system also has shadow formation region **613**, which is projected to screen **615**, which may be temporary and/or removable. The system also has excitation laser source **617** which projects onto the backside of the screen. The excitation laser source which projects through the objective. Other features of the present system have been previously described above, but can also be found throughout this specification.

The method performs a gross alignment step, which aligns the laser, which is on a lower subsystem to the probe tip, which is on an AFM subsystem or assembly. As shown, reference numeral **620** illustrates a projection on the screen, which is transparent in nature. Laser spot is illustrated by reference numeral **623**. The projection also includes a shadow of cantilever **629** and perimeter of field of view **627**. The probe tip, which is coupled to a larger assembly, is adjusted relative to the laser spot. A mis-aligned cantilever along the positive y-axis is shown by reference numeral **620**. A mis-aligned cantilever along the x-axis is shown by reference numeral **630**. An aligned cantilever and laser spot are provided in the illustration of reference numeral **640**. Such aligned cantilever aligns the probe to the laser, which is coupled to the lower optical system.

In a specific embodiment, the method performs another alignment step, which aligns the laser to the probe in a finer manner. Such fine alignment to approximately 1 micron can be achieved by illuminating the cantilever either with monochromatic light or broadband light such that the optics can image the cantilever tip shadow relative to the excitation laser. Piezoelectric actuators can be used to either move the tip until properly aligned with the excitation laser or to steer the excitation laser until it is properly aligned with the tip. Alignment is achieved by way of an optical subsystem, which can be viewed using a display coupled to an image capturing camera or the like.

FIG. **7** is a simplified system diagram **600** including image capturing device which is coupled to a display device. Like reference numerals are used in this diagram as the prior diagram merely for illustration. The system includes lamp **601**, which outputs white light **603**. The cantilever **609** is coupled to prove tip **607**. The probe tip is faced toward cover slip **609**, which also may be a plane of a sample. The microscope objective **611** is coupled to the probe. The system also has photons from the excitation laser diverging from the objective **611**. The system has dichroic mirror **703**, which directs radiation from laser **705** through the objective. An image captured from the probe via white light traverse through eyepiece lens **707** from objective and through

mirror. Such white light is captured via image capturing device **709**, which is a CCD camera or the like. Other features of the present system have been previously described above, but can also be found throughout this specification.

A relationship between the probe tip and laser beam is illustrated by reference numerals **720**, **730**, and **740**. As shown, a display **721** is coupled to the camera, which captures the white light images. The display illustrates laser spot **723** and probe tip **725**. Reference numeral **720** illustrates a mis-aligned probe tip along an x-axis direction from the beam. Reference numeral **730** illustrates a y-direction mis-alignment. An aligned probe tip and laser beam are illustrated by way of reference numeral **740**. Such alignment provides the finer alignment according to an embodiment of the present invention. By way of example only, the relationship between the probe and the laser is adjusted by way of an automated x-y-z state, which has automated and/or semi-automatic control features according to a specific embodiment.

The method also performs a fine alignment between the probe and the laser beam according to preferred embodiments. Referring to FIG. **8**, illustrated is a system including a raster image using an avalanche photo diode or the like. Like reference numerals are used in this diagram as the prior diagram merely for illustration. The system includes cantilever **609** coupled to prove tip **607**. The probe tip is faced toward cover slip **609**, which also may be a plane of a sample. The microscope objective **611** is coupled to the probe. The system also has photons from the excitation laser diverging from the objective **611**. The system has dichroic mirror **703**, which directs radiation from laser **705** through the objective which is backscattered from the probe tip. Back scattered light from the probe traverse through eyepiece lens **707** from objective and through mirror. Such backscattered light is captured via avalanche photo diode **803**. Other features of the present system have been previously described above, but can also be found throughout this specification.

A relationship between the probe tip and laser beam is illustrated by reference numerals **820**, **830**, and **840**. As shown, a display **823** is coupled to the avalanche photodiode, which captures the backscattered images. The display illustrates laser spot **825** backscatter and a center **821** of a raster field of view, which is the alignment point. Reference numeral **820** illustrates a mis-aligned probe tip along an x-axis direction from the beam. Reference numeral **830** illustrates a y-direction mis-alignment. An aligned probe tip and laser beam via raster field of view are illustrated by way of reference numeral **840**. Such alignment provides the finer alignment according to an embodiment of the present invention. By way of example only, the relationship between the probe and the laser is adjusted by way of an automated x-y-z state, which has automated and/or semiautomated control features according to a specific embodiment.

As noted, the method includes fine and ultrafine alignment to as little as a few nanometers. Such alignment can be achieved by imaging the backscatter of the excitation laser either when scanning the laser over the cantilever tip or alternately when scanning the tip over a fixed focus excitation laser. The backscatter image gives a high resolution image via the microscope objective which allows the relative positions of the tip and the laser to be established. Final alignment can then be achieved by either moving the cantilever assembly, moving the cantilever tip or the excitation laser focus point until the excitation laser and the cantilever tip are properly aligned. All of the previously mentioned alignment steps can be carried out separately or in combination. Also they can be carried out in combination with a properly marked sample substrate which incorporates appropriate position reference points and or structures. Alignment can be maintained while imaging in several ways. It can be achieved by imaging the excitation laser back reflection. The imaged diffraction pattern can then be used to monitor changes in relative position which can be used to correct any misalignments which develop if the laser tracks the cantilever tip while imaging a sample. Alternately, information associated with the pattern can be used to provide primary commands to move the excitation laser to track a moving cantilever tip. Finally it can be used to correct other accumulated misalignments including but not limited to thermal drift and strain relaxation, hysteresis, and piezo creep. These techniques can be used to achieve and maintain alignment whether the cantilever tip scans a stationary sample and excitation laser, both the cantilever tip and excitation laser scan a stationary sample, the excitation laser scans a stationary cantilever tip and sample, or a stationary cantilever tip and excitation laser scan a moving sample.

Although the above has been illustrated in terms of specific hardware and/or software features, it would be recognized that many variations, alternatives, and modifications can exist. For example, any of the hardware features can be further combined, or even separated. The features can also be implemented, in part, through software or a combination of hardware and software. The hardware and software can be further integrated or less integrated depending upon the application. One of ordinary skill in the art would recognize many alternatives, variations, and modifications.

FIGS. **9** through **12** are simplified diagrams of packaging systems **900** and methods **1200** for scanning systems according to embodiments of the present invention. These diagrams are merely examples, which should not unduly limit the scope of the claims herein. One of ordinary skill in the art would recognize many other variations, modifications, and alternatives. As shown, the system includes a package **900** to protect an environment of sensitive scanning and measurement equipment. Preferably, the scanning system is an apertureless microscope system for viewing one or more features of samples to a resolution of molecular sensitivity. The system maintains a controlled environment for elements including sample **109** coupled to stage **111**. The elements also include AFM probe **107**, which is coupled to drive **101**, through cantilever member. Source **103** and detector **105** are also enclosed in the environment. Other elements include objective **119** coupled to mirror **120** and laser source **117**. Filter **121** is coupled to sensor **123** and is coupled to detector **125**. Each of these elements are also included in the controlled environment. Of course, some of these elements may be removed while others added without departing from the scope of the claims herein. Preferably, at least the AFM probe **107**, sample **109**, stage **111** and objective **119** are included in the controlled environment.

The controlled environment allows for accurate measurement of one or more features on a sample. Depending upon the embodiment, the controlled environment has a predetermined temperature, lighting, pressure, gas mixture, any combination of these, and the like. The environment can also be free from contaminants, e.g., organic, inorganic. Preferably, the environment is free from coupled mechanical vibration, i.e., equivalent to less than 1% of an output signal of measurement, although others may work as well. Other embodiments may require an oxygen rich environment. Still others may include a non-reactive environment, which is rich with nitrogen bearing particles and/or non-reactive

noble gases, any combination of these, and the like. In many cases, the sample may be maintained and imaged in a biologically relevant fluid environment. Of course, the environment depends highly upon the particular application.

Referring to FIG. **10**, the controlled environment is provided using system **900**. The system has a member **1007** for supporting the apertureless microscope system. A support structure **1001** is coupled to the member to support the member. A plurality of shock absorbing devices **1005** is coupling the support structure and the member. The plurality of shock absorbing devices is capable of substantially eliminating a possibility of mechanical noise from the floor structure. Preferably, the shock absorbing device is a sorbothane manufactured by Sorbothane corp., but can also be others. The shock absorbing device has a suitable length and capable of supporting 2 or more pounds. At least all vibration sensitive elements, and vibration producing elements (e.g. those with fans are included. Preferably, the shock absorbing devices substantially eliminate high frequency (e.g., >10 Hz) noise from entering the controlled environment through the floor structure.

The system also has an enclosure structure **1003** coupled to the member and covering the apertureless microscope system. The enclosure houses the apertureless microscope within an opening confined within the enclosure structure. The enclosure can be made of a suitable material that is rigid and can maintain the environment. Preferably, the enclosure is made of a plastic, a metal, or wood, as well as any combination of these. As merely an example, the enclosure is made of wood, but can also be made of other materials. A cross-sectional-view of the enclosure has been provided by FIG. **11**, which is not intended to be limiting.

As shown, the cross-sectional view includes an outer region exposed to an outer environment **1103** and an inner region exposed to the controlled environment **1115**. The outer environment is often a laboratory or other location where human beings often work. The controlled environment is a region occupied by the scanning system, as previously noted. The enclosure includes rigid structure **1109**. As noted, the rigid structure can be made of a suitable material for supporting the enclosure and overlying materials. The enclosure may also include a frame to support the rigid structure or semi-rigid structure. Such frame can also include walls according to specific embodiments. A sound absorbing member **1111** is coupled to the enclosure structure to substantially eliminate a possibility of acoustic noise from entering into the opening from an external source within the enclosure structure. Preferably, the sound absorbing member is a foam composite, but can also be other sound deadening materials. An inner liner **1107** is also coupled within the opening of the enclosure structure to absorb one or more stray photons within the enclosure structure. The inner liner is generally capable of substantially preventing the stray photons from being released back into the enclosure structure. As an example, the inner liner is a composite manufactured by EAR Composites Inc. A reflective member (e.g., aluminum or other metal, or aluminized mylar or dense plastic) **1105**, **1113** can be formed overlying outer surfaces of the enclosure structure. The outer reflective member is configured to substantially eliminate a desired acoustic noise from entering into the opening within the enclosure structure by reflecting a desired acoustic noise on the reflective surface. Depending upon the embodiment, there can be other layers, which are interposed between any pair of layers described. Some of these layers may be sound absorbing or serve to support the reflective layers. Other embodiments may remove one or more of the layers. Additionally, each layer can be a single material, a composite, or multi-layered, depending upon the embodiment.

Although the above has been illustrated in terms of specific hardware features, it would be recognized that many variations, alternatives, and modifications can exist. For example, any of the hardware features can be further combined, or even separated. Further details of the functionality of the present invention can be outlined below.

According to the present invention, a method for operating a scanning system in a substantially noise free environment is provided as follows.

1. Insert a sample having a molecular feature on a stage of an apertureless microscope system, which has at least a scanning apparatus including a probe coupled to an optical imaging apparatus;

2. Capture information having a feature size of less than five nanometers from a portion of the sample;

3. Maintain at least the stage and the sample in an opening confined by an enclosure structure, which is coupled to a member for supporting a portion of the apertureless microscope system;

4. Maintain at least the stage and the sample free from mechanical vibration noise using a plurality of shock absorbing devices coupling the member, where the plurality of shock absorbing devices is capable of substantially eliminating a possibility of mechanical vibration noise from an external source;

5. Maintain at least the stage and the sample free from acoustic noise using a sound absorbing member coupled to the enclosure structure to substantially eliminate a possibility of the acoustic noise from interacting with the captured information; and

6. Capture one or more stray photons within the opening of the enclosure structure using an inner liner coupled within the enclosure structure to absorb the one or more stray photons within the enclosure structure.

The above sequence of steps is used to perform a method for operating a scanning system in a substantially noise free environment for viewing one or more features of a sample(s) to a resolution of molecular sensitivity. The method allows users of the scanning system to work around it without substantial interference of measurements derived from the system. Further details of the present method are provided throughout the present specification and more particularly below.

Referring to FIG. **12**, the method **1200** begins with start, step **1201**. The method includes inserting (step **1203**) a sample having a molecular feature on a stage of an apertureless microscope system, which has at least a scanning apparatus including a probe coupled to an optical imaging apparatus. An example of such an apparatus has been described above, but can also be outside of this specification according to certain embodiments. Alternatively, the apparatus can be sample scanning with fixed optics and probe, probe scanning with fixed sample and optics, optically scanned with fixed sample and probe, and probe and optically scanned with fixed sample. The optical imaging apparatus is adapted to capture information having a feature size of less than five nanometers from a portion of the sample in preferred embodiments.

Once the sample has been placed on the stage, the method maintains a controlled environment. In a specific embodiment, the method maintains (step **1203**) at least the stage and the sample in an opening confined by an enclosure structure. Preferably, the enclosure structure is coupled to a member for supporting a portion of the apertureless microscope system. The method maintains at least the stage and the

sample free from mechanical vibration noise (step **1207**) using a plurality of shock absorbing devices coupling the member. The plurality of shock absorbing devices is capable of substantially eliminating a possibility of mechanical vibration noise from an external source. Other techniques could also be used, as well.

The method further maintains at least the stage and the sample free from acoustic noise (step **1209**) using a sound absorbing member. Preferably, the sound absorbing member is coupled to the enclosure structure to substantially eliminate a possibility of the acoustic noise from interacting with the captured information. An example of such a sound absorbing member has been provided. The method then has a step of capturing (step **1215**) one or more stray photons within the opening of the enclosure structure using an inner liner. Such inner liner is coupled within the enclosure structure to absorb the one or more stray photons within the enclosure structure. The inner liner is capable of substantially preventing the one or more stray photons from being released back into the opening of the enclosure structure. Depending upon the embodiment, there may be other steps that are included and/or possibly removed.

Although the above has been illustrated in terms of specific hardware and/or software features, it would be recognized that many variations, alternatives, and modifications can exist. For example, any of the hardware features can be further combined, or even separated. The features can also be implemented, in part, through software or a combination of hardware and software. The hardware and software can be further integrated or less integrated depending upon the application. One of ordinary skill in the art would recognize many alternatives, variations, and modifications.

FIGS. **13** through **16** are simplified diagrams of various tip devices according to embodiments of the present invention. These diagrams are merely examples, which should not unduly limit the scope of the claims herein. One of ordinary skill in the art would recognize many other variations, modifications, and alternatives. As shown, the system includes common elements as the prior figures without unduly limiting the scope of the claims herein. The present tip devices are provided within the region surround by the dotted line and indicated by reference numeral **1300**. As shown, the tip **107** is coupled to a cantilever, which is coupled to a drive device. Preferably, the tip is a nanotube based structure, but can also be like structures, depending upon the embodiment. Referring to FIG. **14**, the nanotube structures **1300** include at least a pyramid shaped structure **1301**, which includes tip **1301**. Additionally, such structures include a multi-diameter structure **1305**, which includes tip **1307**. The nanotube structure can be single walled, multi-walled, or any combination of these. Preferably, the nanotube structure is single walled and made of pure or doped carbon. Alternately the nanotube could be made of doped carbon. As merely an example, such single walled structure is a PIT tip from a company called Nanosensors of Germany, but can also be others (for example AC240TM tips from Olympus of Japan). In certain embodiments, the nanotube structure **1311** is coated with an overlying layer **1313**. Here, the nanotube structure can be a semiconductor or conductor. The overlying layer or layers (if multilayered) is a conductor, e.g., metal. The metal's used include platinum, gold, silver alloys, aluminum, platinum-iridium, cobalt and many others. Preferably, the metal is high purity gold or platinum. The nanotube structure can also include a length of less than 250 nanometers in certain embodiments, but will generally have a range of length, e.g., 5-100 nanometers, 10-30 nanometers, depending upon the application.

The metal is deposited using a deposition process. Such deposition process includes evaporation, chemical vapor deposition, sputtering, or molecular beam epitaxy. Preferably, the deposition process is molecular beam epitaxy, which forms a high quality layer of single crystal metal. The thickness of such metal is preferably less than 3 nm, although other thicknesses can be used. The combination of nanotube structure and overlying layer is less than 5 nm diameter near a tip region in preferred embodiments. This compares with commercially available metalized AFM probe diameters of 30 nm from Olympus of Japan. The coated nanotube structures should enhance coupling with an excitation laser light according to certain embodiments. Alternative embodiments are provided by the simplified diagrams of FIGS. **14**A and **14** B, which are nanotube based probes. Such probes include AFM probe **1320** coupled to nanotube probe **1321**. Depending upon the application, there can be many other variations, modifications, and alternatives.

According to an alternative embodiment, metal coating is used for one or more sides of a DNA molecule. Such coated DNA molecule is attached to the probe such that it provides higher resolution images while still modulating the optical signal from the sample being imaged. A DNA molecule coated with gold on one side can have a typical diameter of less than 8 nm.

Other alternative embodiments are illustrated by the photographs **1401**, **1403**, **1405** of FIGS. **14**C, D, and E. Referring to FIGS. **14**C and D, TEM images of shortened nanotube ropes attached by pickup are shown. As shown, nanotube rope dimensions on the right side axis and are approximately 8 nm in width by 62 nm in length. The nanotube tip on the left is approximately 12 nm long and 5 nm in diameter. Referring to FIG. **14**E, scanning electron micrographs of an individual, unshortened carbon nanotube mounted on silicon AFM probe is illustrated. The nanotube was picked up from a flat substrate supporting SWNTs grown by metal catalyzed chemical vapor deposition. Of course, there would be many other alternatives, variations, and modifications.

In a specific embodiment, a method for using the coated nanotube probe can be illustrated by way of FIG. **15**. As shown, the nanotube probe includes a first state **1501** and a second state **1502**. A sample **1505** is also included. The first state has the probe above the sample while the second state is on or in a vicinity of the surface of the sample as shown. As merely an example, an output detected by the present system is shown in the simplified plot of FIG. **16**. The plot includes vertical axis, which is photon count, along probe position. Further details of such plot are provided throughout the specification and more particularly below.

Although certain figures have been described in terms of a specific nanotube structure, one of ordinary skill in the art would recognize many variations, alternatives, and modifications. For example, the nanotube material can be made of homogeneous material, a composite, or even a coated structure. The coating may be a metal, as noted. The metal can include a conductive metal such as platinum, gold, silver, cobalt, and various alloys of such metals such as platinum iridium alloy and the like. Of course, there can a variety of variations without departing from the scope of the claims herein.

Experimental Results:

To prove the principle and operation of the present invention, we performed experiments. The present invention used the FANSOM system, which has been previously described. Such FANSOM used a Digital Instruments BioScope AFM, which had a controller. The controller was a NanoScope IIIa, also manufactured by Digital Instruments of Santa Barbara, Calif. A second closed-loop BioScope AFM has also been used with a NanoScope IV controller. The microscope objective is a 1.3 NA 100× oil immersion objective, which was manufactured by Olympus of Japan.

The system used a PIT tip coated with platinum and iridium manufactured by NanoSensors of Germany. Such tip had a 75 kHz. The samples prepared 20 nanometer (nm) latex beads from a company called Interfacial Dynamics of Portland, Oreg. Such beads were coated with a fluorescent dye, e.g., Nile Red 2 dye. The experiments were performed in room temperature at atmospheric pressure. Although these parameters have been used, there can be many other variations, modifications, and alternatives.

Using the experiment, we demonstrated the probe. Referring to FIG. **17**, as the probe came within a vicinity of a surface of the sample, photon counts decreased. As merely an example, the high photon count corresponded to a 120 nanometer distance between the surface of the sample and the probe. The lower photon counts corresponded to contact between the probe and the sample. As shown, a rate of fluorescence is shown modulated as the cantilever tip oscillates above the sample.

Another example of our experiment is provided by the simplified diagram of FIG. **18**. As shown, a number of photons (y-axis) emitted by a 20 nm fluorescent bead as a function of phase (shown in π radians on the x-axis). At a phase of 0.3 π radians, the tip is closest to the bead and the fluorescence is reduced or even minimized. When the tip is far from the bead the fluorescence is increased or even maximized. The tip is in a stationary X-Y position over the center of the 20 nm bead for a long time, e.g., ten seconds and more. The tip oscillates in the z (vertical) axis and the bead is continuously illuminated. In this combination of illumination (including phase and evanescent components) only a reduced detection rate is illustrated.

Another illustration is provided by the simplified diagram of FIG. **19**, which plots photon count in the vertical axis against radians, i.e., phase, which are along the horizontal axis. A strong polarized evanescent component that has increased fluorescence is seen only when the tip is very close to the bead. At longer range the fluorescence is maximized as the tip to sample distance increases in a manner similar to that seen in FIG. **18**.

We also imaged the bead using AFM only and FANSOM. Referring to FIG. **20**, the 20 nm fluorescent bead has been imaged by AFM (left) and FANSOM (right). The full width-half max (FWHM) diameter is measured on both images as 40 nm. The resolution of the FANSOM is therefore demonstrated to be at least 20 nm for this large sample. Accordingly, FANSOM resolution appears to be limited by the imaging capability of the probe and matches the best available via AFM. In other experiments, we prepared approach curves using a closed loop AFP (See, for example, FIGS. **20**A and **20**B), which provided improved positioning to a resolution of 10 nanometers and better. The closed loop AFM reduced or even minimized the relative drift of the probe over the sample. Partially by minimizing the relative drift error source, it can be expected that 10 nm resolution can be achieved using the present tips. In the present experiments, we used a NanoScope IV controller rather than the IIIa, which had been previously used. As noted above, we used the Digital Instruments BioScope with NanoScope IIIa controller to take the AFM image. Most of the presented FANSOM data was taken with the same optics coupled to a Closed-loop BioScope with NanoScope IV controller. The FANSOM resolution should improve with better probes (e.g. nanotubes) and smaller targets (e.g. quantum dots, biological molecules, etc.).

We also discovered that FANSOM can be used to distinguish different types of materials. For example, images of the bead and a dust particle have been captured. Such images are provided by the diagrams in FIG. **21**. As shown, a 100 nm fluorescent bead and a dust particle are illustrated. On the left hand side using an AFM, the dust particle and bead are nearly indistinguishable (since they each appear as bright spots along a black background.) On the right hand side, they are imaged by FANSOM which clearly distinguishes the fluorescent spherical bead from the dust particle. Depending upon the embodiment, there can be many other variations, modifications, and alternatives.

Although the above has been illustrated in terms of specific hardware features, it would be recognized that many variations, alternatives, and modifications can exist. For example, any of the hardware features can be further combined, or even separated. The features can also be implemented, in part, through software or a combination of hardware and software. The hardware and software can be further integrated or less integrated depending upon the application. One of ordinary skill in the art would recognize many alternatives, variations, and modifications.

FIG. **22** is a simplified diagram of an alignment subsystem **2200** for an optical system according to an embodiment of the present invention. This diagram is merely an example, which should not unduly limit the scope of the claims herein. One of ordinary skill in the art would recognize many other variations, modifications, and alternatives. As shown, a system **2200** for dynamically viewing an increased field of view based upon a smaller field of view to capture an image of features of samples to molecular sensitivity is included. Like reference numerals are used in this figure as the prior figures without limiting the scope of the claims herein. The system has an electromagnetic energy source (in a specific embodiment this can be a laser) **117**, which is capable of emitting a beam. A fixed lens **119** is coupled to the electromagnetic energy source. The fixed lens focuses the beam toward at least one tip of a probe **107**, which is in a vicinity of a feature of a sample to scatter a portion of the beam off a portion of the tip of the probe. A detector **2203** is coupled to the fixed lens. The detector detects the scattered portion of the beam. As shown, the scattered portion of the beam traverses through objective, through mirror **120**, through filter (optional), to the detector. A processor **115** is coupled to the detector via input/output device **2205**. The processor is adapted to process the scattered portion **2201** of the beam to determine a pattern to identify a relationship between the tip and the beam for a spatial alignment between the tip and the beam. As merely an example, conventional image processing techniques can be used. An adjustment device **111** is coupled to the processor. The adjustment device is adapted to adjust a position of the beam based upon at least the pattern to maintain a desired relationship between the tip and the beam. As merely an example, the adjustment device can be an x-y-z state or the like. Further details of the present system can be described with way of the following methods described below.

A method according to an embodiment of the present invention for dynamically viewing an increased field of view based upon a smaller fixed field of view to capture an image of features of samples to molecular sensitivity is provided as follows.

1. Output a beam from a laser coupled to an optical system, which is coupled to an AFM system;

2. Illuminate through a fixed lens coupled to the optical system using the beam of the laser a feature of a sample on a stage coupled to the AFM system;

3. Direct the beam toward at least one tip of a probe coupled to the AFM, which is in a vicinity of the feature of the sample;

4. Scatter a portion of the beam off a portion of the tip of the probe;

5. Traverse scattered portion through the fixed lens;

6. Detect the scattered portion of the beam using a detector;

7. Transfer signal indication from scattered portion being detected to a processor;

8. Process the signal indication of the scattered portion of the beam to determine a pattern to identify a relationship between the tip and the beam for spatial alignment between the tip and the beam;

9. If necessary, adjust a position of the beam used for illumination based upon at least the pattern to maintain a desired relationship between the tip and the beam; and

10. Maintain the alignment between the tip and the beam using one or more of the steps above.

These steps provide a way to align the probe tip of the AFM to the optical subsystem, which is coupled to the AFM. Such steps are provided as the AFM is operational or in-situ in some embodiments. These steps are used by way of a combination of computer hardware and/or software depending upon the embodiment. Further details of these steps are provided throughout this specification and more particularly below.

FIGS. **23** through **24** are simplified diagrams of tip detection alignment methods **2300** for the scanning system according to embodiments of the present invention. These diagrams are merely examples, which should not unduly limit the scope of the claims herein. One of ordinary skill in the art would recognize many other variations, modifications, and alternatives. The scanning system can be one or more of the ones that were previously described, as well as others. As shown, the method begins at start, step **2300**. Here, the method for dynamically (e.g., moving) viewing an increased field of view based upon a smaller fixed field of view to capture an image of features of samples to molecular sensitivity. The method emits a beam from a laser for transfer, step **2303**.

The method also includes illuminating (step **2305**) through a fixed lens using the beam a feature of a sample. The beam is directed toward at least one tip of a probe, which is in a vicinity of the feature of the sample. Next, the method scatters (step **2307**) a portion of the beam off a portion of the tip of the probe. The scattered beam traverses back through the lens. Optionally, the beam also scatters through a filter. The method detects (step **2315**) the scattered portion of the beam using a detector. The detector can include a CCD camera, an avalanche photodiode, or the like.

The method then transfers (step **2317**) signals associated with the detector to a processor. The method then processes (step **2319**) the scattered portion of the beam to determine a pattern to identify a relationship between the tip and the beam for spatial alignment between the tip and the beam. The processing can be done on a conventional signal processor and/or computer or the like. The processor determines of the tip is aligned to the beam, step **2321**. If so, the method continues to transfer the beam, which may have been continuously transferred, as the probe and sample move relative to each other in the scanning method. If not, the method adjusts (step **2323**) a position of the beam used for illumination based upon at least the pattern to maintain a desired relationship between the tip and the beam. Such adjustment may occur using an automated x-y-z stage or the like. The method continues via the branch to step **2303**. The method also stops at step **2313**.

Referring to FIG. **24**, the present method maintains alignment between the probe tip and laser beam. As noted above, such alignment is generally for precision measurement of the features of the sample. The probe tip **2401** should be aligned with the beam **2403**, which can be viewed on display **2400**. Such display can be coupled to the processor, which processes the signals of the image. Of course, there can be other modifications, alternatives and variations.

Preferably, the present method is provided on a secondary illumination system **2500**, which is coupled to the FANSOM. Referring to FIG. **25**, the system **2500** includes various elements, which can be found in the other systems described herein. Additionally, the system includes an independent or secondary illumination sub-system, which transmits and receives scattered light from the probe using a different wavelength of light than the main detector, which is used for the imaging. As shown, the system includes cantilever **2501**, which is coupled to tip **2503**. A sample **2505** such as a bead, fluorophore, DNA, quantum dot, or others is included. The sample is provided on cover slip **2507**. An objective **2509** is coupled to the probe. A tip/tilt mirror **2511** directs light between dichroic mirror **2514** and objective. The dichroic mirror reflects an excitation laser and transmits the backscattered signal. As shown, the excitation laser **2519** transmits light through beam splitter **2517** to the mirror, which transmits the light to the probe. Such probe scatters light and directs it back through the secondary optical subsystem. The scattered light goes from the probe, through the objective, through a secondary eyepiece **2527**, which is coupled to secondary bandpass filter **2529**, which is coupled to a secondary detector **2531**, which receives scattered light from the probe. The system also has primary eye piece **2521** coupled to primary filter **2523**, which is coupled to primary detector **2525**. Control electronics **2517** is coupled to the secondary detector **2531**. The solid arrows and lines represent control signals and the other lines represent light paths. Of course, there can be many variations, alternatives, and modifications.

Although the above has been illustrated in terms of specific hardware and/or software features, it would be recognized that many variations, alternatives, and modifications can exist. For example, any of the hardware features can be further combined, or even separated. The features can also be implemented, in part, through software or a combination of hardware and software. The hardware and software can be further integrated or less integrated depending upon the application. One of ordinary skill in the art would recognize many alternatives, variations, and modifications.

FIG. **25**A is a simplified diagram of a FANSOM system using a closed loop feedback loop according to an embodiment of the present invention. This diagram is merely an example, which should not unduly limit the scope of the claims herein. One of ordinary skill in the art would recognize many other limitations, variations, and modifications. Preferably, the system includes use of a closed-loop AMF position information directly in combination with the tip-tilt mirror position information to maintain alignment while scanning large fields of view or while taking a series of high resolution small FOV images of many samples spread over a larger area (e.g. a 100 micron square region).

According to a specific embodiment to maintain the initial alignment while imaging a series of samples. Alignment established as above, both are commanded to new location, maintaining the earlier established alignment, then imaging commences as above. The location of each of these series of samples could be determined before either by patterning, by taking a large FOV image (for example using a CCD array) and determining the coordinates of each sample within the image, or by taking an AFM image of the sample and

determining the coordinates of each sample. The series of sample coordinates then are used to direct both the closed-loop AFM and the tip-tilt mirror such that the sample is illuminated while maintaining alignment with the probe tip. A high resolution, high sensitivity image can then be taken of each sample in sequence.

Alternately, after achieving alignment, the closed loop AFM can be used to image a large FOV. The position information from the closed loop head can then be used to direct the tip-tilt mirror in such a manner as to maintain alignment as the area to be imaged is rastered over. In an alternate configuration the tip-tilt mirror is commanded to image a large FOV and the position information is used to direct the closed-loop AFM such that alignment is maintained between the probe tip and the excitation laser. Of course, there can be many variations, alternatives, and modifications depending upon the embodiment.

FIGS. **26** through **34** are simplified diagrams of methods and systems for selectively illuminating one or more samples according to embodiments of the present invention. These diagrams are merely examples, which should not unduly limit the scope of the claims herein. One of ordinary skill in the art would recognize many other variations, modifications, and alternatives. As shown, the system includes, among other elements, an AFM source (e.g., laser diode) **2601**. The source is characterized by a certain wavelength of such as λ_A. A clean up filter **2603** is disposed between the source and a focusing lens **2605**. The system includes a plane **2607** for a sample. The plane can be provided on a stage, e.g., x-y stage. The system includes a microscope objective **2609** underlying the sample stage for detecting one or more features from the sample. Other elements include a dichroic mirror **2611** coupled to a laser **2621** λ_E. for sample excitation. A clean up filter **2623** is disposed between the laser and dichroic mirror. The system also includes detector elements such as blocking filter for wavelength λ_A between lens for sample imaging and dichroic mirror. A blocking filter is disposed between the lens and a sample detector **2617**. Depending upon the embodiment, there can also be other elements. Details with regard to the operation of the system can be illustrated by FIGS. **27** through **34**, which are simplified illustrations.

FIG. **27** is a simplified plot of power against wavelength for a spectrum of the AFM laser according to an embodiment of the present invention. The wavelength of the peak emission of the AFM laser is λ_A. FIG. **28** is a simplified plot of power against wavelength for relative positions of wavelengths of predetermined interest. Here, wavelength parameters are defined by λ_E that corresponds to the wavelength of the peak emission from excitation laser, λ_F that corresponds to a range of wavelengths emitted by a sample, λ_{FL} that corresponds to a lower bound of a sample fluorescence, and λ_{FU} that corresponds to an upper bound of a sample fluorescence. FIG. **29** is a simplified plot of transmission plotted against wavelength for a transmission spectrum of the ASE filter according to an embodiment of the present invention. Here, λ_B is the wavelength at which transmission is down to about 10^{-5} and λ_B is higher than λ_{FU}. FIG. **30** is a simplified plot of transmittivity plotted against wavelength for a transmission spectrum of a dichroic mirror according to an embodiment of the present invention. Here, certain characteristics are reflected at (rather than absorption) and transmission from FIG. **31** is a simplified plot of transmission plotted against wavelength for a blocking filter for a wavelength λ_A, which corresponds to a wavelength at which transmission falls to about 10^{-5} and λ_B is higher than λ_{FU}. FIG. **32** is a simplified diagram illustrating power plotted against wavelength for a spectrum of a laser for sample excitation. As shown, λ_E has been illustrated as a single peak. FIG. **33** is a simplified plot of transmission plotted against wavelength of an excitation clean-up filter according to an embodiment of the present invention. Here, λ_C corresponds to a wavelength at which transmission falls to 10^{-5} and λ_C is lower than λ_{FL}. FIG. **34** is a simplified plot of transmission as a function of wavelength. Here, λ_J corresponds to a wavelength at which transmission is about 10^{-5} and λ_J is higher than λ_C. Here, λ_H corresponds to a wavelength at which transmission is about 60% and λ_H is lower than λ_{FL}. Here, λ_G corresponds to a wavelength at which transmission is about 10^{-5} and λ_G is lower than λ_B and also lower than λ_D. Of course, there can be other modifications, alternatives, and variations depending upon the embodiment.

It is also understood that the examples and embodiments described herein are for illustrative purposes only and that various modifications or changes in light thereof will be suggested to persons skilled in the art and are to be included within the spirit and purview of this application and scope of the appended claims.

What is claimed is:

1. A method for measuring a characteristic of biological or chemical objects using detection of photons associated with biological or chemical objects, the method comprising:

providing a liquid environment;

providing a tip of a probe to be movable toward a feature of a biological or chemical sample in the liquid or gas environment to influence an emission of electromagnetic energy associated with the feature of the sample, the feature and the sample being maintained on a stage;

illuminating the tip of the probe using electromagnetic energy comprising a first intensity level as the tip of the probe moves toward the feature of the sample;

capturing a first signal associated with the feature during a first portion of movement of the tip during a portion of time associated with illuminating the tip of the probe with the electromagnetic energy comprising the first intensity level;

moving the tip of the probe using a tapping mode operation toward a vicinity of the feature of the sample during a second portion of movement of the tip;

providing electromagnetic energy comprising a second intensity level associated with the feature of the sample as the tip of the probe moves toward the vicinity of the feature of the sample during the second portion of movement of the tip to cause enhancement of the tip of the probe to the second intensity level;

determining a spatial coordinate of the stage on which the sample has maintained;

determining a distance of the tip of the probe relative to the feature of the sample; and

capturing a second signal associated with the feature to create an image of the feature of the sample.

2. The method of claim **1** wherein the second intensity level is associated with an enhancement or quenching influence of the feature of the sample.

3. The method of claim **1** wherein the first portion and the second portion are provided within an oscillation cycle of the tip of the probe.

4. The method of claim **3** wherein the oscillation cycle is characterized by a predetermined frequency.

5. The method of claim **1** wherein the second intensity level is lower than the first intensity level.

6. The method of claim 1 wherein the vicinity of the feature is when the tip is in contact with the feature.

7. The method of claim 1 wherein the capturing the first signal and the capturing the second signal are among a plurality of capturing steps.

8. The method of claim 1 further comprising scanning the tip of the probe along a spatial surface region of the sample.

9. The method of claim 1 wherein the first signal is associated with a plurality of photons emitted from the feature of the sample.

10. The method of claim 1 wherein the second signal is associated with a plurality of photons emitted from the feature of the sample, the second signal being greater than the first signal.

11. The method of claim 1 further comprising using the probe for capturing information from the biological or chemical sample using an AFM mode of operation.

12. The method of claim 1 further comprising using the probe for capturing information from the biological or chemical sample using an AFM mode of operation or a FANSOM mode of operation.

* * * * *

Appendix E

Two-Color Tip Enhanced Fluorescence Microscope Hardware, Software and Electronics

Design Overview

The basic design of the two color TEFM couples an AFM[1] with a homebuilt optical microscope. The system description will be broken into five parts. The first will deal with the central Microscope Hardware. The second section will define all of the filters and operating configurations. The third section shows the lasers and their associated optics. The fourth section describes the Data Acquisition and Control electronics and software (DAC). The fifth section presents the Matlab scripts used for image processing.

Microscope Hardware:

The assembled microscope is shown in Figure E.1. Figure E.2 shows the section of the microscope where the beams are combined, and then expanded. Figure E.3 shows both optical paths for achieving p-polarization of the evanescent field. One of the paths relies on an optical mask in a similar fashion to that used in the dry TEFM and single-color TEFM. The second incorporates a radial polarization filter, 1:1 telescope and a pinhole that results in a single radially polarized mode being propagated to the sample. Figure E.4 shows the dichroic wheel used to separate the excitation light from the emissed signal. It also shows a tip-tilt mirror used for alignment. Figures E.5 to E.7 show the AFM, sample scanning stage and optical baseplate arrangement. Also included are the 1:1 telescope used in combination with the tip-tilt mirror for beam steering during alignment. Figures E.8 and E.9 show the two optical detection pathways. They also include an optical video camera used for AFM probe-excitation beam alignment.

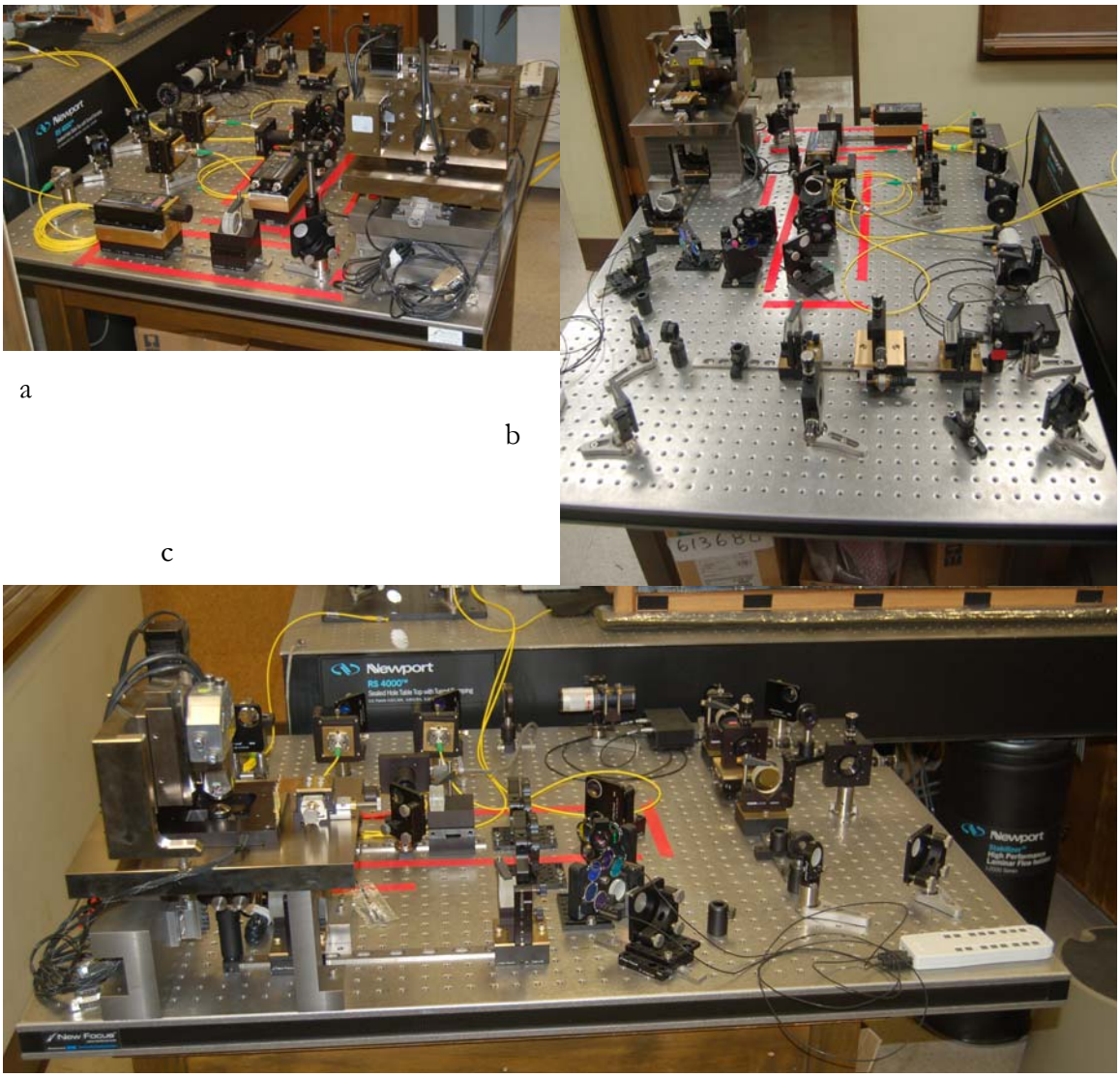

Figure E.1 a, b and c show the complete microscope from three sides.

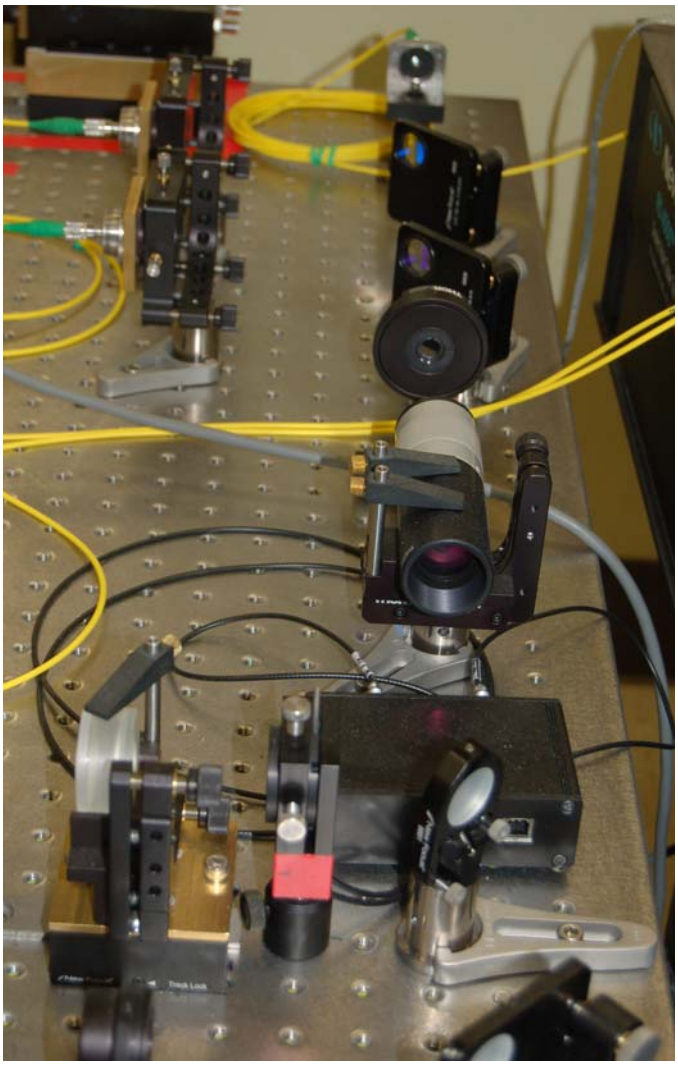

Figure E.2 Three excitation lasers are combined and expanded above. The 543 laser is directly in the beam path. The 502/514 laser is combined next. The 442 nm laser is the last one combined (closest). An apochromatic half-waveplate is provided to ensure uniform linear polarization. A 10x beam expander is also shown.

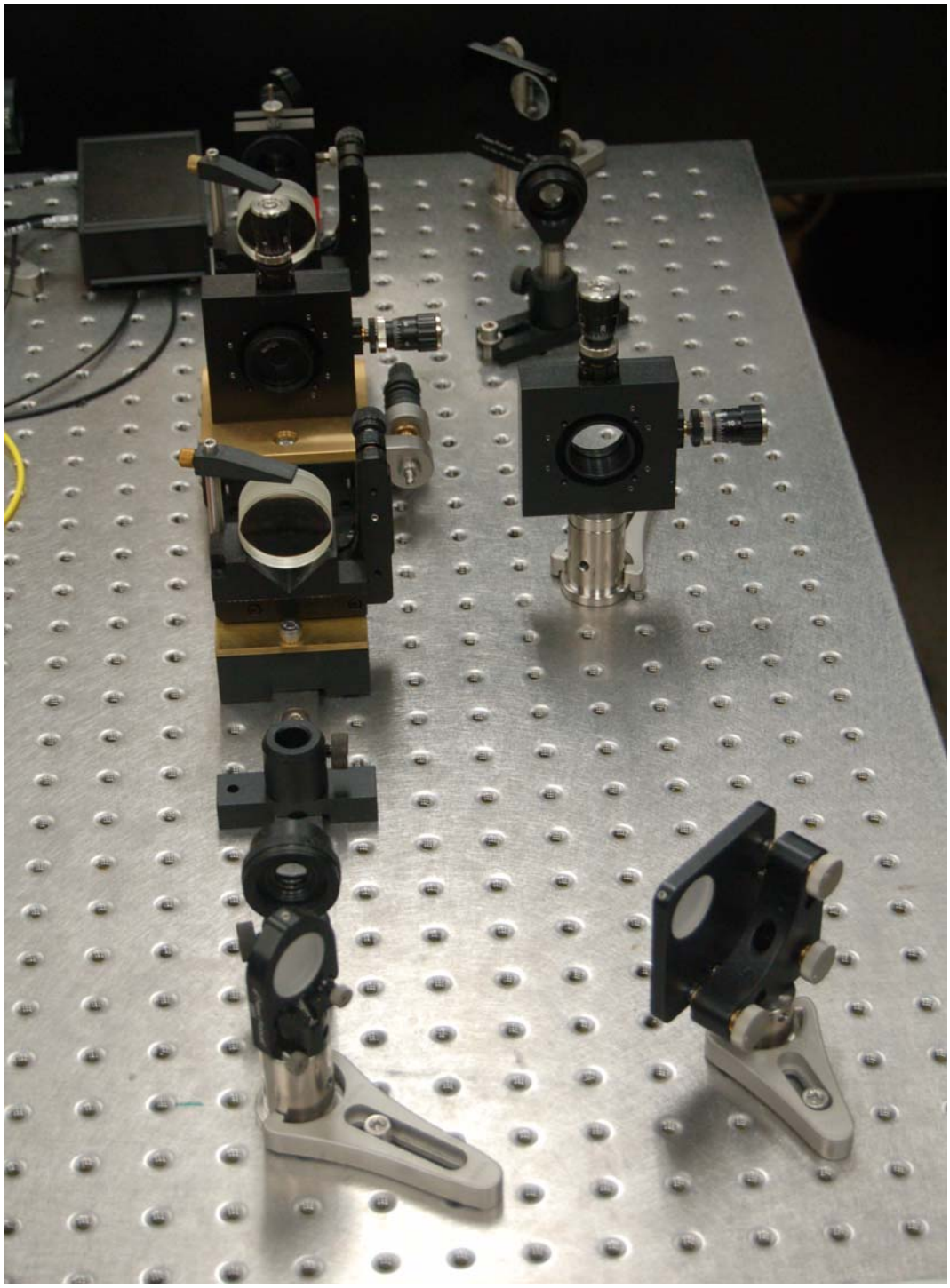

Figure E.3 Two methods for achieving p-polarization of the evanescent field are provided. On the left is the optical path for radially polarizing the excitation light. On the right is the optical path for masking the beam so that only a wedge shaped portion of the back aperture of the microscope objective is illuminated.

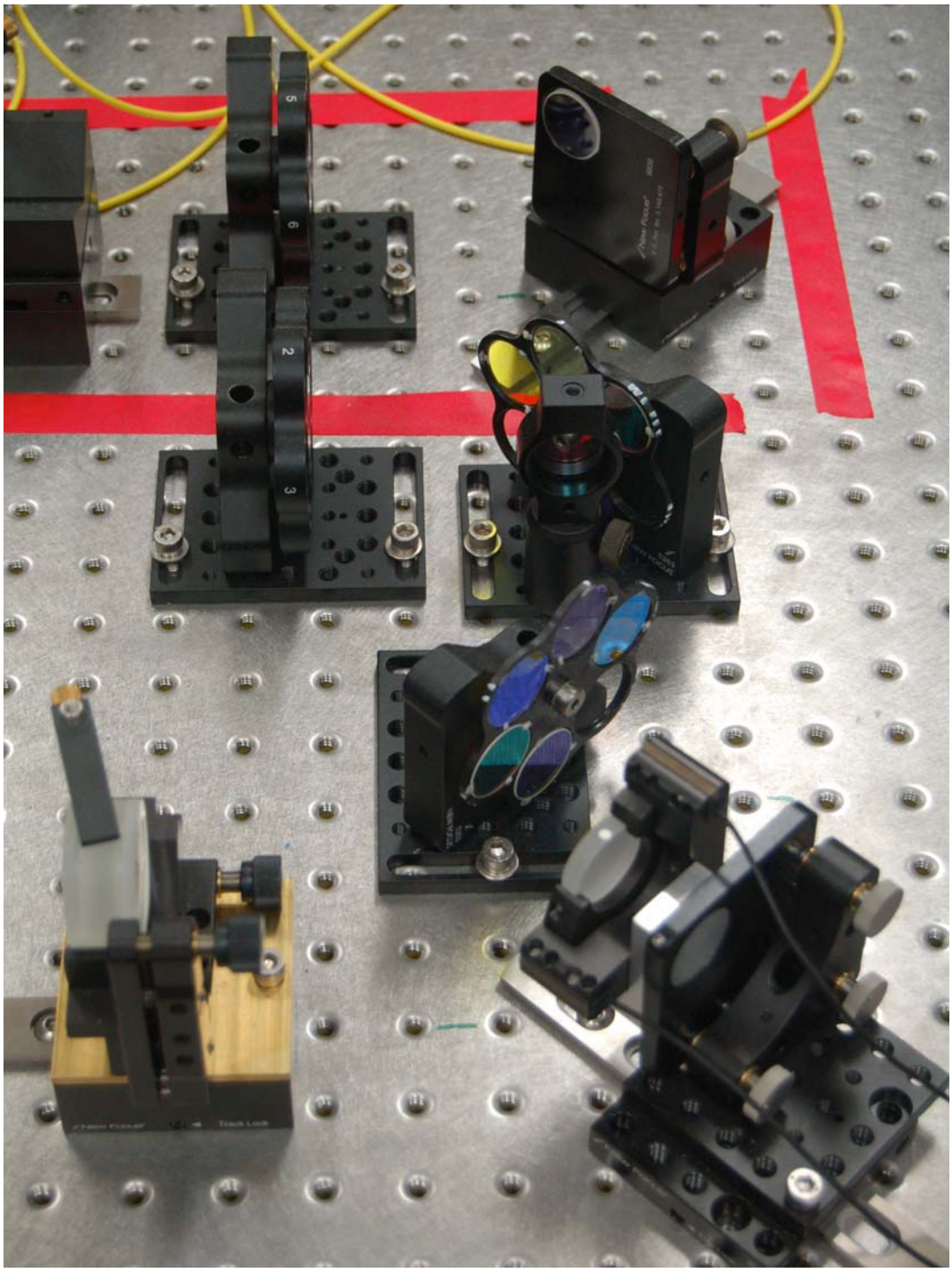

Figure E.4 In the foreground is the dichroic wheel #2 used to separate the excitation beam from the sample emission. The excitation beam then comes forward and reflects off of a dielectric mirror mounted on an actuated tip-tilt fixture. To the left is the first element of the 1:1 telescope that leads to the microscope objective and sample. In the background is the dichroic that splits the emission signal between the two APDs and also the emission filters.

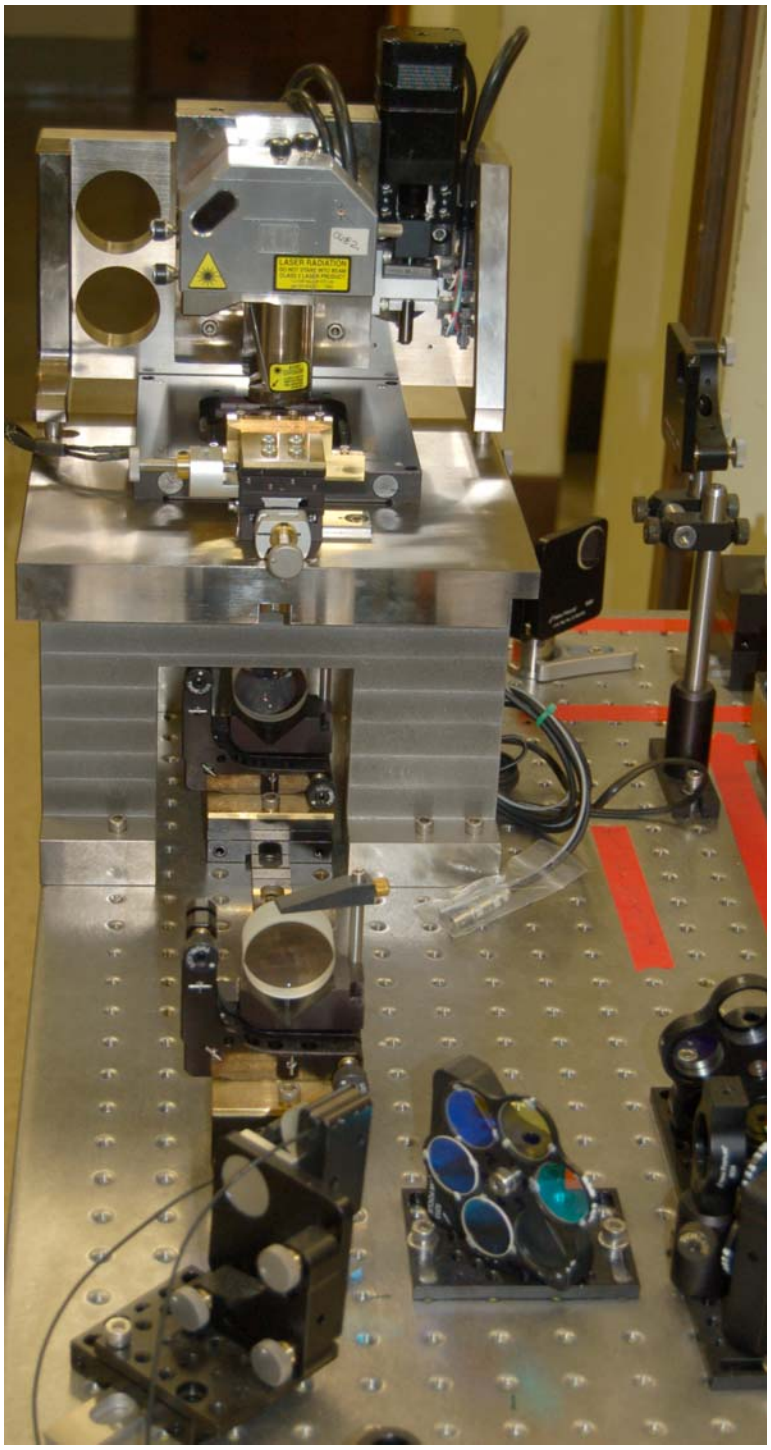

Figure E.5 shows the sample stage, AMF and TIRF microscope. Just to the right of the sample stage is the holder for the laser used to illuminate the AFM probe for alignment.

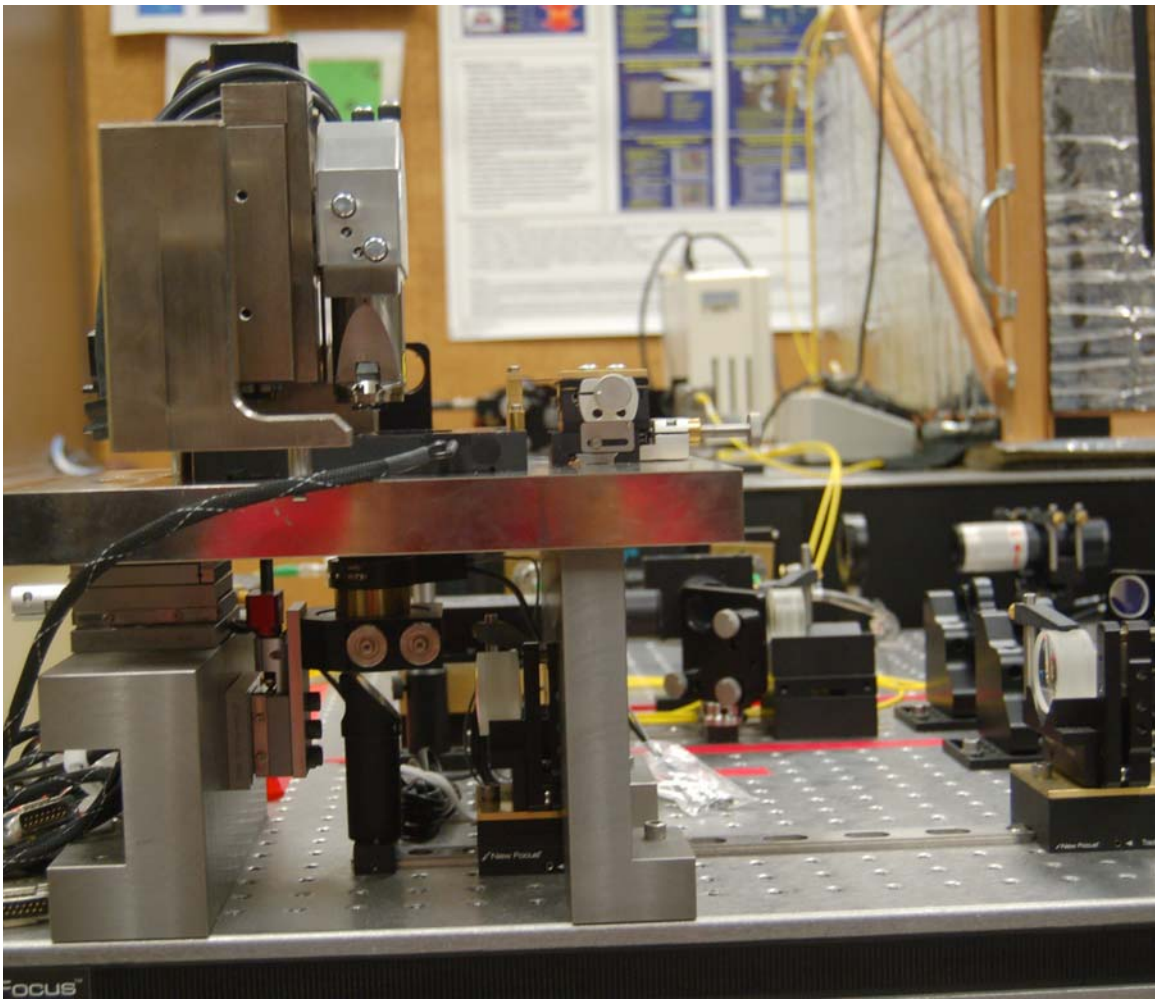

Figure E.6 Shows the AFM and TIRFM from the side.

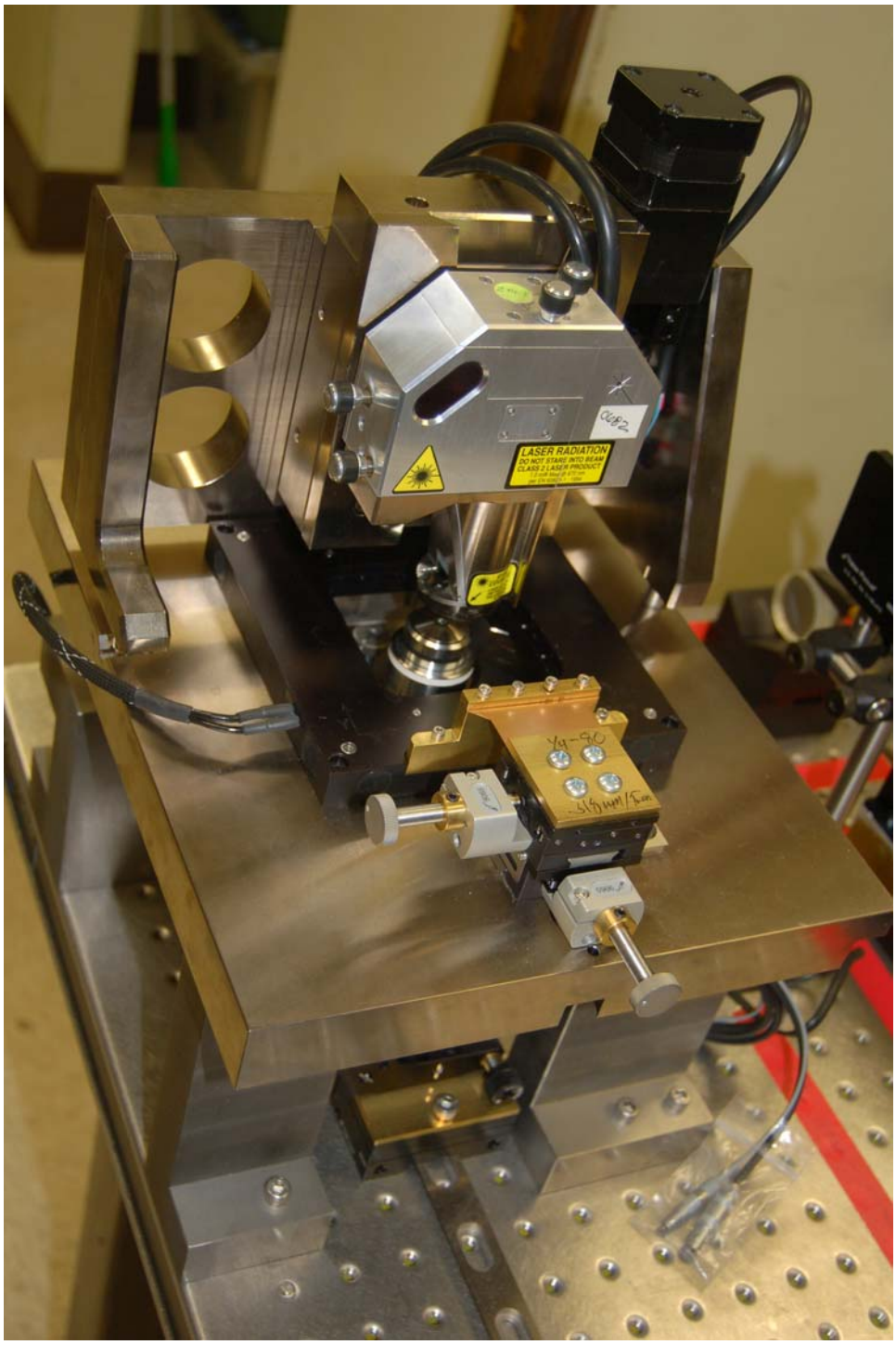

Figure E.7 shows the microscope objective, sample scanning stages (fine and coarse), and the AFM.

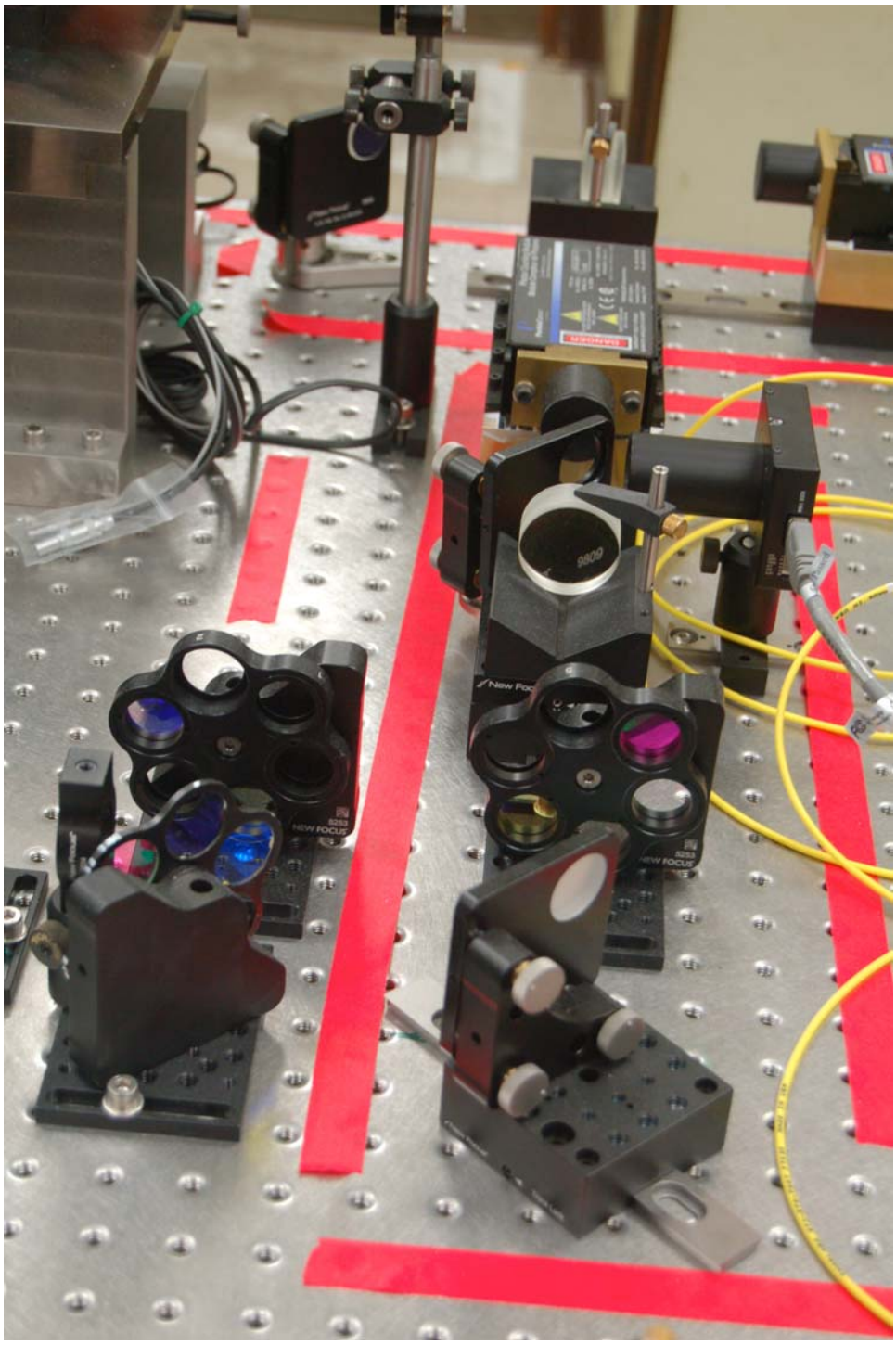

Figure E.8 Dichroic wheels. On the left is shown (starting from the bottom) the dichroic wheel that splits the emission signal between the APD #1 and APD #2. Just above the dichroic wheel is the emission filter wheel for APD #1. At the top of the picture are shown a mirror, a focusing lens, and APD #1. In the center/right you can see (from the bottom to the top) a mirror, an emission filterwheel, a focusing lens, then a clear coverslip used to split ~2% of the light to the right into a camera used for alignment. Just behind/above that 2% beamsplitter is APD #2.

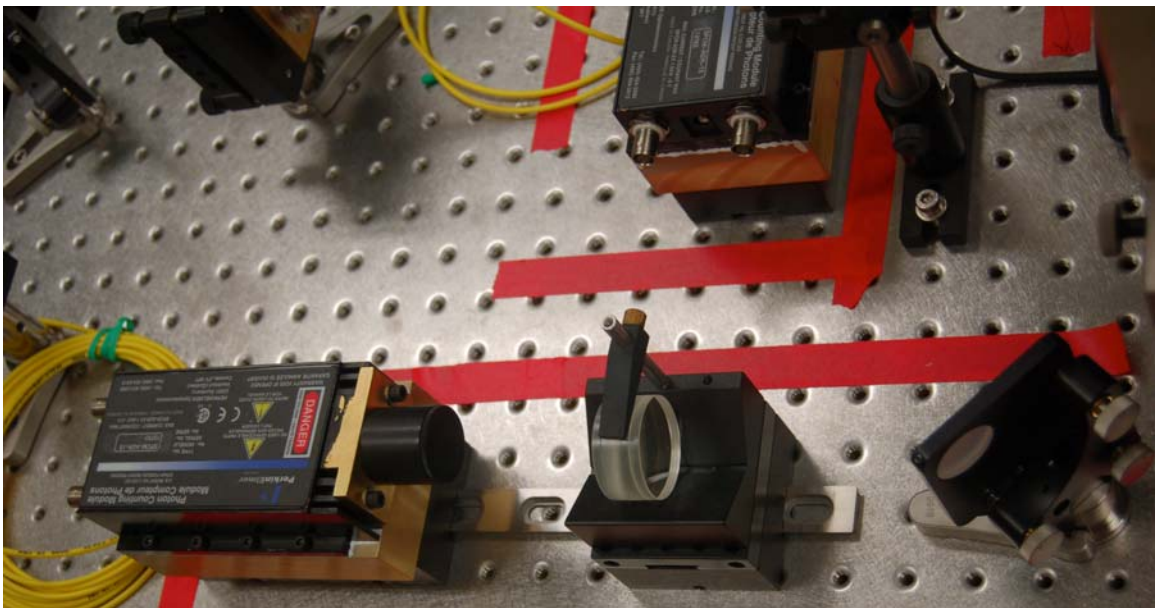

Figure E.9 APD #1 is shown in the bottom left. The focusing lens and a mirror (bottom right) can also be seen. I, the center/top can be seen the back half of APD #2.

Microscope Operating Wavelengths

This microscope was designed to simultaneously detect emissed light in two colors. Three excitation wavelengths are provided. The filters were all custom made by Chroma. The spectral bands were selected to minimize coupling of the targeted fluorophores to more than one of the APDs.

The filter set was designed to accommodate 6 different imaging configurations:

Configuration 1 is for imaging just CFP. The excitation wavelength is 442 nm. The emission band is 460-550 nm.

Configuration 2 is for imaging just YFP. The excitation wavelength is 502 nm. The emission spectral band is 520-600 nm.

Configuration 3 is designed for 2-color excitation and 2-color detection of CFP and YFP. Excitation is provided at 442 nm and 502 nm. The emission spectral bands are 460-485nm and 515-575 nm.

Configuration 4 is designed for 1-color excitation at 514 nm with an emission spectral band of 520-600 nm.

Configuration 5 is designed for 2-color excitation and 2-color detection of CFP and YFP. Excitation wavelengths are 442 nm and 514 nm. The emission spectral bands are 460-500 nm and 525-575.

Configuration 6 is designed for 1-color excitation and detection of mCherry. Excitation is at 543 nm and the emission spectral band is 575-625 nm.

Below are the specific filters (Chroma part numbers) used.

Four excitation filters are provided for the three lasers:

Z442/10X for 442 nm

Z502/10X for 502 nm

Z514/10X for 514 nm

Z543/10X for 543 nm

For excitation beam combination two filters are required. The 543 nm laser is injected directly into the light path. A ZT502RDC dichroic is used to bring 502 and 514 nm lasers in from the side. A ZT442RDC dichroic is used to bring 442 nm laser in from the side.

Dichroic Wheel 2 separates emission signal from excitation signal. This wheel is numbered by position. The filters in each position are:

Pos 1: ZT442RDC used for configuration 1

Pos 2: ZT502RDC used for configuration 2

Pos 3: ZT442/502RPC used for configuration 3

Pos 4: ZT442/514RPC used for configurations 4 and 5

Pos 6: ZT543RDC used for configuration 6

In addition, between the dichroic wheel 2 and the detectors is a 692 blocking filter (to stop the AFM laser): Z692NFRB.

Dichroic Wheel 3 separates longer wavelength emission (to detector 2) from shorter wavelength emission (to detector 1). This filter wheel is also numbered by position:

Pos 1: Z442RDC used for configuration 1

Pos 2: T505LP used for configurations 2 and 3

Pos 4: 515DCLP-XT used for configurations 4 and 5

Pos 6: Z543RDC used for configuration 6

An emission filter wheel is provided for imaging via APD #1. A star by the configuration number indicates the optimal filter choice for that configuration. The filters in the numbered positions are:

Filterwheel Pos 1: ET470/25M for configuration 3*

Filterwheel Pos 3: ET480/40M for configuration 5*

In front of APD #2 an emission filter wheel. A star by the configuration number indicates the optimal filter choice for that configuration. The filters contained in this wheel are:

Pos 1: ET510/80M for configuration 1* (470-550)

Pos 2: ET535/50M for configurations 3 (510-560)

Pos 3: ET540/30M for configurations 2, 3, 4, and 5 (525-555)

Pos 4: ET560/80M for configurations 2*, 3*, 5* (520-600)

Pos 5: ET 595/50M for configurations 1, 4, 6* (570-620)

In addition, just in front of each detector is a filter designed to block the tip illumination laser: ET670SP.

Lasers

The laser assemblies are shown in Figures E.10 - E.12. The three lasers are a 442 nm HeCd laser, an Argon ion laser (selectable for 502 and 514 nm) and a HeNe that operates at 543 nm. Each laser has an Acousto-Optic Modulator (AOM) and a neutral density double optical wheel. Two tip-tilt mirrors are used for coupling into the laser-coupler.

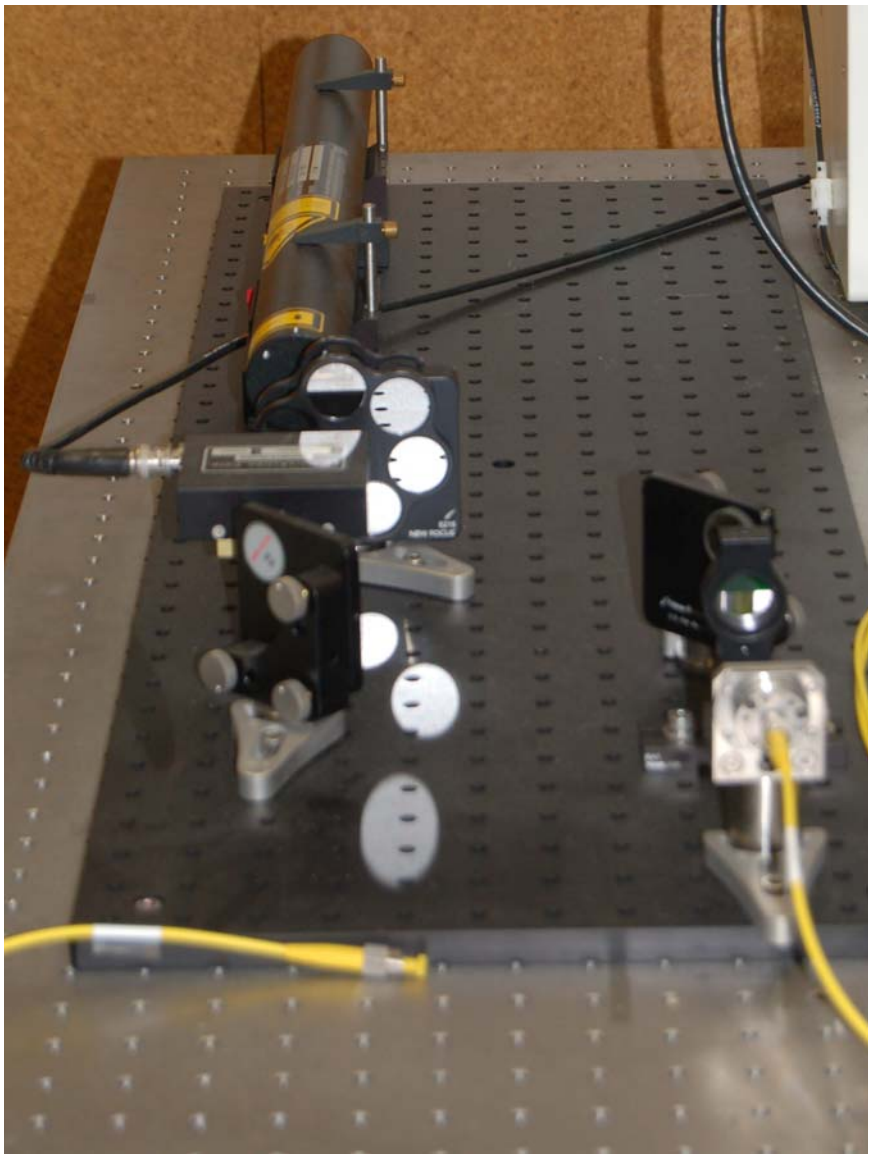

Figure E.10 This shows the 543 nm HeNe laser, AOM, neutral density filter wheels and fiber coupling optics.

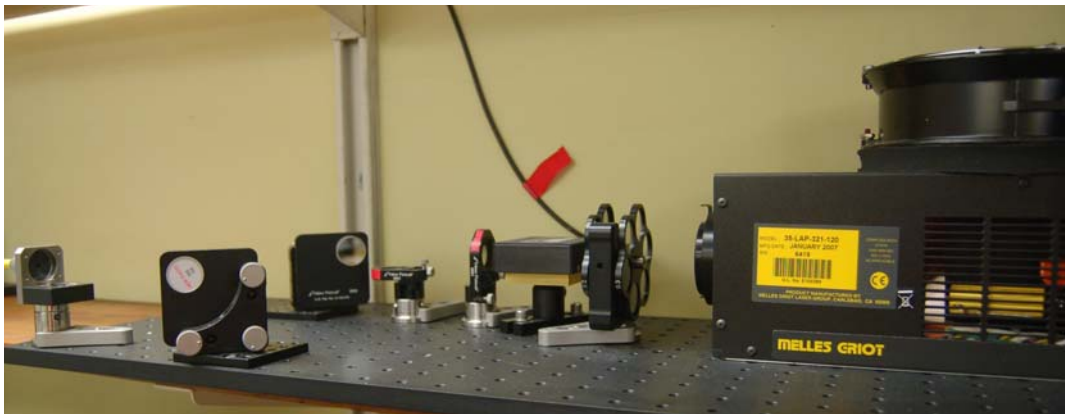

Figure E.11 The 502/514 nm adjustable Argon Ion laser, AOM, neutral density filter wheels and fiber coupling optics.

Figure E.12 The 442 nm HeCd laser, AOM, neutral density filter wheels and fiber coupling optics.

Data Acquisition and Control Electronics and Software

The DAC was designed by me and fabricated at JPL. Below is a report that provides a detailed description of the DAC design. The DAC hardware is shown in Figures E.13-E.15.

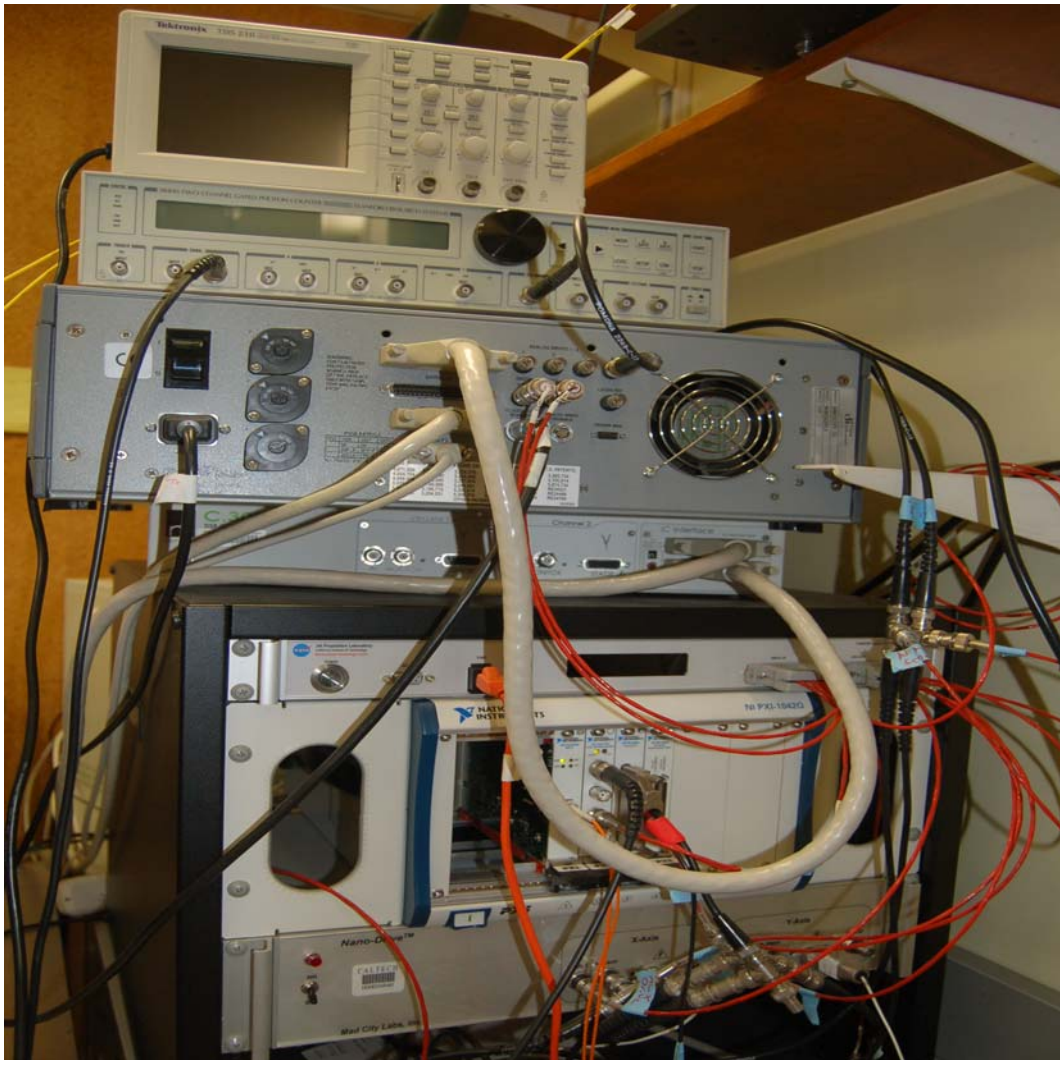

Figure E.13 Several of the DAC electronics boxes are shown above. At the top is an oscilloscope, below that is a SRS400 Gated Photon Counter, then the back of the Nanoscope IV AFM controller, then the nPoint C300 DSP controller (for the fine sample scanning stage), then Box H made by JPL, then the National instruments modules and at the bottom is the Mad City Labs controller for the tip-tilt mirror.

Figure E.14 Top right can be seen the HeCd power supply. In the center can be seen two AOM controllers. Just to the right of the AOM controllers is the side of the Nanoscope IV AFM controller with the gated photon counter on top.

Figure E.15 The tip-excitation laser alignment monitor (top left). Below it is the DAC monitor. The center bottom two monitors are for the AFM computer. The bottom right monitor is for the image-processing monitor.

The next section of this Appendix is a document authored by Brian Franklin and Erik Peterson of the Jet Propulsion Laboratory: 'FANSOM Measurement Technology Center (MTC) Delivery Package.' This document describes the architecture of the data acquisition and control system used in the wet TEFM imaging effort described here. The electronics (pictured in Figure 3.13) were designed and built by Brian Franklin. Erik Peterson wrote the software described in this document. The 'FANSOM Measurement Technology Center (MTC) Delivery Package' is included so that the details of the TEFM would be available to anyone trying to replicate or extend the work reported herein. My role in this work was to define all electrical interfaces, operational modes and the required electronics and software functionalities. I also helped with debugging the system. In addition I funded and directed this work through a JPL Research and Technology Development grant for which I was Principal Investigator.

Later, the data acquisition software described above was further debugged by Mike Gordon (then Caltech and now UCSB) and then significantly upgraded and modified by Jian Li (previously of JPL).

None of the image processing software written by Erik and described in the design delivery package was used for the work reported in this thesis. Instead I used software written by Dan Lo (then a Caltech undergraduate student), which was later replaced by software written by Eyal Shafran. Eyal's software, slightly modified by me, was used to process all of the results included in Chapter 3 and so is included at the end of this Appendix.

FANSOM
Measurement Technology Center (MTC)
Delivery Package

Date: August 10, 2005

Authors: Brian Franklin
Erik Peterson

TABLE OF CONTENTS

TABLE OF FIGURES

1 INITIAL QUOTE

Task Name FANSOM System Automation
Customer Larry Wade, sect. 3543
Phone 4.2272
Cell 818.642.1798
SW Cog. E. Erik Peterson & Brian Franklin

Description
The Fluorescence Apertureless Near-Field Scanning Optical Microscope (FANSOM) system is a novel microscopy technique achieving 10 nm resolution using an apertureless beam forming probe to excite the object being observed at a molecular level.

Requirements

1. Software – The MTC will evaluate all software components of the system and plan an integrated software approach using LabVIEW for the user interface and control software. Some existing code may be integrated into the final product using CIN or functional calls to C. The basic approach will be identified and presented to the customer by 1-2-2005. A data flow diagram and UML model of the current SW and the proposed SW will be presented. Drivers for the commercial hardware will be found and evaluated if possible. Once the detailed plan is presented to and accepted by the customer, development will begin in early January of 2005.
2. Hardware – The MTC will evaluate all commercial and custom hardware and will make a system block diagram of the current system. The Commercial hardware will be re-used. All custom hardware will be evaluated for functionality with a goal of integrating the hardware and providing automated control of the system. New computers and commercial hardware needed to automate the system will be identified and a plan for an integrated and automated system will be produced by 1-2-2005. A system block diagram, description of proposed custom hardware, and a list of needed commercial hardware will be generated as part of the planning process. Development of the integrated system can begin in early 2005 based on acceptance of the plan by the customer.
3. Procurements – The customer prefers to place orders for commercial hardware to allow for development in early January 2005. The team will identify the needed hardware as early as possible to allow for the orders to be processed through Caltech.

Technical Approach

1. Software
    a. Identify current components and functions
    b. Identify controls, measurements, and processing
    c. Produce Data Flow Diagram (or UML)
    d. Define or estimate data processing loads, examine current approach
2. Hardware
    a. Identify current components and functions
    b. Secure Tech data for commercial components

   c. ID functions of all custom components
   d. Produce system block diagram including interconnects
3. System Planning
   a. Define Integrated Software Requirements
   b. S/W development plan (module level)
   c. Define Integrated Hardware requirements (Box Level)
   d. Define Commercial HW list, and custom development plan
   e. Prepare orders for new commercial HW

Acceptance Criteria
The acceptance criterion is split into three parts. The first phase will be for learning the system and proposing the integrated/automated system. The first phase will be completed in early January 2005. The Second phase will be the development of the new software and hardware components. This is expected in late February, but detailed planning is needed to confirm this. The third phase will be the integration and test phase where the new components will be integrated into the system, and tested and refined as needed. This phase is expected to take approximately one work month and will require a high level of customer support.

Deliverables
1. Phase 1 – The Plan – requirements, diagrams, HW and SW plans.
2. Phase 2 – Working Components and Software.
3. Phase 3 – A fully integrated, tested, and documented system.

Schedule
Planning will last until January 2, 2005. Development is expected to be approximately 2 calendar months (TBC). Integration and testing is expected to be 2 weeks. Task completion is currently estimated to be mid March 2005.

Cost
Total cost is expected to be $80-100K with the following breakdown:

Procurements, Parts, Services: $30-40K
Labor (3-4 WM shared) $50-70K

These amounts are preliminary, and are to be verified and agreed upon at the time development begins.

If changes are necessary, the Customer or the Cognizant Engineer, whoever is initiating the change, will notify the other as soon as possible, and this document will be amended.

Appendix A – Preliminary Commercial Equipment List
- SR400 Stanford Research Photon Counter
- Nanoscope IV, Digital Instrument
- MAD CITY Labs Nanodrive

- Bioscope Atomic Force Microscope (cannot be integrated?)
- Uni-phase HV Source Model 1208-1
- Various NI DAC HW

Appendix B – Proposed Software

1. Requirements – The new software shall mimic all features available with the current software with the added feature of capturing AFM tip height waveforms alongside the digital data in Synchronous Mode:
    a. The new software shall be capable of recording photon timestamps in any of the three modes:
        i. Stationary, where photons are captured from a single location for a period of time.
        ii. Optical, where photons are captured over an area of the sample by rastering the laser over the sample and counting photons.
        iii. Synchronous, where photon captures are synchronized with the movement of the AFM head.
    b. Data shall be archived
    c. Analysis code shall be provided to create visual representations of the data files.
    d. Driver software necessary to control the Mad City Labs tip/tilt mirror, the AOMs, and any additional custom hardware shall be provided and integrated. Also of immediate importance is building the software with the intention to add additional channels of DAQ and control, as well as maintenance algorithms to improve the reliability of Synchronous Mode. These features will not be implemented in this phase, but their effect on the architecture shall be considered.
2. Approach – For the new version of the software, the C++ code will be replaced with LabVIEW code and the use of the DAQ hardware will be optimized. All DAQ will be performed in a PXI chassis. The existing PCI NI6602 counter card will be replaced with the PXI equivalent for counting photons, the NI6502 E-series DAQ card will need to be replaced by a PXI M-series card offering additional analog output lines (e.g. NI-6229M) and a scope card (NI-5122) will need to be added to capture the AFM height waveform with high resolution. The following is the planned usage of DAQ channels:

NI 6602			M-series MIO card			Scope Card		
Function	Used	Free	Function	Used	Free	Function	Used	Free
Counters	6	2	Analog Inputs	5	12 DI	Analog Input	1	1
			Analog Outputs	3	1			
			Digital I/O	6	42			

The LabVIEW code will still run independent of the AFM control code, which will need to be set up and run prior to image capture in Synchronous Mode. An improved interface will be developed that will present a separate set of controls and indicators, depending on which of the three operating modes (i.e. Stationary, Optical Raster, or Synchronous) the FANSOM is imaging in. All data captures will be archived on an image by image basis and the analysis software will be integrated into the LabVIEW code, allowing for immediate display of captured

data, or for review of previous data sets, all within the same interface. Analysis code will be rewritten and optimized in LabVIEW. If equivalent or better performance cannot be achieved with LabVIEW, the analysis code will be returned to Matlab and called from LabVIEW.

3. Schedule – Three weeks will be required to write and debug LabVIEW DAQ software with the same functionality of the existing C++ software. The addition of the scope card to capture AFM tip height waveforms will require another two weeks of work and debug. Rewriting the existing analysis code in LabVIEW will take a week. Writing new analysis code in LabVIEW to account for the AFM tip height waveforms will take another week, assuming that the algorithms are specified beforehand. Additional time may be required to create analysis code capable of working in water if the algorithms are not already known. As a total, expect completion after seven weeks of 30hrs/week work. Additional features will be added as requested and are not covered by this plan.

Appendix C – Proposed Hardware

1. Requirements and Purpose – FANSOM project requires upgraded data acquisition hardware and software to enable proper imaging of samples underwater. In addition, the current system is undocumented – Documentation needs to be generated to enable future upgrades and transfer-of-knowledge to future researchers. Also, the current custom electronics are outdated and crudely fabricated. It is desired to replace them in order to improve performance, reliability and future upgradeability, rather than reverse-engineer and repair them.
2. Future Upgrade Requirements – It is desired to add one more laser and three more photon counters in the future. Also, the current system suffers from mechanical and thermal drift problems, and poor coupling between the laser and AFM tip. Future upgrades to address these issues include an automated polarization tune-up algorithm, an automated drift control algorithm, and a moving-stage/fixed-laser-and-optics approach to translating the sample.
3. Existing System Evaluation – Current commercial and custom hardware used by the FANSOM project have been evaluated and an existing system block diagram has been generated as shown in Figure 1. In the upgraded system, all items in blue will be reused and all items in red will be changed.
4. Development Plan – Figure 2 shows the proposed system diagram with incidental hardware removed and future add-ons marked in green. Items in blue are left unchanged and red items are new or rebuilt. Schedule for the following tasks is shown in Figure 3.
    a. Rebuild Box A. Upgrade analog control loop to digital using microcontroller and serial communications link to PC 1.
    b. Replace Box C (comparator) with NI-5122 Scope-Card (100 MS/s, 14-bit, 32MB, $6500). Capture entire z-position waveform from BioScope Electronics Box.
    c. Remove Boxes B, D, E, F, and G. Consolidate into a localized power supply solution.

5. Cost and Schedule – As shown in Figure 3, Total billable hours is estimated to be 23 days @ $120/hr. or $22,080.00 and date of completion is estimated to be March 14, 2005 for a total duration of 7 wks

2 SCHEDULE

2.1 RECAP

After the initial meeting regarding the project in October of 2004, two months were spent coming up with a design that would incorporate the various components from the old system into a new, unified whole. The first cut at the software was completed in early March of 2005, with Box H and its firmware completed later in the month. On the 24th of March the system was integrated at Caltech, where work continued for four more months on the addition of many new features as well as tweaks to original features. As of the end of July, 2005, the system reached a stable, functional state that would be considered complete for Fiscal Year 2005.

2.2 MAJOR MILESTONES

10.28.04 - First meeting

11.04.04 - First trip to Caltech

02.14.05 - Delay of NI order

02.16.05 - Software architecture complete

03.01.05 - First cut of LabVIEW code complete

03.08.05 - NI hardware delivered

03.24.05 - FANSOM system delivered to Caltech

04.06.05 - Budget meeting

06.01.05 - Budget/Progress meeting

06.20.05 - Bug/Feature Meeting

07.05.05 - Box H back at Caltech and fixed

07.06.05 - First run ‘wet’

07.08.05 - Fixed afm image corruptions.

07.19.05 - Got new monitors.

07.20.05 - First full wet run w/ analysis.

07.29.05 - Meeting to discuss final FY05 tasks and documentation

3 SYSTEM SETUP

3.1 DIAGRAM

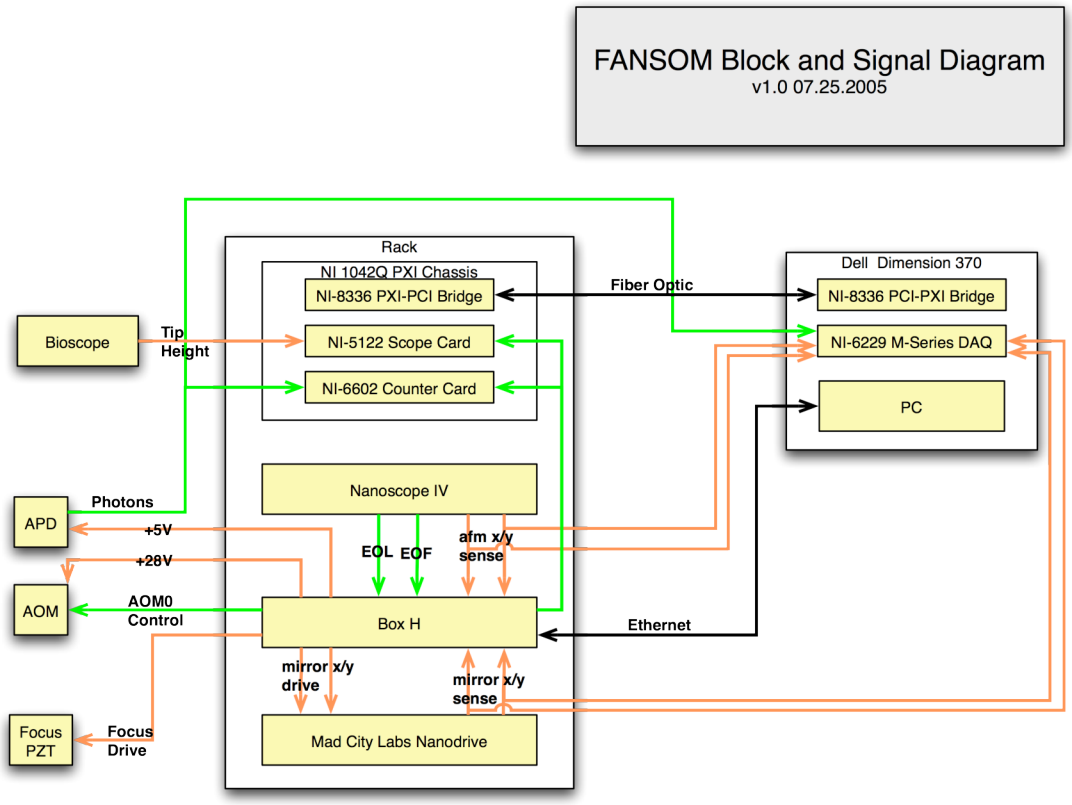

Figure 1 - System Diagram

4 HARDWARE

4.1 DETAILED DESCRIPTION

The custom hardware in the system takes the form of Box H, a 1U rackmount chassis incorporating and improving upon all functionality of the custom hardware in the previous system. It contains a Motorola Coldfire microprocessor, a Xilinx CPLD, a two-line blue LED-backlit LCD display, four ADCs, three DACs, and 6 power supplies.

4.1.1 Motorola Coldfire Microprocessor

The Motorola Coldfire Microprocessor, included in a Netburner package, provides:

- computer-based control of all aspects of Box H's operation through the Ethernet
- a digital control loop used to synchronize the movement of the tip-tilt mirror with the afm
- fast-scan capabilities of the mirror x-axis at user-configurable rate
- programming for the LCD display

4.1.2 CPLD

All digital output and input to and from the Coldfire is passed through an CPLD. This provides several features currently, and will expedite the addition of other features at a later time. The most important feature of the CPLD is to combine the EndOfLine and EndOfFrame signals from the Nanoscope into a LINE signal capable of triggering all of the DAQ hardware in sync with the AFM's movement.

4.1.3 LCD display

The LED display provides information during debug operation of Box H, as well as indication that the Box is running in the form of the word 'FANSOM' spelled across it.

4.1.4 Analog-to-Digital Converters

The four ADCs digitize the analog representation of the mirror and AFM x- and y-axes for use in the digital control loop and reporting back to the host computer.

4.1.5 Digital-to-Analog Converters

Two of the DACs drive the position of the tip-tilt mirror, either in response to direct host computer command or as the result of the digital control loop. The output from a third DAC is amplified to provided the drive voltage for the fine focusing PZT in the microscope's optical system.

4.1.6 Power Supplies

The power supplied provide power internally for Box H's operation and externally to power the AOM and photon detector. The photon detector's power can be enabled or disabled by command from the host computer while the AOM's power is output as long as Box H is powered on.

4.2 SCHEMATICS/DIAGRAMS

4.2.1 Chassis Wiring Schematic

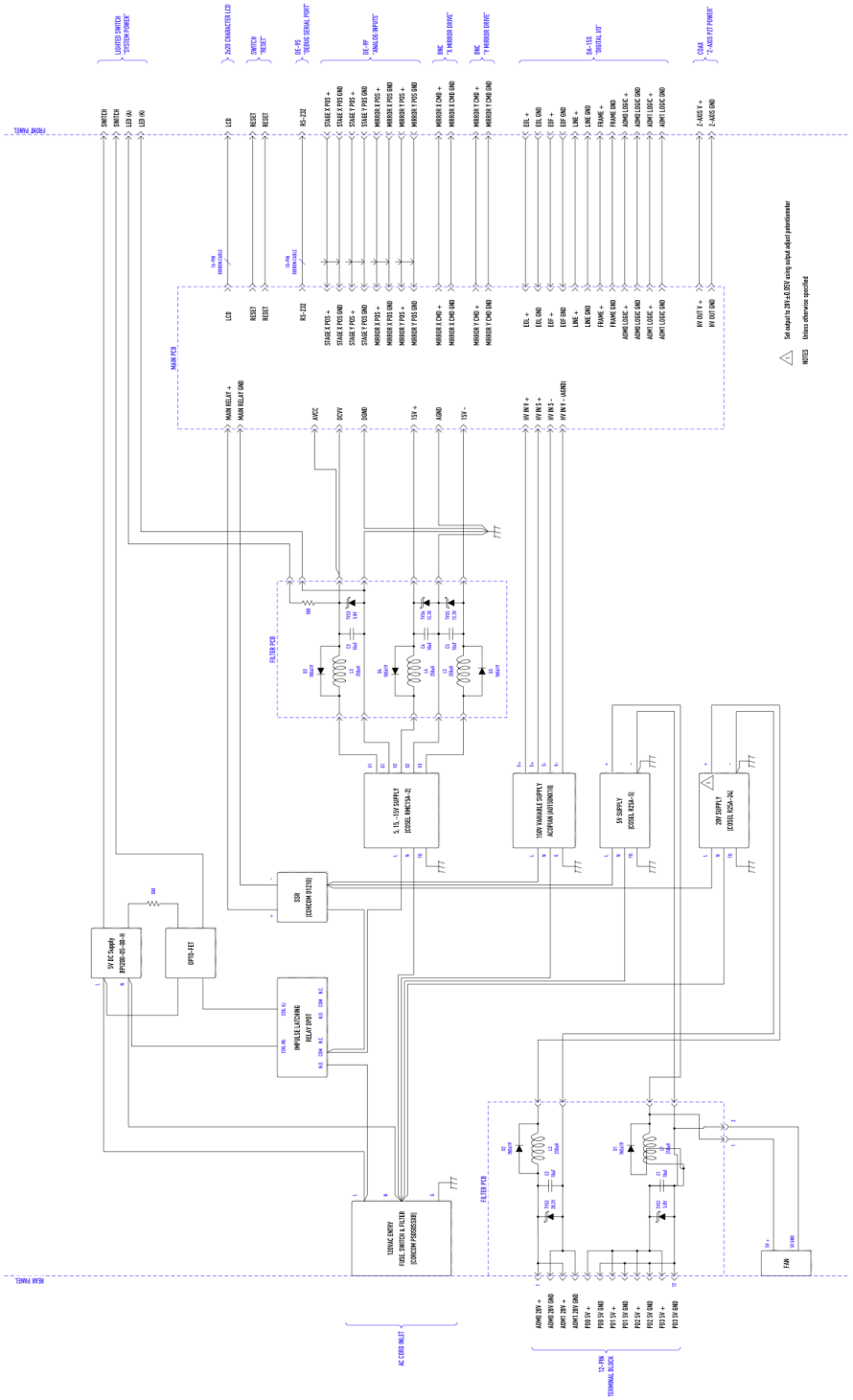

Figure 2 - Chassis Wiring Schematic

4.2.2 Other Schematics

Other hardware schematics can be found in Appendix B – Hardware Schematics.

4.2.3 Firmware Activity Diagram

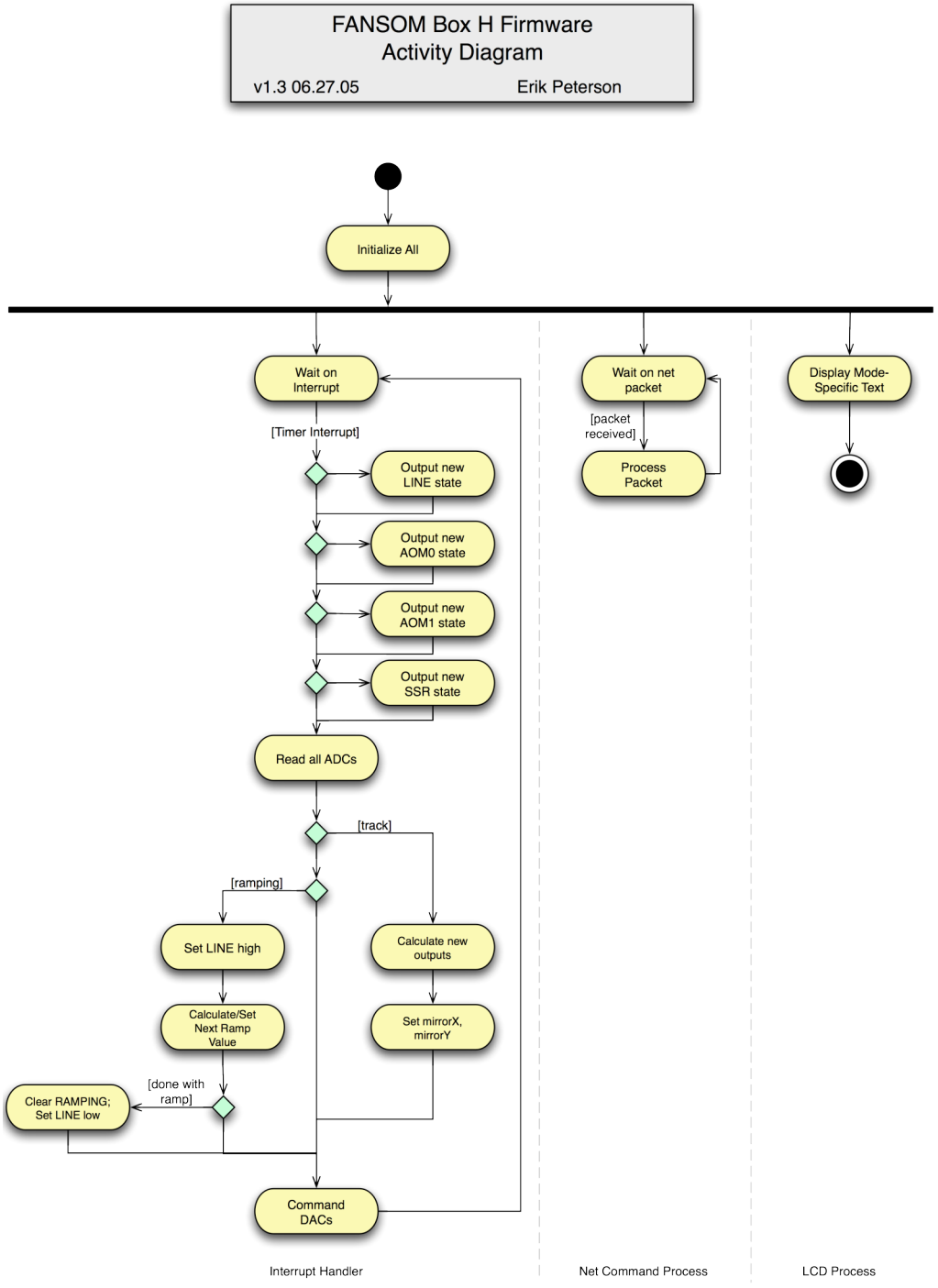

Figure 3 - Box H Firmware Activity Diagram

4.2.4 Signal Connections

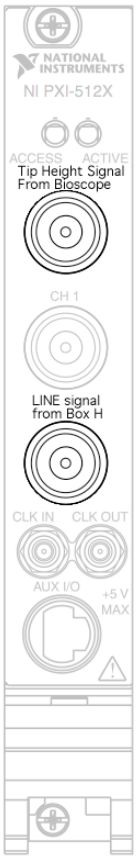

Figure 4 - Scope Card Connections

Analog Signal Connector

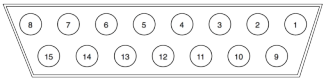

1	AFM X Sense	9	GND
2	AFM Y Sense	10	GND
3	Mirror X Sense	11	GND
4	Mirror Y Sense	12	GND
5		13	GND
6	Mirror X Drive	14	GND
7	Mirror Y Drive	15	GND
8			

Digital Signal Connector

1		14	GND
2		15	GND
3	EOL	16	GND
4	EOF	17	GND
5		18	GND
6		19	GND
7		20	GND
8		21	GND
9		22	GND
10	LINE	23	GND
11	FRAME	24	GND
12	AOM0	25	GND
13			

Figure 5 - Analog and Digital Signal Connectors

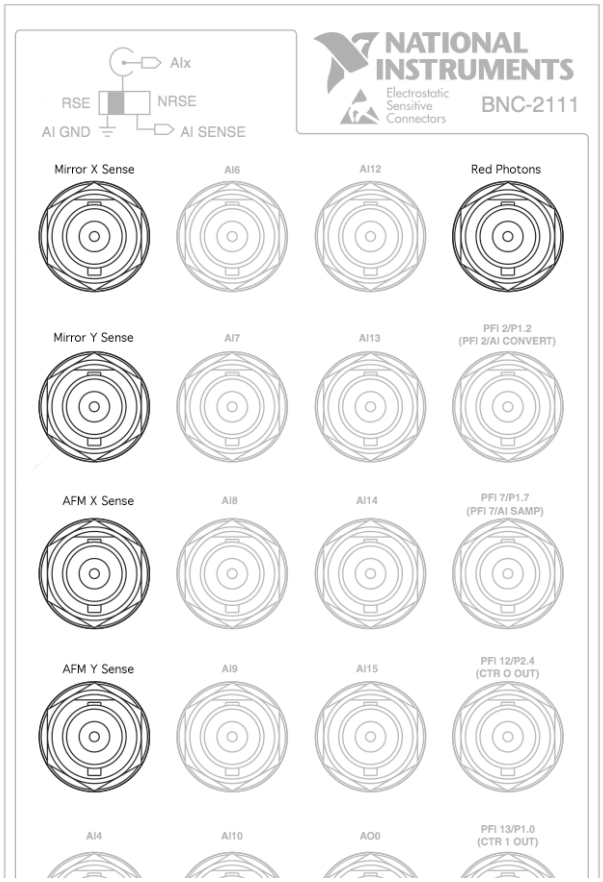

Figure 6 - Debug Signal Connections

4.3 HARDWARE INTERFACE DESCRIPTION

The external interfaces for Box H are: power connectors, an analog signal connector, a digital signal connector, and the Ethernet port.

4.3.1 Power Connectors

On the back of Box H are several connectors for externally-powered devices. On a terminal block there are four connectors, which provide +5V, and two connectors, which provide +28V. Currently, one of the +5V connectors powers the photon detector and one of the +28V connectors powers the AOM. There is also a BNC, which connects to the focus PZT and provides 0-150V.

4.3.2 Analog Signal Connector

On the front of Box H is a 15-pin DSUB connector, which provides input and output of analog signals for Box H.

4.3.3 Digital Signal Connector

On the front of Box H is a 25-pin DSUB connector, which provides input and output of digital signals for Box H. All of these signals pass through the CPLD.

4.3.4 Ethernet Port

On the front of Box H is an Ethernet connection, which provides the command and data gathering capabilities of Box H. A host computer can connect to TCP port 10001 at IP address 192.168.1.5 and send ASCII commands, all terminated with the '\n' character (ASCII 13). A complete listing of the commands available over Ethernet can be found in Appendix A – Box H Ethernet commands

5 SOFTWARE

5.1 HIGH LEVEL SOFTWARE

The main software of the system is written in LabVIEW and offers a user interface for data acquisition, data analysis, and general configuration of the FANSOM system. Separate screens handle configuration and calibration, and a custom wizard handles the preparation of data acquisition or analysis. Once the wizard is completed with a valid set of configuration parameters, several parallel processes are initiated to handle the tasks: the DAQ process, the Archive process, and the Analysis & Display process.

In the case of capturing a new dataset, the DAQ process takes the results of the FANSOM Wizard and preps and executes the necessary data acquisition hardware operations. If archived data is being used the DAQ process is not initiated.

In the case of capturing a new dataset, the Archive process waits for each line of data, in the case of Optical Raster or the FANSOM modes, or the whole duration, in the case of Stationary Optical, to become available. The Archive process next writes the data to a file in the appropriate place in the filesystem. In the case of both new and archived data operations, the Archive process waits for data requests from the Analysis & Display process, which it fills as the data become available in the filesystem.

In the case of capturing a new dataset, the Analysis & Display process requests data lines, performs the necessary analysis on the data, and then displays the data to the user in one of several graph formats.

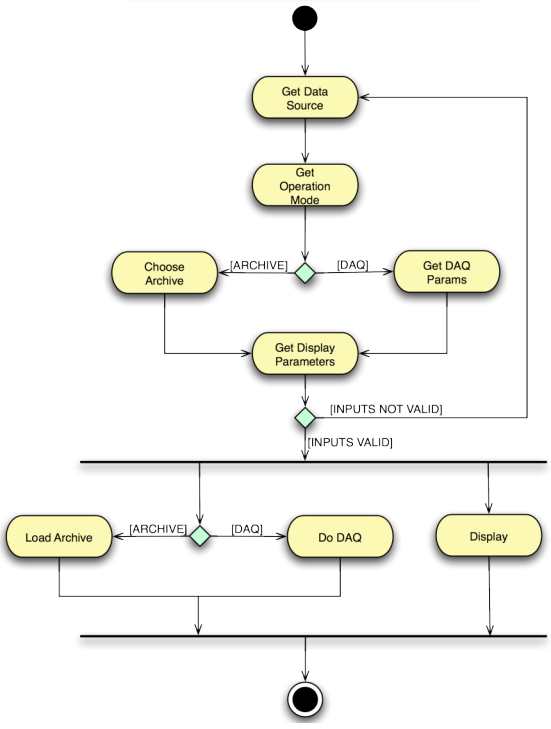

Figure 7 - High Level Software Activity Diagram

5.2 DATA ACQUISITION

Each software mode performs its data acquisition in a slightly different way. There are a few common aspects, which involve how the actual data are taken. In all modes, photons are counted by NI general-purpose counter hardware in Buffered Event Counting mode. In this mode, the counter is constantly being incremented by an internal 20MHz clock. At each photon trigger, the contents of the counter are dumped into a buffer. Thus, at the end of acquisition, the result is a series of photon timestamps with 1/20,000,000 time resolution.

In the FANSOM modes, an NI scope card captures the tip height waveforms. The scope card's buffer is set up based the total amount of time to capture and a 1Megasample/second capture rate.

In all modes but optical stationary, all data acquisition is triggered by LINE triggers coming from Box H.

5.2.1 Optical Stationary

In Optical Stationary Mode, the stage is moved into position, the data acquisition hardware is configured to capture photon timestamps on a software trigger, the AOM is enabled, the software trigger is fired, and the software waits for the specified time. Every 20 ms the software empties the hardware capture buffer into a local array until the acquisition completes, when the data are sent to the Archiver and the stage is returned to (0, 0).

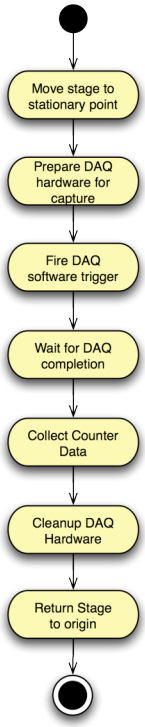

Figure 8 - Stationary Optical DAQ Activity Diagram

5.2.2 Optical Raster

In Optical Raster Mode, first the stage is moved to the beginning of the first line in the image. Then, for each line, the data acquisition hardware is configured to capture photons after a trigger from Box H, the AOM is enabled, and Box H is commanded to perform a ramp along the x-axis at the given rate. When Box H executes the ramp it also sets LINE high, which triggers the data acquisition hardware. Meanwhile, the software polls LINE waiting for it to go from high to low. When this occurs the software empties the data acquisition buffer and sends the data to the Archiver.

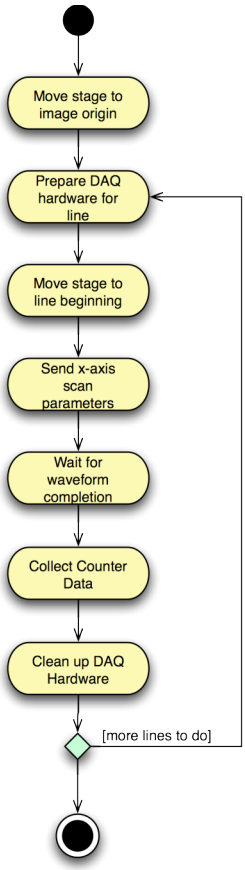

Figure 9 - Optical Raster DAQ Activity Diagram

5.2.3 Synchronous FANSOM

In Synchronous FANSOM Mode, first tip tracking and LINE toggling are enabled in Box H. This forces the mirror to follow the AFM tip (if calibrated correctly) and forces LINE to toggle based on the EOL trigger from the Nanoscope, starting at the top of the image. The AOM, too, toggles in sync with the movement of the AFM tip. Then, for each line the data acquisition hardware is configured to capture both photons and tip heights on LINE triggers. The software waits to see LINE toggle from low to high and back to low again, signaling a capture line has completed, and then empties the hardware buffers, sends the line data to the Archiver, and prepares for the next line. At the end of the image the tip tracking and LINE toggling are both disabled.

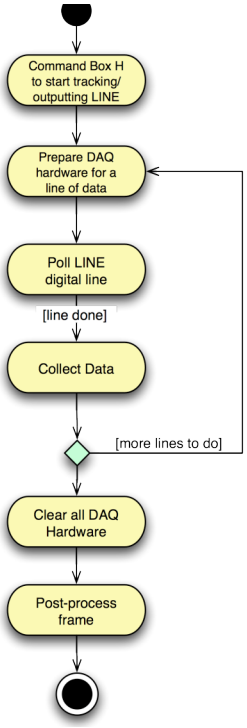

Figure 10 - Synchronous FANSOM DAQ Activity Diagram

5.2.4 Stationary FANSOM

The data acquisition in Stationary FANSOM Mode is the same as it is for Synchronous FANSOM mode, but there is some setup that differs. First, since the mirror remains motionless during this mode, Tip Tracking is not enabled during data acquistion. Instead, the user is prompted to place the AFM in the position where the laser should remain. The Tip Tracking is enabled just long enough for the mirror to orient itself properly. Then Tip Tracking is turned back off, the user is prompted to start the AFM moving again, and data acquisition occurs, line-by-line, the same as in Synchronous FANSOM Mode.

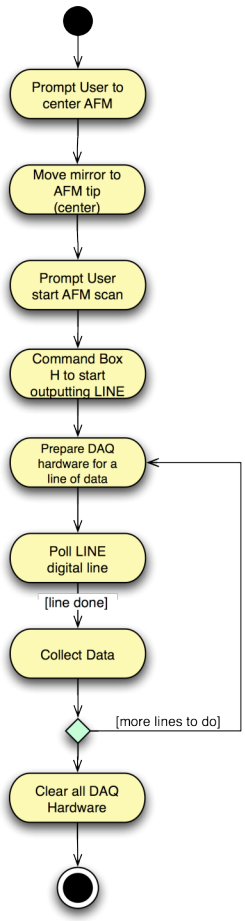

Figure 11 – Stationary FANSOM DAQ Activity Diagram

5.2.5 FANSOM Raster

The data acquisition in FANSOM Raster Mode is very similar to Optical Raster mode, except for two notable differences. First, tip heights are collected as well as photons during each line. Second, the location of the center of the scan is derived from the user-placed position of the AFM tip, which remains stationary during the data acquisition.

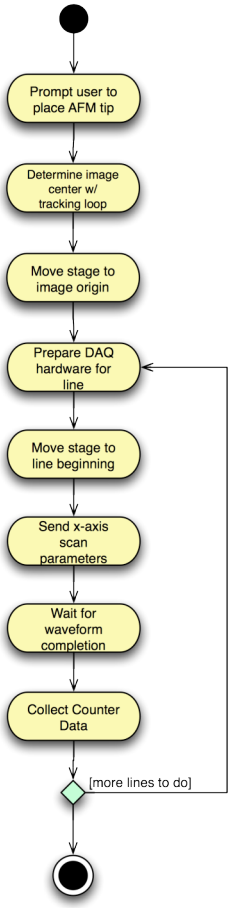

Figure 12 - FANSOM Raster DAQ Activity Diagram

5.3 ANALYSIS

There are essentially three data products in the FANSOM software. They are: evenly-binned photon counts, FANSOM-binned photon counts, and AFM amplitude bins.

5.3.1 Evenly-binned photon counts

This data product is generated for the Stationary Optical Mode graph, as well as for every line in an Optical Raster Mode graph or a Total Power graph for a FANSOM mode. It is generated by taking the total length of time of the group of photons, splitting that time period into as many bins as are requested, and then counting the number of photons (i.e. timestamps) in the group in each bin.

In the case of Stationary Optical Mode, this is displayed as a waveform graph with the x-axis being time and the y-axis being number of photons in the time bin.

In the case of Optical Raster Mode and the Total Power graph for a FANSOM mode, this is displayed as a line in an intensity graph with the x- and y-axes being physical distance and the intensity being number of photons.

These data can be further analyzed in the Optical Raster graph with the Profile feature, whereby a cross-section of an intensity graph is generated between two cursors on the graph by taking the total length of the profile, splitting it up based on the x- and y-axis scales, and then moving along the profile, from one cursor to the other, reading the intensity values and displaying them in a waveform graph.

5.3.2 FANSOM-binned photon counts

The most complicated of the data products is the FANSOM-binned photon count. The main portion of the algorithm starts with a line of photons and tip heights. It then splits both the tip heights and the photons into bins representing pixels in the final intensity plot. Each bin is then processed individually.

For the bin, first the tapping frequency is extracted with a call to the LabVIEW library VI Extract Single Tone Information.vi. With the tapping frequency, then five periods of the waveform are averaged together and the phase offset is determined, i.e. the number of samples from the beginning of the bin's tip height waveform until the first 'zero crossing.' Knowing the first zero crossing and the frequency makes it possible to extrapolate the zero crossings for the entire bin. Then the midpoint between every two zero crossing timestamps is calculated, with this timestamp going into the list of either peaks or troughs. Before the next step, if this is the first bin on the first line of an image, a dialog appears that shows the user a couple of periods of the tip height waveform and the calculated peak and trough within this range. The user can then set three parameters: the window around the peak that should be considered for counting photons, the window around the trough that should be considered when counting photons, and an offset value that will shift all of the peaks and troughs forward or backward in time by some amount. Then the actual counting takes place. The code iterates through each peak and counts the photons with timestamps within the window around each peak. It then does the same for

the troughs in the bin. The last calculation is, if the peak and trough windows are not equal, then the total peak photon count is scaled by the ratio between the two windows.

The bins of peaks and the bins of troughs are generated for the whole image. The final answer generated by subtracting the peaks, i.e. the background photons, from the troughs, or the interaction photons. To try to beat down the background noise one final bit of analysis can be undertaken. A dialog will be displayed for the user to choose which bins to average together for every bin in the image. The pattern is chosen and the software iterates through each pixel in the background, adds together all of the background photons in the pattern, and then divides by number of bins used (to account for coming up against the side of the image and having less than the optimal number of bins).

Then the background signal is subtracted from the foreground signal and the result is displayed as an intensity graph. It can also be sliced into profiles or shown as a 3D representation.

5.3.3 AFM Amplitude Bins

In all FANSOM modes that involve a rastering AFM tip, AFM Amplitude Bins can be generated by taking the full length of a line of tip height data, splitting it up into the proper number of bins, and then taking the amplitude of the waveform within each bin and graphing it as a pixel on an intensity plot with the intensity corresponding to the voltage representation of the tip height. The average amplitude is generated by calling a LabVIEW routine Amplitude and Levels.vi, which returns the amplitude of a waveform.

5.4 USER INTERFACE PANELS

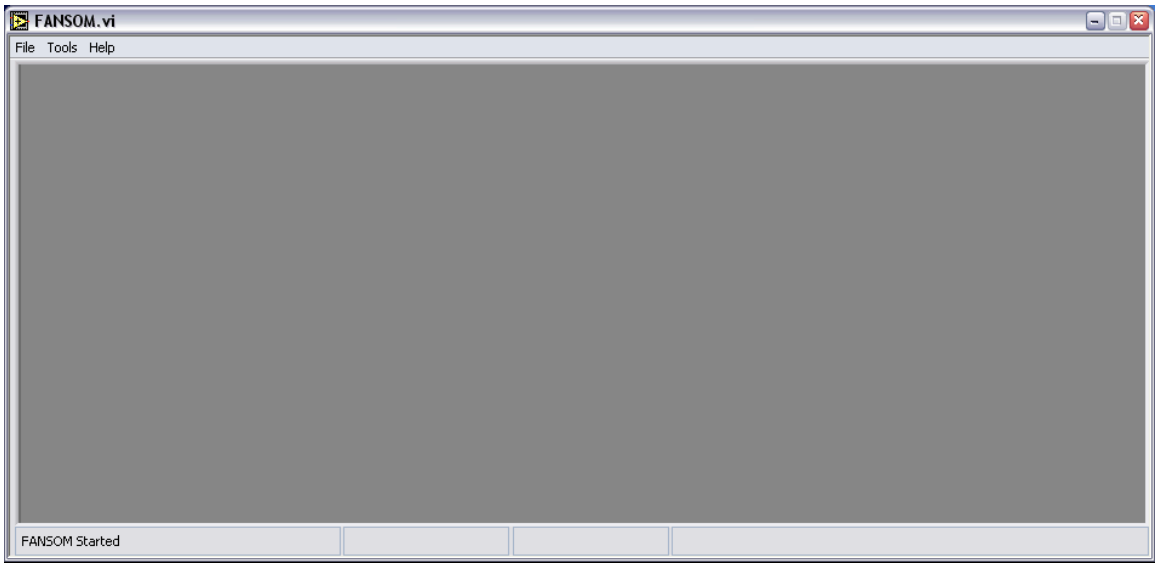

Figure 13 - Main FANSOM User Interface Panel

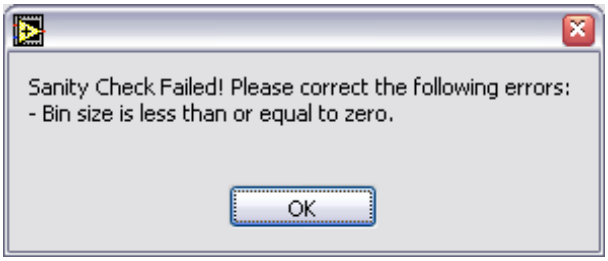

Figure 14 - Sanity Check Failure Box

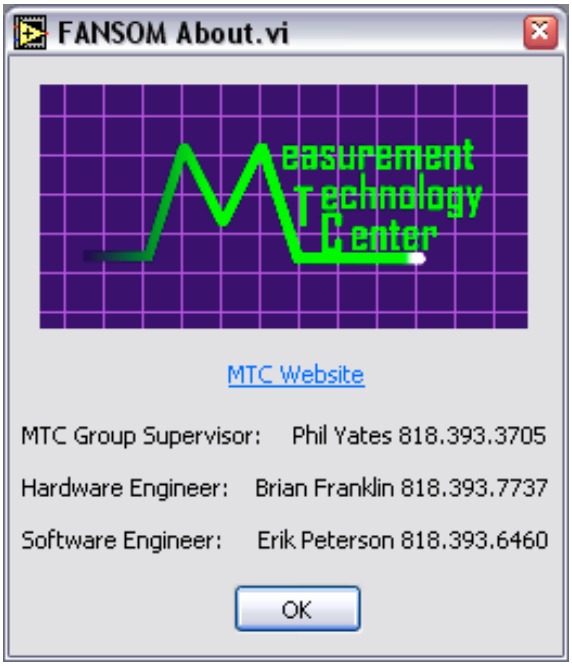

Figure 15 - FANSOM About box

Figure 16 - FANSOM Wizard Panel

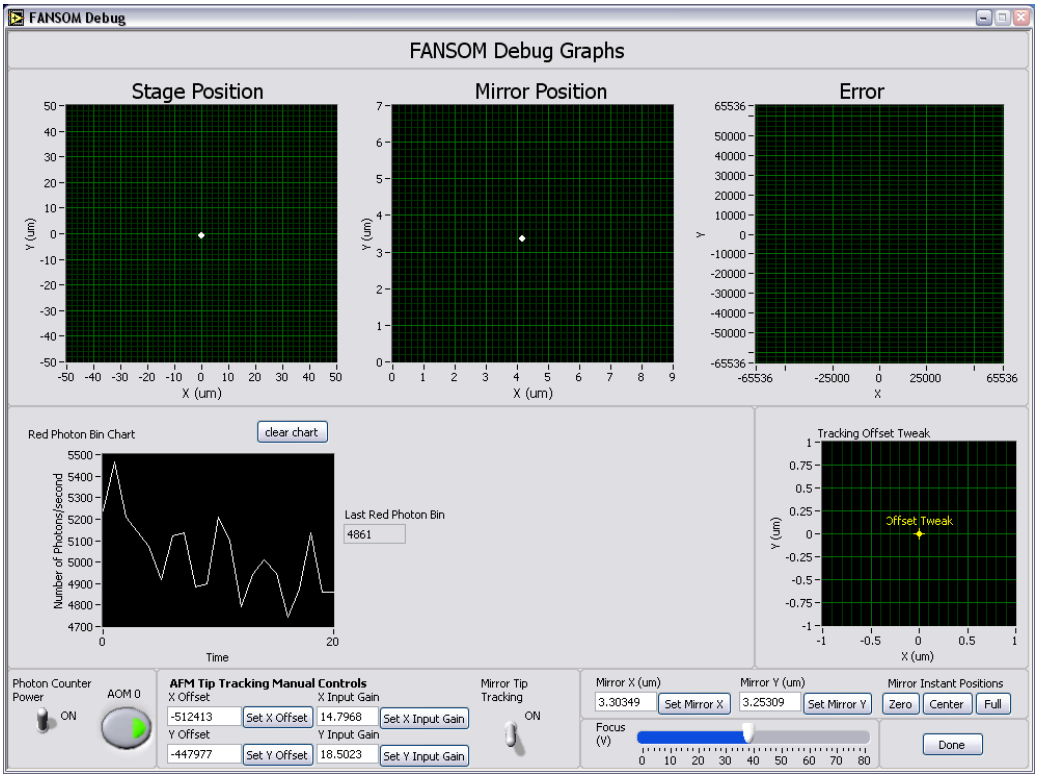

Figure 17 - FANSOM Debug Screen

Figure 18 - FANSOM Calibration Wizard

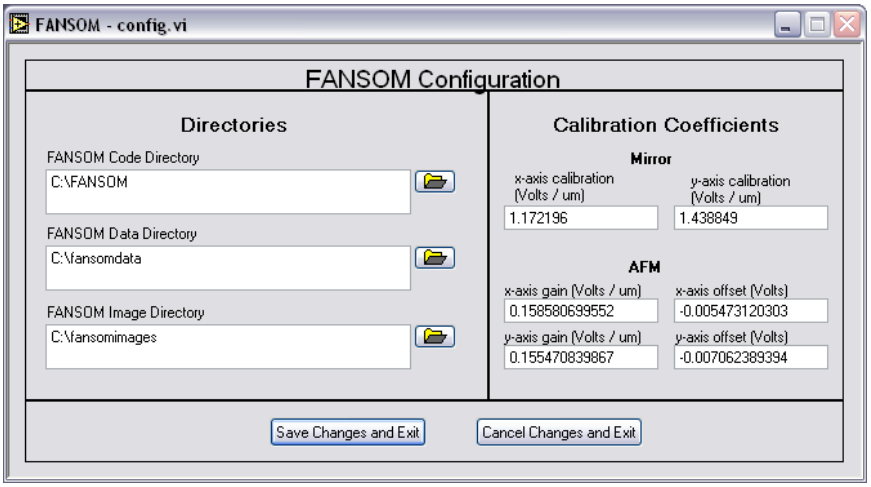

Figure 19 - FANSOM Configuration

(Note: Accessible from the FANSOM Start Menu folder)

6 OPERATING INSTRUCTIONS

6.1 OPERATIONAL OUTLINE

The basic operation of the FANSOM software follows the following scheme:

1. *Focus the objective, ensure operation* - With the debug screen, the user must focus the objective, ensure that photons are being captured, and verify network communication with 'Box H'.
2. *Calibrate tip/mirror control loop* - This must be done once per data acquisition session, or more often as desired.
3. *Capture data* - May it be optical raster images, optical stationary profiles, or synchronous FANSOM images, this involves performing the applicable hardware operations to generate the desired dataset.
4. *Analyze data* - In the case of optical raster and stationary modes, data analysis is performed concurrently with the data acquisition.
5. *Display data* - For optical modes, data are displayed immediately after performing a daq operation. For all modes, data can be loaded to be analyzed and displayed at a later time from archive files.

6.2 FOCUSING THE OBJECTIVE AND ENSURING OPERATION

Before calibrating and using the FANSOM system, it is necessary to focus the objective and ensure that all aspects of the system are operational. These tasks are accomplished on the Debug Screen.

1. First, select **Show Debug Screen** from the **Tools** menu.

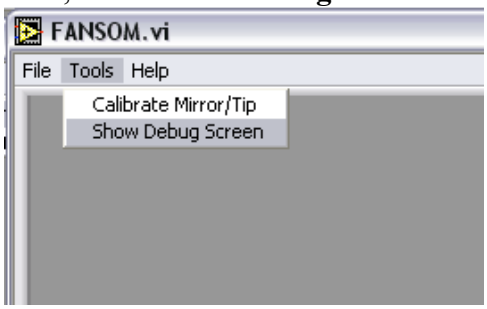

You will be presented with the **Debug Screen**.

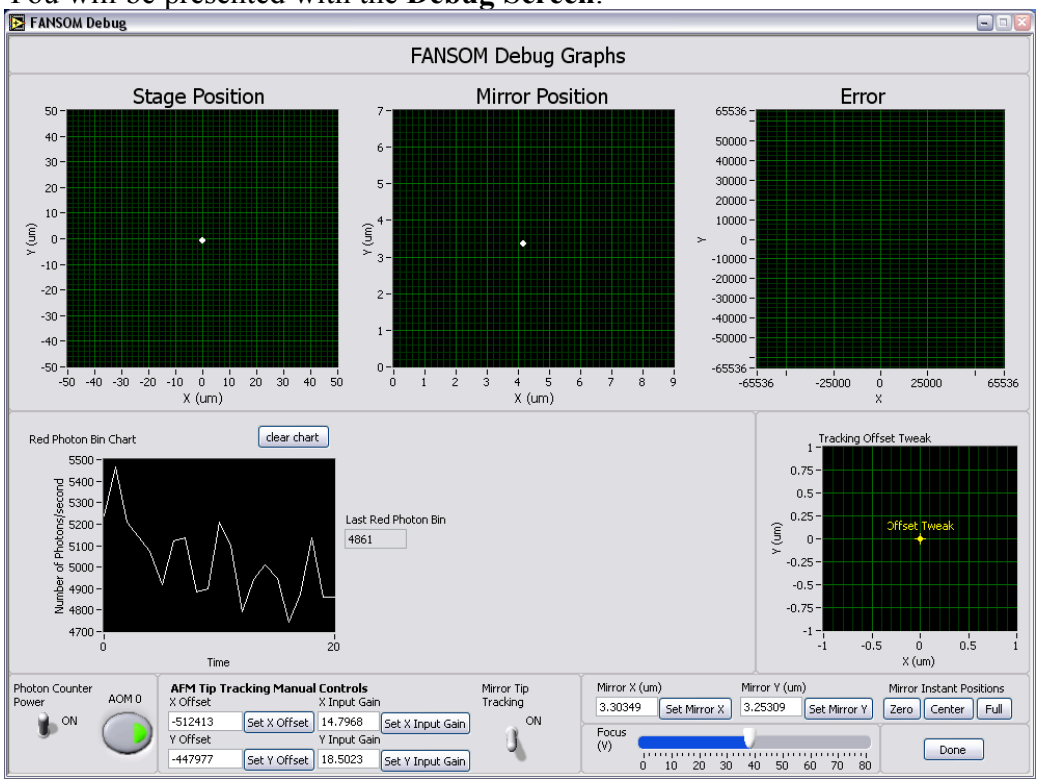

2. Next, ensure that the communication with Box H is operational. Enable laser with the **AOM 0** button.

The laser dot should appear on the tv screen or on the vision system screen on the AFM control computer.

3. Next, focus the laser dot using the **Focus** slider.

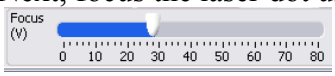

4. Finally, make sure that the **Photon Counter Power** switch is at the ON position

and check to make sure that photons are being collected on the **Red Photon Bin**

Chart.

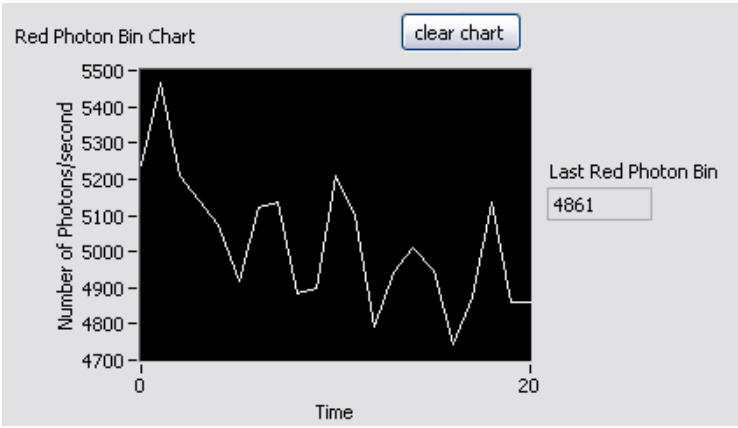

Additional functions on the Debug Screen are:

- activating/deactivating the Mirror Tip Tracking

- setting tip track control loop parameters

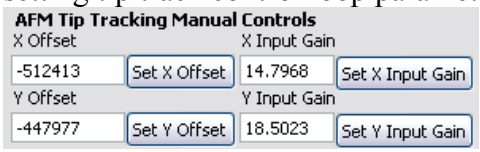

- tweaking tip track control loop offset

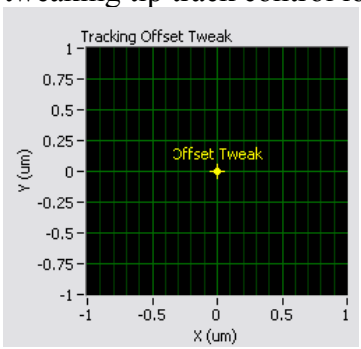

- displaying the positions of both the afm tip and mirror

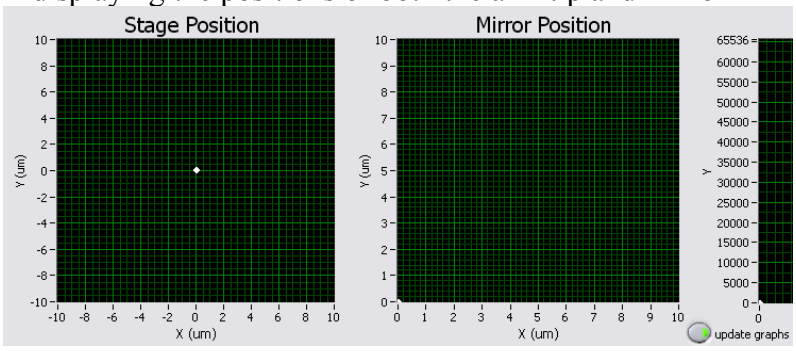

- commanding the mirror to an absolute position

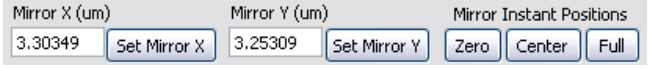

6.3 CALIBRATING

1. Open the calibration wizard by selecting the **Calibrate Mirror/Tip** item from the **Tools** menu.

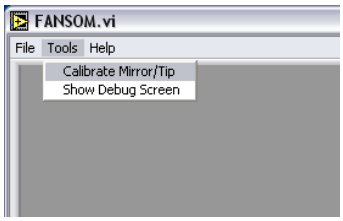

2. Follow the on-screen prompt.

From the Nanoscope control software, using the vision system, align the afm with the location of the blinking laser dot. Click **Next->**

3. Follow the on-screen prompt.

From the Nanoscope control sotware, using the vision system, align the afm with the location of the blinking laser dot. A suggested location will be given on-screen. Click **Next->**

4. Follow the on-screen pro mpt.

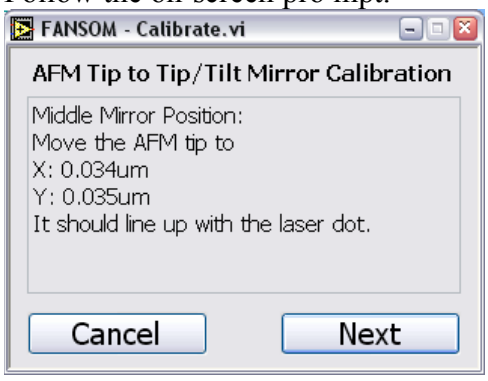

Move the afm to the location specified. If the dot and the afm line up, then the system is calibrated, click **Next->**. If the dot and afm do not line up, click **Cancel** and try again.

6.4 CAPTURE DATA

1. Start a new Wizard by selecting the **New** item from the **File** menu.

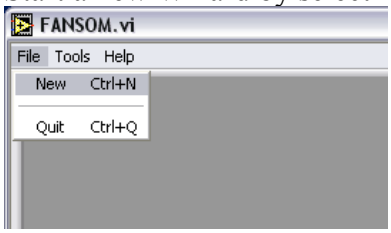

2. Choose **DAQ** as your **Data Source**.

Click **Next->**

3. Choose your desired **Operating Mode**.

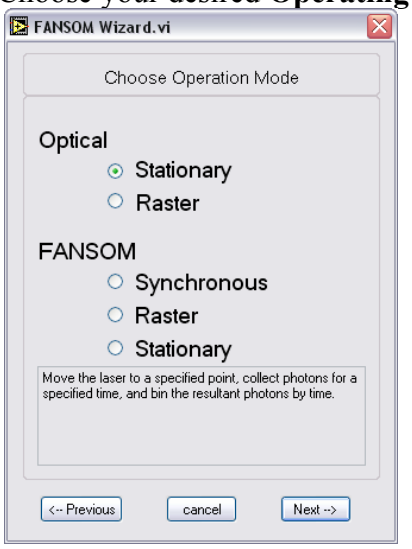

Click **Next->**

4. Fill in the common **DAQ Parameters**.

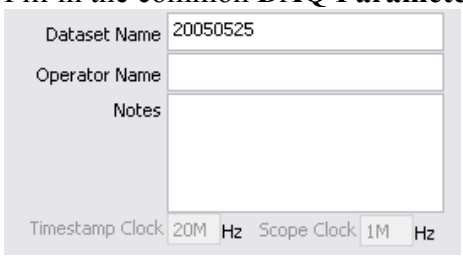

Fill in the Operating Mode-specific **DAQ Parameters**.

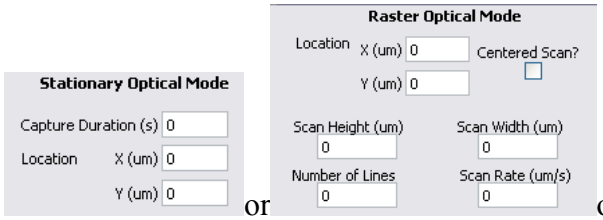

or

or
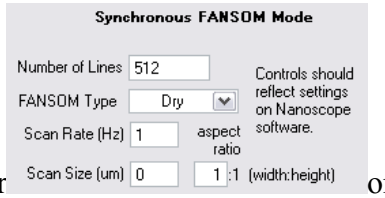

or
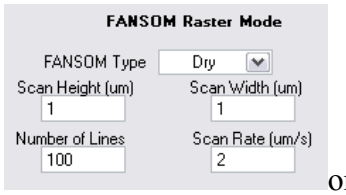

or
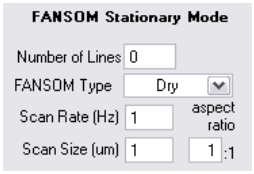

Click **Next->**

5. Fill in the Operating Mode-specific **Display Parameters**.

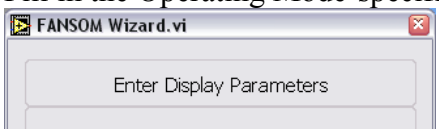

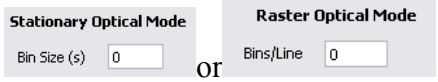

or

(If you choose a FANSOM mode you will not be prompted for Display Parameters because FANSOM mode must be post-processed). Click **Next->** to being the DAQ and, in the case of the optical modes, display of your data

Note: In the case of Synchronous FANSOM and Stationary FANSOM operation, after the Wizard is completed the AFM should be commanded to start from the top of the image.

6.5 ANALYZING ARCHIVED DATA

1. Start a new Wizard by selecting the **New** item from the **File** menu.

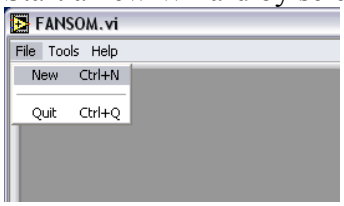

2. Choose **Archive** as your **Data Source**.

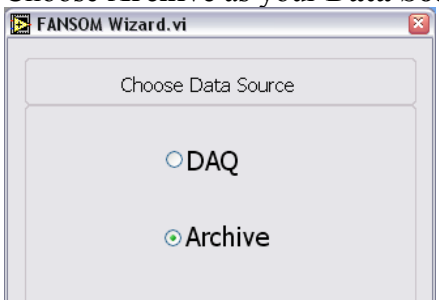

Click **Next->**

3. Choose your desired **Operating Mode**.

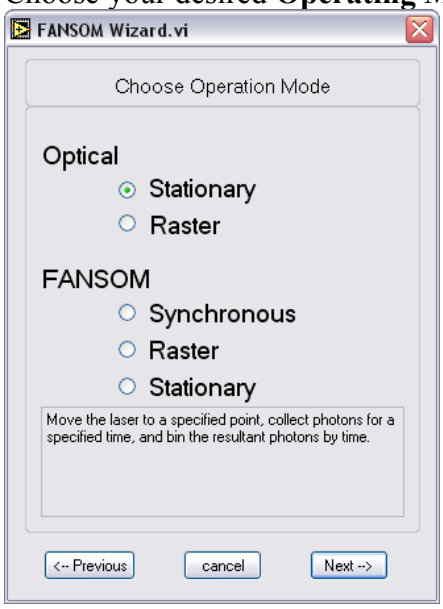

Click **Next->**

4. Choose which Archive you want to open.

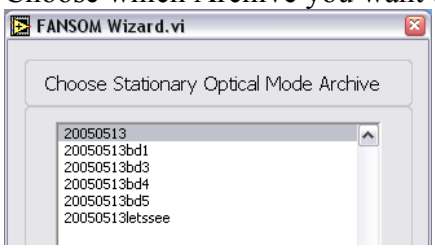

Click **Next->**

5. Fill in the Operating Mode-specific **Display Parameters**.

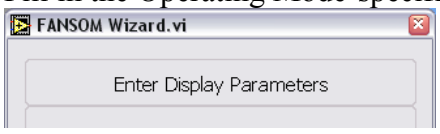

or


or
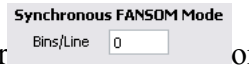

or


or


Click **Next->** to being the processing and displaying of your data.

6. For the three FANSOM modes, the user will have to choose the windows around the peaks and troughs where photons should be counted, as well as an offset for all peaks and troughs, if desired. This is accomplished in the FANSOM Binning

dialog:

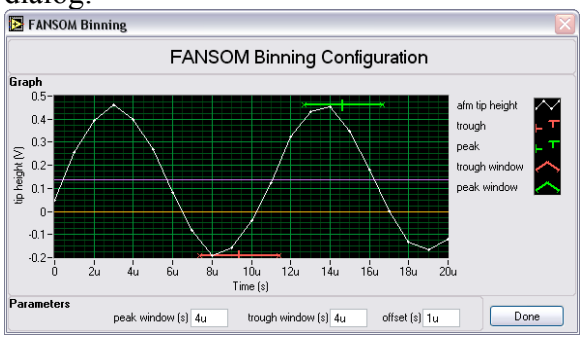

7. Also in the FANSOM modes, when initial analysis has completed, the user will have to define a region for background signal integration. This is done in the FANSOM Integration Dialog:

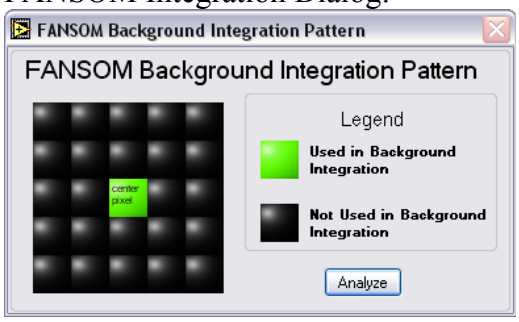

6.6 DISPLAYING DATA

Once analysis has completed, the data will be displayed. The manner in which the data are displayed will vary by mode.

6.6.1 Stationary Optical Data Display

The data product of the Stationary Optical mode is a profile of number of photons vs. time, binned according to a user-specified value. Also displayed is the total number of

photons for the capture duration.

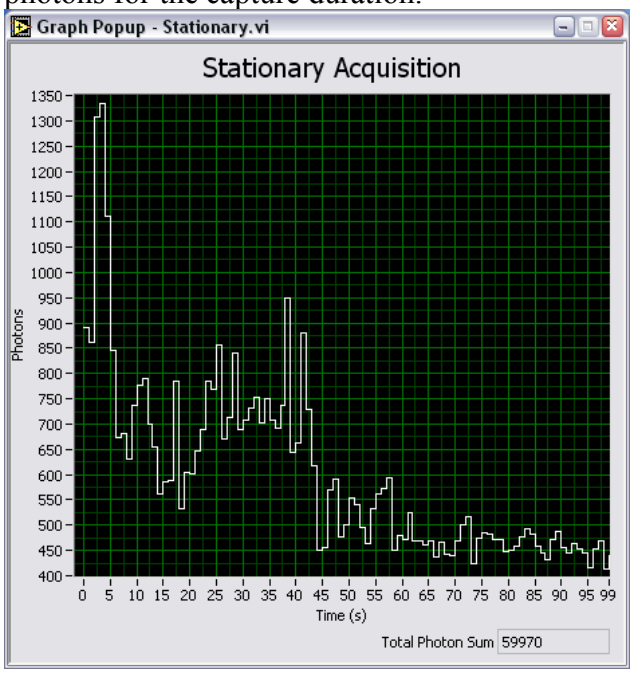

6.6.2 Optical Raster Data Display

The data product of the Optical Raster mode is a three dimensional plot of number of photons per unit area, displayed as a 2-D intensity graph.

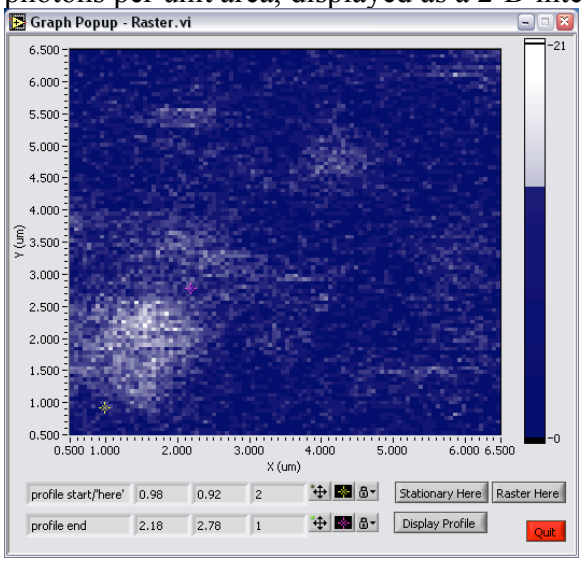

Several additional functions are available once the plot is complete:

- Stationary Here - starts a new DAQ Wizard with Stationary settings at the location of the yellow cursor.
- Raster Here - starts a new DAQ Wizard with Raster settings centered at the yellow cursor.

- Display Profile - displays a 'slice' of the intensity graph from the yellow cursor to the pink cursor.

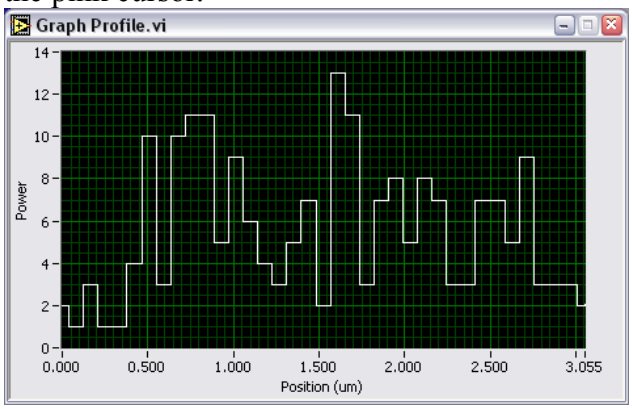

6.6.3 FANSOM Data Display

FANSOM modes offers up three data products. They are:

- AFM Image - A reconstruction of the AFM topographical data.

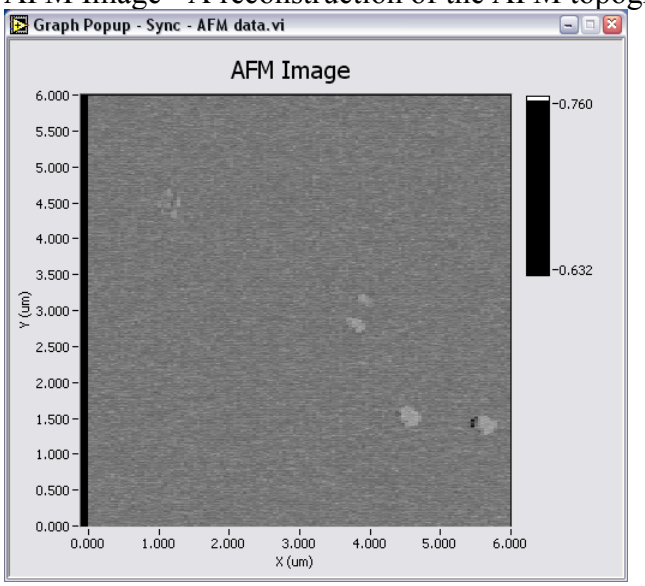

- Total Power - The total number of photons per unit area.

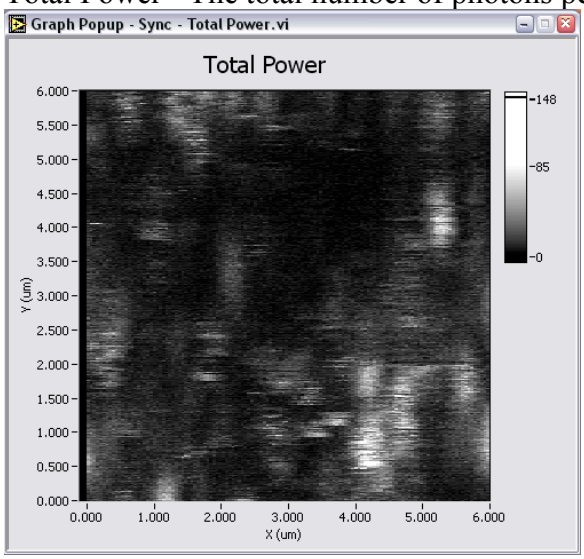

- FANSOM Binning - The total number of photons when the tip is close to the surface minus the background photons, per unit area.

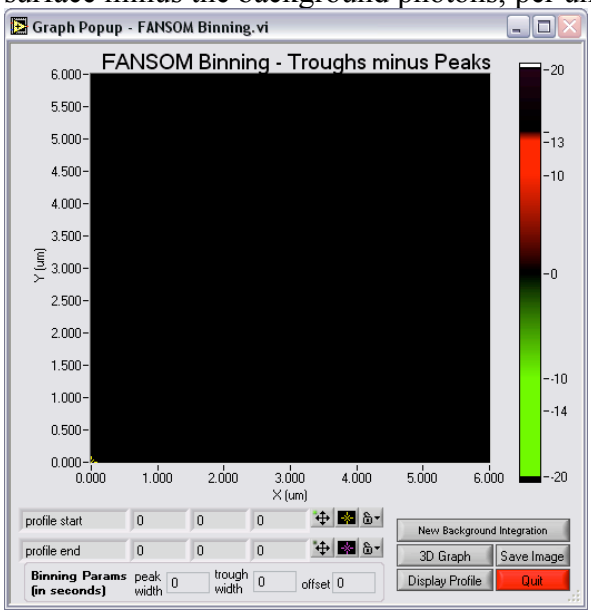

When the plot is complete, clicking…

New Background Integration will display the FANSOM Integration Dialog again and allow the user to pick a new integration pattern

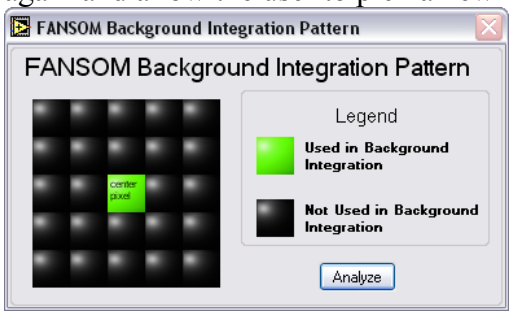

3D Graph will Pops up a 3D version of the binning graph

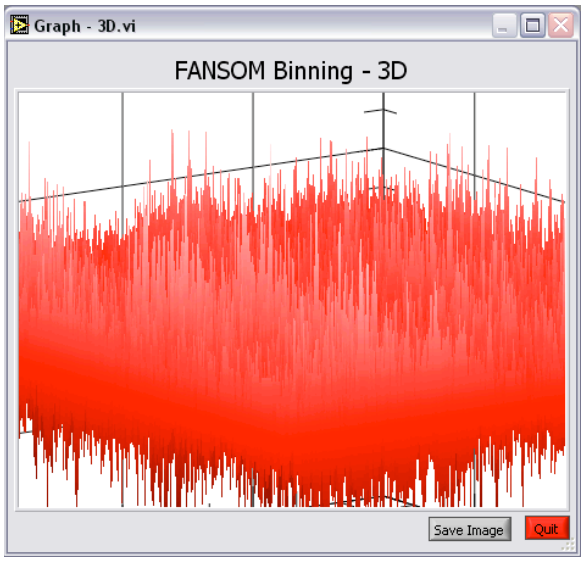

Save Image will allow the user to save another copy of the graph.
Display Profile will display a 'slice' of the intensity graph from the yellow cursor to the pink cursor.

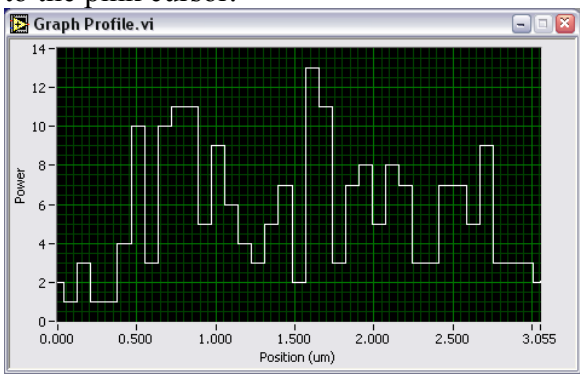

7 SYSTEM CALIBRATION REQUIREMENTS

The software had to be originally calibrated to convert between the voltage representations of the mirror and AFM positions into actual, physical position units. Since the positions are represented as proportional to these voltages, it was a simple matter of moving each to two different positions and doing a linear fit for x and y in terms of voltage.

For the AFM, this is a matter of commanding the tip to two positions with a DMM connected to the sense coax cables. With the commanded positions and the corresponding voltages in hand, perform a linear fit and place the resultant gain and offset values in the FANSOM Configuration screen shown in Figure 19.

In some ways calibrating the Mirror is easier because its offset is zero (i.e. 0 voltage in both axes translates to 0 displacement in both axes). Thus it is only necessary to measure one point, preferably at a known voltage. The method that I used was to drive the mirror full scale (0V-10V) in both axes (with the Full button on the Debug screen), and then use the AFM and the optical screen to measure its travel. Again, a linear fit can be done with the points and the results entered in the FANSOM Configuration screen shown in Figure 19.

If the Nanoscope is recalibrated internally, or the nanodrive is replaced, then these calibrations ought to be performed again. These two calibrations, combined with the calibration described in section 6.3, represent all of the necessary system calibrations.

8 SYSTEM VALIDATION

8.1 VALIDATION DESCRIPTION

The completed system was validated by operation. It was deemed correct by the customer when it was operated in modes, which existed in the previous system, and found to get similar results. Other, secondary indicators also existed. For example, the tip height waveform capture could be shown to be correct by comparing the results with the results captured by the commercial AFM software doing the same analysis. The photon power was shown to be correct by showing, by inspection that the power graph lines up well with the expected locations seen on the AFM image.

9 ISO COMPLIANCE STATEMENT

This system is compliant with JPL's ISO procedure as described in JPL Procedure: Use of Inspection, Measuring and Test Equipment, Rev. 5 (http://dmie.jpl.nasa.gov/cgi/doc-gw.pl?DocID=30312)

10 COMPLIANCE MATRIX

Requirement	System as Delivered Complies?
- System retains the functionality of the previous system.	✓
- Analysis software converted from Matlab to LabVIEW.	✓
- All custom hardware redesigned and combined with placeholders kept for future additions.	✓
- DAQ and interface software redesign with placeholders kept to support future hardware additions.	✓
- Use of COTS hardware optimized.	✓

11 TOTAL COST REPORT

Type of Labor	Hours	Cost/hour	Total
Technician	124.5	$88.00	$10,956.00
Associate	474	$93.00	$44,082.00
Staff	288	$111.00	$31,968.00
Senior	4	$130.00	$ 520.00

Total Hours: 890.5 Labor Total: $87,526.00

(an additional 27 Staff hours and 171 Associate hours were worked and written off as training on several new technologies employed on this task)

Equipment	Quantity	Cost/unit	Total
Adobe Acrobat	1	$190.46	$ 190.46
NI PXI-5211	1	$6,977.62	$6,977.62
NI PXI-1042Q	1	$2517.31	$2,517.31
NI PXI-6229	1	$831.95	$ 831.95
NI PXIPCI-8336 MXI	1	$3107.72	$3,107.72
NI PXI-6602	1	$853.42	$ 853.42
LabVIEW 7.1	1	$2, 141.59	$ 143.59
Tax,S&H	1	$426.43	$ 426.43
Teflon Wire	1	$405.76	$ 405.76
	1	$60.53	$ 60.53
Coldfire/Dev Kit	1	$569.86	$ 569.86
	1	$56.91	$ 56.91
	1	$65.07	$ 65.07
	1	$65.07	$ 65.07
10U Rack	1	$167.45	$ 167.45
	1	$336.06	$ 336.06
Dell Precision 370	1	$2148.10	$2,148.10
	1	$9.71	$ 9.71
	1	$9.71	$ 9.71
	1	$4825.15	$4,825.15
		Procurements Total:	$23,767.88

12 EVALUATION OF SCHEDULE AND COST

The project ended up 10% over the original cost estimate and 166% over the original schedule. There are several factors related to the overrun on each of these metrics.

Schedule, for example, was initially influenced by difficulties with the procurement of all of the National Instruments hardware. Initial delivery of the system to Caltech was completed in a timely fashion, taking this delay into account. Since the March 24 delivery to Caltech, schedule has been influenced by a combination of bug fixing and the addition of new features.

The overruns in cost were due initially to surprises in the implementation of the software and hardware designs, resulting in an early hit to our budget, and later about half and half with the chasing of elusive system bugs and adding new features.

Some of the features added which contribute to the later overruns (estimated to ~10% of the final cost) were not included in the original design and estimate, but were added to facilitate the completion of a truly usable product.

APPENDIX A – BOX H ETHERNET COMMANDS

AOM0 ON|OFF – Controls whether the AOM allows the laser to pass through or not (AOM0 ON : Laser passes through to optical system).

DBG? – Requests a debug packet in the format:
[xxxx,xxxx,xxxx,xxxx,f.fff,f.fff]
With the parameters:
Stage X – the x position of the AFM stage as a four-digit hex value
Stage Y – the y position of the AFM stage as a four-digit hex value
Mirror X – the x position of the mirror as a four-digit hex value
Mirror Y – the y position of the mirror as a four-digit hex value
Error X – the x error from the control loop as a five digit float
Error Y – the y error from the control loop as a five digit float

DISP # - Changes the display mode on the LCD. [Currently inactive]

DUMP – Dumps a full OS state of the Coldfire to the serial port. [Currently inactive]

FOCS xxxx – Sets the Focus PZT DAC output to the value represented as the four character hexidecimal representation xxxx (FOCS 0000 : 0V, FOCS : 140V).

GNNX f.ffff – Sets the digital control loop's AFM input gain to the value represented by the floating-point string f.ffff (GNNX 0.0000 : 0 input gain). **GNNY f.ffff** does the same for the y-axis.

GNDX f.ffff – Sets the digital control loop's D gain to the value represented by the floating-point string f.ffff (GNDX 0.0000 : 0 p gain). **GNDX f.ffff** does the same for the y-axis.

GNIX f.ffff – Sets the digital control loop's I gain to the value represented by the floating-point string f.ffff (GNIX 0.0000 : 0 p gain). **GNIX f.ffff** does the same for the y-axis.

GNPX f.ffff – Sets the digital control loop's P gain to the value represented by the floating-point string f.ffff (GNPX 0.0000 : 0 p gain). **GNPY f.ffff** does the same for the y-axis.

LINE ON|OFF – Controls whether the Coldfire toggles on the LINE pin during each line of the afm's movement (LINE ON : LINE toggles at each line transition).

MIRX xxxx – Sets the DAC output for the mirror's x-axis to the value represented by the four digit hex number xxxx (MIRX 0000 : 0V out). **MIRY xxxx** does the same thing for the y-axis.

OFFX f.ffff – Sets the digital control loop's AFM x-offset to the value represented by the floating-point string f.ffff (OFFX 0.0000 : 0 offset). **OFFY f.ffff** does the same for the y-axis.

POWR ON|OFF – Controls whether the +5V power is output to the photon detector (POWR ON : Power is output).

RMPX xxxx yyyy zzzz – Starts an x-axis ramp starting from the DAC output represented by the four-digit hex value xxxx, going to the DAC output represented by the four-digit hex value yyyy, with as many updates per second as represented by the four-digit hex value zzzz (RMPX 0000 FFFF 1111 : a ramp from 0 to full scale lasting 15 seconds).

RSET : Resets Box H.

RVAR : Resets debug boundary variables. [Currently inactive]

STA? – Requests a state packet in the format:

[f.fff,f.fff,f.fff,f.fff,f.fff,f.fff,f.fff,f.fff,f.fff,f.fff,xxxx,x,x]

With the parameters:

Offset X – the x offset for the afm position as a five digit float
Offset Y – the y offset for the afm position as a five digit float
Gain N X – the x input gain for the afm position as a five digit float
Gain N Y – the y input gain for the afm position as a five digit float
Gain P X – the x P gain for the digital control loop as a five digit float
Gain P Y – the y P gain for the digital control loop as a five digit float
Gain I X – the x I gain for the digital control loop as a five digit float
Gain I Y – the y I gain for the digital control loop as a five digit float
Gain D X – the x D gain for the digital control loop as a five digit float
Gain D Y – the y D gain for the digital control loop as a five digit float
Focus – the focus DAC value as a four digit hex number
Flags1 – a single hex digit whose bits mean
(1 : tracking loop on; 4 : aom0 on; 8 : pd power on)
Flags2 – a single hex digit whose bits mean
(1 : line output high; 2 : frame output high)

TICKS? – Returns the current number of interrupt ticks. Useful for debugging the rate of interrupt of Box G.

TRAK ON|OFF – Controls whether Box H controls the position of the mirror with the digital control loop (TRAK ON : Box H controls the mirror).

APPENDIX B – HARDWARE SCHEMATICS

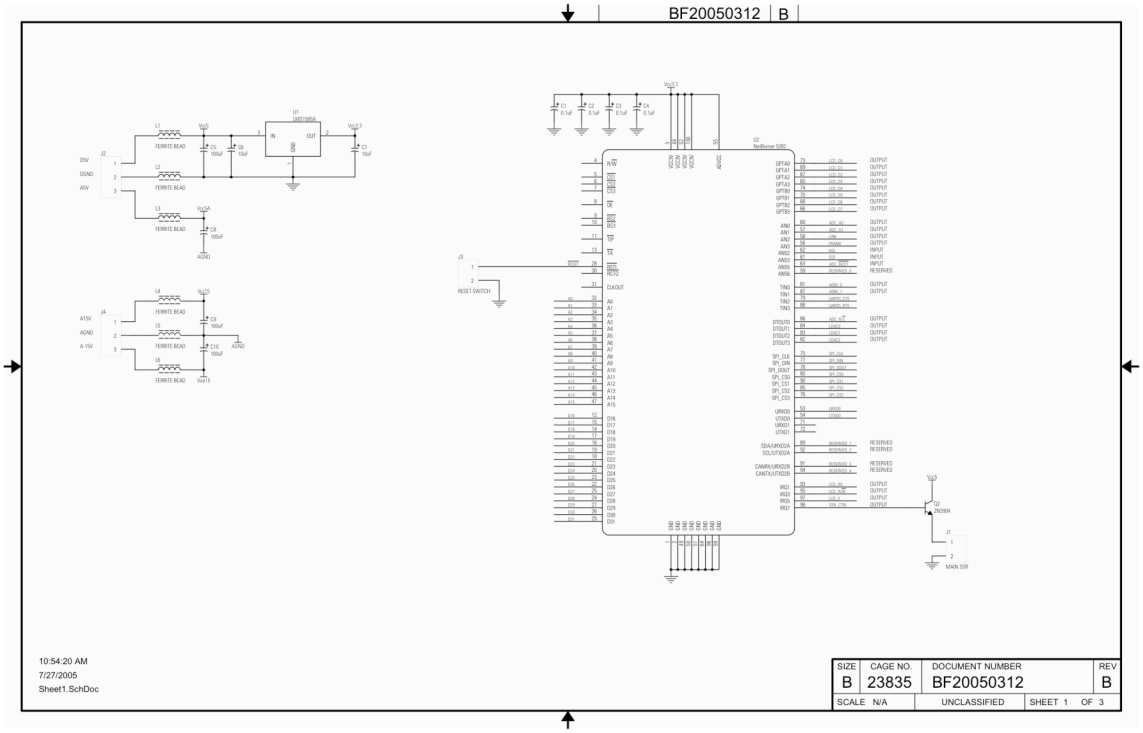

Figure 20 - Main PCB Schematic #1

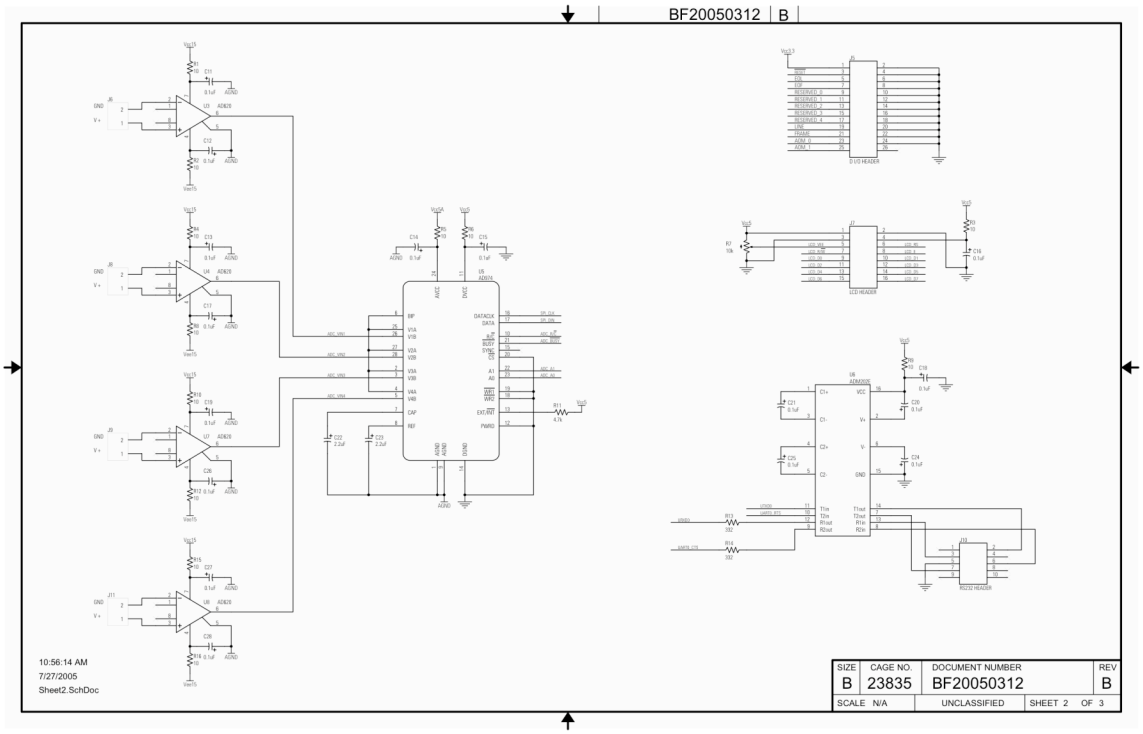

Figure 21 - Main PCB Schematic #2

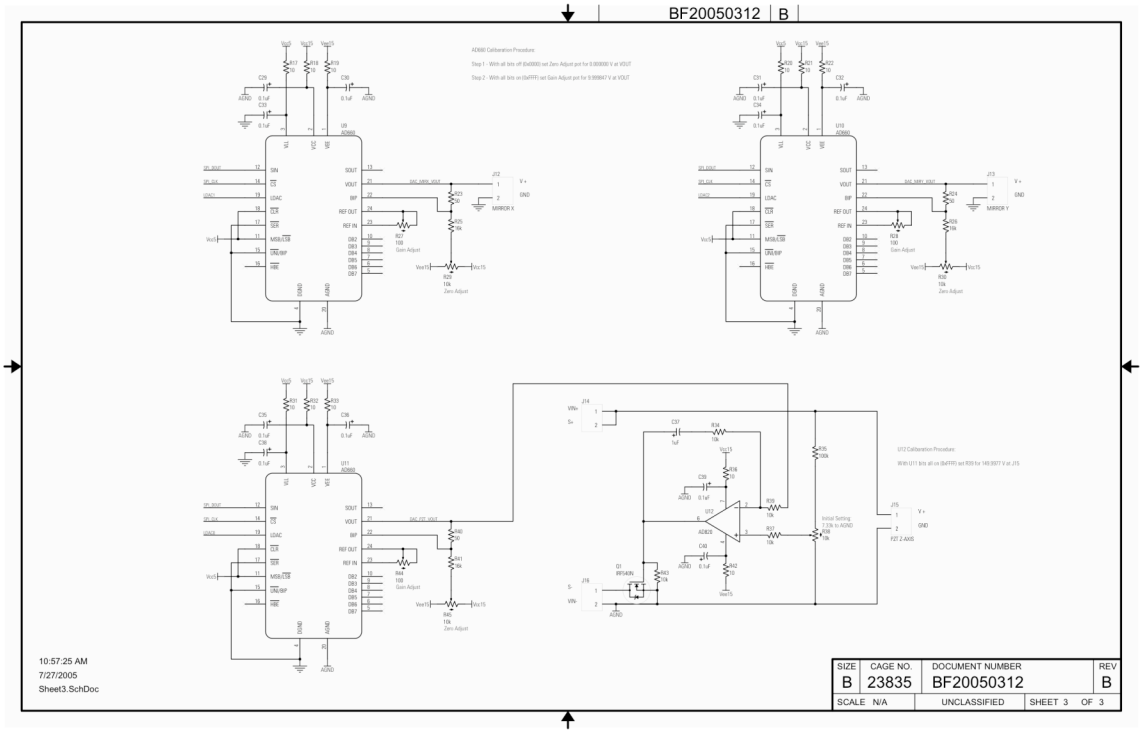

Figure 22 - Main PCB Schematic #3

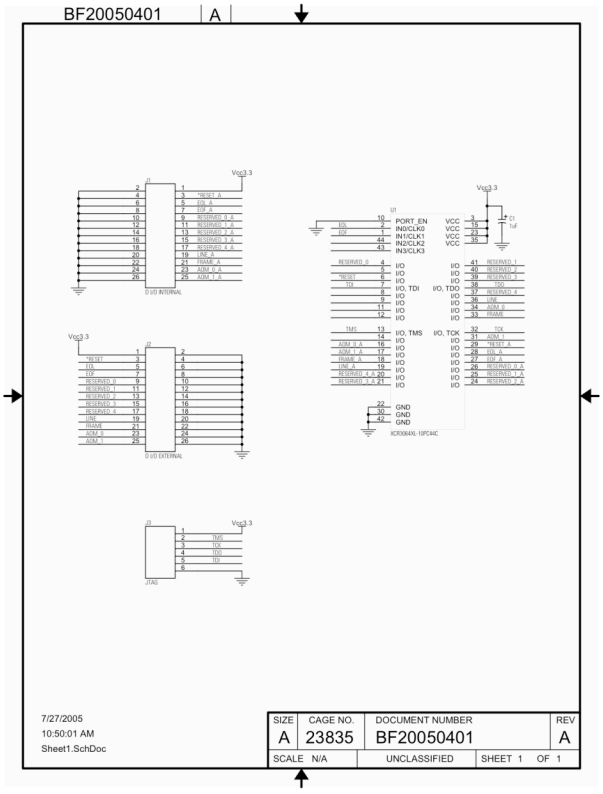

Figure 23 - CPLD Board Schematic

APPENDIX C – PREVIOUS SYSTEM

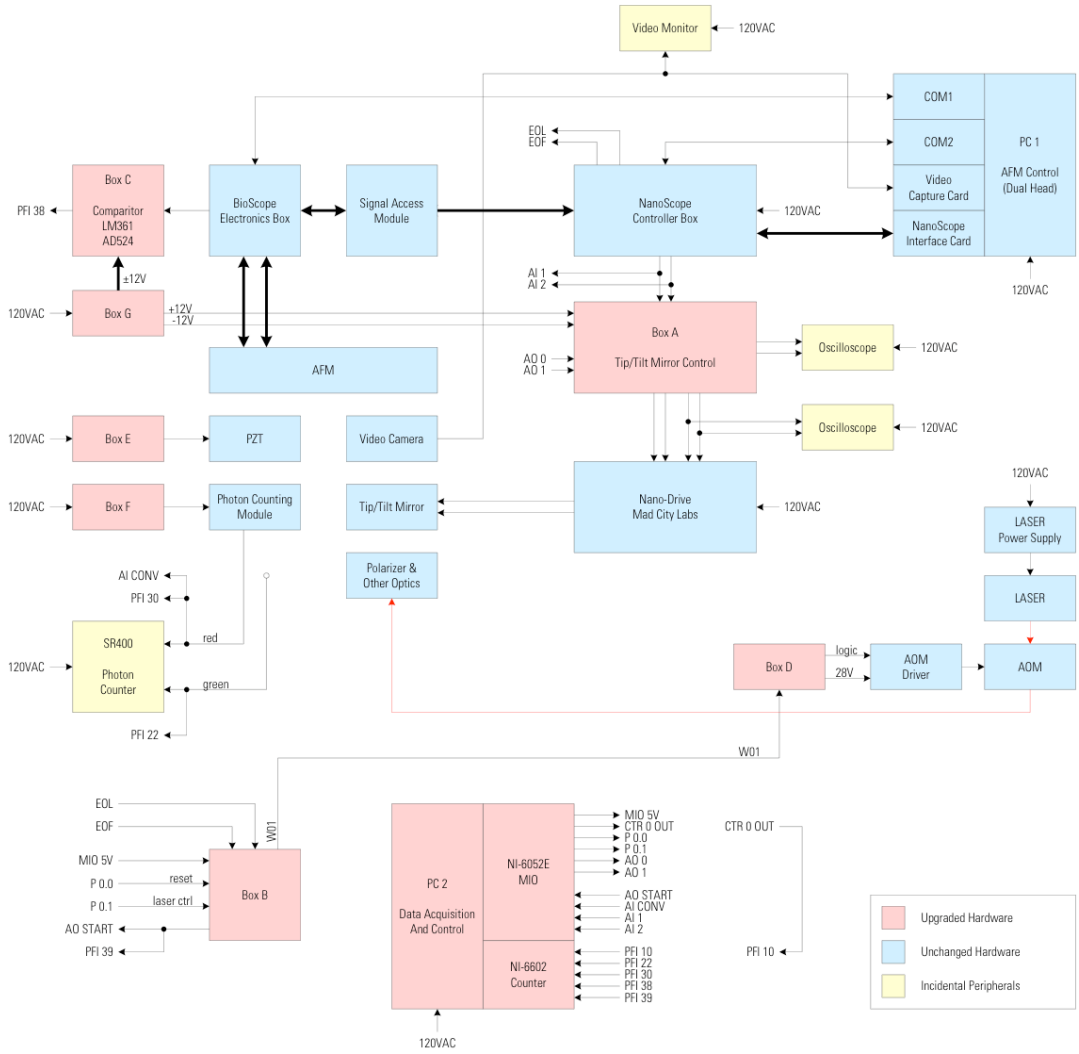

Figure 24 - Previous System Block Diagram

Image Processing Software

The image processing software was written in Matlab by Eyal Shafran with minor modification by me (version 2.2). The code analyzes the data and creates 4 images: Photon, AFM amplitude, Lock-in magnitude and lock-in phase. There are a few subroutines that are called by the main function:

Read_txt_File – Reads the text config file. The following parameters are extracted from the config file: number of lines, scan size, scans rate and aspect ratio.

Larry_load_data – Loads the photon data, afm data or both for a specific line.

Larry_clean_afm_data – Takes the afm data and filters the data with a +- 2kHz band pass filter around the tips frequency. After filtering, the zero crossing are computed and returned to the main program (Essentially this subroutine converts the analog afm data -> timestamps).

Tap_Hist – A c code that finds the phase of each photon.

Vector_Lock_in – Each photon is converted into a unit vector in phase space. For each pixel the vectors are summed. The resulting vector is separated into 2 fields: magnitude and phase.

Before you can use the code the c code needs to be compiled. If you are using a mac download the XTool from the operating system installation disk. Once the XTool is installed type: "mex directory /Tap_Hist.c" in the matlab command window (change directory to the actual directory that the file is in). You might need to choose a compiler. Choose the Lcc-win32 C compiler. If the file can't be compiled try typing mex –setup and choose the compiler you want to use. If the file can't be compiled with any of the compilers available give me a call.

There are a few different options to run the code. All of them assume that the config text files have the same template (if this is not true the code might not work).

Analysis_v1 – A dialog box will be opened. The user needs to select the config txt file. Number of lines is taken from the txt file. The bin number is always equal to the number of lines.

Analysis_v1(base) - The base name is specified. Also looks for the config file. The number of lines is taken from the text file and the number of bins will be the same as the number of lines.

Analysis_v1(base,bin_num) - The base name is specified. The number of bins is specified in bin_num (can be any integer) and is not necessarily equal to the number of lines.

Analysis_v1.m

```
function y = Analysis_v1(varargin)
% ANALYSIS_V1 - Plots photon,afm amplitude, lock-in magnitude and lock-in
% phase images.
% Analysis_v1() - The user needs to select the config txt file. Number of lines is taken from the txt file.
% The bin number is always equal to the number of lines.
% Analysis_v1(base) - The base name is specified. Also looks for the config file.
% Analysis_v1(base,bin_num) - The base name is specified. The number of bins is specified in bin_num (can be any integer) and is not necessarlyequal to the number of lines.

switch nargin
    case 0
        [FileName,base] = uigetfile('*.txt','Choose header file');
        Param = Read_txt_File([base FileName]); % Reads txt config file.
        Lines_num = Param.NumberOfLines;
        M_time = 1/Param.ScanRate/2;
        bin_num = Lines_num;
        k = strfind(FileName, '_config')-1;
        base = [base FileName(1:k)];
    case 1
        base = varargin{1};
        Param = Read_txt_File([base '_config.txt']);
        Lines_num = Param.NumberOfLines;
        M_time = 1/Param.ScanRate/2;
        bin_num = Lines_num;
    case 2
        base = varargin{1};
        Param = Read_txt_File([base '_config.txt']);
        Lines_num = Param.NumberOfLines;
```

```
        M_time = 1/Param.ScanRate/2;
        bin_num = varargin{2};
end;

% Initialize values

Im_amplitude = zeros(Lines_num,bin_num);
Im_Photon = zeros(Lines_num,bin_num);
Im_Magnitude = zeros(Lines_num,bin_num);
Im_Phase = zeros(Lines_num,bin_num);
clock = 1000000;

%Starting main loop

for Line=0:Lines_num-1

    Data = Larry_load_data(base,Line,'all');% Loads the afm and photon data from file
    if(~isempty(Data))
        timestamp = Larry_clean_afm_data(Data.afm); % Cleans the noisy afm data and
returns the afm timestamps
        time = [0:length(Data.afm)]/clock; % Creating a time vector for the afm
        time = time(:);
        bins = 0:M_time/(bin_num):M_time;
        c_photon = histc(Data.data/20000000,bins); % finding the number of photons per
pixel.
        c_photon(end)=[];
        c_Tap = histc(time,bins); % finding the number of taps per pixel.
        c_Tap(end)=[];
        counter_p = 1;
        counter_t = 1;
        index1 = cumsum(c_photon);
        index2 = cumsum(c_Tap);
        amplitude = zeros(bin_num,1);
        Magnitude = zeros(bin_num,1);
        Phase = zeros(bin_num,1);
        Rel_Tap = Tap_Hist(Data.data/20000000, timestamp);% c code that computes the
phase for each photon
        for i=1:bin_num
            Tap = Data.afm(counter_t:index2(i));
            counter_t = index2(i)+1;
            % Doing a fft
            L = length(Tap);
            NFFT = 2^nextpow2(L);
            FT = fft(Tap,NFFT)/L;
            power = abs(FT);
            f = clock*linspace(0,1,NFFT);
```

```
        k = find(f>20000 & f < 100000);
        mc = max(power(k)); % finding the amplitude at the frequency of the tip.
        amplitude(i)= (mc);
        if(~isempty(Rel_Tap(counter_p:index1(i)))) % If there is at least 1 photon
            [Magnitude(i),Phase(i)] = Vector_Lock_in(Rel_Tap(counter_p:index1(i)),M_time/bin_num); % Run vectorial lock-in
        else
            Magnitude(i)=NaN;
            Phase(i)=NaN;
        end;
        counter_p = index1(i)+1;
    end;
    Im_Magnitude(Line+1,:) = Magnitude;
    Im_amplitude(Line+1,:) = amplitude;
    Im_Phase(Line+1,:) = Phase;
    Im_Photon(Line+1,:) = c_photon;
  else
    Im_Magnitude(Line+1,1:bin_num) = NaN;
    Im_amplitude(Line+1,1:bin_num) = NaN;
    Im_Phase(Line+1,1:bin_num) = NaN;
    Im_Photon(Line+1,1:bin_num) = NaN;
  end;

  Line
end;
y.x = linspace(0,1,bin_num)*Param.ScanSize; % creating x vecto
y.y = linspace(0,1,Lines_num)*Param.ScanSize; % creating y vector
y.Magnitude = Im_Magnitude;
y.amplitude = Im_amplitude;
y.Phase = Im_Phase;
y.photon = Im_Photon;
if(Param.ratio==1 && bin_num==Lines_num) % if aspect ratio is 1 and bins=lines the image is scaled properly.
  subplot(2,2,1);imagesc(y.y,y.x,y.photon);axis image; title('Photon');colorbar;
  subplot(2,2,2);imagesc(y.y,y.x,y.amplitude);axis image; title('Amplitude'); colorbar;
  subplot(2,2,3);imagesc(y.y,y.x,y.Magnitude);axis image; title('Lock-in magnitude'); colorbar;
  Phase_hsv = zeros(size(y.Phase,1),size(y.Phase,2),3);
  Phase_hsv(:,:,1) = (y.Phase-min(y.Phase(:)))/max((y.Phase(:)-min(y.Phase(:))));
  Phase_hsv(:,:,2) = (y.Magnitude-min(y.Magnitude(:)))/max((y.Magnitude(:)-min(y.Magnitude(:))));
  Phase_hsv(:,:,3) = 1.0;
                                                    Phase_rgb = hsv2rgb(Phase_hsv);
   subplot(2,2,4);imagesc(y.y,y.x,Phase_rgb);axis image;  title('Lock-in phase'); colorbar;
  Overlay = zeros(size(y.Phase,1),size(y.Phase,2),3);
```

```
   Overlay(:,:,1)          =          (y.amplitude-min(y.amplitude(:)))/max((y.amplitude(:)-
min(y.amplitude(:))));
   Overlay(:,:,2) = (y.photon-min(y.photon(:)))/max((y.photon(:)-min(y.photon(:))));
   figure;
                imagesc(y.y,y.x,Overlay);axis image; title('AFM = Red ; Photon = Green');

else
   subplot(2,2,1);imagesc(y.photon); title('Photon')
   subplot(2,2,2);imagesc(y.amplitude); title('Amplitude')
   subplot(2,2,3);imagesc(y.Magnitude); title('Lock-in magnitude')
   subplot(2,2,4);imagesc(y.Phase); title('Lock-in phase');
end;
```

Larry_afm_images.m

```
function y = Larry_afm_images(base,Lines_num, bin_num, M_time)

for Line=0:Lines_num-1

   Data = Larry_load_data(base,Line,'all');
   clock = 1000000;
   time = [0:length(Data.afm)]/clock;
   time = time(:);
   bins = 0:M_time/(bin_num):M_time;
   c_photon = histc(Data.data/20000000,bins);
   c_photon(end)=[];
   c_Tap = histc(time,bins);
   c_Tap(end)=[];
   counter_p = 1;
   counter_t = 1;
   index1 = cumsum(c_photon);
   index2 = cumsum(c_Tap);
   for i=1:bin_num
      P = Data.data(counter_p:index1(i))/20000000;
      counter_p = index1(i)+1;
      Tap = Data.afm(counter_t:index2(i));
      t = time(counter_t:index2(i));
      counter_t = index2(i)+1;
      L = length(Tap);
      NFFT = 2^nextpow2(L);
      FT = fft(Tap,NFFT)/L;
      power = abs(FT);
      f = clock*linspace(0,1,NFFT);
%     f = clock*(0:(N-1))/N;
      k = find(f>20000 & f < 100000);
      [mc,mi] = max(power(k));
      frequency(i) = f(mi+k(1)-1);
```

```
        height(i)= power(1)/length(Tap);
        amplitude(i)= (mc);%/length(Tap)*2;
    end;
    Im_frequency(Line+1,:) = frequency;
    Im_amplitude(Line+1,:) = amplitude;
    Im_height(Line+1,:) = height;
    Im_Photon(Line+1,:) = c_photon;
    Line
end;

y.frequency = Im_frequency;
y.amplitude = Im_amplitude;
y.height = Im_height;
y.photon = Im_Photon;
subplot(2,2,1);imagesc(y.photon);
subplot(2,2,2);imagesc(y.frequency);
subplot(2,2,3);imagesc(y.amplitude);
subplot(2,2,4);imagesc(y.height);
```

Larry_Analysis.m

```
function Data = Larry_Analysis(bin_num)
% Initialize values
[FileName,base] = uigetfile('*.txt','Choose header file');
Param = Read_txt_File([base FileName]);
Lines_num = Param.NumberOfLines;
time = 1/Param.ScanRate;
Amplitude_image = zeros(Lines_num,bin_num);
Photon_image = zeros(Lines_num,bin_num);
Magnitude = zeros(Lines_num,bin_num);
Phase = zeros(Lines_num,bin_num);
time = time/2;
k = strfind(FileName, '_config')-1;
base = [base FileName(1:k)];
clock = 1000000;

for Line=0:Lines_num-1 % Run code for all the lines

    Data = Larry_load_data(base,Line,'all'); % Loads Photon & AFM data for a given
Line.

    if(~isempty(Data)) % Checking if line is not empty. If Data is empty go to else.
        Data.data = Data.data/20000000; % Divide photon data by card clock to get time.
        [timestamp,Data.afm] = Larry_clean_afm_data(Data.afm); % Cleans the noisy afm
data
```

```
        bins = 0:time/(bin_num):time;
        afm_time = [0:length(Data.afm)]/clock;
        afm_time = afm_time(:);
        c_photon = histc(Data.data,bins); % finds the number of photons per bin.
        c_photon(end)=[];
        c_Tap = histc(afm_time,bins);
        c_Tap(end)=[];
        counter_p = 1;
        counter_t = 1;
        index1 = cumsum(c_photon);
        index2 = cumsum(c_Tap);
        for i=1:bin_num
            P = Data.data(counter_p:index1(i));
            Tap = Data.afm(counter_t:index2(i));
            counter_t = index2(i)+1;
            FT = fft(Tap);
            power = abs(FT);
            N = length(FT);
            f = clock*(0:(N-1))/N;
            k = find(f>20000 & f < 100000);
            [mc,mi] = max(power(k));
            amplitude(i)= (mc)/length(Tap)*2;
            if(~isempty(P)) % If there is at least 1 photon
                counter_p = index1(i)+1;
                Rel_Tap = Tap_Hist(P, timestamp); % Convert photon timetag to phase
                [Data.Lock_in(i),Data.Phase(i)] = Vector_Lock_in(Rel_Tap,time/bin_num); %
Run vectorial lock-in
            else
                Data.Lock_in(i)=NaN;
                Data.Phase(i)=NaN;
            end;
        end;
        Amplitude_image(Line+1,:) = amplitude;
        Photon_image(Line+1,:) = c_photon;
        Magnitude(Line+1,:) = Data.Lock_in;
        Phase(Line+1,:) = Data.Phase;
    else
        Amplitude_image(Line+1,1:bin_num) = NaN;
        Photon_image(Line+1,1:bin_num) = NaN;
        Magnitude(Line+1,1:bin_num) = NaN;
        Phase(Line+1,1:bin_num) = NaN;
    end;
    Line
end;
keyboard;
Data.Amplitude_image = Amplitude_image;
```

```
Data.Magnitude = Magnitude;
Data.Phase = Phase;
Data.Photon_image = Photon_image;
x = 0:Param.ScanSize/(bin_num-1):Param.ScanSize;
y = 0:Param.ScanSize/(Lines_num-1):Param.ScanSize;
figure;
subplot(2,2,1);imagesc(x,y,Photon_image);axis image;title('Photon Image');
subplot(2,2,2);imagesc(x,y,Magnitude);axis image;title('Lock-in Magnitude')
subplot(2,2,3);imagesc(x,y,Phase);axis image;title('Lock-in phase');
subplot(2,2,4);imagesc(x,y,Amplitude_image);axis image;title('Amplitude image');
```

Larry_clean_afm_data.m

```
function [timestamp,afm] = Larry_clean_afm_data(afm)
% LARRY_CLEAN_AFM_DATA(afm) - cleans the afm data and returns timastamps

clock = 1000000;
time = [0:length(afm)-1]/clock;
time = time(:);
FT = fft(afm);
power = abs(FT(1:length(FT)/2));
N = length(FT);
f = clock*(1:N/2)/(N/2)*1/2;
k = find(f>10000 & f < 100000);
[mc,mi] = max(power(k)); % Finds the tips frequency from the power spectrum.
frequency = f(mi+k(1)-1); % Finds the frequency at the peak of the power spectrum.
FT(f< frequency-2000 | f > frequency+2000)=0; % band pass filter with +-2kHz on each
side of the frequency.
afm = real(ifft(FT));
%afm = smooth(afm,5);
timestamp = zero_crossing(time, afm,1/clock); % Finds the zero crossings.
ave_frequency = 1/mean(diff(timestamp));
if(abs(frequency-ave_frequency)/frequency > 0.01)
   [frequency ave_frequency]
   disp('Average frequency for the calculated timestamps is not close to the AFM
frequency from fft ');
end
```

Larry_fft_compare.m

```
function  Larry_fft_compare(Photon,afm)

clock = 1000000;
time = 1/clock:1/clock:length(afm)/clock;
time = time(:);
FT = fft(afm);
```

```
power = zeros(length(FT)/2,1);
power = abs(FT(1:length(FT)/2));
N = length(FT);
f = clock*(1:N/2)/(N/2)*1/2;
b = 0:1/clock:time(end);
F = zeros(length(b),1);
F = histc(Photon,b);
F(end)=[];
FT2 = zeros(length(F),1);
FT2 =fft(F);
%FT(end)=[];
power2 = zeros(length(FT2)/2,1);
power2 = abs(FT2(1:length(FT2)/2));
N = length(FT2);
figure; loglog(f,power/max(power),f,power2/max(power));
figure; plot(f,power/max(power),f,power2/max(power));
```

Larry_load_data.m

```
function y = Larry_load_data(base,line,data_type)
% LARRY_LOAD_DATA(base,line,data_type) - Loads measured line from data. base is
the
% path of the file, line is the line that is being loaded, and data_type is
% one of 3 options - 'photon','afm','all'.


try
   if(strcmp(data_type,'photon'))
      fname = [base '-' num2str(line, '%03d') '-redphotons.raw'];
      file = fopen(fname, 'r', 'ieee-be');
      [y.data, y.count] = fread(file, 'uint32');
      fclose(file);
   elseif(strcmp(data_type,'afm'))
      fname = [base '-' num2str(line, '%03d') '-afmtipheight.raw'];
      file = fopen(fname, 'r', 'ieee-be.l64');
      [y.afm, y.afm_count] = fread(file, 'float64');
      fclose(file);
   elseif(strcmp(data_type,'all'))
      fname = [base '-' num2str(line, '%03d') '-redphotons.raw'];
      file = fopen(fname, 'r', 'ieee-be');
      [y.data, y.count] = fread(file, 'uint32');
      fclose(file);
      fname = [base '-' num2str(line, '%03d') '-afmtipheight.raw'];
      file = fopen(fname, 'r', 'ieee-be.l64');
      [y.afm, y.afm_count] = fread(file, 'float64');
      fclose(file);
```

```
    else
        error('Can not recognize data type. Choose one of the following: photon, afm or all')
    end;
catch
    y = [];
    disp('Line is empty ');
end;
```

Larry_optical_image.m

```
%% QUICK OPTICAL IMAGE

for Line=0:511
    Data = Larry_load_data(base,Line,'photon');
    bins = 0:0.5/511:0.5;
    c_photon = histc(Data.data/20000000,bins);
    Photon_image(Line+1,:) = c_photon;
end;
figure;imagesc(Photon_image); axis image
```

Read_txt_File.m

```
function y = Read_txt_File(path)

fid = fopen(path);
File = fread(fid,inf,'*char')';
fclose(fid);
k = strfind(File, 'NumberOfLines=')+14;
y.NumberOfLines = str2double(File(k:k+4));
k = strfind(File, 'ScanRate=')+9;
y.ScanRate = str2double(File(k:k+4));
k = strfind(File, 'ScanSize=')+9;
y.ScanSize = str2double(File(k:k+4));
k = strfind(File, 'aspectratio=')+12;
y.ratio = str2double(File(k:k+2));
```

Tap_Hist_matlab.m

```
function Theta = Tap_Hist_matlab(Photons, Phase)
m_Photons = length(Photons);
m_Phase = length(Phase);
i=1;k=1;
while (Photons(i)< Phase(1) )
    i = i+1;
    if(i>m_Photons)
```

```
      Theta(1)=-1;
      return
   end;
end;
for j=i:m_Photons
   while (Photons(j)>=Phase(k) && k<m_Phase)
      k = k+1;
   end;
   try
      diff = Phase(k)-Phase(k-1);
      if(diff>=0)
         P = Photons(j)-Phase(k-1);
         d = P*2*pi/diff;
         Theta(j) = d;
      else
         Theta(j)=-1;
      end;
   catch
   end;
end;
```

Tap_Hist.c

```
//Phase_Hist_v6(Photon(k), Ave_Phase, N); Matlab code to run the dll
#include "mex.h"

void Phase_divider(double *Photons, double *Phase, mwSize m_Photons,mwSize
m_Phase, double *Theta)
{

   int i=0,k=0;
   double diff, P,d, PI = 3.141592653589793;
   for(; *(Photons+i)<*(Phase);i++)
      *(Theta+i) = -1; // Taking care of a photon arriving before the first Phase marker

   for (; i <= (m_Photons-1); i++)
   {
      for (; *(Photons+i)>=*(Phase+k) && k<=(m_Phase-1); k++);//Advance Photon
until it is bigger then the Tap
      diff = (*(Phase+k) - *(Phase+k-1));
      if (diff >= 0)
      {
         P = *(Photons+i)-*(Phase+k-1);
         d = (P/diff)*2*PI;
         *(Theta+i) = d;
      }
```

```
        else
            *(Theta+i) = -1;
    }

}



void mexFunction( int nlhs, mxArray *plhs[],
                  int nrhs, const mxArray *prhs[])
{
    double *Photons, *Phase, *z ;
    mwSize m_Photons, m_Phase;

    Photons = mxGetPr(prhs[0]);
    Phase = mxGetPr(prhs[1]);

    m_Photons = mxGetM(prhs[0]);
    m_Phase = mxGetM(prhs[1]);
    if(m_Photons!=0 && m_Phase!=0){
        plhs[0] = mxCreateDoubleMatrix(1,m_Photons, mxREAL);
        z = mxGetPr(plhs[0]);
        Phase_divider(Photons,Phase,m_Photons, m_Phase,  z);
    }
    else{
        plhs[0] = mxCreateDoubleMatrix(1,1, mxREAL);
        z = mxGetPr(plhs[0]);
        *z = -2;
    }


}
```

Vector_Lock_in.m

```
function [R,phi] = Vector_Lock_in(Rel_Tap,Time,varargin)
% Vector_Lock_in(Rel_Tap) is a lock-in code. The magnitude and phase are
% calculated by a vetorial sum on all phases(Rel_Tap)
if(nargin==3)
    beta= varargin{1};
    mu = beta(1);
    sigma = beta(2);
    Rel_Tap(find(Rel_Tap<mu-pi))=Rel_Tap(find(Rel_Tap<mu-pi))+2*pi;
    Rel_Tap(find(Rel_Tap>mu+pi))=Rel_Tap(find(Rel_Tap>mu+pi))-2*pi;
```

```
   Rel_Tap = Rel_Tap(find((abs(Rel_Tap-mu)<sigma) | (Rel_Tap-mu<-pi+sigma) | (Rel_Tap-mu>pi-sigma))); %[-sigma,sigma]
   Time = Time*2*sigma/pi;
elseif(nargin>3)
   error('Too many input arguements')
end
R = sqrt(sum(cos(Rel_Tap)).^2+sum(sin(Rel_Tap)).^2)/Time;
if(sum(cos(Rel_Tap))> 0 )
   phi = atan(sum(sin(Rel_Tap))/sum(cos(Rel_Tap)));
else
   phi = atan(sum(sin(Rel_Tap))/sum(cos(Rel_Tap)))+pi;
end;
```

zero_crossing.m

```
function y = zero_crossing(time, signal,deltaT)
% ZERO_CROSSING(time, signal, deltaT) - finds the zero crossing of an
% oscillating signal. signal and time are the actual signal and the time
% vector of that signal. deltaT is the time difference between to time
% points.

time = time(:);
signal = signal(:);
d = -1*signal(1:end-1)./(diff(signal));
%ZC = time(2:end)+d*deltaT./exp(deltaT*(0.5-d));
ZC = time(2:end)+d*deltaT;
index1 = find(signal(1:end-1).*signal(2:end)< 0 );
if(index1(end)==length(signal))
   index1(end) = [];
end
index1 = index1(find(signal(index1)-signal(index1+1)>0));
y = ZC(index1);
```

References

[1] Closed-Look Bioscope with Nanoscope IV controller, Veeco Metrology, 112 Robin Hill Road, Santa Barbara, CA 93117, USA.

Appendix F

Hue-Saturation-Value Representation and Correlation of Multispectral/Multi-Modal Datasets

Approach

Combining multiple images is a powerful tool for analyzing data provided that it can be done accurately, without distortion to the original image. Combining multiple images corresponding to multispectral or multimodal data allows one to easily and quickly interpret all the data at once. It also allows one to identify correspondences and differences across modes. For example, the method presented in this paper was originally developed for combining images taken by an atomic force microscope and a fluorescence microscope simultaneously. Combining the images gives a detailed topographical image of the sample overlaid with the fluorescence image to show points of interest.

Traditional methods for combining multiple images use red-green-blue (RGB) color space[1], but this often distorts the contrast of the original image. Specifically, RGB images encode grayscale as well as color in each channel. When RGB images are co-added the result inherently becomes darker and darker as the grayscales sum. The author then processes this summed image, using a program such as Photoshop, at a minimum by adjusting brightness and contrast to achieve a visually pleasing image. This undocumented distortion is unrepeatable. At best the result is an image that is visually pleasing, qualitatively correct but quantitatively distorted.

Color can be represented by bases other than RGB and images can be converted between these different color spaces[2,3]. This means that image processing can and should be done in the most convenient format, regardless of the format required for publication or other use. While methods for image fusion have used intensity-hue-saturation (IHS)[4,5] and hue-saturation-value (HSV)[6] color spaces the use of these non-RGB color spaces has been restricted to combining existing multispectral color images. The method we develop here uses HSV to combine multiple monochromatic images that belong to a multispectral into one color image. It can also be used to combine each imaging modality of a multimodal

data set to represent multimodal data sets in a single color image without data loss. Our method is based on performing the combination in the HSV color space as opposed to the RGB color space. In the HSV color space, grayscale and color information are in separate channels, so the combined images do not suffer from the same darkening contrast as images combined in RGB color space. Also, our method provides a visually acceptable image without manipulation through programs such as Photoshop. The result of our HSV-based method is a quantitatively accurate image. The method is repeatable, reversible, and does not suffer from the contrast distortion issues seen in RGB-based combination.

Methods: RGB- HSV Conversions

The conversion between RGB and HSV color spaces is a well-defined process; images can be converted between the two formats without loss of information.

We can convert from RGB to HSV color space using the following set of equations[6]:

$$V = Max(R, G, B)$$

$$S = \begin{cases} \dfrac{V - Min(R,G,B)}{V}, V \neq 0 \\ 0, V = 0 \end{cases}$$

If S = 0, then H = 0.
If R = V, then,

$$H = \begin{cases} \dfrac{60(G-B)}{V - Min(R,G,B)}, G \geq B \\ 360 + \dfrac{60(G-B)}{V - Min(R,G,B)}, G < B \end{cases}$$

If G = V, then,

$$H = 120 + \frac{60(B-R)}{V - Min(R,G,B)}$$

If B = V, then,

$$H = 240 + \frac{60 * (R - B)}{V - Min(R, G, B)}$$

Similarly, we can convert from HSV color space back to RGB color space using the following set of equations.

First, let

$$i = \left[\frac{H}{60}\right]$$

$$f = \frac{H}{60} - i$$

$$p = V(1 - S)$$

$$q = V(1 - S * f)$$

$$t = V\big(1 - S(1 - f)\big)$$

Then,

$R = V, G = t, B = p$	$i = 0$
$R = q, G = V, B = p$	$i = 1$
$R = p, G = V, B = t$	$i = 2$
$R = p, G = q, B = V$	$i = 3$
$R = t, G = p, B = V$	$i = 4$
$R = V, G = p, B = q$	$i = 5$

Methods: Combining two data sets using value and saturation

The following methods for combining images require that the images to be combined are of the same resolution. If they are not, then the individual images must be upscaled or downscaled to a consistent resolution.

To combine two data sets using the value and saturation channels of the HSV color space, one data set is assigned to the value and the other to the saturation. The value channel corresponds to a pixel's grayscale component and the saturation channel corresponds to a pixel's color intensity. For example, whether a pixel is bright red or faintly red is controlled by the saturation. In effect, this method overlays one data set in one color over a grayscale image. This is most useful when the value data set shows more information than the saturation data. The saturation data then points out areas of interest. The hue of the HSV color space image is set to a constant value corresponding to the color desired. The resulting image can be converted into RGB color space for compatibility with computer formats. This process is shown pictorially in Figure F.1.

Methods: Combining two data sets using saturation and hue

The method can be adjusted to combine two data sets using the saturation and hue layers. In this approach, the saturation layer is the average of the two data sets and the hue is set according to the relative values of the color images. The value is set to a constant value, but should not be set to 0 or 1 or the resulting image will be entirely white or black. The resulting image shows each data set as its selected hue with a relative mixture of hues where the data sets overlap. This method is useful for comparing data sets relative to one another. In areas where one data set has large values compared to the other, the hue will correspond to that data set. In areas where the two data sets have comparable intensity, the hue will be between the two individual hues.

More precisely, if at pixel(i,j),

$$data1(i,j) = d1$$

$$data2(i,j) = d2$$

And the hues to represent data1 and data2 are h1 and h2 respectively, then,

$$hue(i,j) = \frac{d1 * h1 + d2 * h2}{d1 + d2}$$

$$saturation(i,j) = \frac{d1 + d2}{2}$$

Methods: Combining three or more data sets

Three or more data sets can be combined using a combination of these methods. One data set can be represented by the value layer and two data sets can be represented using the saturation and hue layers. More data sets can be represented in the saturation and hue values by generalizing the method for two data sets in the saturation and hue layers. For n data sets,

$$hue(i,j) = \frac{\sum_n d_n * h_n}{\sum_n d_n}$$

$$saturation(i,j) = \frac{\sum_n d_n}{n}$$

Results

We compared a combination of two data sets using HSV and RGB-based methods (see Figure F.2). The HSV method uses the saturation and value layers to perform the combination. In the RGB method, one of the original images (Figure F.2a) is converted to grayscale and and the other (Figure F.2b) is added to the green channel. The resulting RGB image (Figure F.2c) has a green tinge to its background and the maxima of the original data are obscured. Furthermore, the horizontal lines from Figure F.2a are also blurred in Figure

F.2c. By contrast, the horizontal lines and the maxima can be clearly seen in the HSV images shown in Figure F.2d.

We also compared a combination of 3 data sets using our HSV-based method (Figure F.3a) and an RGB-based method (Figure F.3b). We start with a grayscale AFM image (Figure F.3c) which is overlayed with two circles, one in blue and one in green. The intensity of color of each of the circles decays with a Gaussian distribution from the center of the circle. In the RGB-based method (Figure F.3b), the contrast of the AFM image becomes distorted while in the HSV-based method (Figure F.3a) there is no contrast distortion.

Significance of results

Using HSV color space to combine multispectral data is an effective and accurate way to combine multiple images. Multispectral data is typically displayed by using the red, green, and blue channels to each display one layer of data. Another method is to color each layer of data differently and then combine the images using an image processing program such as Photoshop to adjust each layer's opacities so that all sets of data are visible. Both methods combine in the RGB color space because computers describe color in an RGB color space. In the first method, only 3 data sets can be effectively combined. In the second method, the manipulation of images in Photoshop could compromise the accuracy of the final image. By definition, adjustments made in Photoshop are done to please the eye. However those adjustments are not recorded or presented with the data. Therefore, the data is intrinsically altered, albeit unintentionally.

The HSV-based method can combine any number up to seven data sets for visual interpretation. There is no mathematical limit to the number of data sets which can be combined since each new data set is simply assigned a new hue. However, the practical number of data sets that can be combined is limited by the number of hues that the human eye can discern. In practice, this number of easily identifiable hues is six: red, yellow, green, cyan, blue, violet. A seventh data set can be displayed in the grayscale of the image. Although multiple colors can be used in RGB color space, multiple layers of data are not independent in the combination: each color is a linear combination of the red, green, and

blue channels. For example, if one layer of data is represented using cyan (a combination of blue and green) and another layer of data is represented using green, when these two layers are added, both data sets are represented in the green of the resulting image. In contrast, the HSV-based method can filter out a certain hue to find the data that corresponds to it. In this way, the original data is preserved. Protecting the quantitative content of the data sets is important for lossless communication between team members. It is also important for subsequent researchers who want to replicate results, analytic conclusions, or apply new analytic tools to these data sets.

Such accuracy to the original data is the main advantage of the HSV-based method. For example, images created in HSV can be converted into an RGB representation for compatibility with digital systems, the new image can be converted back to HSV form since the conversions between RGB and HSV space are well defined. The ability to extract the original data from the HSV-based image is lacking from RGB methods. Combining images in RGB color space, especially in programs like Photoshop, can easily distort individual data sets. The original quantitative data is lost in this process. The HSV-based method for image combination presented in this paper preserves the original data both qualitatively and quantitatively in the final image.

References

[1] S. Fengmei, L. Shutao and Y. Bin, *Robotics and Biomimetics, 2007. ROBIO 2007.* IEEE International Conference 2007, pp. 2043-2048.

[2] W.K. Pratt, *Digital Image Processing,* Edn. Fourth. (Hoboken; 2007).

[3] A. Koschan and M. Abidi, *Digital Color Image Processing.* (Wiley, Hoboken; 2008).

[4] M.M. Huang, J.S. Leng and C.C. Xiang, *Information Science and Engieering, 2008.* ISISE '08. International Symposium 2008, 1 pp. 665-668.

[5] Y. Yi, H. Chongzhao, K. Xin, K. and H. Deqiang, *Automation and Logistics, 2007* IEEE International Conference 2007, pp.1936-1940.

[6] C. Hua-Wen, and L. Shu-Duo, *Wavelet Analysis and Pattern Recognition, 2007.* ICWAPR '07. International Conference 2007, 4 pp. 1585-1588.

Figures

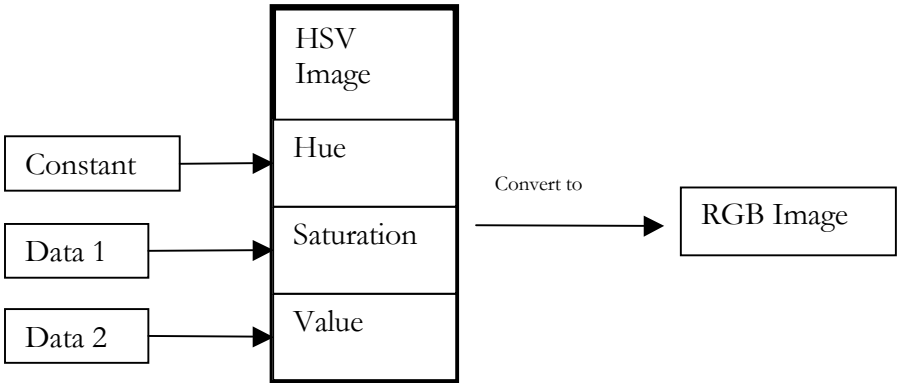

Figure F.1: Block diagram for combining two data sets using saturation and value layers. One data set is used for the saturation layer. The other data set is used for the value layer. The hue is set to a constant value. The HSV image can then be converted to RGB for general compatibility.

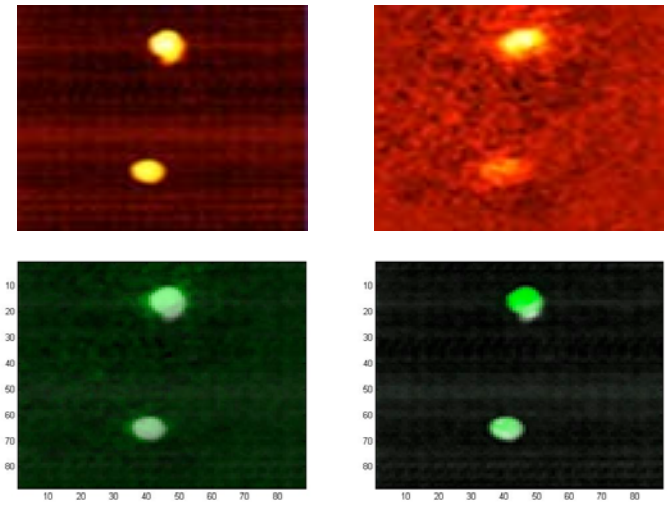

Figure F.2: Comparison of RGB-based and HSV-based image combinations. Images are 90 pixels x 90 pixels. a) First original data image. Yellow corresponds to higher intensity

while dark red corresponds to lower intensity. b) Second original data image using similar coloring as (a). c) Combination of images using RGB-based method with (b) overlaid in green on (a). Note the washed out green across the image. d) Combination of images using HSV-based method with (b) overlaid in green on (a). In this image, the relative intensities of the original image (b) can be seen.

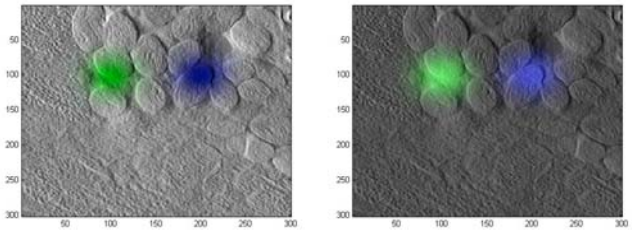

Figure F.3: The original AFM image (a) becomes distorted in the RGB-based image combination (b) as opposed to the HSV-based image combination (c). a) 300x300 HSV-based method for 3 data sets. Two Gaussian circles are overlaid, one in green and one in blue, on an AFM image. b) RGB-based method for the same 3 data sets in (a). c) Original background data set.

Appendix G

US patent 7,211,795
Method for manufacturing single wall carbon nanotube tips

This patent was awarded for a method for the efficient production of nanotube AFM probes. Such probes can image the topography of a sample with extraordinary resolution as part of an atomic force microscope. This method is described in great detail in Chapter 4. Chapter 4 additionally describes the methods used to grow nanotubes on a substrate, their characteristics of the AFM images produced with nanotube tips and finally the physics of nanotube attachment to a silicon AFM probe and of nanotube-nanotube interactions during AFM imaging. This patent was issued on May 1, 2007 to C. Patrick Collier, Ziyang Ma, Steven Quake, Ian Shapiro, and Lawrence Wade. These five inventors made equal contributions to this invention.

US007211795B2

(12) **United States Patent**
Collier et al.

(10) **Patent No.: US 7,211,795 B2**
(45) **Date of Patent: May 1, 2007**

(54) **METHOD FOR MANUFACTURING SINGLE WALL CARBON NANOTUBE TIPS**

(75) Inventors: **Charles Patrick Collier**, San Marino, CA (US); **Ma Ziyang**, Pasandena, CA (US); **Stephen R. Quake**, San Marino, CA (US); **Ian R. Shapiro**, Pasadena, CA (US); **Lawrence Wade**, LaCanada, CA (US)

(73) Assignee: **California Institute of Technology**, Pasadena, CA (US)

(*) Notice: Subject to any disclaimer, the term of this patent is extended or adjusted under 35 U.S.C. 154(b) by 212 days.

(21) Appl. No.: **11/045,240**

(22) Filed: **Jan. 27, 2005**

(65) **Prior Publication Data**

US 2005/0269509 A1 Dec. 8, 2005

Related U.S. Application Data

(60) Provisional application No. 60/542,757, filed on Feb. 6, 2004.

(51) **Int. Cl.**
G21K 7/00 (2006.01)
G01B 5/28 (2006.01)

(52) **U.S. Cl.** **250/307**; 250/309; 73/866.5

(58) **Field of Classification Search** 250/307
See application file for complete search history.

(56) **References Cited**

U.S. PATENT DOCUMENTS

6,002,471	A	12/1999	Quake	
6,743,408	B2 *	6/2004	Lieber et al.	423/447.1
2002/0178846	A1 *	12/2002	Dai et al.	73/866.5

* cited by examiner

Primary Examiner—Nikita Wells
Assistant Examiner—James Leybourne
(74) *Attorney, Agent, or Firm*—Townsend and Townsend and Crew LLP

(57) **ABSTRACT**

A method for fabricating assembled structures. The method includes providing a tip structure, which has a first end, a second end, and a length defined between the first end and the second end. The second end is a free end. The method includes attaching a nano-sized structure along a portion of the length of the tip structure to extend a total length of the tip structure to include the length of the tip structure and a first length associated with the nano-sized structure. The method includes shortening the nano-sized structure from the first length to a second length. The method also includes pushing the nano-sized structure in a direction parallel to the second length to reduce the second length to a third length of the nano-sized structure along the direction parallel to the second length to cause the nano-sized structure to move along a portion of the length of the tip structure.

31 Claims, 15 Drawing Sheets

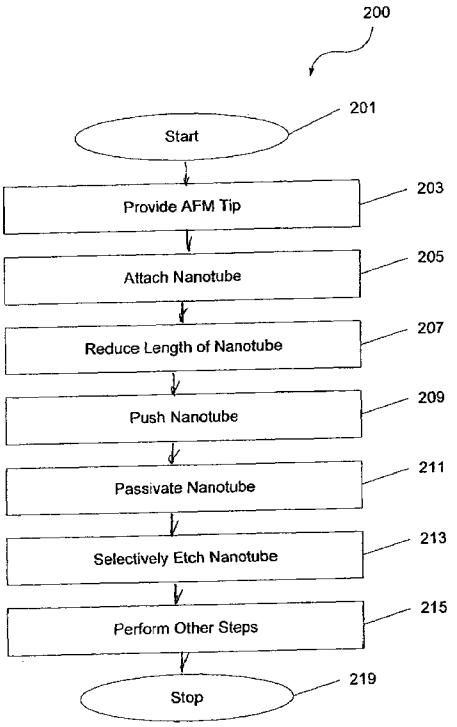

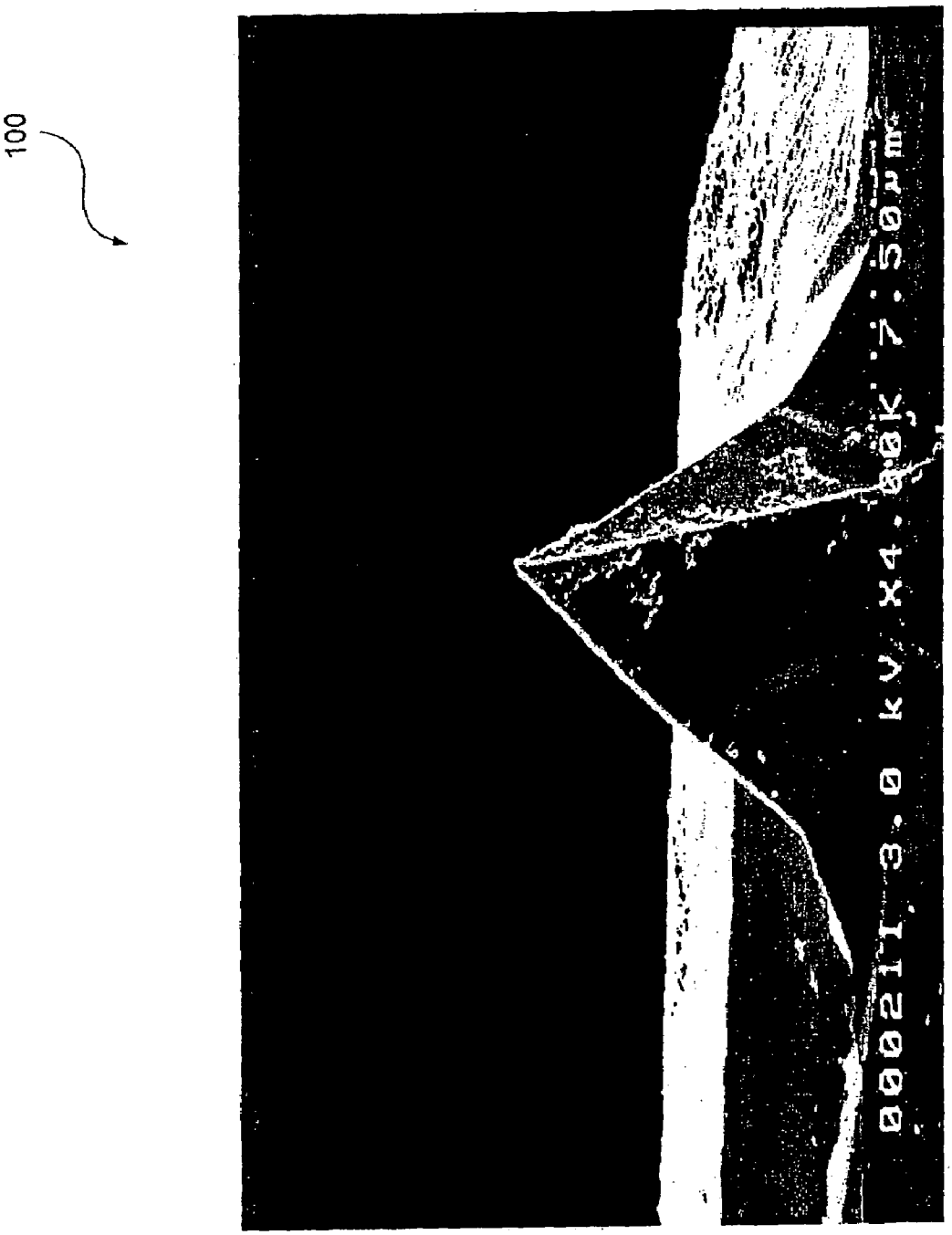

Figure 1

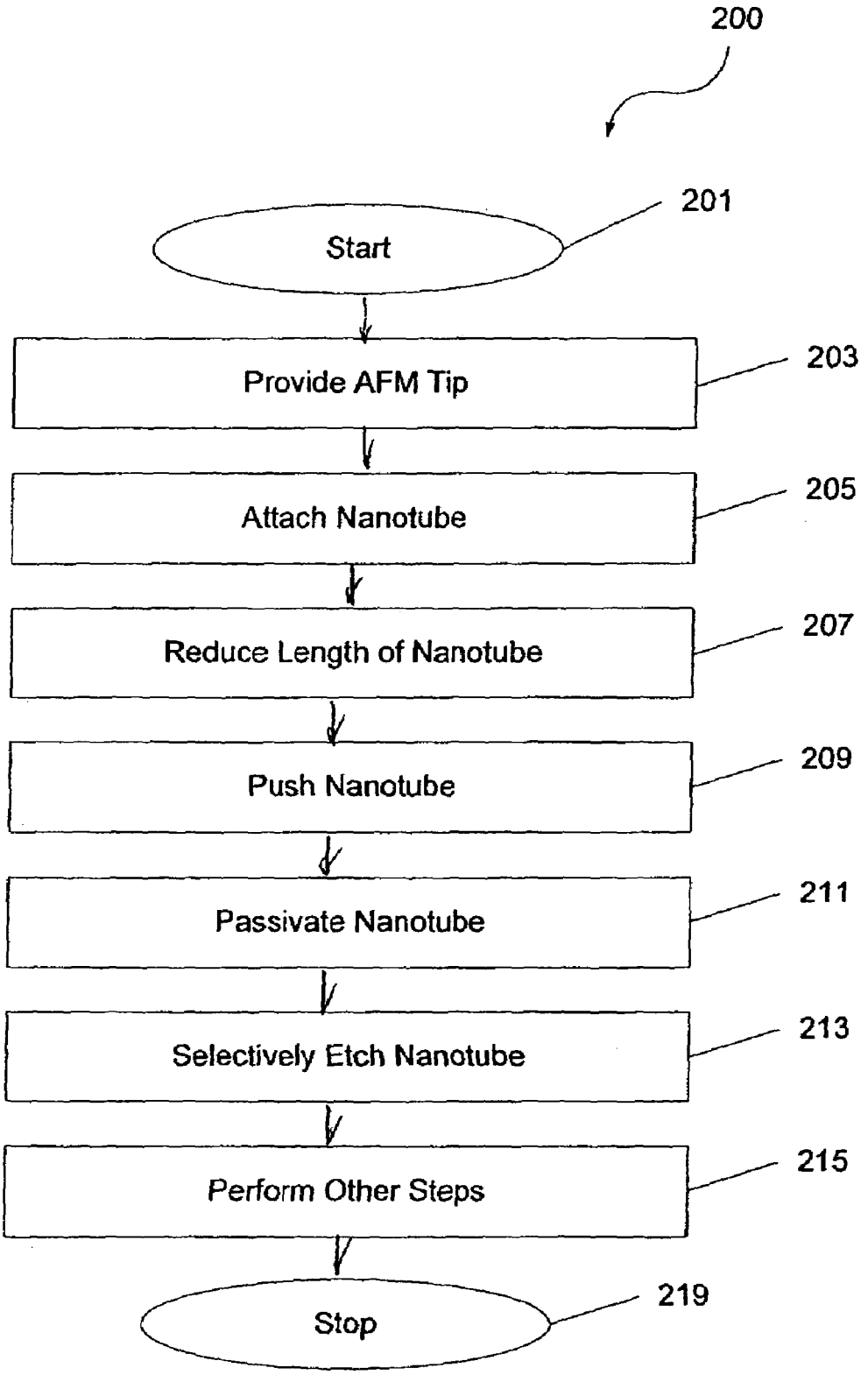
200
201
Start
203
Provide AFM Tip
205
Attach Nanotube
207
Reduce Length of Nanotube
209
Push Nanotube
211
Passivate Nanotube
213
Selectively Etch Nanotube
215
Perform Other Steps
219
Stop

Figure 2

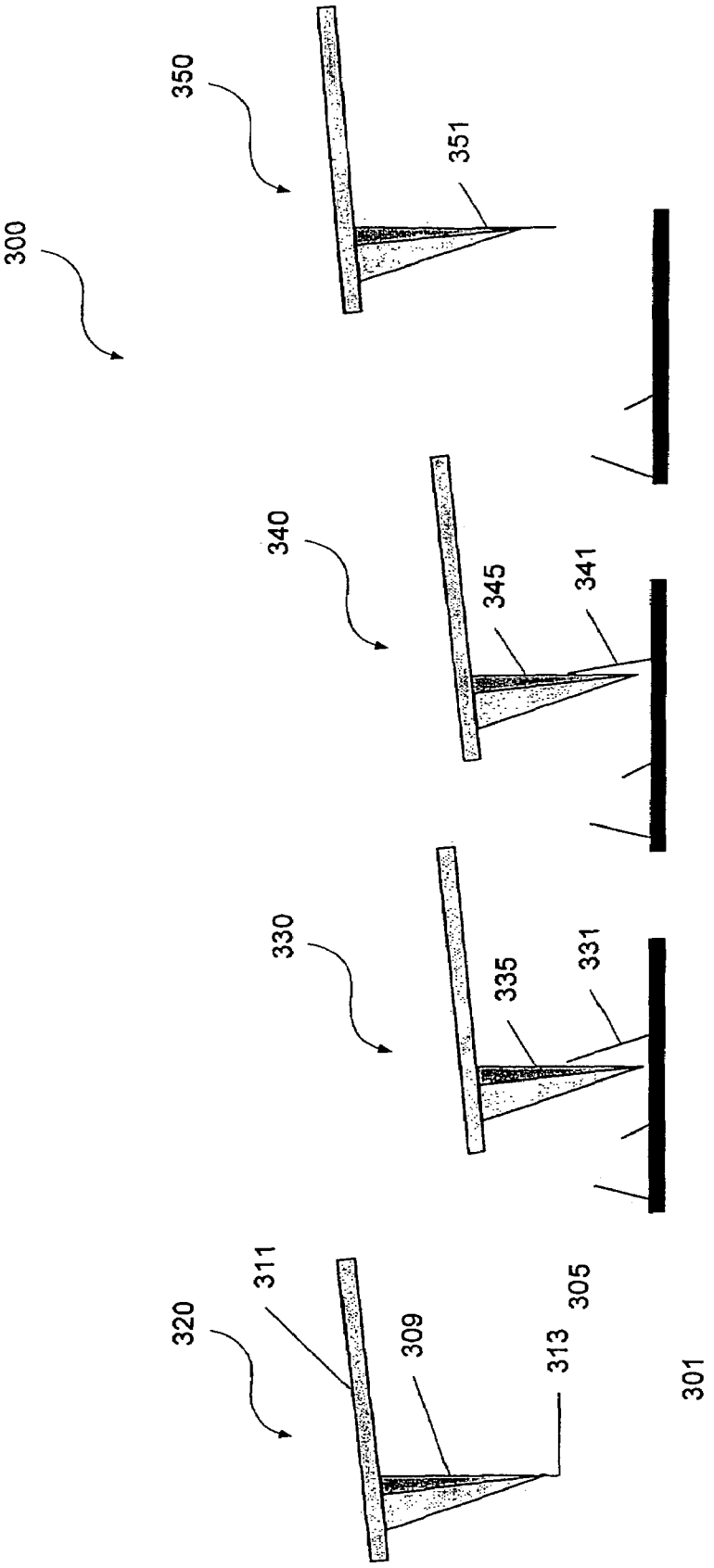

Figure 3

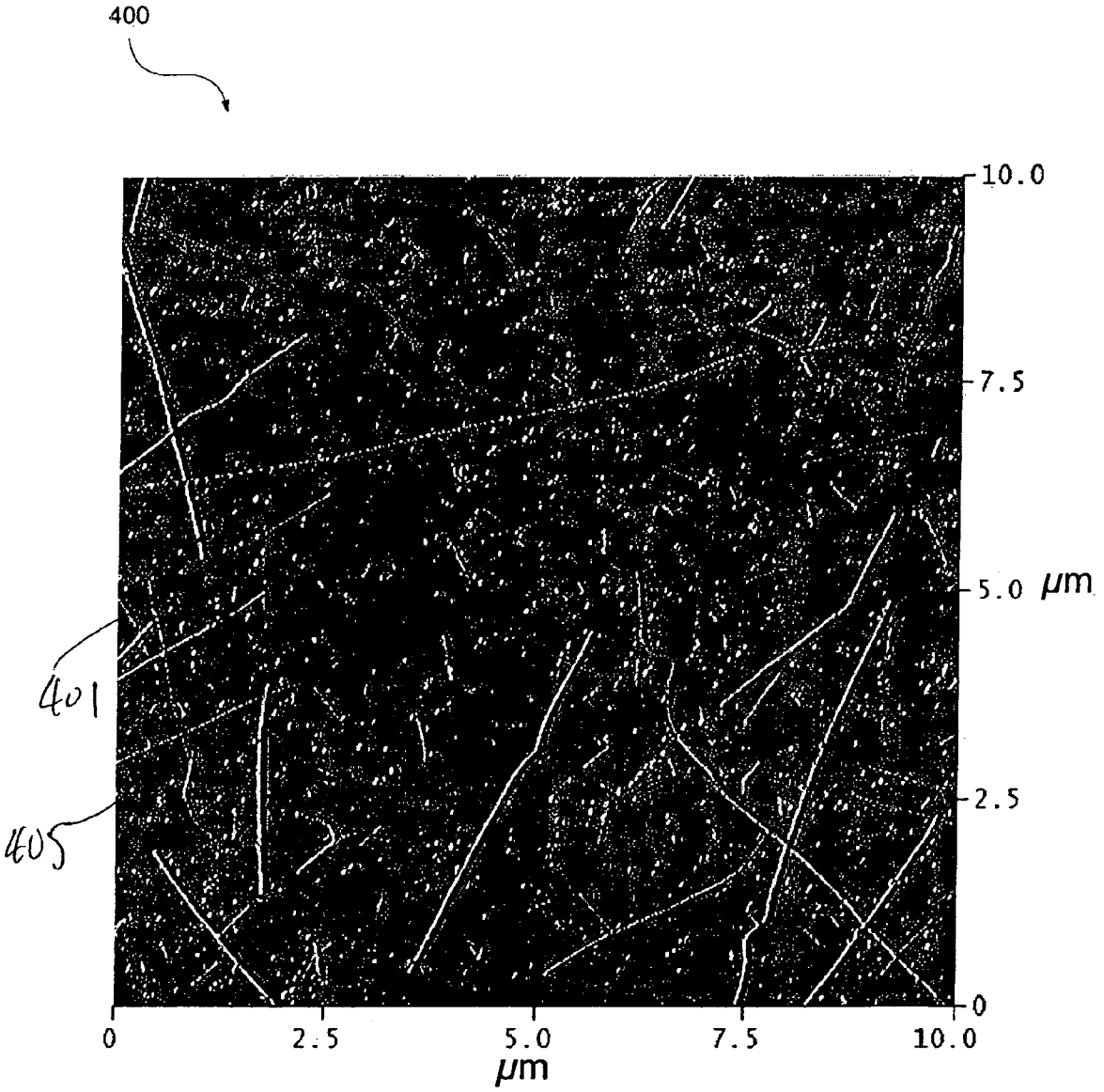

Figure 4

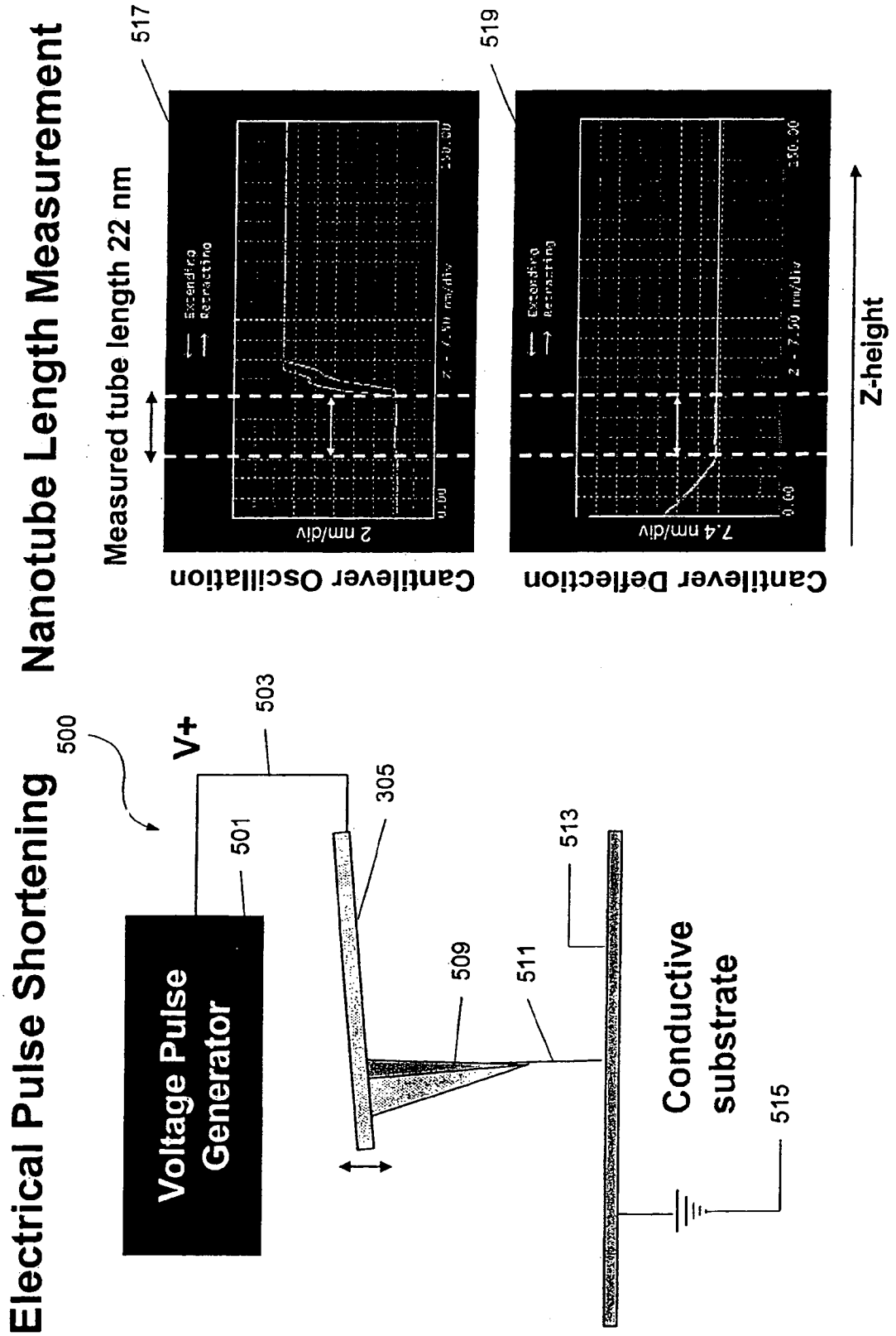
Electrical Pulse Shortening
Nanotube Length Measurement
500
V+
503
501
305
Voltage Pulse Generator
509
511
513
Conductive substrate
515
Measured tube length 22 nm
517
519
Cantilever Oscillation
Cantilever Deflection
Z-height

Figure 5

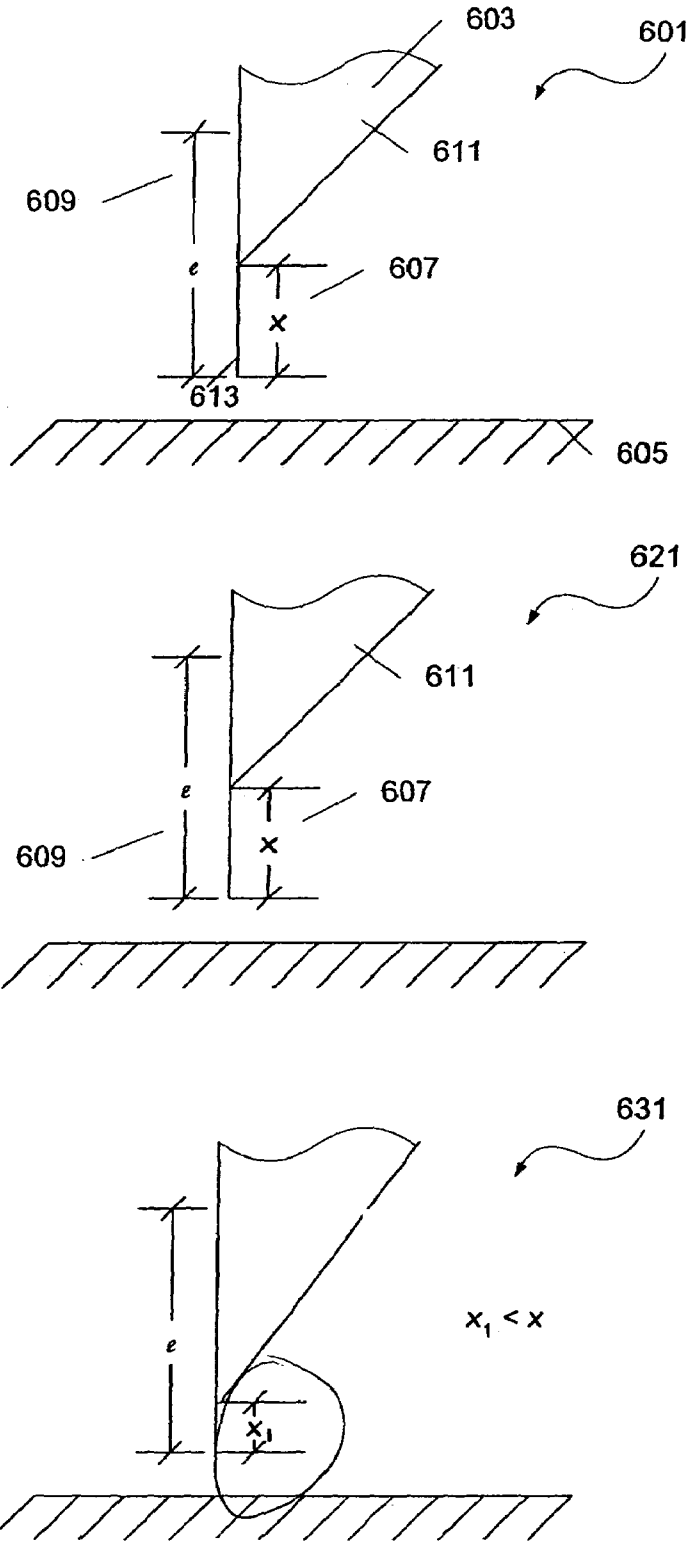

Figure 6

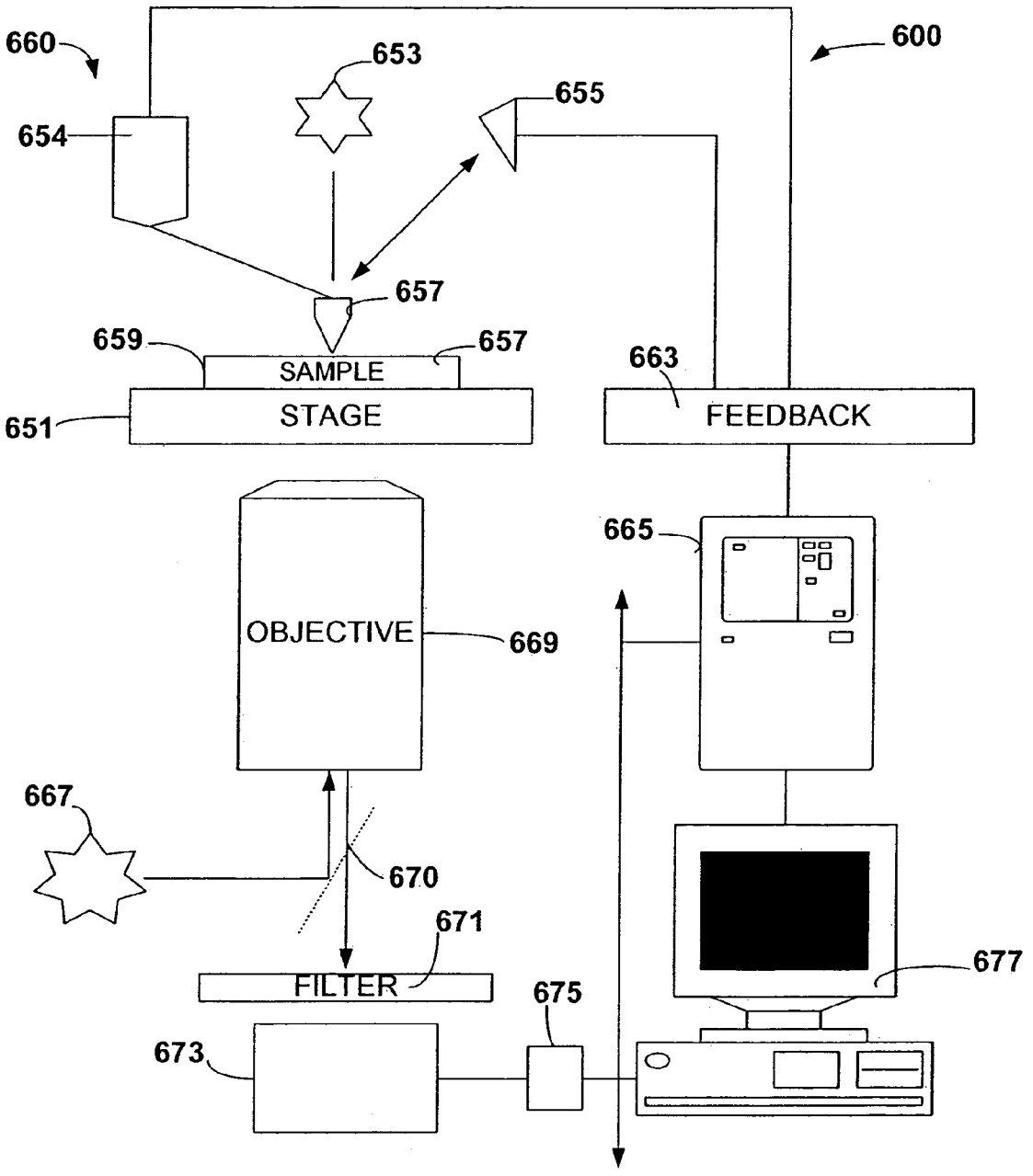
660
653
600
655
654
657
659
657
SAMPLE
663
651
STAGE
FEEDBACK
665
OBJECTIVE
669
667
670
671
FILTER
675
677
673

FIGURE 6A

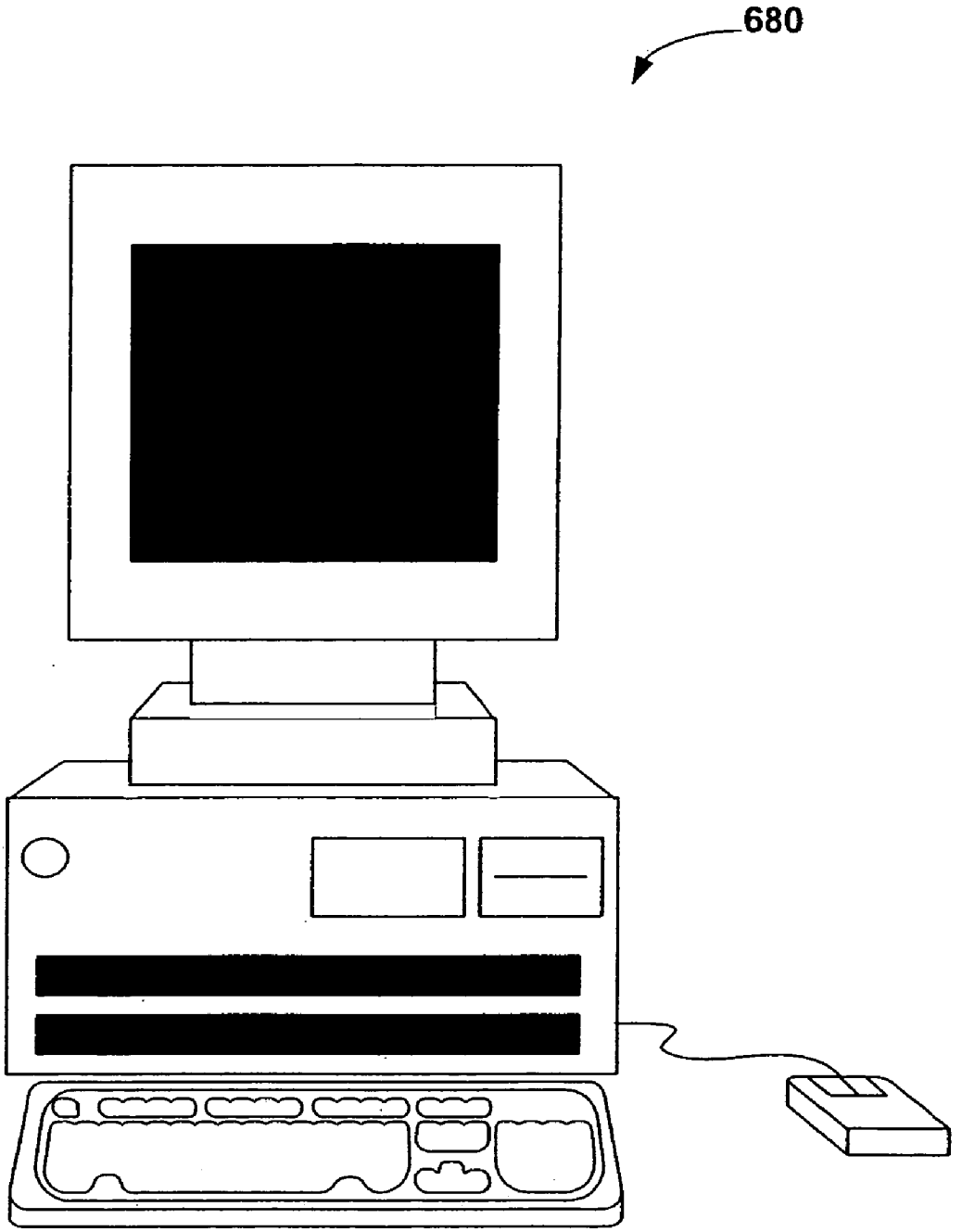
680

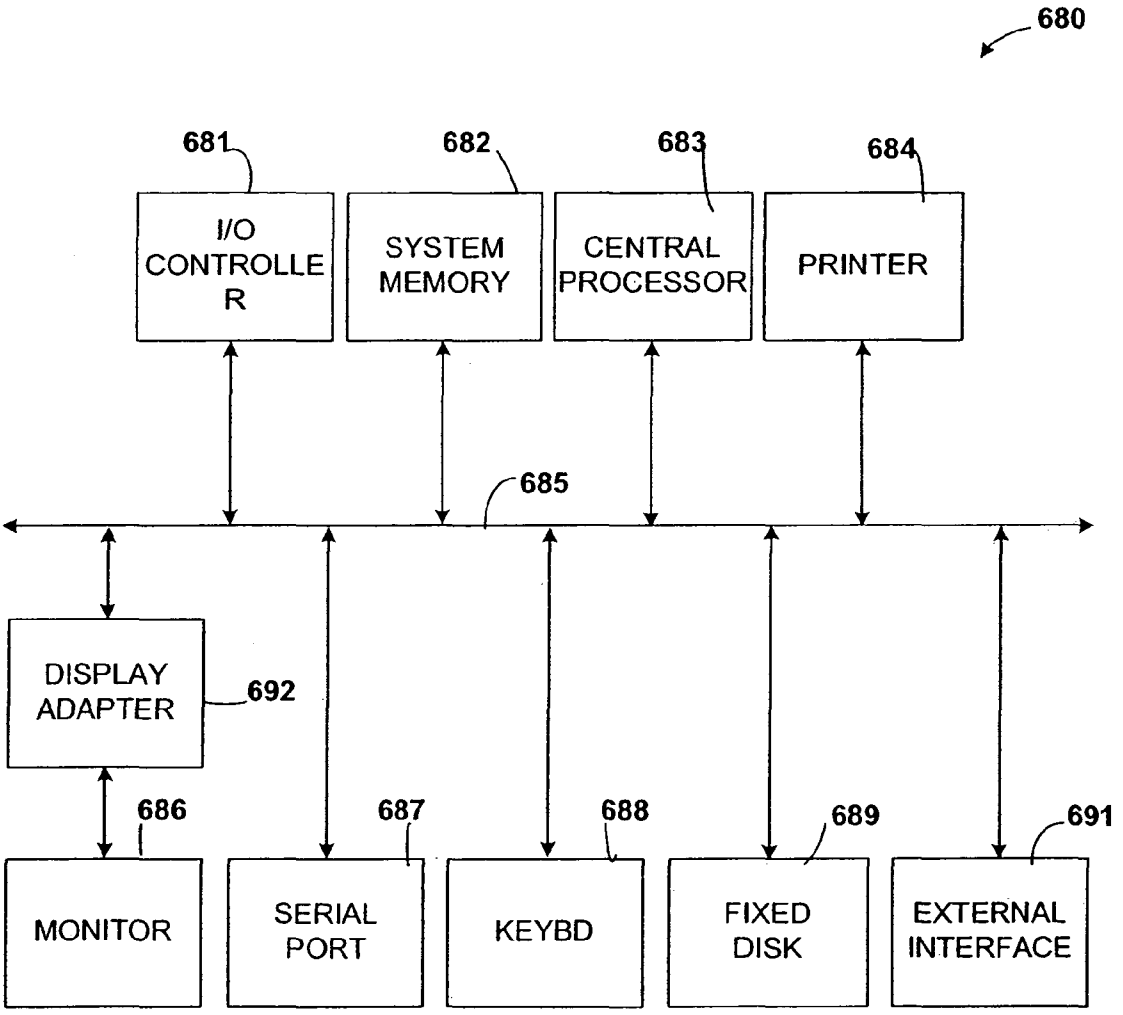
680
681
682
683
684
I/O CONTROLLER
SYSTEM MEMORY
CENTRAL PROCESSOR
PRINTER
685
DISPLAY ADAPTER
692
686
687
688
689
691
MONITOR
SERIAL PORT
KEYBD
FIXED DISK
EXTERNAL INTERFACE

FIGURE 6C

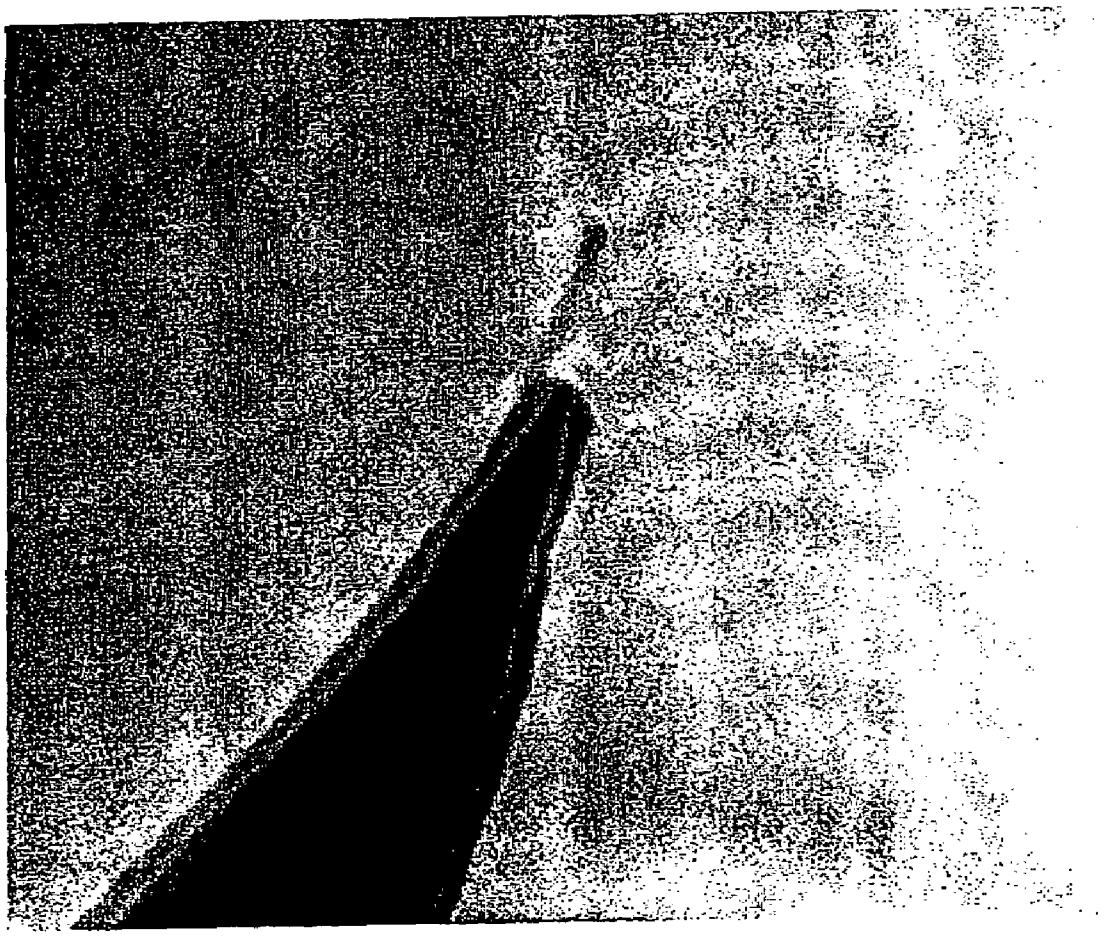

Figure 7

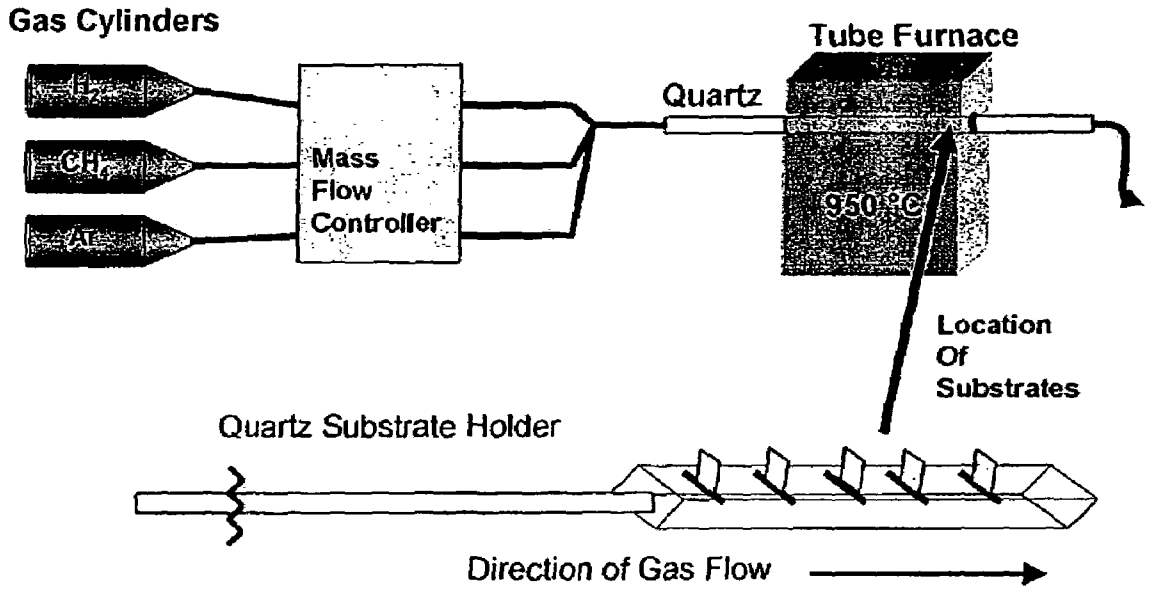
Gas Cylinders
H_2
CH_4
Ar
Mass
Flow
Controller
Quartz
Tube Furnace
950 °C
Location
Of
Substrates
Quartz Substrate Holder
Direction of Gas Flow

Figure 8

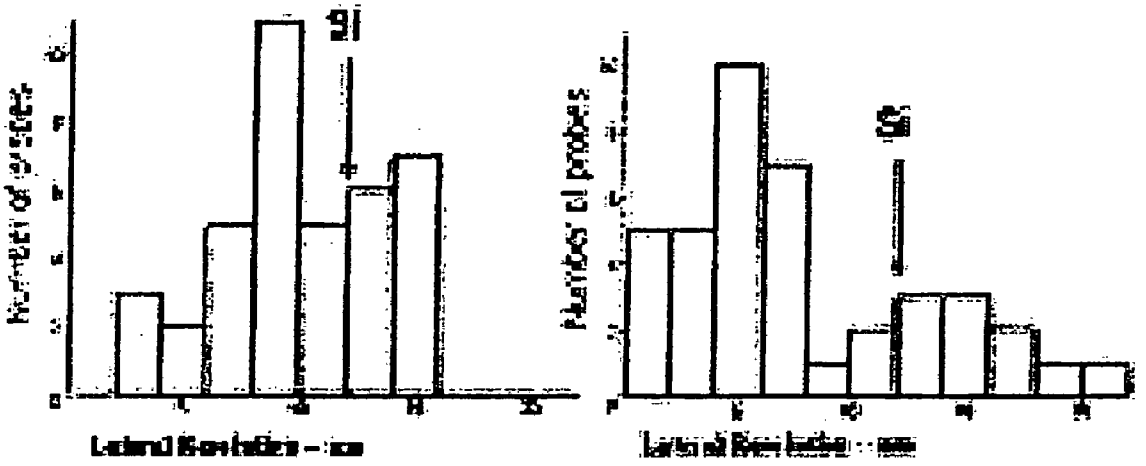

Figure 9

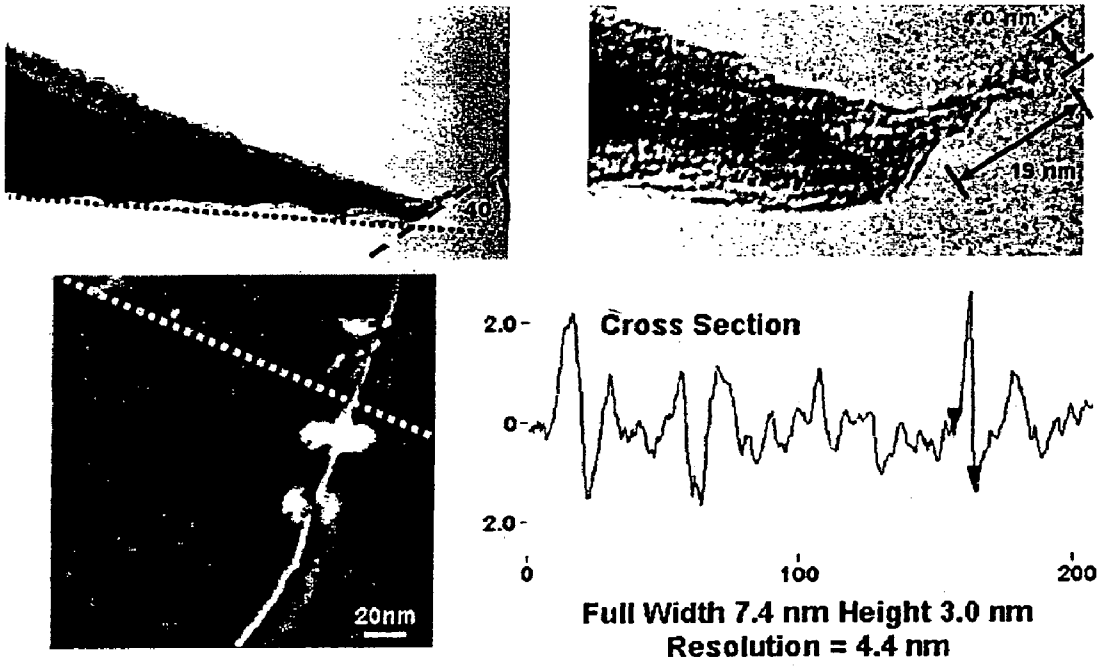
4.0 nm
19 nm
20nm
Cross Section
2.0
0
2.0
0
100
200
Full Width 7.4 nm Height 3.0 nm
Resolution = 4.4 nm

Figure 10

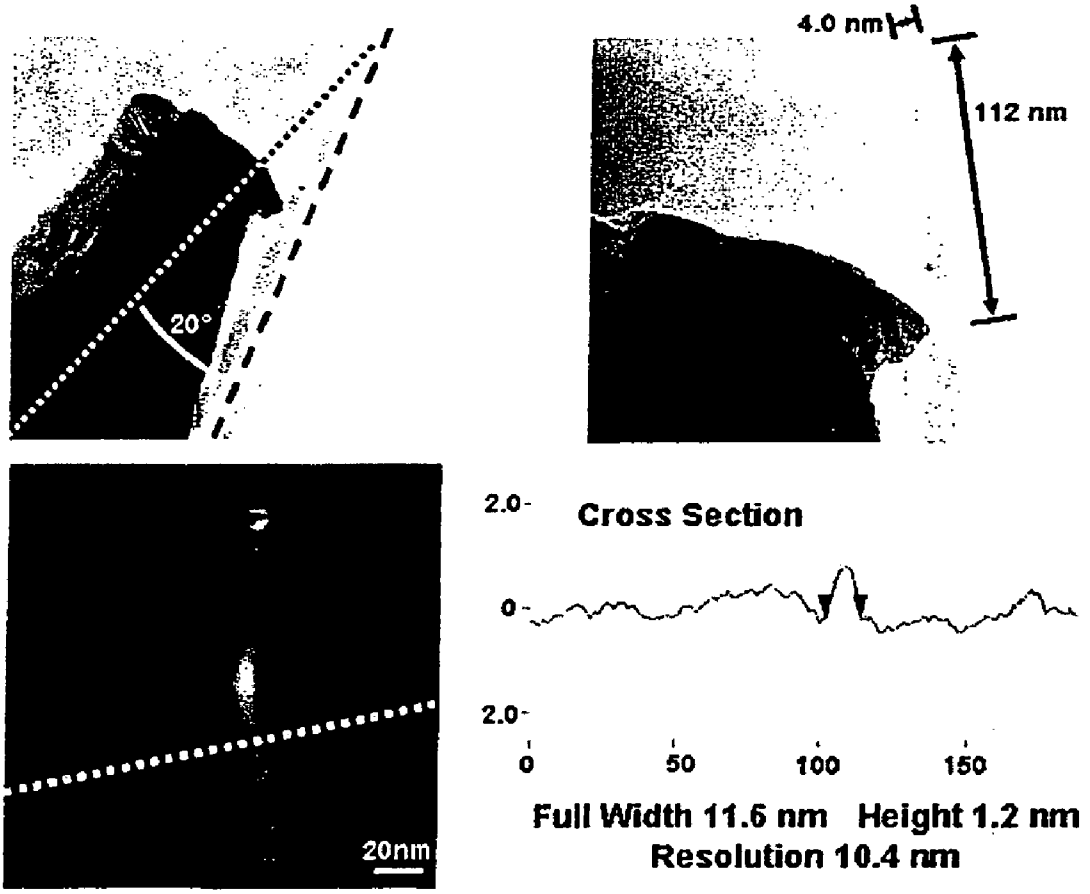
20°
4.0 nm
112 nm
20nm
2.0
Cross Section
0
2.0
0
50
100
150
Full Width 11.6 nm Height 1.2 nm
Resolution 10.4 nm

Figure 11

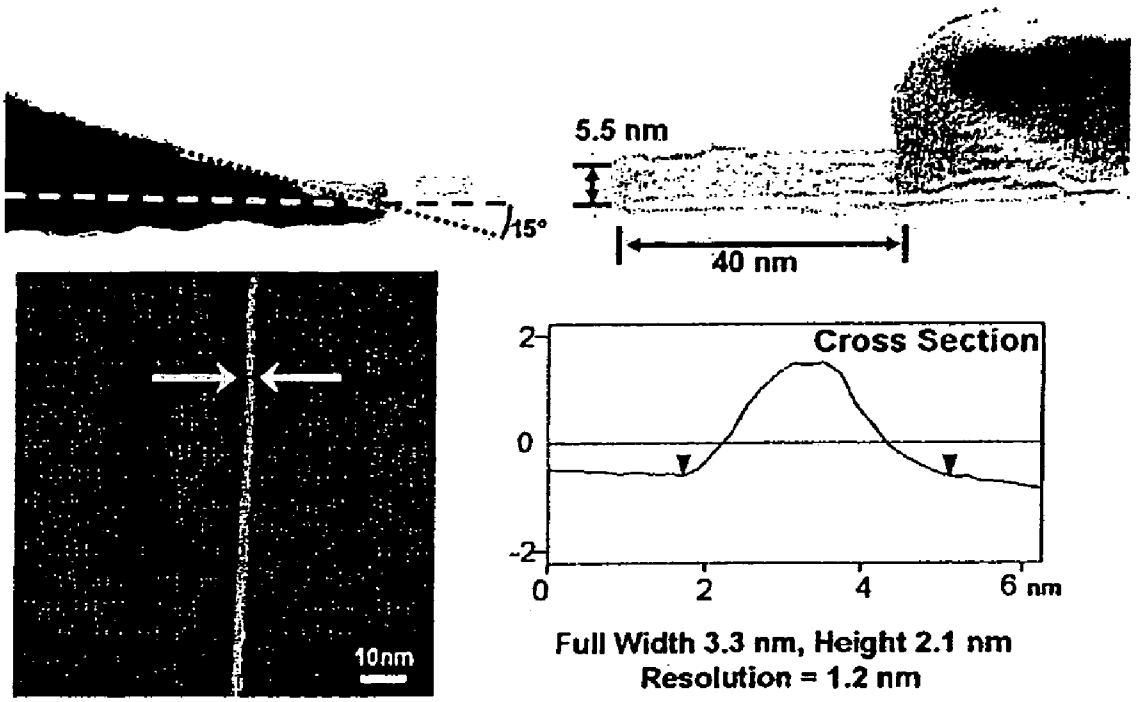
15°
5.5 nm
40 nm
10nm
Cross Section
2
0
-2
0
2
4
6 nm
Full Width 3.3 nm, Height 2.1 nm
Resolution = 1.2 nm

Figure 12

METHOD FOR MANUFACTURING SINGLE WALL CARBON NANOTUBE TIPS

CROSS-REFERENCES TO RELATED APPLICATIONS

This application claims priority to U.S. Provisional Application No. 60/542,757 filed on Feb. 6, 2004, Caltech Ref. No.: CIT-4039, which is hereby incorporated by reference herein in its entirety for all purposes.

STATEMENT AS TO RIGHTS TO INVENTIONS MADE UNDER FEDERALLY SPONSORED RESEARCH OR DEVELOPMENT

N/A

BACKGROUND OF THE INVENTION

The present invention relates generally to manufacture of materials such as nano-sized structures. More particularly, the present invention provides a method and structure for fabricating a nanotube based structure comprising an electrical shortening technique and mechanical forming technique to manufacture carbon based nanotube structures having a desired length. Merely by way of example, the invention has been applied to an atomic force microscope, but it would be recognized that the invention has a much broader range of applicability. For example, the invention can be applied to fluorescent atomic force microscope, commonly called FANSOM, other instrumentation, electronic devices, biological devices, and others.

Over the years, significant development of different types of microscopy has occurred. As merely an example, visible light optical microscopy using far field optics including lenses and light evolved from a simple compound microscope that is capable of resolving sizes of about 200 nanometers and greater. Examples of samples that are capable of being viewed using far field optics include biological cells and tissues, and others, which are often, bulk in nature. The resolving ability of such far field optical microscopy is generally limited by the diffraction of light. The diffraction limit for optical resolution has been stretched somewhat for far field imaging of very specific samples to perhaps 150 nanometers using confocal microscopes and other, related, approaches. Accordingly, atomic force microscopes ("AFM") and scanning optical microscopes including near field scanning optical microscopes were developed. The AFM and near field scanning optical microscopy ("ANSOM") have been developed to overcome certain limitations of far field optics. The AFM and near field scanning microscopes have also found many applications in biology, chemistry, physics, and materials science.

Near field scanning optical microscopy allows one to take optical images with resolutions below the diffraction limit of light. More particularly, light propagating through a waveguide is forced through a subwavelength aperture, which is then scanned in close proximity to a sample. Such subwavelength aperture techniques create other limitations. Here, physical limitations relate to a skin depth of the metal used to coat the waveguide and various scanning artifacts, which yield resolutions of 30 to 50 nanometers, most typically 50 to 100 nanometers. Apertureless near field scanning microscopes have been proposed and demonstrated to overcome these limitations, among others. Conventional ANSOM often involves using an oscillating sharp probe, which is scanned over the sample. The probe perturbs

an incident laser beam, by introducing phase shifts in an electric field or by a periodic occlusion of the sample. Detection techniques are generally used to discriminate light scattered by near field interactions from a far field contribution. Limitations also exist with such ANSOM techniques. Such limitations include contaminated images based upon certain artifacts of the sample topography, and may include others.

A pioneering approach for achieving high resolution spectroscopic information using a scanning microscope is described in U.S. Pat. No. 6,002,471, assigned to California Institute of Technology, Pasadena, Calif., and in the name of Stephen R. Quake ("Quake"). Quake generally provides a system and method for obtaining high resolution spectroscopic information. The system generally includes a support and first optical elements for directing an optical beam at a sample, which is on the support. An optical element for collecting light emitted from the sample to reduce a background noise is also included. Other elements include a spectral dissociating apparatus, a probe, and a probe detection apparatus coupled to the probe. Although significant advances have occurred, certain limitations still exist with these conventional approaches.

Certain advances in technology have occurred with the probe design for conventional ANSOM and FANSOM designs. Such advances have relied upon single wall carbon nanotubes ("SWNTs"). Most particularly, single-wall carbon nanotubes have shown potential as high-resolution scanning microscopy probes. This includes, though is not limited to, application as high-resolution AFM imaging probes. A level of resolution possible for both single molecule imaging and force transduction in AFM is generally limited by size of the structure of the tip. Conventional silicon-based probe tips have radii of curvature of 5–15 nanometers Unfortunately, conventional silicon-based tips are often delicate, leading to substantial variations in tip shape and size even between successive images. SWNTs, on the other hand, have diameters between 1.5 and 6 nm, providing resolution comparable to molecular scale dimensions. Carbon nanotubes are also chemically and mechanically robust, with axial Young's moduli of about 1.25 TPa, resulting in a tip structure that is stable over prolonged imaging periods. SWNTs can be chemically functionalized uniquely at their very ends, permitting a broad array of applications in nanotechnology and biotechnology. Nevertheless, conventional carbon based nanotubes have limitations. That is, carbon based nanotubes are often difficult to reproducibly assemble in large quantities of high-quality single-wall nanotube AFM tips. These and other limitations are described throughout the present specification and more particularly below.

From the above, it is seen that improved high resolution scanning techniques are desired.

BRIEF SUMMARY OF THE INVENTION

The present invention relates generally to manufacture of materials such as nano-sized structures. More particularly, the present invention provides a method and structure for fabricating a nanotube based structure comprising an electrical shortening technique and mechanical forming technique to manufacture carbon based nanotube structures having a desired length. Merely by way of example, the invention has been applied to an atomic force microscope,

but it would be recognized that the invention has a much broader range of applicability. For example, the invention can be applied to fluorescent atomic force microscope, commonly called FANSOM, other instrumentation, electronic devices, biological devices, and others. Additionally, the device(s) and applications can be from a variety of different fields such as electronics, semiconductor, inorganic chemistry, organic chemistry, life sciences, petroleum, biotechnology, financial, and others.

In a specific embodiment, the present invention provides a method for fabricating carbon based nanotubes for atomic force microscope ("AFM") applications. The method includes providing an AFM tip structure, which includes a first end, a second end, and a length defined between the first end and the second end. Preferably, the second end is a free end that protrudes into free space and is free from mechanical attachment. The method also includes attaching a carbon based nanotube structure along a portion of the length of the AFM tip structure to extend a total length of the AFM structure to include the length of the AFM tip structure and a first length associated with the carbon based nanotube structure. The method includes applying an electrical bias between the AFM tip structure and a substrate (e.g., electrically grounded or other reference potential) to cause a reducing of the carbon based nanotube structure from the first length to a second length. In a preferred embodiment, the substrate can be conductive doped-silicon or oxidized doped-silicon or gold plated or otherwise made somewhat electrically conductive. The method also forces the carbon based nanotube structure in a direction parallel to the second length to reduce the second length to a third length of the carbon based nanotube structure using a pushing action along the direction parallel to the second length to cause the carbon based nanotube structure to move along a portion of the length of the AFM tip structure.

In an alternative specific embodiment, the invention provides a method for fabricating carbon based nanotubes for atomic force microscope ("AFM") applications. The method includes providing an AFM tip structure, which has a first end, a second end, and a length defined between the first end and the second end. Preferably, the second end is a free end. The method also includes providing the AFM tip structure along a first portion of a substrate comprising a plurality of carbon based nanotube structures thereon. The method includes attaching at least one of the carbon based nanotube structure from the plurality of carbon based nanotube structures from the substrate along a portion of the length of the AFM tip structure to extend a total length of the AFM structure to include the length of the AFM tip structure and a first length associated with the carbon based nanotube structure. The method provides the AFM tip structure including the carbon based nanotube structure along a second portion of the substrate and applies applying an electrical bias between the AFM tip structure and a substrate (e.g., electrically grounded or other reference potential) to cause a reducing of the carbon based nanotube structure from the first length to a second length. In a preferred embodiment, the substrate can be conductive doped-silicon or oxidized doped-silicon or gold plated or otherwise made somewhat electrically conductive. The method also provides the AFM tip structure including the carbon based nanotube structure of the second length to a third portion of the substrate. The method forces the carbon based nanotube structure in a direction parallel to the second length using the third portion of the substrate to reduce the second length to a third length of the carbon based nanotube structure using a pushing action along the direction parallel to the second length to cause the carbon based nanotube structure to move along a portion of the length of the AFM tip structure.

In yet an alternative embodiment, the invention provides a method for fabricating assembled structures. The method includes providing a tip structure, which has a first end, a second end, and a length defined between the first end and the second end. The second end is a free end. The method includes attaching a nano-sized structure along a portion of the length of the tip structure to extend a total length of the tip structure to include the length of the tip structure and a first length associated with the nano-sized structure. The method includes shortening the nano-sized structure from the first length to a second length. The method also includes pushing the nano-sized structure in a direction parallel to the second length to reduce the second length to a third length of the nano-sized structure along the direction parallel to the second length to cause the nano-sized structure to move along a portion of the length of the tip structure.

In yet an alternative specific embodiment, the present invention provides a method for assembling carbon based nanotubes. The method includes providing a tip structure, which has a first end, a second end, and a length defined between the first end and the second end. Preferably, the second end is a free end. the method includes moving the tip structure along a first region comprising a plurality of carbon based nanotube structures thereon. The method also includes attaching at least one of the carbon based nanotube structure from the plurality of carbon based nanotube structures from the first region along a portion of the length of the tip structure to extend a total length of the tip structure to include the length of the tip structure and a first length associated with the carbon based nanotube structure. The method includes moving the tip structure including the carbon based nanotube structure along a second region. The method includes applying an electrical bias between the tip structure and a substrate (e.g., electrically grounded or other substrate potential) to cause a reducing of the carbon based nanotube structure from the first length to a second length. In a preferred embodiment, the substrate can be conductive doped-silicon or oxidized doped-silicon or gold plated or otherwise made somewhat electrically conductive. A step of removing the tip structure including the attached carbon based nanotube structure is also included. The method repeats the above elements of providing a tip structure; moving the tip structure along a first region comprising a plurality of carbon based nanotube structures thereon; attaching at least one of the carbon based nanotube structure; moving the tip structure including the carbon based nanotube structure along a second region; applying an electrical bias between the tip structure and a substrate (e.g., electrically grounded or other reference potential) to cause a reducing of the carbon based nanotube structure from the first length to a second length; and removing the tip structure including the attached carbon based nanotube structure for N repetitions, whereupon N is 1 or greater or greater than 10; and repeating the above elements at a rate of M repetitions whereupon M equal to N divided by hours, whereupon M is an integer greater than three.

In a specific embodiment, the present invention provides a system for manufacturing nanotubes. The system has a member, e.g., beam. The system has a tip structure (e.g., AFM) coupled to the member. Preferably, the tip structure includes a first end, a second end, and a length defined between the first end and the second end, while the second end is a free end. A first region comprising a plurality of nanotube structures is preferably on a substrate. The first region is within a vicinity of the tip structure. At least one

of the nanotube structures from the plurality of nanotube structures from the first region is attached along a portion of the length of the tip structure to extend a total length of the tip structure to include the length of the tip structure and a first length associated with the nanotube structure. A second region within a vicinity of the tip structure including the nanotube structure is preferably on the substrate. A power source is coupled to the tip structure. The power source is adapted to apply an electrical bias between the tip structure at the end of the first length associated with the nanotube structure and the second region, which is preferably at electrical ground or other reference potential, to cause a reducing of the nanotube structure from the first length to a second length. A third region is within a vicinity of the tip structure including the nanotube structure of the second length. The nanotube structure is forced in a direction parallel to the second length using the third region to reduce the second length to a third length of the nanotube structure using a pushing action along the direction parallel to the second length to cause the carbon based nanotube structure to move along a portion of the length of the tip structure.

Numerous benefits can be achieved using the present invention over conventional techniques. As merely an example, the present invention can provide an AFM-tip structure that is sharp to allow for a tip feature size of about 1/10 of an Angstrom and less. Preferably, a smaller tip size provides for better resolution. In certain embodiments, the present invention can overcome certain limitations of silicon based nanotubes, which often wear down and break after use. In preferred embodiments, the invention provides for carbon based nanotubes that are hard and difficult to wear down. In certain embodiments, the carbon based nanotubes include a dimension ranging from about 1–6 nanometers in diameter as single walled structures. Preferably, the nanotubes can be used with various AFM modes including contact mode, tapping mode (50 to 300 kHz) while scanning at 1 Hertz, and others. The present manufacturing technique can also lead to improved throughput, efficiency, and yield. Depending upon the embodiment, one or more of these benefits may be achieved. These and other benefits are described throughout the present specification and more particularly below.

From the above, it is seen that techniques for improving ways to manufacturing probe designs for microscopes are highly desired.

BRIEF DESCRIPTION OF THE DRAWINGS

FIG. **1** is a simplified cross-sectional view diagram of a nanotube structure for an AFM probe according to an embodiment of the present invention;

FIG. **2** is a simplified flow diagram illustrating a method for manufacturing an AFM probe according to an embodiment of the present invention;

FIG. **3** is a simplified diagram illustrating a method for picking up a carbon-based nanotube according to an embodiment of the present invention;

FIG. **4** illustrates a substrate comprising a plurality of nanotubes according to an embodiment of the present invention;

FIG. **5** is a simplified diagram illustrating a method for shortening a carbon-based nanotube according to an embodiment of the present invention;

FIG. **6** is a simplified diagram illustrating a method for pushing a carbon based nanotube according to an embodiment of the present invention;

FIG. **6**A is a simplified diagram of a system for manufacturing nanotube structures according to an embodiment of the present invention;

FIG. **6**B is a simplified diagram of a computer system according to an embodiment of the present invention;

FIG. **6**C is a simplified block diagram of a computer system according to an embodiment of the present invention; and

FIGS. **7** through **12** are simplified diagram illustrating experimental results according to embodiments of the present invention

DETAILED DESCRIPTION OF THE INVENTION

The present invention relates generally to manufacture of materials such as nano-sized structures. More particularly, the present invention provides a method and structure for fabricating a nanotube based structure comprising an electrical shortening technique and mechanical forming technique to manufacture carbon based nanotube structures having a desired length. Merely by way of example, the invention has been applied to an atomic force microscope, but it would be recognized that the invention has a much broader range of applicability. For example, the invention can be applied to fluorescent atomic force microscope, commonly called FANSOM, other instrumentation, electronic devices, biological devices, and others. Additionally, the device(s) and applications can be from a variety of different fields such as electronics, semiconductor, inorganic chemistry, organic chemistry, life sciences, petroleum, biotechnology, financial, and others.

A method for manufacturing carbon based nanotubes for AFM applications according to an embodiment of the present invention may be outlined as follows:

1. Provide an AFM tip structure, which has a first end, a second end, and a length defined between the first end and the second end, e.g., a free end;
2. Provide the AFM tip structure along a first portion of a substrate comprising a plurality of carbon based nanotube structures thereon;
3. Attach at least one of the carbon based nanotube structure from the plurality of carbon based nanotube structures from the substrate along a portion of the length of the AFM tip structure to extend a total length of the AFM structure to include the length of the AFM tip structure and a first length associated with the carbon based nanotube structure;
4. Provide the AFM tip structure including the carbon based nanotube structure along a second portion of the substrate and applies applying an electrical bias between the AFM tip structure and an electrically grounded substrate at the end of the first length associated with the carbon based nanotube structure to cause a reducing of the carbon based nanotube structure from the first length to a second length. The substrate can be conductive doped-silicon or oxidized doped-silicon or gold plated or otherwise made somewhat electrically conductive in a specific embodiment;
5. Provide the AFM tip structure including the carbon based nanotube structure of the second length to a third portion of the substrate;
6. Force the carbon based nanotube structure in a direction parallel to the second length using the third portion of the substrate to reduce the second length to a third length of the carbon based nanotube structure using a pushing action along the direction parallel to the second length to

cause the carbon based nanotube structure to move along a portion of the length of the AFM tip structure; and

7. Perform other steps, as desired.

The above sequence of steps provides a method according to an embodiment of the present invention. As shown, the method uses a combination of steps including a way of forming a carbon based nanotube probe for AFM applications. Other alternatives can also be provided where steps are added, one or more steps are removed, or one or more steps are provided in a different sequence without departing from the scope of the claims herein. Additionally, the present method can be applied to other applications that are not for AFM techniques. Further details of the present method can be found throughout the present specification and more particularly below.

FIG. **1** is a simplified cross-sectional view diagram of a nanotube structure **100** for an AFM probe according to an embodiment of the present invention. This diagram is merely an example, which should not unduly limit the scope of the claims herein. One of ordinary skill in the art would recognize many variations, alternatives, and modifications. As shown, the AFM probe is characterized by a tip structure. The tip structure is often made of silicon bearing species. The silicon bearing species is from a silicon wafer. The tip structure has a pyramid-like shape that protrudes from a base to an end, as shown. The tip structure has a nanotube base structured coupled thereon. The nanotube structure includes a selected length and width. The length is often less than 200 nanometers and less or less than 100 nanometers, but can also be other dimensions depending upon the application. That is, certain application may include a length of more than 1 micron depending upon the embodiment. Preferably, the nanotube structure is from a carbon based nanotube or other like materials. Details on a method for fabricating the nanotube structure can be found throughout the present specification and more particularly below.

FIG. **2** is a simplified flow diagram illustrating a method **200** for manufacturing an AFM probe according to an embodiment of the present invention. This diagram is merely an example, which should not unduly limit the scope of the claims herein. One of ordinary skill in the art would recognize many variations, alternatives, and modifications. The present invention provides a method for fabricating carbon based nanotubes for atomic force microscope ("AFM") applications, as shown. The method includes providing (step **203**) an AFM tip structure, which includes a first end, a second end, and a length defined between the first end and the second end. Preferably, the second end is a free end that protrudes into free space and is free from mechanical attachment.

The method also includes attaching (step **205**) a carbon based nanotube structure along a portion of the length of the AFM tip structure. The combination of the AFM tip structure and nanotube structure yields a total length of the AFM structure to include the length of the AFM tip structure and a first length associated with the carbon based nanotube structure. The first length of the nanotube structure can be greater than 100 nanometers, but can also be other lengths, depending upon the embodiment.

Preferably, attachment of the nanotube structure occurs using at least attractive forces between the AFM tip structure and the nanotube structure. The attractive forces often include Van der Waal's forces, but can also include other types of forces such as covalent and the like, as well as combination of these forces. Here, a portion of the nanotube structure adheres to a portion of the AFM tip structure. Preferably, the nanotube structure is in parallel with a lengthy of the AFM tip structure, but can also be at other spatial configurations. Once the carbon nanotube has been attached, the method performs other steps, as described more fully below.

The method includes applying (step **207**) an electrical bias between the AFM tip structure and an electrically grounded substrate at the end of the first length associated with the carbon based nanotube structure to cause a reducing of the carbon based nanotube structure from the first length to a second length. Preferably, the substrate can be conductive doped-silicon or oxidized doped-silicon or gold plated or otherwise made somewhat electrically conductive. The electrical bias can cause a reducing of the carbon based nanotube structure from the first length to a second length. In a specific embodiment using carbon nanotubes, the electrical bias can range from about 3 volts to about 50 volts, although others may be used. The electrical bias can be pulsed using one or more pulses. Each of the pulses can be relatively short in duration. The duration can range from about 100 microseconds and less. Depending upon the embodiment, there can be various lengths. For example, the first length can be greater than about 200 nanometers. The second length can range from 80 to 120 nanometers, but can be others. The method finishes the length of the nanotube structure by pushing the cut length down using mechanical force, as described below.

The method also forces (step **209**) the carbon based nanotube structure in a direction parallel to the second length. The force reduces the second length to a third length of the carbon based nanotube structure using a pushing action along the direction parallel to the second length to cause the carbon based nanotube structure to move along a portion of the length of the AFM tip structure. Preferably, the third length is less than 100 nanometers, but can be at other lengths. The method forces the nanotube structure by pressing on an end of the structure. The forces are similar to those of driving a nail into a piece of wood using a hammer. The AFM tip structure can be actuated in the direction parallel to the second length.

The method includes passivating the nanotube structure, step **211**. Next, the method selectively removes (step **213**) a predetermined portion of the passivation to free a portion of the nanotube structure. Further details of these steps can be found in U.S. Ser. No. 10/783,713 filed Feb. 20, 2004, which is CIT-3851), commonly assigned, and hereby incorporated by reference for all purposes.

Depending upon the embodiment, other steps can also be performed, step **215**. The method stops, step **219**. As shown, the method uses a combination of steps including a way of forming a carbon based nanotube probe for AFM applications. Other alternatives can also be provided where steps are added, one or more steps are removed, or one or more steps are provided in a different sequence without departing from the scope of the claims herein. Additionally, the present method can be applied to other applications that are not for AFM techniques. Further details of the present method can be found throughout the present specification and more particularly below.

FIG. **3** is a simplified diagram illustrating a method **300** for picking up a carbon-based nanotube according to an embodiment of the present invention. This diagram is merely an example, which should not unduly limit the scope of the claims herein. One of ordinary skill in the art would recognize many variations, alternatives, and modifications. As shown, the method includes AFM tip structure **309**. The tip structure includes a protruding end **313** that is free. The

tip structure is coupled to arm structure **311**. The tip and arm structures are spatially disposed adjacent to a substrate including a plurality of carbon based nanotube structures, as illustrated by reference numbers **320**, **330**, **340**, and **350**. The substrate can be made using a variety of techniques including chemical vapor deposition, and the like. More particularly, the method provides the AFM tip structure along a first portion **301** of the substrate comprising the plurality of carbon based nanotube structures **305** thereon. The method includes attaching at least one **331** of the carbon based nanotube structure from the plurality of carbon based nanotube structures from the substrate along a portion **335** of the length of the AFM tip structure. The method uses attractive forces between the nanotube structure **341** and AFM tip structure **345**. The attracted nanotube structure extends a total length of the AFM structure to include the length of the AFM tip structure and a first length associated with the carbon based nanotube structure, as illustrated by reference numeral **351**. Of course, there can be other variations, modifications, and alternatives.

FIG. **4** illustrates a substrate **400** comprising a plurality of nanotubes **401**, **405** according to an embodiment of the present invention. This diagram is merely an example, which should not unduly limit the scope of the claims herein. One of ordinary skill in the art would recognize many variations, alternatives, and modifications. As shown, the plurality of nanotubes are carbon based. The nanotube structures have been grown using chemical vapor deposition techniques. Further details of these techniques can be found throughout the present specification and more particularly below.

FIG. **5** is a simplified diagram illustrating a method **500** for shortening a carbon-based nanotube according to an embodiment of the present invention. This diagram is merely an example, which should not unduly limit the scope of the claims herein. One of ordinary skill in the art would recognize many variations, alternatives, and modifications. As shown, the method includes providing an AFM tip structure **509** coupled to arm structure **505**. The arm structure is electrically connected to the AFM tip structure. The arm structure is electrically biased **501** via line **503** using a voltage pulse generator. Preferably, the method applies an electrical bias between the AFM tip structure and an electrically grounded substrate at the end of the first length associated with the carbon based nanotube structure to cause a reducing of the carbon based nanotube structure from the first length to a second length. Preferably, the substrate can be conductive doped-silicon or oxidized doped-silicon or gold plated or otherwise made somewhat electrically conductive. According to a specific embodiment, the arm structure moves the tip of the nanotube onto the conductive substrate **531**, which is maintained at a ground potential **515**. The difference in voltage causes the nanotube structure to reduce in length or ablate depending upon the embodiment.

In a specific embodiment using carbon nanotubes, the electrical bias can range from about 3 volts to about 50 volts, although others may be used. The electrical bias can be pulsed using one or more pulses. Each of the pulses can be relatively short in duration. The duration can range from about 100 micro-seconds and less. Depending upon the embodiment, there can be various lengths. For example, the first length can be greater than about 200 nanometers. The second length can range from 80 to 120 nanometers, but can be others. The method finishes the length of the nanotube structure by pushing the cut length down using mechanical force, as described below. Preferably, the force caused by pushing is parallel to the length of the nanotube structure according to a specific embodiment.

FIG. **6** is a simplified diagram illustrating a method **601**, **621**, **631** for pushing a carbon based nanotube according to an embodiment of the present invention. This diagram is merely an example, which should not unduly limit the scope of the claims herein. One of ordinary skill in the art would recognize many variations, alternatives, and modifications. As shown, the method provides the AFM tip structure **611** including the carbon based nanotube structure **613** of a second length **607** to a third portion **606** of the substrate. As shown, the nanotube structure has total length **609** along a portion of the AFM tip structure. The AFM tip structure comprises silicon bearing material **603**.

The method moves the AFM tip structure including nanotube toward the surface of the substrate, as shown by reference numeral **621**. The tip or end of the nanotube structure is normal to the surface of the substrate. Preferably, the length of the nanotube structure is also normal to the surface of the substrate. As shown via reference numeral **631**, the method forces the carbon based nanotube structure in a direction parallel to the second length using the third portion of the substrate to reduce the second length to a third length of the carbon based nanotube structure using a pushing action along the direction parallel to the second length. The pushing action causes the carbon based nanotube structure to move along a portion of the length of the AFM tip structure. The third length is defined as x_1, which is less than x. Preferably for the carbon based nanotube structure, the third length is less than 100 nanometers but can be at other dimensions, depending upon the application. Further details of the present method and system can be found throughout the present specification and more particularly below.

FIG. **6**A is a simplified diagram of a scanning system **650** according to an embodiment of the present invention. This diagram is merely an example, which should not unduly limit the scope of the claims herein. One of ordinary skill in the art would recognize many other modifications, alternatives, and variations. As shown, the present microscope system **650** includes a mobile stage **651**, which has x-y-z movement capability. The stage can be moved with a tolerance of less than 40 microns for sample positioning and when used for alignment can be moved with a tolerance of <1 nm. A sample **659** is placed on the stage. Depending upon the application, the sample can include the present substrate with a plurality of carbon nanotube structures thereon. Preferably, the sample can also be in liquids, air, inert gas environments, or in vacuum and at specific temperatures (cryogenic, room temperature, warm to extremely high temperatures), depending upon the application.

The system also includes a tapping mode atomic force microscope ("AFM") **660**. In a specific embodiment, the AFM **660** has various elements such as probe **657**, a cantilever to support the probe, which is coupled to a piezo-electric stack **654**. Such piezo-stack provides for dithering and z-motion of the cantilever. The AFM also includes a driving signal, which is coupled to control electronics **663** for signal detection and correction. Preferably, probe **657** has a pyramidal shape and the tip of the pyramid is coated with silver particles. In the present embodiment, the tip includes the nanotube structure to be pushed and/or attached thereon. The AFM also includes a laser source **653**, which is directed to the cantilever or probe. The laser source is used as a position detector, which provides photons that scatter off of the cantilever and/or probe. Such scattered photons are detected by way of photodetector **655**, which is coupled to

control electronics **663**. The AFM may be coupled to an inverted optical microscope, as shown, and further described in co-pending application Ser. No. 10/616,896 filed Jul. 9, 2003, commonly assigned, and hereby incorporated by reference herein.

Preferably, the inverted optical microscope **669** is underlying the AFM, as shown. A laser beam **667** (which in a specific embodiment is from a green HeNe **667** source) is focused on the AFM tip. The laser beam is directed from the source **667** and is adjusted by way of dichroic mirror **670** through the objective **669**, which focuses the beam onto the AFM tip. As the sample is scanned in the x-y plane (which is also in the plane of the paper), fluorescent photons emit from the sample. Such photons pass through the objective through a bandpass filter **671** and are detected by an avalanche photodiode **673**. A gated photon counter **675**, which is coupled to the photodiode, processes the detected photons. The gated photon counter is triggered by a measured height of an AFM cantilever. A signal acquisition and processing apparatus **665** (which includes a microprocessor device and has been used as a "controller" and/or "main controller" herein without unduly limiting the scope of the term processing apparatus), which may be coupled to the counter through a common bus, oversees and performs operation and processing of information. The system also has a display **677**, which can be a computer, coupled to the signal acquisition and processing apparatus. The signal acquisition and processing apparatus is also coupled to the control electronics of the AFM as shown. Of course, there can be other modifications, alternatives, and variations. Further details of the present system can be found in the Quake patent, which has been previously described. Other details of the present system and methods are provided throughout the specification and more particularly below.

FIG. **6**B is a simplified diagram of a computer system **680** that is used to oversee the system of FIG. **6**A according to an embodiment of the present invention. This diagram is merely an example, which should not unduly limit the scope of the claims herein. One of ordinary skill in the art would recognize many other modifications, alternatives, and variations. As shown, the computer system includes display device, display screen, cabinet, keyboard, scanner and mouse. Mouse and keyboard are representative "user input devices." Mouse includes buttons for selection of buttons on a graphical user interface device. Other examples of user input devices are a touch screen, light pen, track ball, data glove, microphone, and so forth.

The system is merely representative of but one type of system for embodying the present invention. It will be readily apparent to one of ordinary skill in the art that many system types and configurations are suitable for use in conjunction with the present invention. In a preferred embodiment, computer system **680** includes a Pentium™ class based computer, running Windows™ NT operating system by Microsoft Corporation or Linux based systems from a variety of sources. However, the system is easily adapted to other operating systems and architectures by those of ordinary skill in the art without departing from the scope of the present invention. As noted, mouse can have one or more buttons such as buttons. Cabinet houses familiar computer components such as disk drives, a processor, storage device, etc. Storage devices include, but are not limited to, disk drives, magnetic tape, solid-state memory, bubble memory, etc. Cabinet can include additional hardware such as input/output (I/O) interface cards for connecting computer system to external devices external storage, other computers or additional peripherals, which are further described below.

FIG. **6**C is a more detailed diagram of hardware elements in the computer system according to an embodiment of the present invention. This diagram is merely an example, which should not unduly limit the scope of the claims herein. One of ordinary skill in the art would recognize many other modifications, alternatives, and variations. As shown, basic subsystems are included in computer system **680**. In specific embodiments, the subsystems are interconnected via a system bus **685**. Additional subsystems such as a printer **684**, keyboard **688**, fixed disk **689**, monitor **686**, which is coupled to display adapter **692**, and others are shown. Peripherals and input/output (I/O) devices, which couple to I/O controller **681**, can be connected to the computer system by any number of means known in the art, such as serial port **687**. For example, serial port **687** can be used to connect the computer system to a modem **691**, which in turn connects to a wide area network such as the Internet, a mouse input device, or a scanner. The interconnection via system bus allows central processor **683** to communicate with each subsystem and to control the execution of instructions from system memory **682** or the fixed disk **689**, as well as the exchange of information between subsystems. Other arrangements of subsystems and interconnections are readily achievable by those of ordinary skill in the art. System memory, and the fixed disk are examples of tangible media for storage of computer programs, other types of tangible media include floppy disks, removable hard disks, optical storage media such as CD-ROMS and bar codes, and semiconductor memories such as flash memory, read-only-memories (ROM), and battery backed memory.

Although the above has been illustrated in terms of specific hardware features, it would be recognized that many variations, alternatives, and modifications can exist. For example, any of the hardware features can be further combined, or even separated. The features can also be implemented, in part, through software or a combination of hardware and software. The hardware and software can be further integrated or less integrated depending upon the application. Further details of certain experimental results can be found throughout the present specification and more particularly below.

Experiments:

To prove the principles and operation of the present invention, we performed various experiments. These experiments have been used to demonstrate the invention and certain benefits associated with the invention. As experiments, they are merely examples, which should not unduly limit the scope of the claims herein. One of ordinary skill in the art would recognize many variations, alternatives, and modifications. Details of these experiments are provided below.

As noted, single-wall carbon nanotubes have shown great potential as high-resolution AFM imaging probes. The level of resolution possible for both single molecule imaging and force transduction in AFM is ultimately limited by the structure of the tip. Commercially available silicon probe tips have radii of curvature of 5–15 nm. The finest commercially available Si tips are very delicate, leading to substantial variation in tip shape and size even between successive images. SWNTs, on the other hand, have diameters between 1.5 and 6 nm, providing resolution comparable to molecular scale dimensions. Carbon nanotubes are chemically and mechanically robust, with axial Young's moduli of about

1.25 TPa, resulting in a tip structure that is stable over prolonged imaging periods. Finally, SWNTs can be chemically functionalized uniquely at their very ends, permitting a broad array of applications in nanotechnology and biotechnology. Nevertheless, it is difficult to reproducibly assemble large quantities of high-quality single-wall nanotube AFM tips. To fully realize the promise of these probes for high-resolution AFM, a better physical understanding is needed of how the geometry of the mounted SWNT on its AFM tip support affects image quality.

Successfully fabricating a probe suitable for AFM imaging in air involves several steps: attaching the nanotube to a silicon AFM tip, shortening it sufficiently to enable high resolution imaging, characterizing its quality, and storing it for later use. Building upon previously reported techniques, we have conducted a comparative survey of fabrication methods to produce a protocol that routinely results in high quality probes. The quality of the AFM images taken with the resultant probes, along with the frequency and ease of success, was used to distinguish between the several approaches studied. In addition, SEM and TEM images of hundreds of nanotube AFM probes were used to evaluate the efficacy of different probe attachment and shortening techniques and to improve the accuracy of our interpretation of AFM imaging and force calibration results. For the first time, the AFM resolution achieved when imaging with nanotube probes was directly correlated to TEM images taken of these same probes. This allowed us to carry out a rigorous examination of nanotube morphology and its influence on image resolution and quality, by directly correlating nanotube geometry, as determined with TEM imaging, with their performance as AFM probes. As a result, we gained significant new insights that are important for research groups performing AFM imaging with SWNT tips.

We summarized the results of these studies and describe a procedure that enables consistently successful nanotube probe fabrication. The lateral resolution of these probes when used to image 3 nm diameter SWNTs was typically less than 4 mm, and in one case, 5 Å. This is an improvement by a factor of 4 over the best resolution reported to date using a SWNT probe, which is 2.0 mm. The systematic correlation of TEM images of SWNT probes with the effective lateral resolution obtained when using these probes for topographical imaging indicates that approximately one-third of the probes demonstrated resolution smaller than the diameter of the nanotube probe itself when imaging nanotubes on a smooth substrate. For example, we have measured 1.2 nm lateral resolution from a SWNT scanning probe that was 5.5 nm in diameter.

These TEM-AFM correlations provide experimental evidence consistent with previous mechanical modeling carried out by Snow, et al. Additionally, whereas previous investigations have shown nanotube buckling to be an elastic process, we have found that under some circumstances, a SWNT probe can buckle inelastically, resulting in probe damage and corresponding image artifacts.

Finally, we have found (L. A. Wade, I. R. Shapiro, Z. Ma, S. R. Quake, C. P. Collier, *Nano Lett.* 2004, 4, 725–731.) that nanotubes picked up by AFM tips can have larger diameters (by about a factor of 2) than the diameters of nanotubes imaged on the surface of the growth substrate, as determined from height measurements with a conventional AFM tip. A better understanding of this discrepancy is needed for optimizing the yield and reproducibility of nanotube probe fabrication. The AFM image resolution statistics we report here underscore the variability between probes fabricated by different methods.

Digital Instruments BioScope and Multimode atomic force microscopes were used with Nanoscope IV controllers for this work. Transmission electron microscopy was performed with a Phillips EM430, and scanning electron microscopy was performed with a Hitachi 4100.

We compared several methods for attaching nanotubes to silicon AFM tips: manual assembly, direct growth, and pickup. Smalley's group reported in Dai, H.; Hafner, J. H.; Rinzler, A. G.; Colbert, D. T.; Smalley, R. E. *Nature* 1996, 384, 147, the first example of the use of carbon nanotubes as AFM tips in 1996. Manual assembly of AFM probes was found to be relatively simple, although the nanotubes had to be large enough to be seen and manipulated under an optical microscope, and thus did not yield high-resolution probes. While direct growth offers the potential for parallel fabrication of SWNT AFM probes, we found that the yield was quite low. We also determined that the rate-limiting step in probe fabrication was the nanotube shortening step rather than attachment. Therefore, we focused our efforts on the pick-up technique for nanotube attachment, as shown in FIG. **7**.

The pick-up technique, developed by Lieber et al., and reported in Hafner, J. H.; Cheung, C. L.; Lieber, C. M. J. Am. Chem. Soc. 1999, 121, 9750, is an efficient and consistent method for mounting SWNTs in the proper orientation. When SWNTs are grown on a flat substrate, a small percentage of the tubes are oriented vertically, and can be picked up when the AFM tip scans across the surface in tapping mode. The nanotube binds to the side of the pyramidal AFM tip via attractive van der Waals forces, and usually remains attached firmly enough that it can be repeatedly pressed into and scanned across the substrate surface. We found that it was important to reduce the field of view (e.g., from 10 μm to 10 nm) or retract the tip as soon as a nanotube was successfully picked up in order to minimize the probability of picking up additional nanotubes. Multiple attached tubes or bundles can lead to AFM image artifacts.

It is also important to note that the ambient humidity appears to affect the efficiency of the pickup method. We found it nearly impossible to pick up nanotubes from a substrate under high humidity conditions. Enclosing the AFM in a glovebag under a flow of dry nitrogen for about 30 min rejuvenated the process. We speculate that an increase in the relative humidity makes it more difficult to pick up nanotubes for two main reasons. First, at higher humidity values, it is harder to overcome capillary forces due to the build up of a surface layer of water on the growth substrate. More force is necessary to pry a prone nanotube off the surface due to increased adhesion. Second, increasing water build up on the tip decreases the attractive interactions of the nanotube to the silicon surface of the AFM tip during pick up. It is known that the van der Waals interactions at the nanotube-AFM tip interface are not strong enough to keep the tube attached to the tip in liquid water. Nanoscopic condensation of water between the AFM tip and the growth substrate at high relative humidity may have an analogous effect on the success rate for picking up a nanotube.

SWNTs were grown via chemical vapor deposition (CVD) on 4 mm to 8 mm square, 500 μm thick p-doped Si wafers. Four different methods were used to coat the substrates with iron catalyst for growing nanotubes suitable for pickup: spin coating a solution of Fe(NO3)3*9H2O in isopropyl alcohol, thermal evaporation of iron onto the substrate, electron beam evaporation of iron onto the substrate, and incubation with ferritin. We achieved the most uniform deposition of small (1–2 nm) catalytic sites with high spatial density by using ferritin-derived iron nanopar-

ticles, prepared as described by Dai and co-workers in Li, Y.; Kim, J. W.; Zhang, Y.; Rolandi, M.; Wang, D.; Dai, H. J. Phys. Chem. B 2001, 105, 11424.

CVD growth was performed in a 22 mm inner diameter Lindberg/Blue M quartz tube furnace with a single heating zone 312 mm long, as shown in FIG. **8**. Five wafers are positioned 12.5 mm apart in a specially designed quartz holder, oriented vertically and with the catalyst-coated side facing away from the direction of the incoming gas. A significant advantage of this holder is that it enables up to three small substrates to be mounted side-by-side in each slot for parallel comparison of growth results under nearly identical temperature and gas flow conditions.

We found that growth was faster (5 μm long nanotubes within one minute) and the distribution of tube lengths increased when the catalyst-coated surface was facing away from the incoming gas flow. We speculate that this is due to increased turbulence of the gas flow at the catalyst coated side after passing over the edges of the substrate. Induced turbulence should minimize the role of diffusion-limited growth relative to nucleation rate in the growth kinetics, but at the expense of uniform growth. These growth procedures generate SWNTs on the substrate with diameters ranging from 1.6 to 3.0 nm, and lengths between 100 nm and 5 μm, as imaged with AFM and SEM.

The distribution of tube diameters varied with the size of the catalytic sites. For example, we found that spin coating many drops of dilute solution of the iron nitrate catalyst to give a high density of small catalytic sites gave a slightly broader tube diameter distribution than did ferritin. In contrast, depositing a few drops of higher density iron solutions yielded broad size distributions and larger average tube diameters. Based on AFM analyses of these substrates, it appears that the larger tube diameters resulted from larger catalytic sites on the substrate. No MWNTs have been observed on these substrates.

The long-term stability of pickup substrates appears to vary depending on how they were prepared. Ferritin and ferric nitrate substrates appear to be substantially less effective for pickup attachment after 4 to 6 months. We hypothesize that this is due to the relatively weak mechanical attachment of the catalytic site to the substrate. Over time, vertically oriented tubes that are attached to loosely bound catalytic sites apparently physisorb onto the substrate. Enclosing the AFM in a glovebag with a flow of dry nitrogen for about 30 min substantially enhanced pickup with these older substrates. In contrast, substrates that had the catalytic sites deposited by molecular beam epitaxy (MBE) have demonstrated reliable pickup of nanotubes with an AFM tip over several years without special care.

The diameters of the picked up tubes measured with TEM were typically between 4 and 6 nm. In comparison, the diameters of nanotubes lying horizontally on the substrate, determined by AFM height measurements, were only 2–3 nm. We have ruled out TEM and AFM calibration errors as the cause of this discrepancy. We have also ruled out compression of the imaged nanotubes by the AFM tip, which would result in a decreased apparent diameter. Deformation of the horizontal nanotubes due to van der Waals forces has also been modeled using realistic molecular dynamics simulations based on quantum mechanical calculations, and found insufficient to explain this discrepancy. It appears that this disparity is real and not just an artifact due to tube distortion or measurement error.

This indicates a strong preference for larger diameter tubes to be picked up by silicon AFM probes. There are two plausible explanations for this disparity. One possibility is that larger diameter nanotubes have a higher probability of remaining vertically oriented on the growth substrate over time than smaller diameter tubes. Only the population of smaller diameter nanotubes adsorbed to the growth substrate can be imaged by AFM. Hence, AFM images will be biased toward this part of the distribution of nanotube diameters.

Alternatively, this disparity may be explained by the binding energy of the nanotube to the AFM cantilever tip relative to the binding energy of the nanotube to the substrate. Once a SWNT has been picked up by a scanning AFM tip, there are two kinds of motions that impose stress on the system. The AFM cantilever has a net motion parallel to the substrate. During pick-up, typical horizontal velocities are on the order of 30 000 nm/s. This motion imposes three kinds of stress on the system: shear, bending, and tension. In addition, the cantilever has a rapid vertical oscillation, typically 70–250 kHz, with an amplitude of 40–50 nm, that imposes additional bending and tension stresses.

The mechanical stresses imposed by the cantilever motion on a nanotube attached on one end to the AFM tip, and on the other end to the surface of the growth substrate, will result in one of two outcomes: the nanotube either slips off the cantilever tip and remains attached to the substrate, or the nanotube separates from the substrate interface and is "picked up". The discriminator between these two outcomes is the binding energy at the attachment site of the nanotube to the silicon tip relative to that of its attachment to the substrate. These binding energies will depend on many factors that are virtually impossible to characterize fully, such as the relative lengths of the nanotube adsorbed onto the tip versus the substrate, as well as details of the chemical, physical, and mechanical interactions between the nanotube and these surfaces during scanning in tapping mode. It is known, however, that binding energy scales with the tube diameter, which can be determined directly from both AFM and TEM images.

The strength of nanotube attachment can be approximated as being linearly proportional to the nanotube diameter using the thin-walled cylinder approximation. At the attachment site with the AFM cantilever tip, the nanotube can be considered fixed until the binding energy is exceeded at this interface by the imposed stresses. This binding force increases linearly with diameter, but at a rate 1.6 times faster for tubes greater than 2.7 nm diameter than it does for smaller diameter nanotubes. The increased binding energy for nanotubes greater than 2.7 nm could result in larger diameter nanotubes being preferentially picked up. The relative adhesion strength of the catalytic particle to the tube versus the substrate could also have a significant influence on the diameters of the tubes that are picked up.

As seen in FIG. **7**, more than 100 nm of a nanotube typically protrudes from the end of the AFM tip after pickup. High-resolution imaging is not possible with such a long nanotube tip due to thermal fluctuations and bending. Pickup SWNT tips were shortened by a combination of push shortening, an approach developed by Hafner and Lieber as reported in an unpublished communication, March 2002, and electrical pulse etching An HP 8114A pulse generator was used in combination with a Digital Instruments signal access module for all of our pulse shortening experiments.

Push shortening is done by incrementally decreasing the tip-sample separation distance during successive force calibrations to push the nanotube up along the side of an AFM tip. This process requires a picked-up tube of very specific length. Tubes longer than 100 nm tend to buckle inelastically during this process, after which they cannot be shortened by

further pushing. Push shortening is superior to pulse etching when further shortening nanotubes less than 100 nm long in very small increments.

We obtain similar results for electrical pulse etching with native oxide coated p-doped silicon, 300 nm thick thermally grown oxide-coated p-doped silicon, and gold-plated silicon substrates. This finding indicates that the entire probe fabrication procedure can be carried out on a single unpatterned, doped-silicon substrate. Thermally grown oxide substrates typically required higher voltages to successfully pulse-shorten than did either native oxide or gold-coated silicon substrates.

Using electrical pulse shortening and push shortening in combination on the same tip relaxes the constraints for obtaining high-quality probes from the nanotube growth substrate and increases yield. Long tubes can be coarsely shortened with electrical pulses until their lengths are less than 100 nm. Push shortening can then be used for finer control in adjusting the probe length.

We frequently found that electrostatic forces would strip nanotubes off the AFM tips when they had been stored in a nonconductive container. An aluminum box with a narrow strip of double-sided tape or a conductive Gel-Pak container both seemed to solve this problem. Prior to use of conductive boxes for nanotube tip storage, we were unsuccessful in TEM imaging the attached nanotube probes.

To characterize the effective resolution of our SWNT probes, we imaged nanotubes resting flat on the silicon growth substrate, using a scanning field of view of 100–350 nm. We define resolution as the full width of the imaged tube measured at the noise floor, minus the measured tube height. While nanotubes are convenient samples for determining resolution, they are not infinitely rigid. Dekker's group has shown in Postma, H. W. C.; Sellmeijer, A.; Dekker, C. *AdV. Mater.* 2000, 12, 1299, that the apparent height of a nanotube measured by tapping mode imaging can decrease substantially at high oscillation amplitudes, even with conventional silicon tips. We have observed similar effects with nanotube probes. For this study, the oscillation amplitude was maintained close enough to its freely oscillating value in air to limit this effect to be within 10% of the true nanotube height.

FIG. **9** shows histograms of the lateral resolutions obtained with SWNT probes fabricated using a growth substrate coated with ferric nitrate catalyst versus those fabricated using ferritin as the catalyst. The variation in nanotube probe performance was greater than we expected based on previous reports. Leiber et al. had examined the image quality of different nanotube types (MWNTs and SWNTs) in Cheung, C. L.; Hafner J. H.; Lieber, C.; M. *Proc. Natl. Acad. Sci. U.S.A.* 2000, 97, 3809. In contrast, we compared 39 SWNTs made from the same iron nitrate-coated substrate and 40 from a ferritin substrate. The wide range in resolution found, between the two different kinds of substrate (ferritin vs iron nitrate), as well as from the same substrate, was surprising and underscores the importance of specific nanotube characteristics in determining the maximum achievable resolution.

There is a clear shift in the distribution toward higher resolution probes when ferritin was used as the catalyst, consistent with a narrower catalyst size distribution. It is not clear how much technique improvements rather than the switch to ferritin from ferric nitrate coated substrates played in the comparative distribution. Most of the latter tips were fabricated using ferritin substrates. By that time, we were more careful to reduce the field of view immediately after pick-up to minimize bundle formation. This could explain why there are fewer 10–15 nm resolution tips. However, it is clear that significantly more probes with resolution better than 5 nm were fabricated using ferritin substrates.

Nearly 100 probes were imaged by TEM to characterize the efficacy of different fabrication techniques. Of these, fourteen SWNT probes imaged by TEM had previously been used for tapping-mode topographic imaging. Table 1 presents a summary of probe characteristics determined by TEMAFM correlations for the fourteen SWNT probes. Entries in bold correspond to probes that demonstrated lateral resolution less than the actual nanotube probe diameter.

Image quality is a function of many factors including: tube diameter and length, contact angle, number of nanotubes extending past the silicon tip, thermal noise, and contamination. These factors can lead to substantial variability in resolution. By correlating probe structure and orientation seen in the TEM images with topographic imaging performance, we can provide experimental evidence consistent with previous mechanical modeling carried out by Snow et al., who have shown that lateral tip-sample forces can bend single-wall nanotubes or cause snap-to-contact behavior when the tubes exceed either a critical length or a critical angle relative to the substrate surface normal. These effects introduce a significant degree of broadening and the appearance of image artifacts.

If the nanotube is presented to the sample surface at an angle deviating from the surface normal by more than ~30°, poor resolution and obvious image artifacts result due to tip-sample forces having a significant component perpendicular to the nanotube axis. For example, FIG. **10** shows a 19 nm long, 4 nm diameter nanotube projecting from the probe tip at an angle of 40°. This probe produced an image that contained a positive height "shadowing" artifact approximately 10 nm in width parallel to each sample nanotube. This artifact resulted from the nonideal orientation of the probe. Additionally, the TEM image showed that the nanotube is buckled near the silicon tip. Previous reports have described reversible elastic buckling of the nanotube, which did not have a serious impact on image quality. Our TEM correlations indicate, however, that buckling can, under some circumstances, be inelastic, resulting in irreversible structural changes. This structural defect results in an effectively lower stiffness for the probe, which we believe is responsible for the decreased resolution and imaging artifacts we observe (shadowing features). Similar artifacts were seen with SWNT ropes (multiple SWNTs bundled together) for the same reason; the layered structure of a bundle of nanotubes attached to the AFM tip results in stiffness variation along the probe length.

In a preferred embodiment, the SWNT probes have aspect ratios less than ~10 to be adequate for imaging purposes. FIG. **11** shows a 4 nm diameter nanotube protruding 112 nm from the end of the AFM tip, but at an angle deviating from the surface normal by less than 20°. The resulting lateral resolution was still 2.5 times the probe tube diameter. This broadening of the image is due in small part to thermal vibrations. However, mechanical modeling studies have indicated that for a nanotube of this geometry, the root-mean-squared thermal vibrations of the end of the tube should be less than 2 Å. Nanotube bending due to lateral tip-sample forces is most likely the principal contribution to the degraded resolution.

Images taken with high quality nanotube probes show no sign of artifacts. These probes all had the nanotubes oriented on the tip at angles close to the substrate surface normal (within 10–20°) and had protrusion lengths ≦40 nm. By directly measuring the nanotube width from each TEM

image and comparing that to the obtained AFM resolution, we have determined the average ratio of AFM resolution to tube diameter for SWNT probes in this class to be 1.17. This is a reasonable value, given that thermal vibrations and bending of the nanotube will always slightly increase its effective imaging diameter.

In about ⅓ of the high quality nanotube probes made from the ferritin substrate, as shown in FIG. **12**, it was found that the effective lateral resolution was significantly better than the nanotube probe diameter measured directly with TEM. FIG. **12** shows a nanotube probe 5.5 nm in diameter that demonstrated a lateral resolution of 1.2 nm, just 22% of the diameter of the nanotube. It is likely that this enhanced resolution occurs when the nanotube contacts the substrate being imaged with either an asperity or at a specific angle such that only an edge of the nanotube is in contact with the substrate. Imaging a small object with an asperity or an open edge of the tube could lead to the high resolutions observed. Molecular dynamics simulations of surface-nanotube and nanotube-nanotube interactions indicate that other phenomena may also be important, including elastic deformation of the sample nanotube relative to the probe nanotube.

In conclusion, we have combined elements from several previously reported techniques for producing nanotube tips suitable for AFM imaging dry samples that significantly reduce the time of manufacture while improving reproducibility and performance. Feedback from SEM and TEM images of the nanotube probes was used to directly evaluate the effectiveness of the different techniques employed for each of the steps in the fabrication procedure. The optimal process involves the following six steps. (1) Grow nanotubes from ferritin-derived iron nanoparticles on conductive silicon substrates coated only with its native oxide. (2) Pick up a SWNT by imaging the substrate with a 10 μm field of view in tapping mode. (3) Quickly reduce the field of view to approximately 10 nm so that additional tubes are not picked up. (4) Shorten the tube to an appropriate length for imaging without changing substrates using a combination of electrical pulse and push shortening techniques. (5) Image a 100–500 nm region of the substrate to characterize the probe quality. (6) Store shortened nanotube probe in a conductive box.

By growing nanotubes directly on a conductive p-doped silicon substrate with either a native oxide layer or a thermally grown oxide surface layer, it is possible to pick up, shorten, and test the probe resolution without having to switch samples. This proved to be a significant timesaving optimization. We have found that the resulting nanotube growths (diameter and length) are very similar for all of the investigated catalyst deposition techniques if the spatial density and diameters of catalytic sites are similar. Rates of production have typically reached one probe per hour for several consecutive hours. On exceptional days, the rate can be as high as several per hour. This success has been duplicated with incoming group members.

Overall, we have found AFM image quality to be consistently and significantly better with nanotube tips than with the best silicon AFM tips. Correlations of TEM images of SWNT probes with the effective lateral resolution obtained when using these probes for topographical imaging with AFM indicate that approximately one-third of the probes demonstrate resolution better than the diameter of the nanotube probe itself when imaging nanotubes on a smooth substrate. The methodology described here has resulted in a sufficiently high level of productivity to enable development of single-molecule probes and sensors using functionalized nanotube tips, and has proven capable of fabricating AFM probes with the highest resolution reported to date.

It is also understood that the examples and embodiments described herein are for illustrative purposes only and that various modifications or changes in light thereof will be suggested to persons skilled in the art and are to be included within the spirit and purview of this application and scope of the appended claims.

What is claimed is:

1. A method for fabricating carbon based nanotubes for scanning probe microscopy, the method comprising:

providing an AFM tip structure, the AFM tip structure including a first end, a second end, and a length defined between the first end and the second end, the second end being a free end;

attaching a carbon based nanotube structure along a portion of the length of the AFM tip structure to extend a total length of the AFM structure to include the length of the AFM tip structure and a first length associated with the carbon based nanotube structure;

applying an electrical bias between the AFM tip structure and a substrate to cause a reducing of the carbon based nanotube structure from the first length to a second length, and

forcing the carbon based nanotube structure in a direction parallel to the second length to reduce the second length to a third length of the carbon based nanotube structure using a pushing action along the direction parallel to the second length to cause the carbon based nanotube structure to move along a portion of the length of the AFM tip structure.

2. The method of claim **1** wherein the electrical bias ranges from about 3 volts to about 50 volts.

3. The method of claim **1** wherein the substrate can be selected from a conductive doped-silicon or oxidized doped-silicon or gold plated or otherwise made somewhat electrically conductive material.

4. The method of claim **1** wherein the electrical bias comprises one or more pulsed voltages.

5. The method of claim **1** wherein the electrical bias comprises one or more pulsed voltages of less than 100 micro-seconds.

6. The method of claim **1** wherein the first length is greater than 2 micrometers.

7. The method of claim **1** wherein the second length ranges from about 10 nanometers to about 200 nanometers.

8. The method of claim **1** wherein the attaching comprises using attractive forces between a portion of the AFM tip structure and a portion of the carbon based nanotube structure.

9. The method of claim **1** wherein the attaching comprises moving the AFM tip structure along a portion of substrate comprising a plurality of carbon based nanotube structures to attract one of the carbon based nanotube structures onto the portion of the AFM tip structure.

10. The method of claim **1** wherein the electrical bias ablates a portion of the carbon based nanotube structure.

11. The method of claim **1** wherein the pushing action is provided using mechanical force on an end of the carbon based nanotube structure in the direction parallel to the second length.

12. The method of claim **1** wherein the electrical bias is applied to the AFM tip structure.

13. The method of claim **1** wherein the third length is less than about 100 microns.

14. The method of claim 1 wherein the attaching comprises substantially Vanderwaals forces between a portion of the AFM tip structure and a portion of the carbon based nanotube structure.

15. A method for fabricating carbon based nanotubes for scanning probe microscopy including atomic force microscope ("AFM") applications, the method comprising:

providing an AFM tip structure, the AFM tip structure including a first end, a second end, and a length defined between the first end and the second end, the second end being a free end;

providing the AFM tip structure along a first portion of a substrate comprising a plurality of carbon based nanotube structures thereon;

attaching at least one of the carbon based nanotube structure from the plurality of carbon based nanotube structures from the substrate along a portion of the length of the AFM tip structure to extend a total length of the AFM structure to include the length of the AFM tip structure and a first length associated with the carbon based nanotube structure;

providing the AFM tip structure including the carbon based nanotube structure along a second portion of the substrate;

applying an electrical bias between the AFM tip structure and an electrically grounded substrate to cause a reducing of the carbon based nanotube structure from the first length to a second length;

providing the AFM tip structure including the carbon based nanotube structure of the second length to a third portion of the substrate, and

forcing the carbon based nanotube structure in a direction parallel to the second length using the third portion of the substrate to reduce the second length to a third length of the carbon based nanotube structure using a pushing action along the direction parallel to the second length to cause the carbon based nanotube structure to move along a portion of the length of the AFM tip structure.

16. The method of claim 15 wherein the substrate is a single substrate being maintained in a stationary position.

17. The method of claim 15 wherein the first portion, the second portion, and the third portion of the substrate are different spatial locations.

18. The method of claim 15 wherein the forcing causes the carbon based nanotube structure to slide along the portion of the length of the AFM tip structure.

19. The method of claim 15 wherein the attaching is provided using Vanderwaals forces between a portion of the AFM tip structure and a portion of the carbon based nanotube structure.

20. A method for fabricating assembled structures, the method comprising:

providing a tip structure, the tip structure including a first end, a second end, and a length defined between the first end and the second end, the second end being a free end;

attaching a nano-sized structure along a portion of the length of the tip structure to extend a total length of the tip structure to include the length of the tip structure and a first length associated with the nano-sized structure;

shortening the nano-sized structure from the first length to a second length, and

pushing the nano-sized structure in a direction parallel to the second length to reduce the second length to a third length of the nano-sized structure along the direction parallel to the second length to cause the nano-sized structure to move along a portion of the length of the tip structure.

21. The method of claim 19 wherein the pushing causes a portion of the nano-sized structure to slide along the portion of the length of the tip structure.

22. A method for manufacturing carbon based nanotubes, the method comprising:

providing a tip structure, the tip structure including a first end, a second end, and a length defined between the first end and the second end, the second end being a free end;

moving the tip structure along a first region comprising a plurality of carbon based nanotube structures thereon;

attaching at least one of the carbon based nanotube structure from the plurality of carbon based nanotube structures from the first region along a portion of the length of the tip structure to extend a total length of the tip structure to include the length of the tip structure and a first length associated with the carbon based nanotube structure;

moving the tip structure including the carbon based nanotube structure along a second region;

applying an electrical bias between the tip structure at the end of the first length associated with the carbon based nanotube structure and an electrically grounded substrate to cause a reducing of the carbon based nanotube structure from the first length to a second length;

moving the tip structure including the carbon based nanotube structure of the second length to a third region of the substrate;

forcing the carbon based nanotube structure in a direction parallel to the second length using the third region to reduce the second length to a third length of the carbon based nanotube structure using a pushing action along the direction parallel to the second length to cause the carbon based nanotube structure to move along a portion of the length of the tip structure;

removing the tip structure including the attached carbon based nanotube structure;

repeating the above elements of providing a tip structure; moving the tip structure along a first region comprising a plurality of carbon based nanotube structures thereon; attaching at least one of the carbon based nanotube structure; moving the tip structure including the carbon based nanotube structure along a second region; applying an electrical bias between the tip structure at the end of the first length associated with the carbon based nanotube structure and the electrically grounded substrate to cause a reducing of the carbon based nanotube structure from the first length to a second length; moving the tip structure including the carbon based nanotube structure of the second length to a third region of the substrate; forcing the carbon based nanotube structure in a direction parallel to the second length using the third region to reduce the second length; and removing the tip structure including the attached carbon based nanotube structure for N repetitions, whereupon N is an integer greater than 1, and

repeating the above elements at a rate of M repetitions whereupon M equal to N divided by hours, whereupon M is an integer greater than three.

23. The method of claim 22 wherein M is an integer greater than five.

24. The method of claim 22 wherein M is an integer greater than ten.

25. The method of claim 22 wherein the tip structure comprises an AFM tip structure.

26. The method of claim 22 wherein the first region, the second region, and the third region are provided on a single substrate, the single substrate being maintained on a stage.

27. The method of claim 26 wherein the stage is moved relative to the tip structure.

28. The method of claim 26 wherein the tip structure is moved relative to the stage.

29. A method for assembling carbon based nanotubes, the method comprising:

providing a tip structure, the tip structure including a first end, a second end, and a length defined between the first end and the second end, the second end being a free end;

moving the tip structure along a first region comprising a plurality of carbon based nanotube structures thereon;

attaching at least one of the carbon based nanotube structure from the plurality of carbon based nanotube structures from the first region along a portion of the length of the tip structure to extend a total length of the tip structure to include the length of the tip structure and a first length associated with the carbon based nanotube structure;

moving the tip structure including the carbon based nanotube structure along a second region;

applying an electrical bias between the tip structure at the end of the first length associated with the carbon based nanotube structure and the second region to cause a reducing of the carbon based nanotube structure from the first length to a second length;

removing the tip structure including the attached carbon based nanotube structure;

repeating the above elements of providing a tip structure; moving the tip structure along a first region comprising a plurality of carbon based nanotube structures thereon; attaching at least one of the carbon based nanotube structure; moving the tip structure including the carbon based nanotube structure along a second region; applying an electrical bias between the tip structure at the end of the first length associated with the carbon based nanotube structure and the second region to cause a reducing of the carbon based nanotube structure from the first length to a second length.

30. The method of claim 29 wherein the substrate is electrically grounded.

31. A system for manufacturing nanotubes, the system comprising:

a member;

a tip structure coupled to the member, the tip structure including a first end, a second end, and a length defined between the first end and the second end, the second end being a free end;

a first region comprising a plurality of nanotube structures, the first region being within a vicinity of the tip structure, at least one of the nanotube structures from the plurality of nanotube structures from the first region being attached along a portion of the length of the tip structure to extend a total length of the tip structure to include the length of the tip structure and a first length associated with the nanotube structure;

a second region within a vicinity of the tip structure including the nanotube structure;

a power source coupled to the tip structure, the power source being adapted to apply an electrical bias between the tip structure at the end of the first length associated with the nanotube structure and the second region to cause a reducing of the nanotube structure from the first length to a second length;

a third region within a vicinity of the tip structure including the nanotube structure of the second length;

whereupon the nanotube structure is forced in a direction parallel to the second length using the third region to reduce the second length to a third length of the nanotube structure using a pushing action along the direction parallel to the second length to cause the nanotube structure to move along a portion of the length of the tip structure.

* * * * *

Appendix H

US patent 7,514,214
Selective functionalization of carbon nanotube tips allowing fabrication of new classes of nanoscale sensing and manipulation tools

This patent was awarded for a method of functionalizing nanotube tips (the manufacture of which was described in US patent 7,211,795). Specifically, it describes methods for coating the nanotube tipped probe to preclude non-specific binding or other chemical interactions with the probe and then chemically functionalizing the end of the nanotube tipped probe with a carboxyl group or amine group so that further chemical modification can be made. This unique chemical functionalization of the nanotube tip can be used to attach a single protein or a specific group of proteins. Such a modified tip can then be used for sensing chemical motilities or triggering a variety of reactions with extraordinary spatial resolution and high chemical specificity. In addition such tips can be used to pattern a substrate for future sensing or chemical logic use. This work builds on that reported in Chapter 4. This patent was issued on April 7, 2009 to Lawrence Wade, Ian Shapiro, C. Patrick Collier, Maria J. Esplandiu, Vern Bittner, Jr., and Konstantinos Giapis. These six inventors made equal contributions to this invention.

US007514214B2

(12) **United States Patent**
Wade et al.

(10) **Patent No.: US 7,514,214 B2**
(45) **Date of Patent: Apr. 7, 2009**

(54) **SELECTIVE FUNCTIONALIZATION OF CARBON NANOTUBE TIPS ALLOWING FABRICATION OF NEW CLASSES OF NANOSCALE SENSING AND MANIPULATION TOOLS**

(75) Inventors: **Lawrence A. Wade**, La Canada-Flintridge, CA (US); **Ian R. Shapiro**, Pasadena, CA (US); **Charles Patrick Collier**, San Marino, CA (US); **Maria J. Esplandiu**, Los Angeles, CA (US); **Vern Garrett Bittner, Jr.**, Pasadena, CA (US); **Konstantinos P. Giapis**, Pasadena, CA (US)

(73) Assignee: **California Institute of Technology**, Pasadena, CA (US)

(*) Notice: Subject to any disclaimer, the term of this patent is extended or adjusted under 35 U.S.C. 154(b) by 1038 days.

(21) Appl. No.: **10/783,713**

(22) Filed: **Feb. 20, 2004**

(65) **Prior Publication Data**

US 2005/0191427 A1 Sep. 1, 2005

Related U.S. Application Data

(60) Provisional application No. 60/499,210, filed on Feb. 21, 2003.

(51) **Int. Cl.**
C12Q 1/68 (2006.01)

(52) **U.S. Cl.** **435/6**; 250/309

(58) **Field of Classification Search** 250/309; 435/6, 5

See application file for complete search history.

(56) **References Cited**

U.S. PATENT DOCUMENTS

5,824,470 A * 10/1998 Baldeschwieler et al. 435/6
2002/0122766 A1 9/2002 Lieber et al.

FOREIGN PATENT DOCUMENTS

WO WO 98/05920 2/1998

OTHER PUBLICATIONS

Carano et al., A Glutathione Amperometric Biosensor Based on an Amphiphilic Fullerence Redox Mediator Immobilised within an Amphiphillic Polypyrrole Film, S.J. Mat. Chem. 12, 1996-2000 (2002).

(Continued)

Primary Examiner—Nikita Wells
Assistant Examiner—Johnnie L Smith, II
(74) *Attorney, Agent, or Firm*—Williams, Morgan & Amerson, P.C.

(57) **ABSTRACT**

Embodiments in accordance with the present invention relate to techniques for the growth and attachment of single wall carbon nanotubes (SWNT), facilitating their use as robust and well-characterized tools for AFM imaging and other applications. In accordance with one embodiment, SWNTs attached to an AFM tip can function as a structural scaffold for nanoscale device fabrication on a scanning probe. Such a probe can trigger, with nanometer precision, specific biochemical reactions or conformational changes in biological systems. The consequences of such triggering can be observed in real time by single-molecule fluorescence, electrical, and/or AFM sensing. Specific embodiments in accordance with the present invention utilize sensing and manipulation of individual molecules with carbon nanotubes, coupled with single-molecule fluorescence imaging, to allow observation of spectroscopic signals in response to mechanically induced molecular changes. Biological macromolecules such as proteins or DNA can be attached to nanotubes to create highly specific single-molecule probes for investigations of intermolecular dynamics, for assembling hybrid biological and nanoscale materials, or for developing molecular electronics. In one example, electrical wiring of single redox enzymes to carbon nanotube scanning probes allows observation and electrochemical control over single enzymatic reactions by monitoring fluorescence from a redox-active cofactor or the formation of fluorescent products. Enzymes "nanowired" to the tips of carbon nanotubes in accordance with embodiments of the present invention, may enable extremely sensitive probing of biological stimulus-response with high spatial resolution, including product-induced signal transduction.

16 Claims, 17 Drawing Sheets

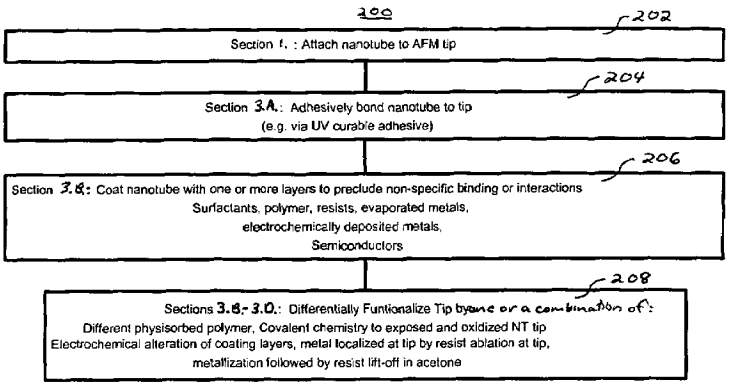

OTHER PUBLICATIONS

Carbon Nanobube Tips for Atomic Force Microscopy, http://cmliris.harvard.edu/html_natalya/research/probes/tip.html, printed Feb. 17, 2004.

Chen et al., Noncovalent Sidewall Functionalization of Single-Walled Carbon Nanotubes for Protein Immobilization, J. Am. Chem. Soc., 123, pp. 3838-3839, (2001).

Cui et al.. Nanowire Nanosensors for Highly Sensitive and Selective Detection of Biological and Chemical Species, Science, vol. 293, pp. 1289-1292, (2001).

Shim et al., Functionalization of Carbon Nanotubes for Biocompatibility and Bio-Molecular Recognition, Nano Lett. 2, No. 4, pp. 285-288 (2002).

Wade et al., Correlating AFM Probe Morphology to Image Resolution for Single-Wall Carbon Nanotube Tips, Nano Letters, 0, No. 0, A-G.

Wong et al., Carbon Nanotube Tips: High-Resolution Probers for Imaging Biological Systems, J. Am. Chem. Soc., 120, pp. 603-604 (1998).

Wong et al., Covalently Functionalized Nanotubes as Nanometer Probes for Chemistry and Biology, Nature, 294, pp. 52-55 (1998).

Wong et al., Covalently-Functionalized Single-Walled Carbon Nanotube Probe Tips for Chemical Force Microscopy, J. Am. Chem. Soc. 120, pp. 8557-8558, (1998).

Xiao et al., Plugging into Enzymes, Nanowiring of Redox Enzymes by a Gold Nanoparticle, Science, 299, 1877-1881, (2003).

Shim et al. Functionalization of Carbon Nanotubes for Biocompatibility and Biomolecular Recognition, Nano Lett, Jan. 2002, vol. 2, No. 4, pp. 285-288.

* cited by examiner

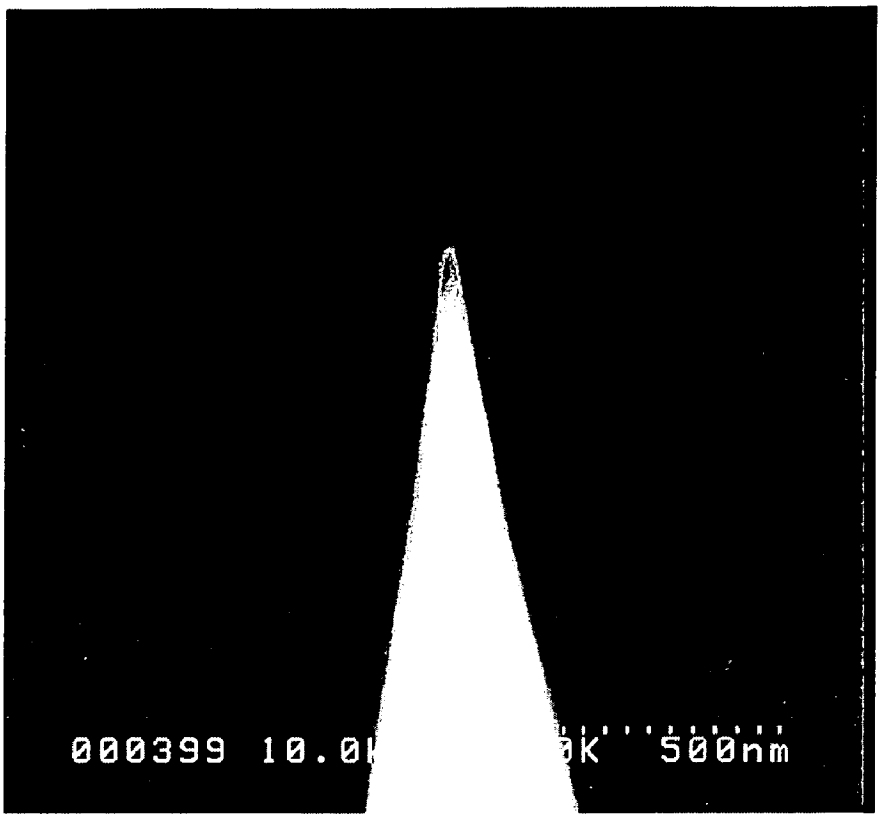

Figure 1A

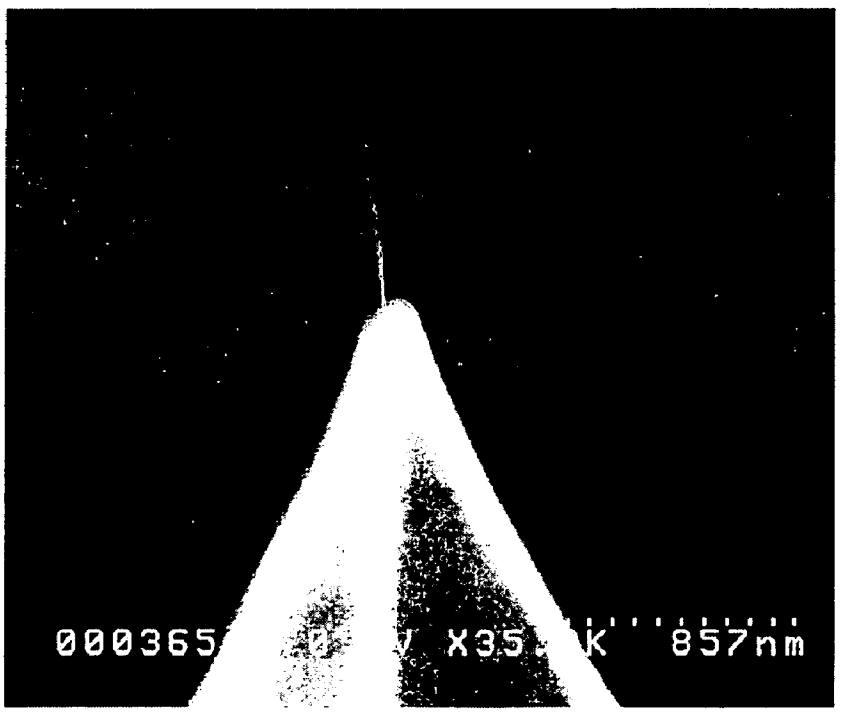

Figure 1B

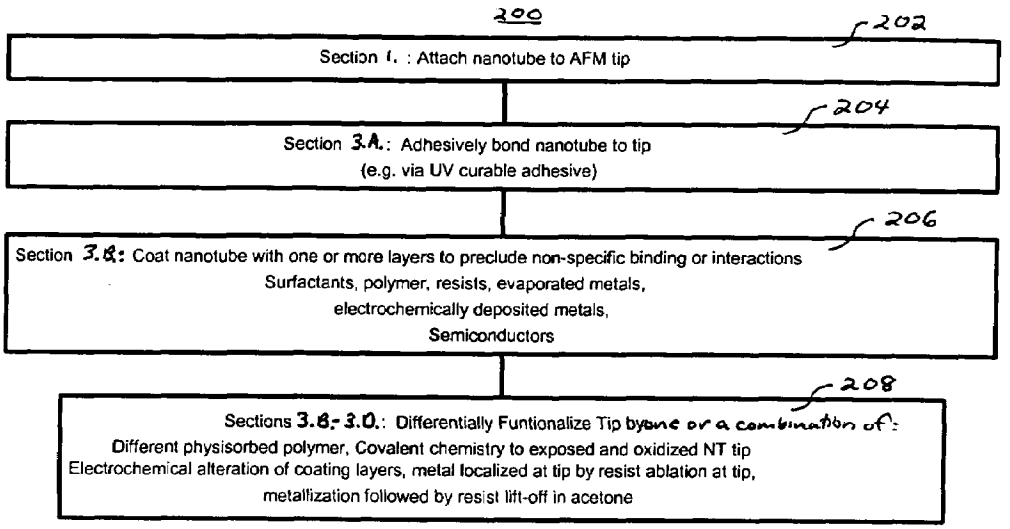

Figure 2

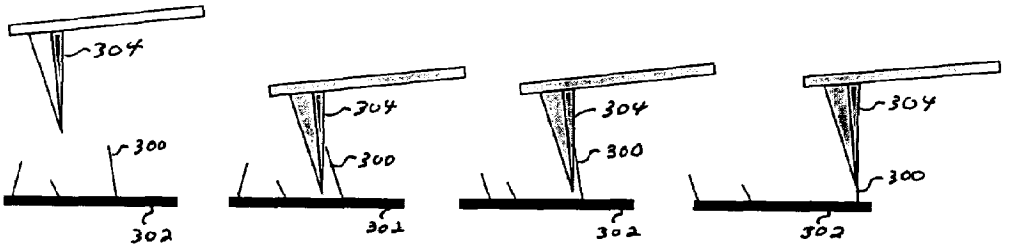

Figure 3

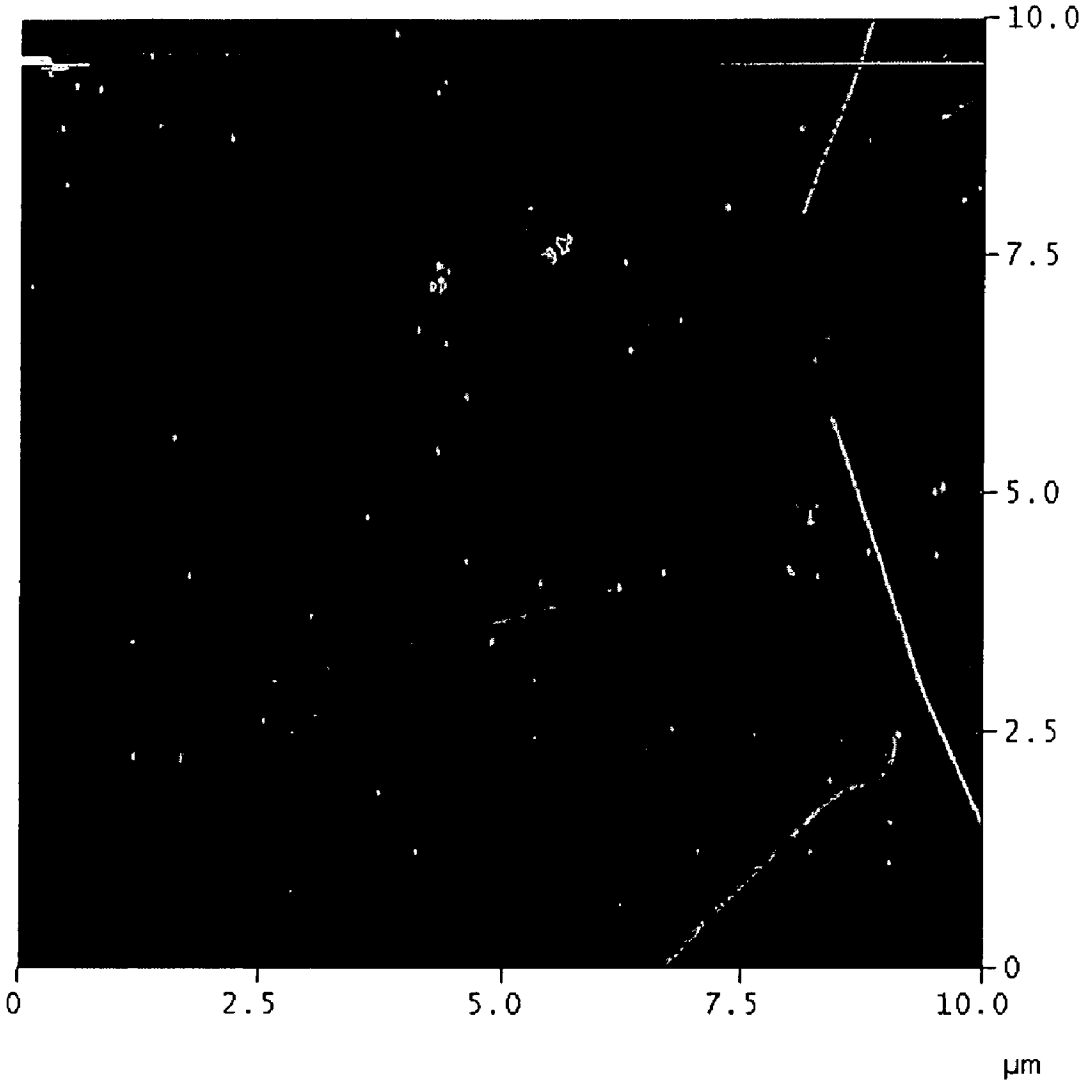

Figure 4

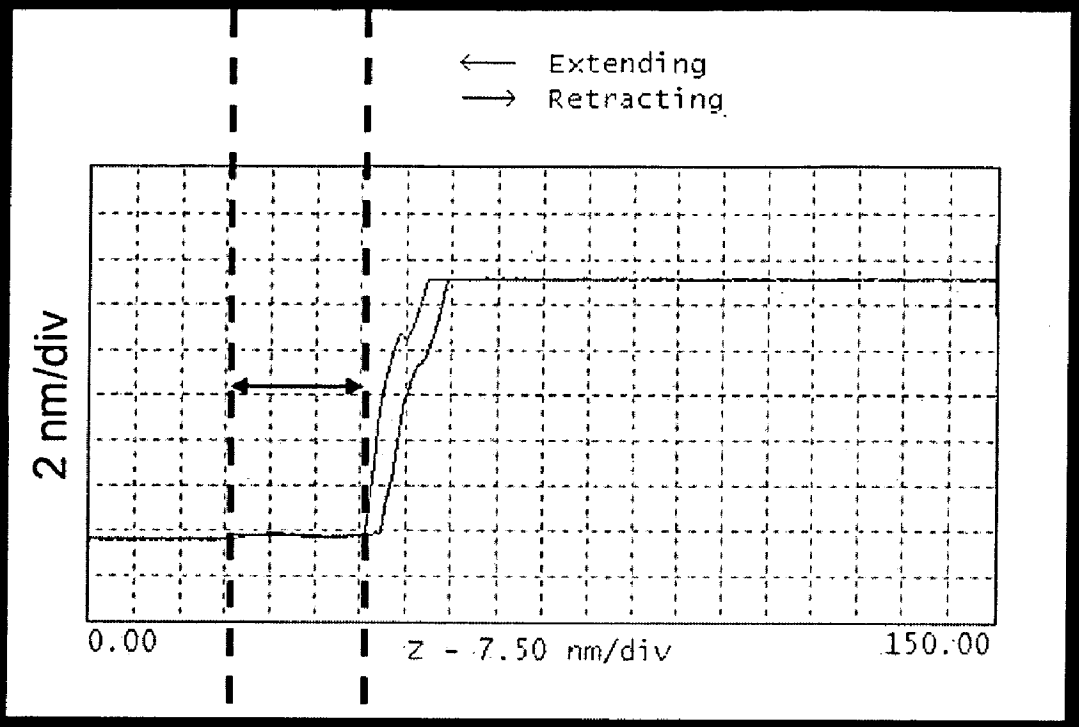

Figure 5A

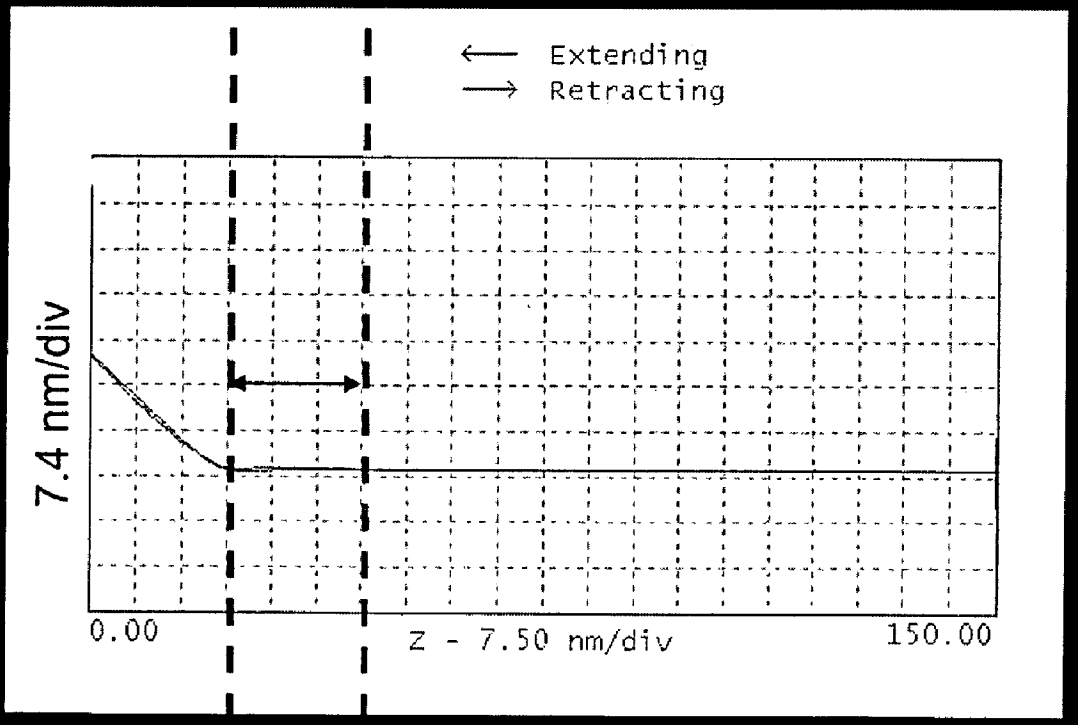

Figure 5B

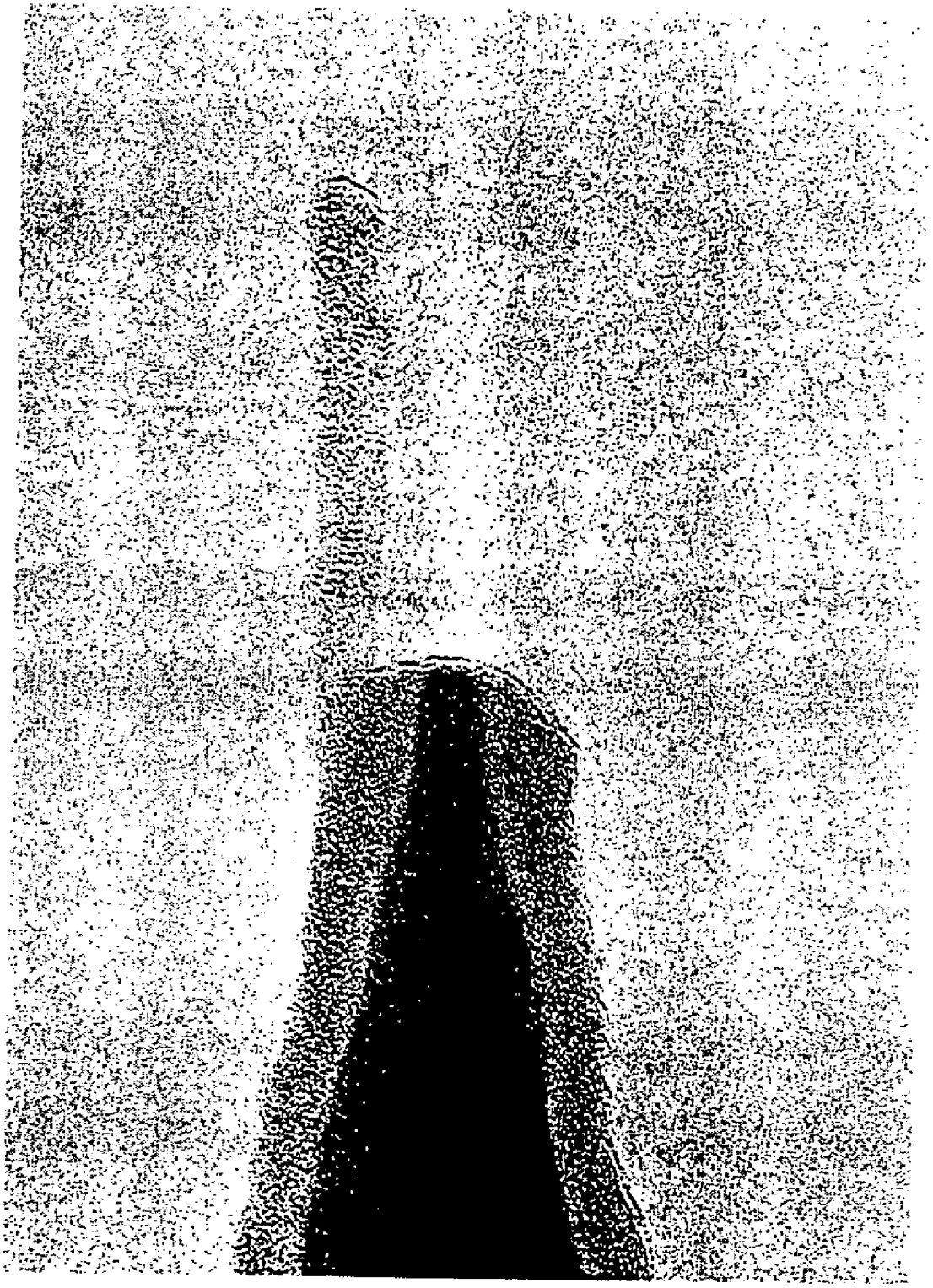

Figure 6

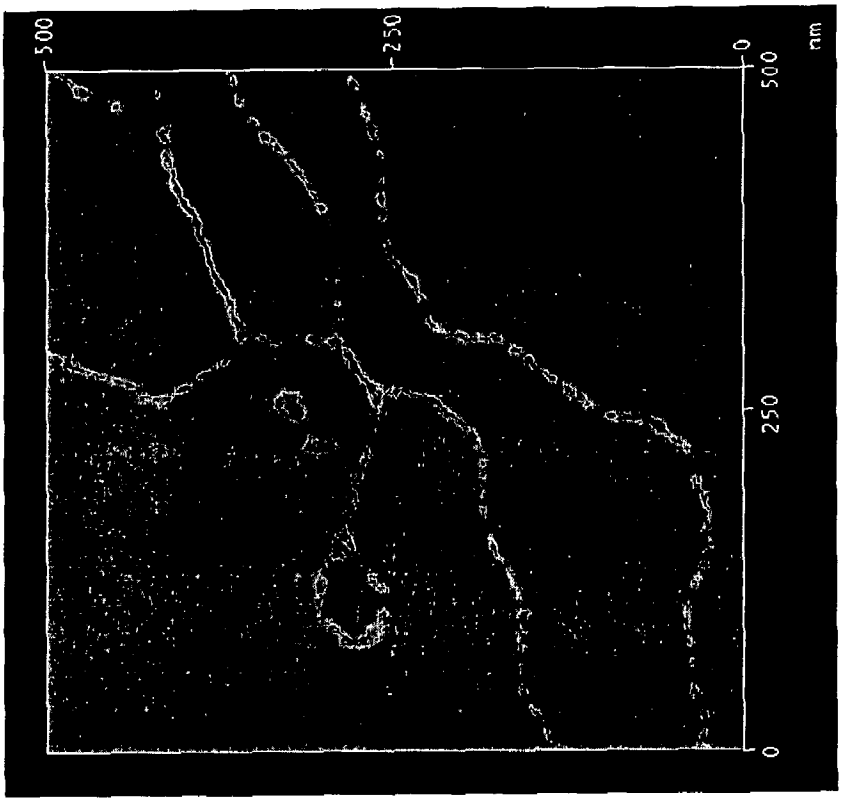
500
250
0
0
250
500
nm

FIG. 7B

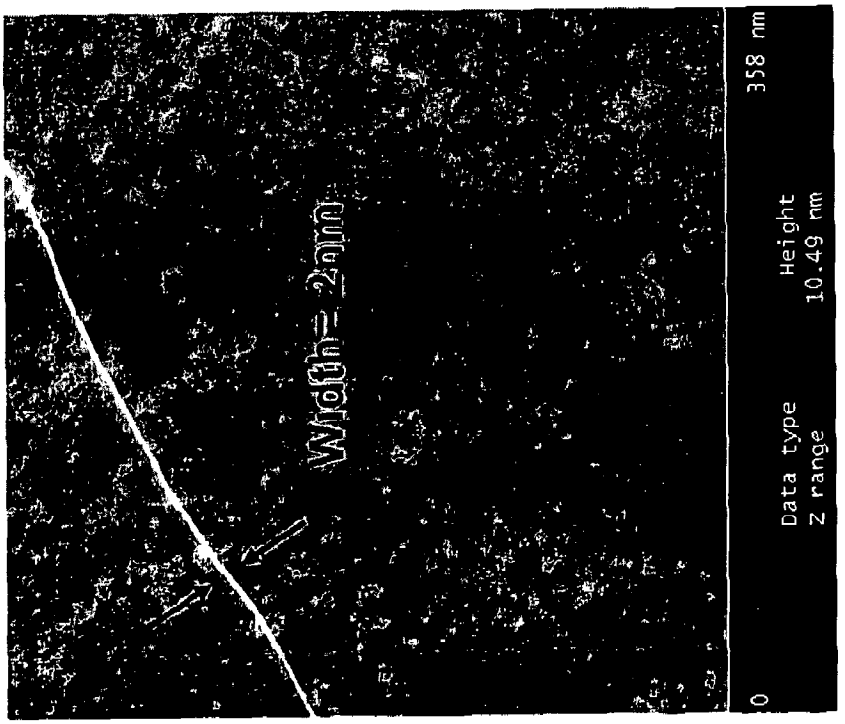
Width= 2nm
358 nm
Height
10.49 nm
Data type
Z range
0

FIG. 7A

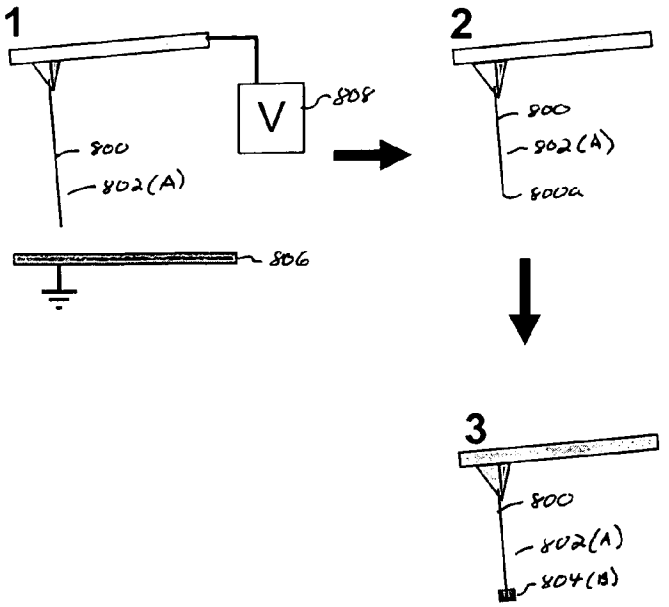

Figure 8

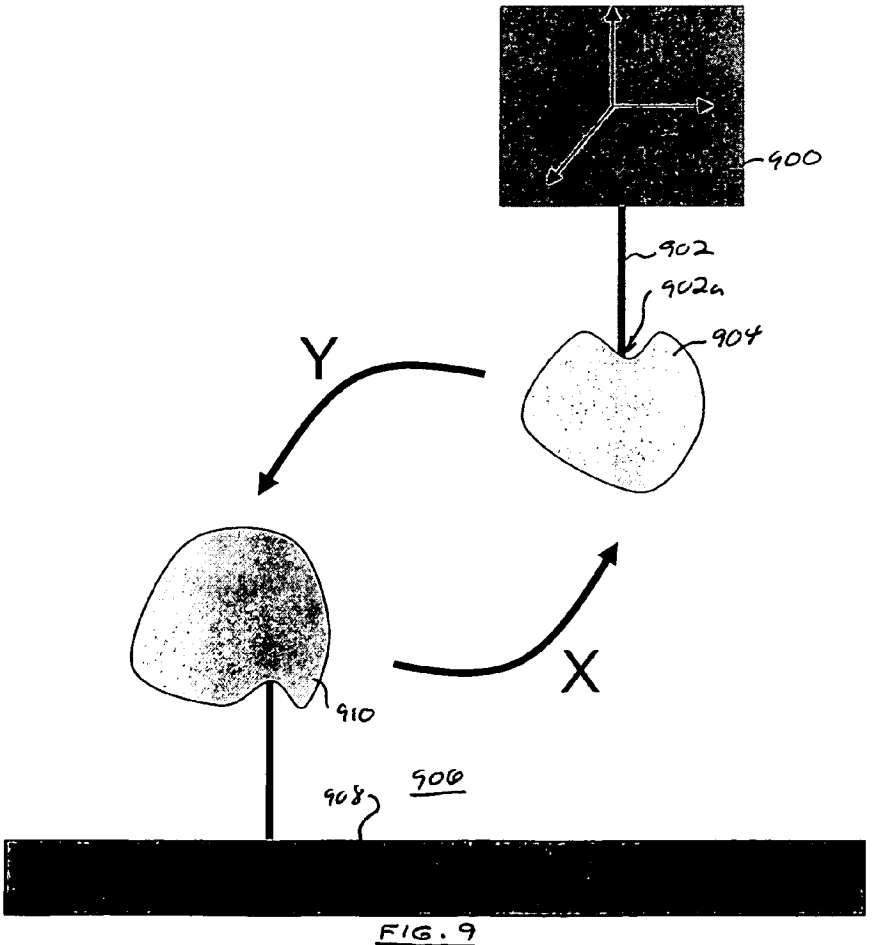

FIG. 9

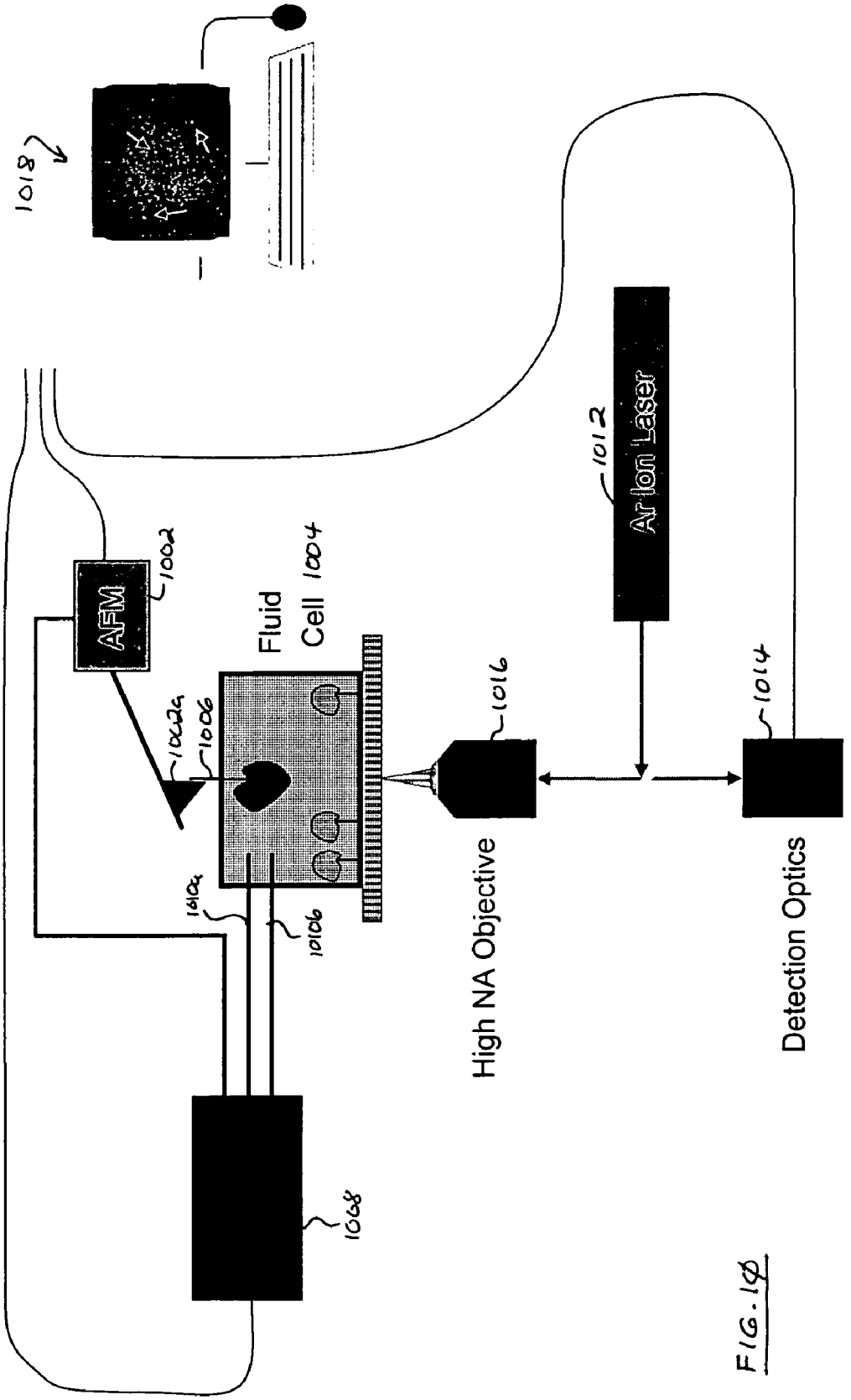
1018
AFM
1002
Fluid Cell 1004
1002a
1006
1010a
1010b
1008
Ar Ion Laser
1012
1016
High NA Objective
1014
Detection Optics

FIG. 10

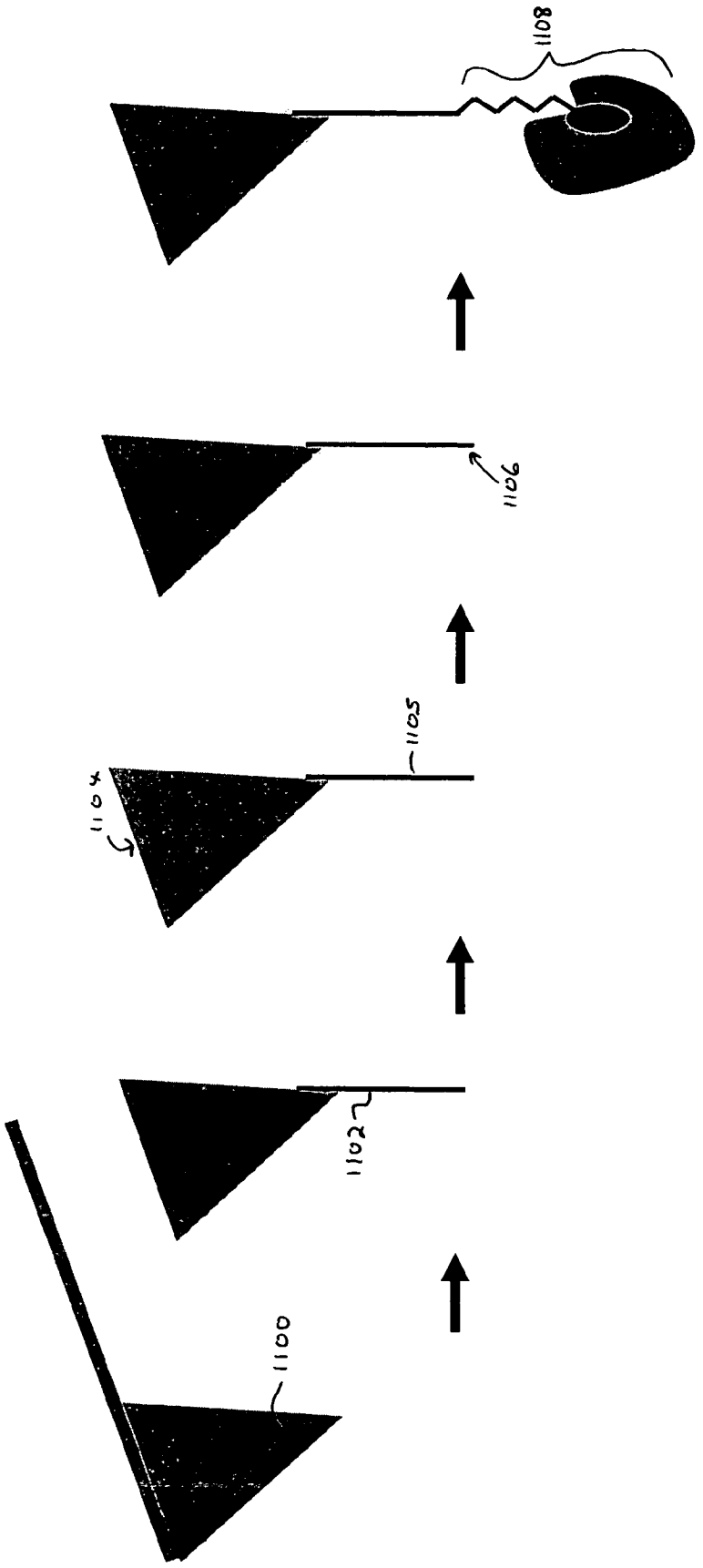
1108
1106
1105
1104
1102
1100
Assembly
Passivation
Etching
Functionalization

FIG. 11

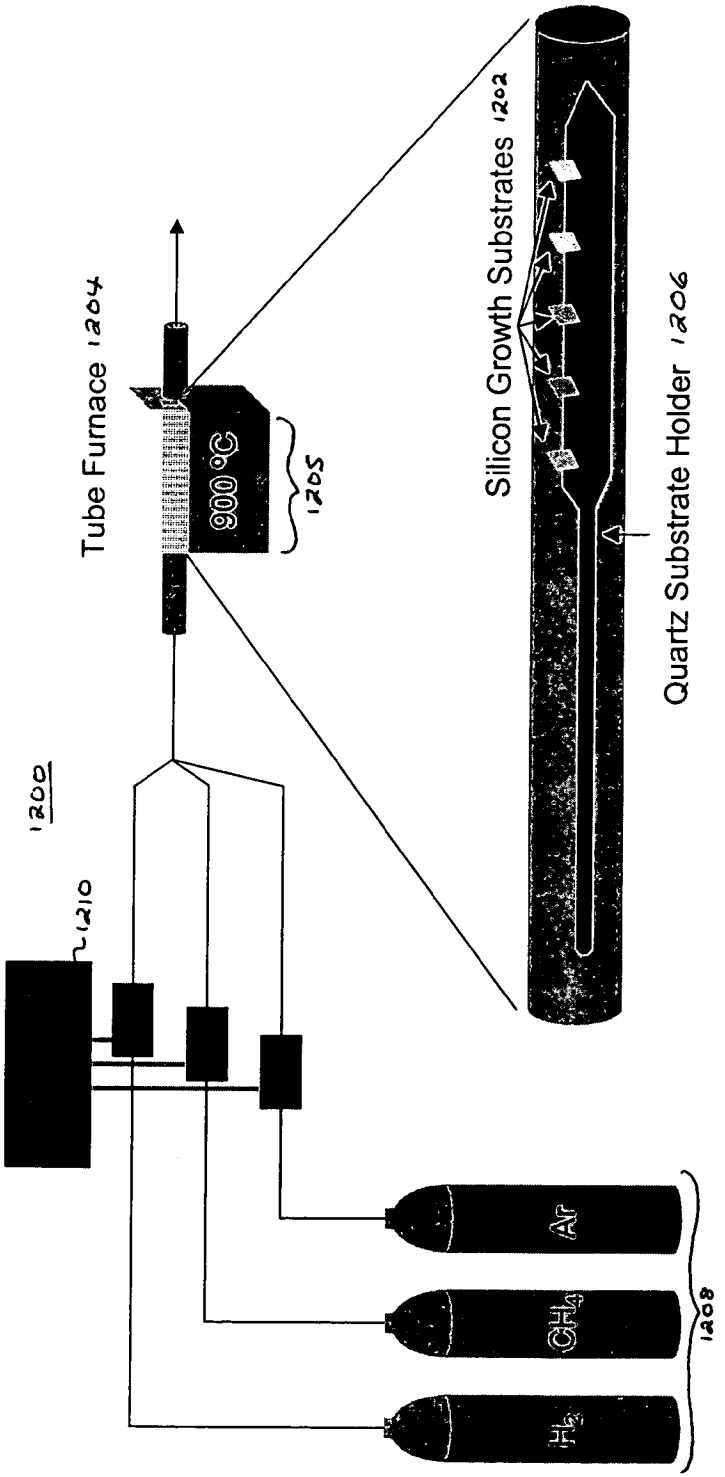

FIG. 12A

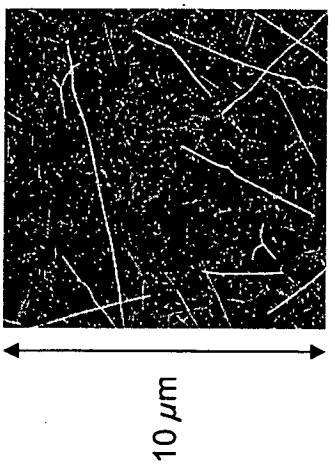

FIG. 12B

FIG. 13A

FIG. 13B

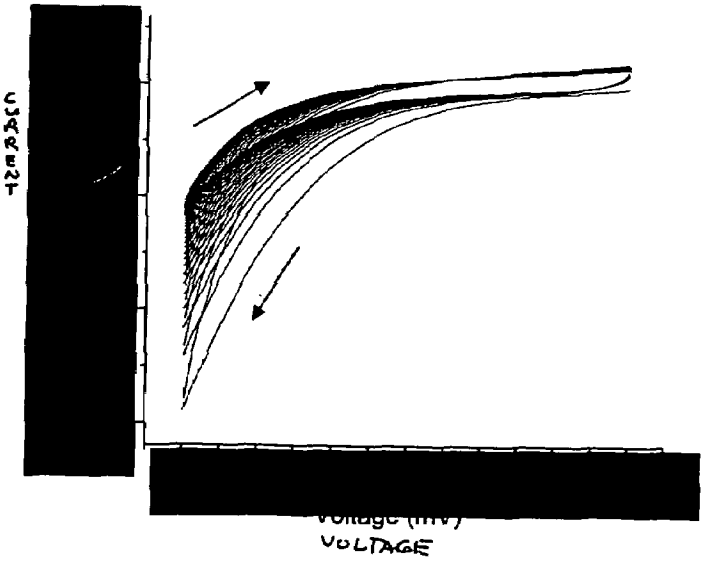

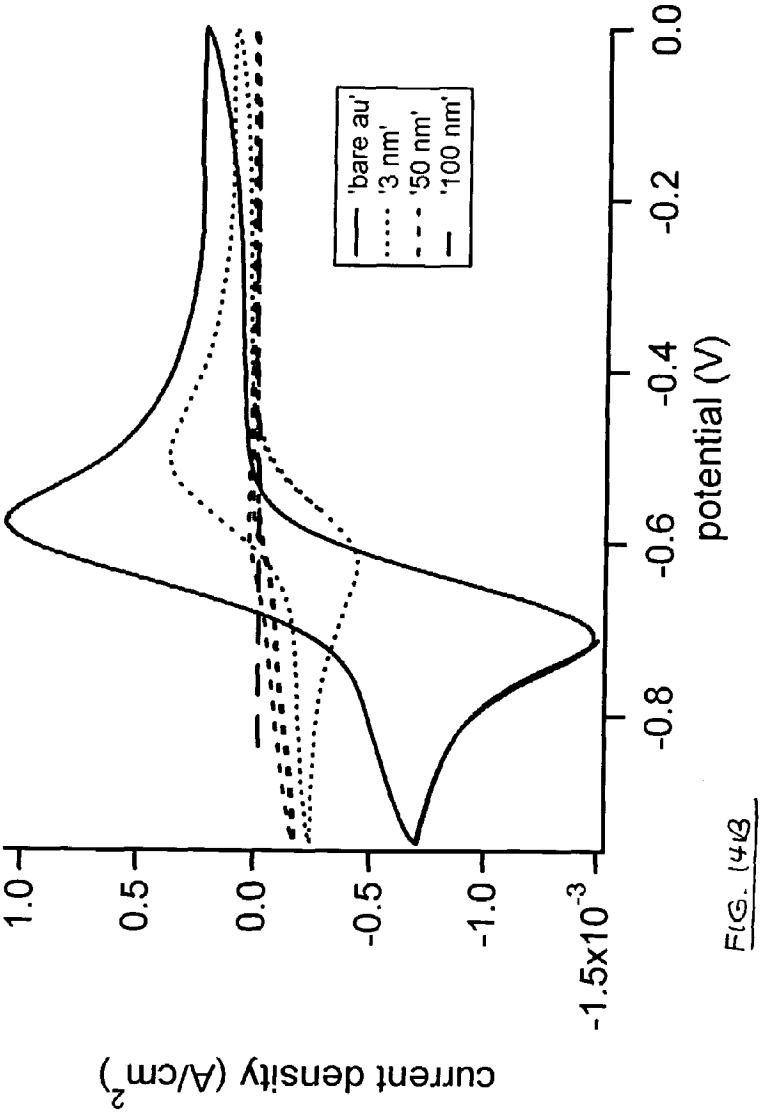

FIG. 14B

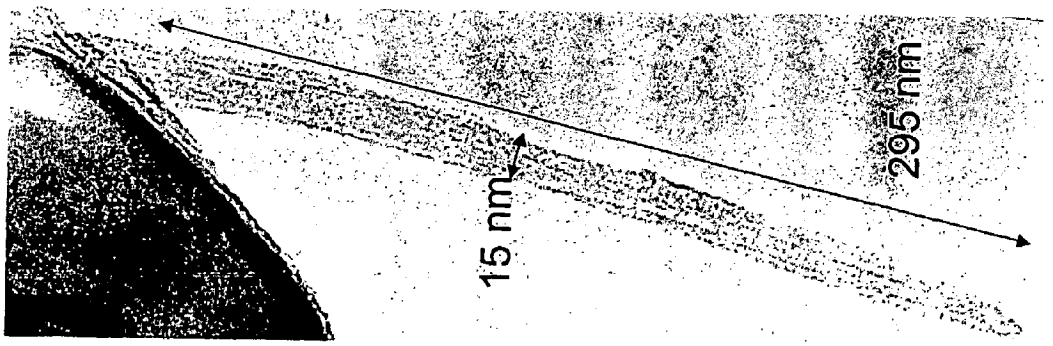

FIG. 14A

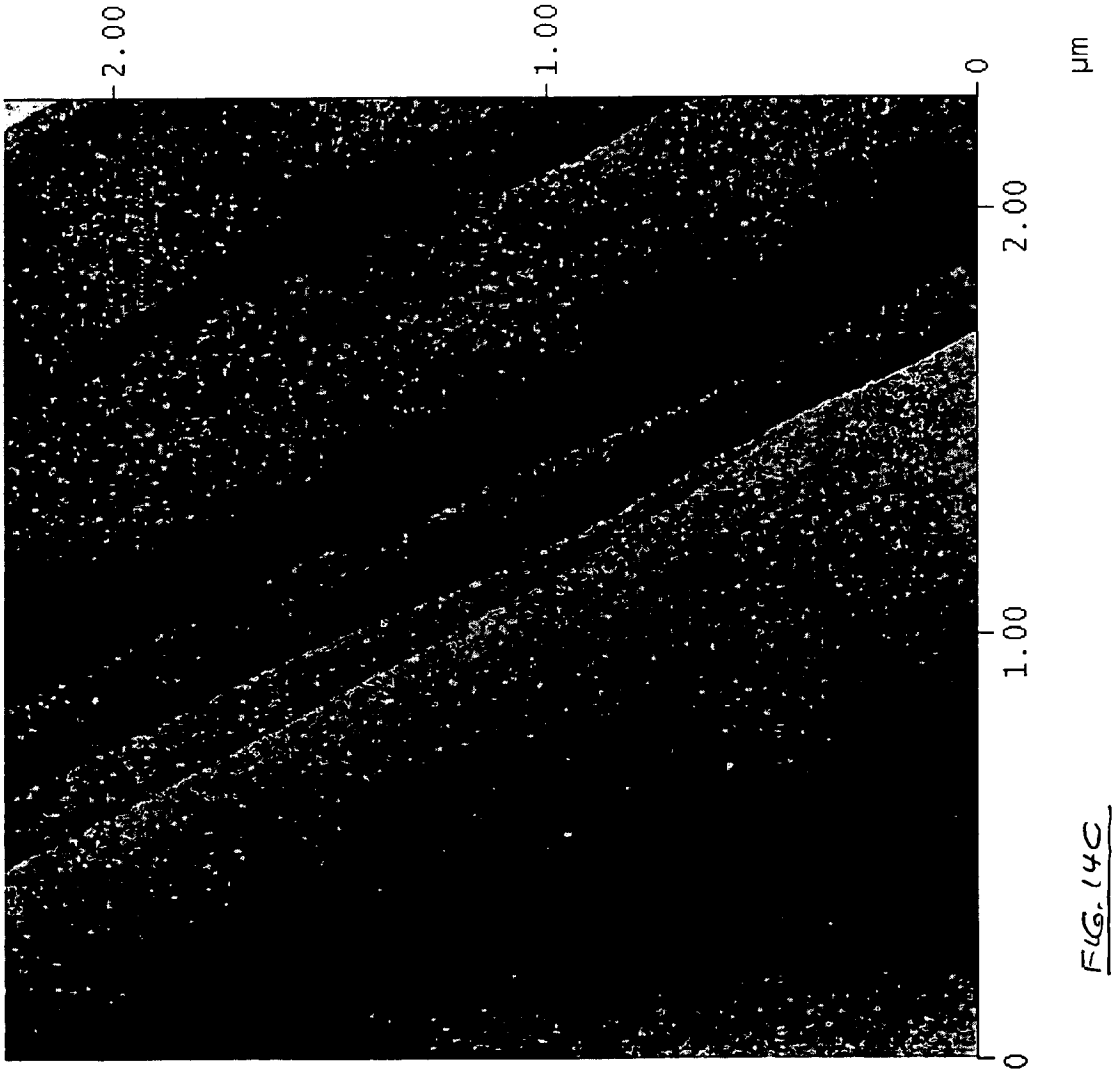

FIG. 14C

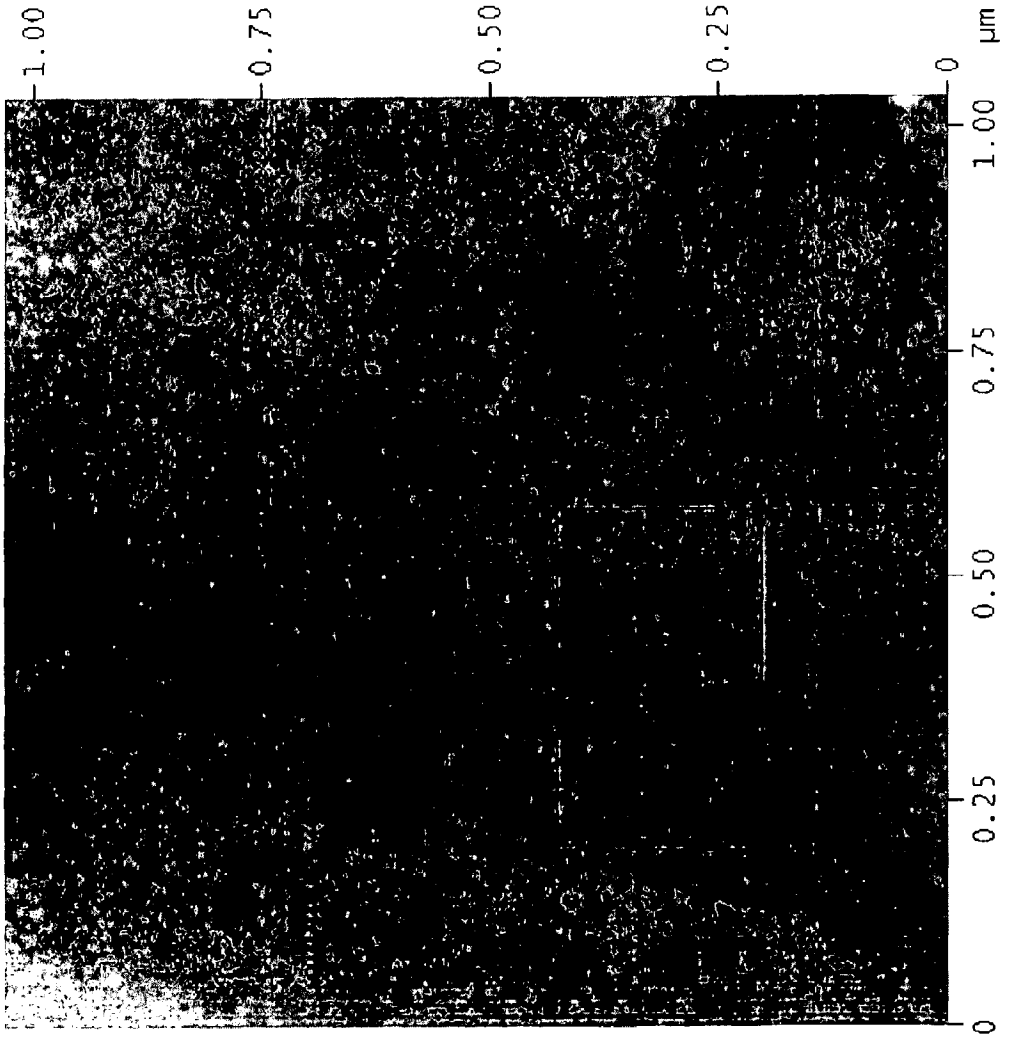

FIG. 14D

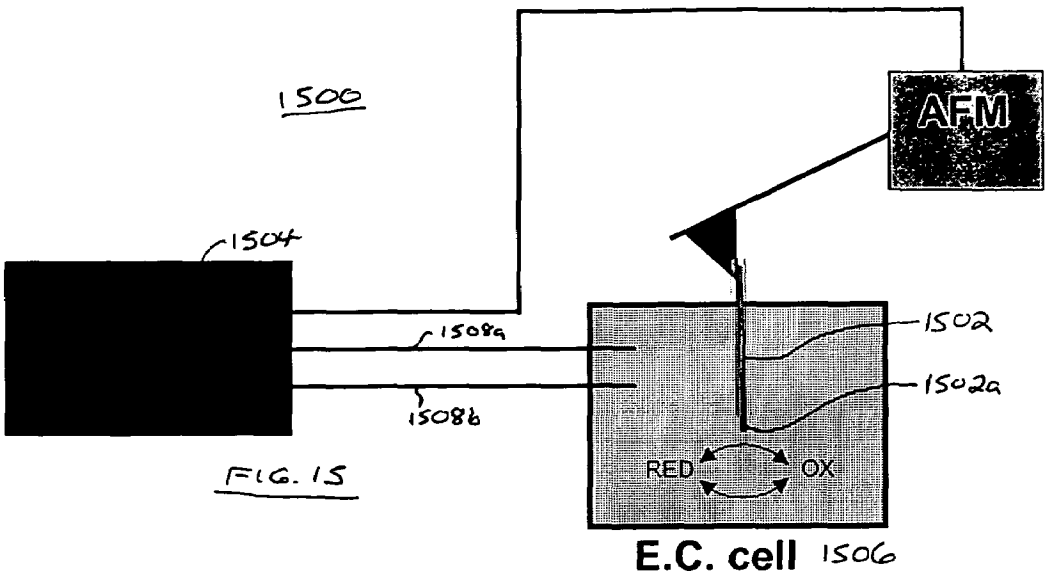

FIG. 15

$$Ru(bpy)_3^{2+} \rightarrow Ru(bpy)_3^{3+} + e^-$$

$$Ru(bpy)_3^{3+} + TPA \rightarrow Ru(bpy)_3^{2+} + TPA^+$$

$$TPA^+ \rightarrow TPA^\bullet + H^+$$

$$Ru(bpy)_3^{3+} + TPA^\bullet \rightarrow Ru(bpy)_3^{2+*} + products$$

$$Ru(bpy)_3^{2+*} \rightarrow Ru(bpy)_3^{2+} + hv$$

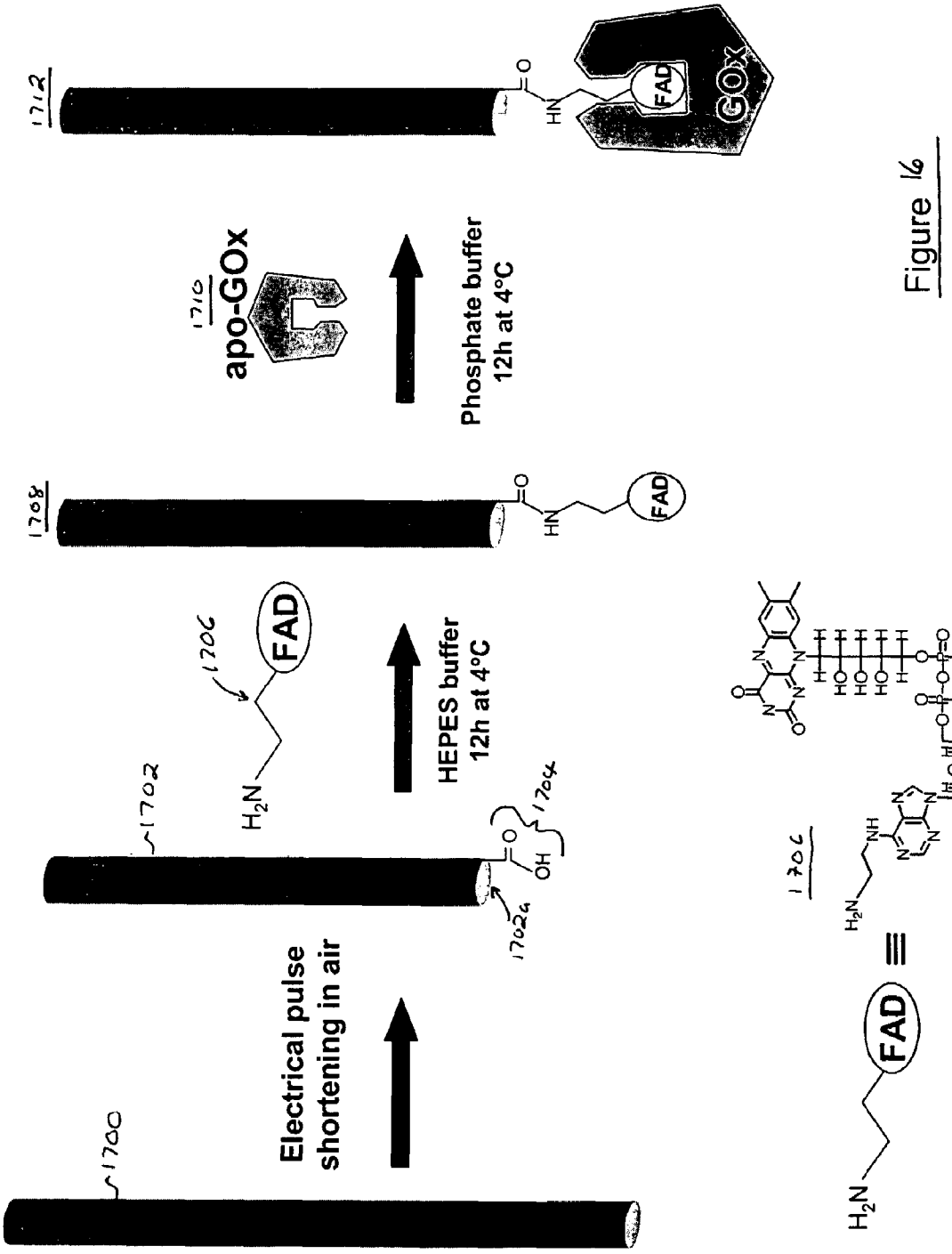
1712
GOx
FAD
apo-GOx
1710
Phosphate buffer
12h at 4°C
1708
FAD
HEPES buffer
12h at 4°C
1706
FAD
1702
1704
1704a
Electrical pulse
shortening in air
1700
1706
FAD

Figure 16

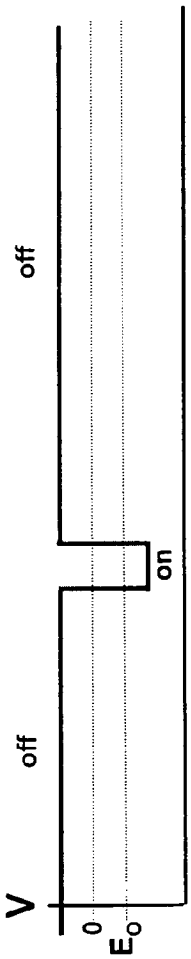

FIG. 17B

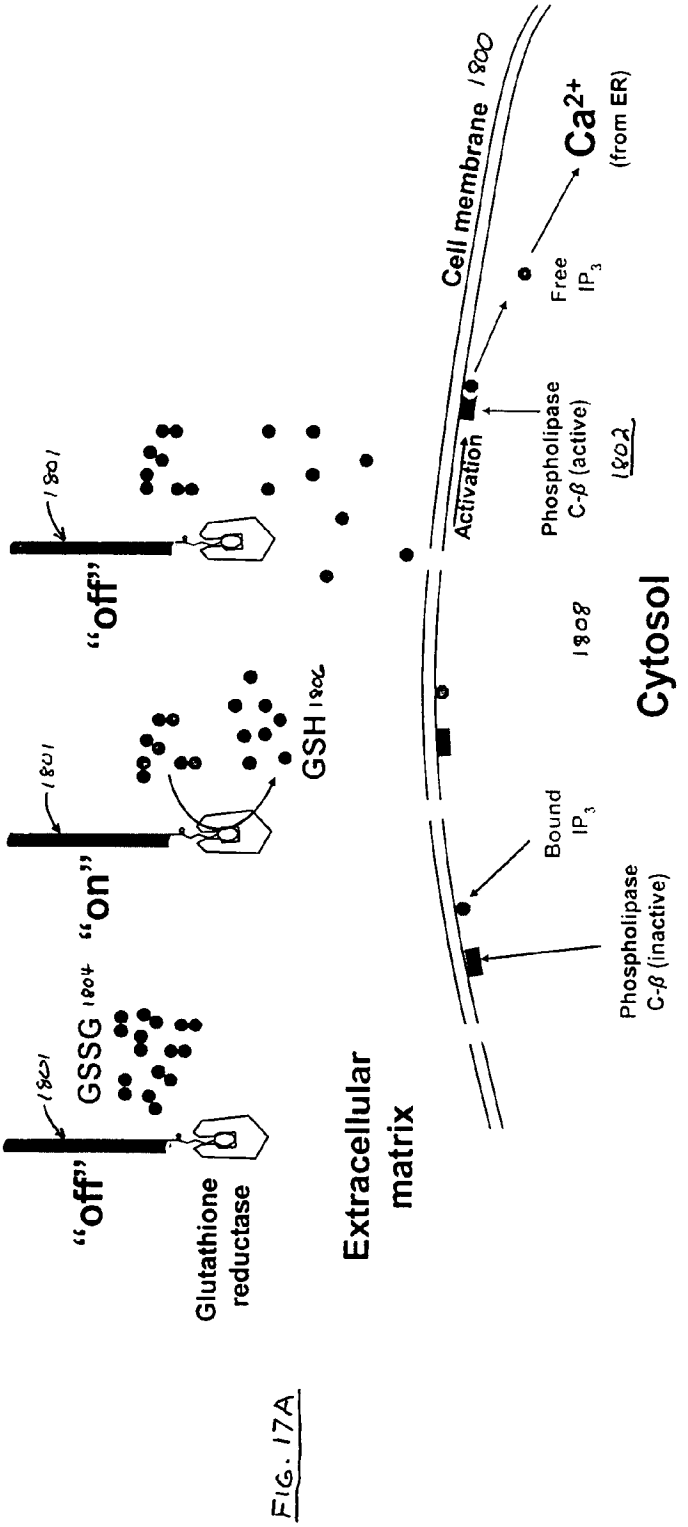

FIG. 17A

SELECTIVE FUNCTIONALIZATION OF CARBON NANOTUBE TIPS ALLOWING FABRICATION OF NEW CLASSES OF NANOSCALE SENSING AND MANIPULATION TOOLS

CROSS-REFERENCES TO RELATED APPLICATIONS

This application claims priority to U.S. Provisional patent application No. 60/449,210 filed Feb. 21, 2003, commonly assigned and incorporated by reference herein for all purposes.

STATEMENT AS TO RIGHTS TO INVENTIONS MADE UNDER FEDERALLY SPONSORED RESEARCH OR DEVELOPMENT

Work described herein has been supported, in part, by the Caltech President's Fund, which is co-administered between JPL (NASA contract NAS7-1407). The United States Government may therefore have certain rights in the invention.

BACKGROUND OF THE INVENTION

Carbon nanotubes hold great promise in many areas of science and technology, due to their unique physical properties and molecular-scale dimensions. A significant technological advance for these materials has been their incorporation as specific molecular transducers in nanosensors, molecular electronics and as molecular manipulation tools. This potential is based on the remarkable molecular recognition capabilities of carbon nanotubes through covalent chemical bonding, surface charge transfer or electrostatic changes when a specific molecule binds to a tube.

In order to achieve this specificity, nanotubes can be chemically, physically or biologically functionalized to recognize a particular target molecule and reject others in a complex environment. In addition, proof-of-principle demonstrations of nanotube functionalization for sensing or binding specific molecules in the gas and liquid phases have been successfully made.

The most commonly used geometry for nanotube based sensors is a chemically or biologically sensitive "field effect transistor". The nanotube serves as a wire connecting lithographically defined source and drain metal electrodes on a doped silicon substrate having a thin insulating silicon oxide surface layer. Binding occurs over the length of the sides of the nanotubes in these devices. The electrically-conductive doped silicon serves as a backgate; noncovalent binding of target molecules is detected by changes in conductance of the device.

Recent advances in nanotube fabrication and AFM imaging with nanotube tips have demonstrated the potential of these tools to achieve high resolution images. Carbon nanotubes have been attached or grown on silicon AFM tips as high resolution AFM probes.

FIGS. **1**A-B show a scanning electron micrographs of individual carbon nanotubes mounted to a silicon AFM probe tip by our team. The nanotube was picked up from a flat substrate supporting SWNTs grown by metal catalyzed chemical vapor deposition.

SWNTs are in many respects, ideal high resolution probe tips for AFM. SWNTs are single carbon atom thick hollow cylinders that are microns in length with diameters ranging from 0.7 to 5 nm. They can be used as high aspect ratio probes with radii comparable to molecular scale dimensions.

Carbon nanotubes are chemically and mechanically robust. They are the stiffest material known, with Young's moduli of about 1.2 Tpa, which limits the noise due to thermal vibrations and bending from degrading the ultimate obtainable resolution. Unlike other materials, carbon nanotubes buckle elastically under large loads, limiting damage to both the tips and the sample. Because SWNTs have well-defined molecular structures, interpreting AFM data becomes much easier since the tip-sample interaction is well characterized and reproducible.

As shown by Wong et al., "Covalently-Functionalized Single-Walled Carbon Nanotube Probe Tips for Chemical Force Microscopy", *J. Am. Chem. Soc.* 120, 8557-8558 (1998), incorporated herein by reference for all purposes, SWNT AFM probe tips have been chemically functionalized uniquely at their very ends. This can be initiated by an electrical etching process, which is also used to shorten the attached SWNTs in order to achieve lengths suitable for high-resolution imaging. However, this approach still leaves the sides of the SWNT susceptible to non-specific binding of molecular species.

When SWNT tips are etched in an oxidizing environment (for example, in O_2 ambient), the ends become functionalized with one or more carboxyl groups, based on bulk measurements carried out on chemically oxidized nanotubes. The tip can be chemically modified further by coupling organic amines to the carboxylate to form amide bonds. Alternatively, by etching the SWNT in a nitrogen environment, SWNT ends become functionalized with one or more amine groups, directly. The use of reactive amino chemistry is a common biochemical conjugation technique, and can be exploited further to take advantage of a wide range of chemical and biological means available for attaching fluorophores, antibodies, ligands, proteins or nucleic acids to the ends of the nanotubes with well-defined orientations.

The manipulation of a ligand-protein interaction with specific single molecules chemically and biologically coupled to the nanotube tip has been measured with AFM by Wong et al, "Covalently Functionalized Nanotubes as Nanometer Probes for Chemistry and Biology", *Nature*, 394, 52-55 (1998), incorporated by reference herein for all purposes. However, nonspecific binding of molecules to the sidewalls of the nanotube is still frequent.

Often this is due to the hydrophobic nature of nanotubes. Hydrophobic sections of proteins or other biological molecules will bind to, and heavily coat, the nanotube sidewalls in a non-specific location. For example, in "Functionalization of Carbon Nanotubes for Biocompatibility and Bio-Molecular Recognition," *Nano Lett.* 2, 285 (2002), incorporated by reference herein for all purposes, Shim et al. have shown that the protein streptavidin nonspecifically binds to as-grown SWNTs unless this nonspecific binding is prevented by coating the nanotubes with a surfactant, such as Triton, and poly (ethylene glycol), PEG.

Thus while known approaches have offered promise, improved techniques for employing carbon nanotubes for sensing and other functions are highly desirable.

BRIEF SUMMARY OF THE INVENTION

Embodiments in accordance with the present invention describe a series of techniques, which used alone or in combination, enable the manufacture of a variety of nanoscale devices and sensors, including single-molecule sensors. Furthermore, these techniques enable the devices to be uniquely manufactured at a specific location. Typically, this is achieved through the use of an individual single wall carbon nanotube

(SWNT) attached to a scanning atomic force microscope (AFM) tip as a structural scaffold. In alternative embodiments, the location of the functionalized SWNT may be changed relative to a target utilizing a nanoscanner, nanopositioner, or other manipulating device, as described in detail below.

Embodiments of the present invention enable construction of a wide variety of novel nanometer scale devices located at the sensing or exposed end of a nanotube AFM tip. These devices can be used for characterizing molecular conformations, chemical dynamics and behavior, intermolecular dynamics, and a wide variety of materials and devices at nanometer length scales. These devices will extend the utility and sensitivity of scanning probe microscopy in general.

Embodiments in accordance with the present invention rely on the concept of selectively modifying the (free) end of a functionalized SWNT AFM probe through electrical or electrochemical means, thereby fundamentally changing the chemical, electrical, and/or mechanical properties of the tube end relative to the rest of the probe. This modification can be carried out by electrically charging the SWNT through application of an electrical potential between the AFM cantilever and the substrate, leading to ablation or modification of material coating the nanotube tip.

The concept is general, and applies equally well in describing the construction of nanoscale probes based on SWNT functionalization using soft materials for possible use in biological applications, as well as metals, semiconductors and insulators, for building nanoscale solid-state electrical, magnetic and optical devices. The ability to incorporate specific device designs with high-level functionality into scanning probes represents a significant advance in the utility of scanning probe microscopy for nanotechnology, materials science and biophysics.

An embodiment of a method in accordance with the present invention for fabricating a nanostructure, comprises, coating a nanostructure with a passivation layer, and altering the passivation layer at a first position.

An embodiment of a device in accordance with the present invention, comprises, a nanostructure having a surface, and a passivation layer coating all but a unique site on the surface, the unique site exhibiting at least one of chemical, biological, electrical, and physical activity.

An embodiment of a method in accordance with the present invention for interacting with a local environment, comprises, providing a nanostructure having a surface coated by passivation excluding a unique site which exhibits at least one of chemical, biological, electrical, and physical activity. The unique site is then positioned in communication with the local environment.

Various additional objects, features and advantages of the present invention can be more fully appreciated with reference to the detailed description and accompanying drawings that follow.

BRIEF DESCRIPTION OF THE DRAWINGS

FIGS. **1**A-B show scanning electron micrographs (SEM) of individual carbon nanotubules mounted on an atomic force microscope (AFM) tip.

FIG. **2** shows a simplified flowchart of steps of one embodiment of a method in accordance with the present invention.

FIG. **3** shows simplified views of pick-up attachment of a single wall carbon nanotube (SWNT) in accordance with an embodiment of the present invention.

FIG. **4** shows an AFM image of SWNTs grown on a pick-up substrate.

FIG. **5**A plots an oscillation amplitude signal for an AFM tip for a shortened SWNT.

FIG. **5**B plots a cantilever deflection signal for an AFM tip for the shortened SWNT of FIG. **5**A.

FIG. **6** shows a transmission electron micrograph of a shortened nanotube at the end of an AFM cantilever tip.

FIG. **7**A shows an AFM image of SWNTs on an oxidized silicon substrate, taken using shortened pick-up nanotube tips.

FIG. **7**B shows an AFM image of DNA on mica, taken using shortened pick-up nanotube tips.

FIG. **8** shows simplified views of a basic process flow for unique functionalization of the free end of a SWNT.

FIG. **9** shows a simplified schematic view of control over biomolecular dynamics on the molecular scale.

FIG. **10** shows a simplified schematic view of a hybrid AFM/optical microscope apparatus allowing manipulation of functionalized SWNTs.

FIG. **11** shows simplified schematic views of the process of wiring biomolecules to carbon nanotube scanning probes.

FIG. **12**A shows a schematic view of an apparatus for achieving SWNT catalyzed vapor deposition growth.

FIG. **12**B shows an AFM image of SWNTs grown on a pick-up substrate utilizing the apparatus shown in FIG. **12**A.

FIG. **13**A shows an electron micrograph of a nanotube probe passivated by an electrochemical polymerization process.

FIG. **13**B plots current versus voltage to illustrate the passivation by electrochemical polymerization, of the nanotube probe of FIG. **13**A.

FIG. **14**A shows an electron micrograph of a nanotube probe passivated by gas phase polymerization in an inductively coupled plasma.

FIG. **14**B plots current density versus potential for such a Teflon-like polymer film formed on gold electrodes by the same type of gas-phase reaction responsible for forming the passivation layer on the SWNT shown in FIG. **14**A.

FIG. **14**C shows an AFM image of a planar graphite substrate coated by a Teflon-like polymer film formed by the same type of gas-phase reaction responsible for forming the passivation layer on the SWNT shown in FIG. **14**A.

FIG. **14**D shows a roughness analysis of the substrate whose AFM image is shown in FIG. **14**C.

FIG. **15** shows a simplified view of the use of a SWNT probe in connection with a localized electrochemical reaction.

FIG. **16** is a simplified schematic view of the nanowiring of an enzyme to a carbon nanotube.

FIG. **17**A is a simplified schematic view showing use of a nanowired enzymatic probe.

FIG. **17**B plots voltage versus time for the enzymatic probe of FIG. **17**A.

DETAILED DESCRIPTION OF THE INVENTION

Embodiments in accordance with the present invention exploit the unique molecular recognition capabilities, mechanical and electronic properties, and length scale of carbon nanotubes, to construct molecule-specific actuators and manipulators integrated on scanning probes. These probes can also function as biosensors capable of detecting specific molecules, and sensing changes in (inter)molecular dynamics in combination with fluorescence detection. Interactions between SWNTs and specific biomolecules can be engineered through functionalization of the SWNTs, employing techniques previously developed to construct electronic biosensors based on nanotube transistors.

However, the devices described herein function substantially differently from conventional nanotube-based sensors detecting molecules through electronic transport measurements. In particular, the SWNT probe will serve as a molecular-scale structural support for fabrication of a specific device, through attachment of ligands, enzymes or other biomolecules. Embodiments of devices in accordance with the present invention will induce in biological systems, well-defined biochemical reactions or conformational changes amendable to spectroscopic detection. Fluorescence imaging correlated with one or more of the plurality of data channels an AFM supports, can be used to not only detect and identify single biomolecules, but also to study and eventually control intermolecular dynamics. Electrical conduction through the SWNT can further expand the probe's functional capability.

Conventionally, electronic sensors based on nanotube transistor geometries on planar supports have functioned primarily as static assays. Such conventional devices can sensitively detect and identify specific analytes, but are not intended to interact with or further perturb the sample. By contrast, embodiments in accordance with the present invention are designed to continuously probe a dynamic biological system in real time, and to ultimately influence the organizational evolution and functional capabilities of complex assemblies of individual interacting biomolecules.

Embodiments in accordance with the present invention comprise methods that enable a single active location to be created for sensing or characterization at the free end of a nanotube. This nanotube is attached to a structural substrate that enables the sensor to be very precisely located. The precise location capability enables a wide variety of high resolution studies, characterization and manipulation to be conducted with unprecedented resolution and sensitivity. A typical process of achieving this is outlined in FIG. **2** and described below.

Embodiments in accordance with the present invention start by attaching a nanotube, single-wall, multi-wall or a rope or bundle of single-wall nanotubes to a supporting structure such as an AFM tip. For AFM tips this can initially be accomplished either by direct growth or more preferably by the pickup technique. Once attached this tube can either be adhesively attached to the tip or left attached via van der Waals forces. The adhesives used can vary considerably. The range covers many common water tolerant adhesives such as Norland Optical Adhesive and other UV curable adhesives and even adhesion via metallization, vapor deposited polymers and electrochemical polymerization of coating materials.

In one embodiment, the adhered tip is coated with surfactant and a polymeric material such as PEG to preclude non-specific binding. This coating may be the same material used to increase adhesion of the nanotube to the supporting substrate or separate material or materials used in sequence or combination. The coating can be either chemisorbed or physisorbed onto the tube. For purposes of the instant patent application, the term "chemisorbed" refers to formation of a covalent bond between the nanotube and the coating.

The formation of a covalent bond can alter the electronic properties of the nanotube. In accordance with a preferred embodiment, the coating layer will be physisorbed onto the nanotube. For purposes of the instant patent application, the term "physisorbed" refers to formation of other than a covalent bond between the nanotube and the coating.

Examples of coating to achieve specific purposes include surfactants, polymers, resists, metals, electrochemically deposited metals, polymers, or semiconductors. One or more layers of any of these materials can be applied in succession.

The nanotube tip is then shortened, most commonly through application of a short voltage pulse, to a length suitable as a scanning probe. This length is typically less than 500 nm, and may be less than about 250 nm. In another embodiment, this length is less than about 200 nm and may be less than about 100 nm. In still other embodiments, this length is less than about 100 nm, may be less than 50 nm, and can be as short as about 10 nm.

Application of an electrical pulse, while the coated nanotube tip is in contact or near contact with a grounding substrate, is made to remove coating used to inhibit non-specific binding at the very tip. In one case this material may be a surfactant/PEG solution. This is accomplished through ablation and/or oxidation of the remaining tube end. When performed in an oxidizing environment, the exposed carbon nanotube tip is chemically functionalized with a carboxyl (COOH) group. When performed in a nitriding environment, the exposed carbon nanotube tip is chemically functionalized with an amine (NH_3) group.

A specific sensing material can be attached to the end of the nanotube at this unique location. This can be accomplished through covalent chemical bonds to the carboxyl or amine groups at the free end of the nanotube.

Alternately, this attachment can be accomplished via physisorption to the end of the tip. Physisorption could be carried out either by dipping it in the desired material or by touching the end on a very thin deposit of the desired material and lifting off a small deposit at free end of the nanotube. The very thin layer could be created by many commonly known techniques such as spin coating or dip pen lithography.

Alternately, the properties of the nanotube coating material can be electrochemically altered via application of the electrical pulse in different ways than ablation or oxidation, such as reduction. Alternately, several coating of materials could be applied sequentially to gain specific sensing capabilities.

In one specific example of this invention, the adhered nanotube could be coated with metal. In another example of this invention, the nanotube could be coated with several metal layers. In some cases, these metal layers are coated with an insulating material such as a nonconductive polymer. Ablation or oxidation of the end will leave an exposed ring or tip of metal and carbon while protecting the insulating qualities of the assembly.

Differential functionalization is achieved at the free end of the nanotube. It could be achieved through physisorption or chemisorption of a different polymer layer than the initial coating layer or layers. Or it could be achieved by electrochemically altering the coating first applied. Or metal could be localized at tip through resist ablation at tip, metallization, lift-off in acetone, etc. Alternately, the bare tip could be used directly as a nanoelectrode.

FIG. **2** shows a simplified flow chart of process **200** employing basic techniques for creating nanoscale or single molecule sensors, manipulators, and devices. In first step **202** described in detail below in Section 1., a nanotube is attached to an AFM tip.

In a second step **204** described in detail below in Section 3.A., a nanotube may be adhesively bound to an AFM tip utilizing UV curable adhesive, epoxy or other adhesive. In a third step **206** described in detail below in Section 3.B., the nanotube may be coated with one or more layers to preclude non-specific binding or interactions with another material, and/or electrically isolate the nanotube from the surrounding environment. Examples of passivating coatings for use in accordance with the present invention include, but are not limited to a surfactant, a polymer, a resist, an evaporated metal, an electrochemically deposited metal, and a semicon-

ductor. In some cases a coating will also serve to increase the adhesion between the nanotube and its supporting substrate.

In a fourth step **208** described in detail below in sections 3.B.-3.D., the tip may be differentially functionalized utilizing a number of techniques, alone or in combination. For example, functionalization may be accomplished through use of (1) different absorbed polymer, (2) covalent chemistry to exposed and oxidized NT tip; (3) electrochemical alteration of coating layers, (4) metal localized at tip by resist ablation at tip; or (5) metallization followed by resist lift-off in acetone.

FIG. **11** shows simplified schematic views summarizing the process of wiring biomolecules to carbon nanotube scanning probes in accordance with embodiments of the present invention. In a first stage, the probe is assembled by causing the AFM tip **1100** to pick up nanotube **1102**. In a second stage, the assembled probe **1104** is passivated with material **1105**. In a third stage, tip **1106** of the assembled probe exposed by etching. In a fourth stage, the probe is functionalized by interaction between the exposed probe tip and a chemical species **1108**. A single sensing assembly comprising one or more molecules is then attached at this uniquely functionalized site and used to probe or sense a variety of samples.

1. "Pick-Up of Individual SWNTs from Flat Substrates

We have found the most success in our labs in following the procedure of growing individual SWNTs on flat surfaces, and using the silicon probe tip to pick up vertically oriented tubes during imaging of these substrates in tapping mode. As described by Wade et al., "Correlating AFM Probe Morphology to Image Resolution for Single-Wall Carbon Nanotube Tips", *Nano Lett.* 10.1021/n1049976q (2004), incorporated by reference herein for all purposes, both the growth conditions of SWNTs as well as the conditions for mounting them on AFM probes with the optimal geometry, are more controllable and better defined with this approach.

FIG. **3** shows a simplified schematic view of the pick-up attachment of SWNTs **300** grown on substrate **302**. The as-grown nanotubes can be attached to a scanning AFM probe **304** by van der Waals forces. Once the SWNT has become attached to the AFM tip, the bond between them can be reinforced by gas phase polymerization coating in a plasma reactor, electrochemically deposited coatings, metallization, or curing of a precoated adhesive such as epoxy.

To contrast the relative yield between the pickup and direct catalyst growth methods: in one week we have picked up and shortened 20 SWNT AFM tips to between 10 and 25 nm in length. Estimates for optimal production of direct catalytic tube growth on tips are only 1 useful tip per 2 days, for a dedicated researcher with complete co-located facilities, as described by Wong et al, "Carbon Nanotube Tips: High Resolution Probes for Imaging Biological Systems", *J. Am. Chem. Soc.* 120, 603-604 (1998), incorporated by reference herein for all purposes.

Van der Waals forces between the silicon apex and the picked-up SWNT are believed to hold the nanotube to the tip firmly in air. For imaging in fluids, the silicon pyramidal apex could be pre-conditioned by applying an adhesive to the tip before pick-up followed by curing (with a UV lamp for example). Alternately, evaporative metallization may be an effective tool for strengthening of the attachment site while still preserving the conductive properties of the SWNT tips. Further alternately, plasma deposition of a polymer may be an effective tool for strengthening of the attachment site while still preserving the conductive properties of the SWNT tips.

The primary indication used to tell that a SWNT has been picked up during imaging, is a step change in the Z height. Once a SWNT has been picked up and shortened, the probe can be transferred to a sample for high-resolution imaging, biomolecular manipulations, or force spectroscopy. As evidenced by the large number of SWNTs shown in FIG. **4**, the same SWNT substrate can be used thousands of times to prepare SWNT AFM tips easily and reliably.

A. CVD Growth of SWNTs on Pick-Up Substrates

FIG. **12**A shows a schematic view of an apparatus **1200** for achieving SWNT catalyzed vapor deposition growth. Growth of SWNTs is carried out by CVD on square 500 μm thick Si/SiO_2 wafers **1202** with dimensions between 4 mm and 8 mm.

The wafers are first coated with an iron catalyst by spin-coating at 3000 rpm with 12 drops of a 100 μg/ml solution of $Fe(NO_3)_3.9H_2O$ in isopropyl alcohol. Alternatively, the concentration of $Fe(NO_3)_3.9H_2O$ may range from between about 5-30 μg/ml. Between applications of each drop of catalyst solution, the wafer is spun for several seconds to allow the solvent to evaporate. Catalyst deposition is preferably, though not necessarily, carried out in a clean room.

Alternately, catalyst deposition of metals such as iron, nickel and iron-nickel can be carried out using sputtering, thermal evaporation, molecular-beam epitaxy (MBE). Alternately proteins such as Ferritin can be used to deposit iron catalytic sites uniformly. Alternately nickel-based catalysts can be used on unoxidized silicon substrates.

CVD is performed in a 22 mm inner diameter Lindberg/Blue M quartz tube furnace **1204** with a heating zone **1205** that is 312 mm long. Five wafers are positioned 12.5 mm apart in a specially designed quartz holder **1206**, oriented vertically and with the catalyst coated side facing away from the direction of the incoming gas from sources **1208** regulated by mass flow controller **1210**. The most rapid nanotube growth is obtained when the holder is positioned at the leeward end of the quartz tube, with the last wafer approximately 2 mm from the end of the heating chamber/zone.

The quartz tube is then flushed for 15 minutes with argon gas (Matheson, 99.9995% purity, 440 sccm). The furnace is heated at 950° C. for approximately 20 minutes, and then held at 950° C. for 15 minutes, both under a flowing atmosphere of Ar (440 sccm) and H_2 (Matheson, research grade, 125 sccm). The furnace is held at this temperature for 5 additional minutes while being flushed with Ar (440 sccm). Growth of nanotubes is then carried out for 1-5 minutes at 950° C. with CH_4 (Air Liquide, Ultra High Purity, 1080 sccm) and H_2 (125 sccm).

Following this growth step, the furnace is again flushed with Ar (440 sccm) and held at 950° C. before rapidly cooling to less than 250° C., after which the substrates are exposed to air and removed from the furnace. FIG. **12**B shows a scanning electron micrograph of SWNTs grown on a pick-up substrate.

This procedure is offered as an example of one of the many which we have used to grow nanotubes. There are many available variations in gas mixture, growth temperature, mass flow rates and procedure step times.

2. SWNT Pick-Up and Shortening Procedure

The growth procedure generates SWNTs on the substrate with diameters ranging from 1.6 to 3.0 nm, and lengths between 100 nm and 5 μm, as imaged with SEM and TEM. Most of the tubes are oriented horizontally with respect to the substrate surface, and can be imaged with standard AFM.

The results from a typical growth are depicted in FIG. **4**, which shows a micrograph of SWNTs grown by CH_4/H_2CVD on a pick-up (Si/SiO_2) substrate. This image, and the force spectroscopy curves displayed below in FIGS. **5**A-B were taken with a MultiMode AFM instrument in Collier's lab, controlled by a Nanoscope IV controller, both from Digital Instruments of Santa Barbara, Calif.

A small percentage of tubes are oriented vertically, and can be picked up by scanning the AFM cantilever across the surface. Typically, 1 to 4 tubes can be picked up from a 10 μm×10 μm square region. The tube binds to the side of the pyramidal AFM tip through Van der Waals attractive forces, and usually remains attached firmly enough that it can be repeatedly pressed into or scanned across the substrate surface. The pick-up of a nanotube is readily observed by monitoring the Z height while looking for a significant step change in the average position.

In almost all cases, more than 100 nm of nanotube protrudes from the end of the AFM tip, making high resolution imaging impossible due to thermal fluctuations and bending without first shortening the tube to lengths between 10 and 100 nm for a 2 nm diameter SWNT. The length of the nanotube protruding from the end of the AFM tip can be measured indirectly by observing the oscillation amplitude and deflection of the cantilever as it is brought into contact with a hard surface.

Consider first the profile of a bare tip in contact with a substrate. As the approaching tip begins to interact with the surface, the oscillation amplitude decreases quickly, reaching zero when the tip is in full contact. At this point of contact, the cantilever deflection signal begins to rise linearly as the tip is pressed further into the surface.

A tip with a protruding nanotube will show a different profile, as depicted in FIGS. **5**A-B, which plot oscillation amplitude and cantilever deflection signals, respectively, for an AFM tip with a SWNT shortened to about 22 nm. In FIGS. **5**A-B, the length of the tip is depicted by the length between the two vertical dashed lines.

The oscillation of the tip undergoes rapid damping as soon as the nanotube makes contact with the surface. However, the SWNT buckles elastically at higher loads and does not deflect the cantilever.

Only when the rigid Si tip apex itself makes direct contact with the substrate is the deflection detected. The distance between the point at which the oscillation amplitude decreases to zero and the point at which the deflection of the cantilever is detected indicates the protrusion length of the nanotube. In this region, the tube is elastically bending or buckling, which is reversible: when the probe is retracted, the buckled tube can reform to its original shape.

FIG. **6** shows TEM image of shortened nanotube at the end of a silicon AFM cantilever tip. This tip was attached via the pickup method and shortened to 65 nm using electrical pulses as described above. The diameter of this tip is approximately 6 nm. Due to the structure at the end of the nanotube and the angle at which it is mounted relative to the surface, it images with a resolution of approximately 3 nm.

The procedure to shorten the SWNT in air comprises applying +3 to +50 volt pulses of 20 to 100 μs duration between the AFM tip and a grounded, conductive silver substrate. These pulses are supplied from a Hewlett-Packard 8114A pulse generator and routed to the tip through a Digital Instruments Signal Access Module, or "break-out" box, which is connected to the MultiMode AFM. Presumably the nanotube is shortened by ablation resulting from the very high electric field generated at the nanotube end. The pulses are applied while tapping the surface at approximately 70-300 kHz, which is near the resonance frequency of the cantilever.

For a given SWNT tip, larger voltage pulses shorten the tube in larger increments, as do pulses of longer duration. But the voltage necessary to carry out shortening varies drastically between individual tubes. This is believed due to the widely varying conductivities associated with nanotubes of slightly different molecular structure, for example, between semiconducting and metallic nanotubes.

Nanotubes can be shortened precisely with steps as small as 2 nm per pulse. The main drawback to this technique is that the electrical pulsing can dislodge the nanotube electrostatically from the AFM tip. However, this effect can also be exploited to controllably deposit nanotubes precisely on substrates for device fabrication.

FIG. **7**A shows AFM images of SWNTs on oxidized silicon substrate taken using a shortened pickup nanotube tips grown by our team. The SWNT AFM images seen in FIG. **7**A determine the equivalent resolution that we have been able to obtain so far to be 0.5 nm.

The resolution is defined as being the difference between the measured height of the cylindrical nanotube and the width at the noise floor. In this case the 1.6 nm diameter nanotube was measured to have a 2.1 nm width at the noise floor. Hence the very conservative estimate of 0.5 nm resolution. Typical silicon tips are 10-30 nm in diameter. AFM resolution in the X-Y plane is proportional to the tip radius. The resolution seen here is ~20-30 times better than can be achieved with a conventional silicon tip.

FIG. **7**B shows AFM images of DNA on mica taken using a shortened pickup nanotube tips grown by our team.

3. Functionalization of SWNT AFM Probes

A. Adhesion of Picked-Up SWNT to AFM Tip for Operation in Liquids

If necessary, the silicon apex of the AFM tip can be precoated with a very thin layer of an adhesive (for example Norland Optical Epoxy Number 60) before picking-up a SWNT from the growth substrate. This involves bringing the AFM cantilever assembly mounted on a XYZ micromanipulator into contact with a very thin layer of adhesive. The neck of a drawn-out filament from a bead of epoxy coated on a wooden applicator has been found to be a sufficiently thin coating. The process is performed under 10× to 110× magnification in a stereo zoom microscope.

Once a SWNT has been picked up from the substrate by the scanning AFM, the adhesive is cured. In the case of the Norland optical adhesives, this is accomplished with a UV lamp. The bulk resistivity of the optical epoxies is high but the layer can be thin enough to allow sufficient electrical contact between the silicon AFM tip and the nanotube.

Other adhesives, with lower resistivities, will enable improved electrical contacts to be achieved. Curing of the adhesive can be accomplished either after pickup and before pulse shortening, or after pickup and shortening are completed. Alternatively, polymer or metal coatings can be applied after pickup to improve adhesion.

B. General Description of Differential Functionalization of SWNT Tips

The as-grown SWNT can be coated with one, two, or many different materials depending on the specific embodiment envisioned. FIG. **8** shows a simplified schematic view of the basic process flow for unique functionalization of the free end of a nanotube **800**. The process starts with coating with a material **802** that inhibits non-specific binding. In the second step, an electrical pulse is then used to ablate or vaporize the end of the tube exposing the tip **800***a*. The tip can then be uniquely functionalized, as shown in the third step.

In the embodiment shown schematically in FIG. **8**, the process uses a single initial coating, A, (**802**) which can then be modified with the application of a potential difference between the AFM tip and the scanned surface to give coating layer B, (**804**) having fundamentally different chemical, biological and/or physical characteristics. Depending on the particular embodiment, the voltage may be of any magnitude,

polarity and duration. In the embodiment shown in FIG. **8**, the probe tip is positively charged relative to grounded conductive substrate **806** as a result of connection with voltage pulse generator **808**.

The high electric field density between the SWNT tip and the surface will localize the physical extent of layer B to, at most, a few nanometers from the resulting tip end. Specific examples of changes in the characteristics of layer B relative to layer A will depend on the details of the specific embodiment envisioned and may result from procedural steps carried either before, during or after the application of the electrical potential.

The role of the electrical event in any process will be to either ablate material from the tip of the SWNT probe, possibly including but not limited to the nanotube core, or electrically/electrochemically change the nature of the initial coating formulation at the tip relative to the rest of the tube due to the vastly increased density of electric field lines emanating from the sharp tube end.

The modification will involve charge injection at the region of modification, and may or may not be accompanied by measurable electrical current. The electrical modification process may be monitored in real time by correlating measurements of the voltage difference between tip and surface or current flow between the two, with observation of tip oscillation amplitude or tip deflection similar to the description of tube shortening in section 2 above.

C. Specific Embodiments of SWNT Functionalization and Applications

In one general class of modifications, SWNTs attached to AFM probes can be functionalized to serve as single molecule manipulation and sensing devices. FIG. **9** shows a simplified schematic view of such an embodiment, wherein AFM probe **900** includes nanotube **902** functionalized to bear molecule **904** at its tip **902***a*. AFM tip **900***a* may be translated along the x-, y-, or z-axes to bring molecule **904** into proximity with environment **906** (here represented as surface **908** bearing feature **910**). Based upon interaction (X/Y) between the probe and the environment, control of biomolecular dynamics at the molecular scale may be accomplished utilizing techniques such as single-molecule manipulation, single-molecule fluorescence, or electrochemical triggering of biochemical reactions. In addition, kinetics of chemical or biological activities may be either monitored, controlled, triggered, or catalyzed by such devices.

FIG. **10** shows a simplified schematic view of one embodiment of a hybrid AFM/optical microscope utilizing functionalized SWNTs. Device **1000** comprises atomic force microscope (AFM) **1002** having probe **1002***a*, in fluid communication with fluid cell **1004**. Probe **1002***a* bears nanotube **1006** bearing functionalized end **1006**.

Fluid cell **1004** is in electronic communication with potentiostat **1008** through electrodes **1010***a* and **1010***b*. Fluid cell **1004** is in optical communication with light source **1012** (e.g. an Ar Ion laser) and detection optics **1014** through high NA objective **1016**. Computer **1018** is in electronic communication with the AFM, potentiostat, and detection optics.

Such SWNTs attached to AFM probes can be functionalized as single molecule manipulation and sensing devices using a three-step procedure.

A first step involves initial coating to ensure that non-specific binding is inhibited. In certain embodiments, the initial coating step on the SWNT may take place while the tube is still on the growth substrate, before it is picked up by the AFM tip.

An initial coating formulation that has been shown to effectively resist non-specific binding of molecules such as proteins to SWNTs involves co-adsorption of a neutral surfactant such as Triton-X **100** and PEG. Triton is surfactant containing a hydrophobic aliphatic chain, terminated by a short hydrophilic PEG group. Binding of Triton to SWNTs is favorable due to hydrophobic interactions and has been a well-used method for preparing stable suspensions of SWNTs in aqueous solutions.

Like many other polymers, PEG can be irreversibly adsorbed onto SWNTs. However, coating of SWNTs by Triton-X or PEG alone does not result in complete passivation of the SWNT; both materials are needed for uniform passivation of the nanotube.

Alternatively, or in conjunction with forming passivation through exposure to surfactant(s), a passivation layer can be formed over a SWNT utilizing an electrochemical polymerization process. In accordance with one embodiment of the present invention, a SWNT may be passivated with a phenylenediamine polymer resulting from electrochemical oxidation of phenylenediamine monomer. FIG. **13**A shows an electromicrograph of a SWNT passivated in this manner.

FIG. **13**B is a cyclic voltammetry plot taken during formation of the passivated SWNT shown in FIG. **13**A. The reduced current (y-axis) at later cycles reveals the reduction in conductivity of the SWNT, and hence the thickness/strength of the passivation layer formed.

Moreover, passivation of a SWNTs is not limited to exposure to surfactants or electropolymerized materials as just described. In accordance with still other alternative embodiments of the present invention, a passivation layer may be deposited by gas phase polymerization. FIG. **14**A shows an electron micrograph of a nanotube probe passivated by gas phase polymerization in an inductively coupled C_4F_8 (octofluorocyclobutane) plasma, to form a Teflon-like layer on the nanotube.

FIG. **14**B plots current density versus potential for such a Teflon-like polymer film formed on gold electrodes by the gas-phase reaction of C_4F_8. The insulating properties of FIG. **14**B were determined by measuring the current involving the oxidation of ruthenium (II) hexaammine:

$$Ru(NH_3)_6^{2+} \rightarrow Ru(NH_3)_6^{3+} + e^-$$

as a function of film thickness in an electrochemical cell. Similar behavior was observed with graphite electrodes.

FIG. **14**C shows an AFM image of a planar, highly oriented pyrolytic graphite (HOPG) substrate coated a Teflon-like polymer film formed by the same type of gas-phase reaction responsible for forming the passivation layer on the SWNT shown in FIG. **14**A. The thickness of the deposited polymer film is 3 nm. FIG. **14**C shows the conformal nature of the coating, as the polymer layer closely follows the step edges.

FIG. **14**D shows a roughness analysis of the substrate whose AFM image is shown in FIG. **14**C. Root-mean-square (rms) roughness in the boxed region is 0.238 nm. FIG. **14**D shows that polymer coating is very smooth. Step edges in the graphite are clearly identifiable, indicating that coating is conformal.

The various techniques for forming coatings just described, may be employed alone or in combination. Thus formation of a coating by gas phase deposition of a polymer, in the presence or absence of a plasma, may be performed in conjunction with surfactant exposure.

A second step of functionalizing such SWNTs attached to AFM probes involves removing or modifying this inhibiting coating at the free end of the nanotube, typically through application of an electrical pulse. In one set of embodiments,

this passivating coating is removed at the free end of the SWNT by ablation from the electrical pulse.

The exposed free end of the SWNT could be left uncoated, and serve as a scanning probe nanoelectrode. The nanoelectrode could function as an amperometric electrode or as a potentiometric electrode.

The nanoelectrode device would be useful in single molecule electrochemical studies, including but not limited to use in a novel scanning patch clamp apparatus for measuring and/or stimulating ion channel, G-coupled protein receptors, or other transmembrane protein activity, both in in vitro reconstituted systems as well as in cells. This probe could be brought within the Debye length (~10 Å) of a protein like an ion channel, enabling one to measure local currents and/or electrical potentials at and in the vicinity of single ion channels.

New bioelectrochemical experiments can be envisioned utilizing such nanoscale scanning probes in accordance with embodiments of the present invention. Such applications include but are not limited to the detection, or production via reduction-oxidation chemistry, of physiologically active ligands, such as hormones, neurotransmitters, nucleotides and peptides as a function of electrode potential.

FIG. **15** shows a simplified view of apparatus **1500** utilizing an uncoated tip **1502***a* of a SWNT **1502** as a probe for detecting a localized electrochemical reaction. By utilizing potentiostat **1504** to measure a changed voltage on SWNT **1502**, the electrochemical environment within cell **1506** could be monitored on a highly localized level.

Apparatus **1500** of FIG. **15** could also be utilized to influence or trigger an electrochemical reaction on a highly localized scale. Specifically, application of electronic energy in the form of a potential or current to the SWNT, would create an electric field at the exposed end of the SWNT structure.

In one approach, the changed electrical environment resulting from the application of electrical energy from the exposed SWNT tip, could be detected by electrodes **1508***a* and **1508***b* present in cell **1506** and in direct communication with potentiostat **1504**. However, the small amount of voltage applied in an extremely small area may render detection in this manner difficult or unfeasible.

Alternatively, the successful application of electrical energy to a localized environment may be detected indirectly through electrochemical luminescence. Consider the following electrochemical reaction sequence:

$$Ru(bpy)_3^{2+} \rightarrow Ru(bpy)_3^{2+} + e^-$$

$$Ru(bpy)_3^{2+} + TPA \rightarrow Ru(bpy)_3^{2+} + TPA^+$$

$$TPA^+ \rightarrow TPA^{\bullet} + H+$$

$$Ru(bpy)_3^{3+} + TPA^{\bullet} \rightarrow Ru(bpy)_3^{2+*} + products$$

$$Ru(bpy)_3^{2+*} \rightarrow Ru(bpy)_3^{2+} + hv$$

The probes may also produce electrochemiluminescence. Oxidation of ruthenium bipyridine by the probe in the presence of a primary alkyl amine (such as tripropylamine) results in the formation of electronically excited triplet-state ruthenium bipyridine, which phosphoresces to the ground electronic state. Since this approach involves the detection of photons in a zero-background experiment, it may be more sensitive than measuring ultra-small electrical currents directly.

A third step in the functionalization of SWNTs attached to AFM probes involves attaching material, either through a covalent or non-covalent process, that enables specific interaction or binding at that fixed location.

As described in connection with the second step, the SWNT tip of the probe could be freed from passivation through the application of electrical energy. Such electrical pulsing in air also results in functionalization of the remaining end of the carbon nanotube with one or more carboxylate groups (—COOH).

Pulsing in other gases than air, such as H_2 or N_2, will introduce different functionality to the carbon nanotube end, allowing for an expansion of possible chemical coupling techniques.

Covalent coupling chemistry of the carboxylate moiety with reactive amino species, with EDC (1-ethyl-3-(3-dimethylaminopropyl) carbodiimide) as a catalyst, allows for the covalent attachment of many types of organic and biological species via formation of amide bonds. Examples of molecules attached in this way include but are not limited to DNA, proteins and fluorophores. Photo-activated or "caged" molecules, such as those presenting groups like benzophenone, could also be attached for light-directed capture of target molecules.

Alternately, the free end may have a different polymeric material adsorbed to it, with specific functionality for attachment of molecules of interest. For example, derivatives of PEG containing amino groups, thiol groups, cyano groups, biotin, or antibodies may be uniquely physisorbed at the free end to capture specific molecules in a complex sample.

Alternately, lower voltages or currents may be used to electrochemically modify a redox-active polymer, polyelectrolyte or self assembled monolayer (SAM) at the tube end to change its physical and chemical properties and affinity for specific analytes, either reversibly or irreversibly, but without destruction of the coating.

Alternately, an initially neutral coating at the tip may be electrically charged by application of the pulse, for electrostatic attraction of molecules. Examples of materials that could be used in this regard include, but are not limited to, polyaniline and polypyrrole and self assembled monolayers comprised of ferrocenyl thiols.

Alternately, a photoactive conjugated polymer, such as PmPV [poly{(m-phenylenevinylene)-co-[(2,5-dioctyloxy-p-phenylene)vinylene]}] or PPyPV [poly{(2,6-pyridinylenevinylene)-co-[(2,5-dioctyloxy-p-phenylene)vinylene]}] could be adsorbed. SWNTs wrapped with these polymers have shown interesting photogated effects on charge transport, including rectification and amplification of current flow.

These optoelectronic effects were pH dependent. A scanning probe fabricated with such material may serve as a nano-pH electrode.

Embodiments in accordance with the present invention may allow observation and even electrochemical control over single enzymatic reactions, allowing monitoring of fluorescence from a redox-active cofactor or the formation of fluorescent products. Enzymes "nanowired" to the tips of carbon nanotubes in accordance with embodiments of the present invention, may enable extremely sensitive probing of biological stimulus-response with high spatial resolution, including product-induced signal transduction.

In accordance with certain embodiments, covalent attachment of electrically active or fluorescent species such as some redox-active enzymes or cofactors used by these proteins to a functionalized SWNT nanoelectrode, could be used to study the effect of charge injection on enzyme activity. Analogous macroscopic electrode systems containing electronically coupled enzymes such as glucose oxidase are well known. For example, in "Plugging into Enzymes: Nanowiring of Redox Enzymes by a Gold Nanoparticle", *Science* 299, 1877-1881 (2003), Xiao et al. showed that by quickly changing the

potential applied to their "nanowired" electrode from 0 V to 0.7 V, glucose oxidase could be switched from an enzymatically inactive state to an active one.

In accordance with embodiments of the present invention, application of electrical potentials to functionalized SWNT probes will permit electrochemical control over individual redox events occurring during enzymatic turnovers of glucose oxidase, thereby permitting development of a single-molecule "enzymatic switch". Such an enzymatic switch integrated on a SWNT-based scanning probe will create a mechanism to deliver an exact number of product molecules to a specific location with precise spatial positioning.

For example, FIG. **16** shows fabrication of such a nanoelectrode in accordance with one embodiment of the present invention. As shown in FIG. **16**, nanotube **1700** attached to an AFM tip (not shown) and coated to preclude non-specific binding, is shortened by exposure to an electrical pulse in air, producing SWNT **1702** having tip **1702***a* bearing carboxylate group **1704** (COOH). The cofactor flavin adenine dinucleotide (FAD) **1706** is then covalently attached to the SWNT tip (in HEPES buffer for 12 hours @ 4° C.) to form nanoelectrode **1708**.

Nanoelectrode **1708** in turn allows an apo-enzyme such as apo-glucose oxidase (apo-GOx) **1710** to reconstitute an active site around the immobilized FAD (in phosphate buffer for 12 hours @4° C.). The result is nanoelectrode **1712** functionalized with a single enzyme, glucose oxidase. Nanoelectrode **1712** allows for transduction of enzymatic activity to a measurable electrical current or fluorescence signature.

Moreover, this concept could be generalized to operate with any redox-cofactor containing enzyme that can be reconstituted from its corresponding apo-protein. For example, a nanoelectrode fabricated with a single glutathione reductase (GR) enzyme could be used as a sensitive probe for glutathione-modulated Ca^{2+} signal transduction cascades triggered by membrane bound N-methyl-d-aspartate (NMDA) receptors in neurons.

GR uses both FAD and NADPH (nicotinamide adenine dinucleotide phosphate) cofactors during the reduction of dimeric glutathione (GSSG) to its monomeric species (GSH). GSH has been implicated as a relatively uncharacterized neurotransmitter and neuromodulator in both the brain and central nervous system. Extracellular GSH initiates the inositol-1,4,5-triphosphate (IP_3)/Ca^{2+} signal transduction cascade via a NMDA-receptor activation event, while GSSG appears to have an inhibitory effect.

In "A Glutathione Amperometric Biosensor Based on an Amphiphilic Fullerene Redox Mediator Immobilised within an Amphiphilic Polypyrrole Film", *S. J. Mat. Chem.* 12, 1996-2000 (2002), Carano et al. successfully demonstrated integration of GR into amperometric electrodes which can be "turned on" at appropriate voltages.

A GR-functionalized SWNT enzyme probe in accordance with embodiments of the present invention could be switched on for a specific amount of time for the generation of an appropriate, predetermined amount of GSH molecules in the vicinity of a single NMDA receptor or a cluster of receptors. The subsequent evolution of the intracellular Ca^{2+} concentration could then be monitored in real time using a Ca^{2+}-dependent cell-permeant fluorophore such as Fluo-3 (Molecular Probes). This would permit observation of the transduction cascade triggered from a point source, as well as determination of the threshold GSH stimulus.

FIG. **17**A shows a process for measuring the threshold stimulus required for initiating an intracellular calcium signal transduction cascade. FIG. **17**B plots the electrical voltage signal of the nanoelectrode driving this process.

Electrode **1801** comprising glutathione reductase (GR) nanowired to the SWNT tip, is positioned adjacent to membrane **1800** of target cell **1802**. A potential is applied to the SWNT and the GR is electrochemically activated. As a result of this activation, the GR reduces a predetermined amount of dimeric glutathione (GSSG) molecules **1804** to the monomeric thiol (GSH) species **1806**.

The GSH **1806** then binds to membrane bound protein-coupled receptors **1808**, initiating the inositol triphosphate signal transduction pathway and triggering a rise in intracellular Ca^{2+}. This rise in the intracellular Ca^{2+} ion may be observed with a calcium-dependent fluorophore.

The above discussion introduces a general method for studying the initiation and propagation of biochemical reaction pathways using enzymatically-driven chemical triggers precisely defined in spatial and temporal coordinates, and in chemical magnitude. By carefully selecting an appropriate biochemical process, such as a signal transduction cascade, this method could elucidate the signal propagation rate and timing between individual chemical steps, or determine the minimum biochemical threshold for initiation.

By contrast, the conventional bulk studies related to the single-molecule, single-stimulus experiments described above, can only determine thresholds in ligand concentrations. These conventional studies would therefore be unable to distinguish repeated stimulation of a single receptor, from single stimulation of multiple receptors.

By contrast, experiments conducted utilizing functionalized SWNT probes in accordance with embodiments of the present invention could make this distinction. SWNT-functionalized probes in accordance with embodiments of the present invention should also exhibit enhanced sensitivity to the effects of receptor clustering and other receptor-receptor interactions, revealing interconnectivity details of multiple signaling pathways in both space and time.

Embodiments of applications for probes in accordance with the present invention are not limited to covalent bonding to the SWNT tip. In accordance with other embodiments, a noncovalent bonding mechanism could also be exploited.

For example, in "Noncovalent Sidewall Functionalization of Single-Walled Carbon Nanotubes for Protein Immobilization", *J. Am. Chem. Soc.* 123(16), 3838-9 (2001), Chen et al. report noncovalent functionalization of SWNT sidewalls with bifunctional molecules having a pyrenyl group on one end and a succinimidyl ester on the other end. The pyrenyl group is highly aromatic and interacts strongly with the basal plane of graphite and the sidewalls of carbon nanotubes by van der Waals interactions. The succinimidyl esters on the other end of the linker molecules are highly reactive toward amine groups on the surface of most proteins to form amide bonds. Embodiments in accordance with the present invention could utilize similar non-covalent interactions to functionalize the tips of SWNT probes.

4. Solid-State Coatings and Their Uses in the Fabrication of Nanomanipulators and Localized Sensors

Another general class of embodiments of the invention relate to coating SWNT scanning probes with one or more solid-state materials in conjunction with, or in addition to the soft materials described above. Examples include, but are not limited to, metals, semiconductors and insulators. These materials may be deposited onto the SWNT AFM tip by evaporation, plasma deposition, sputtering, molecular beam epitaxy or through electrochemical means such as electroplating or chemical condensation reactions.

In addition to expansion of possible biophysical applications, further specific embodiments of the invention may include electronic, magnetic, optical and superconducting solid-state nanosensors.

Many of these devices have analogs in microelectronics. Most solid state devices rely on junctions (Schottky barriers, tunnel junctions, etc.) to create a property. By properly matching the material layers, such junctions, or energy barriers, can be fabricated using the nanotube allowing creation of nanometer scale devices and sensors. Many of these will uniquely benefit though creation of either an active or conductive site or material properties alteration achieved by application of a final shortening pulse. The exposed material is highly localized at the free end of the nanotube.

In one embodiment, the combination of such devices with a scanning probe microscope, such as a closed-loop controlled scanning probe microscope (SPM) such as an atomic force microscope (AFM), will enable ultraprecise position and probing of samples, materials and devices. The small size of these devices will enable exploration of properties for nanoelectronics and even molecular circuitry.

In one subset of embodiments, the SWNT AFM probe may be coated by a metal that has a specific chemical, biological or physical affinity for a target molecule of interest, or it may be further functionalized with a soft material such as a polymer or a self assembled monolayer for capture of a target molecule. Specific examples include, but are not limited to, chemisorption of alkyl thiols on gold surfaces and nitrilotriacetic acid on nickel (NTA-Ni). Alkyl thiols can have their free ends terminated with the same chemical moieties outlined in the previous section for attachment of molecules to derivatized PEG polymers. NTA-Ni has a strong affinity for histidine residues and is a common route for immobilizing proteins and polypeptides.

Metals may be either localized at the SWNT tip or they may be ablated exclusively off the tip. To fabricate a SWNT probe with metal only within a few nanometers from the free end, a resist may be coated onto the SWNT in preliminary step. The resist could comprise a polymer layer or other appropriate material applied to the probe, that can be selectively removed by exposure to an appropriate solvent in a subsequent step. Following ablation of the resist layer from the nanotube tip, the assembly is coated with the metal of interest. Subsequent lift-off of the resist in a suitable solvent (such as acetone) leaves a metal coating only at the very end of the nanotube.

Alternately, the coating could include multiple metals or combinations of metals, semiconductors, insulators (such as oxides) and soft materials. This will extend the types of applications and devices that may be constructed with this invention. Ablation of such a composite coating will result in the formation of a ring structure with a carbon nanotube core at the end face of the nanotube tip.

Composite layers consisting of metals, insulators and semiconductors are fundamental building blocks in many macroscopic solid-state devices. Examples include, but are not limited to, thermocouples based on the Seebeck effect, including Peltier heaters or refrigerators, superconducting quantum interference devices (SQUIDs), transistors, diodes and capacitors. This invention provides for the possibility of fabricating nanometer sized equivalents of these devices, located on the tip of a scanning AFM probe. Alternately these devices could be located on a substrate or structure such that nanopositioning stages can be used to control the relative locations of the materials, molecules, receptors, substrates and devices being characterized, probed, tested or controlled.

Alternately bi- and tri-metallic or polymer coatings or polymer/metallic coatings will enable electrically, thermally and chemically actuated manipulators to be constructed with a range of motion on-order of tube length and a precision on the order of 1 Å or less.

In summary, the localization of the functionalized or active sensing site, together with the ability to attach highly specific molecular sensors at this site, in combination with coatings which prohibit non-specific binding, enables construction of sensors, probes and devices with precise control of location. By combining these tools with existing technologies such as scanning probe microscopes (like AFM), we have the ability to control the position of these nanoscale sensors in such to study samples with exquisite sensitivity and resolution.

Alternately, the localization will enable the manufacture of sensors with active sites of sizes on order of a nanometer in diameter. These sensors and devices will enable extremely high precision and spatial resolution measurements to be conducted to characterize materials, and devices at the nanometer scale. In addition they will enable new classes of devices capable of characterizing and even controlling the behavior of molecular circuits. Finally these devices could be embodied as a new class of nanomanipulators.

And while the present invention has been described in connection with the translation of a functionalized SWNT relative to a target utilizing an AFM tip, embodiments in accordance with the present invention have a much broader range of applicability. In accordance with one alternative embodiment, a functionalized SWNT could be translated proximate to a target environment utilizing other than an AFM tool, for example a nanopositioner or nanoscanner as manufactured by Mad City Labs of Madison, Wis., or by Physik Instrumente (PI) of Karlsruhe, Germany. Still other possible techniques for positioning the functionalized nanotube involve translation of the sample relative to a stationary probe, for example by flowing a sample solution past a functionalized SWNT fixed in a microfluidic flow channel.

It is understood that the examples and embodiments described herein are for illustrative purposes only, and there can be other variations and alternatives. Various modifications or changes in light of the above description thereof will be suggested to persons skilled in the art and are to be included within the spirit and purview of this application and scope of the appended claims.

What is claimed is:

1. A device comprising: a nanostructure having a surface and a passivation layer coating all but a unique site on the surface, the unique site exhibiting at least one of chemical, biological, electrical, and physical activity, wherein the nanostructure comprises a carbon nanotube, wherein a material is attached to the unique site, and wherein a moveable probe is connected to the nanostructure.

2. The device of claim **1**, wherein the carbon nanotube is selected from the group consisting of a single-wall carbon nanotube (SWNT), a multi-wall carbon nanotube, and a bundle or rope of SWNTs.

3. The device of claim **1** wherein the passivation layer comprises at least one of a polymer, a semiconductor, and a metal.

4. The device of claim **1** wherein the moveable probe is selected from the group consisting of a scanning probe microscope (AFM), a nanoscanner, and a nanopositioner.

5. The device of claim **1** wherein the unique site comprises an exposed portion of the nanostructure in communication with a source of electrical power.

6. The device of claim 1 wherein the material is selected from the group consisting of a carboxyl group, an amine group, and a molecule covalently bound to one of a carboxyl group and an amine group.

7. The device of claim 1 wherein the material comprises a molecule bound at the unique site with a covalent bond.

8. The device of claim 1 wherein the material comprises a molecule bound at the unique site with other than a covalent bond.

9. A device comprising: a carbon nanotube, wherein the carbon nanotube has a surface and two ends, wherein the carbon nanotube is connected to a moveable probe and wherein one of the ends of the carbon nanotube has a tip; wherein the surface and all but the tip of the carbon nanotube is coated with one or more layers of a material selected from the group consisting of a polymer, a metal, a semiconductor material and an insulator material, wherein the tip of the carbon nanotube exhibits at least one of chemical, biological, electrical, and physical activity.

10. The device of claim 9, wherein the carbon nanotube is selected from the group consisting of a single-wall carbon nanotube (SWNT), a multi-wall carbon nanotube, and a bundle or rope of SWNTs.

11. The device of claim 9 wherein the moveable probe is selected from the group consisting of a scanning probe microscope (AFM), a nanoscanner, and a nanopositioner.

12. The device of claim 9 wherein the tip of the carbon nanotube is in communication with a source of electrical power.

13. The device of claim 9 further comprising a material attached to the tip of the carbon nanotube.

14. The device of claim 13 wherein the material is selected from the group consisting of a carboxyl group, an amine group, and a molecule covalently bound to one of a carboxyl group and an amine group.

15. The device of claim 13 wherein the material comprises a molecule bound at the tip of the carbon nanotube with a covalent bond.

16. The device of claim 9 wherein the material comprises a molecule bound at the tip of the carbon nanotube with other than a covalent bond.

* * * * *

UNITED STATES PATENT AND TRADEMARK OFFICE

CERTIFICATE OF CORRECTION

PATENT NO. : 7,514,214 B2
APPLICATION NO. : 10/783713
DATED : April 7, 2009
INVENTOR(S) : Lawrence A. Wade et al.

It is certified that error appears in the above-identified patent and that said Letters Patent is hereby corrected as shown below:

Title Pg, Item (60) "Related U.S. Application Data":

delete "No. 60/499,210" and insert -- No. 60/449,210 --.

Signed and Sealed this

Nineteenth Day of May, 2009

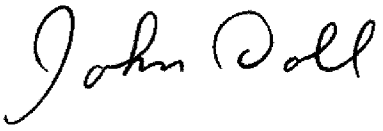

JOHN DOLL
Acting Director of the United States Patent and Trademark Office